Geological mapping in the proterozoic Mt. Isa Inlier, Queensland, Australia, using radiometric and multispectral remotely sensed data

Stuart Harry Marsh

GEOLOGICAL MAPPING IN THE PROTEROZOIC MT. ISA INLIER, QUEENSLAND, AUSTRALIA, USING INTEGRATED RADIOMETRIC AND MULTISPECTRAL REMOTELY SENSED DATA

A thesis presented for the degree of

Doctor of Philosophy

by

Stuart Harry Marsh

University of Durham

Department of Geological Sciences

September 1992

DEDICATION

To Harry Marsh, who always saw pictures in numbers.

DECLARATION

The work contained in this thesis has not been submitted elsewhere for any other degree or qualification and that unless otherwise referenced it is the author's own work.

STATEMENT OF COPYRIGHT

ABSTRACT

Landsat Thematic Mapper, NS001 Aircraft Thematic Mapper, Geoscan Mk. II. Multispectral Scanner and Airborne Gamma Radiometric data have been used to address a variety of geological problems in the Mary Kathleen area, 60 km east of Mt. Isa, NW Queensland. This area forms part of the Cloncurry Complex, a structurally complicated mass of diverse igneous and metamorphic rocks in the Precambrian Mt. Isa Inlier for which many stratigraphic problems remain to be solved.

The Landsat Thematic Mapper data have been the most extensively used in this study. They are the least problematic data type and provide new geological information at scales up to 1:50 000. The NS001 Aircraft Thematic Mapper data have similar spectral but superior spatial resolution in comparison with the satellite data. They suffer from increased geometric and noise-related problems, but the increase in spatial resolution has allowed the solution of problems, at scales up to 1:10 000, which could not be comprehensively addressed with the satellite data. The higher spectral resolution Geoscan Mk. II Multispectral Scanner aircraft data used in the latter part of the study can be used to remotely identify surface mineralogy.

The logarithmic residual technique has proved the most successful approach to enhancing the radiance data sets. When applied to the lower spectral resolution data the technique achieves good discrimination of most lithologies, produces an albedo image useful for structural mapping and yields more information than can be extracted using conventional techniques. When applied to the higher spectral resolution data the technique allows remote mineral identification. Many of the geological problems in the area have been wholly or partially solved using suitably processed radiance data.

The Airborne Gamma Radiometric data have the lowest spatial resolution. Only discrimination has been possible with this data set. These data contain no terrain information and are therefore difficult to use in the field. Integration of the gamma radiometric data with satellite data has been successful in overcoming this problem. The gamma radiometric data have allowed the separation of some lithologies which cannot be separated using the radiance data sets but have contrasting radiometric counts.

ACKNOWLEDGEMENTS

I thank my Mum for teaching me that anything is possible and making certain that it was in numerous ways over the years. My fascination with maps was instilled by Ian Bradley, my brother-in-law, at an early age. I thank Dr Frank Moseley for showing me such an interesting way to make them.

This work was initiated by Dr Tim Munday who has provided direction and comments at various stages along the way. I am grateful to Dr David Hirst of the Geology Department for stepping in as Supervisor when Dr Munday left the Department and for doing an excellent job in difficult circumstances. Ron Hardy was a great help with the XRD analyses and Dave Stevenson kept the computer working despite my best endeavours. Dave Asbery helped a lot of important things happen, and Ian Billing, Angela Williams and other inhabitants of Room 223 over the three years are thanked for companionship.

I thank NERC, for funding the work under Studentship GT4/88/GS/31, and the Commonwealth Scientific Industrial Research Organisation in Australia, who were the CASE body for this work. They kindly provided office and computing facilities in Australia, much of the data used in the study, a vehicle for two field seasons and most importantly a wealth of experience. Particular thanks are due to Dr Jon Huntington, who acted as my supervisor in Australia, Dr Andy Green, who was full of helpful suggestions, Dr Jack Churchill and Dr Maurice Craig, who kept me smiling when the VAX was down, and Chris Horsfall, who did likewise when I was down.

CRAE Pty. Ltd. in Canberra provided data, advice and assistance in the field, for which my thanks go to Dr Kerry O'Sullivan in particular. Geoscan Pty. Ltd. also provided data for the project and I thank Dr Bob Agar for taking an interest in my work. I would also like to thank the members of the BGS Remote Sensing Group for valuable discussions over the last year, and for not asking me when I would finish too often. Jim Evans of BGS Photographic and all the staff who operate the colour laser copier also deserve thanks and more notice next time.

My time in Australia was made all the more pleasant by hospitality from the Munday family, the Huntington family, Margot Walker and Dianne Woodlands. The latter also had the dubious pleasure of sharing a house with me and a guitar, as did Lisa Mather. Thanks to Mark Janos, for introducing me to Australian wines and providing the said guitar. My life would not be the same had Lawrie Joseph not taken me to a few games of Aussie Rules and introduced me to Coopers.

My inventive spelling is notorious and I hope it kept Dr Hirst, my wife Alison and her Dad amused while they kindly proof read various bits of this document. Thanks to Lisa Goodacre who typed a chapter when I was getting worried and helped me get there, as did Margaret Gardner. If it started with my Mum, it ended thanks to Alison who kept me smiling, helped out in the field, typed a chapter or so, stuck labels on numerous spectra, helped set the document out, created the contents pages, experienced her first nights without any sleep and showed enormous patience over the final year. At long last, life could be...

TABLE OF CONTENTS

LIST OF FIGURES

CHAPTER ONE

CHAPTER TWO

CHAPTER 3

CHAPTER 4

CHAPTER 5

CHAPTER 6

CHAPTER 7

CHAPTER 8

LIST OF PLATES

CHAPTER 1

CHAPTER 2

CHAPTER 4

CHAPTER 5

CHAPTER 6

CHAPTER 7

CHAPTER 8

LIST OF TABLES

CHAPTER 3

CHAPTER 4

CHAPTER 5

CHAPTER 6

CHAPTER 7

CHAPTER 8

LIST OF ENCLOSURES

CHAPTER 2

Enclosure 2.1 The geology of the study area at 1:100 000 scale as depicted on the MARABBA and MARY KATHLEEN sheets.

CHAPTER 5

Enclosure 5.1 TM LR colour composite with the geology of the study area for comparison.

CHAPTER 6

Enclosure 6.1 AGR colour composite with the geology of the study area for comparison.

CHAPTER 8

Enclosure 8.1 A revised map for the NE Corella Formation based on the TM LR data and with inputs from all other data sets used.

LIST OF ACRONYMS

AGR	Airborne Gamma Radiometric
AMG	Australian Map Grid
AVIRIS	Airborne Visible/Near-infrared Imaging Spectrometer
CMM	Covariance Matrix Method
CSIRO	Commonwealth Scientific Industrial Research Organisation
DN	Digital Number
EOSAT	Earth Observation Satellite Corporation
GCP	Ground Control Point
GMS	Geoscan Mark II Multispectral Scanner
HMM	Histogram Minimum Method
HSI	Hue Saturation Intensity
IRIS	Infrared Intelligent Spectroradiometer
KWIK	Computationally fast approximation to Logarithmic Residuals
LR	Logarithmic Residuals
LSFIT	Least Square Fit
MSS	Multi Spectral Scanner
NASA	National Aeronautics and Space Administration
NS001	NS001 Airborne Multispectral Scanner
MAF	Maximum/Minimum Autocorrelation Function
PC	Principle Component
RIM	Regression Intersection Method
TM	Landsat Thematic Mapper

Cartography, the most aesthetically pleasing of the sciences, draws its power from the greatest of man's gifts - courage, the spirit of inquiry, artistic skill, man's sense of order and design, his understanding of natural laws, and his capacity for singular journeys to the most distant places. They are the brightest attributes and they have made maps one of the most luminous of man's creations.

Paul Theroux, 'Mapping the World', 1981.

CHAPTER 1. INTRODUCTION

1.1 Background

Laboratory studies during the late nineteen sixties and early nineteen seventies showed that minerals and other materials such as vegetation reflect, absorb and transmit characteristic amounts of energy at particular wavelengths. This work, summarised in Hunt (1977) and Hunt (1980) demonstrated that if the parameter reflectance is plotted against wavelength, commonly between 0.4 μm and 2.5 μm, the resultant reflectance spectrum can uniquely identify the minerals found in rocks and soils. Continued research in the geological community has led to the U.S. Geological Survey recently publishing a digital spectral library consisting of 414 fully documented reflectance spectra from 182 different minerals (Clark et al, 1990b). A similar spectral library containing the reflectance spectra of 160 common minerals has been published by Grove et al (1992).

The utility of the parameter reflectance for geologists is increased by the fact that spectroscopic measurements can be made remotely from an airborne or spaceborne platform. Early remote sensing instruments performing spectroscopy, such as the Landsat Multispectral Scanner (MSS), measure too few and too broad portions of the electromagnetic spectrum for the data to be used to produce mineral specific spectra (Goetz et al, 1983). These instruments can be used to discriminate between lithologies but identification of a particular mineralogy is not possible (Podwysocki et al, 1983).

Refinements of such instruments have led to more measurements over narrower portions of the electromagnetic spectrum, focused on wavelengths with known features. With sensors such as the Landsat Thematic Mapper (TM) and the NS001 Airborne Multispectral Scanner (NS001) information can be extracted from the data that allows more than simple discrimination. Of the satellite borne sensors currently in operation TM has the best spectral resolution. The spectral resolution remains too poor for the identification of specific minerals, but areas of broad mineral groupings such as "iron-oxides" and "clays" can be delineated (e.g. Sultan et al, 1986).

During the last decade a number of airborne sensors have been developed which make measurements over a sufficient number of narrow portions of the electromagnetic spectrum for the production of reflectance spectra. Identification of minerals from such remotely derived spectra has been demonstrated with the Airborne Visible/Near Infrared Imaging Spectrometer (AVIRIS) (Carrere, 1990; Kruse, 1990a, 1990b), with the Geoscan Mk.II Multispectral Scanner (GMS) (Huntington et al, 1990) and with other similar sensors. Spectroscopy is the only analytical technique for identifying minerals which can be operated remotely. Remote sensing thus allows the remote discrimination and identification of lithologies, mineral groups and minerals to be coupled with delineation of their surface disposition over large areas, enabling geologists to improve the accuracy with which geological problems are addressed more rapidly and at less expense than is possible by conventional means (Huntington et al, 1989).

There have been many geological studies utilising satellite borne sensors such as TM, of relatively low resolution, in arid areas such as Egypt (Sultan et al, 1986), Oman (Rothery, 1987) and Spain (Crosta and Moore, 1989). This work with TM data has focused solely on discrimination enhancing techniques such as principal component analysis and band ratios. Huntington et al (1989) have made clear the need for the goal of remote sensing to be identification. Studies with higher resolution data such as that from the AVIRIS sensor, also in arid areas such as the western United States, achieve this goal by analysing geological problems in terms of reflectance retrieved from the data (Kruse, 1990a, 1990b; Green, 1990; Hook, 1990). Whilst identification of specific minerals may not be possible with TM data, the processing of this lower resolution data with aims other than discrimination is yet to be fully investigated.

Studies in arid areas include work on lithological mapping (e.g. Rothery, 1987) and mineral exploration (e.g. Hook, 1990). Vegetation is sparse and weathering often minimal, so that conditions are ideal for geological remote sensing. Less work has been done in semi-arid areas with more extensive weathering (Drury and Hunt, 1988). Where vegetation is more extensive, the emphasis has been on mineral exploration and, in particular, the detection of anomalous spectral responses rather than detailed lithological mapping (Fraser et al, 1986; Hook, 1989). The need for studies in vegetated and weathered environments which are less well-exposed is stated in Huntington et al

(1989). In the prime exploration area of NW Queensland there is a need to extend the application of remotely sensed data beyond localised mineral exploration to the sort of lithological mapping previously restricted to arid areas. The surface materials must be related to the solid geology, taking account of weathering, erosion and transport (Drury and Hunt, 1988), as well as any obscuring vegetation cover (Fraser and Green, 1987). The variety of natural surfaces encountered in geological studies means that spectral data must continue to be added to the available libraries, especially from less understood environments. Huntington (1984) noted a lack of reference in the literature to the reflectance in the short wave infrared of the calc-silicates, smectites and amphibole rich rocks typical of the Mt.Isa region of NW Queensland and stated the need for further research with high resolution data sets in this area.

Remotely sensed data contain the geologically useful parameter reflectance, but it is modified by the irradiance of the source, the transmittance along the atmospheric path, the albedo and radiance of the surface under study, the atmospheric path radiance and the gains, offsets and noise introduced at the sensor (Drury, 1987; Mather, 1987). Processes for the removal of each of these complicating factors and the production of reflectance spectra from airborne data are being developed and implemented on higher resolution data sets (e.g. Green and Craig, 1985; Crippen, 1987; Green, 1990) and require further evaluation for a variety of data types and environments. If the spectral information content of TM and NS001 data is also investigated using techniques which produce reflectance, reflectance data with a variety of spectral resolutions, acquired from a variety of remote sensing platforms, can be compared, preferably over the same field area, and the data requirements of geologists defined.

Previous studies using GMS data in semi-arid Australian environments, such as that by Derriman and Agar (1990), have not attempted to fully exploit the spectral resolution of the data, using only techniques such as band ratios and band differences in an exploration context. Huntington et al (1990) applied the techniques of Green and Craig (1985) to a GMS data set from Cuprite, Nevada, an arid part of the western United States, and outlined the need for studies retrieving reflectance from GMS data in less arid Australian test sites. Lyon and Honey (1989) used linear regression methods to produce "apparent" reflectance from GMS data with some success. Windeler and Lyon

(1991) calibrated GMS data by deriving offsets from the reflectance of laboratory spectra, but did not attempt to remove other factors such as gains and multiplicative atmospheric effects. This calibration, whilst simple and quick, is described by the authors as rudimentary and the values obtained for comparison to laboratory reflectance spectra are consistently too high in the visible. Few studies have been published which follow the approach of Green and Craig (op. cit.) and Huntington et al (op. cit.) with GMS data in a semi-arid Australian environment.

The effects of spatial resolution on geological mapping have received little attention. Abrams and Brown (1985) investigated the effects of spatial resolution on the scale at which objects can be identified in imagery and suggested that further work is required. Changes in spatial resolution also have implications for the effective spectral resolution (Barnsley and Kay, 1990) which should be investigated. This also requires the study of a variety of data sets collected over the same area and processed in the same way. Such a variety of data sets are likely to exist in exploration environments but the amount of use a particular data type is put to depends not only on its success in mapping but also the extent of any processing it requires to be operational. Mineral exploration relies increasingly on the combination of different data sets (Harding and Forrest, 1988) and methodologies for the integration of different types of data from different sensors are only beginning to be explored (Green and Craig, 1984; Chavez et al, 1991; Fernandez-Alonso and Tahon, 1991) and require further investigation.

1.2 Objective and specific aims of the study

The primary objective of this study is to **assess the utility of a variety of remotely sensed data for improving and refining the process of geological mapping in the important mineral exploration area of NW Queensland.**

Within this objective, there are several related aims:

1. To keep the **physical meaning** of the data central to the analysis at all stages.

2. To compare the ease with which data from each sensor can have problems of **geometry** and **noise** removed, and thus assess the operational use of the data for geologists.

3. To compare the **spatial resolutions** of satellite and airborne multispectral sensors and define the **scale** at which different data sets make the maximum contribution to the understanding of geological problems.

4. To explore the effect of **spectral resolution** on lithological discrimination and geological analysis.

5. To understand the complicating effects of the **atmosphere** and **vegetation cover**, and the processes of **weathering**, **erosion** and **transport** in a semi-arid environment.

6. To explore methodologies for the retrieval of the physically meaningful parameter **reflectance**, which can be interpreted with a sound geological basis, from all the radiance data sets.

7. To establish which of the processing techniques **rapidly** produce useful geological information and from which data sets.

8. To explore the benefits of the **integrated** study of several types of data for geological mapping.

1.3 Choice of field area

The field area covers 900 km^2 and is located 60 km east of Mt. Isa in NW Queensland, centred on the Mary Kathleen uranium and rare-earth open pit mine. It straddles the MARY KATHLEEN and MARRABA 1:100 000 geological map sheets. The following information on geology, climate, vegetation and physiography is taken from Derrick et al (1977). The area is suitable for the study for the following reasons:

1. A large number and variety of remotely sensed data sets are available which cover the region.

This allows the role of scale, spatial and spectral resolution, as well as sensor and platform type, to be investigated. The application of data processing techniques to different types of data provides an opportunity to assess the techniques' consistency and wider application. The contribution of data integration to successful geological mapping with remotely sensed data can be studied.

2. The geology is varied, including a Proterozoic crystalline basement, flanked by Carpentarian metasediments and metavolcanics and intruded throughout by acidic and basic igneous rocks. There is significant uranium, rare earth and base metal mineralisation in the area, which is deformed by major NE-SW faults and N-S fold structures.

The variety of geology means that the area is suited to the study of geological mapping by remote sensing, while the extensive mineralisation provides an economic incentive for the mapping to be improved.

3. Whilst parts of the area are mapped in detail at scales up to 1:10 000, particularly in the vicinity of the Mary Kathleen mine, much of it is mapped by traverses and air photograph interpretation alone at a scale of 1:100 000.

These differing levels of existing mapping provide an opportunity to assess the contribution remote sensing can make at a variety of scales. Many aspects of the area's geology are in dispute and there are thus specific geological reasons for further work in the area.

4. Though the area is reasonably remote, access is possible to all but the most rugged and isolated parts using a four wheel drive vehicle.

Remote sensing is of particular use where conventional mapping is difficult, but access is still possible to provide ground truth.

5. Vegetation cover consists of spinifex grasses, acacia scrub and low, stunted eucalypt trees. Larger river gums, ti-trees and pasture grasses cluster in the normally dry creeks.

Rainfall is 430 mm/year, making the region semi-arid, and 90 % falls between November and March as a result of monsoonal activity. Vegetation is thus greater than in some arid regions previously studied providing an opportunity to study the problems it causes. It is not so extensive, however, as to pose insurmountable problems for geological remote sensing. The typical amount and type of vegetation on outcrops is shown in Plate 1.1 while Plate 1.2 shows the increased vegetation found in creeks.

6. Exposure varies from poor to excellent, relief varies from minimal to moderately rugged. Weathering has continued since Precambrian times and is extensive, but not to the point where laterite development obscures the underlying geology.

The area includes immaturely dissected plateaux, ridges, high plains and maturely dissected hill country. The variety of relief means that problems caused by erosion and transport of weathered material can be addressed. In places the weathered material relates directly to the outcrop below, but elsewhere the relationship is more complicated.

The field area was visited twice, for a month in 1989 and six weeks in 1990. Work was concentrated on known problem areas identified through the work of others in the area, and through study of the remotely sensed data prior to the field season. Traversing and sampling made up the bulk of the mapping, though some areas were mapped in more detail where appropriate. As well as hard copy of the processed remotely sensed data, 1:25 000 colour stereo air photographs were used for location purposes and as a map base. The samples taken have been analysed in the laboratory by X-Ray Diffraction (XRD) and reflectance spectroscopy using an Infrared Intelligent Spectroradiometer (IRIS).

1.4 Data types utilised

The remotely sensed data used in this study are of two types, those involving a measure of radiance and those which are a measure of gamma radiation. Whilst in many ways complementary, the two types of data require different approaches to correction and enhancement and will be described separately. The Landsat TM, NS001 and GMS data are all radiance data, form the bulk of the study, and will be discussed in chapters 3, 4, 5 and 6. The Airborne Gamma Radiometric (AGR) data form a lesser part of the study, and will be discussed in chapters 3 and 6.

1.4.1 The TM data

The Landsat TM data are the lowest spatial and spectral resolution radiance data used in this study, but have the largest areal coverage. They were acquired by the Landsat 5 satellite, part of a series developed since the early 1970s by the US National Aeronautics and Space Administration (NASA) and subsequently operated by the Earth Observation Satellite Corporation (EOSAT). This carries several instruments, including that of concern here, the Thematic Mapper. The data studied here are from Path 99 Row 74 acquired on 16th of March 1987 and were made available for this study by the Commonwealth Scientific Industrial Research Organisation of Australia (CSIRO). The TM data set has received the most attention in this study, as it was available from the outset and TM data are widely available to geologists with almost universal coverage.

1.4.2 The NS001 data

The NS001 data set has higher spatial resolution than the TM data, but has similar spectral resolution and a smaller areal coverage. It is derived from three overlapping flight lines within the boundaries of the TM subscene, acquired as part of the US/Australia Joint Scanner Project carried out in 1985 by NASA and CSIRO. The plane carried several instruments including the NS001 airborne multispectral scanner and was flown in the Mary Kathleen area on October 15th 1985. The flight lines studied here were made available by CSIRO.

1.4.3 The GMS data

The GMS data have higher spatial and spectral resolution than TM data. Though each flight line has a smaller areal coverage than TM, taken together they cover the majority of the study area. Of eight overlapping flight lines three are within the boundaries of the TM subscene and two of these are studied here. They were acquired in 1989 by Geoscan Pty Ltd, who have made them available for this study. As this data set was only made available in the final year of the study it has not been analysed in the same depth as the TM and NS001 data.

1.4.4 The AGR data

The AGR data set has lower spatial resolution than the TM data set, covers the whole of the study area and consists of gridded flight lines which go well beyond the boundaries of the TM subscene. It was made available for this study by the Canberra office of CRAE Pty. Ltd.

1.5 Approach taken and thesis structure

For the study as a whole the approach was to:

1. Investigate what is known of the geology of the area.

This was done through study of the literature, discussions with geologists who have worked in the area and study of available maps, as discussed in chapter 2.

2. Understand the operation of the instruments and the physics behind the data they produce.

In chapter 3 details are given of the data types studied and the sensors that acquired the data. The physical basis for remote sensing is explained. Decisions are then made concerning the data processing techniques necessary and the order in which they should be implemented.

3. Perform any data processing necessary to highlight and extract the geological information content of the radiance data.

Chapter 4 concerns the removal of those features of the data, identified in chapter 3, purely related to the sensor itself and the atmosphere between it and the surface under study. These include noise, gains and offsets and the additive atmospheric path radiance. The aim was to reduce the data to ground radiance.

Chapter 5 discusses further processing of the data aimed at highlighting the geological component of the ground radiance. The processes discussed are principal component analysis, band ratioing, least squares fit residuals and logarithmic residuals, applied with the aim of reducing the data to reflectance.

4. Investigate the complementary nature of the radiance and gamma radiometric data and methods for their integration, including geometric correction of the remotely sensed data.

Chapter 6 includes the details of geometrically correcting each of the radiance data sets and an assessment of the geological advantages of doing so. Processing of the AGR data is discussed as well as their integration with the TM data.

5. Use all the available data to address the geological problems of the field area.

Chapter 7 examines the problems involved in applying the remotely sensed data to geological mapping. The results of fieldwork and the laboratory analysis of field samples by both IRIS and XRD are discussed.

Chapter 8 is a geological analysis of the remotely sensed data and addresses the geological problems identified in chapter 2.

6. Propose revisions to geological maps for the area and draw conclusions concerning the aims of the study.

Chapter 9 summarises the findings of the study and draws conclusions about the data studied, the processing techniques used on those data and geological mapping using remotely sensed data in this field area, as well as any other points which have arisen.

The timing of visits to the study area dictated that the data sets be studied sequentially. Thus the study commenced with detailed work on the TM data and introductory study of the AGR data, after which these two data sets were taken into the field. Detailed study of the NS001 data followed, along with the integration of the TM and AGR data and the second field season. Work on the GMS data only occurred at the end of the study when that data set became available. This sequential study of data sets, illustrated in Figure 1.1, leads to problems being re-addressed in progressively greater detail and the cumulative build up of findings.

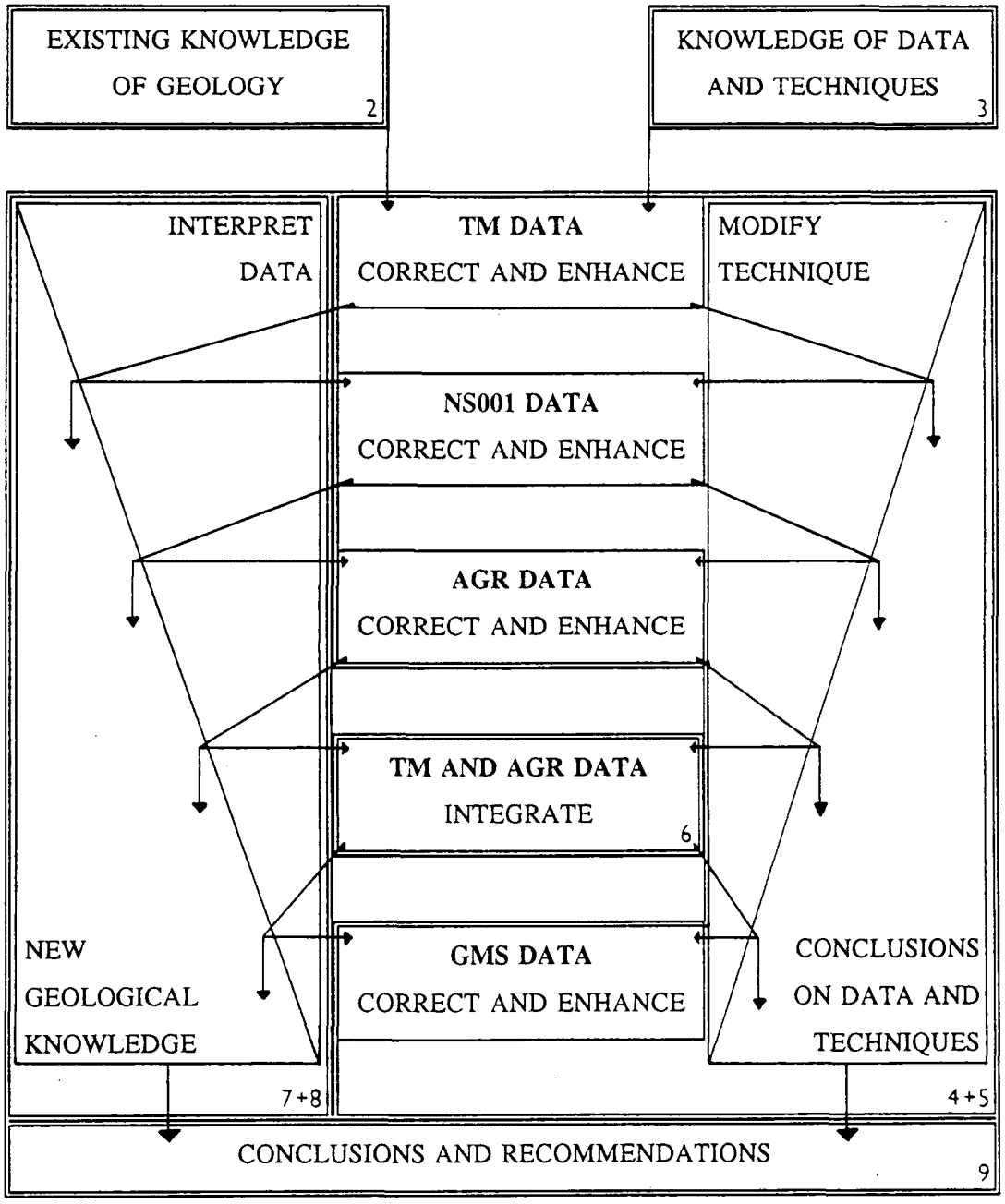

Figure 1.1 The way the approach taken in this study relates to the thesis structure. Flow arrows show the work sequence, with stages outlined as single line boxes. The double line boxes and chapter numbers show where these stages are reported in the thesis.

Plate 1.1 The mixture of cover types typical of exposed surfaces in the field area. The foreground shows clearly the low level of the vegetation cover. The apparent increase in vegetation density as the look angle decreases is well displayed.

Plate 1.2 The increased vegetation density typical of the normally dry creeks at locality 115 by the Cameron River.

CHAPTER 2. THE GEOLOGY OF THE STUDY AREA

2.1 Introduction

Later chapters describe the nature of the remotely sensed data acquired over the Mary Kathleen area and various processing techniques which can be used to highlight the geological information contained in the data. Before the processed data are used to address the problem of improving geological mapping in the area, it is necessary to detail the existing level of geological knowledge and this is done in section 2.2. Except where others are referenced, the geology of the area is described as it appears in the memoir which accompanies the 1:100 000 geological map MARY KATHLEEN (Derrick et al, 1977). Further general information, particularly on the regional geology and the age of some lithologies, is taken from Day et al (1983). Specific detail on the area around the Mary Kathleen uranium mine is derived from Scott and Scott (1985).

The geological outline making up the first part of this chapter forms a useful framework in which various controversial aspects of the area's geology can be addressed with the remotely sensed data. A series of studies question aspects of the published geological maps, and their interpretation, and these form the basis for section 2.8. These studies, alongside discussions with geologists working in the area, define a series of problems to be addressed with the remotely sensed data. In addition to producing new maps which add to or contradict the old ones, the study is thus guided by the previous geological work and considers practical problems.

2.2 Regional geological setting

All the rocks under study are Precambrian and form part of the Cloncurry Complex, a structurally complicated mass of diverse igneous and metamorphic rocks within the Mt. Isa Inlier in NW Queensland. The Inlier consists of an Early Proterozoic to Carpentarian (pre-1800 m.y.) basement high, the Kalkadoon and Leichhardt Block. This block is aligned N-S and is flanked to east and west by N-S aligned basins as shown in Figure 2.1. The basins contain a Carpentarian (1800-1400 m.y.) metasedimentary and metavolcanic sequence, intruded by a variety of igneous rocks, termed the Eastern and

Western Successions respectively. The study area, shown in Figure 2.1, is dominated by the Eastern Succession. A fault-bounded upthrust block of the Early Proterozoic to Carpentarian basement (the Blockade Block), consisting of metamorphosed plutonic and volcanic rocks with some intercalated sediments, occurs in the west. The Western Succession is not represented in the study area.

2.3 Stratigraphy

The stratigraphic column for the area is summarised in Figure 2.2. and the basic geology in Figure 2.3. The basement is represented in the Blockade Block by the Tewinga Group, which is intruded by the Kalkadoon and Wonga Granites. The Malbon Group lies unconformably on the basement sequence in the extreme southeast of the area. The Mary Kathleen Group, which is the most widespread lithology in the area, lies unconformably on both the Tewinga Group and the Malbon Group. In the west of the area the Mount Albert Group completes the sequence, and is conformable or locally unconformable on the Mary Kathleen Group. The sequence is intruded by the Hardway and Burstall Granites, the Tommy Creek Microgranite and the Lunch Creek Gabbro, as well as numerous dolerite dykes at five different stratigraphic levels. The whole is subject to varying degrees of faulting, folding, metamorphism and mineralisation.

2.3.1 Tewinga Group

The oldest rocks exposed in the area are the Leichhardt Metamorphics (**Pel**). They consist of the metamorphosed equivalents of rhyolite and rhyodacite flows and sills and possibly ash-flows and their mineralogy is dominated by quartz, plagioclase, potassium feldspar and biotite. In the field area the Blockade Block is restricted to the western margin, the Leichhardt Metamorphics are not widely represented and thus were not sampled. The Kalkadoon Granite (**Pgk**) is dated between 1930 and 1785 m.y. and intrudes the Leichhardt Metamorphics, together with dolerite dykes ($\mathbf{do_1}$). The outcrop of the granite, however, is just to the west of the field area.

The Magna Lynn Metabasalt (**Pem**) is disconformable on the Leichhardt Metamorphics and consists of massive and amygdaloidal metabasalt with intercalated minor tuff,

epidosite, quartzite, siltstone and amphibolite. The metabasalt contains pillow structures and has copper mineralisation as chalcopyrite and malachite, filling amygdales, associated with faulting. Shallow marine - subaerial extrusion in a N-S trough is inferred and the uniform thickness of the unit suggests extrusion from a fissure. The Magna Lynn Metabasalt outcrops in the west of the field area and has been sampled in several places. It is seen in Plate 2.1.

Conformably overlying the Magna Lynn Metabasalt is the Argylla Formation (**Pea**) which has been sampled in a number of places. It consists of a series of rhyolite lavas, ignimbrites, tuffs, granite metaporphyry sills and dykes with minor beds of conglomerate, quartzite and metasiltstone. The rhyolite which dominates this formation is quartz and potassium feldspar rich and is shown in Plate 2.2. The base of the Argylla Formation is defined as the first acid flow above the Magna Lynn Metabasalt. An extrusive origin for the rhyolites is inferred by the intercalated sediments. The environment was probably shallow marine or subaerial. The Argylla Formation is intruded by dolerites (**do_2**) and the Wonga Granite (**Pgw**). The latter is dated between 1738 and 1665 m.y. and gives a minimum age for the formation.

2.3.2 Malbon Group

The Cone Creek Metabasalt (**Pnc**) is the only member of the Marraba Volcanics to occur in the field area. In the extreme southeast it lies conformably on the Tewinga Group and consists of metabasalt with intercalated sediments. It is overlain by the Mitakoodi Quartzite (**Pnm**), a medium grained cross-bedded sandstone with finer sandstone and siltstone which includes the Wakeful Metabasalt (**Pnm_2**). Outcrop in the field area is limited and these rocks have not been sampled. They may be lateral facies equivalents of the more widely developed Mary Kathleen Group.

2.3.3 Mary Kathleen Group

The base of this group is marked by the Ballara Quartzite (**Pkb**) which appears unconformably above the Argylla Formation in the west of the field area. At the base of the Ballara Quartzite a discontinuous lenticular conglomerate containing clasts of the

Argylla Formation is found in places ($\mathbf{Pkb_1}$). The majority of the formation ($\mathbf{Pkb_2}$) consists of coarse to medium grained quartzite with minor limestone and metabasalt. The formation thins eastward. It has been sampled in a number of localities and usually forms resistant ridge tops as shown in Plate 2.3. The top of the unit is marked by the first substantial calcareous sediments, which are assigned to the Corella Formation (**Pkc**). The Ballara Quartzite passes conformably into the Corella Formation and no time gap is envisaged.

According to Derrick et al (1977) the Corella Formation is "of special interest because of its diversity of carbonate, pelitic, and psammitic rock types, and the presence of uncommon metamorphic mineral assemblages". Examples of the lithologies represented are shown in Plate 2.4. The status of this formation is one of the most contentious issues in the area, as will be discussed in section 2.8. This formation occurs throughout the field area and is the most widely sampled in this study. Broadly speaking, in the east it is calcareous and carbonaceous, while in the west it is more pelitic and arenaceous and less structurally complex. There are, however, representatives of all the following lithologies in all the Corella sequences mapped in the area: calc-silicate granofels (a textural term which describes granoblastic metamorphic rocks without a distinct lineation or foliation), metasiltstone, metashale, feldspathic quartzite, limestone, marble, slate, pelitic schist, amphibolite, metabasalt (e.g Lime Creek Metabasalt, **Pkl**), tuff, micaceous sandstone and marl. The formation is divided into three members based on a type section in the northeast of this field area. The lower member ($\mathbf{Pkc_1}$) and the upper member ($\mathbf{Pkc_3}$) mainly consist of granofels, limestone, marble and slate. The middle member ($\mathbf{Pkc_2}$) is far less calcareous and includes many more pelites, quartzites and arenites than both $\mathbf{Pkc_1}$ and $\mathbf{Pkc_3}$. Representatives of most lithologies are found in each member however, and abrupt sedimentary facies changes are common. It is difficult to recognise the three members in many outliers and even in the type section.

Member $\mathbf{Pkc_2}$ in the Mary Kathleen Mine area is further divided into three units by Scott and Scott (1985). The lower unit is mafic and contains calc-silicates, schists, granofels and amphibolite. The middle unit is felsic and consists of calc-silicates, minor quartzite and marble. The upper unit, or mine sequence, is characterised by quartzite, felsic and mafic calc-silicates, diorite and conglomerate. This more detailed sequence

is the result of mapping over 10 years and of the mine drilling programme. It is unlikely to be recognised elsewhere without a similarly detailed study.

The scapolite found widely throughout the Corella Formation is interpreted by Ramsey and Davidson (1970) as replacement of original evaporitic halite in the marls and shales. In the southeast of the area the Overhang Jaspilite (**Pkj**) outcrops. It is thought to be a lateral facies equivalent of $\mathbf{Pkc_1}$ and may be of organic origin. Many of the units in the Corella Formation are finely laminated but lack other sedimentary structures. Deposition of the group, therefore, probably took place in a near-shore evaporitic carbonate shelf environment. The Ballara Quartzite formed during the original marine transgression onto the basement. The more quartzitic and arenaceous member of the Corella Formation, $\mathbf{Pkc_2}$, may represent a further regression-transgression event.

The Burstall (**Pgb**) and Hardway Granites (**Pgh**), the Tommy Creek Microgranite (**Pgt**), the Lunch Creek Gabbro (**Pbk**) and numerous dolerite dykes (**do**, $\mathbf{do_3}$, $\mathbf{do_4}$, $\mathbf{do_6}$) intrude the Mary Kathleen Group.

2.3.4 Mount Albert Group

In the west of the area the Deighton Quartzite (**Ppd**) is unconformable on the Corella Formation in several large discrete masses. These form high, steep-sided, deeply dissected plateaux with little soil and sparse stunted vegetation. Fine grained siltstone and shale grade upwards into coarser feldspathic quartzite with lenses of calcareous and pyritic siltstone. Parts of the quartzite are highly feldspathic and weather to white, friable, kaolinitic sandstone. There are cross-beds, slump structures, mud-cracks and rain marks, all of which suggest a shallow subaqueous environment with some emergence. Palaeocurrent directions suggest this is a fluviatile sand deposit. The White Blow Formation (**Ppw**) is conformable, or locally unconformable, on the Deighton Quartzite in restricted basins. It consists of schist, phyllite and limestone but the field area contains no good exposures of this rock type.

The igneous rocks which intrude the Mary Kathleen Group are also thought to postdate the Mount Albert Group, but dating of many of these intrusives is contentious, as will be discussed in section 2.8.

2.3.5 Intrusives

The oldest granite exposed in the field area is the Wonga Granite (**Pgw**) which forms an elongate N-S belt characterised by a low plain in which the granite outcrops as small tors, such as that shown in Plate 2.5. The granite intrudes the Argylla Formation throughout the centre of the field area. The main lithology is grey, medium to coarse foliated granite, but there are many inhomogeneities including microgranite plugs and dykes, syenogranite, monzogranite and aplite, mafic pods and numerous dolerite and amphibolite dykes (Plate 2.6). The granite has a high K content, and the mineralogy is dominated by potassium feldspar, quartz, plagioclase, biotite and amphibole. It is strongly deformed, causing the foliation illustrated in Plate 2.7 and its relationship to the Corella Formation is not known as they are not seen in contact. The memoir indicates that the Wonga Granite postdates the Argylla Formation but precedes the Malbon and Mary Kathleen Groups. Age determinations range from 1665-1738 m.y. but its age is not accurately known.

The other important granite exposed widely in the area is the Burstall Granite (**Pgb**), which is thought to be associated with the uranium-rare earth mineralisation at Mary Kathleen. It forms two conspicuous masses in the central part of the field area with high ground, steep slopes and extensive rugged outcrop, as seen in Plate 2.8. The main lithologies are massive, coarse- to medium-grained granite and leucogranite. There are few inhomogeneities in the granite and dolerite dykes are less numerous in comparison to the Wonga Granite; the Burstall Granite is also far less deformed. The mineralogy is similar to that of the Wonga Granite, being dominated by potassium feldspar, quartz, plagioclase, biotite and hornblende. The granite is seen to intrude the Corella Formation and the Lunch Creek Gabbro and the memoir places it at the top of the stratigraphic column. A date of 1740 m.y. obtained from U-Pb dating of zircons may be too old.

The Hardway Granite (**Pgh**) also outcrops in three masses on the western edge of the field area. These probably formed one large mass before being split by dextral displacements during the extensive strike-slip faulting which has affected the area. The terrain over this granite has similarities in places with both the Wonga and the Burstall Granite. The majority of the granite is coarse grained, though there is also medium grained tonalite. Deformation is less extensive than for the Wonga Granite and the mineralogy is dominated by quartz, microcline, plagioclase and biotite (Plate 2.9). The Hardway Granite intrudes the Tewinga Group, is dated at 1668 m.y. and may thus be a separate igneous body. Alternatively it may represent the Wonga Granite to the west of the main mass, where deformation was less extensive. It is also reported to intrude the Corella Formation, however, and may thus be similar in age to the Burstall Granite. All three of these granites have been extensively sampled.

In the inaccessible northeast of the area a small part of the Tommy Creek Microgranite (**Pgt**) is exposed. It is formed from a leucocratic microgranite and porphyritic rhyolite, is dated at 1607 m.y. and intrudes the Corella Formation. The MARRABA map suggests that the Tommy Creek Microgranite is similar in age to the Burstall Granite. It has not been sampled.

Basic intrusives are represented in the area by numerous dolerite dykes and by the Lunch Creek Gabbro (**Pbk**). The latter is a coarse grained, weakly layered elongate tholeiitic intrusion intimately associated with the Burstall Granite. The intrusion is dominantly an olivine-pyroxene gabbro with minor diorite and tonalite and contains olivine, orthopyroxene, clinopyroxene, plagioclase and biotite. It intrudes the Corella Formation, is dated at around 1740 m.y. and is intruded by the Burstall Granite.

Five periods of dolerite intrusion occur in the area (**do_1, do_2, do_3, do_4, do_6**). Metadolerite dykes are ubiquitous in the basement and form a north-trending anastomosing network. They consist of biotite schist, biotite amphibolite and amphibolitised dolerite and are dominantly mapped as undifferentiated **do**. All five ages of dolerite intrusion are probably represented. The Wonga and Hardway Granites are intruded by N and NE trending metadolerites. Some may be contemporaneous with the granites but most are later and are mapped as undifferentiated **do**. Far fewer dolerite

dykes intrude the Burstall Granite but one, the northeast trending Lake View Dolerite, clearly postdates the granite, being almost unmetamorphosed. It is the youngest dolerite found in the area ($\mathbf{do_6}$), and is dated at 1140 m.y..

The Eastern Succession does not contain representatives of $\mathbf{do_1}$ or $\mathbf{do_2}$. Dyking is relatively scarce compared to the basement, which may be due to the metasedimentary sequence being poorly jointed and fractured. In the dykes which are present the NE trend remains strong. Rocks up to and including the Mary Kathleen Group are intruded by $\mathbf{do_3}$, $\mathbf{do_4}$ and $\mathbf{do_6}$. Important examples include metadolerite and amphibolite sills in the cores of the Rosebud and Little Beauty Synclines and an unnamed metadolerite dyke which runs NE from Lake Corella through the Corella Formation and is conspicuous in the TM imagery ($\mathbf{do_3}$). This is termed the Lake Corella Dolerite, for the purposes of this study, and is shown in Plate 2.10. The dykes all stop at the top of the Mary Kathleen Group. This may be because they exploit older pre-existing fractures which do not penetrate the Mount Albert Group, or more likely because the final period of dyking predates deposition of the Deighton Quartzite and the White Blow Formation.

2.4 Metamorphism

Throughout the basement and the Eastern Succession the metamorphic grade ranges from lower greenschist (quartz - biotite - chlorite - scapolite) to upper greenschist (garnet - tremolite - actinolite - biotite) facies although locally within the Eastern Succession amphibolite facies is reached. In pelites this is marked by the appearance of cordierite and staurolite in association with andalusite. In Ca-rich lithologies diopside replaces tremolite, and andesine and hornblende develop in basic rocks. Two other important assemblages in the metasediments are anthophyllite - cordierite and andalusite - kyanite - sillimanite.

The greenschist facies metamorphism is associated with folding during regional deformation between 1600 and 1450 m.y.. Low pressure, high temperature thermal metamorphism is found in rocks adjacent to granite intrusions and is characterised by the presence of sillimanite. During faulting, the last stage of metamorphism in the area,

temperatures were still high enough for retrogressive growth of kyanite porphyroblasts with chlorite and muscovite along and near faults.

2.5 Structure

The Kalkadoon-Leichhardt Block is broadly anticlinal and is underlain by granite. The earliest $\mathbf{D_1}$ structures are N-S normal or high-angle reverse faults with an associated north trending, steeply dipping foliation. NE and NW conjugate fractures are found representing dextral and sinistral movement respectively. These are related to E-W compression. All these fault structures are also seen in the Eastern Succession, but are complicated by later structures. $\mathbf{D_1}$ deformation is thought to be related to the first phase of deformation in the area. This involved the isostatic uplift of the basement block in response to the sedimentation which occurred on its flanks in the Eastern and Western Successions.

The most conspicuous structures in the Eastern Succession are $\mathbf{D_2}$ folds and $\mathbf{D_3}$ faults. The synclinal troughs which lie to east and west of the basement high have been exaggerated by E-W compression to form major synclines with N-S axes. In the field area these are represented by the Little Beauty, Rosebud and Mary Kathleen Synclines. The discrete masses of the Deighton Quartzite in the west of the field area are also in synclinal troughs. The synclines are separated by broadly anticlinal masses of granite (**Pgw** and **Pgb**). There has also been some gentle cross-folding on E-W axes which causes the axes of the major N-S folds to plunge to N and S. This is anticlinal between the Little Beauty and Rosebud Synclines, and synclinal between the separate masses of the Deighton Quartzite. Minor folding, often very complex, occurs adjacent to faults. These $\mathbf{D_2}$ structures are related to the beginning of the second major phase of deformation. Increasing E-W compression, related to the close of the basin in which the Eastern Succession was deposited, caused N-S folds and regional metamorphism and was accompanied by granite intrusion. Late granite intrusion was accompanied by thermal metamorphism, overprinting the regional effects.

The $\mathbf{D_3}$ structures are major NE trending and less well developed NW trending conjugate strike-slip faults. Displacement on the NE trending faults is large. In the field

area dextral movement is recorded for the Wonga Fault (3 km), the Cameron Fault (up to 2 km) and the Fountain Range Fault (up to 25 km). The best developed NW trending structure in the field area, the Greens Creek Fault, has sinistral displacement of less than 1 km. These major $\mathbf{D_3}$ strike-slip faults represent further E-W compression during the closing stages of the second deformational phase.

2.6 Mineralisation

Copper mineralisation is very widespread with the only lithologies free from Cu-mineralisation being the Lunch Creek Gabbro, the Deighton Quartzite and the White Blow Formation. Most of the mineralisation is stratabound, although some is igneous-related, and all involves a degree of structural control. There is a concentrated zone of mineralisation in the upper Argylla Formation, probably related to the volcanic activity at that time. A second zone of extensive mineralisation occurs in the lower to middle Corella Formation and is exploited in numerous small operations such as that shown in Plate 2.11. This is related either to erosion of a crystalline source with deposition in restricted basins and concentration by diagenesis and metamorphism, or to circulating fluids within the sedimentary pile. **Gold**, **silver** and **nickel** are recovered as by-products of the smelting of the Cu ores and **calcite** is mined for smelting flux from larger, coarse grained lenses and veins within the Corella Formation. Trace elements suggest the calcium was mobilised from the calc-silicates by hot fluids during metamorphism and dyking.

Uranium, **thorium** and **rare-earth** elements were mined from the Corella Formation, at Mary Kathleen, until 1985 and there are many other radioactive anomalies in the area. The mineralisation occurs as uraninite enclosed by allanite, honeycombed through garnet-rich sediments. It is closely associated with the Mary Kathleen shear, the Burstall Granite intrusion, related acidic dykes which extend from the granite to within 400 m of the orebody and dioritic rocks along-strike. The genesis of this major orebody, shown in Plate 2.12, is still in dispute and will be discussed in section 2.8.

Quartz occurs along fault planes and **iron staining** is ubiquitous but, although magnetite accompanies Cu-mineralisation, there are no economic deposits in the area.

Many other minerals occur in quantities or qualities of little economic potential. These include **kyanite, garnet, fluorite** and **staurolite.**

2.7 Synthesis

Starting possibly before 1930 m.y., acid volcanics of the Leichhardt Metamorphics were extruded onto an old land surface which is no longer exposed. Granite emplacement accompanied this activity and the Kalkadoon Granite may represent the source magma for these volcanic rocks. The $\mathbf{do_1}$ dolerites were also intruded at this time. Volcanism became basic with the extrusion of basalt sheets some of which may be sub-marine as implied by the presence of pillow structures in the Magna Lynn Metabasalt. A return to acidic volcanism is accompanied by an increase in the volume of sediments in the Argylla Formation particularly in the east, suggesting marine conditions became more widespread and that volcanism became more intermittent. Intrusion of the Wonga and Hardway Granites and $\mathbf{do_2}$ dolerites may have commenced at this time and 1740 m.y. is the maximum age for granite intrusion. The period ended with uplift of the basement block by normal faulting dated at 1700 m.y., accompanied by the formation of basins to east and west.

The onset of sedimentation in the eastern basin is marked by local basal conglomerates and the accumulation of near shore and shallow shelf sediments of the Ballara and Mitakoodi Quartzites. Carbonate rocks may have been deposited further into the basin at the same time. Deepening of the basin or marine transgression is marked by an increase in these carbonate and pelitic sediments seen in the Corella Formation. Quartzite/carbonate variations may represent ?local transgression and regression.

Renewed uplift of the basement led to erosion of all previous rocks and further faulting, accompanied by intrusion of the $\mathbf{do_3}$ dolerites. On the Corella land surface a river system led to deposition of the fluviatile or estuarine fan sands of the Deighton Quartzite. Minor transgression formed restricted basins on this land surface in which the calcareous and argillaceous sediments of the White Blow Formation accumulated. Further uplift of the basement and the Eastern Succession led to the end of sedimentation. The eastern basin closed with E-W compression causing folding,

regional metamorphism dated at 1550 m.y., intrusion of the Lunch Creek Gabbro and $\mathbf{do_4}$ dolerite, further granite intrusion (Burstall, ?Hardway) and strike-slip faulting. A post-metamorphic $\mathbf{do_6}$ dyke is dated at 1140 m.y., by which time tectonic activity had largely ceased. The entire area has been uplifted and eroded since Precambrian times.

2.8 Problems to be addressed

It is clear from the above outline, from the literature and from discussions with geologists working in the area that several aspects of the area's geology remain contentious. The relationships and ages of the various granites are yet to be clearly established. Some authors question the presence of major structures, or propose the existence of ones which do not appear on the maps. The cause of the uranium-rare earth mineralisation at Mary Kathleen is still debated. Many units mapped as intrusive dolerites may in fact be extrusive lithologies.

The most common problem relates to correctly establishing the stratigraphy, which has proved difficult for the Argylla Formation, Corella Formation and Mount Albert Group in particular. Stratigraphic correlations are complicated by repetitions of similar lithologies, intrusions, folding, faulting, metamorphism and the scarcity of reliable isotopic age data (Blake, 1980). For example, quartzites occur in the Argylla Formation, the Ballara Quartzite, the Corella Formation, the Malbon Group and the Mount Albert Group and are, according to Blake (ibid.), "notoriously difficult to distinguish". As two of these lithologies, the Argylla and Corella Formations, contain significant mineralisation at certain stratigraphic levels it is an economic exploration imperative to improve the stratigraphy. In particular, whilst the stratigraphy at some localities is well known one of the major problems is fitting outliers of the same lithology into this framework. The improved mapping which the remotely sensed data may afford presents an opportunity to contribute to the solution of these stratigraphic problems, and may have a direct bearing on the discovery of new orebodies.

2.8.1 Stratigraphic problems of the Argylla Formation

The Argylla Formation cannot be distinguished from the older Leichhardt Metamorphics in the Rosebud area in the opinion of Ramsey and Davidson (1970). Within the Argylla Formation no consistent stratigraphic relations can be found for individual members (Derrick et al, 1977). Holcombe and Fraser (1979) attempted to map out some of the individual units within this formation and proposed that east of the Wonga Granite units mapped as Argylla Formation may be much younger and equate with the Corella Formation. This possibility has also been raised by Blake (personal communication). The top of the formation is a further matter of dispute. In Blake (1980) the Argylla Formation is envisaged as passing into the Ballara Quartzite of the Mary Kathleen Group without a significant break. Evidence is given in Derrick et al (1977), however, that the Ballara Quartzite is derived from erosion of the Argylla Formation and that there is thus a significant unconformity between the two.

2.8.2 Stratigraphic problems of the Corella Formation

The debate about the Corella Formation began with Blake (1980), who observed that the sequences mapped as Corella Formation in the Wonga Granite area are thicker and the rocks more varied, deformed and metamorphosed than those to the east and west of the Wonga belt. He also observed concordant contacts between the Ballara Quartzite and the Argylla Formation in the Wonga belt. Blake (ibid.) thus proposed that the rocks in the Wonga belt belong to an older sequence more properly equated with the basement rocks. Derrick and Wilson (1981) disagreed, contending that there are no differences in thickness between the two areas, that all the Corella Formation displays variation and that concordant contacts with the underlying Argylla Formation also exist outside the Wonga belt. Derrick and Wilson (ibid.) claimed that the Corella Formation, as mapped, is a single sequence with a restricted time range.

A detailed account of the problems faced when mapping the Corella Formation is given in Blake (1982). Within the field area under study here, the Corella Formation is divided in to Zone A, contained in the Rosebud and Little Beauty Synclines west of the Wonga belt, and Zone B, the Mary Kathleen Syncline, Wonga belt and the area to the

northeast of the Burstall Granite (Figure 2.4). In Zone A, the Corella Formation is readily divisible into three conformable members with the calcareous-pelitic-calcareous sequence described in section 2.3.3 almost complete. This sequence, overlying the Ballara Quartzite and overlain by the Deighton Quartzite, is proposed as the true type section of the Corella Formation. In Zone B there is no easy division into three members but rather a complex of lithologies with uncertain relations, both to each other and to the Ballara and Deighton Quartzites. The sequence is thicker, more calcareous and contains more felsic and mafic units, interpreted as extrusive. The original Corella Formation type section northeast of the Burstall Granite is folded, faulted and intruded and contains too many deficiencies to be retained. At least two different stratigraphic units are envisaged, the older around the Burstall Granite (1740 m.y.) and the younger in the northeast around the Tommy Creek Microgranite (1607 m.y.), which may be an extrusive unit within the Corella Formation rather than a granite body. Consequently it is proposed by Blake (ibid.) that the rocks in Zone B be referred to as the Corella Beds until their stratigraphic relations are more clear.

Some of the difficulties raised by Blake are recognised by Wilson (1983), but the type section in the northeast is retained, bounded by faults, and the full Corella Formation sequence recognised in both Zones confined by two unconformities. The suggestion that the Corella Formation be downgraded to the Corella Beds in the northeast is refuted. Recent work in the area northeast of the Burstall Granite, however, has again found that the recognised Corella sequence is not seen in that area and the divisions shown on the 1:100 000 map are open to question (Blake, personal communication) and may be more like those shown in Figure 2.5. The stratigraphy of the Corella Formation remains unresolved.

The work of Loosveld and Schreurs (1987) also has implications for the Corella Formation. This work suggests that a thrust rather than a depositional unconformity separates the top of the Corella Formation (Mary Kathleen Group) from the Deighton Quartzite (Mount Albert Group). The Deighton Quartzite-White Blow Formation sequence has broad similarities with the Ballara Quartzite-Corella Formation sequence below it. Loosveld and Schreurs (ibid.) have proposed that the Mount Albert Group is part of the Mary Kathleen Group, thrust above itself, and thus that the Mount Albert

Group is not a separate stratigraphic sequence. Alternatively, the Mount Albert Group may be a lateral facies equivalent of the Mary Kathleen Group, overthrust above it.

2.8.3 Age and relationships of the granites

Matheson and Searl (1956) did early work in the area and thought the Wonga and the Burstall Granites to be the same age, "contrary to previous ideas". Differences in homogeneity, deformation and field expression between the two granites are related to their formation at different levels within one irregular batholith. This explanation is not accepted in the memoir (Derrick et al, 1977) where it is suggested that the Wonga Granite is older than Burstall Granite. This view is supported in Wilson (1978), where the Wonga is envisaged intruding only as far as the Malbon Group at 1760-1660 m.y. but the Burstall is thought to be intruded at 1400 m.y. into the Mary Kathleen Group. The isotopic data may be inconclusive, however, and the problems involved are illustrated by Holcombe and Fraser (1979) using three alternative published stratigraphies (Figure 2.6). Many of these difficulties stem from the fact that the Wonga has no contact relations with the Mary Kathleen Group. This is acknowledged by Holcombe and Fraser (ibid.), but they claim that it is seen to intrude metaporphyry dykes which themselves intrude the Ballara Quartzite at the base of the Mary Kathleen Group. Based on this they suggest that the Wonga Granite must be younger than at least some of the Mary Kathleen Group.

Evidence is given by Cruickshank et al (1980) that regional metamorphic effects, associated with the Wonga Granite, are overprinted by the hydrothermal effects of the Burstall Granite which must thus postdate regional metamorphism and is therefore younger than the Wonga Granite. This is questioned by the work of Jacques et al (1982), however, which suggests that the relationship between the granites and the metamorphism is unclear. The problem is illustrated by the isotopic data of Page (1983), which date the Burstall granite at 1740-1730 m.y. (c.f. 1400 m.y. above) and regional metamorphism between 1620 and 1500 m.y., after the Burstall is emplaced. This is countered by the claim of Oliver et al (1985) that acidic dykes from the Burstall Granite cut across the structural grain of the Mary Kathleen Syncline and thus the granite must be at least syntectonic, being intruded at the close of deformation. In

summary, the age and relations of the granites remain unclear, but there are differences, in foliation for instance, between the Wonga and the Burstall Granites (Scott and Scott, 1985).

The place of the Hardway Granite in the stratigraphy is also unclear. The memoir reports that it intrudes the Mary Kathleen Group, is less deformed than the Wonga and is therefore correlated with the Burstall Granite. This interpretation is questioned by Wilson (1978), who has dated the Hardway Granite at 1660 m.y., possibly correlated with the Wonga Granite. The Hardway and Burstall Granites are placed together by Jacques et al (1982), as on the 1:100 000 Mary Kathleen map.

Work with the remotely sensed data cannot yield information on the ages of the various granites. It may be possible, however, to comment on the relationship of one granite body to another based on field expression and spectral characteristics. Improved mapping may better constrain the stratigraphy in the area and allow the relative ages of the granites to be determined.

2.8.4 The status of some igneous rocks

According to Blake (1982), the Tommy Creek Microgranite is in fact made up of extrusive rhyolite flows within the Corella Formation and many units mapped as dolerite dykes are also extrusive units within the Corella Formation. Some basic, lenticular units within the Corella Formation near the Mary Kathleen Mine are interpreted as extrusive flows by Scott and Scott (1985). As there are known metabasalts and known dolerites it may be possible to discern spectral distinctions between the two and identify units whose origin is uncertain as one or the other. Even if the composition does not vary in this way, improved mapping for example may suggest that an igneous unit cuts across the strike of the metasediments and is thus likely to be intrusive. The volume of extrusive material in the Corella Formation is an important factor in the stratigraphic problems discussed in section 2.8.2. and the mapping of these rocks and their correlation between different outliers may be improved using the remotely sensed data.

2.8.5 Structures

Most authors accept the existence of the Mary Kathleen Syncline in the region around the Mary Kathleen uranium mineralisation. In the view of Hawkins (1975), however, the synclinal structure cannot be substantiated in the mine area, as units cannot be consistently mapped and lens out along-strike, with rapid facies changes. In their detailed synthesis of ten years mapping and drilling Scott and Scott (1985) acknowledged that the Corella Formation in the syncline is very variable. Some beds however, such as a quartzite marker unit, do repeat across the structure and a synclinal structure is indicated by Scott and Scott's work (ibid.).

The memoir places a depositional unconformity between the Mary Kathleen Group and the Mount Albert Group, but this is replaced with a thrust plane by Loosveld and Schreurs (1987). Section 2.8.2 discusses the stratigraphic implications this may have. The synoptic view afforded by the remotely sensed data, together with an improvement in the mapping, may make the presence or otherwise of such structures clear.

2.8.6 Mineralisation

There has been almost continuous debate for over 30 years concerning the genesis of the uranium-rare earth orebody at Mary Kathleen. Most authors agree that the mineralisation is closely associated with granite intrusion, shearing, acid dyking, and garnetisation, but disagree on the significance of each factor.

Matheson and Searl (1956) considered that the mineralising solutions were late stage emanations from the Burstall Granite magma. Access to the favourable host rocks of the Corella Formation was provided by faulting and jointing associated with regional deformation and garnetisation was strongly related to ore formation. The shears were seen as providing a structural trap for a high temperature metasomatic deposit. Most aspects of this model are accepted by Hawkins (1975) but an alternative source for the uranium is suggested; remobilisation from within the sedimentary pile by metamorphism. As the sediments have U contents close to world averages and this U has an even distribution, it is however unlikely that large scale extraction of U from the

sediments has taken place (Derrick, 1977). The most U-rich lithologies, with values well above world averages, are the Burstall Granite and its associated rhyolite dykes. The genetic connection between rhyolite, granite, metasomatism, skarn formation and mineralisation described by Derrick (ibid.), suggests that the U was introduced from the granite by the rhyolite dykes, as a late metasomatic event, when the Burstall Granite was intruded into the Corella Formation. A similar hypothesis is put forward by Cruickshank et al (1980).

Problems with this model are introduced when the isotopic data are considered. Page (1983) obtained a date of 1550 m.y. for the uraninite in the mineralisation, which is younger than his date for granite intrusion of 1740-1730 m.y. but older than the granite age of 1400 reported by Wilson (1978). The age for the mineralisation correlates with that for regional metamorphism. The metasomatic origin of the deposit is again questioned by Scott and Scott (1985), as the chemical reactions required for the metasomatism imply the expulsion of silica and no significant free silica is seen in adjacent rocks. They also question whether metasomatism can produce the same garnet composition in Si-rich, Ca-poor rocks as in Si-poor, Ca-rich rocks as is the case here. They report that U and rhyolite dykes are not always found with garnetisation and that the pattern of garnetisation does not suggest a close relationship between garnetisation and the Burstall Granite.

A new model is thus proposed in Scott and Scott (ibid.). In this model, basic, lenticular rocks within the Corella Formation of the Mary Kathleen Syncline are interpreted as flows similar to the Lime Creek Metabasalt in the Corella Formation to the north of the Wonga Fault, and may contain pillows and flow top breccias. The U concentration is zoned around the orebody, which is largely stratabound. A volcano-sedimentary origin is proposed where the origin of the garnet is related to the volcanism and the U is formed by hydrothermal activity within the sediments. Maas et al (1987) have found problems with this model, however, as the ores are isotopically distinct from the sediments. They have suggested that the mineralisation is the metamorphosed, recrystallised equivalent of an older, granite-related U-rare earth mineralisation.

The gamma radiometric data may indicate possible sources for the U in the Mary Kathleen deposit. The structures involved in the mineralisation may be clear in the remotely sensed data, and the orebody and associated rocks may have distinct spectral signatures which provide more evidence of the relations between the deposit and its host rocks.

2.8.7 Summary

There are many aspects of the geology which require further input if satisfactory solutions to mapping problems in the area are to be found. The main questions which should be addressed with the remotely sensed data are:

1. Can a consistent stratigraphy be worked out for the Argylla Formation?

2. Is the established stratigraphy for the Corella Formation correct, especially in the area northeast of the Burstall Granite?

3. Is the Mount Albert Group more correctly part of the Mary Kathleen Group?

4. What are the relationships and **relative** ages of the granites?

5. Are there compositional differences between extrusive and intrusive basic rocks within the Corella Formation which allow them to be distinguished?

6. What is the structure within the Corella Formation in the Mary Kathleen Mine area?

7. Is the contact between the Corella Formation and the Deighton Quartzite a depositional unconformity or a thrust?

8. Is there structural and compositional information in the remotely sensed data which highlights the important factors in the formation of the Mary Kathleen uranium-rare earth deposit?

Various lithologies may have distinctive spectral responses in the remotely sensed data and the synoptic view may allow these to be correlated over wide areas. Structures may have a topographical expression visible in the remotely sensed data or be seen due to improvements in the mapping. Structural and stratigraphic problems may thus be resolved. The remotely sensed data may make a less direct input to other controversies, such as the factors involved in the mineralisation, but any new structural and stratigraphic insights will also address these problems. Answers to these questions will influence future mineral exploration in the area. For example, once the structure at Mary Kathleen, the stratigraphy of the Corella Formation and the important factors in the Mary Kathleen mineralisation are known it may be possible to use the remotely sensed data to propose other localities which may be similarly mineralised.

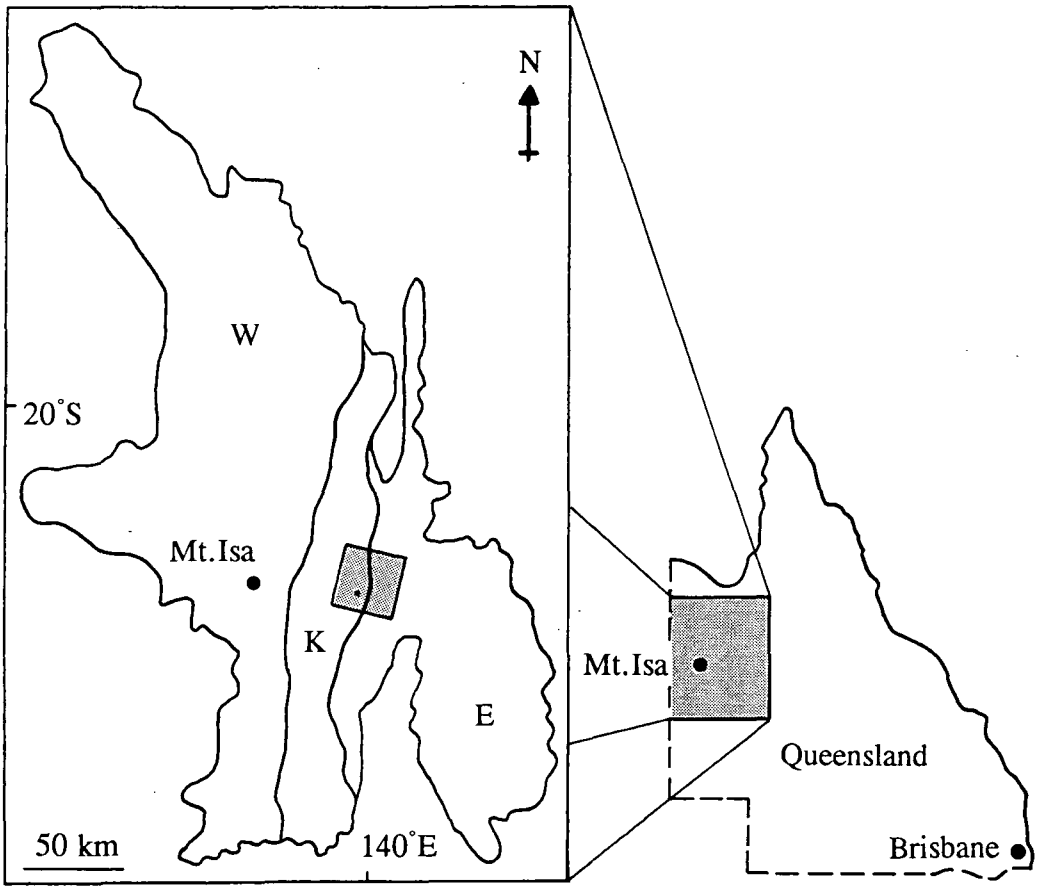

Figure 2.1 Location of the Mt.Isa Inlier (shaded on right) and the study area (shaded on left). Small circle = Mary Kathleen, W = Western Succession, K = Kalkadoon - Leichhardt Block, E = Eastern Succession (after Blake and Page, 1988).

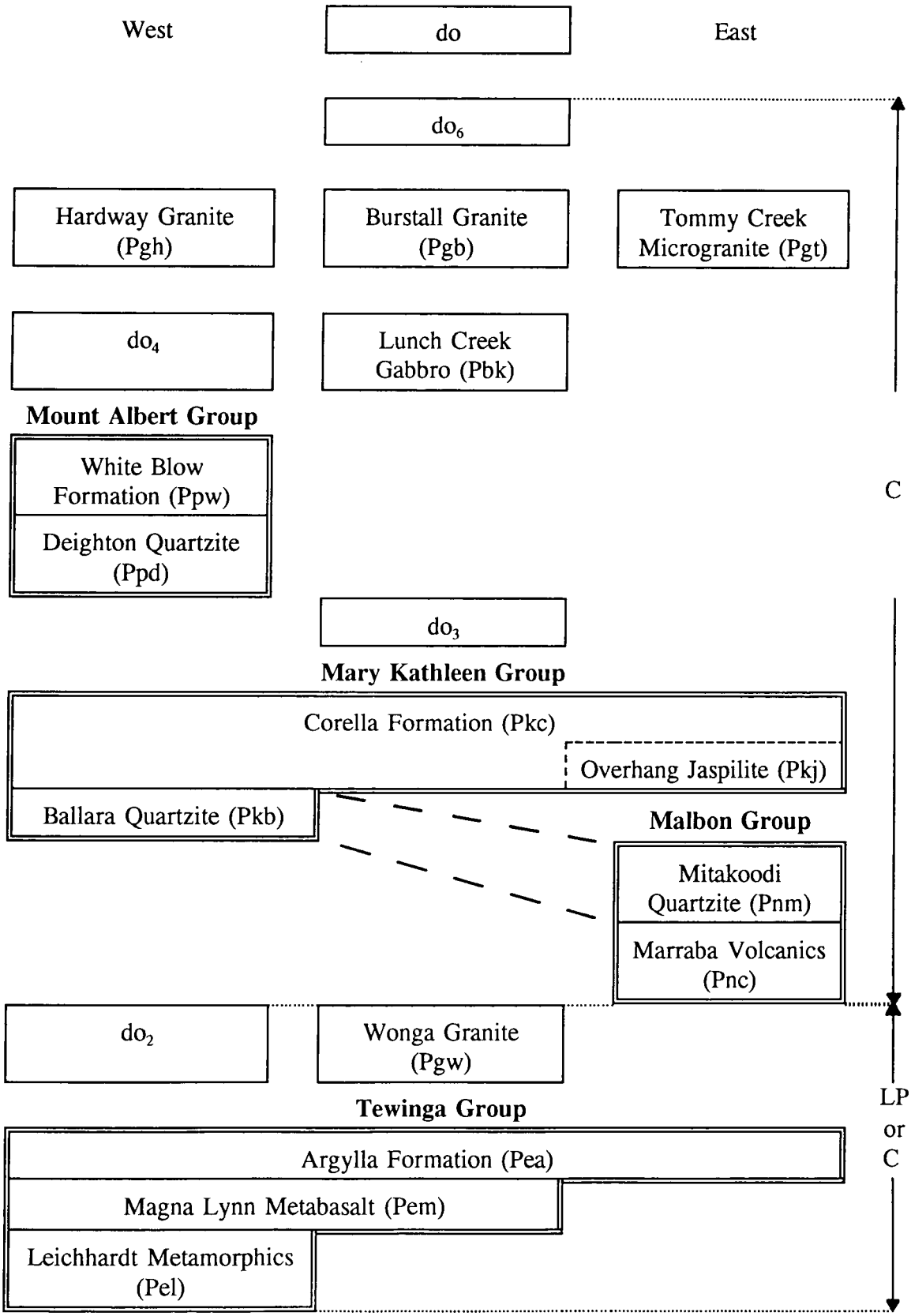

Figure 2.2 The stratigraphy for the area, compiled from the MARABBA and MARY KATHLEEN sheets. LP = Lower Proterozoic, C = Carpentarian, do = dolerite. Abbreviations for formation names are given in brackets.

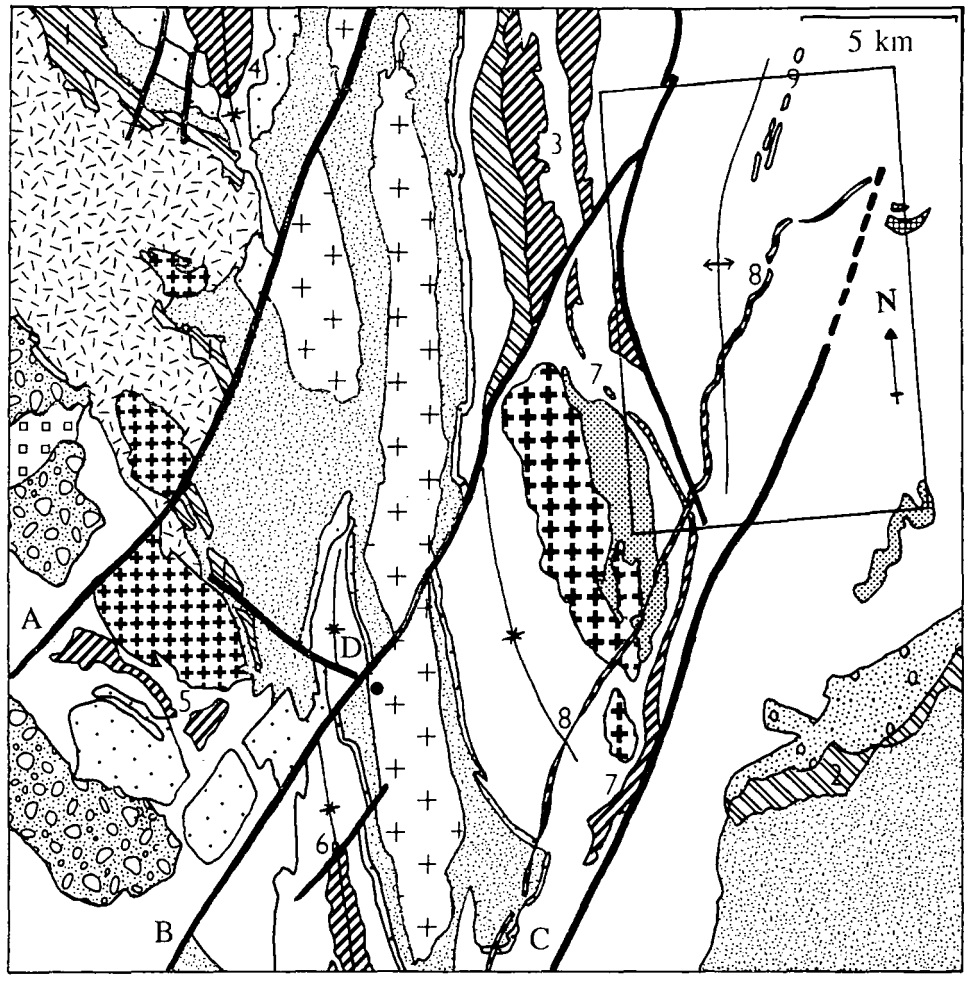

Syncline; Anticline

Dolerite

Metabasalt

Lunch Creek Gabbro

Tommy Creek Microgranite

Hardway Granite

Burstall Granite

Wonga Granite

Major Faults

White Blow Formation

Deighton Quartzite

Corella Formation

Ballara Quartzite

Mitakoodi Quartzite

Argylla Formation

Leichhardt Metamorphics

Figure 2.3 The Geology of the study area simplified from the MARABBA and MARY KATHLEEN sheets. The area's geology is shown in full at 1:100 000 in Enclosure 2.1. Circle = Mary Kathleen. Dolerites and Metabasalts: 1 = Magna Lynn, 2 = Cone Creek, 3 = Lime Creek, 4 = Little Beauty, 5 = Dog Bone, 6 = Rosebud, 7 = Lake Corella, 8 = Lake View. Burstall Pegmatite dykes = 9. Faults: A = Wonga, B = Cameron, C = Fountain Range, D = Greens Creek. Box indicates area of detail for Corella Formation shown in Figure 2.5.

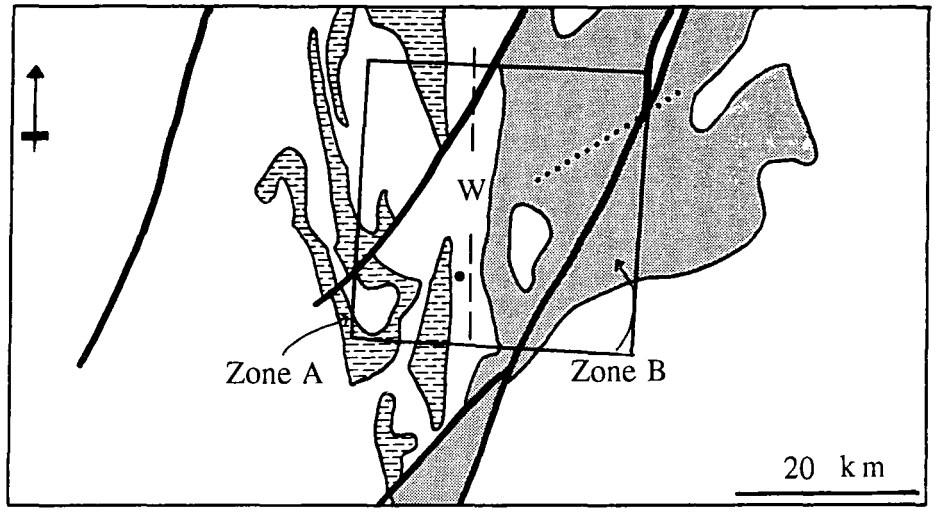

Figure 2.4 The distribution of Zone A and Zone B Corella Formation as defined by Blake (1982). W = Wonga Belt, dotted line = original type section, box = study area.

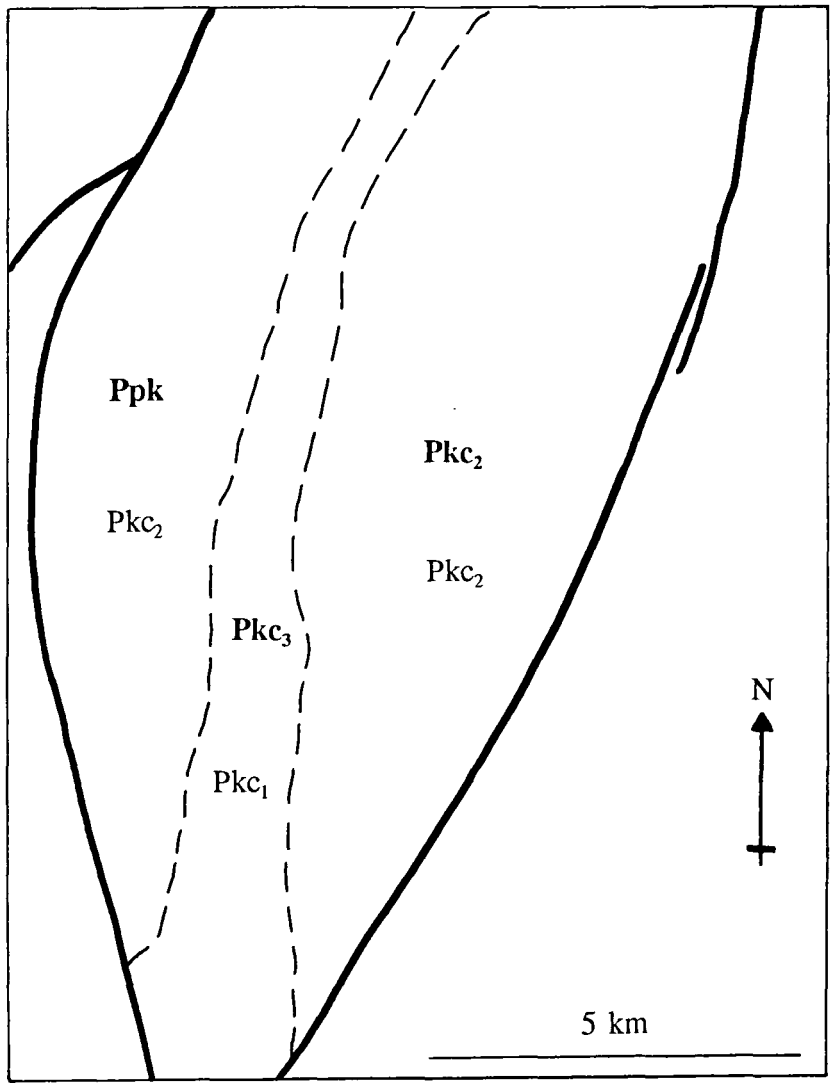

Figure 2.5 The Corella Formation NE of the Burstall Granite. The member names in ordinary type are from the MARABBA sheet. The alternative interpretation is shown in bold.

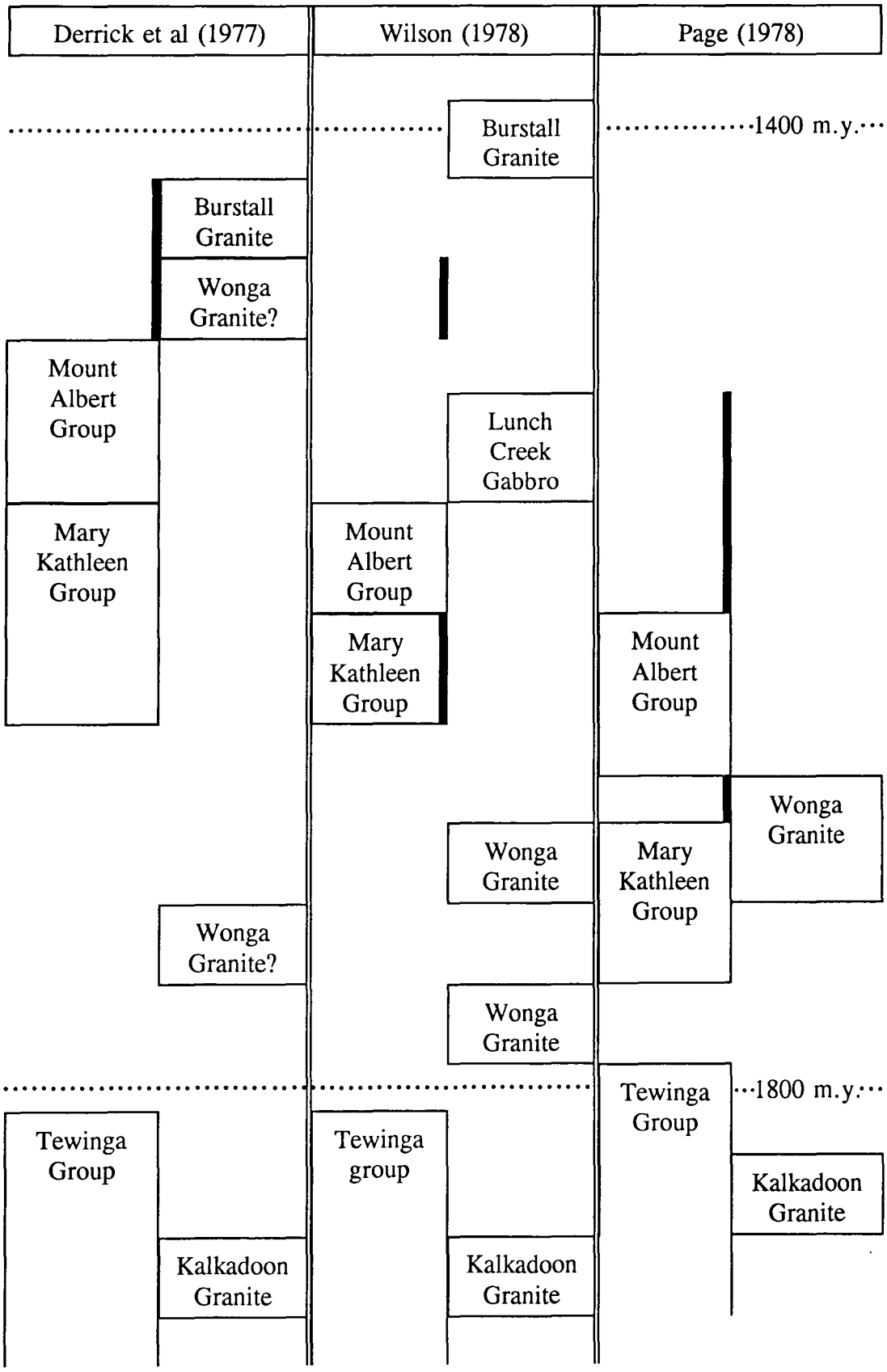

Figure 2.6 Three alternative stratigraphies for the study area (after Holcombe and Fraser, 1979). Proposed periods of metamorphism are indicated by thick vertical lines.

Plate 2.1 Outcrop of the Magna Lynn Metabasalt near the Greens Creek fault. A thick iron oxide enriched weathered crust is seen in the far outcrop which has been removed by flash flooding from those outcrops in the creek (foreground).

Plate 2.2 Outcrop of the Argylla Formation near the Dog Bone Dolerite. At this locality the Formation consists of deformed rhyolite.

Plate 2.3 Outcrop of the Ballara Quartzite (foreground) and with an example of its distinctive ridge topography along-strike (background). This locality (223) is on the east limb of the Rosebud Syncline, northwest from Mary Kathleen.

a)

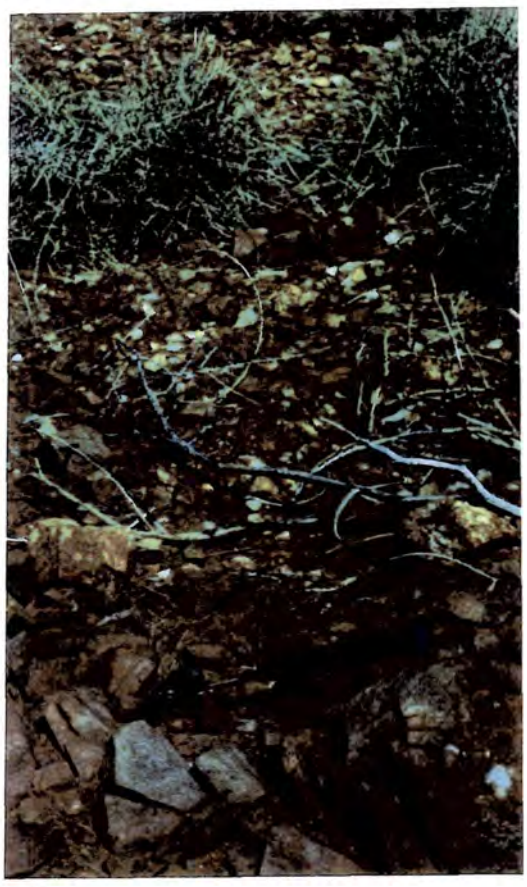

b)

c)

Plate 2.4 Examples of the Corella Formation. a) Calcareous metasediment with pitted weathering typical of member Pkc_1, locality 17. b) Epidotic metamorphics typical of Pkc_2 at locality 51. c) Cordierite-biotite schist within member Pkc_2 at locality 29 in the core of the Rosebud Syncline. Strange, tomato-sized fruit for scale.

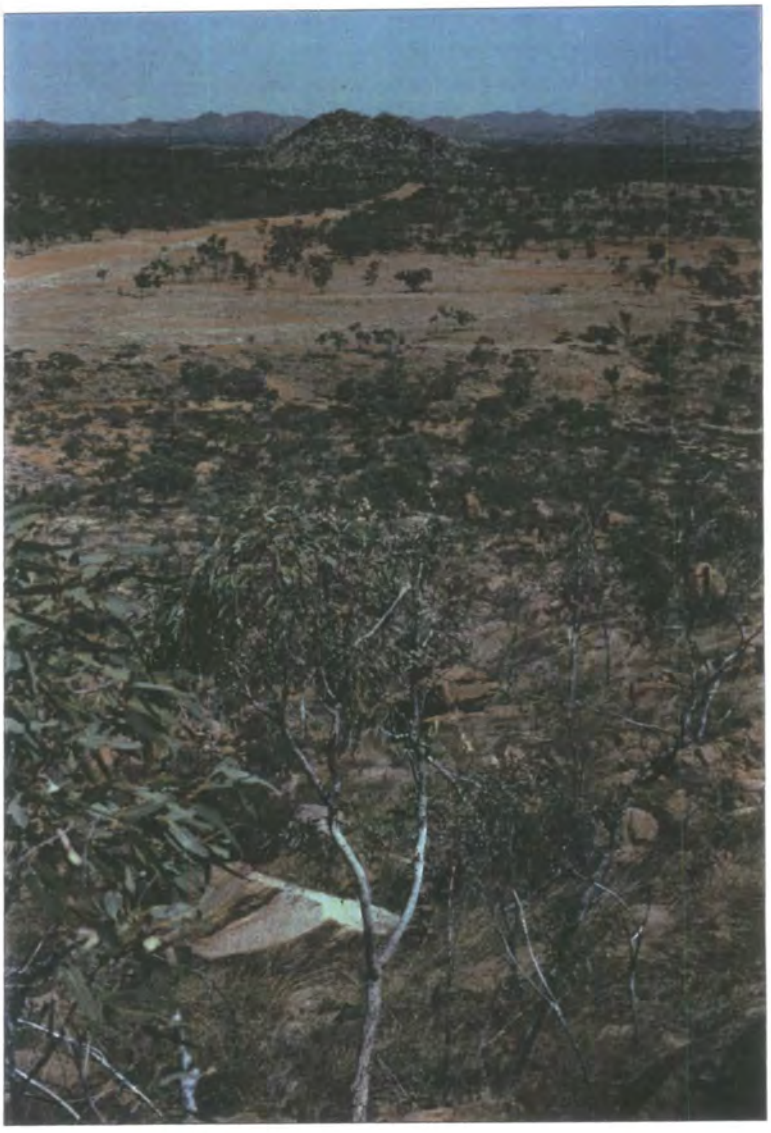

Plate 2.5 Wonga Granite plain with outcrop in the form of tors. Taken looking south from the airstrip north of Mary Kathleen township.

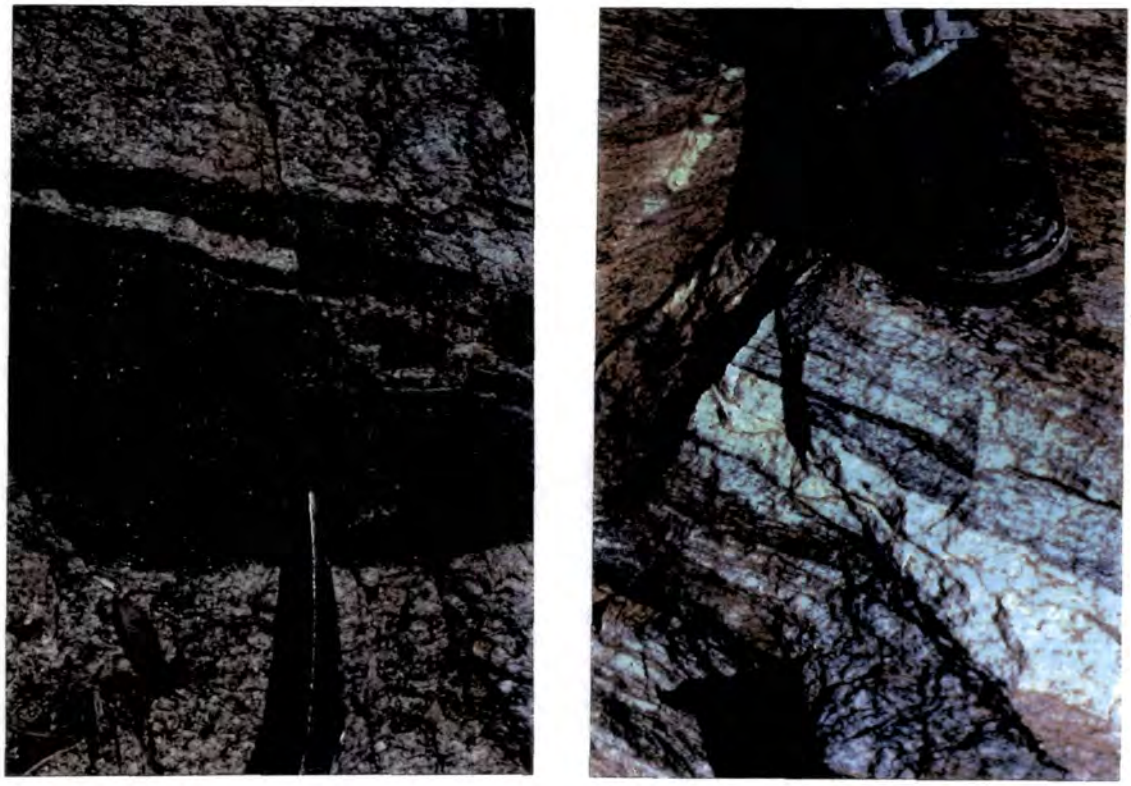

(a) (b)

Plate 2.6 Examples of mafic separations (a) and banding (b) in the Wonga Granite from exposures 1 km (a) and 2 km (b) due south of Mary Kathleen.

Plate 2.7 Foliation in the Wonga Granite at south end of Mary Kathleen airstrip.

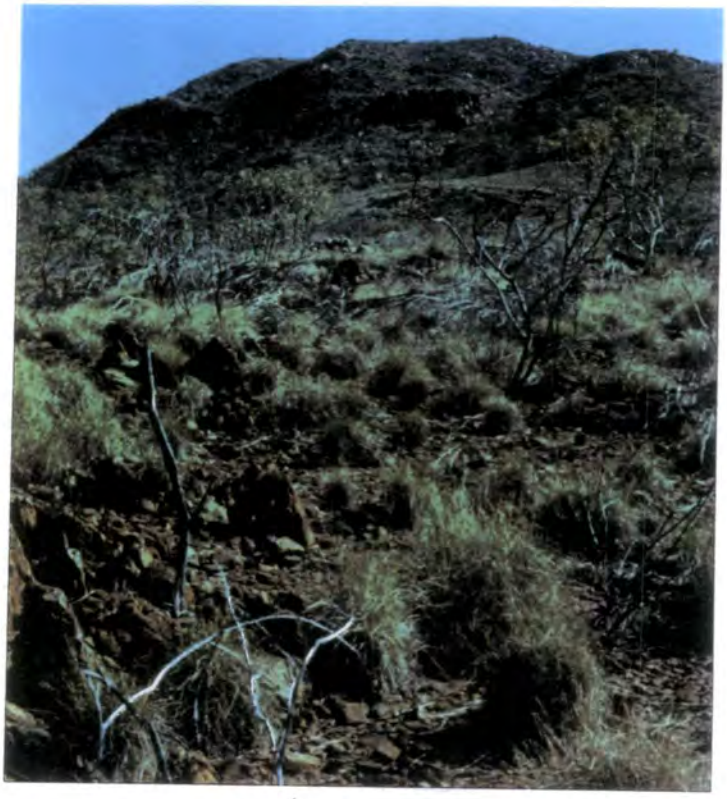

Plate 2.8 The high rugged outcrop of the Burstall Granite's southern mass viewed from locality 99 on the Lake Corella Dolerite to the southeast.

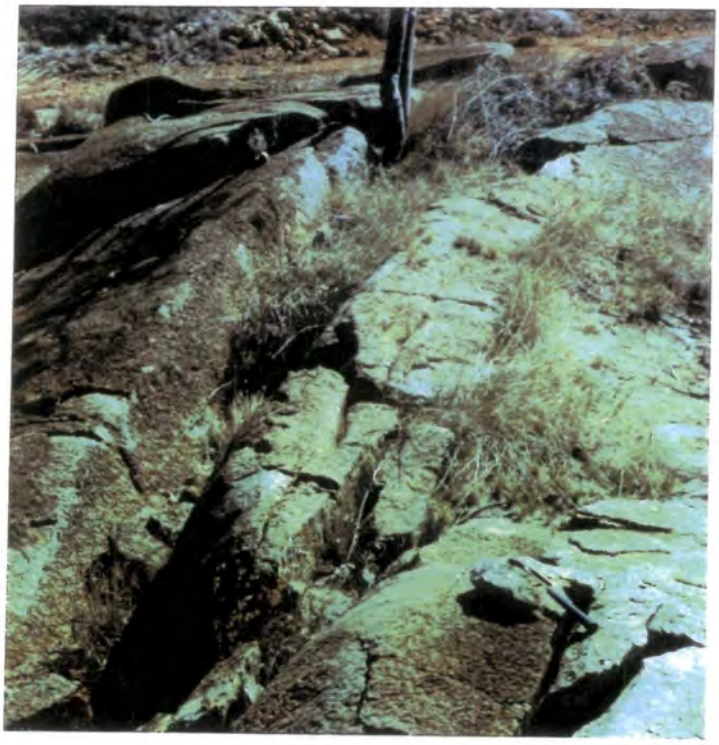

Plate 2.9 Low tor of the Hardway Granite 2 km north of the eastern-most Dog Bone Dolerite exposure, showing iron oxides developing on weathered surfaces.

Plate 2.10 Red-brown iron-rich soil of the Lake Corella Dolerite (left) against paler Corella Formation soils (right) at locality 98 east of the southern Burstall Granite.

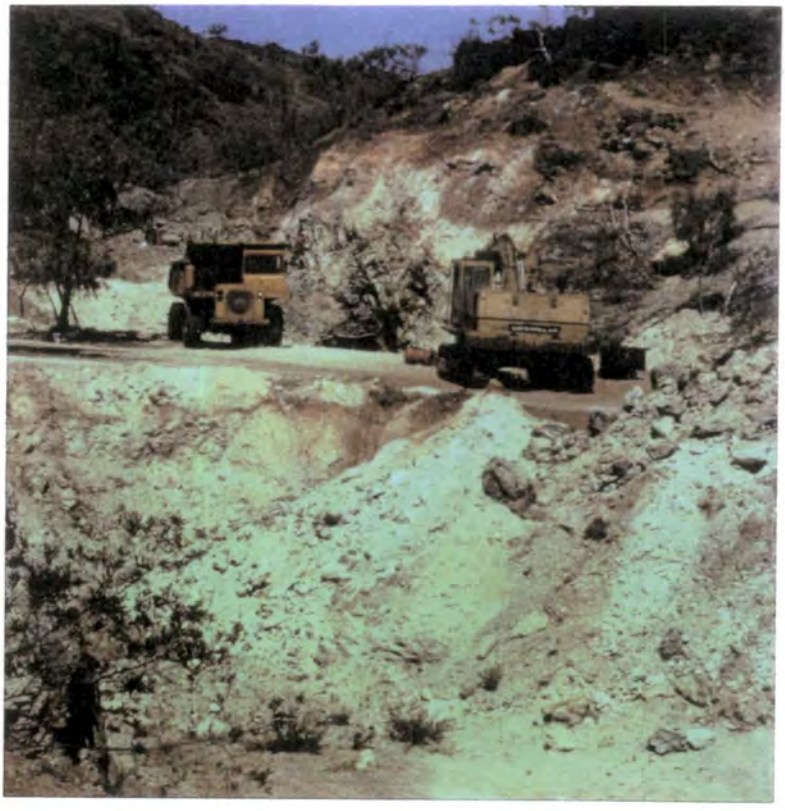

Plate 2.11 Small scale one-person copper mine in the Corella Formation 1 km north of the Greens Creek Fault in the Rosebud Syncline.

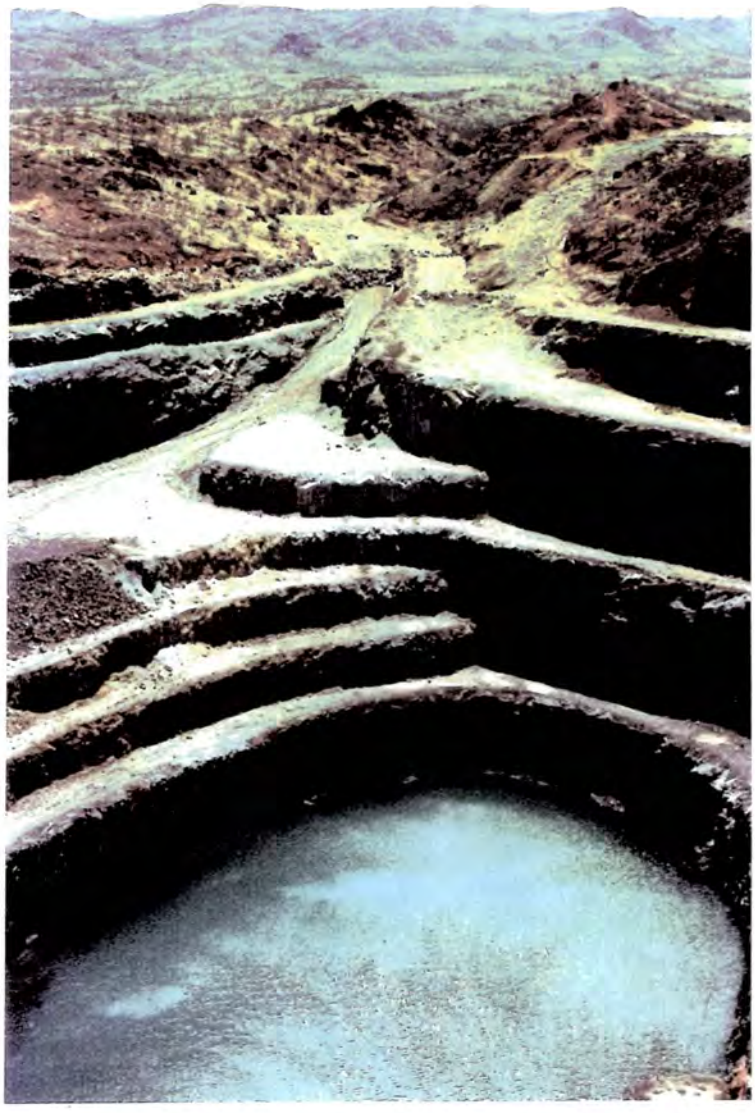

Plate 2.12 View of the open pit at the Mary Kathleen uranium-rare earth mine in the Corella Formation, 5 km northeast of Mary Kathleen township.

CHAPTER 3. THE DATA STUDIED

3.1 Introduction

This chapter describes the acquisition and nature of each of the four data sets studied. It includes details on the various sensors, as well as the physics behind both the radiance and gamma radiometric data. An understanding of the physical basis of remote sensing and the nature of the data allows decisions to be made regarding data processing. The majority of the chapter deals with the radiance data which form the bulk of this study. The remainder deals with the gamma radiometric data.

3.2 Characteristics of the TM sensor and data set

The Thematic Mapper's characteristics are given in Table 3.1 and Figure 3.1. The parameters given in this section are from CSIRO (personal communication), Harris (1987) and USGS (1984). TM is a scanning radiometer in which incident radiation is focused by a mirror and lenses directly onto detectors located in the primary focal plane of the telescope optics. The response of the detectors is digitised and the quantisation range is 256 levels, giving digital data in the range 0-255 Digital Numbers (DN). Each scan of the mirror measures sixteen lines of data, in both the forward (west-east) and reverse (east-west) scans. Radiation is measured in seven wavelength ranges, three in the visible, one in the near infrared, two in the short wave infrared and one in the thermal infrared wavelength regions. Each measurement is made over an area on the ground 28.5 m by 28.5 m, giving the pixel size for this data set. In the thermal infrared measurement is over 120 m by 120 m but this study makes little use of the thermal infrared band (band 6), as it is primarily concerned with reflectance data. The swath width is 185 km, and the nominal repeat cycle for any one location is 16 days. Near real-time relay of the data to ground stations is achieved by the use of the Tracking and Data Relay Satellite and US Domestic Communications Satellite systems.

The TM data set studied here is a cloud-free subscene 1024 pixels square and is used to define the boundaries of the field area (Figure 3.2).

3.3 Characteristics of the NS001 sensor and data set

Details of this sensor's characteristics are given in Table 3.1 (CSIRO, personal communication). The NS001 optics operate in a similar way to that described for TM and the response of the detectors is again digitised to give digital data in the range 0-255 DN. For this sensor each scan of the 45° rotating mirror measures one line of data only and there is no reverse scan. The data are stored on 1600 bpi computer compatible tapes, band interleaved by line. Radiation is measured in eight wavelength ranges, three in the visible, one in the near infrared, three in the short wave infrared and one in the thermal infrared wavelength regions. This study does not make use of NS001's thermal infrared band (band 8), as it is primarily concerned with reflectance data. The instrument has a field of view of 1.75 radians and an instantaneous field of view of 2.5 x 2.5 milliradians. It was operated at a height of 4000 m, giving a nominal pixel size of 10 m at nadir and a swath width of 9.534 km.

Two adjacent E-W flight lines and one intersecting N-S flight line were flown on October 15th 1985, centred on the Mary Kathleen open-cast mine. The N-S flight line largely repeats the coverage of two E-W flight lines and so was not studied in detail. The more northerly E-W flight line (Flight Line 2) is 3452 lines by 750 pixels, 700 pixels of which are image data, and the rest of which are flight data. It was flown at 1300 hours in hazy but cloud-free conditions, and was designated 100% successful. The southern E-W flight line (Flight Line 3) is 2025 lines by 750 pixels and overlaps Line 2 by 3 km (Figure 3.2). It was flown at 1315 hours in hazy conditions with 1% cloud, and was also deemed 100% successful.

3.4 Characteristics of the GMS sensor and data set

Details of the sensor characteristics, as provided by Geoscan, are given in Table 3.1. The GMS operates in a similar way to the NS001 sensor and records data in the range 0-255 DN. Each scan of the mirror measures one line of data, which are stored on 5.25 inch optical disks and can be analysed in-flight at the time of acquisition. Radiation is measured in twenty four wavelength ranges selected from a possible forty six detector channels, thirty two in the visible/near infrared, eight in the short wave infrared and

six in the thermal infrared wavelength regions. In this case all the short wave and thermal infrared bands were recorded and ten in the visible/near infrared. This study makes some use of the GMS thermal infrared data as there are sufficient bands in this wavelength region to make this worthwhile. This is not the case with TM or the NS001 sensor, which only have one band in the thermal infrared as described above. The instrument was operated at a height of 4774 m, has a field of view of 92° and an instantaneous field of view of 2.1 milliradians, giving a nominal pixel size of 10 m at nadir for this data set. The swath width at this height is 9.887 km.

Eight adjacent N-S flight lines were flown in the area on 11th of November 1989. Of these, the two adjacent flight line portions 5b, over the mine, and 6a, in the east, cover the geology of interest (Figure 3.2). The log for these flight lines, recorded at approximately 1300 hours, records no cloud or turbulence. The portion of Flight Line 5b studied is 2800 lines by 768 pixels, all of which are image data, and for Flight Line 6a this portion is 1601 lines by 768 pixels. The difference in the number of lines is due to differing start and finish points for each flight line and to restricting the lines studied to the geology of interest. The flight lines overlap by approximately 1 km.

3.5 The physics of remote sensing between 0.4 and 2.5 μm

All sensors described in the previous sections are passive remote sensing instruments operating over the wavelength range 0.4 to 2.5 μm and record the earth's radiant electromagnetic energy, modified by the atmosphere (Mather, 1987). The proportion of energy reflected, absorbed or transmitted at a particular wavelength by the earth's surface is dependent on its chemical composition. If these parameters are plotted against wavelength, a reflectance, transmittance or absorbance spectrum results which can be used to uniquely identify rocks and minerals (Hunt, 1977; Hunt, 1980).

3.5.1 The radiance measured by the sensor

The source for the electromagnetic energy incident on the earth's surface is the sun, which emits radiant energy between 0.1 and 100 μm (Figure 3.3). This irradiates the earth's surface after interaction with the atmosphere. The total radiance reaching any

surface therefore comprises a direct radiance from the sun and a diffuse radiance scattered onto the surface by the atmosphere. This energy can be reflected, absorbed and re-emitted, or transmitted by the earth's surface. The energy reflected and emitted reaches the sensor after further interaction with the atmosphere, which causes attenuation of the radiance but also adds energy through atmospheric scattering in the direction of the sensor (Hunt, 1980; Slater, 1980). Gains and offsets at the sensor, set to ensure the measurement falls within the radiometric sensitivity of the instrument, modify the measurement further. Finally, noise may be introduced by electrical or mechanical defects in the instrument. The above sequence is shown in Figure 3.4. Excluding the noise, the measurement made can be described mathematically by the following equation derived from Slater (1980):

$$X_\lambda = [E_\lambda t_\lambda A(\rho_\lambda + L_{\lambda T}) + a_\lambda]G_\lambda + O_\lambda \qquad (3.1)$$

where

X_λ	=	Radiance measured at sensor at wavelength λ
E_λ	=	Irradiance of source reaching surface at wavelength λ (direct + scattered)
t_λ	=	Atmospheric transmittance (up) at wavelength λ
A	=	Slope and aspect based effects for the surface
ρ_λ	=	Reflectance of surface at wavelength λ
$L_{\lambda T}$	=	Thermal emittance of surface at wavelength λ
a_λ	=	Atmospheric path radiance at wavelength λ
G_λ	=	Gain applied at the sensor at wavelength λ
O_λ	=	Offset applied at the sensor at wavelength λ

Equation 3.1 expands to:

$$X_\lambda = E_\lambda t_\lambda A(\rho_\lambda + L_{\lambda T})G_\lambda + a_\lambda G_\lambda + O_\lambda \qquad (3.2)$$

The earth's ambient temperature is such that between 0.4 and 2.5μm it does not emit significant amounts of energy (Figure 3.3) and so, for the wavelengths studied here, the reflectance spectrum is the most useful to geologists. At a given wavelength reflectance

is the ratio of reflected energy over incident energy (Drury, 1987). At the wavelengths and temperatures under study here $L_{\lambda T} = 0$ and the equation becomes:

$$X_\lambda = E_\lambda t_\lambda A \rho_\lambda G_\lambda + a_\lambda G_\lambda + O_\lambda \qquad (3.3)$$

3.5.2 Reflectance spectra of rocks, soils and minerals

Rocks, soils and minerals constitute either rough or particulate surfaces and cause bidirectional reflection of incident energy. This energy is measured when the source and the sensor are both above the sample, whether in the field or the laboratory. The plot of reflectance against wavelength forms a reflectance spectrum. This has features in it which are due to absorptions by surface materials which reduce the energy reflected. Between 0.4 and 2.5 μm incident energy is absorbed by electrons undergoing electronic and vibrational transitions within atoms and molecules of the surface under study, as outlined by Hunt (1977; 1980).

Electronic transitions are caused by several effects:

1. Crystal field effects, which involve the absorption of energy by electrons as they change to a new energy level in an ion that forms part of a mineral's structure. The most common ions involved in this are Fe^{2+} and Fe^{3+}, others being manganese, copper, chromium and nickel ions. The new energy value and consequently the resulting spectral feature are determined by the ion's valency state, coordination number and site symmetry. Many different spectral features can all be due, for example, to Fe crystal field effects, because Fe exists in two valency states and can occupy many sites.

2. Conduction band transitions, which involve electrons absorbing sufficient energy to leave an ion and become free electrons in what is known as a "conduction band" within the crystal structure. Only the more conductive materials requiring less energetic photons for the transition, such as sulphides, produce features at wavelengths considered here.

3. Charge transfer transitions, also involving the liberation of electrons from an ion, but only as far as a neighbouring ion. The most important is the Fe-O charge transfer which produces an intense absorption in the visible causing the red colour of iron oxides.

4. Finally, variable absorptions can occur in the visible due to electrons trapped in crystal defects moving to higher energy states. As they lead to colouration of the mineral, these crystal defects are known as colour centres.

The element Fe, which often features in the electronic transitions described above, is common in minerals due to its place in numerous mineral structures and its ability to substitute into Al, Mg and even Si sites in other mineral structures. The minerals of most importance to remote sensors include the weathering products hematite, goethite and limonite and many rock forming minerals such as fayalite, pigeonite and the amphiboles. Examples of spectral absorptions caused by electronic transitions are shown in Figure 3.5.

Vibrational transitions require energy levels which only cause absorption features beyond 2.5 μm. If, however, multiples of these energy levels interact with a surface, overtones may be produced at multiples of the fundamental transition frequency. When combined with fundamentals from other atoms these are responsible for features at shorter wavelengths. The most important molecule responsible for such interactions is OH, present in rocks as OH in mineral structures or as molecular water. This may be interstitial, absorbed on the rock's surface, or part of the crystal structure usually in combination with Al, Fe or Mg. Minerals which contain OH in their structure include kaolinite, dickite, chlorite, talc, montmorillonite, muscovite and epidote while gypsum and quartz have associated molecular water (Gribble and Hall, 1985). The other molecule with vibrational overtone transitions of importance at these wavelengths is CO_3, which is present in calcite, dolomite and other carbonates. Figure 3.6 shows spectra which contain absorptions due to vibrational transitions.

Table 3.2 shows the wavelength positions of the most important absorptions, the transitions and elements responsible for them and minerals and rocks of which these are important constituents.

3.6 Implications of the physics for geological remote sensing

Geological mapping consists of the discrimination of units, delineation of their boundaries and structures and identification of rock types and minerals present. Unprocessed TM data have been used to analyse geological problems with some success (e.g. Qari, 1989). Such analysis can yield valuable structural information and discriminate between some rock units, effectively giving improved photogeological interpretation. This approach does not, however, fully exploit the information contained in the data. Much of the information contained in remotely sensed data relates to albedo and is highly correlated between different wavelengths. Albedo information is useful for structural mapping, but the discrimination and identification of different lithologies rely on emphasising or retrieving the small amount of uncorrelated information contained in the mineral-specific absorptions.

3.6.1 Discrimination

In equation 3.3 the factor A is large and correlated between wavelengths. Discrimination is improved by the application of data processing techniques which reduce this correlation. Techniques such as principal component analysis have proved successful at highlighting the uncorrelated information of use to the geologist (Rothery, 1987). Band ratioing aims to remove the factor A by division, as it is the same at all wavelengths, and this technique has been successfully used in geological studies (Abrams et al, 1983). The additive components of equation 3.3, $a_\lambda G_\lambda$ and O_λ, should be removed before these discrimination enhancing techniques are implemented. The factor A cannot be removed by ratioing if the additive component is not removed, and the detrimental effect on ratio images if this is not done has been demonstrated by Crippen (1988).

3.6.2 Identification

For rocks and minerals over wavelengths in the visible, near infrared and short wave infrared regions of the spectrum, identification of lithologies or minerals can only be achieved if the parameter reflectance (ρ_λ) is retrieved from the data and the spectrum of reflectance at different wavelengths plotted (Hunt, 1980). The geologically significant information often consists of subtle absorption features in this spectrum at particular wavelengths which may form as little as 4% of the signal (Green et al, 1985). The values of ρ_λ the data contain are modified by several factors, many of little or no geological interest; noise, offsets, gains, additive atmospheric path radiance, multiplicative atmospheric transmittance, the topographic factor and the irradiance of the source. Logarithmic residuals (Green and Craig, 1985) is one technique which aims to retrieve ρ_λ by removing those factors which are multiplicative (E_λ, t_λ, A and G_λ in equation 3.3). Study of equation 3.3 shows, however, that the additive components $a_\lambda G_\lambda$ and O_λ must be dealt with before this can be done. Thus, it is important in identification as well as discrimination to perform radiometric correction of the data, involving the removal of $a_\lambda G_\lambda$, O_λ and, if possible, the gain and atmospheric transmittance.

3.6.3 Notation convention for absorptions in the radiance data

The sensors used in this study have wide band widths each measuring radiation over a wavelength range covering several different absorption features. Thus low TM band 7 values caused by absorption at 2.2 μm are "absorption in TM band 7", rather than "absorption at 2.2 μm". In this study, where several sensors are used, this notation is confusing. For example, absorption at 1.65 μm would be referred to as "absorption in TM band 5", but also as "absorption in NS001 band 6" (Table 3.1). The concept of bands is sensor specific and not suited to a study where several types of data are used together. It is better to refer to the data in terms of wavelength, which is consistent for all the sensors used. Thus in this study absorption in any band is referred to by that band's centre wavelength. This notation allows meaningful comparison of a "1.65 μm absorption in the TM data" with a "1.65 μm absorption in the NS001 data". As the majority of the TM and NS001 bands are broad, the bands centred on 0.485 and 2.215 μm will be rounded to three significant figures and referred to as the 0.49 μm and

2.22 μm bands to be consistent with the other bands (Table 3.1). The spectral resolution of the GMS sensor, however, warrants the retention of four significant figures when referring to its bands.

3.7 Other considerations

3.7.1 Effects of time and season

Season and time of acquisition affect the magnitude of the solar irradiance and the sun-angle. At the acquisition times in this study variation in solar irradiance should be small but a significant change in sun-angle, and hence slope and aspect effects, will occur between the TM data, acquired mid-morning in late summer, and the airborne data sets, both acquired around mid-day in early spring. However, techniques used in this study, such as logarithmic residuals, remove irradiance and slope and aspect terms. The effects of this variation have not been investigated in the present study. Season also affects the amount of vegetation present. The airborne data sets were acquired at the end of the dry season, to minimise the vegetation problem. The TM data, acquired in March, can be expected to display more vegetation-related problems.

3.7.2 Noise removal and cross-track shading

Several processing techniques aim to remove the correlated information and highlight the uncorrelated, subtle features often associated with particular minerals. Instrument noise, however, is also uncorrelated information. Techniques such as band ratioing designed to highlight the weak geological signal therefore emphasise noise also. Where possible, noise should be eliminated or reduced prior to data enhancement.

With airborne sensors the large variation in look angle affects the radiance measured at the sensor. For a simple case with the sun overhead, the radiance at nadir is a maximum and diminishes to either side of the flight track, due to surface reflectance varying in different directions, and to different proportions of the shade component being seen at different across-track positions (Barnsley and Kay, 1990). Correcting this effect forms part of the radiometric correction and, as the methods used do not change the variance of the data, this can be done before further processing of the data.

3.7.3 Geometric correction

Remotely sensed data, in common with air photographs, have inherent geometric distortions due to the geometry of their acquisition. Correction of an image's geometry requires the data to be resampled, involving averaging and replication or replacement of some pixels' data values. It thus represents a potential distortion of the radiance measurements. This correction is commonly only required for production of a final product image and is often best done after spectral processing, with the non-geometrically corrected data retained for comparison. As each instrument acquires data in a different manner, at a different altitude, and from a different platform, each data type displays different problems requiring instrument-specific corrections.

3.8 The order of processing steps

The physical principles described in section 3.5 and the other considerations detailed in section 3.7 combine to dictate the order of processing steps. The first correction which should be performed on the radiance data is the removal of noise. It has been shown that, before the implementation of techniques designed both to improve discrimination and to facilitate identification, the gain and offset of the sensor and the additive atmospheric path radiance should be corrected for. Chapter 4 therefore deals with noise removal and radiometric correction of the data. Further processing aimed at improved discrimination or the retrieval of reflectance is an enhancement of the radiance data. These data enhancements are explained in chapter 5. Finally, geometric correction is required to remove spatial distortions introduced by the satellite orbit or aircraft flight path and the viewing geometry. This is covered together with data integration in chapter 6.

3.9 Characteristics of the AGR sensor and data

The aircraft-mounted gamma ray spectrometer measures radiation at energy levels which correspond to gamma rays emitted by the decay of the isotopes ^{40}K, ^{232}Th, ^{238}U and ^{235}U. The amount of radioactivity at a given energy level is measured by the frequency with which gamma rays of that energy are intercepted. The resultant data are

recorded in four channels which are measures of the U, Th and K concentration and the total count radioactivity for a point source on the ground. The response of the detectors is recorded as real *4 data, giving real data with a precision of 7 significant figures.

The data were acquired by CRAE Pty Ltd at a 250 m line spacing and a nominal terrain clearance of 70-80 m (Smith, 1985). They have been corrected for background, altitude and Compton scattering and gridded on a 100 m x 100 m grid, projected to Australian Map Grid (AMG) Zone 54. After gridding this data set is a pseudo-image 1000 pixels square, with a pixel size of 100 m, and thus covers 10 000 km^2 (Figure 3.2). It was made available for this study by the Canberra office of CRAE Pty Ltd, who are also the source for many of the parameters given above, in addition to Drury (1987).

3.9.1 The physics of remote sensing through gamma radiometry

The measurement at the sensor is a radioactivity count. When an element on the ground decays it emits gamma rays at a range of specific energy levels, which pass upwards through the atmosphere to the sensor. The data only give an indication of the concentration of the elements U, Th and K and the total radioactive count (Drury, 1987).

3.9.2 Other considerations

Noise may be introduced at the sensor. Radioactive elements in the atmosphere may contribute by their decay to the measurement attributed to a point on the ground. In this case the energy level of the gamma ray emitted by the atmospheric halogens is similar to one of those measured for uranium (A. Green, personal communication). This atmospheric component is apparent after gridding as irregular striping in the image and can be treated as noise. The data, a series of point measurements all made from a similar height and geometry, are not in the form of an image when collected and so contain no geometric distortions after griding.

3.9.3 Processing of gamma radiometric data

There is no potential for the identification of minerals and the main geological use of the data is lithological discrimination through the detection of differing amounts of the elements U, Th and K in different rocks. The effects of the atmosphere and noise can be treated. The information is correlated between the U, Th and K bands, so there is potential for some processing aimed at reducing this correlation such as band ratioing. The data do not contain a parameter equivalent to reflectance which further processing can enhance or retrieve. As the data are registered to AMG, no geometric correction of the data is required. The majority of the processing implemented on this data set concerns its integration with the TM data.

All processing of the AMG data is described in chapter 6, along with the geometric correction of the radiance data sets.

3.10 Summary

Radiance data sets can be applied to geological problems without processing, but the large amount of information correlated for all wavelengths hinders discrimination. Processes aimed at reducing correlation to enhance discrimination are more effective if the data have had noise treated and a radiometric correction applied to remove effects related to sensor and atmosphere alone. The parameter reflectance can be used to identify rocks, soils and minerals due to characteristic absorption features in their reflectance spectra which are dependent on chemical composition and crystal structure. This parameter may be retrieved from the data by further processing, which can also be considered an enhancement of the radiance data. Geometric correction should be applied as a final stage of processing, as it may change any radiance and reflectance values calculated and geometric precision is only required in final image products.

The gamma radiometric data can also be applied to geological problems without any processing. Processing of these data is limited to noise removal and the reduction of correlation between bands. The use of the data is limited to discrimination, because it does not contain a parameter which can uniquely identify rocks and minerals. No

geometric correction is required, as the mode of acquisition does not introduce distortions and the data are registered to the AMG.

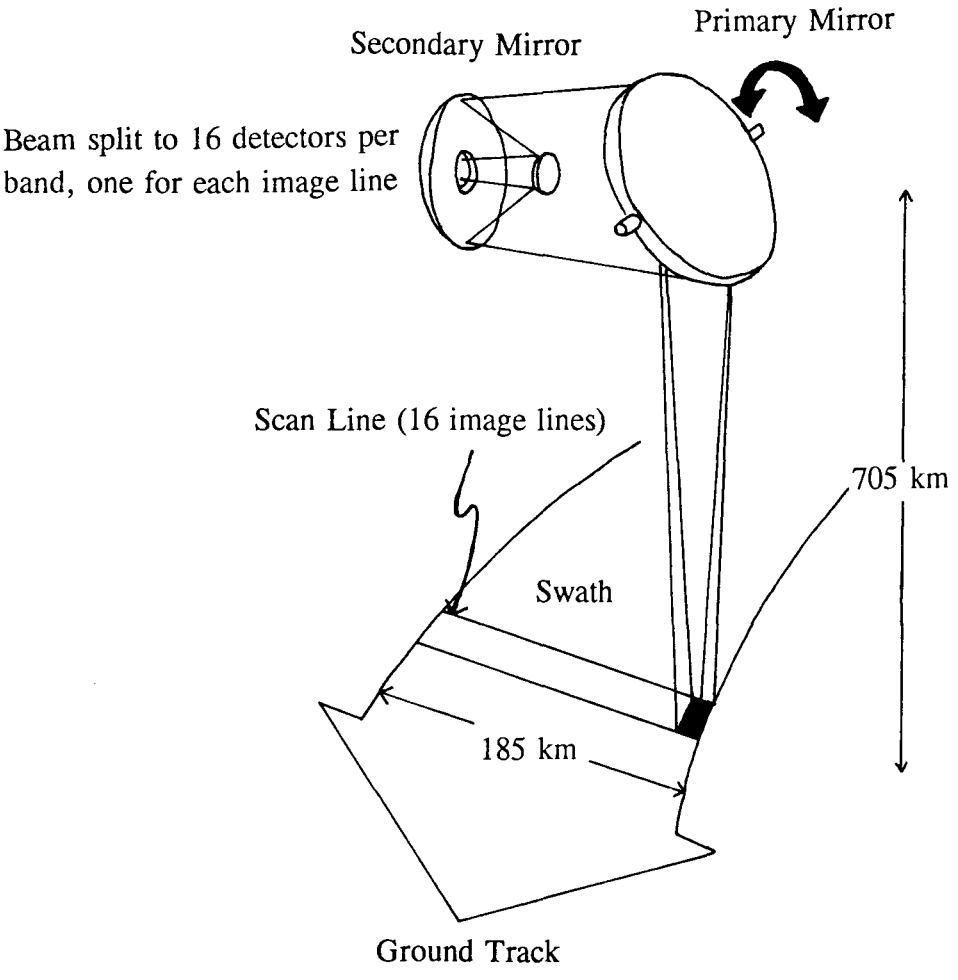

Figure 3.1 The mode of acquisition for TM data (after USGS, 1984).

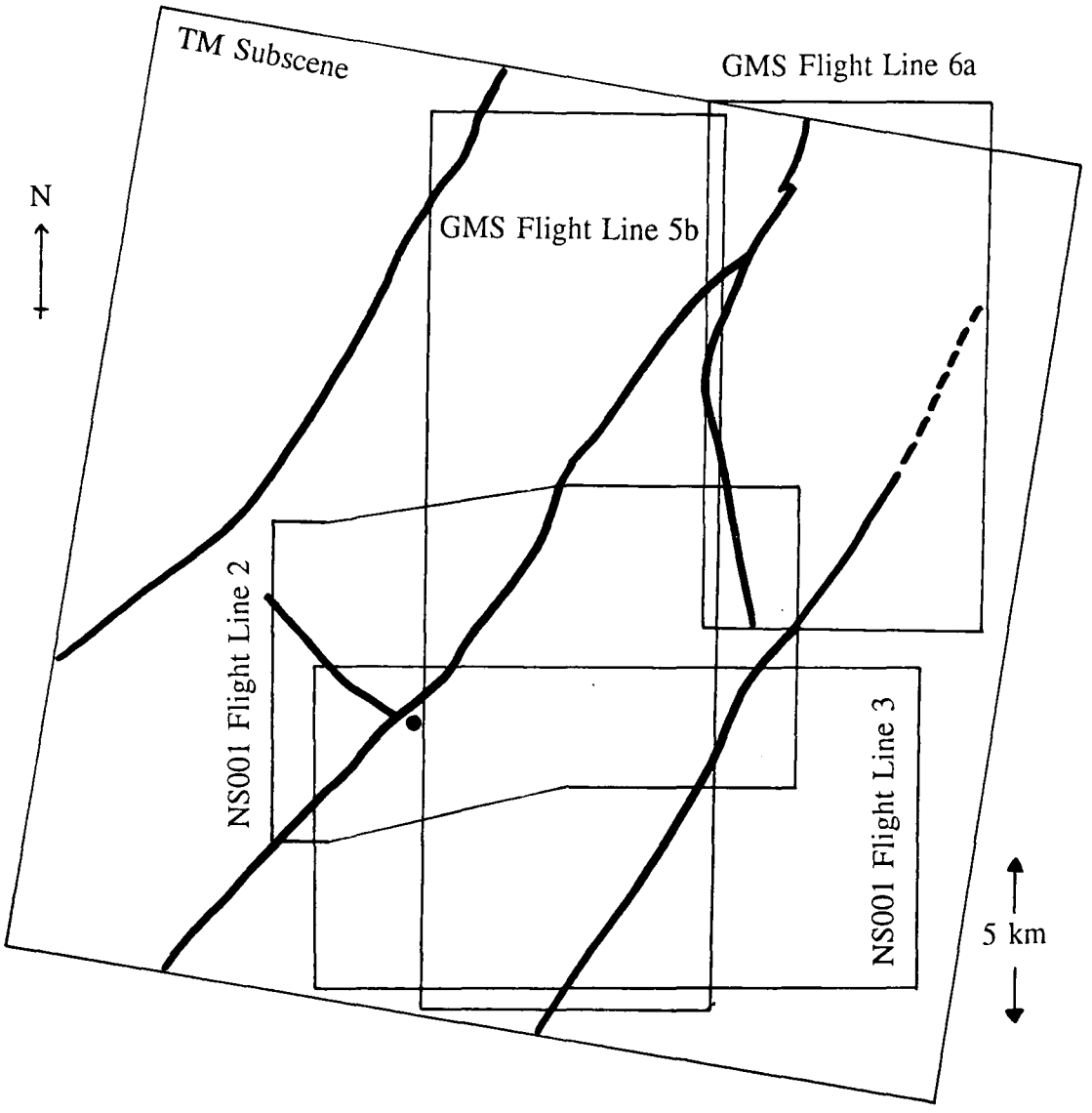

Figure 3.2 The boundaries of the data sets used in the study. NS001 Flight Line 3 is described as drifting to the south on the flight log, and two areas of yaw corresponding to this are seen in the data. The AGR data cover the entire region around the field area.

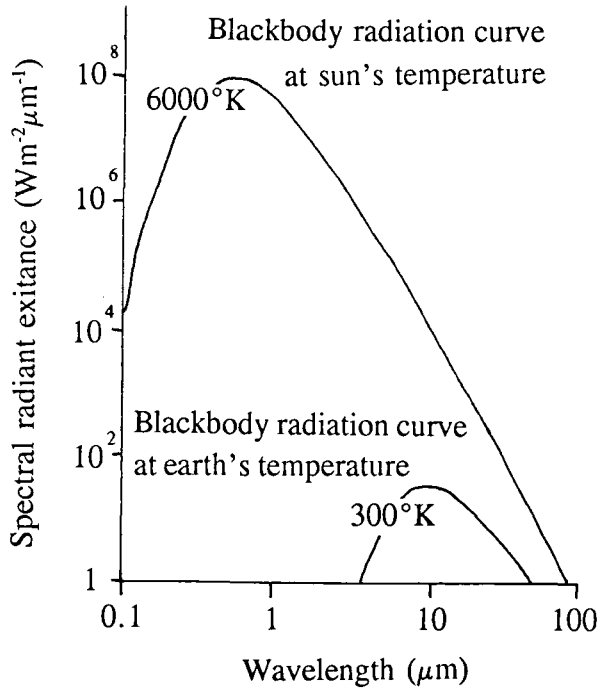

Figure 3.3 Spectral radiant exitance curves for black bodies at the temperature of the earth and the sun (after Lillesand and Kiefer, 1987).

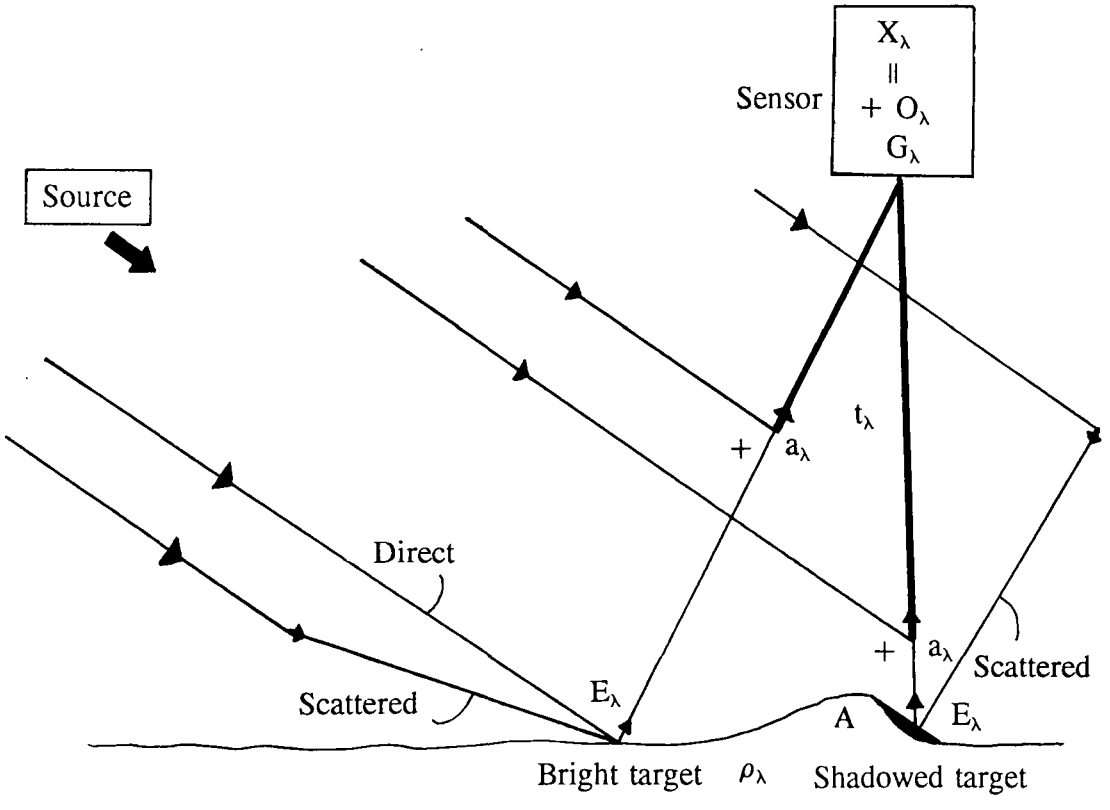

Figure 3.4 Schematic representation of the physics behind equation 3.1 for two cases. In the first the look angle is such that the sensor sees a bright target (left), while in the second the sensor looks into deep shade (right).

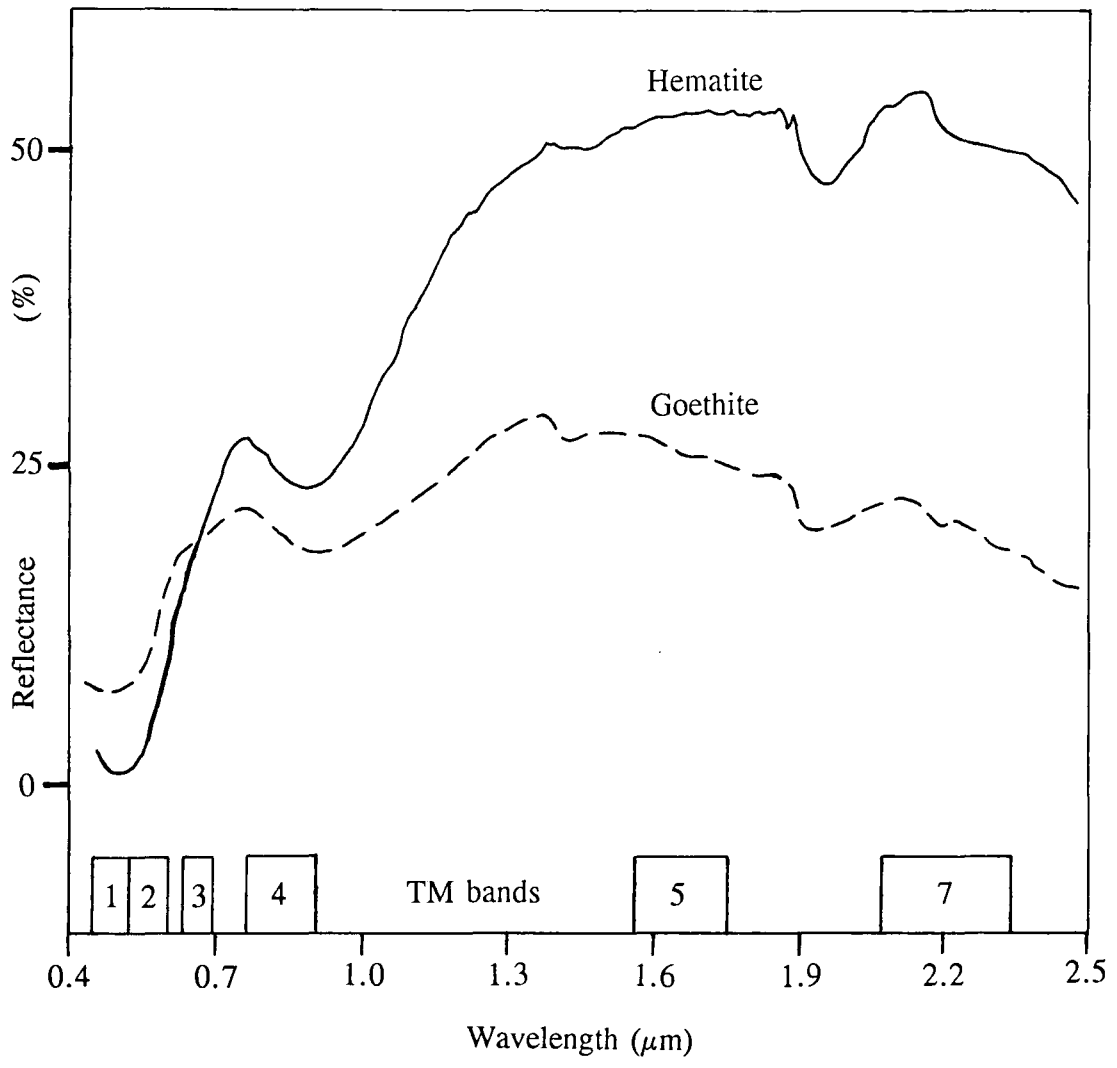

Figure 3.5 Two reflectance spectra with electronic transition related absorption features (source: CSIRO).

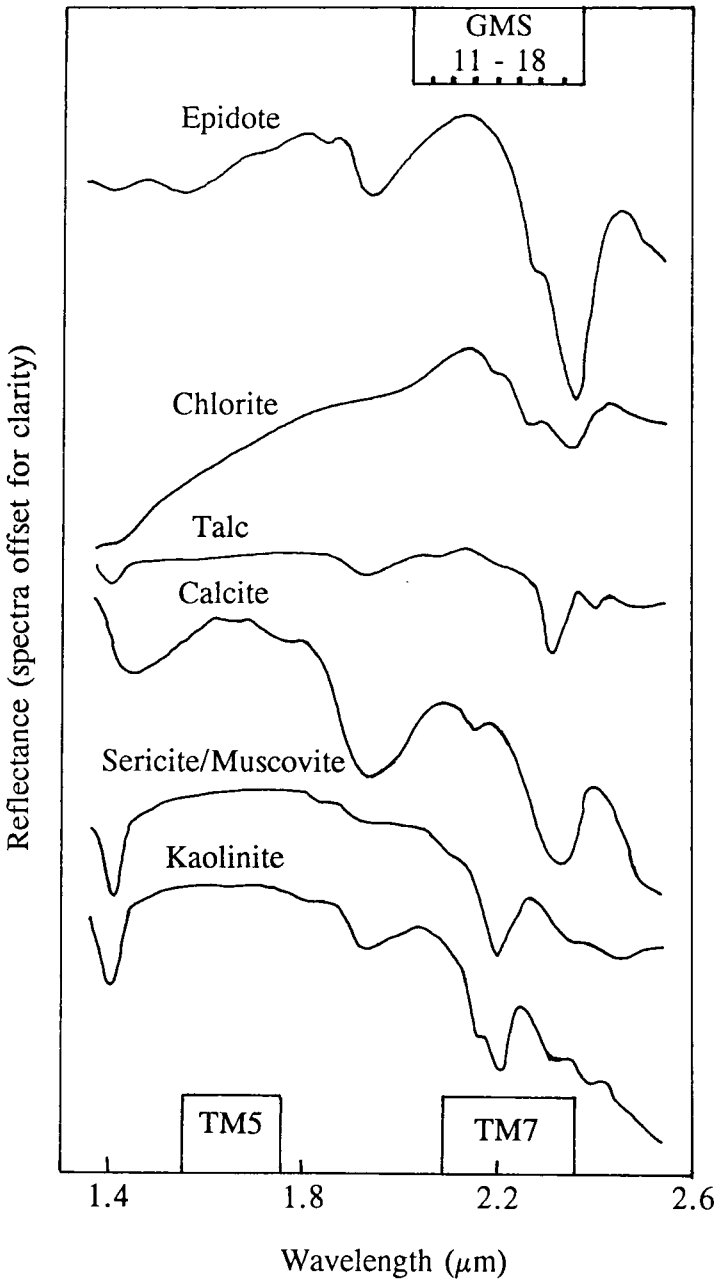

Figure 3.6 Six reflectance spectra showing absorptions due to vibrational overtones in Al-OH (kaolinite, muscovite, epidote, chlorite), Mg-OH (talc, chlorite) and C-O (Calcite) (source: Geoscan).

	TM BANDS			NS001 BANDS			GMS BANDS		
	28.5 m pixels			10 m pixels @ nadir			10 m pixels @ nadir		
		Wavelength (μm)			*Wavelength (μm)*			*Wavelength (μm)*	
	#	*Centre*	*Width*	*#*	*Centre*	*Width*	*#*	*Centre*	*Width*
V	1	0.485	0.070	1	0.485	0.070			
							1	0.522	0.042
	2	0.560	0.080	2	0.560	0.080			
I							2	0.583	0.067
S							3	0.645	0.071
	3	0.660	0.060	3	0.660	0.060			
							4	0.693	0.024
							5	0.717	0.024
							6	0.740	0.023
N	4	0.830	0.140	4	0.830	0.140	7	0.830	0.022
I							8	0.873	0.022
R							9	0.915	0.021
							10	0.955	0.020
				5	1.150	0.300			
	5	1.650	0.200	6	1.650	0.200			
							11	2.044	0.044
							12	2.088	0.044
S							13	2.136	0.044
W							14	2.176	0.044
I	7	2.215	0.270	7	2.215	0.270			
R							15	2.220	0.044
							16	2.264	0.044
							17	2.308	0.044
							18	2.352	0.044

a)

Table 3.1 Band centres and band widths for the TM, NS001 and GMS sensors. a) Visible (VIS), near infrared (NIR) and short wave infrared (SWIR) wavelength regions. b) Thermal infrared wavelength region (sources: CSIRO, Geoscan).

	TM BANDS			NS001 BANDS			GMS BANDS		
	120 m pixels			10 m pixels @ nadir			10 m pixels @ nadir		
		Wavelength (μm)			*Wavelength (μm)*			*Wavelength (μm)*	
	#	*Centre*	*Width*	*#*	*Centre*	*Width*	*#*	*Centre*	*Width*
							19	8.640	0.530
							20	9.170	0.530
T							21	9.700	0.530
I							22	10.220	0.533
R							23	10.750	0.533
				8	11.040	1.240			
							24	11.280	0.533
	6	11.450	2.100						

b)

Absorption (μm)	Cause	Minerals	Lithologies
0.4 - 0.55	Charge Transfer, Fe	Limonite	Almost any rock containing Fe which can be released in solution, particularly basic rocks such as dolerite and basalt.
Near 0.48	Charge Transfer, Fe	Goethite	
Near 0.58	Charge Transfer, Fe	Hematite	
0.68	Crystal Field Effect, Fe	Goethite	
Near 0.84	Crystal Field Effect, Fe	Hematite	
0.90 - 0.92	Crystal Field Effect, Fe	Goethite	
0.86 - 0.92	Crystal Field Effect, Fe	Limonite	
0.8 - 1.2	Crystal Field Effect, Fe	Olivine/Pyroxene	Basic rocks
Near 1.4	Vibrational Overtones: H_2O 0-H	 Quartz, Gypsum Montmorillonite Kaolinite Muscovite	Acid rocks, sandstone, schist, evaporite, weathered rocks.
1.9 - 2.0	Vibrational Overtones: H_2O	 Gypsum, Quartz Montmorillonite	Acid rocks, sandstone, evaporites.
Around 2.2	Vibrational Overtones: Al-OH H_2O	 Kaolinite Muscovite Gypsum Montmorillonite	Acid rocks, sandstone, schist, evaporites.
2.3 - 2.4	Vibrational Overtones: Mg-OH/Al-OH C-O	 Amphibole Talc Chlorite Epidote Calcite	Metamorphic rocks, carbonates.

Table 3.2 Some common absorption features, their causes and the minerals and lithologies with which they are associated (sources: Hunt (1977, 1980), CSIRO, Geoscan, Grove et al (1992)).

CHAPTER 4. RADIOMETRIC CORRECTION OF RADIANCE DATA

4.1 Introduction

This chapter concerns the removal of noise, the radiometric correction of the radiance data and the benefits of performing these operations to the geological analysis of the data. Noise is dealt with first, followed by gains and offsets, which are related to the sensor alone, and the atmospheric path radiance and transmittance. Finally, for airborne sensors, variations in the recorded radiance as the view angle varies across-track are addressed.

4.2 Noise removal

Noise removal has been thought of as a "cosmetic operation" (Mather, 1987) but it is of greater importance than this. Noise has a deleterious effect on the geological analysis of remotely sensed data for the following reasons:

1. Delineation of lithological boundaries is impaired by the visual manifestation of noise in the imagery (Drury, 1987).

2. Any processes used to highlight uncorrelated geological information will highlight noise as it is also uncorrelated information.

3. Identification of minerals is impaired by random noise (Mackin, 1989). Geological information in the form of subtle absorptions in reflectance spectra can easily be masked if noise with a similar or greater amplitude to this signal is present.

4.2.1 Noise in the TM data

A study at CSIRO showed striping in a TM scene of extreme contrast containing ocean, rainforest and small areas of highly reflective cloud (C. Horsfall, personal communication). There are no such extreme contrasts in the data set under consideration

here, however, and noise problems are minor. Noise is uncorrelated information, and so a technique aimed at highlighting uncorrelated information, such as principal component (PC) analysis or logarithmic residuals, should make noise obvious. Little noise is apparent in the logarithmic residual TM data and although PC analysis reveals some striping and high frequency noise in the sixth PC this is very minor, does not interfere with data analysis, and has not been treated.

4.2.2 Noise and mis-registration of wavelengths in the NS001 data

The NS001 data contain more noise than the TM data, but this has been successfully removed. Two types of noise were encountered in analysing the raw data, both the result of dropped pixels due either to faults in the instrument or corruption of the data whilst on tape. For each line of the raw 0.49 μm data from Flight Line 2 pixel 650 has a value of 252 DN, and this appears as an anomalously bright column in the image. As it occurs once per line, this is attributed to a cyclical fault in the machinery. It has been corrected by replacing the noisy column with the average of columns 649 and 651, on the principle that spatial changes in reflectance are likely to be gradual over a few pixels rather than sudden and isolated. The second type of noise consists of odd pixels or small groups of pixels along lines being set to an anomalous value. This is apparent in the imagery as short horizontal stripes or spots (Plate 4.1), and has been removed by a similar averaging process.

In addition to the noise described above the 0.49 μm data are mis-registered to the data for all other wavelengths by a fraction of a pixel, leading to a slight blur in colour composites involving this wavelength. This is thought to be due to a timing problem and has been reported elsewhere for TM data (Dwivedi, 1991). This mis-registration is important if unmixing and PC analysis are performed on the data, as for a given pixel different wavelength data will be covering different percentages of the mixed materials in question (M. Berman, personal communication). In this case no correction has been attempted as PC and unmixing analyses have not been performed on the NS001 data and visual distortion is minimal.

4.2.3 Noise in the GMS data

The GMS data contain much more noise than either the TM or NS001 data, particularly in the visible and near infrared wavelength regions. The noise in the GMS data can be split into striping and high frequency "salt and pepper" noise. The removal of this noise had to be addressed prior to the spectral processing of this data.

Many sensors have noise problems, and consequently there are a number of techniques available for noise removal. For example, Mackin (1989) found that data from the Airborne Imaging Spectrometer 1 scanner contained horizontal and vertical striping, random noise and data spikes and described algorithms designed to overcome these problems. Over the operational lifetime of an instrument these problems are commonly reduced, as has been the case with the AVIRIS sensor (Porter et al, 1990). It is to be hoped that this will be the case with the Geoscan Mk.II sensor, as noise renders the 0.522 μm data useless thus reducing to nine the effective number of bands in the visible and near infrared wavelength regions.

4.2.3.1 Striping

Horizontal striping between individual lines occurs in the raw data from bands centred on 0.74 μm, 0.83 μm, 0.873 μm and 0.915 μm. This is visually apparent as sudden changes in average brightness from one line or group of lines to the next. The initial approach to this problem involved collecting line means, and plotting a smooth curve through them. Any line means exhibiting a sudden change in brightness are data outliers to the mean curve, and have been adjusted to have the mean indicated by the curve. This process does not change the variance of the data, and was thus acceptable at this early stage of processing. Implementing this correction noticeably reduced striping, striping was still present to a lesser degree and a second correction was required.

A method of improving the correction has been developed at CSIRO which separates the signal from the noise so that subsequent attempts to remove the noise have minimum affect on the signal. Details are given in Green et al (1988). The noise is separated from the signal for each wavelength using a difference image created by

subtracting the data corrected as above from the same data translated by one line, one pixel or both. The signal is highly correlated between adjacent data points and is therefore the same in both these images. The noise is uncorrelated for adjacent data and so is different in each image. Each wavelength's difference image thus contains little of that wavelength's signal and the majority of that wavelength's noise.

The next step involves a technique developed for overcoming inter-wavelength correlation, known as principal component (PC) analysis. The mathematics of this widely-used technique are explained by Gillespie (1980) and Figure 4.1 is a graphical representation. If all the data for any two wavelengths are plotted on orthogonal axes, they will lie in an elliptical area. Information is correlated between the axes and the maximum variation lies along a new axis at an angle to both original axes, the principal axis of variation. A second axis exists orthogonal to the principal axis, describing the second largest amount of variation and having no correlation with the first. Each datum has a value obtained by projection onto these new axes, giving two new sets of values which have more variation than the original wavelength data values and are independent of each other. Each of these new sets of values for the data is known as a principal component (PC). In an extension of this technique, known as the decorrelation stretch (Gillespie et al, 1986), the data ellipse is linearly stretched so that the variance of PC2 is as great as that of PC1 and the data occupy the maximum space between the PC axes (Figure 4.2). Once this has been done the decorrelated data are projected back onto the original axes. For three bands, the spread of data becomes a "cloud", described by three PC axes. For n bands there are n PCs, all independent of each other, and the data can be stretched to occupy the maximum portion of the n-dimensional space .

If the noise has equal variance in all bands, an ordinary PC transformation will isolate the noise into a small number of the higher order components, as often is the case with TM data (Figure 4.3a). With aircraft data, however, the noise is often unequally distributed between bands, as has been described for the GMS data in this study. In this case a PC analysis does not produce sequential PCs with increasing noise. The CSIRO technique (Green et al, op. cit.) has been developed for this latter scenario. A PC transformation is performed on both the original image and the noise image to determine the distribution of the noise within the signal. The original image is then

decorrelation stretched so that all bands have the same noise variance (Figure 4.3b). PC analysis is then used to produce PCs with decreasing noise and increasing signal, known as maximum/minimum autocorrelation function (MAF) bands.

When the MAF process was applied to GMS data from Flight Line 5b, omitting the very noisy 0.522 μm data, the result was 12 MAF bands dominated by noise (e.g. MAF band 8, Plate 4.2) and 5 MAF bands dominated by signal. With data from Flight Line 6a, again omitting the noisy 0.522 μm data, the result was similar. Images of the noisy MAF bands show some striping still present in the data and so the de-striping process was repeated, but to more effect as the remaining noise had been isolated. Plate 4.3 shows MAF band 8 from Flight Line 5b after this re-run of the de-striping process. Comparison with Plate 4.2 shows that further removal of striping has been achieved.

4.2.3.2 High frequency noise

The techniques available for the removal of high frequency noise all involve the replacement of data values in pixels defined as noise. Noisy pixels are defined as those markedly darker or brighter than adjacent pixels; for example all pixels which differ from their neighbours by more than 10 DN. The replacement value could be the mean of the pixels in the chosen mask area, or some other real data value from those inside the mask. This flexibility allows the correction to be tailored to a particular problem. All these processes involve a reduction in the total volume of data, either by averaging where a mean is used as the replacement value or by duplication where a real data value is used. If the pixel to be replaced is entirely noise this does not matter, but if the pixel is a mixture of data and noise its replacement results in a reduction in the total data volume, which should be avoided. Techniques dealing with high frequency noise should therefore be applied to the noisy MAF bands, in which the noise has been isolated from the signal, rather than to the original data.

MAF band 8 from Flight Line 5b is shown in Plates 4.2 and 4.3. The high frequency noise is clear and was treated by passing a 3 x 3 box filter over the data which replaced noisy pixels with the median of the pixels in the mask. The result (Plate 4.4) shows that the high frequency noise has been subdued, but a smoothing effect is apparent on

comparison with Plate 4.3. The scene detail, however, varies on a longer frequency than that at which the smoothing has taken place and so the residual geological information in the MAF band has been preserved. High frequency noise in other MAF bands was also treated in this way.

After the noise was dealt with the inverse transformation was applied to restore the original bands. As shown in Plate 4.5 this process largely removed the noise. A difference image of the raw data minus the data cleaned using the MAF transformation, shown in Plate 4.6, illustrates the noise which has been removed and also demonstrates that minimal scene detail has been sacrificed. Plate 4.7 shows a second difference image of the data when cleaned in normal data space minus the data when cleaned by the same processes in conjunction with the MAF transformation. The second difference image contains noise, demonstrating that more noise has been removed in the latter case. It also contains scene detail, demonstrating that useful geological information has been removed by the application of the noise removal techniques before the isolation of the noise from the signal.

MAF bands from Flight Line 6a also contain high frequency noise. This was treated using a similar box filter, in this case designed to replace the noisy pixel with the mean of the mask, with similar results.

4.2.4 Conclusions

1. Noise is not apparent in the raw TM data. Even the application of techniques which highlight uncorrelated information reveals only minor noise not warranting treatment.

2. The raw NS001 data display "bad" pixels, lines or columns in no particular pattern. This noise is easily removed by simple averaging processes.

3. Extensive noise removal is required for all the visible and near infrared wavelengths of the GMS data, the 0.522 μm band of which contains almost no signal at all and cannot be used.

4. Extensive treatment of noise is more successful after its separation from the signal using the MAF process. This prevents the noise removal processes from having any detrimental affect on the geological information present in the data.

4.3 Radiometric correction

In this section, Equation 3.3 will be referred to frequently:

$$X_\lambda = E_\lambda t_\lambda A \rho_\lambda G_\lambda + a_\lambda G_\lambda + O_\lambda$$

All three radiance sensors used in this study produce data in the form of raw DN in the range 0-255. Radiometric correction involves the removal of the gain and offset factors G_λ and O_λ, purely attributable to the sensor under consideration, the atmospheric path radiance a_λ and atmospheric transmittance t_λ. It has been performed on these data sets because of the following benefits to the geological analysis of the data:

1. Discrimination of geological materials is enhanced if the influence of non-geological factors on the data is reduced.

2. Identification of particular minerals requires the DN values to be transformed into the meaningful physical parameter reflectance, allowing comparison between different data sets and sensors as well as with field and laboratory measurements. The retrieval of reflectance from the data first involves the retrieval of ground radiance.

4.3.1 Instrumental gain and offset

For each sensor, full use of the radiometric sensitivity of the instrument is achieved by setting an appropriate multiplicative gain factor, G_λ, and additive offset factor, O_λ, for each wavelength. Many variables influence the setting of these factors, from the nature of the terrain flown over to the radiometric sensitivity of the instrument at different wavelengths, and so these factors differ between instruments and different flights of the same instrument. They are non-geological factors and may mask the subtle geological

information which the data contain, particularly as they are wavelength dependent. They should be removed after noise has been treated.

4.3.2 Atmospheric effects

The second part of the additive component of the radiance measured at the sensor is due to the spectral radiance along the atmospheric path, a_λ. This radiance is caused by atmospheric particles scattering the source radiation, as described by Rayleigh's Law. This states that the degree of scattering is inversely proportional to the fourth power of the wavelength (Drury, 1987). The magnitude of the effect thus varies, being large in the visible and decreasing to almost nothing in the short wave infrared region of the spectrum. Reflectance features of interest to the geologist are often small and wavelength specific (Hunt, 1977) and the identification of these features is hindered if the data contain an additive component which varies with wavelength. Such a component will, for example, be a large distorting factor in any ratio of two wavelengths (Crippen, 1988). Equation 3.3 shows that omitting the correction for atmospheric path radiance will cause problems in any transformation to reflectance, where it is needed to model the physics involved.

The atmosphere also has a multiplicative effect, due to the spectral transmittance along the atmospheric path, t_λ. During its passage through the atmosphere, radiation interacts with water vapour, ozone and carbon dioxide by vibrational and rotational transitions which all cause energy to be absorbed (Drury, 1987). Fortunately between 0.4 μm and 2.5 μm atmospheric absorption is the dominant effect across only a small number of narrow wavelength ranges and the sensors studied here do not make measurements across these (Figure 4.4). At other wavelength ranges between 0.4 μm and 2.5 μm the effect merely reduces atmospheric transmittance by around 20 % (Drury, op. cit.), but this multiplicative effect should be removed during calibration to reflectance. This effect, which again varies with wavelength, is another distorting factor present in the data which could bias other processing techniques such as band ratioing and further mask the geological signal.

4.3.3 Removal of the gains, offsets and atmospheric effects

There are two possible approaches to the removal of gains, offsets and atmospheric effects; the use of known calibration values, or the calculation of the calibration values from the data themselves.

The gains and offsets may be known for the data under study, in which case they can be accurately removed. For the TM sensor, the gain and offset values at launch are known (Markham and Barker, 1986). The NS001 sensor records the gains and offsets at the time of the flight (Gabell et al, 1985) and an example of the calibration of this data is given in Hook (1989). If the gains and offsets are known, this is a straightforward correction.

The atmosphere may be modelled to compute its contribution via models such as LOWTRAN (e.g. Carrere, 1990). In principle this is a good approach, as it attempts to quantify the processes involved rather than simply correct for them. In practise, problems are numerous. Large amounts of data must be collected at the time of the flight or satellite overpass for input to the model, such as local pressure, temperature and humidity. If a local atmospheric profile is not routinely available this involves fieldwork with radiosondes and other instruments. The work of Kealy (1990), who used the LOWTRAN model with data from the Thermal Infrared Multispectral Scanner for an inland area in N.W. Australia, illustrates the problems involved. The nearest atmospheric profile available for the time of data acquisition was from a radiosonde 950 km from the field area, on the coast. Even if suitable atmospheric data exist, the atmosphere is not yet fully understood and modelling of its profile is incomplete.

If it is not possible to collect the atmospheric data required by the model, one alternative is to use a standard atmosphere as the input to the LOWTRAN model, modified where possible to suit the data and study area. As the atmospheric conditions at the time may not be known, however, it is difficult to know whether the standard atmosphere is appropriate for most data sets. Finally, with high spectral resolution sensors, such as Airborne Visible/Infrared Imaging Spectrometer (AVIRIS), it is possible to compute individual atmospheric effects from the data themselves using

absorptions around 1.4 and 1.9 μm due to atmospheric gases (Green, 1990). With data of the spectral resolution and coverage dealt with here this is not possible.

In this study the calibration values available were, to greater or lesser degree for each instrument, considered unreliable. Markham and Barker (op. cit.) have specified a 10 % uncertainty for the TM calibration values post-launch, and have described a known continuous change in gain while in orbit. Other TM studies have used calibration techniques which rely on the TM data alone for these same reasons (e.g. Hill and Sturm, 1991). In the case of the NS001 data, calibration values recorded at the time of the flight may no longer be reliable due to corruption of portions of the data. No calibration values are recorded for the GMS data. The radiance data sets used had been collected at an earlier date and local atmospheric data were not reliably known for any of the dates in question. Appropriate correction values have therefore been calculated from the data themselves.

Study of Equation 3.3 shows that the instrument offsets (O_λ) and the atmospheric path radiance (multiplied by the instrument gains - $a_\lambda G_\lambda$) can be considered as a gross additive component. The removal of this gross additive component leaves the atmospheric transmittance and the effect of the instrument gains on the rest of the radiance equation to be accounted for. These are both multiplicative effects, as are all remaining factors in the radiance equation. The gain and atmospheric transmittance are less significant distortions of the ground radiance than the additive atmospheric path radiance. They are more easily dealt with at the same time as the other multiplicative factors and will be considered for each of the data enhancements utilised in chapter 5.

4.3.4 Removal of the gross additive component

In theory, for a ground surface in full shadow E_λ is zero. A ground surface which absorbs or transmits all energy incident on it has ρ_λ equal to zero. For these cases, equation 3.3 reduces to:

$$X_\lambda = a_\lambda G_\lambda + O_\lambda \qquad (4.1)$$

Thus ground surfaces of any reflectance in full shadow, or under any illumination which reflect no light, have DN values purely attributable to the gross additive component. This could be dominated by effects such as atmospheric backscattering at shorter wavelengths, or by offset values at longer wavelengths where atmospheric effects are reduced. Once found for each wavelength, this gross additive component can simply be subtracted from the data.

Three methods were used to compute the gross additive component. These were the methods of Switzer et al (1981), Crippen (1987), and Chavez et al (1977). The first two are methods which rely on there being spectrally homogeneous areas with good topographic variation within them in the study area. They were developed for use in arid areas of the United States and it was thus of value to try them in the semi-arid conditions of Australia, with the increased vegetation providing a test of their wider application. The third method involves the data minima and requires less computation, but a lot of care in implementation. They all assume that the atmospheric profile does not vary significantly across the scene so that a_λ is constant for all pixels. Recent work has shown that this assumption may be invalid (R. Green, 1990), but the variation in a_λ over scenes of the size dealt with here should still be small. The techniques were tested on the TM data and only the most successful used on the NS001 and GMS data.

Additive component values purely attributable to atmospheric path radiance will approximate closely to the solar irradiation curve after its interaction with the atmosphere (Figure 4.4). Bearing in mind the contribution of any wavelength dependent instrument offset values, this provides a test of success for all these techniques.

4.3.4.1 The covariance matrix method

A pixel with zero illumination, or which reflects no energy, has a DN value at each wavelength representing the additive component at that wavelength. However, due to atmospheric scattering of diffuse radiation into areas in shadow (Figure 3.4) and the reflection of energy from bright surfaces into shadow, such a pixel rarely exists in practise. This has been noted for TM's 0.83 μm band in particular by Hill and Sturm (1991). The covariance matrix method (CMM) aims to find the gross additive

component statistically by regression from the data (Switzer et al, 1981). It requires there to be an area of homogeneous reflectance in the scene, such that all variation seen is due to differing illumination (Figure 4.5). The additive component for one wavelength is assumed to have some arbitrary value. The additive components for the remaining wavelengths are calculated by the simultaneous regression of all other bands against the chosen band in order to calculate their intercepts with the chosen band at the chosen value (Figure 4.6 shows the principle for two wavelengths).

For Landsat Multispectral Scanner data, Switzer et al (ibid.) chose zero as the arbitrary value in the band centred on 0.95 μm. For the Landsat TM data in this study, the arbitrary value was chosen for the 2.22 μm band, where the atmospheric effects are a minimum as given by Rayleigh's Law. Values used ranged from zero, chosen assuming no effect at that wavelength, through 3, the scene minimum for that wavelength, to 27, the scene minimum for that wavelength excluding lakes and the open cast pit (i.e. the darkest shadow). These values were tried with a 512 x 512 pixel area of low homogeneity as a control, and two areas of the Burstall Granite which appear homogeneous, one 173 x 61 pixels and the second 50 x 40 pixels.

The results are shown in Table 4.1. The closest approximation to the solar illumination curve was obtained by selecting 0 in band 7 using the smaller area of granite. These correction values, highlighted in the table, were acceptable except for the bands centred on 0.83 μm and 1.65 μm, which gave higher values than anticipated. High values at these two wavelengths are a common feature of the results and could be attributed to the presence in the shadows of green (0.83 μm) and dry (1.65 μm) vegetation, assuming instrument offsets do not vary with wavelength by that amount. These materials have a high reflectance at these wavelengths and may thus raise the radiance in shadow for these bands. The moderate vegetation cover present in most pixels prevents the selection of an area for the statistics which avoids this effect and so this method was not considered successful in this setting.

Although the vegetated nature of this semi-arid field area may prevent the success of the whole approach, it was felt that this warranted further investigation. As the same general approach lies behind Crippen's (op. cit.) method, but it removes the need to

arbitrarily select a value for the gross additive component at one wavelength, this method was implemented next.

4.3.4.2 The regression intersection method

Crippen (1987) also noted the necessity for data adjustments to correct atmospheric path radiance and sensor calibration offsets. To avoid arbitrarily choosing a gross additive value for one wavelength as in the CMM approach, he developed the regression intersection method (RIM). This relies on there being at least two areas of homogeneous material in the scene, preferably with a strong spectral contrast. The data from these areas are plotted for any two wavelengths, and a regression line drawn for each material (Figure 4.7). If they are truly homogeneous, the data for each will lie along a line ranging from the lightest pixel down to the darkest, as the only difference between each pixel should be its degree of shading. In the absence of the gross additive component the intersection point of these two lines would be at the origin, and thus represents the true location of data values corresponding to deep shade. The gross additive correction for the two wavelengths plotted is simply the offset from the origin of the intersection point on their respective axes. Once the intersection point is translated to the origin, a ratio of the two wavelengths for each homogeneous material will be constant, allowing their discrimination from each other. This process is then repeated for other wavelength pairs until a solution has been determined for all.

The results from the application of this technique to the TM data were poor. For all areas selected, the distribution of data on a two-wavelength plot showed that, despite the areas each containing only one rock type, they are not homogeneous. An example is shown in Figure 4.8. The data plot within broad, elliptical areas, and any regression lines are therefore very poorly constrained. In this and most other cases infrared wavelengths have larger computed additive component values than the visible wavelengths. This is the reverse of the pattern expected due to the atmospheric radiance, which diminishes at higher wavelengths as Rayleigh scattering declines. Although instrument offset values may differ between wavelengths, they are not likely to vary enough to be the cause of this effect.

The failure of this technique is attributed to the non-homogeneity of single surface materials, caused by the ubiquitous moderate vegetation cover. On the two-wavelength plots, the principal axis of variation for a given area results from changes in illumination due to shading, but there is a second axis orthogonal to this, probably due to the varying amounts of vegetation in a pixel. Any regressions are poorly constrained because of this spread of data. This can also cause the data fields for two different surface materials to overlap, giving even less constraint to any intersection. A small change in the angle of a regression line leads to a much larger change in the value of the gross additive component indicated by that regression. The RIM was less successful than the CMM, probably because of the requirement for two homogeneous surface materials rather than one.

Whilst in principle Crippen's (1987) method finds the gross additive component from the data themselves, with no assumptions, its satisfactory execution is unlikely in environments where significant mixing of surface cover types occurs. It is more suited to the arid environments previously studied. In this semi-arid environment a small but significant amount of vegetation is present in almost all pixels. The values for the gross additive component produced by this technique do not closely approximate the solar irradiation curve and so were not utilised in this study.

4.3.4.3 The histogram minimum method

Described by Chavez et al (1977), the histogram minimum method (HMM) is simple in principle, but requires care in application, as several pitfalls exist. It is based on the assumption that a pixel which is in complete shade or has zero reflectance does exist somewhere in the scene. In the absence of the gross additive component such a pixel would thus register zero DN and thus that pixel's actual DN values are attributable to the gross additive component and give the desired correction value. When such a pixel is found its reliability must be checked in the image, as reliance on values from any one pixel is dangerous. The selected pixel could represent noise. A visual check, coupled with background knowledge about expected values for the area in question, should be enough to detect such pixels. The pixel could also come from an area such as the open cast pit or its slag tips. Whilst such areas contain low reflectance materials such as

water, and also large amounts of shade, they may also contain other low reflectance material associated with mining activities, such as black plastic. It is difficult to be certain of the reason for a low DN value, so such areas are best omitted from any statistics.

With the TM data, scene minima have been found for two cases, one omitting Lake Corella and the other including it. Inspection of the image showed that correction values found represent shadow (no illumination) and water (low reflectance) respectively, allowing a comparison to be made. Figure 4.9 shows the values of the additive component at each wavelength for these two cases. The qualitative fit of the values from shadow to the solar irradiation curve is poor, showing that significant diffuse radiation enters shadowed areas. In contrast, the qualitative fit of the Lake Corella values to the solar irradiation curve is good. The lake is a large water supply reservoir in the south of the area with still, deep and relatively clean water. The reflectance of water is shown in Figure 4.10 (Mather, 1987). At longer wavelengths water has zero reflectance and is therefore a suitable dark object. It must be noted that water is not so suitable as a dark target in the visible wavelengths. Despite this, the correction values calculated are better than those calculated by the CMM and RIM techniques. A correction for the gross additive component was therefore performed by subtracting the scene minima values for each wavelength, all from Lake Corella, from all data at that wavelength.

The use of the same technique on the NS001 data provided a useful opportunity to test the validity of deriving the gross additive component from the water scene minima. Flight Line 3 passes over the lake, but the Flight Line 2 does not, allowing the choice of a correction for the gross additive component based on Lake Corella to be further tested. For Flight Line 3, the minima are all from pixels in the lake except for the two shortest wavelength bands, where the water values are just 2 and 4 DN higher than the minima. Once again, the values give a good approximation to the solar illumination curve when plotted against wavelength (Figure 4.11). The Flight Line 2 minima all lie in shadow and as predicted from the work with TM are consistently higher, by up to 5 DN, than those for Flight Line 3, though they still approximate the solar irradiation curve in shape (Figure 4.11). Correction for the gross additive component was again

performed by the subtraction of the flight line minima values at each wavelength from the rest of the flight line's data at that wavelength.

The GMS data were supplied unprocessed, but pre-processing had been done on the data during the flight. In theory this sensor's gains and offsets are set in a dummy run over similar terrain to the prospective flight line such that the brightest object registers 255 DN and the darkest 0 DN, the mean for each wavelength is 128 DN and the available data range is fully used (Windeler and Lyon, 1991). The gains and offsets may thus compensate for the atmospheric path radiance and effectively correct the gross additive components, as stated by Windeler and Lyon (ibid.). Analysis of the statistics for both Flight Line 5b and Flight Line 6a revealed minima of zero at all wavelengths, located either in Lake Corella or in billabongs in the dry creeks. No additive correction has been performed on this data set as it appears to be unnecessary, although there is no way of knowing for certain if this is the case. The offsets could have been set such that the atmospheric path radiance is in fact over-compensated. The only possibility which can be excluded is that of under-compensation, as this would lead to values greater than zero within Lake Corella. Other GMS data sets may not be so well calibrated, as other workers have found (J. Huntington, personal communication). If this is the case, some type of correction for the offset and additive atmospheric component will still be required, in which case all that has been discussed for the TM and NS001 data would also apply to this instrument's data.

4.3.5 Discussion

The gross additive correction for the NS001 data is significantly higher than for the TM data, despite the smaller amount of atmosphere through which light must pass in order to reach the sensor (8 km rather than 1410 km). This may be due to higher offset settings for the NS001 data, but could also be due to different atmospheric conditions prevailing at the time. The conditions for the TM overpass are not known but it was after the wet season and before the dry winter. The NS001 flights were at the end of the dry season and before the start of the wet season, when bush fires are most common, and atmospheric conditions are described in the flight log as "hazy". There

is also visual evidence of fresh fire scars in the imagery. A higher atmospheric path radiance at this time is not unexpected.

The Lake Corella DN minima values from Flight Line 3 are lower than the deep shadow DN minima values from Flight Line 2. As the two lines were acquired within 15 minutes of each other under almost identical atmospheric conditions, this is unlikely to reflect a real change in the atmospheric path radiance portion of the gross additive component. On sequential flights over similar terrain offsets should be unchanged. The difference in the gross additive component found for the two flight lines demonstrates that minima values from deep shadow are not as valid an approximation to this component as those from still, deep, clear water.

4.3.6 Conclusions

1. In the absence of reliable calibration data and an atmospheric profile, the gross additive component must be calculated from the data themselves.

2. The approach taken to calculating the gross additive component in the CMM and RIM techniques is unsuccessful for this area, and is likely to be so for other semi-arid areas. The ubiquitous moderate vegetation cover means that the required homogeneous reflectance surfaces cannot be found within the image. The CMM is more successful than the RIM, however, as only one homogeneous surface is required for the former as opposed to two for the latter.

3. The gross additive component must be estimated from the scene minima, with care taken to check which material is responsible for these minima.

4. Where a body of still, deep, clear water exists it represents the best material from which to estimate the gross additive component, being a very low reflectance material.

5. The close approximation of the gross additive component found using scene minima to the solar irradiation curve suggests that the atmospheric path radiance

forms the majority of the gross additive component and offset differences between wavelengths are small.

6. In scenes with no such water body the shadow minima values which are utilised instead may provide a poor estimation of the gross additive component. Even the most complete shadow must have diffuse light scattered in and light from adjacent bright surfaces reflected in, which it will in turn reflect.

As this study concerns the use of these data for geological purposes and the additive correction based on scene minima worked well, this was implemented. A large amount of time could not be dedicated to finding another approach for cases where no bodies of water exist. The very fact that no water body exists would suggest that arid conditions prevail and that the techniques of Crippen (op. cit.) and Switzer et al (op. cit) may be applicable.

4.4 Cross-track shading

One of the major problems afflicting imagery acquired by aircraft-borne sensors is that the measured radiance varies as a function of the across-track position. This effect is related to the sun's position in the sky relative to the flight line in question and the variation in view angle at different across-track positions. It has been documented in the past and various causes and corrections proposed (Kimes, 1983; Hook, 1989). For TM data the variation in view angle is so small that no noticeable effect occurs. For the NS001 sensor the view angle varies by 50° on each side of nadir and there is a systematic across-track change in the measured radiance. The effect has been corrected in this study because:

1. The visual effect produced by cross-track shading in an image impairs the delineation of geological boundaries.

2. These non-geological radiance variations make comparison of radiance, or the reflectance derived from it, impossible between different parts of the image.

4.4.1 Background to the problem

For particulate soils backscatter is strong and forward scatter is weak (Kimes, 1983). For a flight line with the sun shining parallel to the flight direction, the measured radiance is a maximum for the central pixel. This is because the strong backscatter of the exposed particulate soil or rough rock surface is directed towards the sensor (Figure 4.12). Moving towards the edges of the swath the number of surfaces producing backscatter directed towards the sensor decreases, leading to a decrease in the measured radiance. This effect is not related to the shade component in this case, which does not systematically vary across swath. The position of maximum measured radiance (the central pixel in the above case) is known as the antisolar point. As the position of the sun moves to one side of the swath, the antisolar point moves to the other side, at the point where the view angle is the same as the illumination angle (Figure 4.13). In addition, the proportion of the shade component seen by the sensor now varies across the swath, such that no shade is seen at or beyond the antisolar point and an increasing amount of shade is seen moving from the antisolar point towards the sunward side.

The mean for each column will ideally be composed of all spectral responses and thus represent the average column brightness. The cross-track shading effect can thus be displayed graphically via a plot of column means against cross-track position (Figure 4.14). Methods for the removal of cross-track shading rely on this plot. The column means are not always reliable, however, especially if the strike of the geology is parallel to the flight line and the mean is thus dominated by one spectral response. This leads to several complications when attempting a correction. NS001 E-W Flight Line 2 cuts across a mixture of lithologies striking N-S but the strike swings towards E-W in the south of the field area and the more southerly E-W Flight Line 3 therefore covers many lithologies striking sub-parallel to the flight line. This allows the correction techniques to be fully evaluated with these data. Additional problems due to the atmospheric path radiance have also been found which have not previously been documented, and these are described below.

4.4.2 Correcting cross-track shading in NS001 data

For the NS001 data the flight lines were E-W, the season was spring and the time was 1300 hours. The sun was at a position to the north of the flight line (the solar azimuth). The angle its illumination made with the ground (the solar zenith) can be calculated from appropriate tables. This solar position and image geometry mean that there is a pronounced cross-track shading effect in both of the NS001 flight lines studied, as can clearly be seen in any colour composite image (Plate 4.8).

Two methods of correction making use of the column means have been tested on the NS001 data. The first involves normalising all column means to the central column mean on the assumption that this represents the correct average radiance for the scene. The means are collected avoiding anomalous areas such as the mine dumps. These areas are often very bright or very dark and thus bias the column means, leading to over or under-correction apparent as vertical banding in the image for affected columns. This technique worked quite well when applied to Flight Line 2 but less well when applied to Flight Line 3. In the latter case geology, such as the Wakeful Metabasalt, which is sub-parallel to the direction of flight causes bias in the column means, thus leading to banding.

The second method involves fitting a smooth curve through the column means to avoid any that are biased (Irons and Labovitz, 1982). The curve used is a Tchebychev Polynomial (Figure 4.15), whose degree can be varied to best fit the data. In practise the choice of polynomial degree involves a compromise between choosing an order high enough to be a good fit to the data and one low enough to provide a good average across biased column means. For Flight Line 2 the best fit to the column means plot is a 4th degree polynomial (Figure 4.16) and the improvement in results when applying this and a 3rd order polynomial are shown in Plate 4.9. The calculations avoided mine dumps and areas of yaw-induced anomalies (see chapter 6). A good test of the technique's success is the calculation of band ratios, which highlight any banding present. As no banding was seen in the ratio image the correction was accepted. This technique also allows for an off-centre antisolar point, rather than always normalising to the centre column.

The correction was not so successful when applied to Flight Line 3, which covers too many areas of sub-parallel geology. Enough column means contain bias for this bias to be reflected in the fitted polynomial. If the column means are collected using all lines, omitting only those from anomalous areas (Figure 4.17), they must reflect the geology and the resultant image has banding. If the areas of sub-parallel lithologies are omitted from the mean calculation there is an improvement but some problems remain (Plate 4.8, Figure 4.18). If more areas of problem geology are omitted, there comes a point at which the column means are collected from so few lines that they are inevitably biased and become irrelevant. Using only 25 % of the lines in the image to calculate the column means reduces the influence of the geology but there is still banding in the resultant image. A difference image produced from corrected data minus uncorrected can be calculated to demonstrate the correction which has been applied. Plate 4.10 shows this difference image, which still contains scene detail when it should only contain shading.

The above problems might be avoided by using the column mean curve smoothed with a moving filter (S. Fraser, personal communication). This smoothing process would, however, be prone to the same dilemma as that involved in the selection of the correct degree polynomial, in that a large filter would over-smooth the curve and a small filter would fail to remove the bias from individual column means.

Data outliers due to anomalies such as mine dumps could be avoided automatically by using column modes rather than means, but modes are more difficult to calculate and would still be prone to bias from sub-parallel geology.

The flaws inherent in techniques to remove cross-track shading are in the approach itself, rather than in any one method. No attempt is made to model the physics of the system in fitting the curve but despite this the results are acceptable. The prospects for improvement lie in modelling the processes taking place, but the improvements are unlikely to justify the extra processing steps.

4.4.3 Information contained in the column mean plot

It may be possible to isolate the contribution to the cross-track shading of each of the processes described in section 4.4.1. This would allow the physics involved to be modelled, and has been investigated for the NS001 data.

Using astronomical tables the solar zenith was found to be 14.9° for Flight Line 2 and 17.2° for Flight Line 3. The antisolar point was calculated by trigonometry to be pixel 371 for the former and pixel 353 for the latter, on the assumption that the sun was due north giving an azimuth of 360°. For lower solar azimuths the antisolar point moves back towards the centre of the swath until an azimuth of 270° when the antisolar point is the centre pixel for an E-W flight line. The solar azimuth was found to be 324° for Flight Line 2 and 314° for Flight Line 3, and so the true antisolar point lies somewhere between the calculated position and the centre of the swath. It is difficult to measure the actual antisolar point from the column mean plots to the accuracy possible by calculation because the radiance peak is broad (Figures 4.14 and 4.18).

The relationship between azimuth and antisolar position for Flight Line 2 is shown in Figure 4.19. For the longer wavelengths, the observed antisolar point plots on a line joining the antisolar points calculated for orthogonal (360°) and parallel (270°) sun angles. Where the atmospheric contribution is minimal, the relationship is governed by geometry alone and is linear. The antisolar point varies systematically with wavelength, however, being further from the centre of the swath for the shorter wavelengths (see also Figure 4.14 and Figure 4.18). This movement of the antisolar point away from the centre of the swath for the short wavelengths is attributed to the increased thickness of atmosphere between the target and the sensor as the look angle increases towards the swath edge (Figure 4.12). The increased atmospheric thickness will in turn increase the atmospheric path radiance towards the swath edge and this increased radiance is thought to compensate for the usual fall-off in radiance moving towards the swath edge. The position of maximum measured radiance thus moves towards the edge of the swath. This effect may also be responsible for an upturn at the edges of the column mean curve observed for the shorter wavelengths alone (Figures 4.14 and 4.18).

Cross-track shading thus combines at least a shade and backscatter effect due to the sun/sensor geometry and an atmospheric effect due to the changes in the magnitude of the atmospheric path radiance with varying view angle. Analysis of the column mean curves suggest that these effects can be isolated. For example, the atmospheric effects could be isolated by dividing each wavelength's curve by that for the longest wavelength with minimum path radiance, this effect being corrected before that due to the sun/sensor geometry is dealt with. The antisolar position measured from the data, if found to be reasonable by comparison with that calculated from astronomical tables, could be used to constrain the cross-track position of the maximum for any fitted curve so that the curve models the physics as well as fitting the data. In practise, however, further processing steps would be added to make only a minor improvement in the correction applied in all but the most extreme examples. This study sets out to produce geologically useful products rapidly as is often the requirement in industry. If this type of data is to be widely used, the corrections implemented must be kept to a minimum. The fitted 4th degree polynomial-based correction is adequate (Plate 4.8), even where there is geology striking parallel to the flight line, and has been implemented for both flight lines. Investigation of cross-track shading and its correction continues with the GMS data.

4.4.4 Cross-track shading in the GMS data

The GMS flight lines run N-S, and were acquired close to midday in early summer. Cross-track variation in brightness is thus not as obvious as for the NS001 data. The effect is still present, however, and requires investigation.

In order to avoid geological detail causing bias in the column means a further refinement of the process described in section 4.4.2 was introduced for the GMS data. Before the cross-track shading effect was corrected in the GMS data it was separated from the geological signal using the modified PC transformation, MAF, previously implemented during noise removal (Green et al, 1988). This approach was used with the GMS data only, rather than the NS001 data, so that the time involved in investigating cross-track shading was spread more evenly between data sets.

In the north of the field area, where the geology commonly strikes N-S, the N-S GMS flight lines are parallel to the geological strike. The MAF process separates high frequency variation from low frequency variation. Across a flight line, the geology may vary on a scale of tens of lines to hundreds of lines but the cross-track shading varies on an even lower frequency, being a smooth variation over the entire swath. The cross-track shading should therefore be concentrated in the last, lowest frequency MAF band and images produced from the MAF bands for each flight line show that the effect is indeed isolated in MAF band 17 (only GMS bands 2-18 have been used in this study, so only 17 PCs are produced). It has been removed using a 3rd degree polynomial, applied to MAF band 17, prior to inverting the MAF transformation. A difference image of a raw band (0.583 μm) minus the same band after correction demonstrates that significant shading has been removed even though it was not obviously present in the raw data (Plate 4.11). It is also apparent in this image that in addition high frequency noise and striping have been removed by processing in MAF space, as described in section 4.3.2., and that the geological signal has not been affected.

The cross-track shading effect, as isolated in MAF band 17, represents a linear combination of the shading effect at all wavelengths. Once the total effect has been treated the shading component for each wavelength is removed and is thus not restored to the original data by the inverse MAF transformation. This is reasonable if the only thing which varies with wavelength is the **magnitude** of the effect. The increase in the effect at swath edges in the lower wavelengths however, observed with the NS001 data, shows that the **nature** of the effect may also vary with wavelength. It is not known whether this would stop the gross cross-track shading effect being isolated with the MAF transformation into a single band. Where the total cross-track shading is a combination of several different effects, each of these may be isolated into a different MAF band.

4.4.5 Conclusions

1. Correction of the cross-track shading effect, by normalisation of image radiance to the centre column, is prone to bias from geology if this strikes parallel to the flight line. It also ignores the sun/sensor geometry.

2. Replacement of the column mean profile with a fitted polynomial provides a partial solution, but in the more extreme cases problems due to geology remain.

3. This problem can be avoided if the cross-track shading effect is separated from the geological signal, using the MAF process, before it is treated.

4. The gross cross-track shading effect is a composite of at least two effects, one due to the changing proportions of shade and reflected energy at different view angles and the other due to the increased length of the atmospheric path as the view angle increases. These effects can be both seen in the column mean plot.

4.5 Summary

Noise is a significant problem only in the GMS data, where its presence is enough to hinder geological analysis. Treatment improves this imagery significantly, especially when the signal is first separated from the noise by the MAF process, but noise remains a problem in the visible and near infrared wavelength regions.

Radiometric correction is performed using values from the data themselves, due to the absence of reliable calibration data, simultaneous field measurements or atmospheric data. There are two sets of factors which must be considered, those due to the instrumentation and those due to the atmosphere. The offsets and the additive atmospheric path radiance can be treated as a gross additive effect, calculated, and removed by subtraction. The gross additive component can be calculated in a number of ways, but those which rely on the presence in the scene of areas of homogeneous reflectance are unsuccessful for these data sets. This is because the ubiquitous presence of moderate vegetation cover in this semi-arid area causes all surfaces to be spectrally inhomogeneous mixtures of rock, soil and vegetation. The only alternative is to use values based on the darkest pixels in the scene. For this area, this approach works well as there is a body of still, clear, deep water which forms a good low reflectance material. Plots of these water values for the gross additive component against wavelength are a good fit to the sun's irradiance curve. Comparison of values from

water with those from the darkest shadow demonstrates that a correction based on the latter is less likely to be accurate as even deep shadow receives diffuse radiation. Shade-based corrections should be avoided if possible.

The radiance varies with across-track position, causing difficulties in analysis of the data where this effect is strong. This effect may be removed as part of the radiometric correction by normalising the data using the column mean curve, or a polynomial fitted to this. The MAF process can be used to separate this effect from the data prior to their treatment and overcome problems caused by geological bias in the column mean curves.

The gain and the atmospheric transmittance are multiplicative factors, as are all those that remain after radiometric correction. These multiplicative factors are removed as a consequence of a later data enhancement, covered in chapter 5.

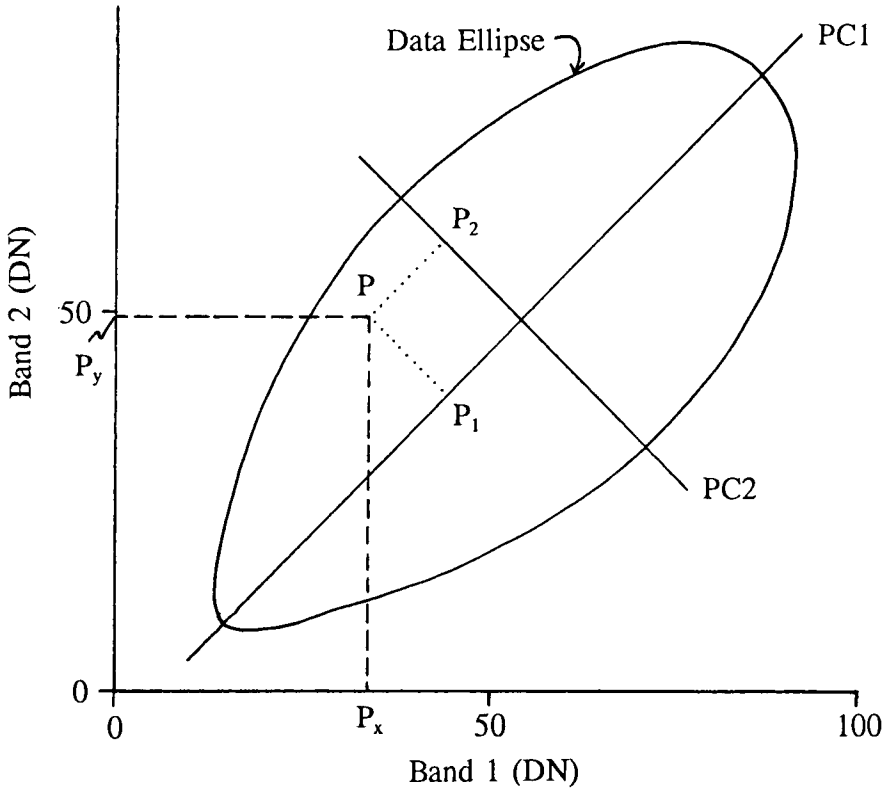

Figure 4.1 Principal component analysis for two bands. Point P, whose data values in band 1 and band 2 were P_x and P_y, has a value of P_1 on axis PC1 and P_2 on axis PC2.

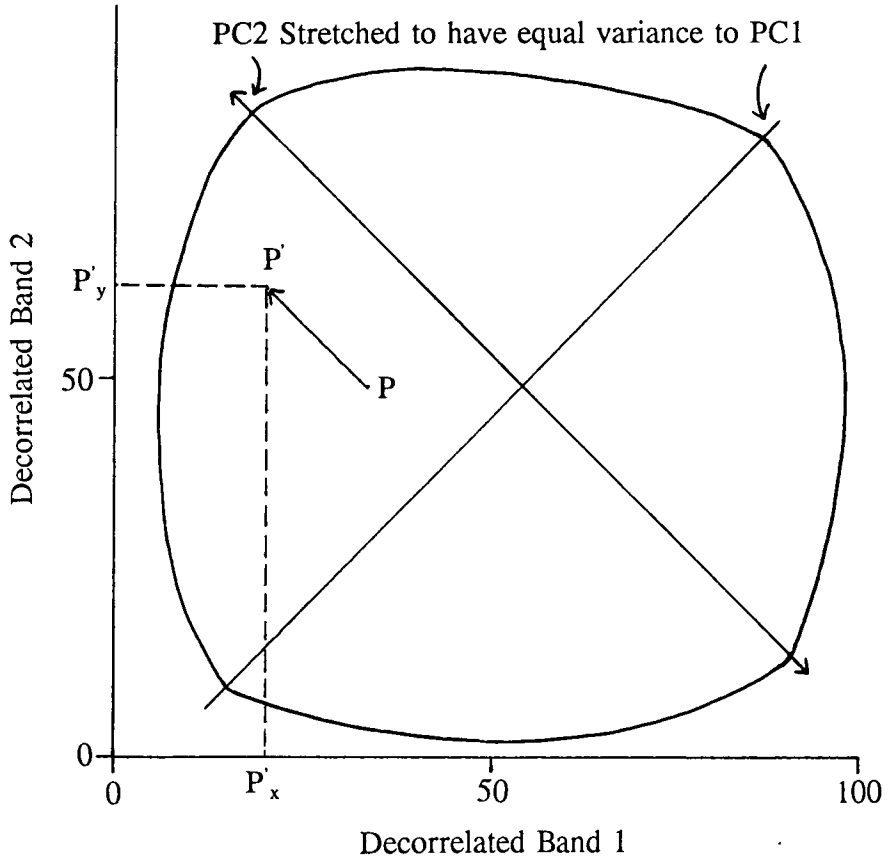

Figure 4.2 Decorrelation stretch for two bands. The point P is translated to the point P', and has new values of P'_x in band 1 and P'_y in band 2. For point P, the relationship between the two wavelengths has changed. A point at the intersection of PC1 and PC2 is not translated at all under this transform and retains its original data values.

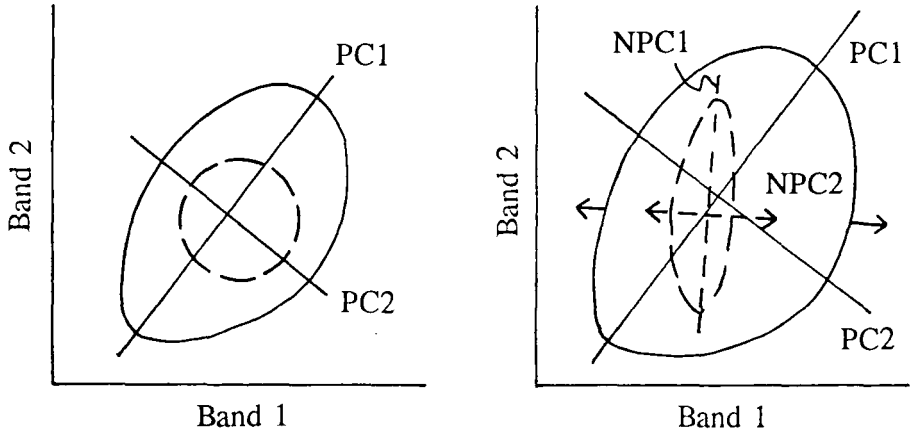

Figure 4.3 The MAF transform. a) Noise (dashed line) has equal variance at all wavelengths. b) Majority of noise is in band 2 and PC analysis of the data would lead to noise in both PCs. The distribution of the noise is found by performing a PC analysis on the noise image to give NPC1 and NPC2. The data are then stretched along NPC2 so that the noise has equal variance in each band, as in a). A PC analysis of the stretched data is then performed to produce one PC with the majority of the noise (PC2 in a)) and one comparatively noise-free PC (PC1 in a)).

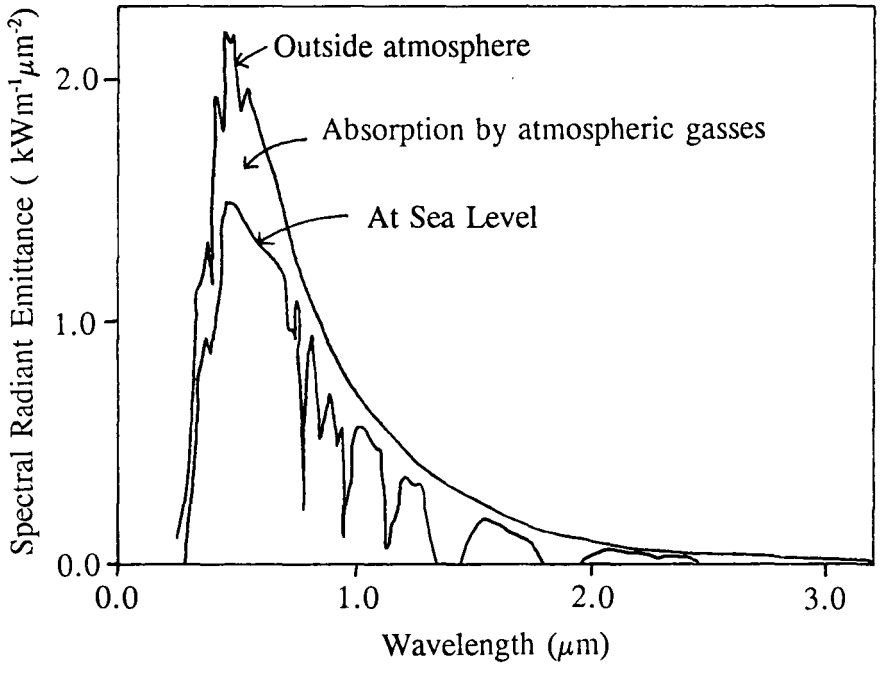

Figure 4.4 Radiance of the sun outside the atmosphere and at sea-level to show how much incoming radiation the atmosphere absorbs (after Lillesand and Kiefer, 1987).

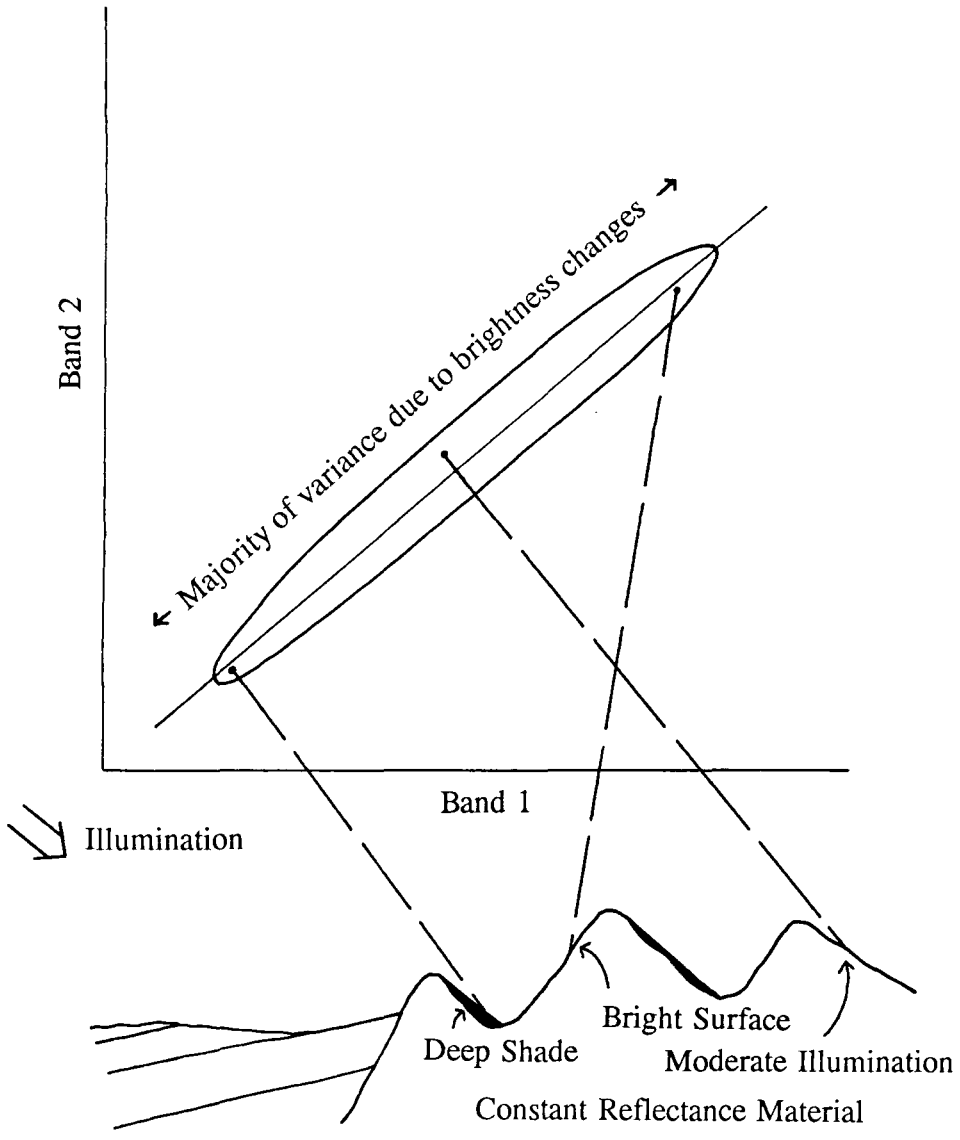

Figure 4.5 Required conditions for calculation of the additive component by the CMM.

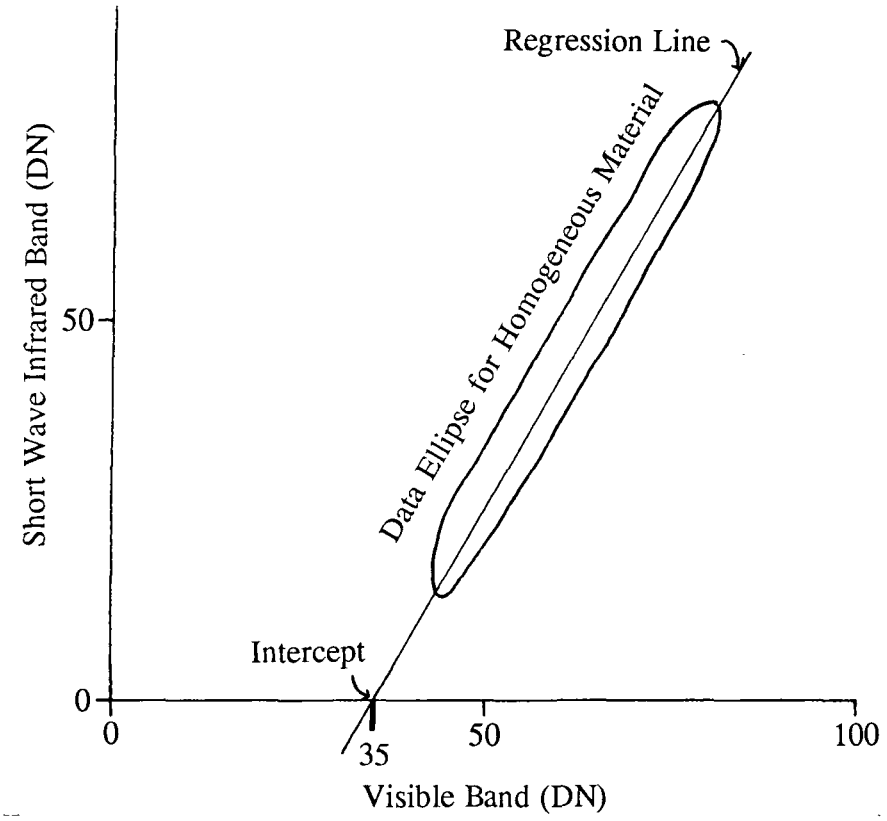

Figure 4.6 The principle behind the CMM. The additive component in a short wave infrared band is assumed (0 here) and the correction value for a visible/near infrared band (35 here) is given by the intercept of the regression line and the line y = 0.

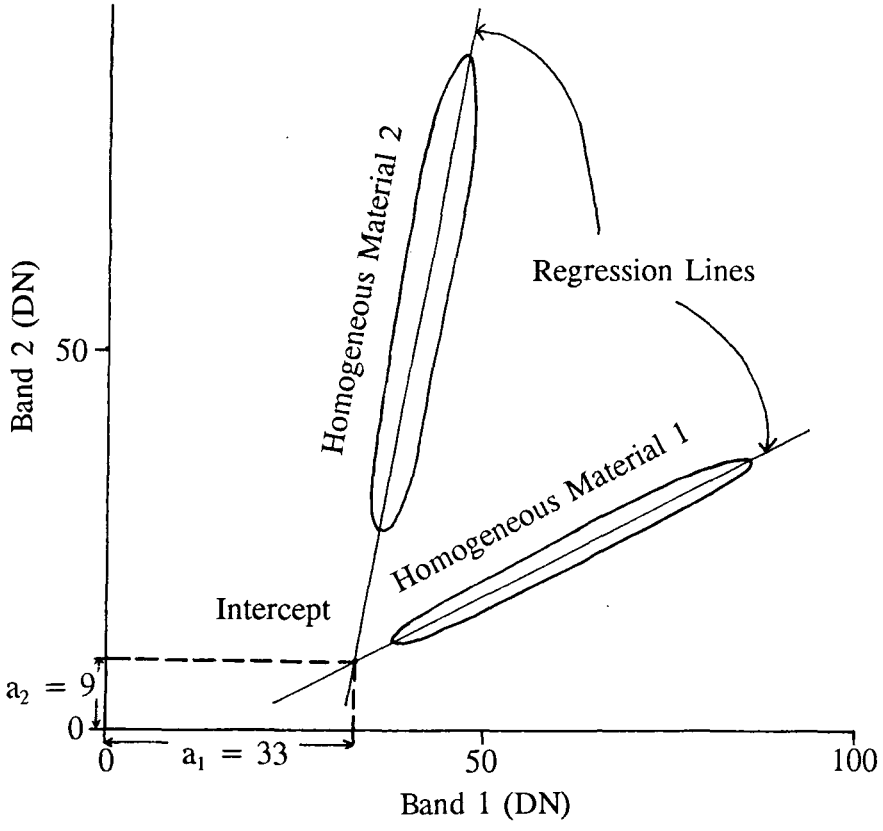

Figure 4.7 The principle behind the RIM. No values need be assumed because two homogeneous materials are used and the value of the regression lines' intercept is read off each axis to give an additive component of 33 for band 1 and 9 for band 2.

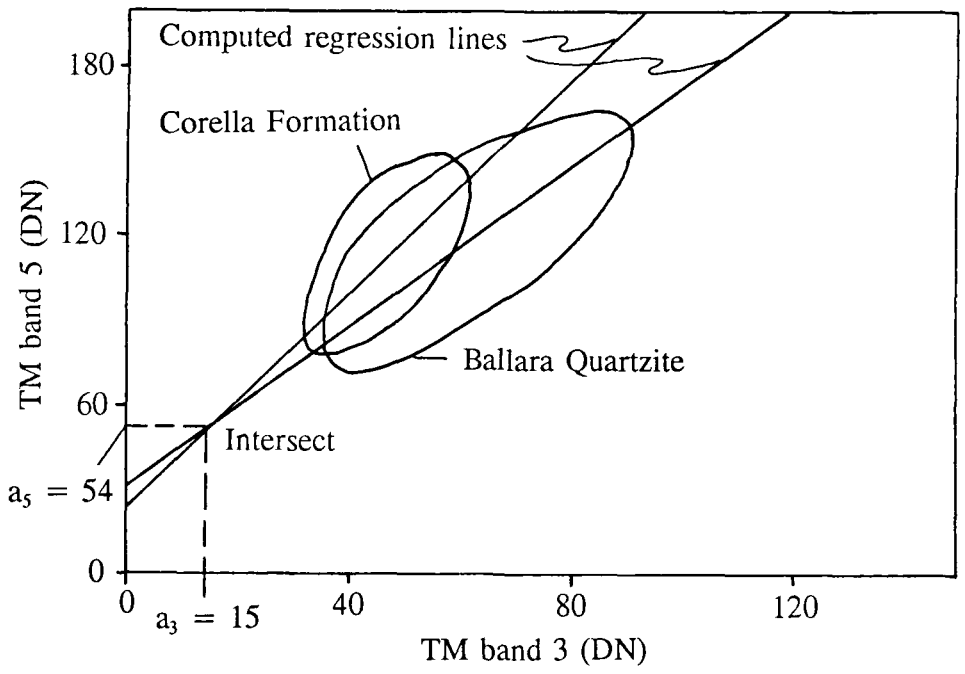

Figure 4.8 An example of the application of the RIM to this TM data, using two apparently homogeneous lithologies. The correction values obtained are larger for the short wave infrared band than for the visible band, the reverse of what is expected.

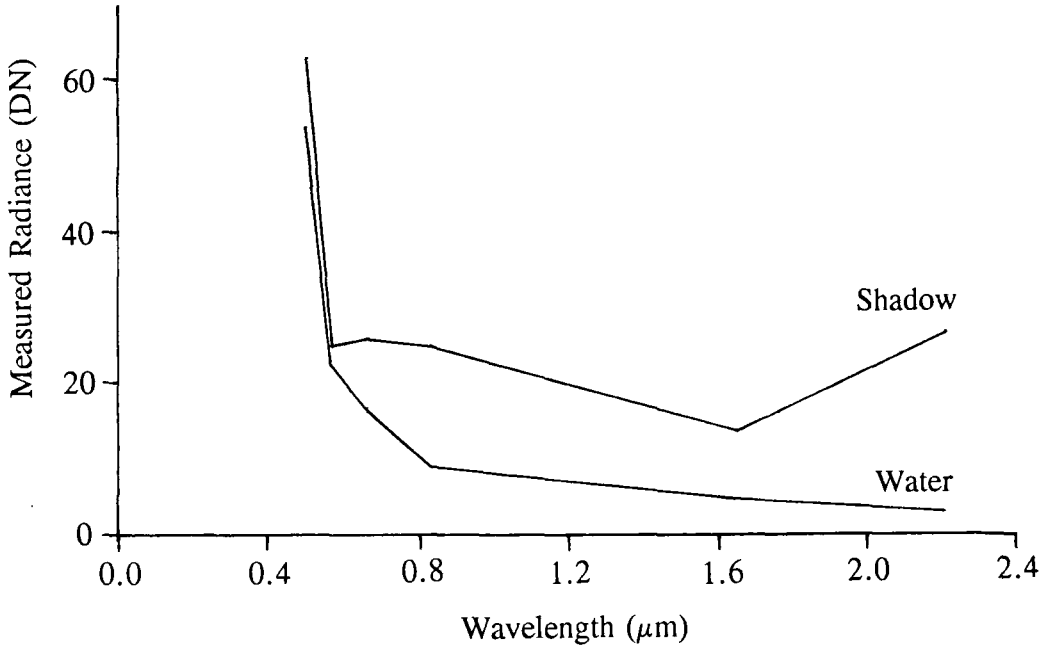

Figure 4.9 HMM additive correction values for the TM data.

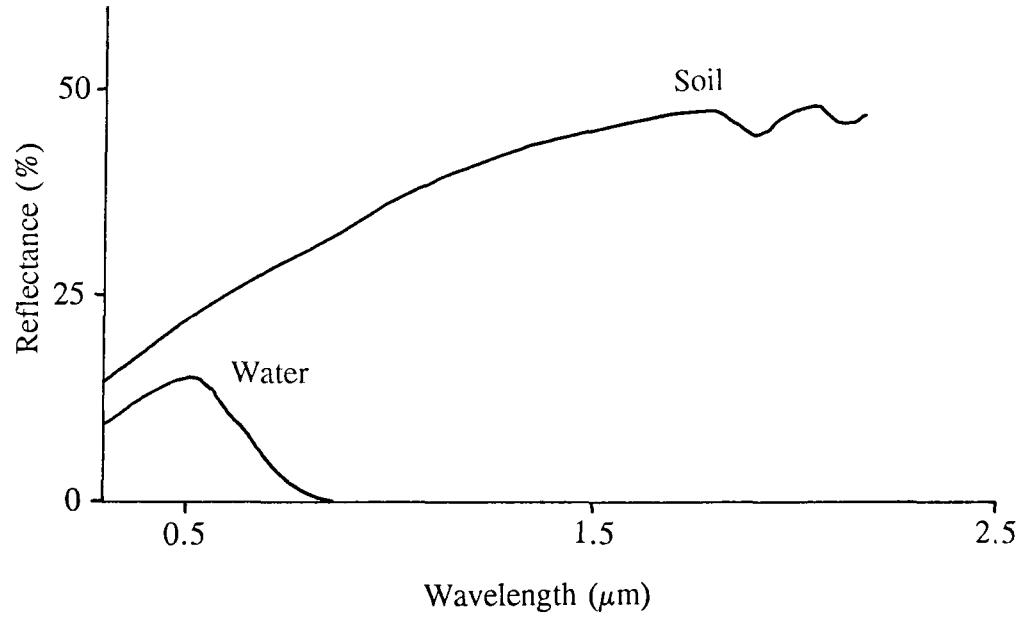

Figure 4.10 The typical reflectance of water and soil (after Mather, 1987).

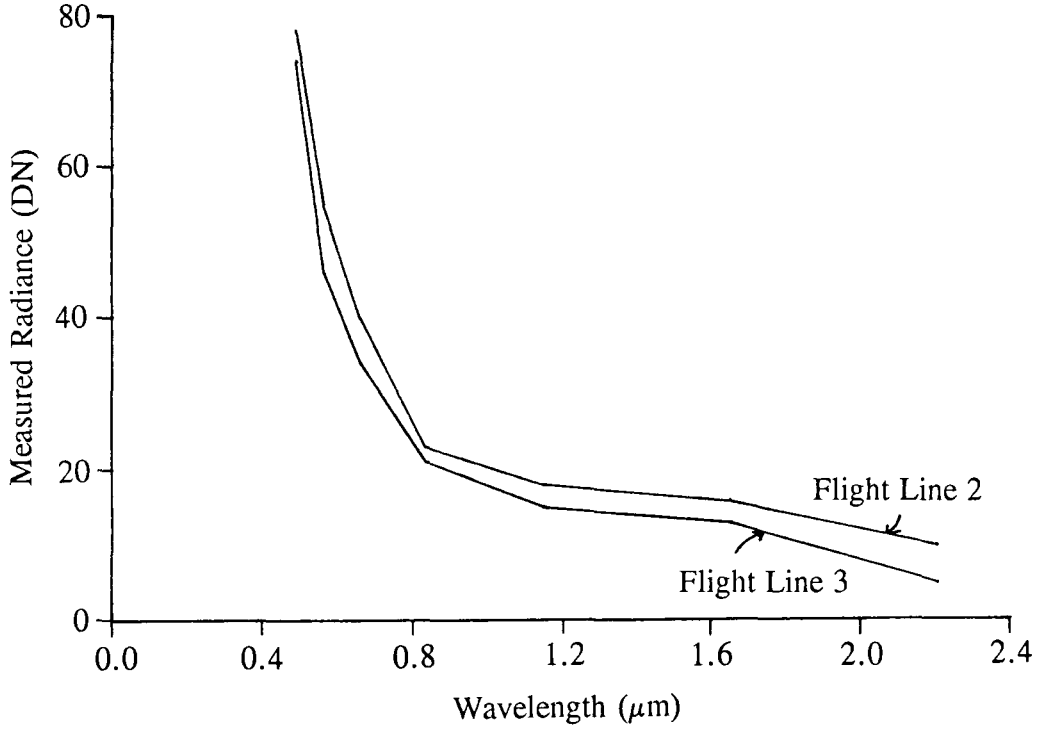

Figure 4.11 HMM additive correction values for the NS001 data.

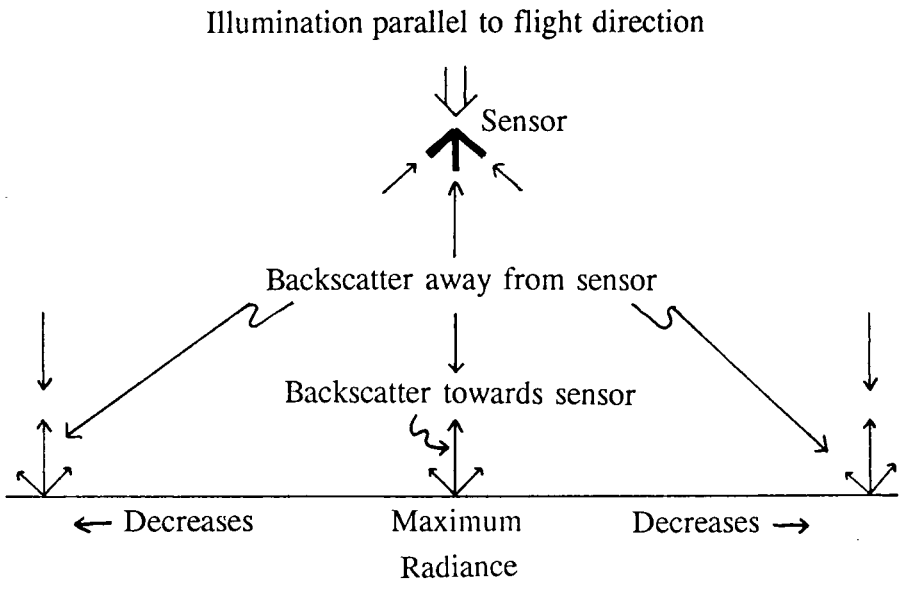

Figure 4.12 The effects of look angle on the radiance measured at the sensor.

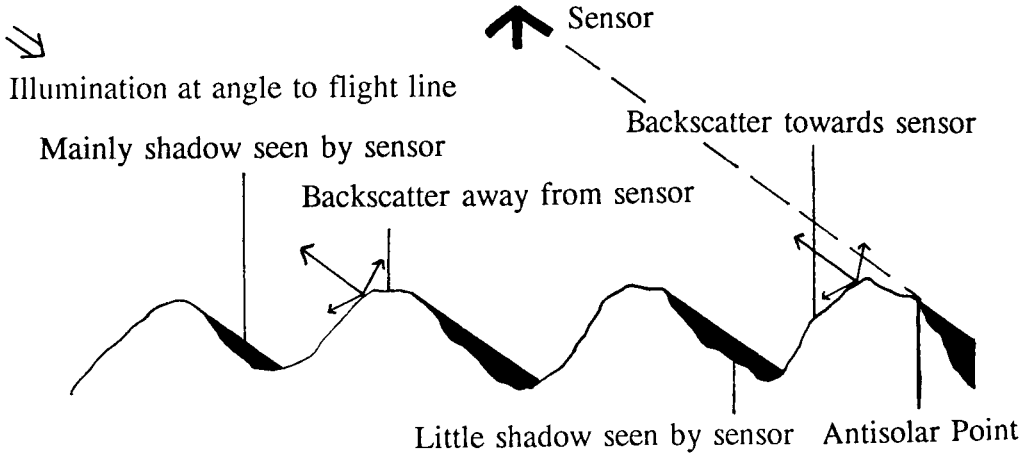

Figure 4.13 The effects of look angle and solar position on the radiance measured at the sensor.

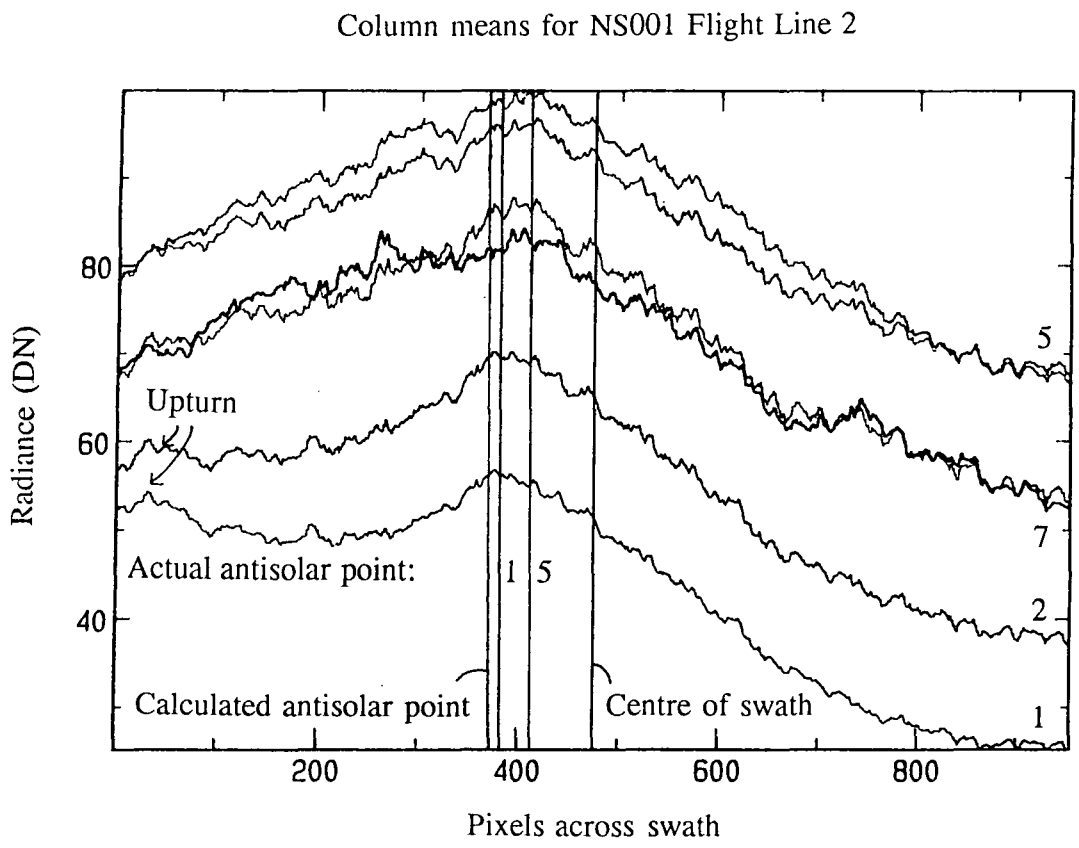

Figure 4.14 Column means for NS001 Flight Line 2, illustrating the effects of cross-track shading for this sun/sensor geometry. Numbers indicate particular bands.

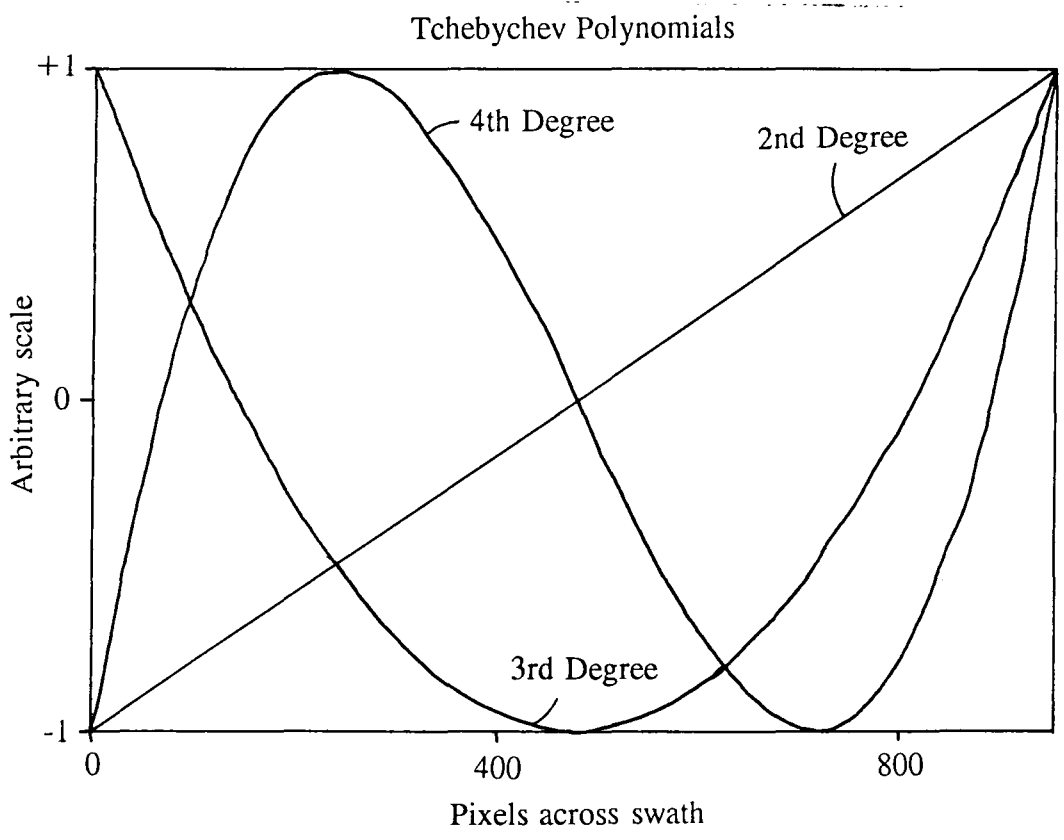

Figure 4.15 2nd, 3rd and 4th order Tchebychev polynomials.

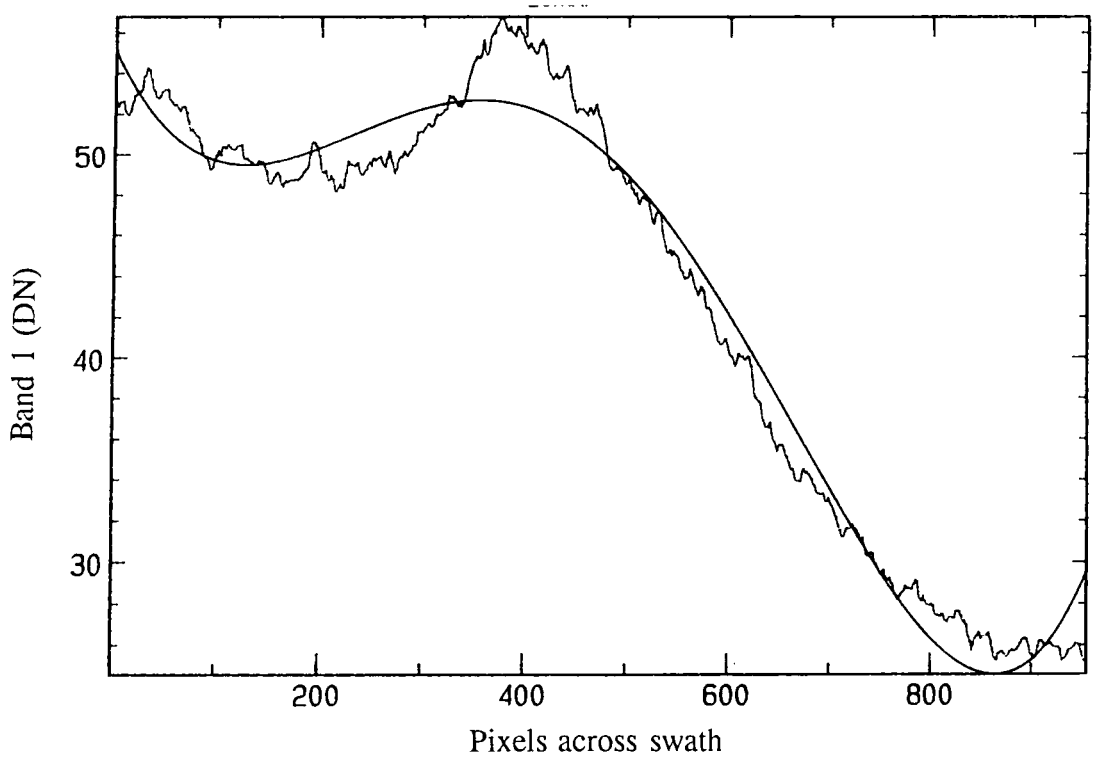

Figure 4.16 A 4th degree polynomial fitted to the column means for the 0.49 μm band of NS001 Flight Line 2.

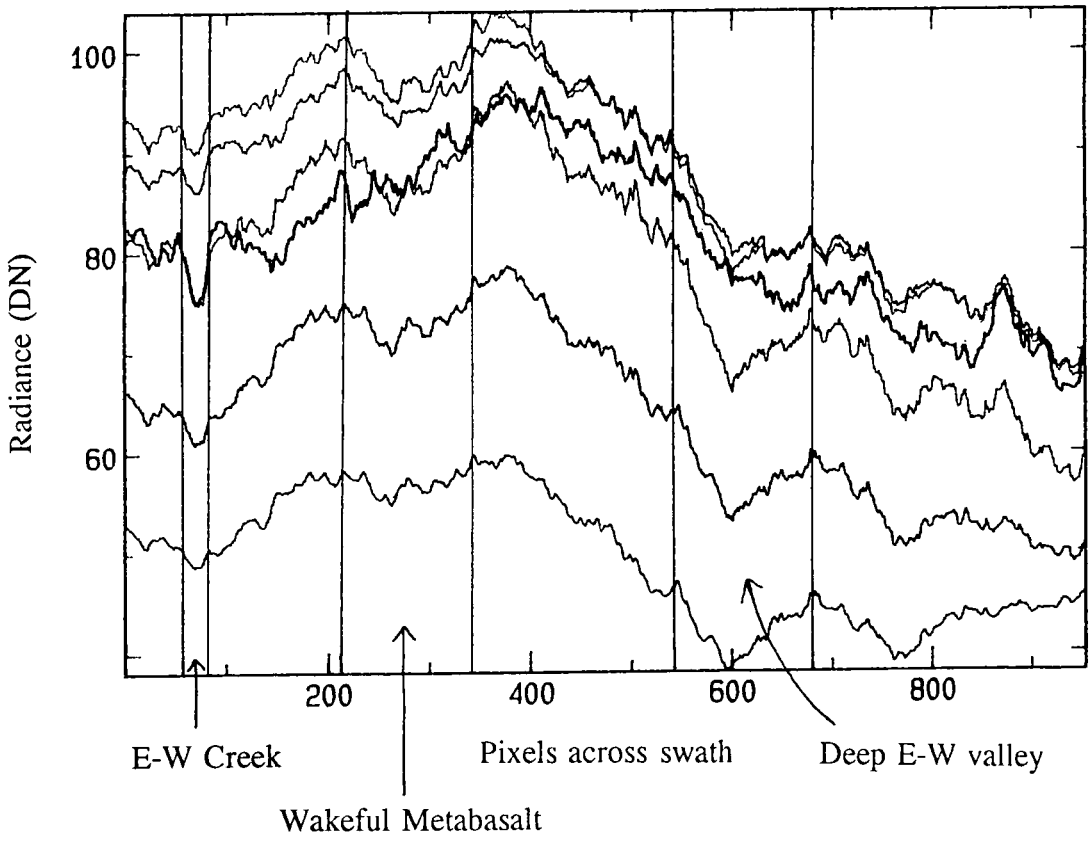

Figure 4.17 The influence of geology and other scene detail on the column means for NS001 Flight Line 3.

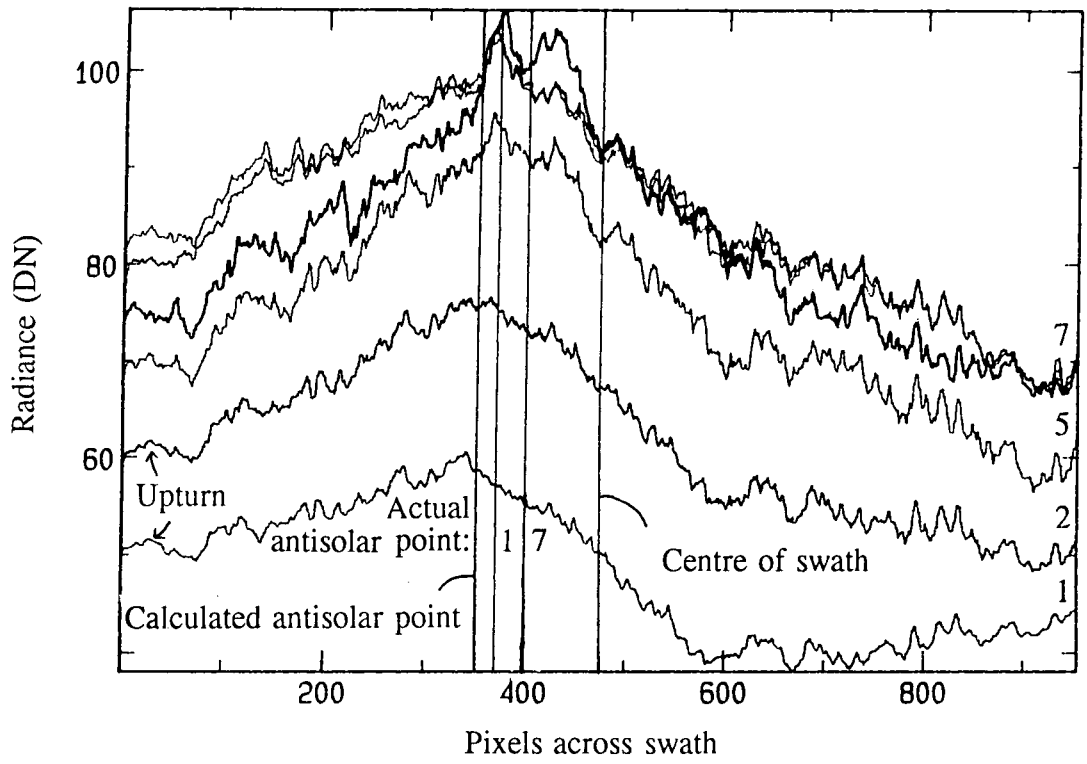

Figure 4.18 Column means for NS001 Flight Line 3 collected to avoid areas where the strike is parallel to the flight direction, illustrating the effects of cross-track shading for this sun/sensor geometry. Numbers on right indicate NS001 bands.

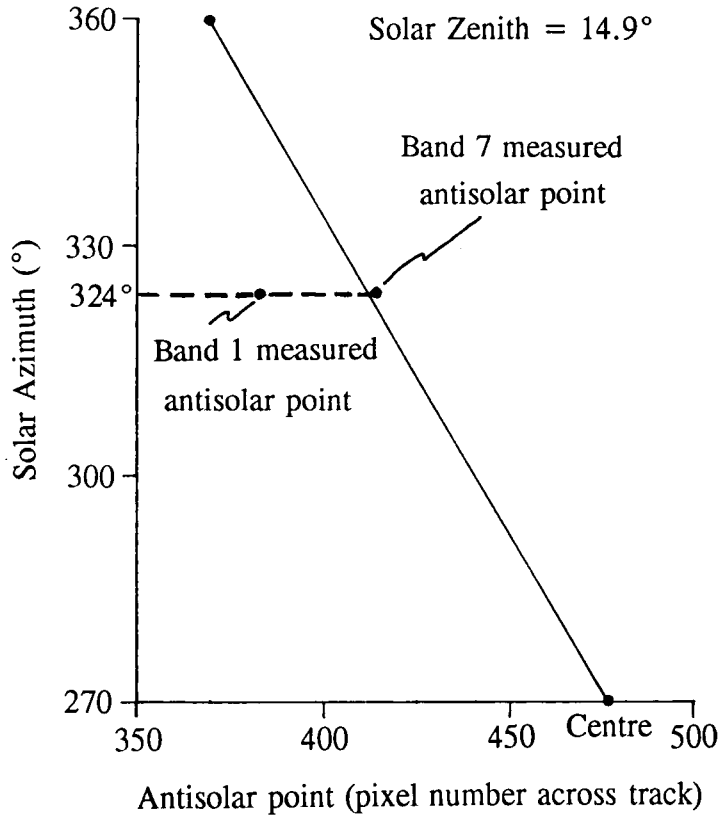

Figure 4.19 Antisolar point's relationship to the sun's azimuth, NS001 Flight Line 2.

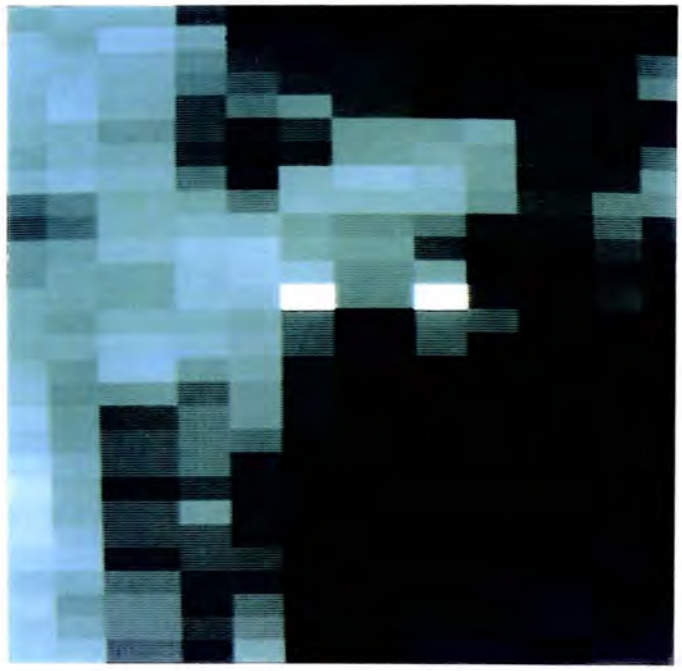

Plate 4.1 Two anomalously bright pixels from NS001 Flight Line 3. Also depicted are the effects of the nearest-neighbour resampling employed during geometric correction, causing a duplication of pixels for every second or third pixel across the track.

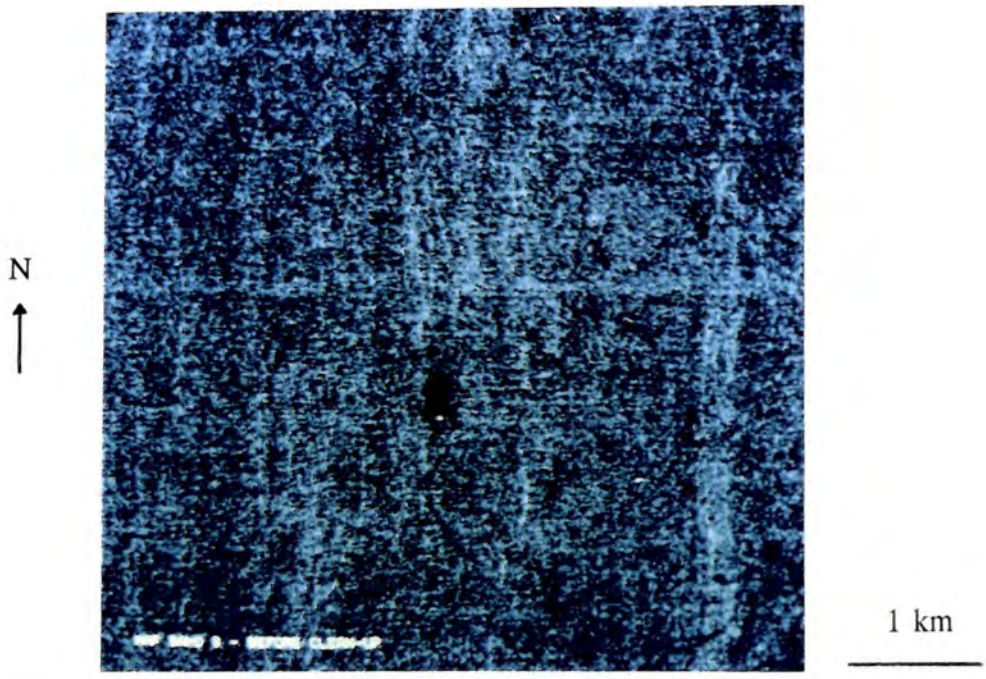

Plate 4.2 GMS Flight Line 5b MAF band 8, before noise removal.

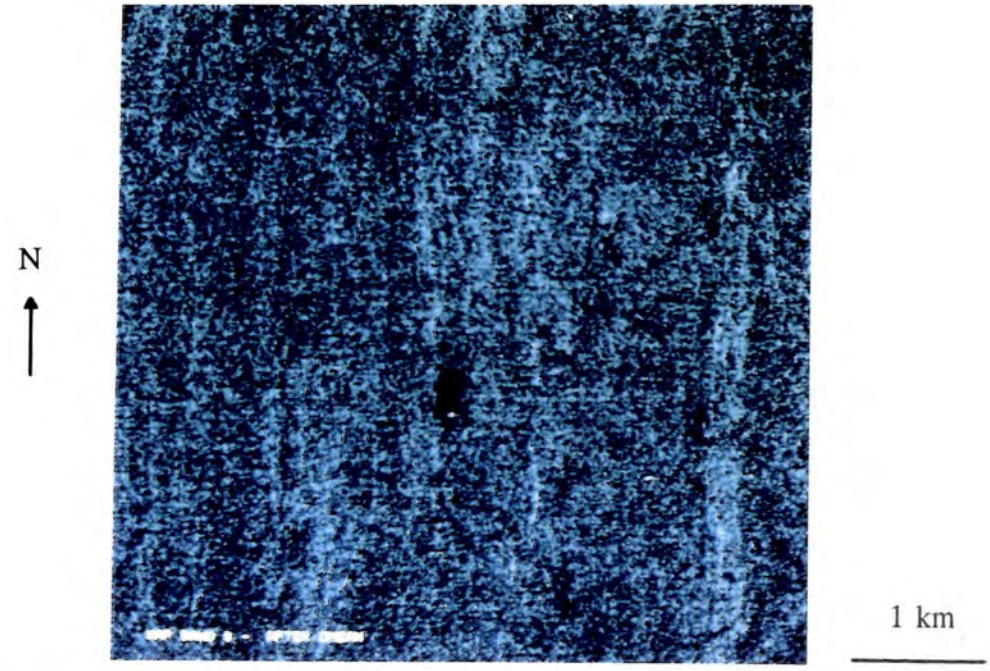

Plate 4.3 GMS Flight Line 5b MAF band 8, after the removal of striping.

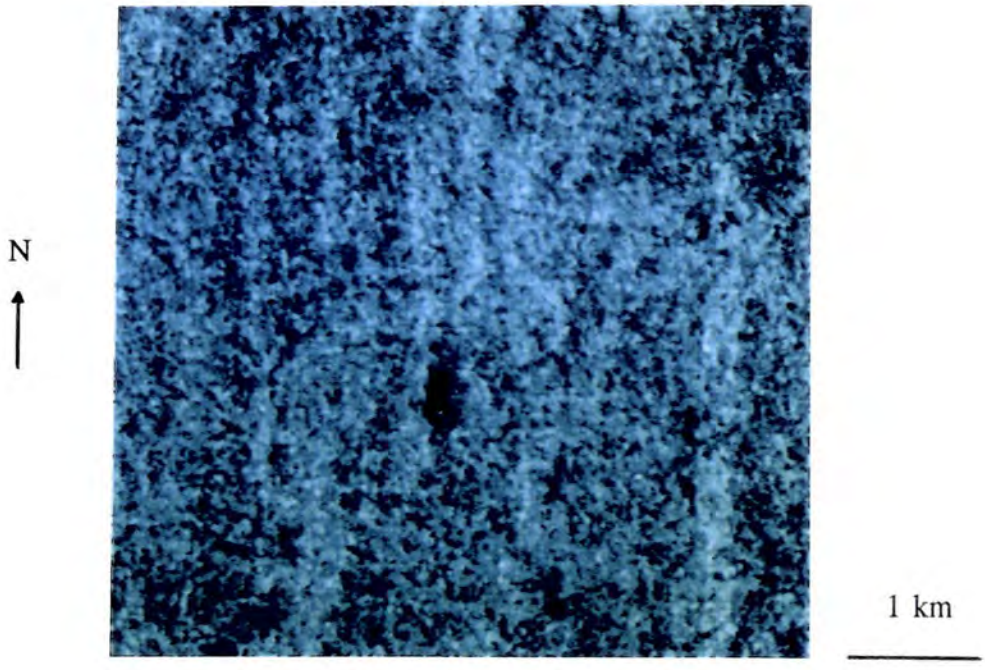

Plate 4.4 GMS Flight Line 5b MAF band 8, after removal of salt and pepper noise.

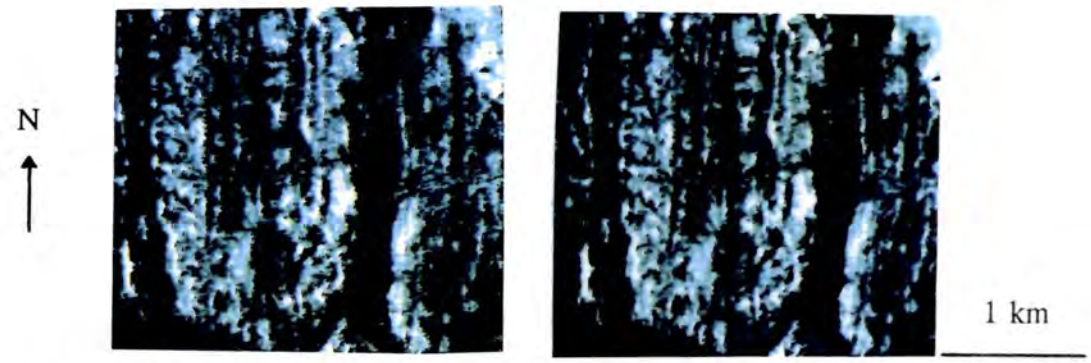

Plate 4.5 GMS Flight Line 5b 0.83 μm band before (left) and after (right) noise removal.

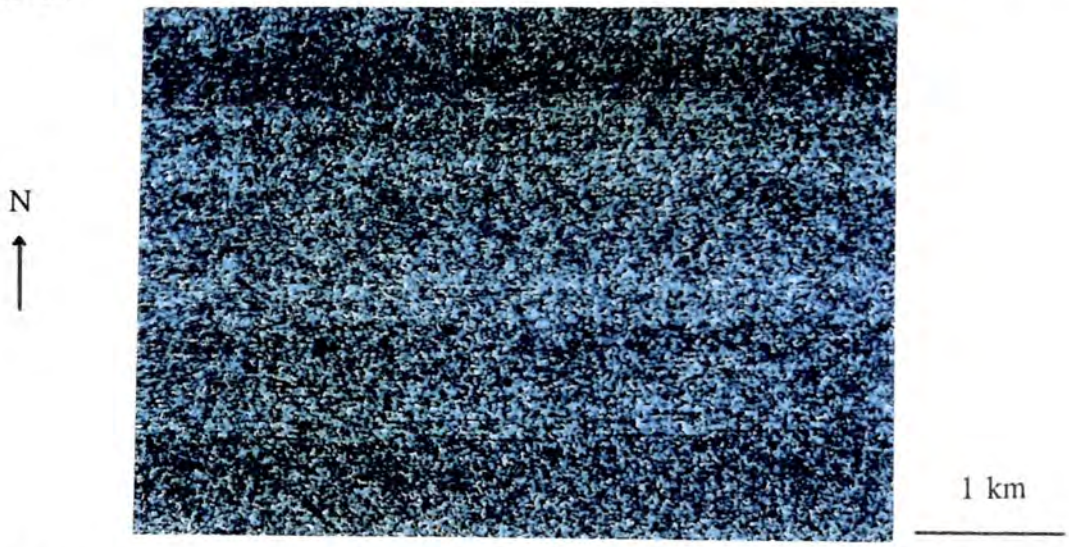

Plate 4.6 GMS Flight Line 5b 0.83 μm band. A difference image of before and after noise removal to illustrate the noise which has been removed in MAF space.

Plate 4.7 GMS Flight Line 5b 0.955 μm band. A difference image of noise removal in normal space and noise removal in MAF space, showing that the former does not remove as much noise as the latter and also removes scene detail.

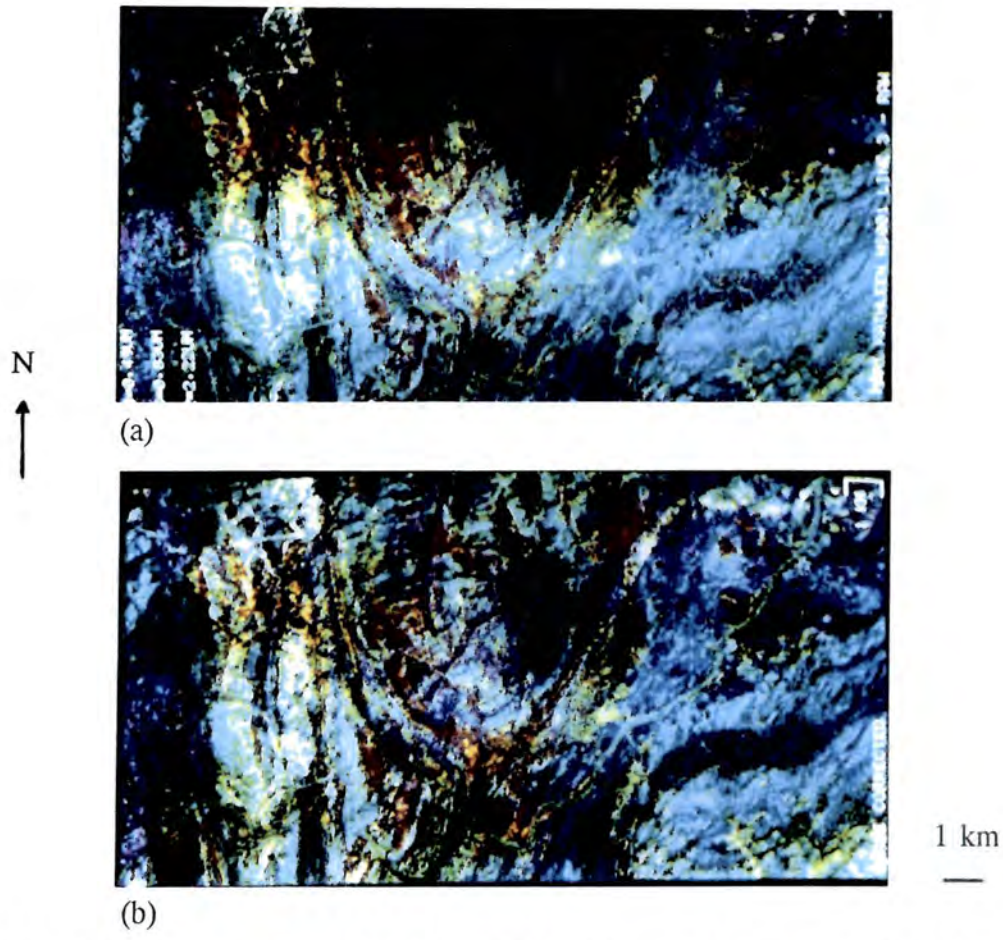

Plate 4.8 Colour composite of NS001 Flight Line 3 with 2.22 μm in red, 0.83 μm in green and 0.49 μm in blue, before (a) and after (b) removal of cross-track shading.

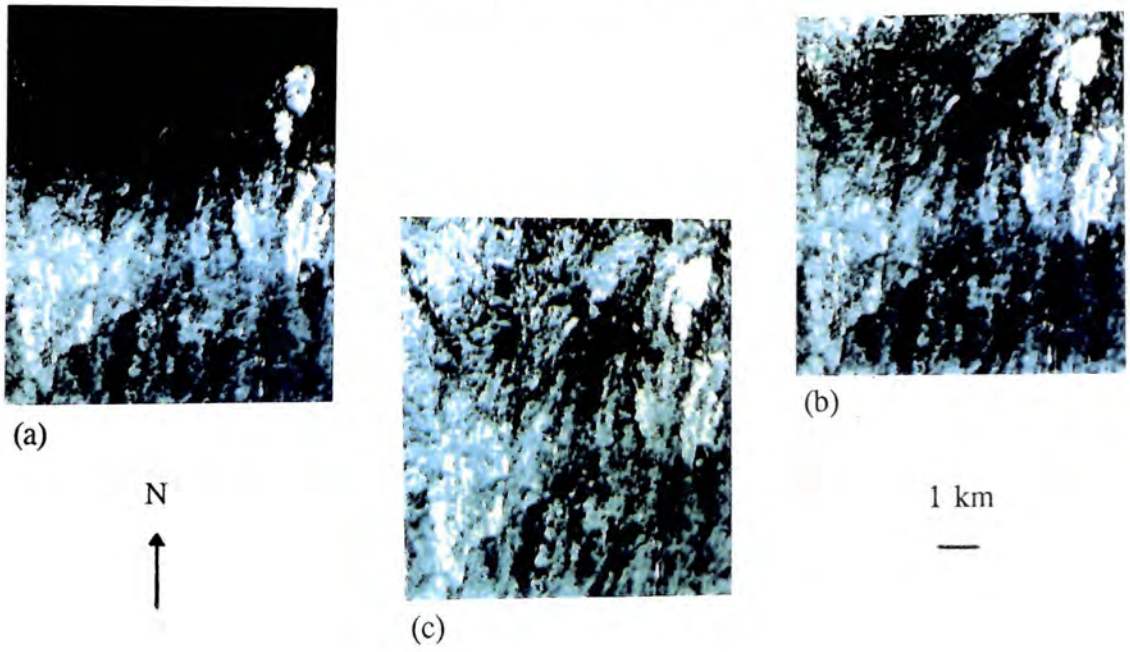

Plate 4.9 NS001 Flight Line 2, 0.49 μm band before removal of cross-track shading (a) and after its removal, using a third (b) and a fourth (c) degree polynomial.

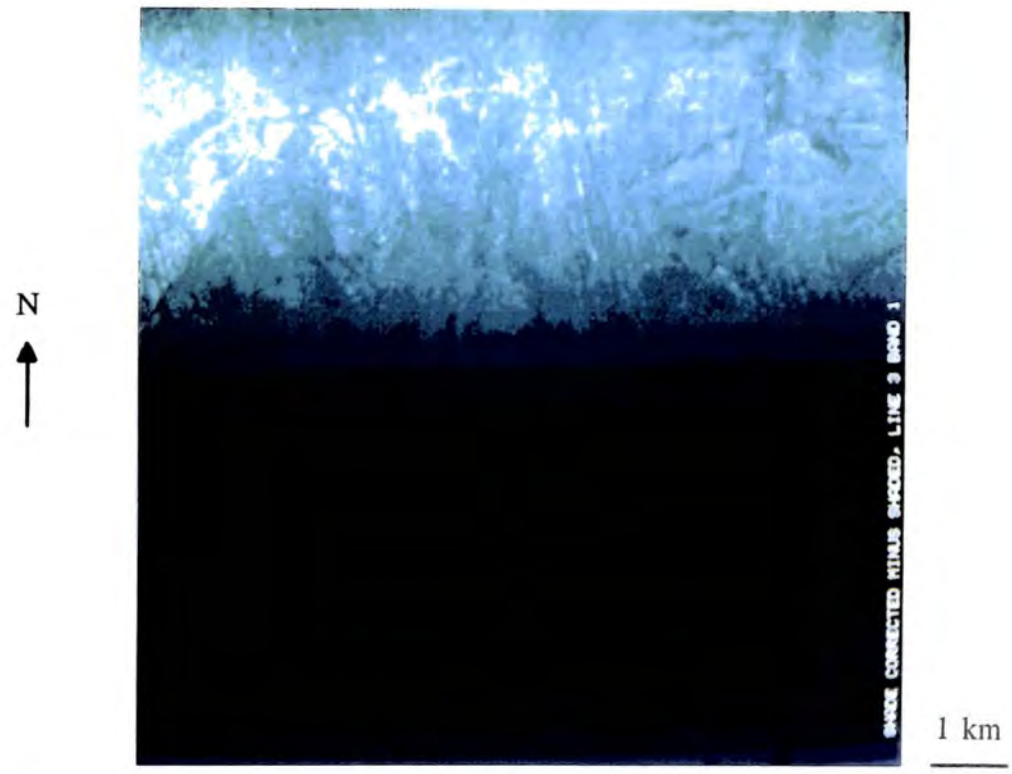

Plate 4.10 A difference image of uncorrected minus shade-corrected data for the 0.49 μm band of NS001 Flight Line 3, showing both the cross-track shading removed and the scene detail also affected.

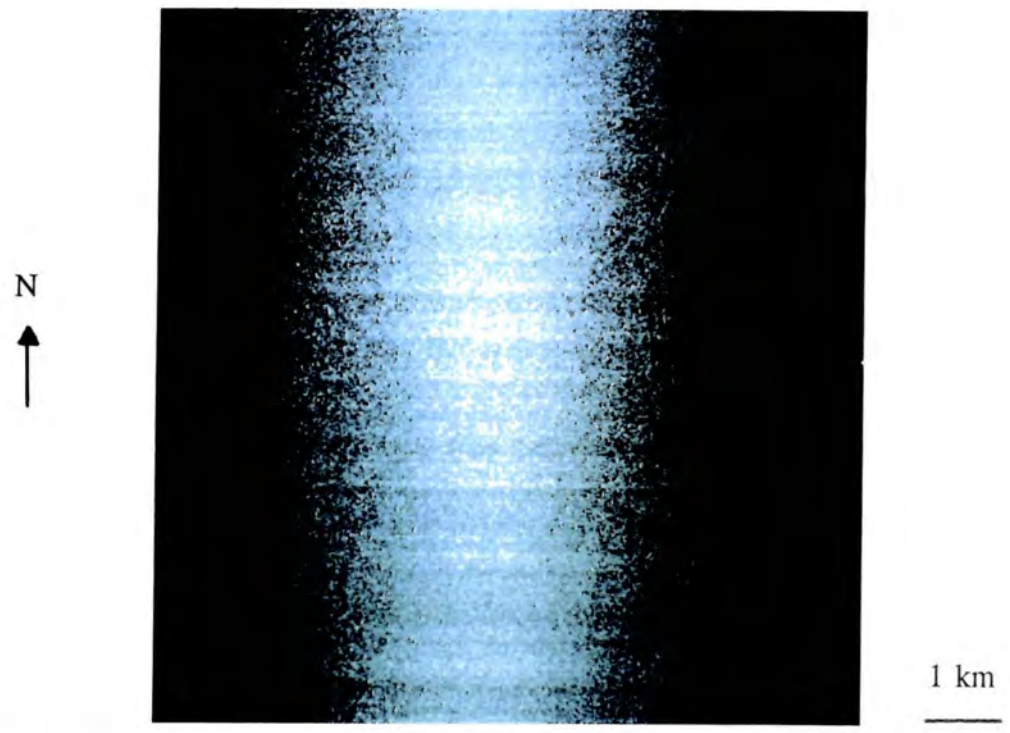

Plate 4.11 A difference image of GMS Flight Line 6a 0.583 μm band before and after the removal of cross-track shading and noise in MAF space.

Chosen band 7 value	Reason for choice	Computed value in band:					
		1	2	3	4	5	7
512 x 512 non-homogeneous control area							
0	Arbitrary	71	25	15	16	13	0
3	Scene minimum	72	26	17	17	18	3
16	Minimum, avoiding lake	74	29	24	25	38	16
20	Minimum, no lake/mine	75	30	27	28	44	20
27	Manually chosen shadow	76	32	31	32	55	27
173 x 61 pixel area of Burstall Granite							
0	Arbitrary	69	25	20	23	10	0
3	Scene minimum	69	26	22	25	15	3
16	Minimum, avoiding lake	72	29	28	31	37	16
20	Minimum, no lake/mine	73	30	30	33	43	20
27	Manually chosen shadow	75	32	34	37	55	27
50 x 40 pixel area of Burstall Granite							
0	**Arbitrary**	**59**	**18**	**9**	**12**	**14**	**0**
3	Scene minimum	60	19	11	14	18	3
16	Minimum, avoiding lake	65	24	20	24	39	16
20	Minimum, no lake/mine	67	25	23	27	46	20
27	Manually chosen shadow	70	28	29	32	57	27

Table 4.1 The results of the CMM method for this TM data. The best results are shown in bold.

CHAPTER 5: ENHANCEMENTS OF THE RADIANCE DATA

5.1 Introduction

Chapter 4 has described techniques that remove the gross additive component. Once this has been removed, the data are a close approximation to ground radiance, although still modified by the gain and the atmospheric transmittance. Enhancements of the radiance data can be performed which increase their use for geological mapping by removing or isolating one or more of the remaining multiplicative factors. These techniques aim to reduce correlation between wavelengths. The logarithmic residual technique does this as a consequence of retrieving the geologically significant parameter reflectance from the radiance data (Green and Craig, 1985). This chapter describes these techniques, the data they produce and the ways in which these data are analysed.

5.2 Methods of data analysis

5.2.1 Colour compositing

The discrimination of different geological units is achieved by combining data for three wavelengths in a red-green-blue (RGB) image. The data for each wavelength are stretched to optimally occupy the range 0-255 DN on the display. This is done by interactive contrast stretching on the display device in most cases, although some processing techniques produce data already in this range. Colour composites have been studied of the data at all stages of processing, from raw through atmospherically corrected to all subsequent enhancements described in this chapter.

5.2.2 Spectral analysis

Depending on the way the radiance data are enhanced and which sensor recorded them, direct identification of rock types and even particular minerals can be achieved through the analysis of pixel spectra. This relies on the detection of known absorptions by comparison to spectral libraries (e.g. Grove et al, 1992) and reference to the literature as summarised by Hunt (1977; 1980). In this study, comparisons have also been made

with a library of laboratory spectra from field samples and pure minerals collected and measured by the author and a library of pure mineral laboratory spectra measured by Hook (1989).

The ideal analysis system involves the display of remotely sensed data as imagery and pixel spectra simultaneously, with on-line spectral libraries for comparison. Such spectral analysis packages are becoming available for personal computers (e.g. Donoghue et al, 1990). The move towards spectral analysis in no way removes the need for the spatial perspective provided by colour composites.

5.3 Analysis of the radiance data prior to enhancement

After minimal processing, involving only removal of the gross additive component, the radiance data were analysed through the production of black and white and colour composite imagery. At this stage only discrimination was possible, although some lithologies could be putatively identified.

5.3.1 TM data

Data from single wavelengths displayed as black and white images contain less lithological information than three band colour composite images. Spatial information is prominent in any single band, however, aiding structural mapping and field location.

The selection of wavelengths for colour composites has been based on the degree of inter-wavelength correlation and the position of absorption features. A colour composite with 0.83 μm, 0.66 μm and 0.56 μm in red, green and blue (Plate 5.1) is far less discriminating than one with 2.22 μm, 0.83 μm and 0.49 μm in the same colours (Plate 5.2). The latter composite consists of three well spaced wavelengths, thus reducing correlation, and is optimally targeted on specific reflectance features. These are due to iron oxide absorption at 0.49 μm, the vegetation reflectance peak in the near infrared at 0.83 μm and the clay and carbonate absorptions around 2.2 μm (Figure 5.1). It has been the most effective radiance colour composite for lithological discrimination, rendering iron oxides red, vegetation green and clays blue. Plate 5.2 shows that this

colour composite is still dominated by the effects of topography and albedo and can provide only limited information on the lithologies involved.

5.3.2 NS001 data

The experience gained in working with the TM data was the basis of the wavelength selection process. The colour composites used have therefore had 2.22 μm in red, 0.83 μm in green and 0.49 μm in blue. Interpretation criteria remain the same.

5.3.3 GMS data

Geoscan have developed an image display system, GIPSy, to analyse the data from their instrument. This system deals with the data without any processing to reflectance, but nevertheless has some features which make it useful. Several different colour composites of the same area can be analysed at the same time by placing them in different windows of the display screen, or by superimposing them in turn. It is also possible to look at a histogram of the DN values at all wavelengths, though not with the correct wavelength spacing. This system has been used for a first look at the raw radiance data at all wavelengths, in a variety of combinations, and to analyse the thermal data in particular, on which no data processing has been performed. The increased number of wavelengths measured by the GMS make processing to reflectance particularly attractive and so colour composites of the radiance data have not been extensively studied.

5.4 Approaches to data enhancement

There are two approaches to the enhancement of remotely sensed data for geological purposes, one aimed at maximum **discrimination** and the other at **identification.**

5.4.1 Choice of approach

Approaches aimed at maximum discrimination start from the position that the main use for the data will be in producing a map which can be field checked at some point.

Discrimination is maximised by highlighting the variation in the data in some way. As this does not involve a calibration to reflectance it cannot lead to the clear remote identification of particular minerals, groups of minerals, or even rock types. In this study principal component analysis (Gillespie, 1980) has been used in order to investigate the correlation reduction approach and whether PCs can have physical meaning ascribed to them. An extension of this technique, the decorrelation stretch (Gillespie et al, 1986), has not been used. It is a non-linear extension of the PC transform, which is itself a linear combination of the data at all wavelengths (Figure 4.2). It is difficult to ascribe physical meaning to data resulting from a PC transform, so performing a decorrelation stretch makes this harder still. Such imagery must be subject to extensive field checking, as there is no other way of ascribing meaning to it. If discrimination alone is the goal, however, the decorrelation stretch remains an important technique used successfully in many studies with this approach (e.g. Drury and Hunt, 1988).

Discrimination is only one part of the mapping process. Huntington et al (1989) have argued that geological mapping by remote sensing should have identification, the second important part of the mapping process, as the ultimate aim. When the goal is changed from discrimination to identification PC analysis cannot be used as it produces PCs with different meanings in different environments (Conel and Alley, 1985). Band ratioing (Abrams et al, 1983) has been used in this study as it aims to identify particular mineral groups by highlighting absorptions in their reflectance spectra, though it cannot achieve unequivocal mineral identification. Least squares fit (LSFit) residuals (Fraser et al, 1986) have also been used and aim to highlight subtle spectral features of geological significance which are masked by the strong response of vegetation, a problem in parts of this semi-arid area. Unequivocal mineral identification cannot be achieved with this technique, either. This can only be achieved by performing some form of calibration to reflectance on data collected over many narrow, contiguous spectral bands.

There are a variety of techniques which attempt to retrieve reflectance from radiance data. Many of these rely on the remotely sensed data being normalised to ground-based reflectance measurements of known bright and dark target materials. One example of such an approach is the empirical line method described by Conel et al (1987). The

extensive field work required, ideally at the time of the data acquisition, removes a major advantage of remote sensing: reduced reliance on field work in remote places. It also precludes processing of the data before fieldwork begins, removing the advantage of being able to take reflectance imagery into the field. Crippen (1987) gives a good summary of the other difficulties involved in attempting such calibration. Other approaches to the problem of calibration to reflectance, relying only on the data themselves, are in their infancy (R. Green, 1990). In this study, extensive use has been made of the logarithmic residuals (LR) process which aims to perform calibration to near-reflectance based on the data alone (Green and Craig, 1985).

Approaches aimed at increasing discrimination alone can be complementary to those aimed at achieving identification, though they may in fact add little. The techniques used for identification often allow equal or better discrimination than techniques with discrimination as their aim. Hook (1989) and Kealy (1990) have described two methods both aimed at identification, logarithmic residuals and alpha residuals respectively. Both produce images on which geological boundaries can be discriminated as well or better than is possible on images formed after applying decorrelation stretches aimed solely at enhancing discrimination.

5.4.2 The approach taken with each data set

The TM data form the major part of this study and so all the processing techniques being assessed have been applied to this data set. The NS001 data have been examined in comparison to the TM data so that the impact of the improved spatial resolution and extra spectral coverage on geological mapping can be discovered. Consequently the processing techniques employed are those found to be most successful with the TM data.

The GMS data contain sufficient spectral information, particularly in the short wave infrared region, for the production of pixel spectra which can be profitably compared with laboratory resolution reflectance spectra (Huntington et al, 1990). The intention with these data was to rapidly reduce them to reflectance and to define an operational process which does this and is repeatable, so that the utility of these high spectral

resolution data for geological mapping can be investigated. Hence, after the gross additive correction and noise removal only the logarithmic residuals technique has been applied to these data. As the GMS data were available late in the study, the aim was to assess what was possible with these data rather than fully analyse all the geological problems in the area.

5.5 Principal component Analysis

PC analysis has been described in chapter 4, as it is also used in the noise removal process for the GMS data. For data measured over n wavelengths there are n principal components, all independent of each other, which describe the majority of the variance in the data. The values of the original data on the new PC axes can be treated as normal data and an RGB image produced from three of these PC bands (Canas and Barnett, 1985). As the low order PCs have the maximum variance and least noise, RGB images using them allow good discrimination. They are, however, difficult to interpret, as it is not clear what each PC represents. The first PC often appears to represent albedo (Conel and Alley, 1985), although this is difficult to prove. There may be multiple causes for the variation of a particular PC because it represents a mathematical combination of the radiance information at all wavelengths. In one scene a particular PC may be due to the coincidence of a particular soil with a certain type of vegetation in one topographic setting while in another the same PC may represent iron oxide abundance. In all cases therefore these PC interpretations are scene specific. If these problems cannot be overcome, such imagery will be restricted to discrimination and the identification of possible end members in unmixing analysis.

5.5.1 TM data

When applied to TM data the technique produces six new PC bands (omitting TM's thermal infrared data from the calculation). PC1 appears to represent the albedo of each pixel. PC2, PC3 and PC4, when combined in a colour composite image, allow very good discrimination of the lithologies in the area. This is because they are highly uncorrelated, with the maximum non-shade variance for this data set, and contain minimal topographical and vegetative information. Without extractable compositional

information, however, this is of limited use. Other techniques such as logarithmic residuals (Green and Craig, 1985) yield spectral information diagnostic of lithological and mineralogical composition and can allow equal or better discrimination than PC analysis (Hook, 1989). In applying the PC technique to the TM data the intention was therefore to make progress on the question of what each PC means.

Conel and Alley (1985) have used the weighting of the eigenvectors for each new PC on the original wavelength band axes to suggest which wavelengths and hence absorption features have the largest influence on each PC. These weightings are shown for these TM data in Table 5.1. Figure 5.2 indicates that, as with the data studied by Conel and Alley (ibid.), PC1 is equally influenced by all wavelengths and represents the average radiance, supporting the visual analysis that it is a measure of albedo (although strictly speaking albedo is the reflectance averaged over all wavelengths). PC5 is positively influenced by the 0.83 μm band (near infrared vegetation reflectance peak) and negatively influenced by the 1.65 μm band. It visually correlates with ?dry vegetation away from creeks. PC6 is positively influenced by the 0.56 μm band (visible vegetation green peak) and negatively by bands at 0.49 and 0.66 μm (absorption on either side of the peak). It most closely correlates with areas of green vegetation near creeks. PC2 is negatively influenced by the 0.49 μm band (iron oxide absorption, charge transfer effects). PC3 is negatively influenced by the 0.83 μm band (iron oxide absorption, crystal field effects). Both visually correlate with basic rocks, though by no means exclusively. PC4 is positively influenced by the 2.22 μm band (clay absorption) and it appears to be inversely related to lithologies which contain clay minerals in their weathering product. The good discrimination achieved in a PC2, PC3, PC4 RGB image is thus due to these three PCs largely having mineralogical explanations, while PC1, PC5 and PC6 have topographical/vegetational explanations. These explanations are not, however, consistent throughout the image. A similar explanation of 6 PCs from TM data has been described by Laughlin (1991).

5.5.2 NS001 data

The technique has not been applied to this data set, as the work with the TM data indicated that other processes were more useful for geological analysis of the data.

5.5.3 GMS data

Whilst this processing technique has not been performed as part of the geological analysis of the GMS data, it is the basis of the MAF transformation, described in chapter 4, designed to separate the signal from the noise during noise removal. The MAF bands containing the lowest frequency variation are almost noise-free, and the information varying on this scale is mainly geological in nature (excepting the cross-track shading). A colour composite image of MAF bands 15, 16 and 17 allows detailed discrimination of the geology for both flight lines studied. No attempt has been made to ascribe meaning to each MAF band, in the way that has been done for TM PC bands, as those MAF bands other than 15, 16 and 17 are dominated by the noise they are designed to isolate.

5.5.4 Discussion

The data's variance is due to the mix of materials in the scene, which changes for each scene. Consequently the meaning of the PCs which describe the variance is always scene dependent. Shade and at least a minor amount of vegetation are present in the majority of scenes and so certain of the PCs will consistently measure these components. The meaning of the other PCs will change depending on the dominant components of the scene in question and even where the technique appears to produce data with a physical meaning this cannot be compared directly with the PC data from another area. For example Conel and Alley (1985) found that PC2 from one study area equated with PC4 from another. The explanation of PCs will always require prior knowledge about the area under study.

The PC transformation is performed on radiance data so the input data at each wavelength also contain information on non-geological factors such as atmospheric transmittance. These factors also influence each PC. To ascribe physical meaning to the PC data as described in section 5.5.1 they must ultimately be considered in relation to the original wavelength data; "PC1 has equal contribution from all wavelengths, PC4 is primarily due to absorption at 2.22 μm". In isolation the PC data have no absolute physical meaning.

In the two dimensional case only, it is possible to exercise more control by performing the PC transformation on ratios of wavelengths designed to highlight a particular material, rather than on single wavelengths. This approach, known as directed principal component analysis (Fraser and Green, 1987; Fraser, 1990a), is one way of ensuring that the shade component is not described and the PCs are controlled by geological information. Likewise, Laughlin (1991) has attempted to control the information each PC isolates by restricting the number of wavelengths used as the input for PC analysis. For example, to produce PCs focused on clay minerals most wavelengths with features due to iron oxide are avoided in the PC analysis. Each PC may still, however, contain information on more than one material and a further PC analysis of the first PCs may be required to overcome this problem.

The approaches of Fraser (op. cit.) and Laughlin (op. cit.) have not been attempted in this study as they are more suited to focused mineral exploration than general mapping. Another way of ensuring the PCs calculated relate more directly to mineral species considered by the author was the application of PC analysis to the reflectance data rather than radiance data. Each PC might be more directly correlated with a geological feature as the non-geological multiplicative factors would have been removed. Information on shade would also have been removed freeing one PC, which may instead describe a geological variable. In practise however, once the data are transformed to reflectance discrimination of a standard achieved by PC analysis is already possible and the further issue of identification can be addressed. A PC analysis of such data still requires explanation by reference to the original wavelength data and was therefore considered unnecessary.

5.6 Band ratioing

One of the reasons that the radiance data do not allow maximum discrimination between rock types is that they contain information which can hinder rather than help this process. The purely geological information content of radiance data can be lower than 4 % (Green et al, 1985). The largest proportion of each pixel's data is information about its slope and aspect, A, and hence over an image the albedo and topography of the scene. Whilst this may be useful in its own right, particularly for structural

mapping, it dominates radiance imagery to the extent that the geological information contained in the reflectance is obscured. After removal of the gross additive component as discussed in chapter 4:

$$X_\lambda = E_\lambda t_\lambda A \rho_\lambda G_\lambda \qquad (5.1)$$

where

X_λ = Radiance measured at sensor at wavelength λ
E_λ = Irradiance of source reaching the surface at wavelength λ
t_λ = Atmospheric transmittance (up) at wavelength λ
A = Slope and aspect based effects for the surface
ρ_λ = Reflectance of surface at wavelength λ
G_λ = Gain at sensor at wavelength λ

One method widely used to remove the slope and aspect related effects is band ratioing (Abrams et al, 1983), which takes advantage of the fact that, unlike atmospheric effects, A is not wavelength dependent. Hence, the division of a pixel's radiance at one wavelength by that at another gives:

$$X_{\lambda 1}/X_{\lambda 2} = \rho_{\lambda 1} E_{\lambda 1} t_{\lambda 1} G_{\lambda 1} / \rho_{\lambda 2} E_{\lambda 2} t_{\lambda 2} G_{\lambda 2} \qquad (5.2)$$

The constant slope and aspect related factor, A, has been removed.

This technique, which only succeeds if the additive correction has been correctly performed, produces topographically "flat" imagery. If it is assumed that the remaining multiplicative factors do not vary over the scene, the ratio value for a homogeneous area with uniform surface reflectance will be a constant (Figure 5.3) and will be directly proportional to the ratio of the reflectances. Such ratio imagery is therefore better for discrimination than the raw radiance data. Ratios are quick to calculate and retain the relationship between the bands chosen, simply expressing it differently. Indeed, band ratios are usually designed to highlight certain mineralogical features. Figure 5.1 shows that a ratio of 0.66 μm/0.49 μm should be large for a pixel dominated

by iron oxide, which has an absorption near 0.49 μm, and smaller for a pixel dominated by clay minerals, which has the same high reflectance at both wavelengths. Ratios have been used in this study which aim to putatively identify certain mineral groups. Ultimately, however, this technique is a discriminatory aid requiring field checking.

Crippen (1988) has shown the importance of performing a correction for the additive terms before calculating ratios. A constant ratio value cannot be found for homogeneous reflectance surfaces if the additive component has not been removed (Figure 5.3). A further problem which may result if an additive correction is not performed is that a ratio may fail to highlight an absorption feature as desired. The ratio 0.66 μm/0.49 μm was described above as targeting iron oxide-related absorption. If a large additive component is present at 0.49 μm which is not present at 0.66 μm, the ratio value for iron oxide will no longer be large. For clay minerals this ratio, which was approximately one, now tends towards zero. As both ratios tend towards zero the separation achieved between the two materials, even after contrast stretching, may decrease (J. Huntington, personal communication). This effect has been investigated with the TM data and the results are described below.

5.6.1 TM data

Several combinations of band ratios have been calculated and analysed for the TM data set, and many more are possible. Podwysocki et al (1983) suggest that, for strongly contrasted rock types, band ratios can be selected by the analysis of reflectance curves for the dominant materials. In this study, band ratios have been chosen to highlight strong contrasts in reflectance at different wavelengths for clay minerals, iron oxides and vegetation, as shown in Figure 5.1, and the following have been the most effective. Iron oxides have high reflectance at 0.66 μm and absorb strongly at 0.49 μm. Both wavelengths are characterised by high reflectance for the clay minerals, and this fact can be used to discriminate between the two groups. A ratio of 0.66 μm/0.49 μm should be large for a pixel dominated by iron oxide, and smaller for a pixel dominated by clay minerals. In contrast, clay minerals have a major absorption around 2.2 μm, not shared by the iron oxides, while both have high reflectance at 1.65 μm. A ratio of 1.65 μm/2.22 μm is therefore large for clay minerals and smaller for iron oxides.

Vegetation has a reflectance peak in the near infrared, and as rocks and soils commonly have higher reflectance at 1.65 μm than at 0.83 μm the ratio 0.83 μm/1.65 μm is generally larger for vegetation than any other material in the scene.

In all cases there can be no direct identification of these materials, as it is possible for other materials to produce a similar response. For example, the ratio 1.65 μm/2.22 μm used to highlight clay minerals may also be large for vegetation, as vegetation's reflectance drops off sharply in the short wave infrared (Fraser and Green, 1987; Figure 5.1). It is possible that carbonate may also give a similar response to clay minerals for sensors of the resolution of TM (Figure 5.4).

Colour composite imagery with 1.65 μm/2.22 μm in red, 0.66 μm/0.49 μm in green and 0.83 μm/1.65 μm in blue is shown in Plate 5.3. These TM ratio composites are more effective for lithological discrimination than colour composites of the radiance data because the contrasts between different lithologies are enhanced in the ratio imagery by the removal of the correlated, non-geological signal. Delineation of geological boundaries is much easier. The data still contain multiplicative effects such as the atmospheric transmittance but the technique allows more to be said about the materials responsible for some of the responses seen. Vegetation appears purple, having large values in both the vegetation-targeted and clay-targeted ratios. Iron oxides appear green and areas of clay minerals appear red.

The effect of the additive correction on the value of the ratios calculated was investigated for the TM data by calculating the 0.66 μm/0.49 μm ratio value for 36 randomly selected pixels from a variety of rock types both before and after the gross additive component had been removed. Figure 5.5 shows the histograms for these two cases. A greater separation of high and low ratio value rock types was achieved with the corrected data, confirming the hypothesis that the ratio technique may fail to highlight a particular absorption as effectively without an additive correction. Visual analysis for the two cases showed that this difference is partly overcome during image display by the contrast stretch applied. Nevertheless ratio images calculated after removal of the gross additive component are superior for geological analysis to those calculated before this correction.

Plate 5.4 shows the ratio 0.66/0.49 μm before and after the additive correction. The non-constant ratio value for homogeneous materials in the uncorrected data is clear. Despite two strong reasons for a radiometric correction prior to the calculation of ratios, they are often employed without prior atmospheric correction (e.g. Sultan et al, 1986).

5.6.2 NS001 data

The NS001 sensor covers almost the same wavelengths as the TM sensor. In order to keep imagery from the two sensors compatible, the NS001 ratio images also have 1.65 μm/2.22 μm in red, 0.66 μm/0.49 μm in green and 0.83 μm/1.65 μm in blue. The criteria for interpretation of these images remain unchanged.

5.6.3 GMS data

The ratio technique was not used with this data set. It has high spectral resolution and so processing was focused on the retrieval of reflectance with the goal being the identification of minerals and lithologies.

5.7 Least squares fit residuals

The details of the least squares fit residual technique are given in Fraser et al (1986) and Hook (1989). It is designed to solve two specific problems. The first is the removal of noise where it is isolated in one band, as with the gamma radiometric data. This will be further discussed in chapter 6.

The second problem involves the masking of areas of absorption due to clay minerals in the 2.2 μm wavelength region by the similar reflectance of vegetation at these wavelengths. The reflectance at 2.2 μm can be predicted from the reflectance at shorter wavelengths. The shorter wavelengths do not contain any absorptions with which to predict the presence of clay minerals. Absorption at 2.2 μm is not therefore predicted for pixels with clay minerals. In contrast, vegetation does have such features at shorter wavelengths; low 2.2 μm reflectance related to vegetation is predicted. The least

squares fit residual is the difference between the observed reflectance and the predicted. For vegetation the observed and predicted 2.2 μm value are the same and the residual is zero. For clay minerals the observed 2.2 μm value is affected by an absorption which the predicted does not account for and is much smaller than the predicted. The residual is therefore large for clay minerals. Where the 2.2 μm band showed absorption due to both materials, the LSFit residual shows only absorption due to clay minerals.

An LSFit residual has been calculated for TM's 2.22 μm band and analysed as a black and white image and also used to replace the 2.22 μm data in logarithmic residual colour composites. The success of the separation achieved will be discussed when the data are applied to geological problems.

5.8 Logarithmic residuals

Given the lack of calibration and atmospheric data available for the data sets used in this study, the aim of producing reflectance from the raw data was best pursued using the logarithmic residuals technique. Initially described by Green and Craig (1985) for radiance data between 0.4 and 2.5 μm, the LR technique has since been modified by Hook (1989) to extend its use to the thermal infrared wavelength region. Its application in mineral exploration has been described by Hook (1989) and Huntington et al (1990). There are, however, few case studies which use the LR technique extensively enough to provide a full assessment of its success for geological mapping, especially with TM data. This study presented an opportunity to implement this technique with data from three sensors for the same area, providing insights into its consistency and a chance to experiment with various options in its application.

5.8.1 The logarithmic residuals model

The following is modified from Green and Craig (1985). Assuming the irradiance of the source, the transmittance of the atmosphere and the instrument gain are constant for the scene, and a gross additive correction has been performed, for a single pixel i equation 5.1 becomes:

$$X_{i\lambda} = E_\lambda t_\lambda A_i \rho_{i\lambda} G_\lambda \qquad (5.3)$$

If the remaining multiplicative effects can be removed the surface reflectance at each wavelength can be derived from the measured radiance. For this to be possible, the factors E_λ, t_λ, A_i and G_λ must be found from the data themselves as they are unknowns. The logarithmic residuals technique attempts this by the calculation of two geometric means for the scene in question. These are a mean over all wavelengths for each pixel (spectral mean) and a mean over all pixels at each wavelength (spatial mean). The spectral mean is calculated in order to remove the wavelength independent slope and aspect effects. The spatial mean is calculated in order to remove the spatially independent illumination, atmospheric transmittance and instrument gain effects. The spectral mean for pixel i derived from equation 5.3 is:

$$X_{i.} = E_. t_. A_i \rho_{i.} G_. \qquad (5.4)$$

where

. = the geometric mean over all wavelengths (other symbols as previously explained).

Division of equation 5.3 by equation 5.4 gives

$$X_{i\lambda}/X_{i.} = (\rho_{i\lambda}/\rho_{i.})(E_\lambda t_\lambda G_\lambda / E_. t_. G_.) \qquad (5.5)$$

The slope and aspect related factor A_i has been removed.

Using the same notation for the geometric mean over all pixels, the spatial mean of equation 5.5 is:

$$X_{.\lambda}/X_{..} = (\rho_{.\lambda}/\rho_{..})(E_\lambda t_\lambda G_\lambda/E_. t_. G_.) \quad (5.6)$$

Division of equation 5.5 by equation 5.6 gives

$$(X_{i\lambda}/X_{i.})/(X_{.\lambda}/X_{..}) = (\rho_{i\lambda}/\rho_{i.})/(\rho_{.\lambda}/\rho_{..}) = L_{i\lambda} \quad (5.7)$$

where

$L_{i\lambda}$ = the logarithmic residual at wavelength λ for pixel i

The gain, irradiance of the source and atmospheric transmittance factors have been removed.

All the multiplicative effects are approximated in this way and removed. In practise, the use of geometric means dictates that this be done by the subtraction of logarithms, hence the term logarithmic residuals. LR do not represent purely the reflectance of a pixel at one wavelength ($\rho_{i\lambda}$), since they retain contributions from mean reflectances for the whole scene at all wavelengths ($\rho_{..}$), sample i at all wavelengths ($\rho_{i.}$), and wavelength λ for all samples ($\rho_{.\lambda}$). The residuals do, however, contain only reflectance terms, and represent a close approximation to reflectance (near-reflectance).

5.8.2 Problems with the model

If the term '$\rho_{..}/(\rho_{i.}\rho_{.\lambda})$' approximates to one the logarithmic residual value will approximate to the reflectance $\rho_{i\lambda}$ as desired. The further the mean spectra depart from this ideal the greater the artifacts introduced into the residual, and thus the further $L_{i\lambda}$ becomes from the actual reflectance. If these means contain spectral information, such as $\rho_{.\lambda}$ incorporating a near-ubiquitous absorption at wavelength λ, this will be absent in the residuals and that absorption will not be found anywhere in the scene. If a few pixels do not exhibit this absorption they may display an anomalous peak at that

wavelength. Green and Craig (1985) report the presence of a "**not** Ca-clay" feature in spectra over grass and soil, as areas of Ca-clay were common in the mean calculated.

It is important to consider potential inaccuracies involved in the calculation in each case, so that any deviation from actual reflectance can be predicted, or if possible avoided. The term '$\rho_{..}/(\rho_{i.}\rho_{.\lambda})$' is unlikely to equal one in practise but at best will be a constant so that $L_{i\lambda}$ will be proportional to the true reflectance. This should be true for all pixels except those which are bright at all wavelengths or dark at all wavelengths. In collecting the statistics for the LR calculation, care has been taken to avoid any obvious anomalies such as mine dumps and clouds, and to include the broad range of materials found in the scene so that this may be achieved. Vegetation and iron oxide, which are present in nearly all pixels, are probably the only materials which cause a feature in the mean spectra. These components are thus incorporated in the multiplicative effects, and are likely to have been removed from the residuals. In practise, however, this is advantageous. Although the true "pixel reflectance" should contain a portion of the vegetation and iron oxide components, these components may be deleterious to geological analysis of the data. The identification of minerals of interest may even be hindered by them and much effort may be expended in unmixing them from the geologically significant reflectance of the pixel (see section 5.7).

The assumptions made must also be borne in mind, and a gross additive correction must have been performed, or the atmospheric effects and instrument gain removed in another way, prior to the calculation. As noise is minimised by averaging, it is absent in the mean spectra and will be highlighted in the residuals. It should be removed at an earlier stage. Comparisons of LR spectra to field and laboratory spectra will then be valid.

5.8.3 Analysis of logarithmic residual data

The byte LR data are analysed as colour composite imagery and the real LR data as pixel spectra, with the LR values each plotted at the correct wavelength spacing. For display as colour composite images, the residuals may be scaled to byte values optimally stretched between 0 and 255 DN. In addition, the lookup table of the display

device should be inverted as this renders the low logarithmic residual values which represent absorption features bright in the chosen display colour. If the 2.22 μm band is displayed in red, absorption at that wavelength is imaged in bright red, standing out. Non-inverted display would render low logarithmic residual values representing absorption dark in the chosen display colour. In the above case, absorption at 2.2 μm would then be displayed as "absence of red". Depending on the material's values at other wavelengths, this could equate to either green, blue or a shade of cyan.

An advantage of this method of removing topographic effects over a method such as band ratioing is that the spectral mean value for each pixel i, X_i. ($E_i t_i A_i \rho_i G_i$ as shown in equation 5.4), is not discarded but stored in a separate band. A_i and ρ_i are the only factors in X_i which vary for each sample. As A_i is the slope and aspect of the pixel and ρ_i is the average reflectance, a measure of albedo, the spectral mean values when imaged in black and white give a very useful indication of topography. This image, seen in Plate 5.5, can be used along side the LR imagery to aid fieldwork and also forms the basis for much of the integration work described in chapter 6.

5.8.4 Options in implementing logarithmic residuals

In implementing the logarithmic residual model there are two options. The spectral and spatial means can be geometric or arithmetic and the LR data can be recorded as real or byte data.

1. The type of mean used.

The means used in the logarithmic residuals model to remove the unwanted multiplicative effects are geometric means, which are the nth root of the product from 1 to n. Division using geometric means can remove all of the A_i, E_λ and t_λ terms because the denominator in equation 5.7 is a product. Residuals can be calculated much more rapidly from arithmetic means, which are the sum from 1 to n divided by n. If this is done the denominator is a summed series ($E_{\lambda 1} t_{\lambda 1} A_i \rho_{i\lambda 1} G_{\lambda 1} + E_{\lambda 2} t_{\lambda 2} A_i \rho_{i\lambda 2} G_{\lambda 2} +$ .....) and thus it is not possible to remove all the A_i, E_λ and t_λ terms through a division operation. The calculation of residuals using arithmetic means thus introduces potential

artifacts into the residual. Work at CSIRO has shown, however, that the differences do not affect geological analysis of the data. Geometric means are preferred but for ease and speed of calculation arithmetic means are often used. (A. Green, personal communication). This produces KWIK residuals, named after the program which calculates them, and this quicker option has been used throughout this study.

2. Record the residuals as real or byte data.

The LR process can produce real or byte data. The latter result from linear scaling of each wavelength's LR values between 0 and 255 DN, independently of the range of LR values at other wavelengths. As byte data take up less disc space and are required by image displays they are often the preferred option. If pixel spectra are produced from byte data, however, they may contain artifacts due to the wavelength-dependant scaling. This has not yet been systematically investigated (A. Gabell, personal communication).

When the contrast stretch applied to a particular wavelength at the end of the LR process is defined, the spread of data for that wavelength is considered in isolation from the rest of the data. If the same stretch was applied to all wavelengths, as shown in Figure 5.6, byte residuals from wavelengths containing little contrast would convey little information compared to byte residuals from those with more contrast. Differential stretching enhances the colour composite display of the residuals by maximising the contrast at each wavelength and thus the discrimination in colour composites. The use of the byte data to produce spectra, however, may cause problems. If, for the scene, the maxima and minima at each wavelength represent absolute maxima and minima in a wider (global) sense, such as water and cloud, the spread of data and stretch applied at each wavelength is likely to be similar and no problems arise. If this is not the case, however, the stretch applied after the logarithmic residual process will be different at each wavelength, leading to the masking or creation of absorption features and reflectance peaks as shown in Figure 5.7.

Consider a scene containing iron oxides with low values at 0.49 μm which contains no bright objects at that wavelength but does contain bright and dark objects at other wavelengths. The 0.49 μm real residual data will contain an iron oxide absorption

because the value at that wavelength is low in comparison to all reflectances at all wavelengths. In the 0.49 μm byte residual data, however, the low maximum value in that band leads to the data being over-stretched compared to other wavelengths. Low values are boosted compared to other wavelengths and the absorption is masked. Byte spectra may thus contain scaling artifacts and not portray accurately reflectance, which is the parameter desired for comparison with laboratory and field spectra. This problem has been investigated with the TM data.

5.8.5 TM data

Lithological discrimination is greatest with a colour composite image based on the same wavelengths as those used for the radiance data before enhancement. In order to highlight absorption features this is, however, displayed inverted and this changes the interpretation criteria. Blue means absorption at 0.49 μm (charge transfer effects) and suggests iron oxides, green means absorption at 0.83 μm (crystal field effects) which also suggests iron oxides and red means absorption at 2.22 μm and suggests clay/carbonate/sulphate minerals. With the broad band passes of TM, division of the image into areas of these mineral groups has often been the limit of geological studies. However, the use of two wavelengths for the detection of iron oxides may make possible the further division of this mineral group into different iron oxides such as hematite and goethite, as is possible with laboratory reflectance measurements. This has not been previously demonstrated with satellite data of TM's spectral resolution (Kruse, 1990a). Recent work by Fraser (1990a) using Directed PC Analysis also suggests that this separation can be achieved with TM data. The analysis of information from all wavelengths simultaneously by pseudo-spectra (they are not full spectra, as they do not contain reflectance information for contiguous wavelengths across the range of the instrument) allows the separation of different minerals causing 2.22 μm absorption (Marsh et al, 1992).

Analysis of the TM LR colour composite imagery in Plate 5.6 allows mineral groups and lithologies to be better discriminated than was possible using band ratios or the radiance data without enhancement. Pseudo-spectra for pixels or groups of pixels picked out of the colour composite have been compared with laboratory reflectance spectra,

and the dominant mineral group for a particular pixel identified in some cases. Field work and the analysis of reflectance spectra for field samples followed this to add detail.

KWIK residuals have been created in both real and byte format for the Landsat TM data over this study area. TM LR pseudo-spectra from 60 individual pixels have been generated from both types of data and compared. In some cases the results are almost identical and using the byte version would lead to the same interpretation as using the real data. There are 18 cases where minor differences occur in such things as the depth of an absorption and in a further 18 cases an absorption is lost or falsely created. Figure 5.8 shows an example of the latter for a pixel over a dolerite dyke whose surface minerals are dominated by iron oxides. The pseudo-spectrum from the byte data (a) displays an increase in reflectance towards the shorter wavelengths which may suggest that the additive atmospheric radiance has not been correctly removed. The pseudo-spectrum from the real data (b) contains the expected iron oxide absorption at shorter wavelengths and shows that the increased short wavelength reflectance in the byte spectrum was an artifact of the differential stretch applied at each wavelength.

Problems occur in 60 % of the byte pseudo-spectra studied (36 out of 60). Only the real values should be used for spectral interpretation. If the byte data are kept for visual analysis, the stretch values for each band should be recorded and removed before pseudo-spectra are plotted. All pseudo-spectra generated by KWIK residuals for spectral analysis in this study are from the real data, with no stretch applied.

5.8.6 NS001 data

In order to keep NS001 imagery consistent with TM imagery, the LR colour composite used from the NS001 data has 2.22 μm in red, 0.83 μm in green and 0.49 μm in blue, each inverted. The criteria for the analysis of these images are the same as for the TM data. When the NS001 LR data are used for the production of pseudo-spectra, information from all available wavelengths is analysed, including NS001's third short wave infrared band which TM lacks. In this form, comparison of the data with spectra from other data such as TM, as well as laboratory measurements, has been possible.

5.8.7 GMS data

The visible and near infrared data have been processed separately from the short wave infrared data as they are recorded by two separate spectrometers, with differing gains, offsets and albedo. Treating the two spectrometers separately maximises the information in the residuals. The visible wavelengths in particular still contain noise despite extensive treatment. As this is effectively anomalous information, the logarithmic residual process highlights it. This is not a problem for the short wave infrared data which are virtually free of noise after treatment, a further reason for separate processing of the visible/near infrared and the short wave infrared data.

A greater number of wavelengths are available for study with the GMS data, and so several different colour composites can be formed and used. For compatibility with TM and NS001 LR colour composites, one GMS LR colour composite has 2.22 μm in red, 0.83 μm in green and 0.583 μm in blue, all inverted and interpretable in the usual manner. This does not, however, take full advantage of the information available from the increased number of wavelengths. Two other combinations have been used, selected by the analysis of spectral curves for typical surface materials in the area, one for the visible/near infrared and one for the short wave infrared data. The first combination has 0.955 μm in red, 0.83 μm in green and 0.74 μm or 0.583 μm in blue and is an attempt to separate hematite, with an absorption at 0.84 μm, from goethite, with a broad absorption around 0.92 μm (Figure 3.5). The second combination has 2.352 μm in red, 2.176 μm in green and 2.044 μm in blue and is designed to discriminate between kaolinite with an absorption at 2.17 μm and carbonates with absorption around 2.35 μm (Figure 5.4). At 2.044 μm the edge of absorptions at shorter wavelengths due to calcite, chlorite, montmorillonite or epidote may be detected.

The images are used for the selection of pixels or groups of pixels from which to plot spectra, allowing information from all wavelengths to be analysed. The visible/near infrared wavelength bands are not evenly spaced and are of varying width and response function, but are well spread across that wavelength region (Figure 5.9). The short wave infrared wavelength bands are evenly spaced every 0.044 μm, are all 0.044 μm wide and have identical response functions, providing contiguous coverage over that

wavelength region (Figure 5.10). This allows the production of full near-reflectance spectra from the GMS short wave infrared data.

5.9 Summary

Visual analysis of the data has been done in the form of colour composite imagery. The radiance data produced by the gross additive correction do not permit good discrimination as the majority of the information is correlated between wavelengths and the uncorrelated geological information is masked. Techniques such as band ratios and principal component analysis have been used to enhance the uncorrelated information, improving discrimination, but cannot address the further goal of identification. With principal component analysis in particular there are problems in assigning consistent physical meaning to the data produced.

The logarithmic residual technique aims at producing the geologically meaningful parameter reflectance from the data and allows the production and analysis of near-reflectance spectra. It has identification rather than discrimination as its goal but discrimination is also much improved, as correlated information such as topographic shading is removed. If implemented with care it can produce near-reflectance from the data which is the reflectance modified by several reflectance means. A strict application of the logarithmic residual model requires the means used to be geometric means but in practise the quicker and more easily calculated arithmetic means can be used.

If the logarithmic residual data are to be analysed as spectra and compared with field and laboratory reflectance spectra, the residuals should be recorded as real data, because scaling to byte data introduces spurious features in the residual spectra. A by-product of the logarithmic residual process is a spectral mean image which is a good representation of the albedo in the scene and is useful for pinpointing a location in the field and for structural mapping.

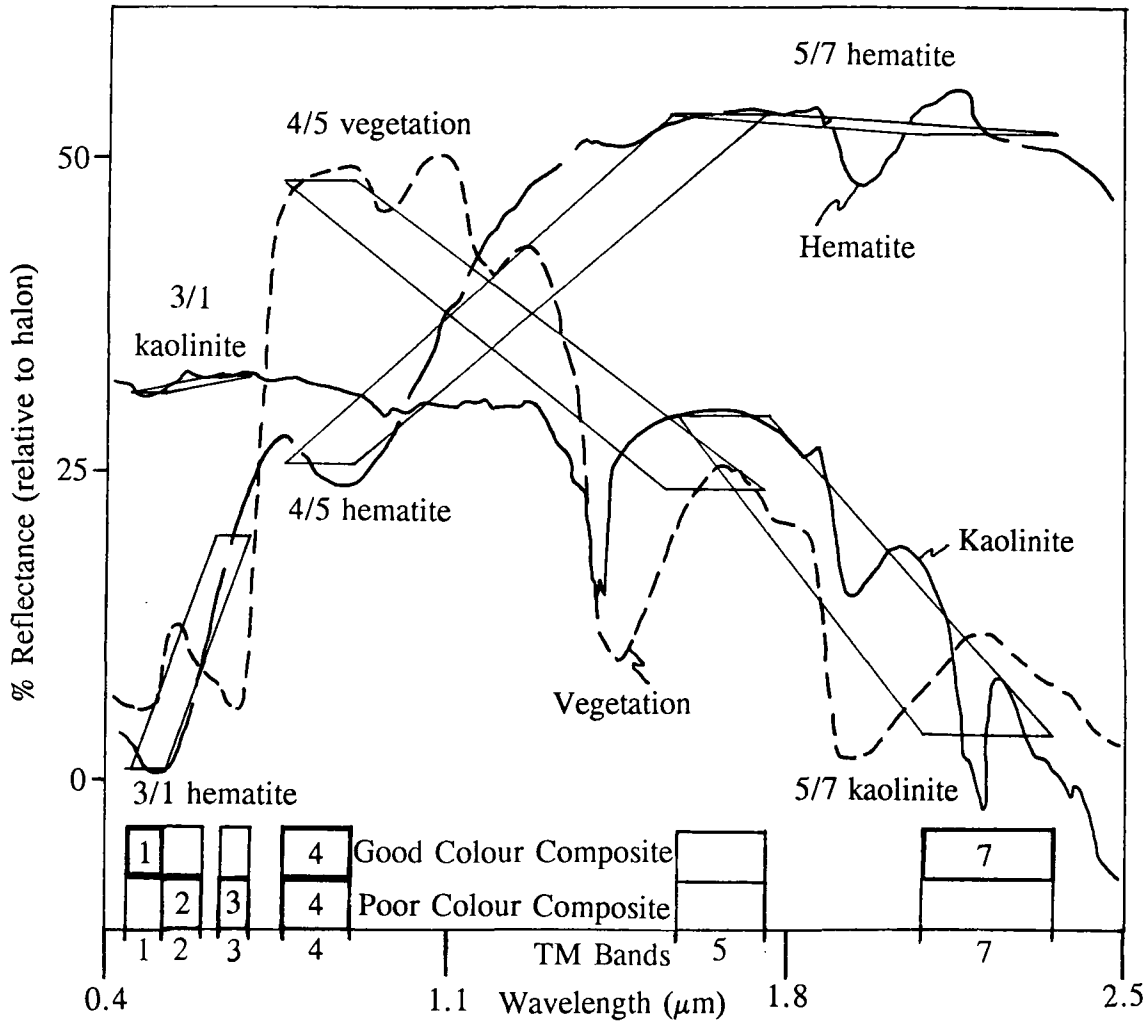

Figure 5.1 An illustration of the way in which the reflectance spectra of clay minerals, iron oxides and vegetation have been used to select the best bands for colour composites (lower boxes) and band ratios (illustrated by polygons on spectra) (spectra: CSIRO).

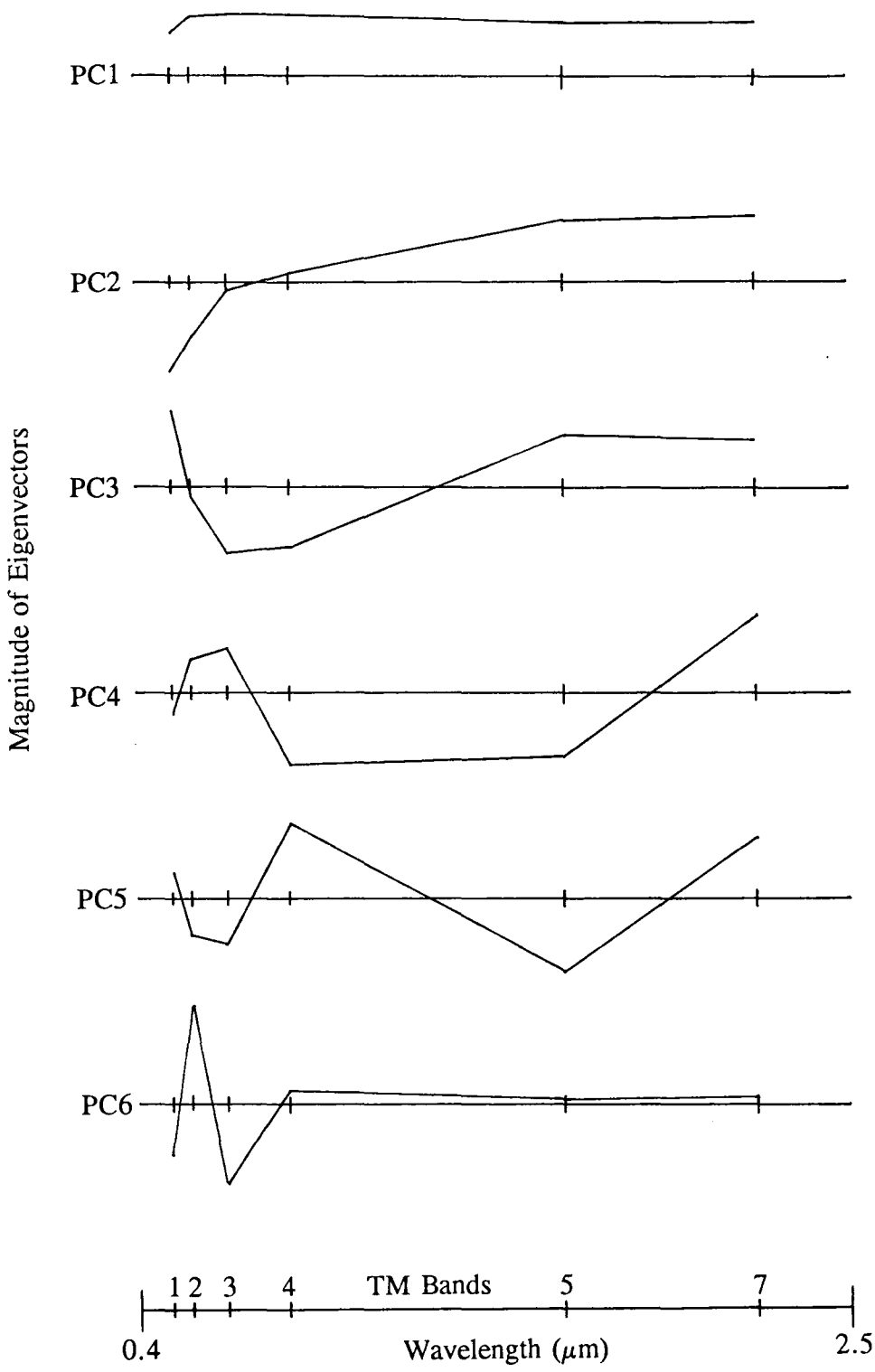

Figure 5.2 Plots for all six PCs calculated for the TM data showing the eigenvector weightings on each wavelength band.

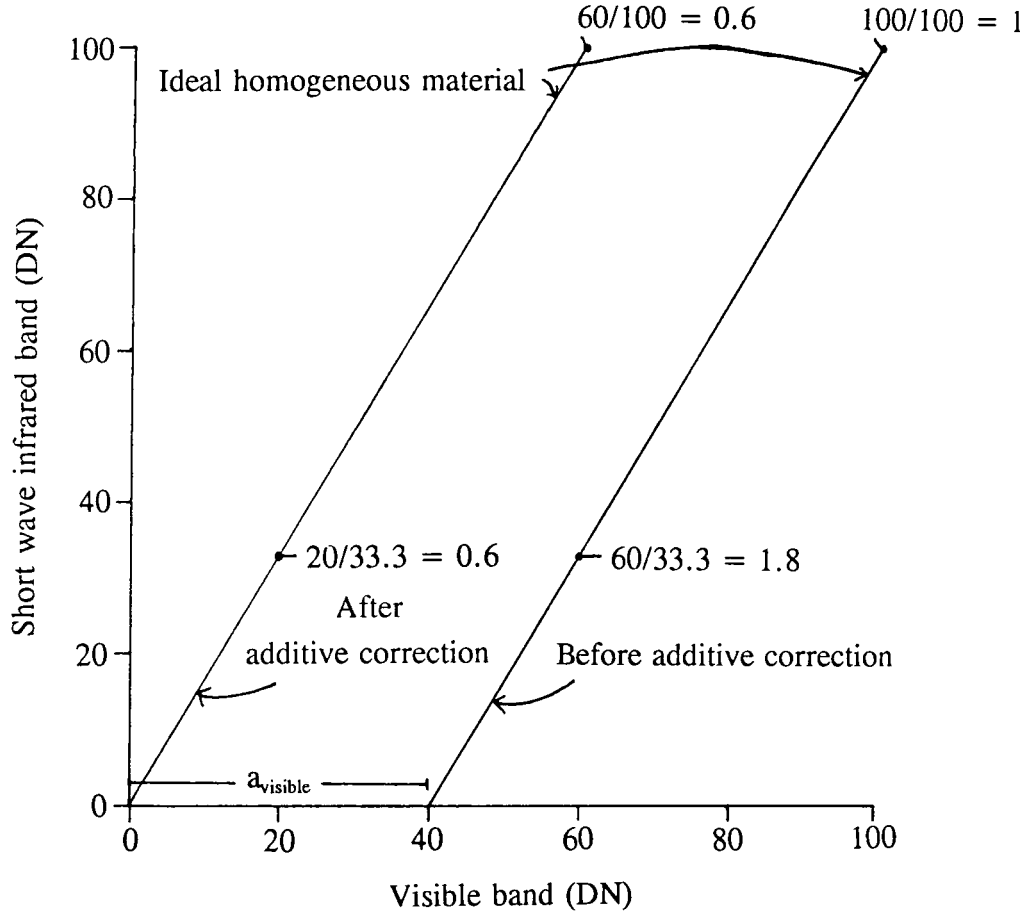

Figure 5.3 An illustration of the fact that a constant ratio value for a homogeneous material is only achieved when the additive correction has been performed (subtraction of $a_{visible}$ in the visible band - correction assumed to be 0 in the short wave infrared).

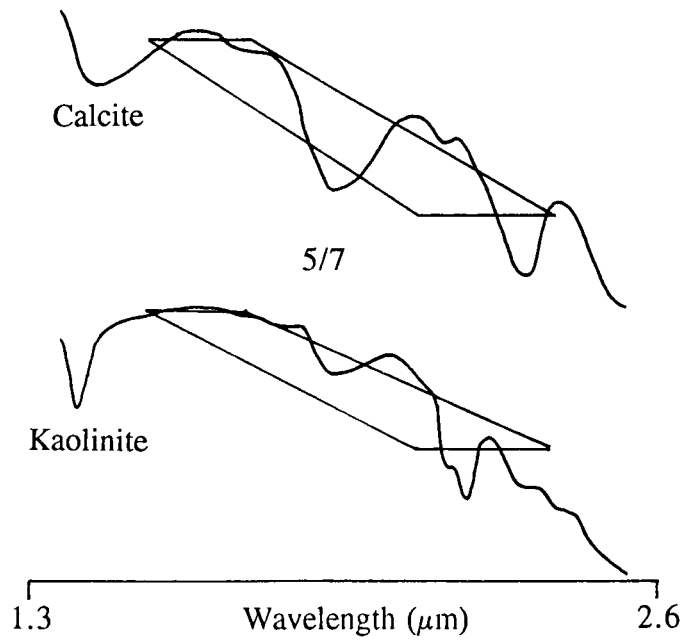

Figure 5.4 The reflectance spectra of calcite and kaolinite may give a similar 1.65/2.22 μm ratio for a sensor of TM's low spectral resolution, as shown by the polygons on the spectra between the two band passes in question (spectra: Geoscan).

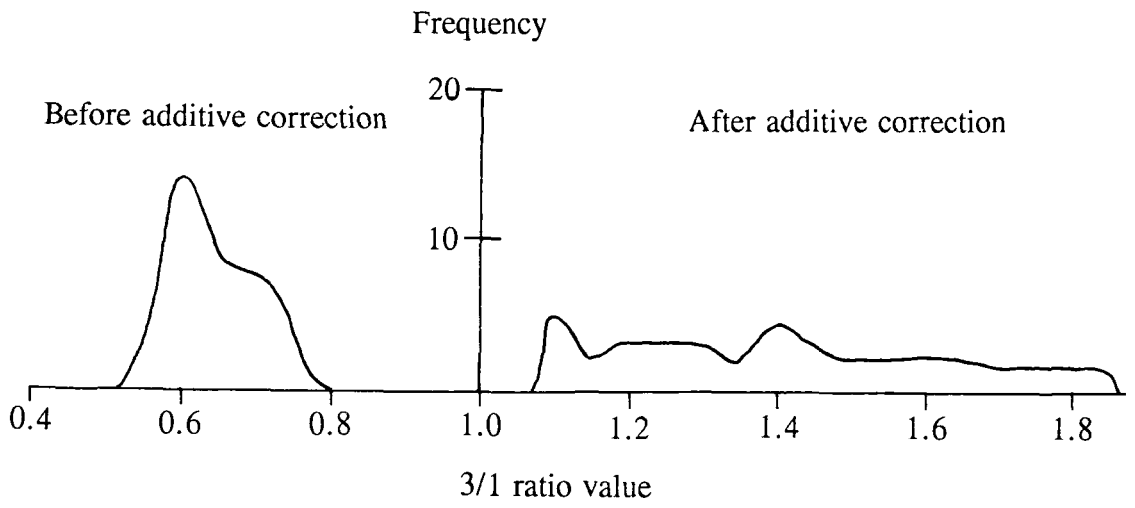

Figure 5.5 A histogram of the ratio 0.66/0.49 μm before and after the additive correction for 32 randomly selected pixels from the TM data, showing the better separation of high and low ratio materials after the correction.

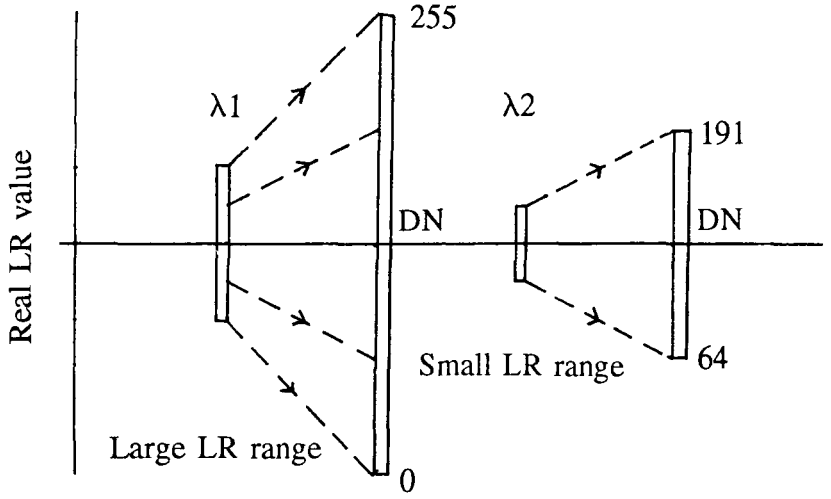

Figure 5.6 A contrast stretch based on the band with the highest variance (λ1) leads to lower variance bands (λ2) having poor contrast.

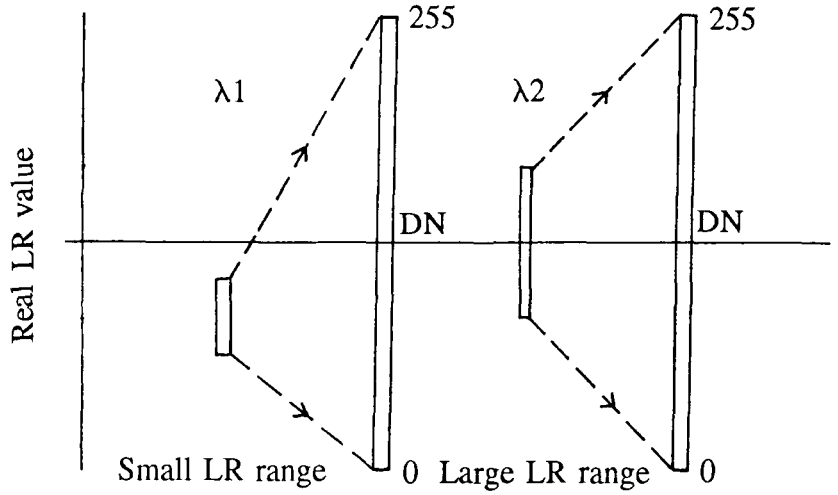

Figure 5.7 Stretching the data at each wavelength separately distorts the relationship between those wavelengths. All the data at λ1 has low reflectance relative to the data at λ2, but after the stretch is applied it appears as if high λ1 reflectance is the same as high λ2 reflectance, and only the lowest λ1 values are still seen as absorption.

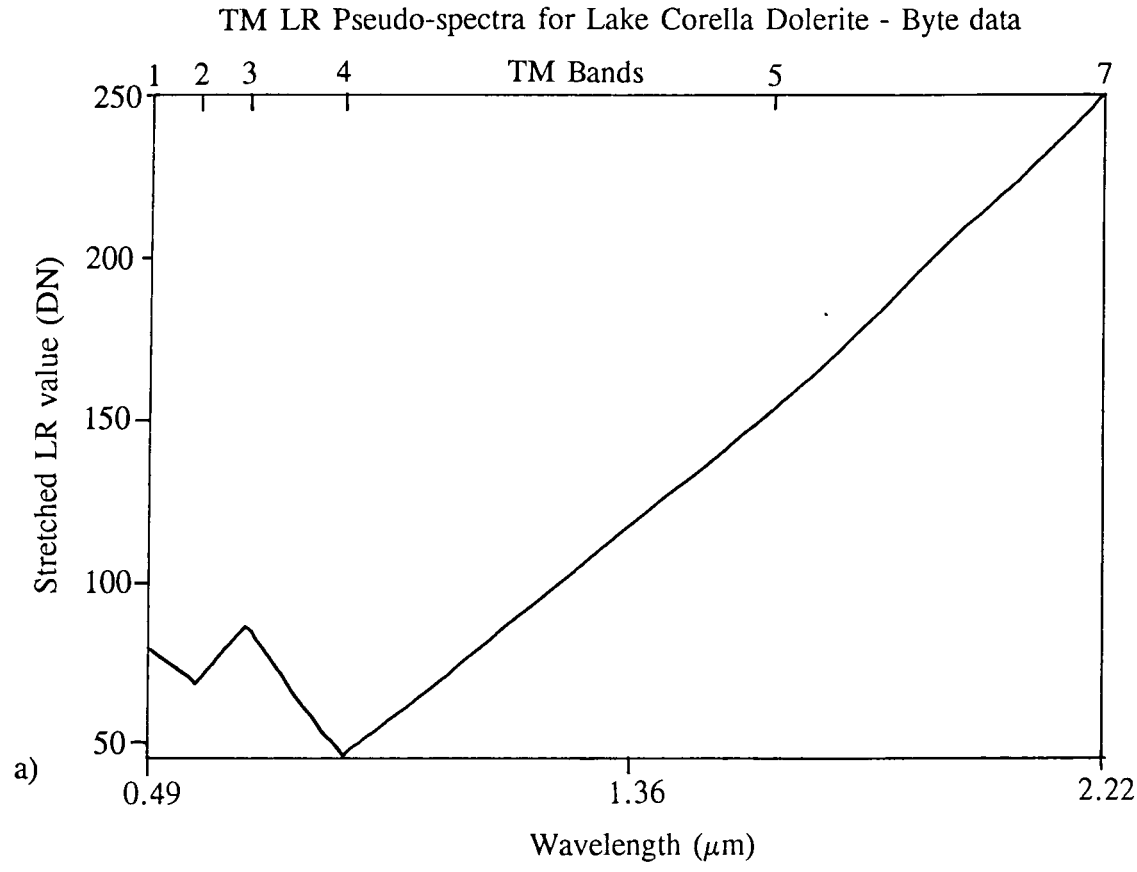

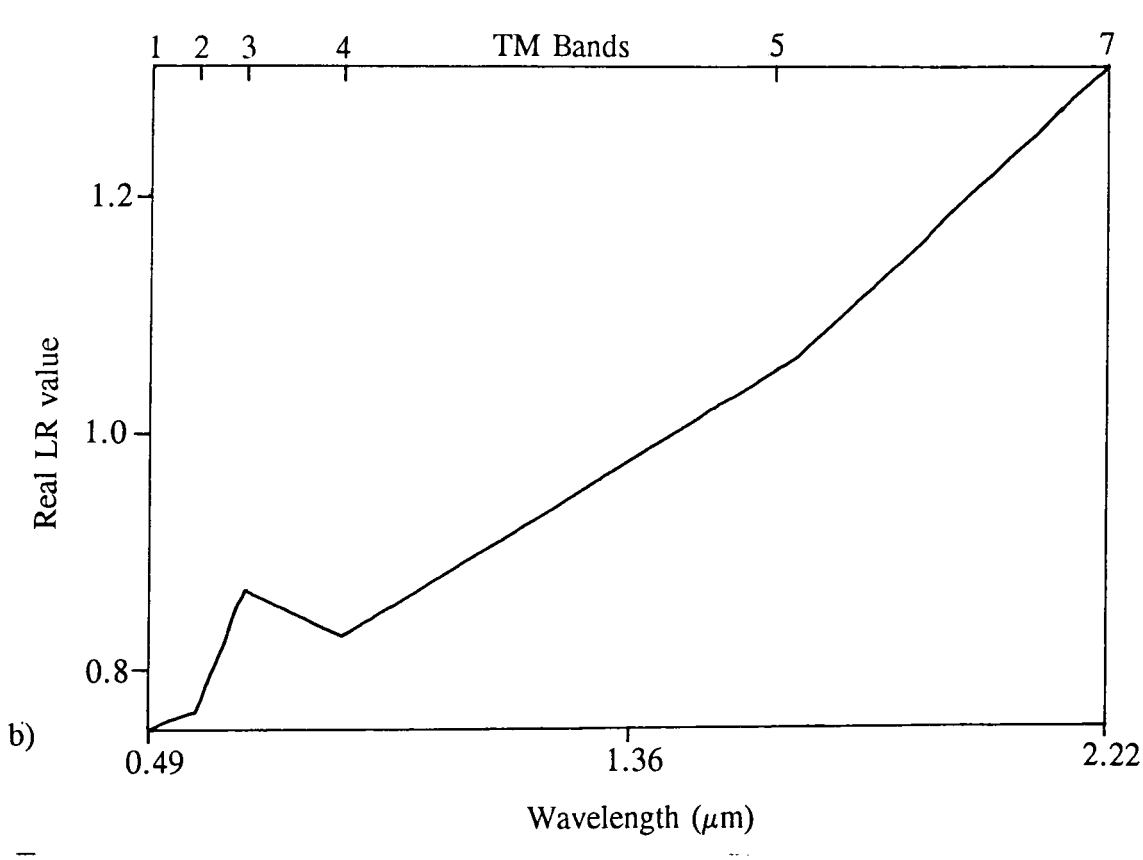

Figure 5.8 a) A TM LR pseudo-spectrum for the Lake Corella Dolerite from a single pixel of the byte data. b) The same pixel pseudo-spectrum from the real data.

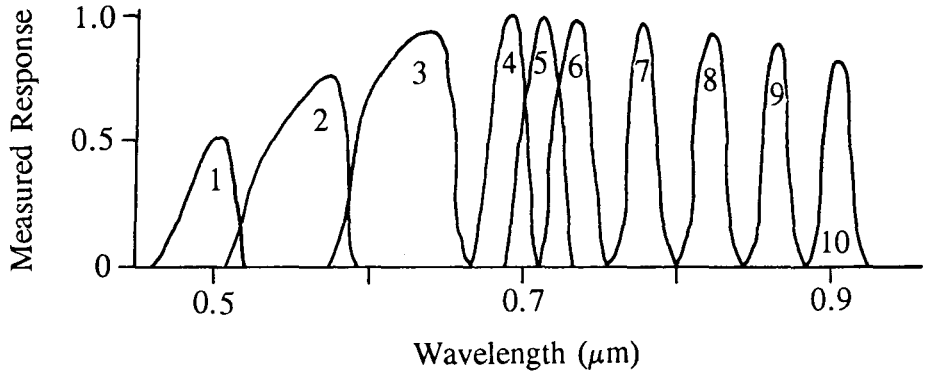

Figure 5.9 Detector response functions for the GMS visible and near infrared bands used in this study (source: Geoscan).

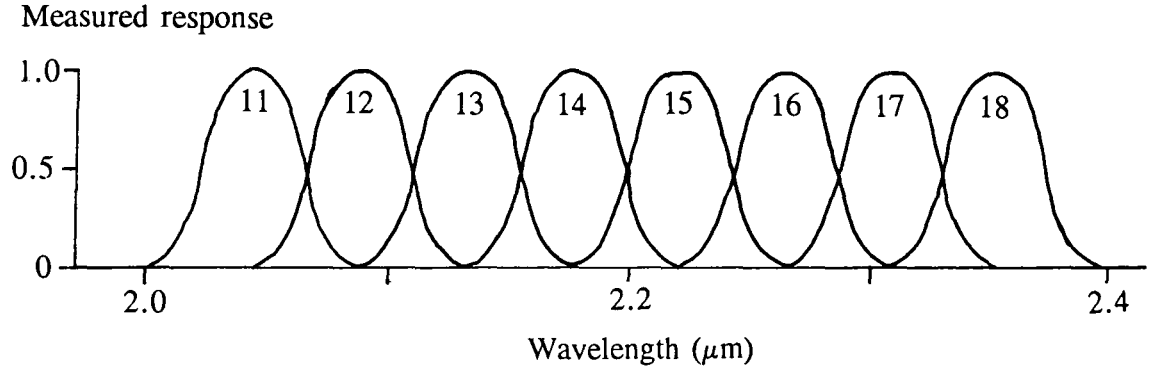

Figure 5.10 Detector response functions for the GMS short wave infrared bands (source: Geoscan)

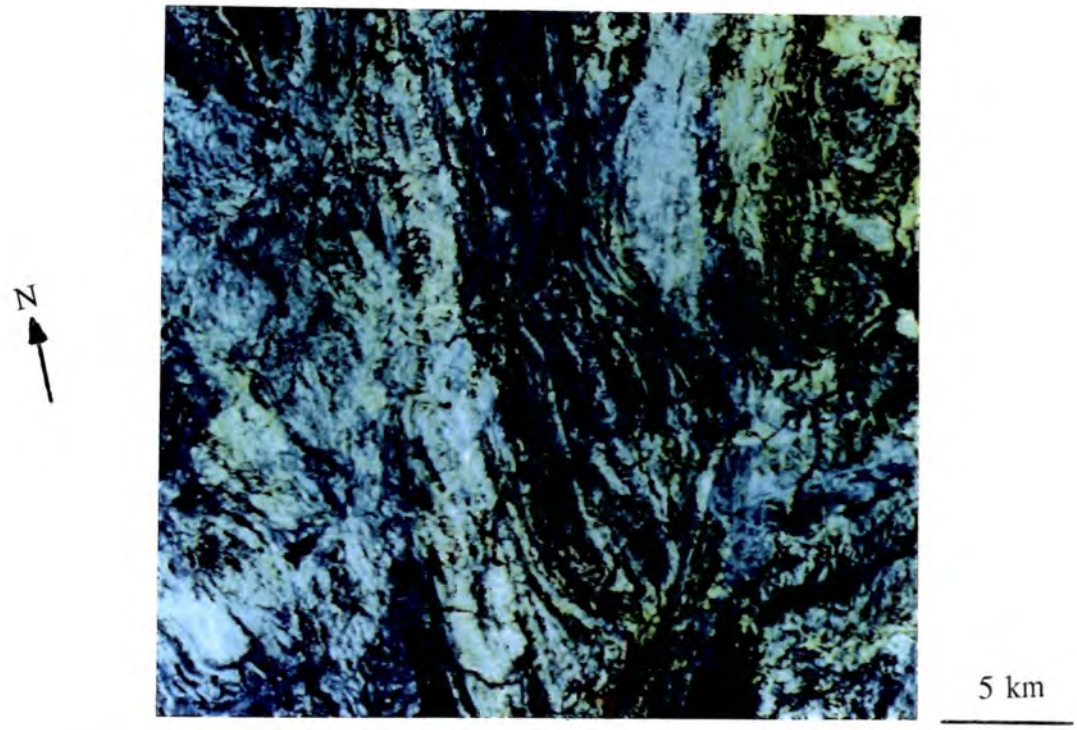

Plate 5.1 TM colour composite of the whole study area, before geometric correction. Red = 0.83 μm, green = 0.66 μm, blue = 0.56 μm, after atmospheric correction.

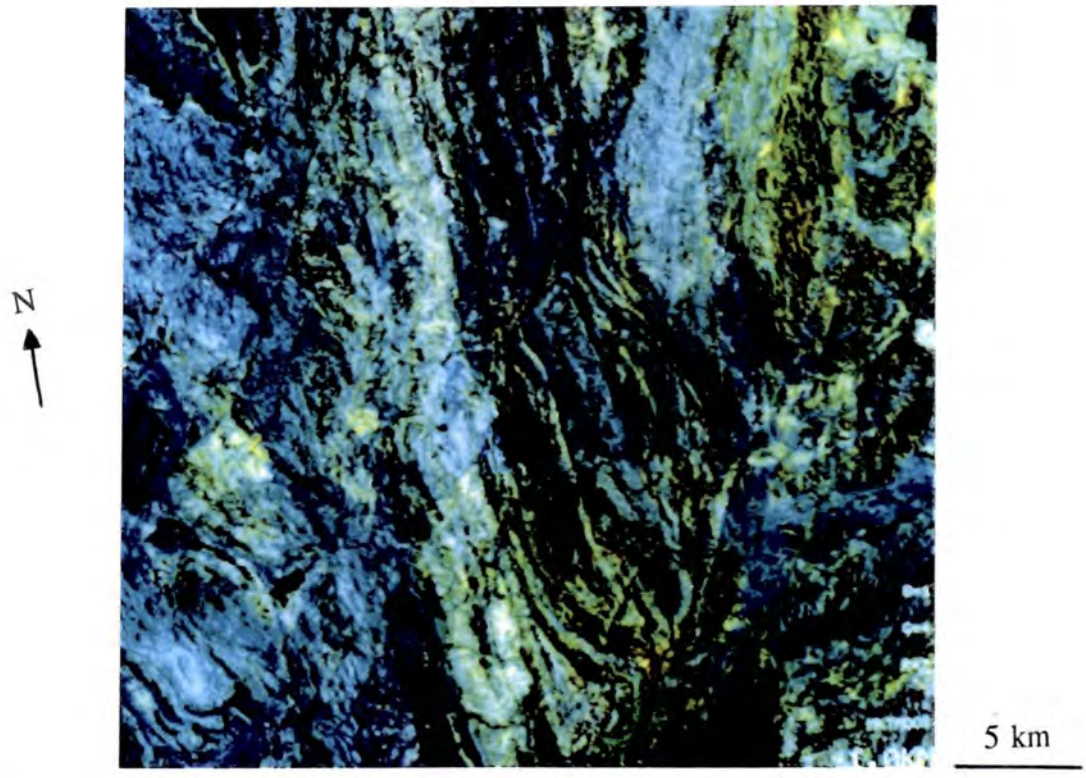

Plate 5.2 TM colour composite of the whole study area, before geometric correction. Red = 2.22 μm, green = 0.83 μm, blue = 0.49 μm, after atmospheric correction.

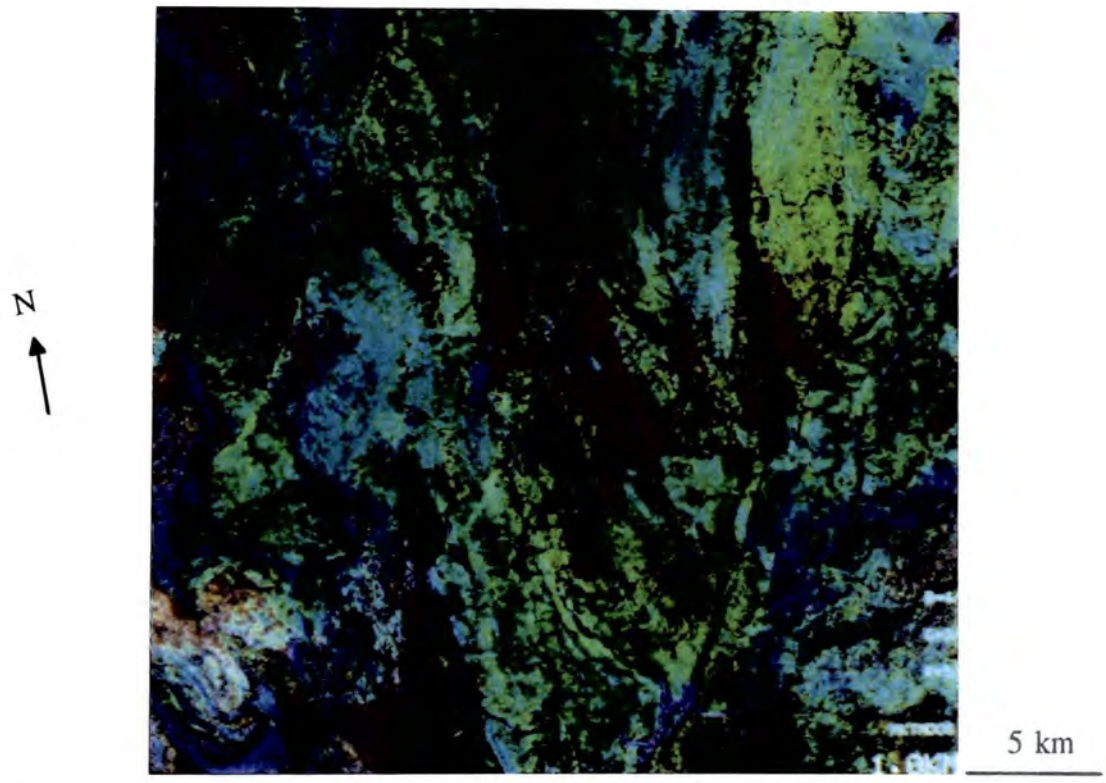

Plate 5.3 TM ratio colour composite of the whole study area, before geometric correction. Red = 1.65/2.22 μm, green = 0.83/1.65 μm, blue = 0.66/0.49 μm.

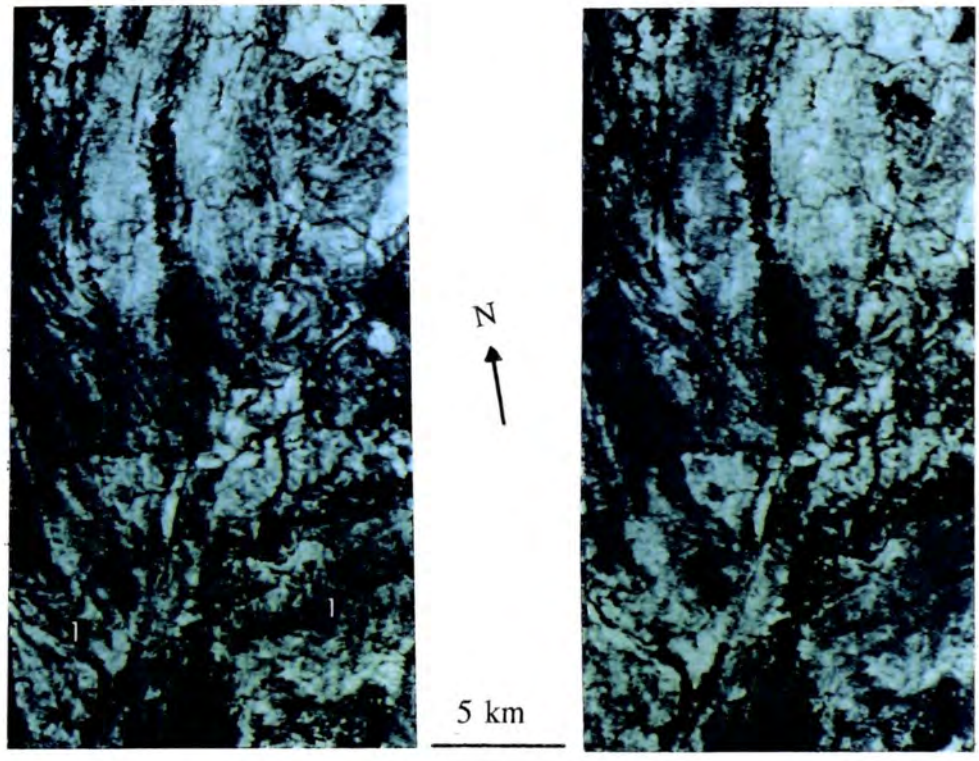

Plate 5.4 TM 0.66/0.49 μm ratio for the eastern half of the scene, before (left) and after (right) the gross additive correction has been performed. 1 = residual topography in the ratio data not corrected for the gross additive component.

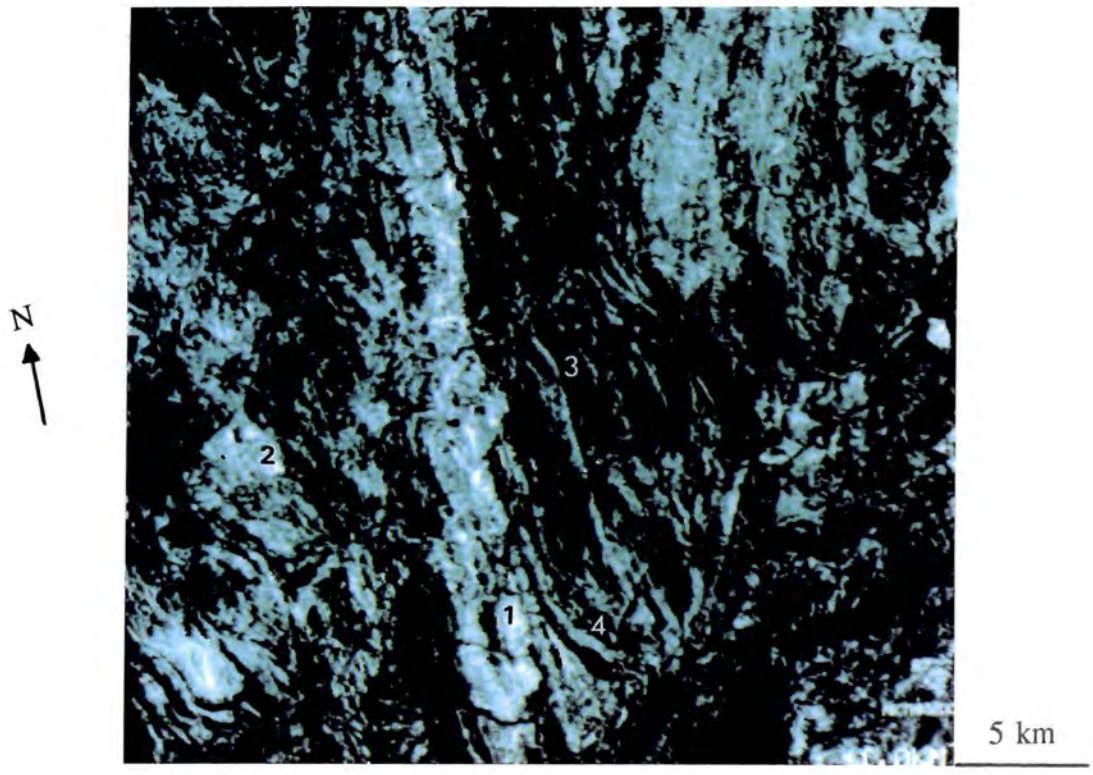

Plate 5.5 TM LR spectral mean image of whole study area before geometric correction. Granites: 1 = Wonga, 2 = Hardway, 3 = Burstall. 4 = Mary Kathleen syncline.

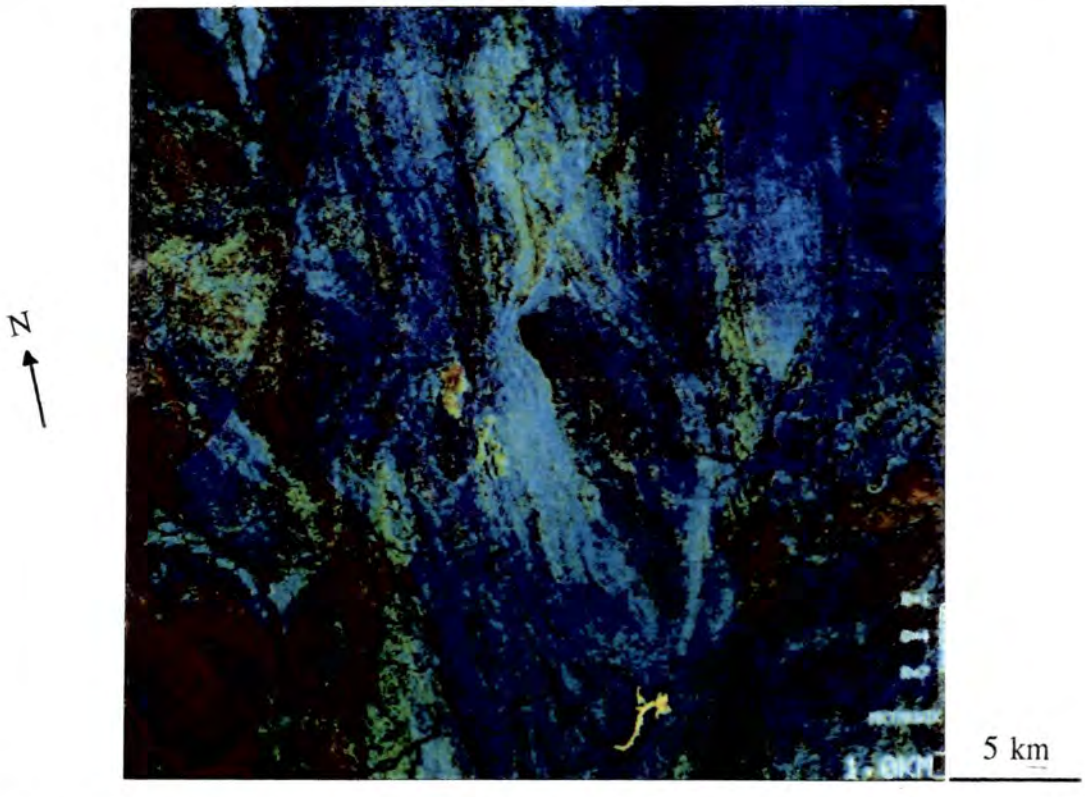

Plate 5.6 TM LR colour composite of the whole study area, before geometric correction. Red = inverted 2.22 μm (absorption at 2.22 μm), green = inverted 0.83 μm (absorption at 0.83 μm), blue = inverted 0.49 μm (absorption at 0.49 μm). This image is included loose in the back pocket as Enclosure 5.1.

Band	λ	PC1	PC2	PC3	PC4	PC5	PC6
1	0.49	+0.32	-0.64	+0.55	-0.15	+0.18	-0.36
2	0.56	+0.42	-0.40	-0.08	+0.25	-0.26	+0.72
3	0.66	+0.45	-0.04	-0.49	+0.33	-0.33	-0.58
4	0.83	+0.45	+0.06	-0.44	-0.53	+0.55	+0.10
5	1.65	+0.40	+0.45	+0.36	-0.47	-0.54	+0.02
7	2.22	+0.39	+0.47	+0.35	+0.56	+0.44	+0.03

Table 5.1 Eigenvector weightings for each TM PC on the original wavelength bands.

CHAPTER 6. GEOMETRIC CORRECTION, AIRBORNE GAMMA RADIOMETRIC DATA AND DATA INTEGRATION

6.1 Introduction

This chapter describes all the processes needed to integrate the Airborne Gamma Radiometric (AGR) data and any of the three radiance data sets. The radiance data have already been spectrally processed so that any further processing should not alter the radiometric characteristics of the data without this being obvious. The radiance data must first be geometrically corrected, which involves the removal of distortions associated with the motion of the platform and the viewing geometry. The data set to be integrated with the AGR data, in this case the TM data, must then be registered to the Australian Map Grid (AMG). The AGR data have already been registered to the AMG, but has had no processing beyond standard corrections for altitude, background and Compton scattering. Further processing of the AGR data has aimed at noise removal, co-registration with the TM data, compensation for the overall radioactive intensity and the combined display and analysis of the two data types. The latter includes simple techniques for joint display as well as more complex techniques which merge compositional information from the AGR data with spatial information from the TM data.

6.2 Geometric correction

The motion of the platform on which the sensor is mounted and the geometry of the look-angle required to acquire the data both cause distortions in image geometry. The distortions due to platform motion may be expected, such as those due to a satellite's orbit, or they may be due to deviations from the expected platform motion, such as an aircraft making a course correction. Distortions due to the viewing geometry are mainly caused by the changes in look angle needed to get a reasonable lateral coverage for an image. As these things vary between sensors each is better considered separately, though some of the corrections are common to several sensors.

6.2.1 TM data

TM data have only minor geometric distortions because the high altitude of the platform means that a small look angle of 15° (Goetz et al, 1983) is sufficient to provide the required areal coverage. Pixel size varies by only 0.5 m between nadir and the edge of a scene and thus does not change appreciably for this subscene within the resolution of the sensor. Along-track the speed of orbit is constant, meaning that there is no need for correction in this direction either. Each scan of the mirror is out of step laterally with the previous scan because the earth is rotating beneath the satellite track. This distortion should be removed during processing at the receiving stage, and does not present a problem in this case. Due to the angled track of the satellite's orbit the image acquired is rotated eastward relative to AMG by an angle of 9 degrees. This rotation is seen but does not hinder the analysis of the data or their use in the field. Its removal is only necessary for the production of maps and the integration of TM data with other data types, as discussed in section 6.4.

The data were acquired before the establishment of the Australian Centre for Remote Sensing, which now processes the data received at the Alice Springs Landsat receiving station. Consequently, the procedures in place at the receiving stage for this data set were not perfect and changes in mirror scan speed are not always adequately corrected. This leads to a residual error on some scans (at some multiples of sixteen lines) which appears as a varying displacement of a line-segment, line or block of lines across-track. This has no predictable pattern and is thus impossible to remove en-masse. An error-by-error correction would be possible in some cases, but would be time-consuming. In practise, it is not worth removing the minor distortions involved with specific corrections, as the integration of this data with the gamma radiometric data leads to the majority of the required geometric corrections being performed.

6.2.2 NS001 data

There are two big differences between airborne data such as NS001 and satellite data such as TM which lead to the former having greater geometric distortions. When the platform is an aircraft the lower altitude means that a large field of view is needed to

image a reasonable area on the ground. The sensor position is also less stable and more difficult to know accurately. Thus geometric problems also fall into two groups, those due to angular distortion and those due to variations in platform position and attitude. It is important to consider these effects and their correction, as the use of such data in industry is unlikely if the image geometry is too poor to allow its use alongside other products which are easily registered to maps.

6.2.2.1 Angular distortions

The distance between the sensor and the ground is typically a few kilometres for an aircraft rather than a few hundred kilometres as it is for a satellite. The geometry dictates that in order for the ground area covered to remain adequate the field of view must increase. At the height of the Hercules C130 survey aircraft used to acquire these data, the field of view must be 100° to give a swath width of around 10 km. Consequently the viewing geometry for an individual pixel varies significantly according to its across-track location, leading to a pixel covering a larger area on the ground at the edge of the swath than at the centre (Figure 6.1). The pixel size at different view angles for this data set is shown in Figure 6.2 and ranges from 10 m for a pixel at nadir to 24.3 m for a pixel across-track at the edge of the swath. The relationship is non-linear, involving the tangent of the view angle, and so the effect is much stronger at the edge of the swath than closer to nadir. This causes a progressive compression of features at each side of the image as successively larger ground areas are imaged as pixels of constant size.

This distortion is solely due to the system's viewing geometry. It is therefore predictable and can be routinely removed by what is known as a tan-theta correction. This involves an across-track nearest-neighbour resampling by a factor which is determined by the scan angle. For example, a pixel at a view angle of 45° has an across-track size of 20 m, and so is resampled into two new pixels. This effect can be seen in Plate 4.1. A pixel at ~35° has an across-track size of 15 m, and so becomes 1.5 new pixels. The central pixel is not resampled at all. After this process, the original across-track pixels are replaced by 954 pixels all with 10 m resolution. Plate 6.1 shows the raw data and the data after tan-theta correction.

The function of this correction is purely to produce geometric accuracy. It cannot alter the real spatial resolution of the sensor's measurements, which still decreases towards the edges of the image. The loss of spatial resolution cannot be made up. Barnsley and Kay (1990) have observed that the image variance is inversely related to the viewing angle, decreasing where the view angle is high. This is because at high angles the spatial resolution decreases, the overlap of adjacent elements increases, and the proportion of various end members visible to the sensor changes. For this area in particular, the shade and vegetation components may dominate at the swath edges and cause problems, for example in the spectral analysis of these data by the logarithmic residual technique.

6.2.2.2 Platform instabilities

As detailed by Drury (1987) and illustrated in Figure 6.3, a number of sudden changes can occur in the sensor's position and orientation relative to the ground. The aircraft can experience roll, which leads to across-track under- or over-sampling, visible in the image as lateral compression or extension respectively, orthogonal to the flight direction. Up to 15 % roll is accommodated by the instrument during the flight, and correction above this is almost impossible without access to flight parameters. A similar along-track effect can be caused by the pitch of the aircraft changing, and is equally difficult to correct. No serious examples of these effects have been identified in these data. If the aircraft yaws, the data will be over-sampled along-track at one edge of the track and under-sampled at the other, leading to along-track extension on one side of the image with corresponding compression on the other. An example of this type of distortion is shown in Plate 6.2 from Flight Line 2. This geometric distortion cannot easily be corrected. Finally, there could be changes in altitude or course, which will alter the scene dimensions for their duration. Plotting of the image boundaries on a map detects such distortions and allows their correction through the calculation of the new scene geometry, pixel size and an appropriate resampling factor. Figure 3.2 shows that for these two flight lines the scene dimensions remain reasonably constant, excepting the southward drift of Flight Line 2 associated with the yaw described above.

On plotting the image boundaries on a map as described, another problem becomes apparent. Flight Line 2 has 3452 lines, and at the desired sample rate (100 lines/km to give 10 m pixels), should be 34.52 km long. Its actual length is 19.23 km, representing a sample rate of 179.4 lines/km giving an along-track pixel size of 5.57 m. As the across-track pixel size is 10 m, the aspect ratio of the image is 1.8:1 rather than 1:1. This over-sampling has been caused either by the aircraft flying too slowly or by the scanner operating at too high a scan rate. It has been corrected by resampling along-track to give the correct aspect ratio, in this case leading to an along-track data compression with a factor of 0.56 (Plate 6.1). Hook (1989) found that NS001 data for a study area near Charters Towers in NE Queensland also had an aspect ratio of approximately 2:1. This suggests that the problem is consistent and is more likely to be due to an incorrect scan rate than the aircraft flying at half the required speed.

In the above example, the aspect ratio was found to be fairly constant over the entire length of the image. Further problems occur, however, where the aircraft speed actually varies during the data acquisition. This is demonstrated by Flight Line 3 where, by calculating the aspect ratio for different 500-1000 line portions of the flight line, the aspect ratio is seen to vary between 1.73:1 and 2.16:1 (Table 6.1). This represents a variation in along-track pixel size in the most extreme case from 5.78 m to 4.63 m, or 1.15 m in every 5.78 m ($\sim$20 %). It is possible to split the image up into smaller portions and correct the individual aspect ratio of each portion before re-assembling the full image. If this is to be attempted it is not obvious at what scale it should be done. An aspect ratio of 2.16:1 over 930 lines is itself an average, and may contain as much variance as does the entire flight line. Being compiled from fewer samples it is more prone to being influenced by one anomalous section with a very poor aspect ratio, due for example to a local, short lived change in aircraft pitch. The use of this type of aspect correction requires that the aspect be measured over as many lines as possible to minimise the influence of such anomalous areas. Flight Line 3 was thus judged to have an aspect ratio of 1.94:1 based on the average of several measurements over the entire length of the flight line and this led to an along-track data compression at a factor of 0.52.

6.2.2.3 Accuracy of the geometric correction

The accuracy of the techniques used to geometrically correct the NS001 data can be assessed by comparing the same portion of the study area as imaged in the two different flight lines, where they overlap. Plate 6.3 shows logarithmic residual colour composites for Flight Lines 2 and 3. There are clear geometric differences between the two flight lines, but these are of a type which cannot be removed by the correction techniques described. For example, an outcrop of the Ballara Quartzite strikes slightly east of north in Flight Line 2 and slightly west of north in Flight Line 3. Under-sampling or over-sampling can lead to a change in strike, but Figure 6.4 shows that these effects cannot take the strike past N-S or E-W lines at the most extreme, as occurs in the change of orientation for this lithology. The cause is likely to be the aircraft yawing and drifting southwards, for which there is evidence in Flight Line 2 at the same point in the image as the occurrence of the lithology in question. Removal of these distortions would require the registering of the data to another, corrected, data set, or AMG. The overall geometry of the imagery is good enough for field mapping and no further geometric correction of this data set has been attempted.

6.2.3 Geometric correction of the GMS data

The Geoscan Mk.II sensor is mounted on a gyroscopically stabilised optical platform in the aircraft so no problems exist due to the aircraft's roll, yaw, or pitch. The scan rate is well coordinated with the flight speed, so there are no along-track aspect problems. The remaining geometric problems are associated with the variation in across-track view angle and so the number of geometric problems is vastly reduced in comparison to the NS001 data, though more exist than in the TM data. The remaining distortions are routinely corrected by a tan-theta correction as described in section 6.2.2.1. This processing stage may already have been completed for any given data set and it is important to find out if this is the case. This study started with raw unprocessed data so that control could be retained over the processing steps implemented. A tan-theta correction must therefore be applied as the final processing stage with this data set involving an across-track resampling after which each line contains 1024 pixels measuring 10.125 m across-track.

6.3 Registering the TM data to the AMG

The satellite borne TM data contain far fewer geometric distortions than the aircraft borne radiance data sets, even after the aircraft data are geometrically corrected. Creasy (1990) successfully integrated SPOT (Satellite Probatoire de l'Obseravation de la Terre) satellite data and data from Geophysical Environmental Research's 64 band aircraft spectrometer, but found there were many more difficulties than existed if only satellite data were co-registered. The TM data have therefore been chosen to investigate integration of the radiance and AGR data. The final stage in the geometric correction of the TM data in preparation for their integration with the AGR data involved registering them to the AMG, to which the AGR data had already been registered. The AMG-registered TM data have also been used as a base for new maps.

The TM data were registered to the AMG by the use of ground control points (GCPs) which define the orientation of the AMG with respect to the TM data. The GCPs used included the junctions of major creeks or roads, recognisable both in the image and on the 1:100 000 topographic map. Fernandez-Alonso and Tahon (1991) used 50 GCPs to register a TM scene covering over 17,000 km^2 to a coordinate system. For the far smaller scene in question here, covering only 900 km^2, and a correspondingly smaller number of GCPs can be used. They should include a minimum of one in each corner plus one in the centre of the image. The TM image can then be warped so that the AMG becomes correctly oriented. The warp used was a simple bivariate linear warp using only x, y and xy terms. It is unlikely that the TM data contain sufficiently complex geometric distortion to warrant the use of higher order quadratic and cubic terms in the warp. A nearest-neighbour resampling has been employed in the warp so that the spectral distortion is minimal. As a check on this, the LR and LSFit data were used and the original LR and LSFit data retained for comparison.

6.3.1 Steps involved in registering the TM data to the AMG

1. GCPs were chosen spaced as described above.

2. The grid reference of each GCP was read off the relevant map sheet as an easting and northing and the map zone recorded.

3. The pixel coordinates of GCPs were read off the TM image.

4. The eastings, northings and map zones were converted to latitudes and longitudes.

5. The **chosen GCPs only** were warped to the map coordinates defined by the longitudes and latitudes.

6. The root mean square (rms) error was checked for each GCP, badly constrained GCPs redefined or replaced and the warp re-run until the rms errors were less than a defined tolerance level.

7. These final GCPs were used to define a warp for the **whole image**, registering it to the coordinate system defined by the latitudes and longitudes.

6.3.2 The accuracy of the warp

Any warp of this form is as accurate as the defined tolerance level. In selecting this many factors must be considered:

1. The maps used to measure the eastings and northings were made in 1971 but the satellite data were acquired in 1987. In a semi-arid environment prone to sudden flooding creeks may move significantly in this time and tracks are frequently relaid from year to year.

2. In reading the eastings and northings off the map, the best possible accuracy allows a point to be defined to the nearest 1/4 mm. This represents 25 m and is almost equivalent to one TM pixel.

3. Creeks are visible in the image because of the vegetation along their courses. The junction of two creeks as defined on a map may be different to the position where the vegetation meets.

4. Creeks are often several tens of meters across so that their junctions may straddle more than one pixel in the image. Smaller creeks, where this will be less of a problem, have less vegetation and therefore are not so clear in the image.

5. Major roads are not prone to these problems, but the area only contains one road large enough to be seen in TM imagery. The tracks which form junctions with it are too small to be seen and their position may be unreliable.

Any one GCP could therefore be out by at least two pixels. As shown in Figure 6.5 six GCPs were used with this data set and so the accuracy which can reasonably be expected increases. Rms errors less than one pixel have been accepted and in the warp performed none exceeded 0.7 pixels. The addition of another GCP increased rms errors. This may have been due to the new GCP being particularly badly located, or because the new GCP revealed an existing local error which none of the previous GCPs was in the correct place to highlight. Thus, while the overall geometry of the image has been corrected to the stated accuracy, local errors may be of greater magnitude.

For an image of this size the six GCPs chosen are sufficient (J. Creasy, personal communication). The accuracy of the warp can be further checked as the warped image has a user coordinate system attached to it, allowing new points to be selected and their latitude and longitude in the image checked against the map. The worst error found in this way was 100 m, but most points checked were less than 50 m out. Given the uncertainties listed above, an error for any given point of 1-3 pixels in 1024 pixels (up to 1 mm on the map) is as good as can be expected and no further improvements have

been attempted. The visual effects of the warp are seen in Plate 6.4 (compare with plate 5.6) and the warped data have 1159 lines by 1237 pixels, with the extra pixels created at the image margins set to the 0 DN. The pixel size for the warped image was set to 30 m at the resampling stage.

6.4 Analysis of the AGR data

AGR data are usually analysed in the form of colour composites such as that shown in Plate 6.5 where the potassium values are imaged in red, the thorium values in green and the uranium values in blue. Smith (1985) looked at the same data set for the whole region in this way and found that the AGR data were a good complement to the 1:100 000 geological map and added detail in places. Smith (ibid.) made no attempt to compensate for the overall radiometric intensity. In this study the data have also been looked at in this way, but at a larger scale at which the noise in the uranium data is more apparent and hinders geological analysis. This noise was therefore treated before integration of the AGR data with the TM data. Further processing aimed at compensating for the overall radiometric intensity and adding spatial information to the AGR data from TM data. Methods for the joint display of complementary information from each data set have been investigated.

6.4.1 Noise removal

The uranium data contain noise due to the decay of atmospheric halon which can be removed before gridding. If this is not done imagery of the uranium data contains the halon component as high frequency noise and discontinuous striping (Plate 6.6), as noted but not treated by Fernandez-Alonso and Tahon (1991). The thorium and potassium data do not suffer from the same problem. Noise removal with radiance data has to cope with noise spread through most or all wavelengths. This is not the case here as two out of three bands are noise-free. Consequently, a different approach has been taken using the LSFit technique of Fraser et al (1986) described in section 5.7.

The uranium, thorium and potassium data are strongly correlated with each other as all measure radioactivity. The U data can therefore be predicted from the Th and K data.

These predicted U data are shown in Plate 6.7. The predicted data have been subtracted from the observed data leaving a difference image dominated by noise but also containing any information unique to the U data. This difference image is seen in Plate 6.8 and one clear U anomaly occurs over the tailings dam of the Mary Kathleen mine. As with the MAF technique described in chapter 4, the noise has been separated from the majority of the signal and the noise-dominated difference image can now be treated.

Striping has been treated by normalising line means to a smooth curve fitted through them. High frequency noise has been treated using a moving box filter. Both techniques were fully described in section 4.2., and they were again successful in the majority of cases. Problems were found where a stripe only persists along a line for a few tens of pixels. A technique has been developed by the author for treating these short stripes, based on the usual treatment for high frequency noise. The short stripes are effectively elongate spots and can be removed using a modification of the box filter. Rather than using a 3 line x 3 pixel box, the dimensions of the box are changed so that a 1 line x 199 pixel horizontal box is used. Short stripes along a line are replaced by the average of the 199 pixels along the same line to either side, mimicking the removal of high frequency noise. If the noise has not been largely isolated from the signal this technique cannot be used as it would have a large effect on the signal. The result of the application of these noise removal techniques to the noisy difference image is shown in Plate 6.9. The noise has been largely removed, but the residual geological signal remains unaffected.

The cleaned difference image was then added back to the predicted uranium data to give the cleaned uranium data shown in Plate 6.10. Comparison with Plate 6.6 shows there has been a significant improvement between these and the original uranium data. As the total count values represent radiation measured for all three elements they also have a noise component from the atmospheric halon and this can be treated in the same way.

6.4.2 Integration of the AGR data with the TM data

The TM and AGR data sets have both been registered to the AMG and so share a common coordinate system. The TM data set has 30 m pixels and the AGR data set

100 m pixels so one of the data sets had to be resampled to the spatial resolution of the other before they could be integrated. As the TM data contain the spatial information, it was sensible to preserve this by resampling the AGR data to the spatial resolution of the TM data. This was done by nearest-neighbour resampling to preserve the radiometric information in the AGR data. After this was done the common coordinate system allowed a sub-area of the AGR data to be selected which matched the warped TM data and had the same dimensions in lines and pixels. The accuracy of the match depends on the accuracy of the warp applied to the TM data, as discussed in section 6.3.2, and the accuracy with which the AGR data have been registered to the AMG. The AGR data have been registered to the AMG with the same accuracy as the TM data (M. Hornibrook, personal communication). The two data sets should therefore have been registered to $\pm$ 100 m, allowing their integrated analysis.

6.4.3 Ratio normalisation of the AGR data

Table 6.2 contains the statistics for the AGR data and shows that this data set has a very large dynamic range. It is therefore difficult to scale the data for display between 0 and 255 DN in a way which allows information to be extracted from very high or very low response areas, which saturate at 255 DN or get truncated to 0 DN respectively. A granite may be saturated at 255 DN for all three radioactive elements, when in fact the response due to uranium could be higher than that due to either the thorium or the potassium. A dolerite may be scaled to 0 DN for all three elements when the small response present is dominated by uranium. This potentially useful information is hidden by the overall intensity of the radioactivity, as mentioned by Smith (1985).

A similar problem has been described for the radiance data sets. These are dominated by the intensity variations due to slope and aspect and this has been overcome by employing the band ratioing technique. The ratioing approach can be used again with the AGR data. The total count value for each pixel is a measure of the overall radioactive intensity and can be ratioed against each of the uranium, thorium and potassium data values. It then becomes apparent which element contributes the most to the high intensity values, and which element dominates the low intensity areas. A large uranium/total count value means that uranium is a large contributor to the recorded

intensity. A colour composite with the potassium/total count ratio in red, the thorium/total count ratio in green and the uranium/total count ratio in blue was created and is shown in Plate 6.11. It reveals detail in those areas previously saturated black or white. Any remaining noise is highlighted by this technique but it provides a valuable approach to increasing discrimination in otherwise saturated areas such as granites.

6.4.4 Combined colour composites of the AGR and TM data

One of the stated aims is to investigate the complementary nature of the AGR and TM data sets. Once registered they can be placed in different bands of the same image file and colour composites formed from any combination of the two data types. The TM data provide information on the surface mineralogy of the rocks, dominated by the elements Fe, Al, Mg, Ca, O and H. U and Th data are likely to contain information on the more minor mineral constituents of the rocks as these elements are not abundant in comparison to the former even when occurring in economic mineral deposits. They are therefore unlikely to provide information which is related to that provided by the TM data. Of the elements on which the AGR data provide information, K is the most closely related to the TM data. It has a comparable abundance to the elements detected by TM in crustal rocks. K is a constituent of feldspars, a very common crustal mineral which weather to clays such as illite, kaolinite and montmorillonite (Gribble and Hall, 1985). Correlation might therefore be expected between high K values and areas thought by analysis of the TM data to be dominated at the surface by clay minerals. The AGR data may give information on the whole rock composition where the TM data highlight the minerals produced during the weathering of that rock.

Two colour composite images have been used to study this potential association. The first, shown in Plate 6.12, has inverted TM LR 2.22 μm data in red, K data in green and inverted 0.49 μm TM LR data in blue. Under this scheme, iron oxide areas should be imaged in blue, K areas in green, clay areas in red and areas where K and clays coincide in orange or yellow. The second, shown in Plate 6.13, has an LSFit residual of the 2.22 μm TM data, designed to highlight clays, in red, inverted 0.83 μm TM LR data in green and K data in blue. This should render K dominated areas blue, iron oxide dominated areas green and clay areas red, with any K - clay association imaged in

purple. The second scheme is designed to highlight a different iron oxide absorption to the first and attempts to highlight clays in areas where they may be masked by vegetation, as discussed in section 5.7. These images will be referred to when geological problems are addressed in chapters 7 and 8.

6.4.5 Giving the AGR data a spatial context

The AGR data contain valuable lithological information but only their registration to the AMG gives this a spatial context. This weakness was particularly apparent when the AGR imagery was used in the field, where pinpointing a location often requires the use of terrain features. Air photographs and the radiance data sets contain this information, which generally speaking is of two types; the drainage pattern and the albedo. Once the AGR and TM data sets have been co-registered and share the same spatial framework it is possible to add spatial information from the TM data to the AGR data.

6.4.5.1 Drainage pattern

The drainage pattern could simply be traced off a map and superimposed in some way on the AGR imagery, either physically or digitally. As previously noted, however, the most recent maps are 20 years old whereas the TM data are 4 years old. A more accurate drainage pattern can therefore be produced from the TM data and combined easily with the AGR data since the two data sets are in a common image file.

The usually dry creeks which dominate the drainage pattern are seen in the TM imagery because green vegetation, absent elsewhere in the area, clusters densely along their courses (Plate 1.2). A vegetation density map created from the TM data thus accurately delineates the drainage pattern. One of the most widely used vegetation index is the normalised difference vegetation index, which employs the difference between the red and near infrared responses of vegetation (e.g. Dudgeon et al, 1990). In this study the most effective vegetation index was found to be the ratio of these two responses, using the wavelengths 0.83/0.65 μm for the TM data. The discrimination was maximised by calculating the ratio using the LR data in which the absorption at 0.65 μm has been highlighted. This ratio could be used to produce an image with a range of values from

no vegetation in black to 100 % vegetation in white, but this would not easily combine in a three colour composite with the AGR data. It was therefore necessary to create a creek map from this image in which creeks have one value and all other terrain types have another. Such a binary map is suited to display in the graphics plane of the display device and can thus be superimposed on the colour composite.

Visual inspection of the vegetation image scaled for display between 0 and 255 DN showed that most values greater than 240 DN are confined to creeks. All values above 240 DN were set to 1 and all values below 240 DN to 0, resulting in a binary creek map of the type required. Some of the more minor creeks appeared disjointed and were "sewn together" using a low pass box filter designed to set pixels in a 3 line x 3 pixel box to 1 if a value of 1 is encountered. Isolated patches of increased vegetation not associated with creeks were treated in the opposite way as if they were noise using a high pass filter. Plate 6.14 shows an example of an AGR colour composite with the binary creek map overlaid in white and illustrates one problem with this scheme. The Burstall Granite in the lower left of the image is saturated to white for all three elements and so causes a potential confusion with the binary creek map. Elsewhere the creek pattern is clear and features such as creek junctions can be used to pin-point localities.

6.4.5.2 Slope and aspect

Fernandez-Alonso and Tahon (1991) have used the 1.65 μm TM band as a representation of topography, which is unsatisfactory as it contains spectral as well as spatial information. Albedo information is well-represented in these TM data by the spectral mean values (Plate 5.5) calculated as part of the logarithmic residual technique of Green and Craig (1985). These data have therefore been used as the basis for adding topographic information to the AGR data. Two approaches have been taken to the integration of the data sets.

The first approach is similar to that of Fernandez-Alonso and Tahon (1991), who added half the DN value of the 1.65 μm TM data to each of the U, Th and K values and rescaled the resultant values to produce a colour composite of the combined data sets.

In this case the U, Th and K data and the spectral means were first scaled to have the same range of DN. The spectral means were then added to each of the U, Th and K bands so that a portion of the intensity in the resulting data was controlled by the albedo from the TM data. The resulting data were then rescaled between 0 and 255 DN for display. In some areas this technique successfully combined the radiometric data and TM albedo information. In other areas however the approach caused confusion as it produced imagery with intensity controlled by both topography and gamma intensity. For example, the Burstall Granite has high gamma intensity and low albedo while the Wonga Granite has high gamma intensity and high albedo. The relationship between the gamma radiometric values for these two rocks was not clear in the combined data because of the introduction of intensity variations due to topographic differences between the two lithologies.

The second approach was an attempt to prevent confusion of the two intensities by removing the radiometric intensity altogether and replacing it with the albedo values from the TM data. This was done by using the hue saturation intensity (HSI) transformation described in Mather (1987) and Drury (1987). The mathematics are given in Gillespie et al (1986), who have used the technique to overcome problems of inter-wavelength correlation. Blom and Daily (1982) used the technique to combine Seasat Single Aperture Radar data with Landsat MSS data for lithological analysis. Chavez et al (1991) found that when the technique was used to combine spectral information from TM with higher resolution spatial information from the SPOT satellite some spectral distortions were introduced. This was attributed to the failure of the assumption that the intensity for the two data sets was equivalent. In this study the gamma radiometric intensity was to be replaced with the TM albedo information. As the two were not expected to be equivalent the problem described by Chavez et al (ibid.) did not prevent the technique being applied.

The HSI transformation takes advantage of an alternative colour space to the RGB colour space used so far in this study. The conical HSI colour space is a close analogue to human colour vision and is shown in Figure 6.6. The apex of the cone is a common origin for the coordinate system of both colour spaces and represents black in both. A datum situated on the line R=G=B, the central axis of the cone, is a shade of grey and

its position along that axis represents its intensity. At any point along this axis a circular cross section can be drawn. The colour or hue of a datum is represented by its angular position around this circle and the saturation by the distance the datum lies from the central axis.

Data with three variables represented in RGB colour space can be transformed on most image processing systems to give three new sets of values for the data, their hue, saturation and intensity. Hue ranges from 0 to 255 DN, representing angles between 0° and 360° such that, if 0 DN is blue, 85 DN (120°) is green, 170 DN (240°) is red and 255 DN (360°) is blue again. Saturation also ranges between 0 and 255 DN and represents the angle between the central axis and a line drawn from the origin through the datum. The intensity varies between 0 (black) and 255 (white) DN.

The above transformation has been performed on the U, Th and K data and the intensity values then replaced by the TM spectral mean values, scaled between 0 and 255 DN. The transformation was then inverted to give U, Th and K data with a pixel's colour and saturation controlled by the amount of each element present and intensity controlled by the albedo of the pixel. These data, with K in red, Th in green and U in blue are shown for the whole area in Plate 6.15. Plate 6.16 shows an area over the Mary Kathleen Syncline both before and after the HSI integration of the two data sets. The colour information is preserved in the integrated data but a valuable spatial context is clearly added by the TM albedo information. Areas which are white in the standard AGR data have no colour assigned to them and so their appearance in the integrated image is controlled by the intensity due to their slope and aspect alone. Consequently they appear as shades of grey.

Plate 6.17 shows a further combination of the two data sets. The compositional information is due to the three radioactive elements, with K in red, Th in green and U in blue. Spatial context has been added from the TM spectral means using the HSI transformation and this has been augmented by displaying the drainage pattern in white in the graphics plane. This combination of the two types of terrain information and the AGR data also avoids the potential confusion of white creeks with white granites, as the latter now appear in shades of grey. Such data combinations greatly increase the ease

with which the AGR data can be used in the field and also allow the potential effects of the geomorphology of the area on the measured radiometric response to be investigated in the laboratory as well as in the field.

6.4.6 Threshold images

The technique used to isolate areas dominated by vegetation has also been used to delineate high concentrations of other materials of more geological interest. For example, if the K data are scaled for display between 0 and 255 DN any pixel with a value over 200 DN has a high K response. The value 200 DN has been used as a threshold, with any values greater than the threshold set to 1 and other values set to 0, and a binary high-K threshold image produced. Other threshold images have been created from the TM data, such as 0.49 μm iron absorption, 0.83 μm iron absorption and 2.22 μm ?clay absorption.

In order to compare the distributions of these materials, a spatial context has again been added. The TM spectral mean values are used as a base greyscale image on which the threshold images can be displayed as colours. This has been done by displaying the TM spectral mean values in the red, green and blue channels of the display device, so that a black and white image results, representing the albedo. If a binary threshold image is added to TM spectral mean values in the blue channel only, portions of the image with the value 1 have increased brightness in the blue channel alone and thus those areas are mapped in blue on top of the albedo greyscale. In practise this is not visible to the human eye if only 1 DN is added, so the threshold image must be multiplied by an appropriate factor before it is added to the topography. The factor chosen must be large enough that enough colour is added to the image for the areas above the threshold value to be delineated, but low enough that the albedo information is not obscured. If the same process is repeated for two more threshold images in the green and red channels the result is a threshold image such as the one in Plate 6.18. Red areas highlight iron absorption at 0.83 μm, green areas have deep 0.49 μm iron absorption and blue areas have high K responses.

Such images are one approach to producing mineral distribution maps. Whilst not as sophisticated an approach as the unmixing techniques being developed by Settle (1990) and others, the images produced have the advantage of being very easy to compute, to the extent that they can be experimented with in real-time. The threshold images integrate two different types of data without confusing the information present in each. It would be easy to add further co-registered data types, such as geochemical data, to this scheme, or even an unrelated variable such as gravity data. These images will be referred to again when geological problems are addressed.

6.5 Summary

Satellite data contain far fewer geometric distortions than aircraft data as both the stability of the platform and the viewing geometry are superior. Many of the geometric problems encountered with aircraft data can be overcome by processing, or by mounting the sensor on a gyroscopically stabilized platform in the aircraft, as is the case with the GMS data. However, problems remain for which no simple correction is available. This means that the TM data are more suited to integration with the AMG-registered AGR data than either the NS001 or the GMS data.

The TM data have been registered to the AMG using a simple bivariate linear warp based on ground control points. The AGR data have been treated for noise, resampled to the spatial resolution of the TM data and an area has been chosen which matches the TM data. A file has been created which contains both data sets under a common coordinate system. The joint display of the two data sets has been achieved in a variety of ways. The influence of the overall radiometric intensity has been reduced using a ratioing technique analogous to that used with the radiance data to remove the topographically controlled intensity variations.

Spatial information from the TM data can be added to the AGR data. The simple additive approach to this integration of the two data sets was not successful, confusing the albedo and gamma ray intensities. The most successful method involves using a HSI transformation as the basis for replacing the radiometric intensity with the albedo information contained in the TM spectral mean data calculated during the logarithmic

residual process. Further spatial context can be provided by overlaying the drainage pattern, derived from a TM vegetation enhancing ratio, on the AGR imagery. The TM spectral mean data can be used as a topographic map on which the mineralogical and chemical information derived from the two data sets can be concurrently displayed. Such information may be extracted using a simple thresholding technique with both the TM LR and the AGR data.

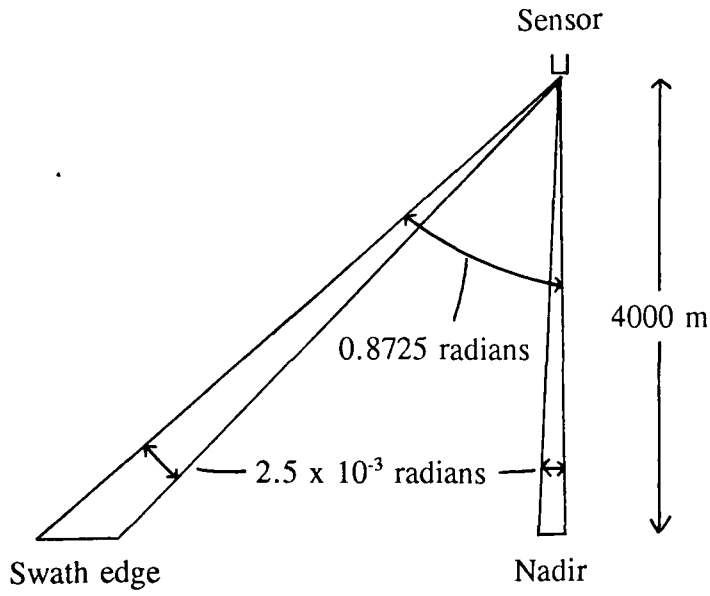

Figure 6.1 At nadir, NS001 pixel size = 4000 (tan 2.5 x 10^{-3}) - 0 = 10 m (across-track). At swath edge, pixel size = (4000 tan 0.8750) - (4000 tan 0.8725) = 24.3 m.

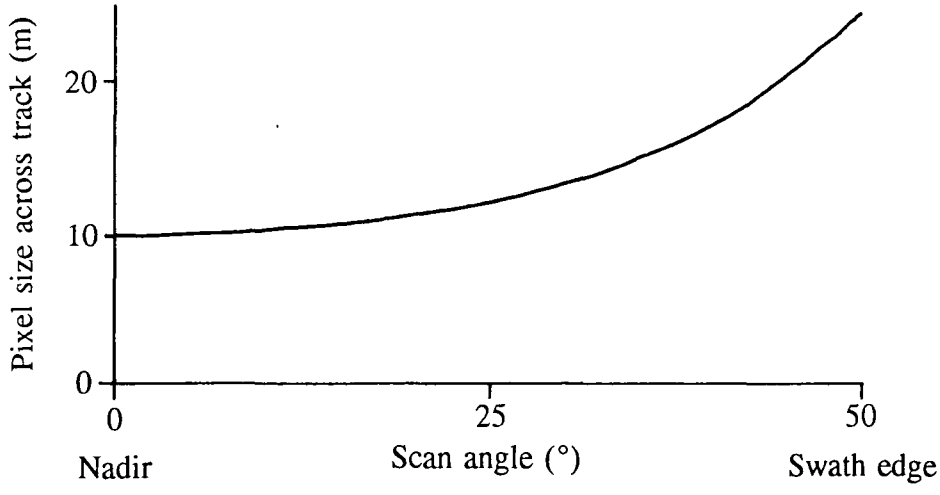

Figure 6.2 The variation of pixel size across-track for the NS001 sensor.

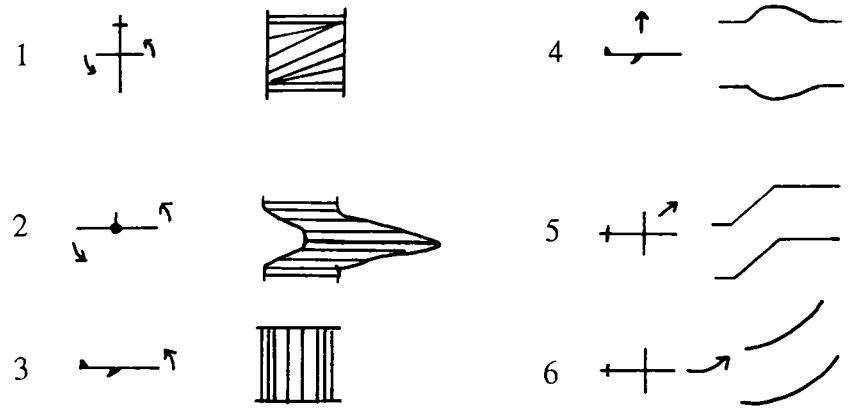

Figure 6.3 Distortions of image geometry due to the motion of the aircraft. 1 = yaw, 2 = roll, 3 = pitch, 4 = altitude change, 5 = drift, 6 = turn.

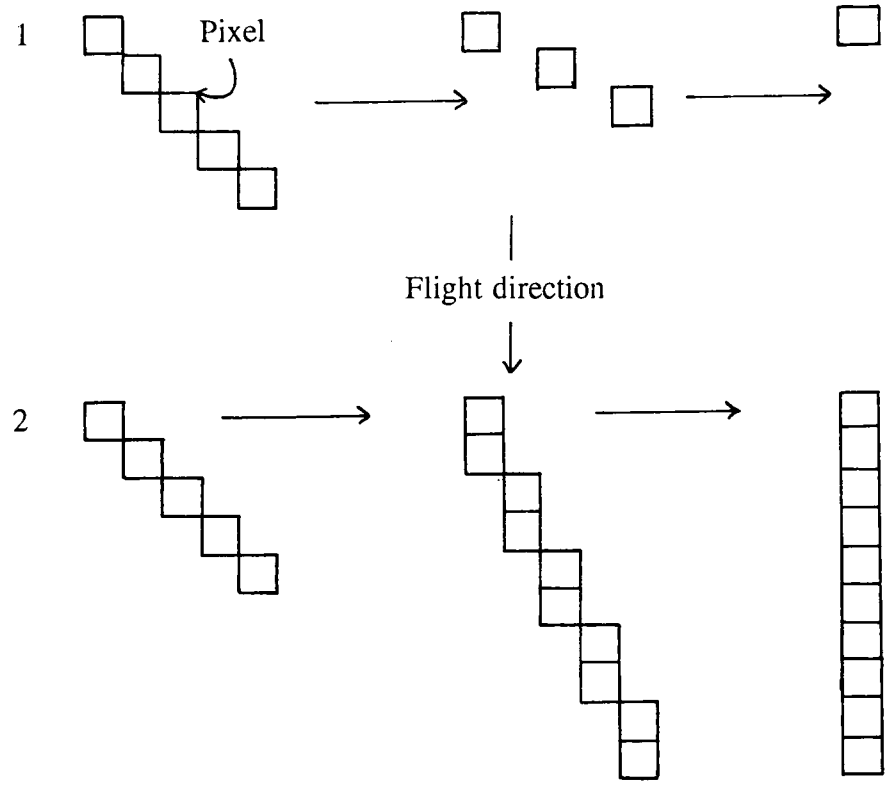

Figure 6.4 The effects of 1) under- and 2) over-sampling on the appearance of a unit striking at 45° to the flight direction. In 1) the strike appears to swing away from the flight direction until ultimately the object is no longer seen. In 2) the strike appears to swing toward the flight direction until in the extreme case the two are parallel.

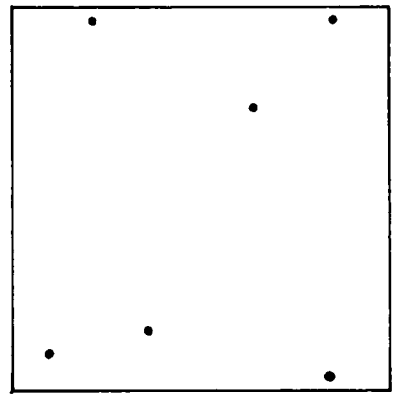

Figure 6.5 The distribution of the six ground control points within the TM image.

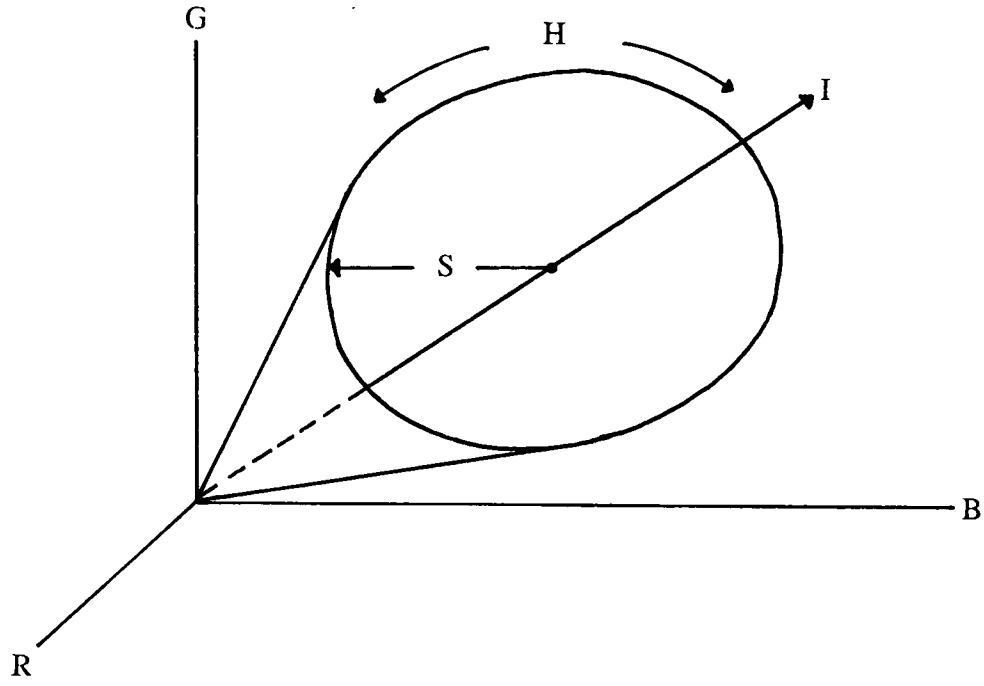

Figure 6.6 The relationship between HSI and RGB colour space (after Drury, 1987).

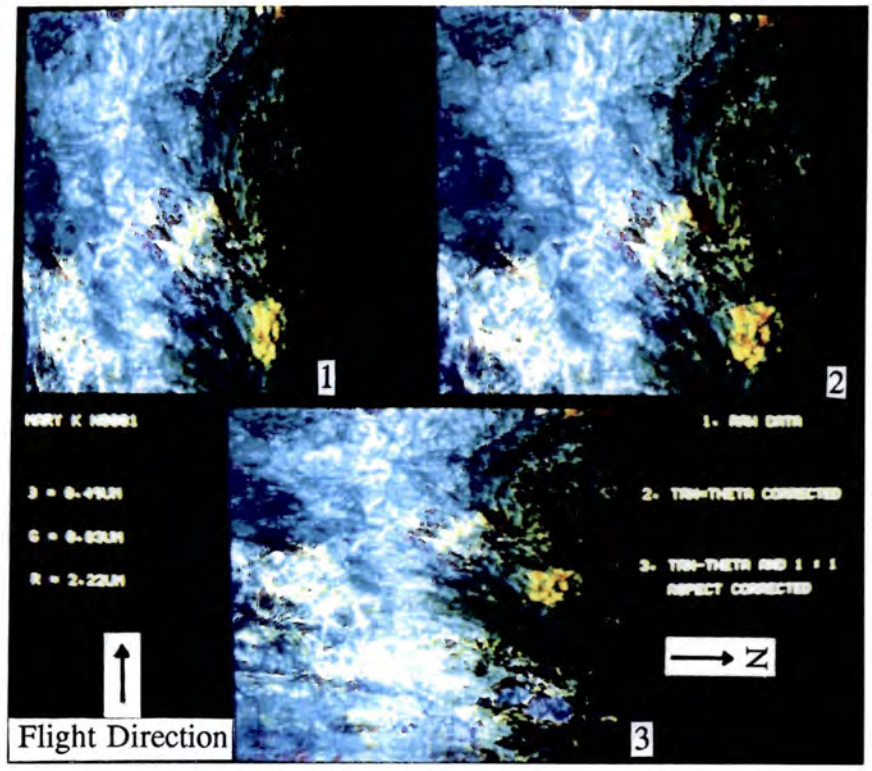

Plate 6.1 NS001 Flight Line 2, red = 2.22 μm, green = 0.83 μm, blue = 0.49 μm. 1 = uncorrected, 2 = tan-theta corrected, 3 = tan-theta and aspect ratio corrected.

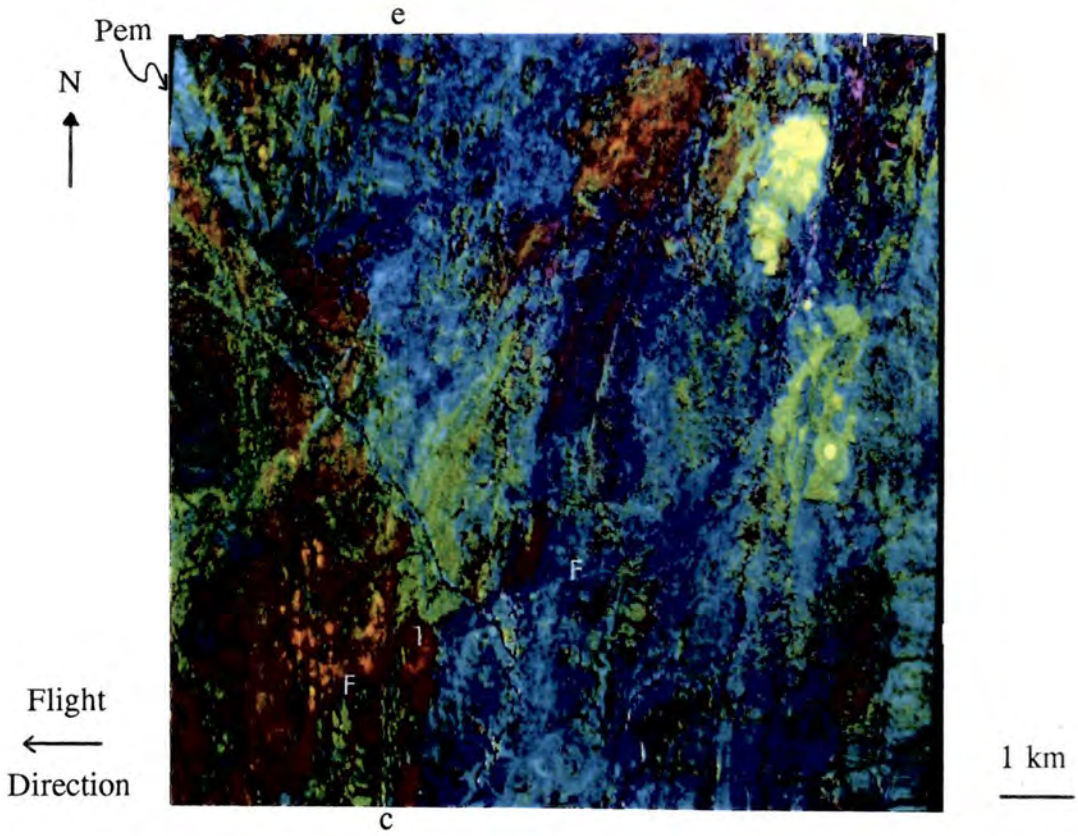

Plate 6.2 NS001 Flight Line 2 inverted LR data. Red = 2.22 μm, green = 0.83 μm, blue = 0.49 μm, highlighting yaw-induced extension (e) opposite compression (c). Pem = Magna Lynne Metabasalt, F = Cameron Fault, 1 = Argylla Formation debris.

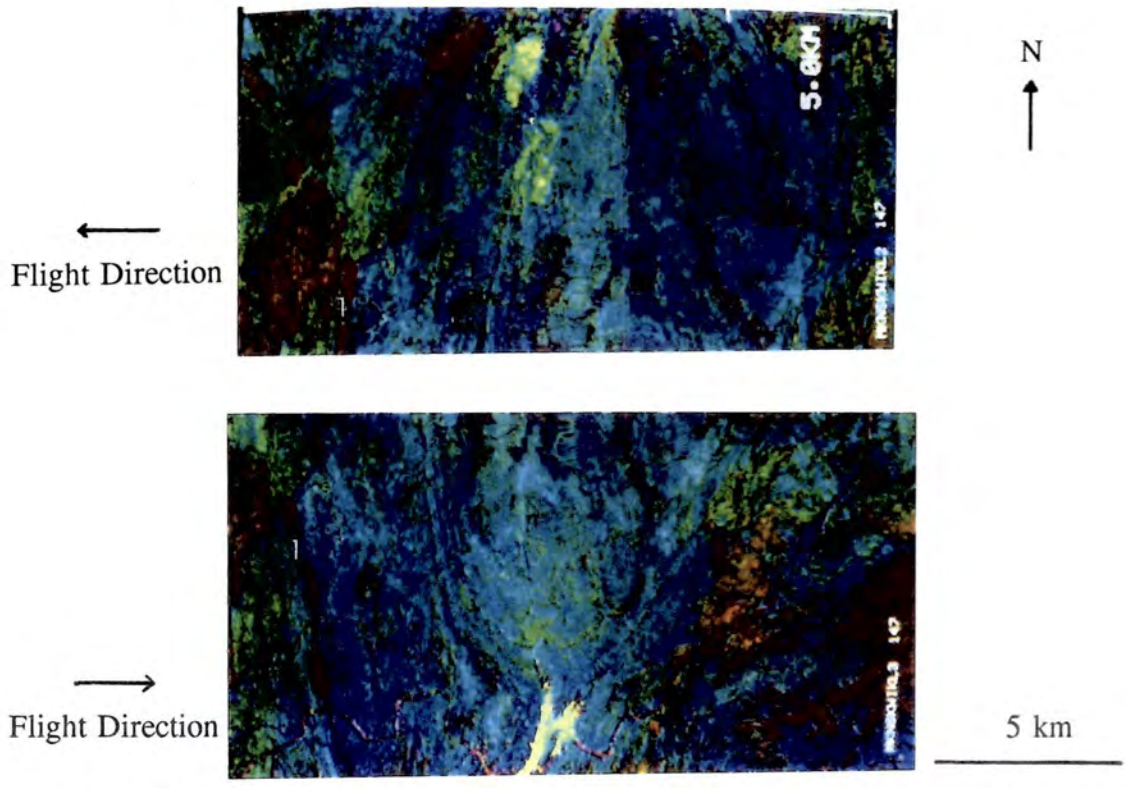

Plate 6.3 NS001 Flight Line 2 (top) and Flight Line 3 (bottom) inverted LR data. Red = 2.22 μm, green = 0.83 μm, blue = 0.49 μm. Note change in strike of the Argylla formation in the west from one flight line to the other (1).

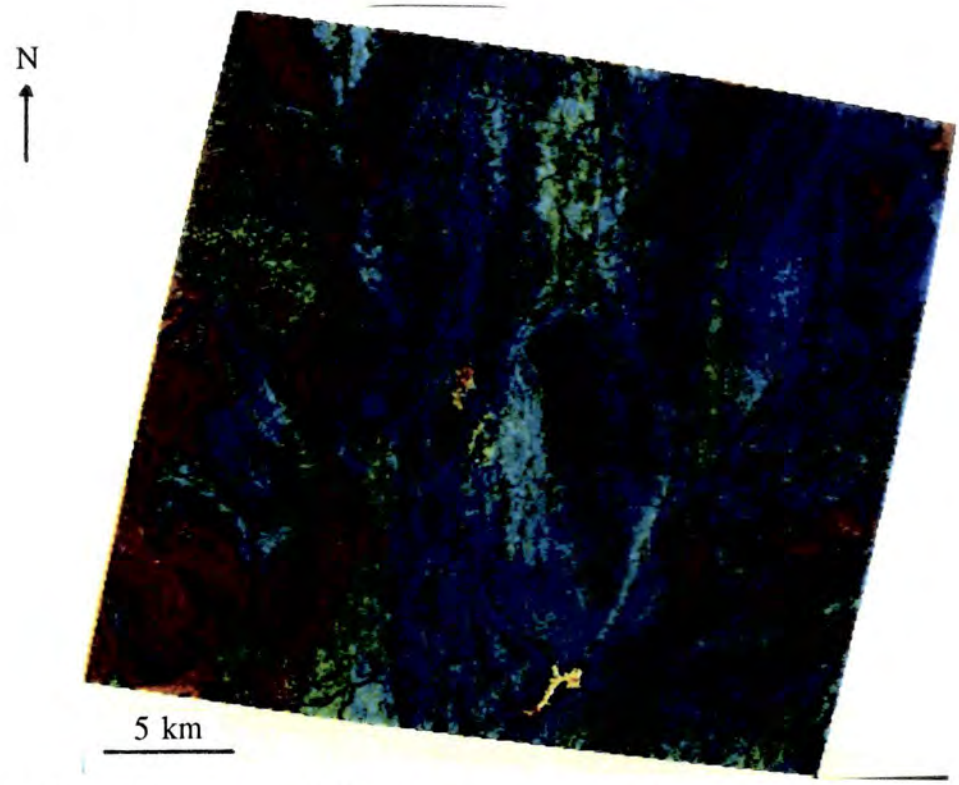

Plate 6.4 TM inverted LR colour composite of whole area. Red = 2.22 μm, green = 0.83 μm and blue = 0.49 μm. The image margins show the effects of the warp to AMG.

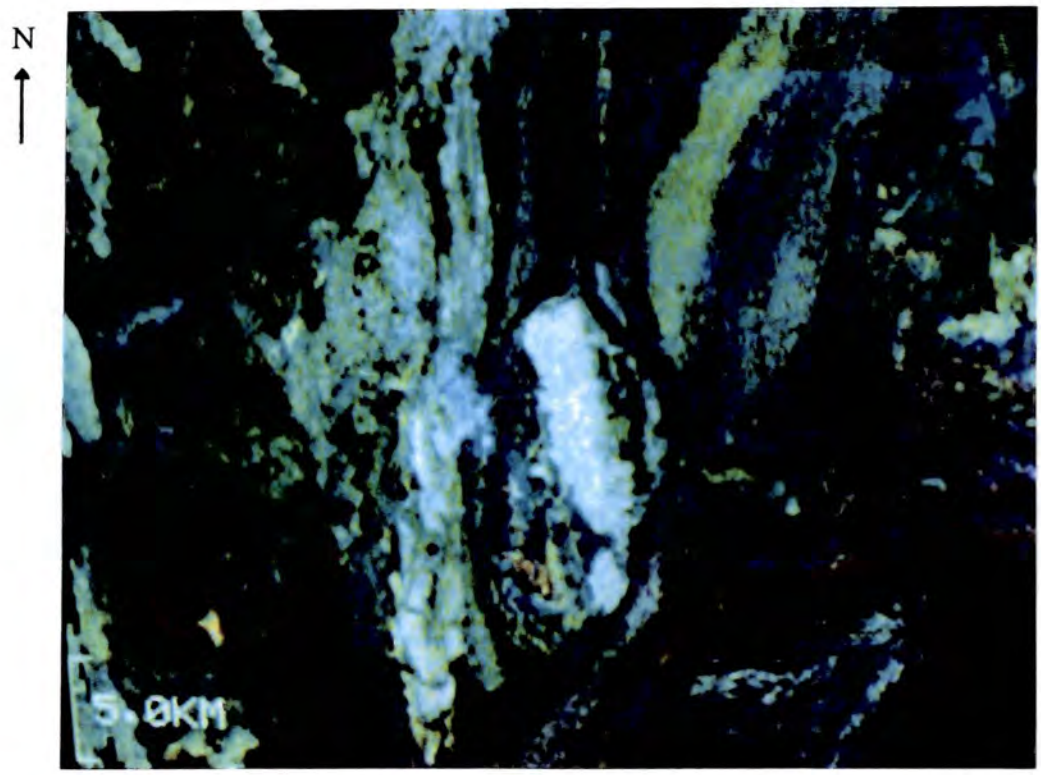

Plate 6.5 AGR colour composite for the region around the field area, with potassium in red, thorium in green and uranium in blue. This image, with an accompanying geological map, is reproduced as Enclosure 6.1 in the back pocket.

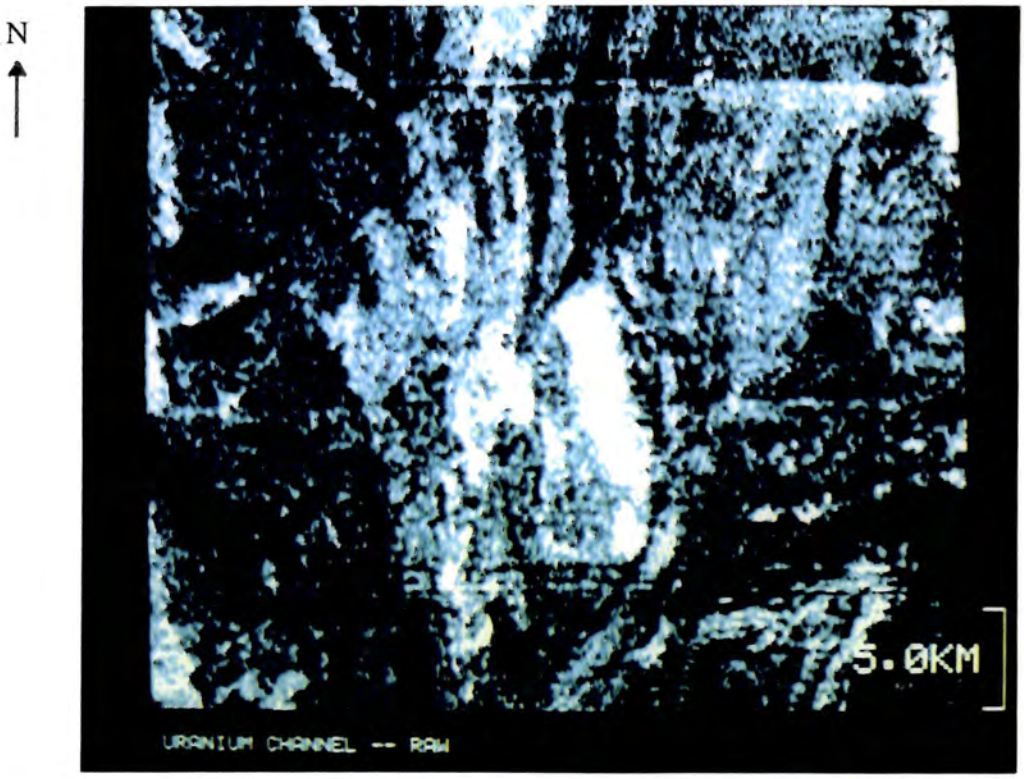

Plate 6.6 The noisy uranium band.

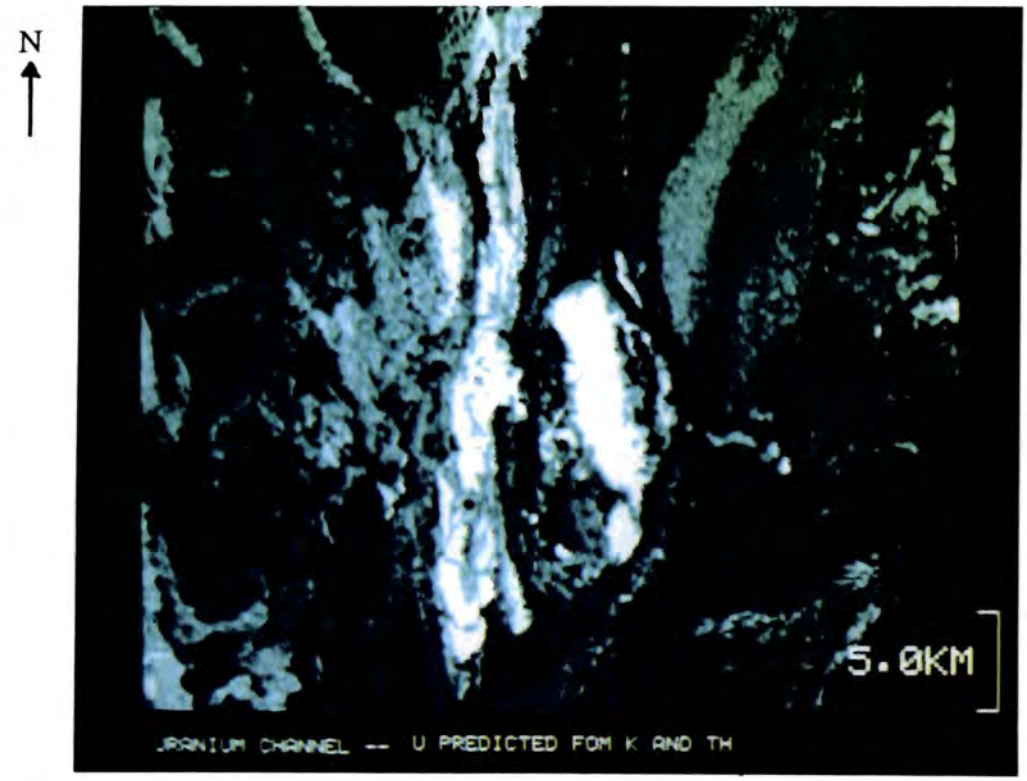

Plate 6.7 The predicted uranium band.

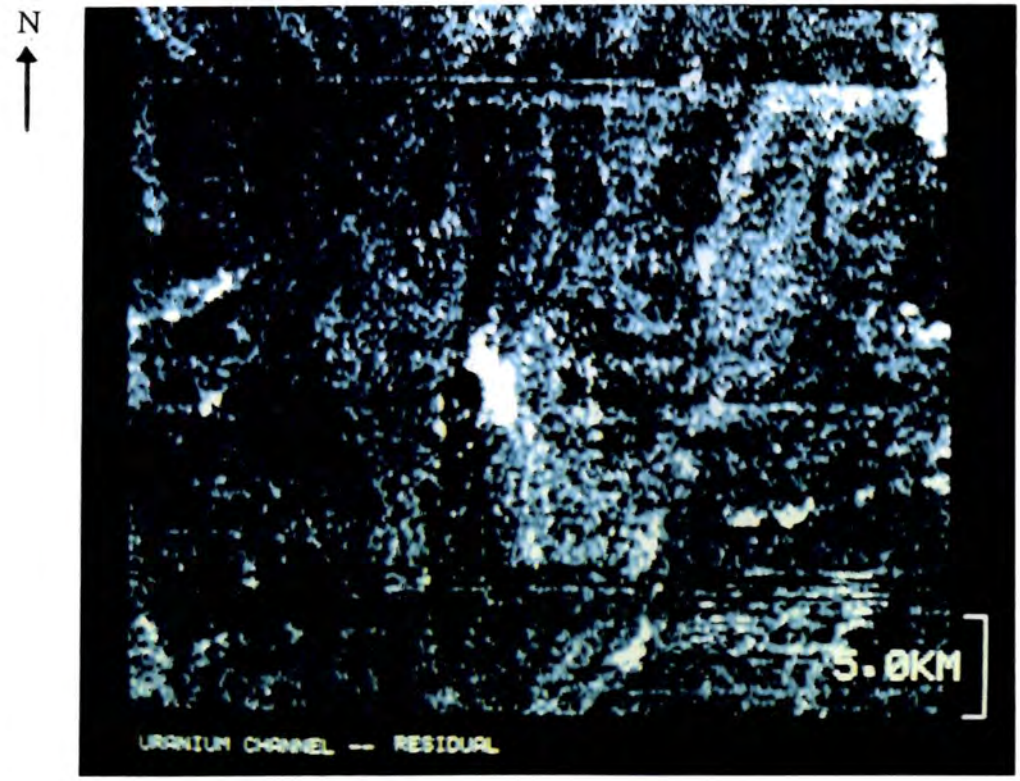

Plate 6.8 The residual uranium band (observed minus predicted). As well as striping and high frequency noise, geological information unique to the uranium band is seen.

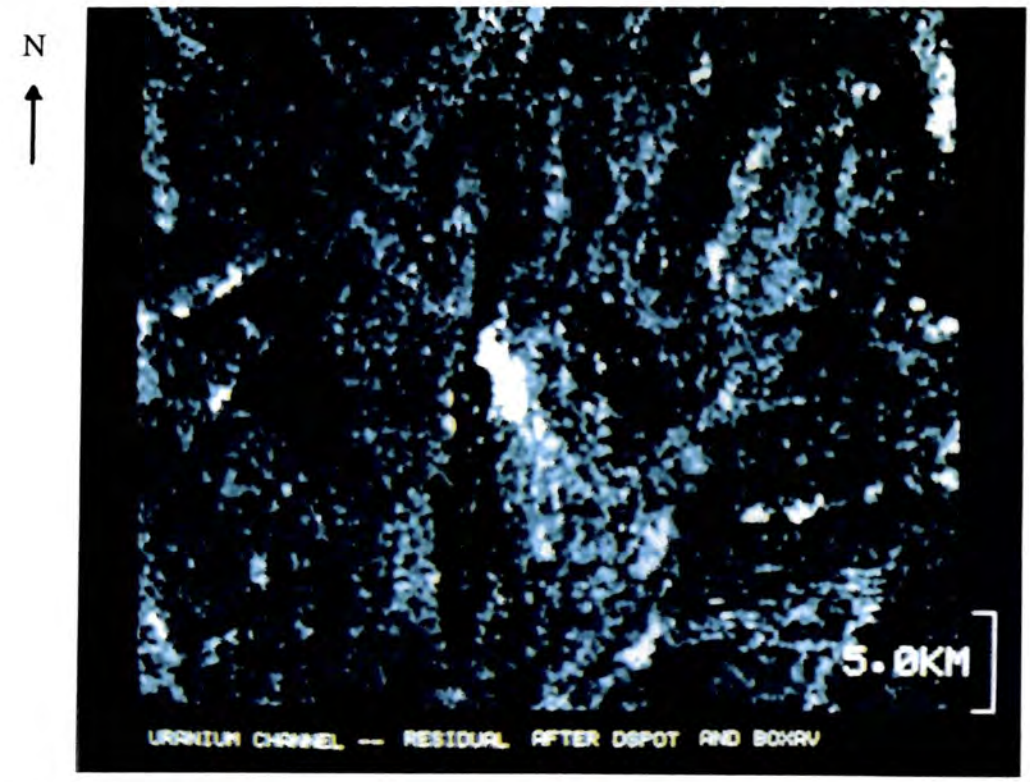

Plate 6.9 The residual uranium band after the removal of striping and high frequency noise. The residual geological information has been preserved.

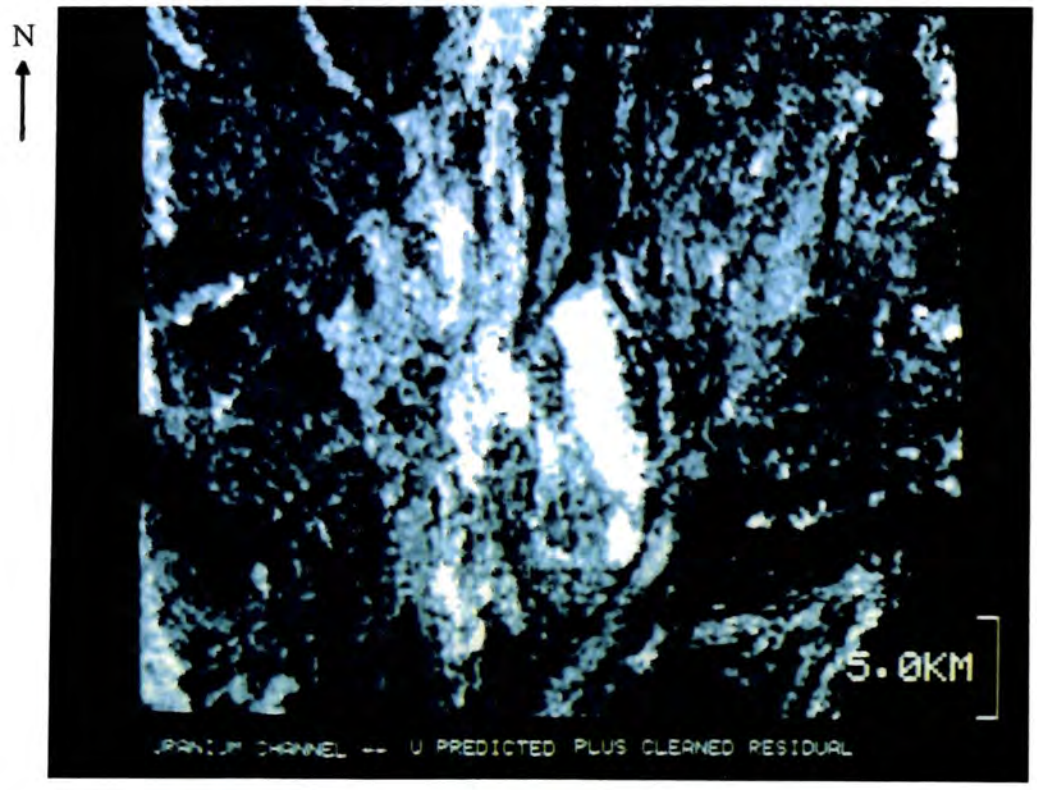

Plate 6.10 The restored uranium band (predicted plus cleaned residual). Comparison with Plate 6.6 shows that considerable noise has been removed.

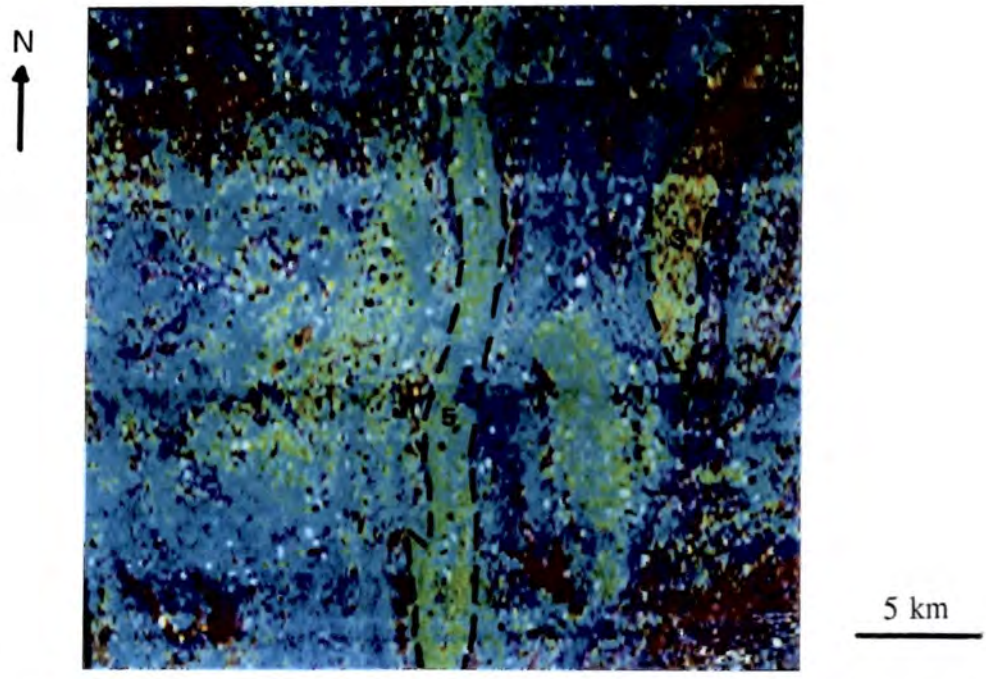

Plate 6.11 AGR ratio composite. Red = K/total count, green = Th/total count and blue = U/total count. 1 = Northward increase in K within Leichhardt Metamorphics, 2 = Magna Lynn Metabasalt, 3 = Pkc_2 west, 4 = Pkc_2 east, 5 = Wonga Granite.

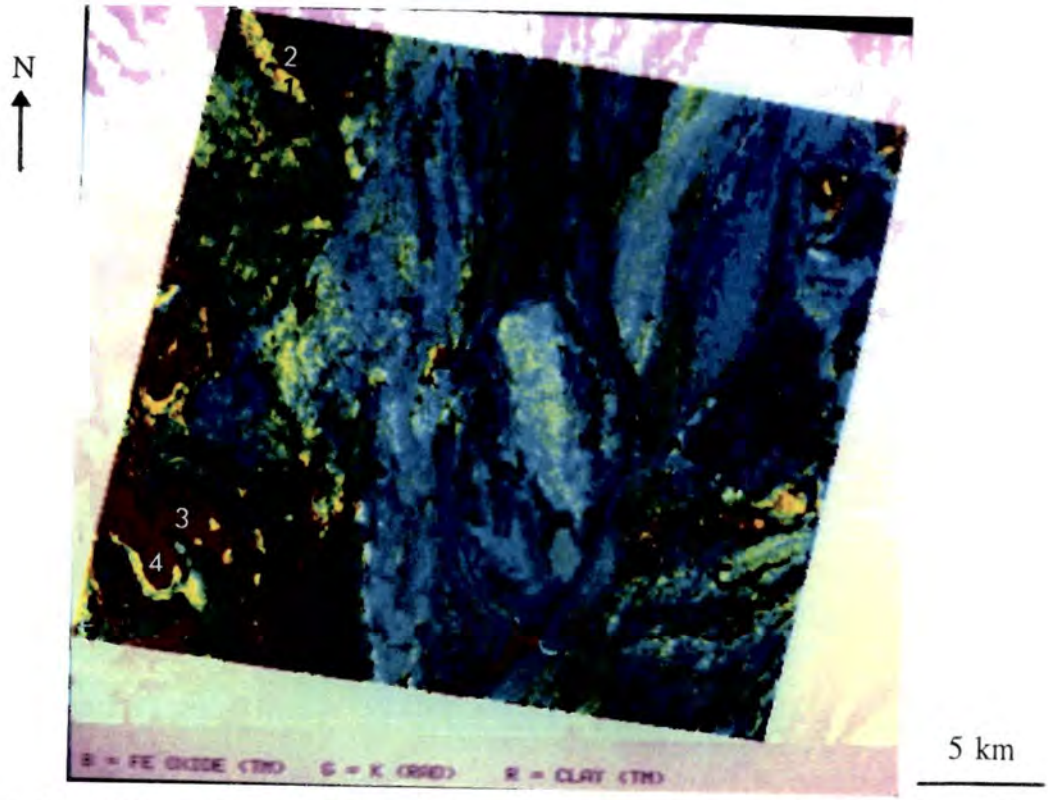

Plate 6.12 AGR and TM LR colour composite. Red = 2.22 μm absorption, green = high potassium count, blue = 0.49 μm absorption. Areas of coincident potassium and clay minerals are imaged in yellow/orange. Note separation of Argylla Formation (1) and Ballara Quartzite (2) in the Little Beauty Syncline. Elsewhere, the Ballara Quartite (3) cannot be separated from other quartzites, such as the Deighton (4).

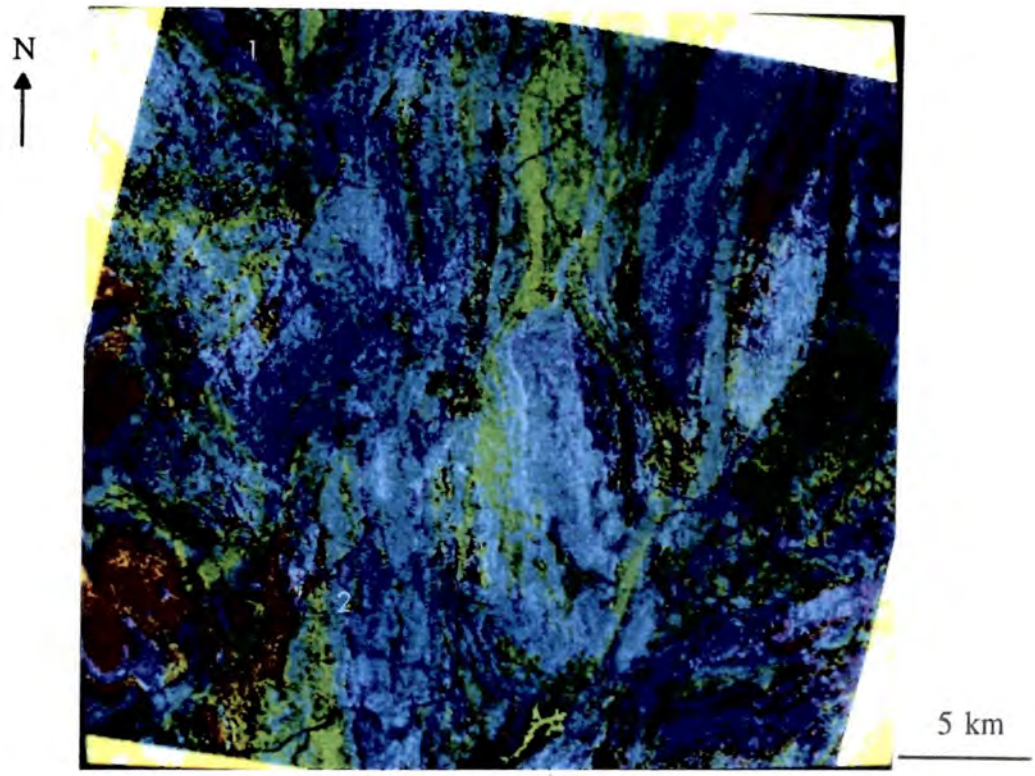

Plate 6.13 AGR and TM colour composite. Red = LSFit residual (2.22 μm absorption not attributable to vegetation), green = 0.83 μm absorption, blue = high potassium count. Coincidence of potassium and clay minerals gives purple hues. The Argylla Formation (purple) and Ballara Quartzite (red) can be separated in the Little Beauty Syncline (1), and this discrimination extended into the Rosebud Syncline in places (2).

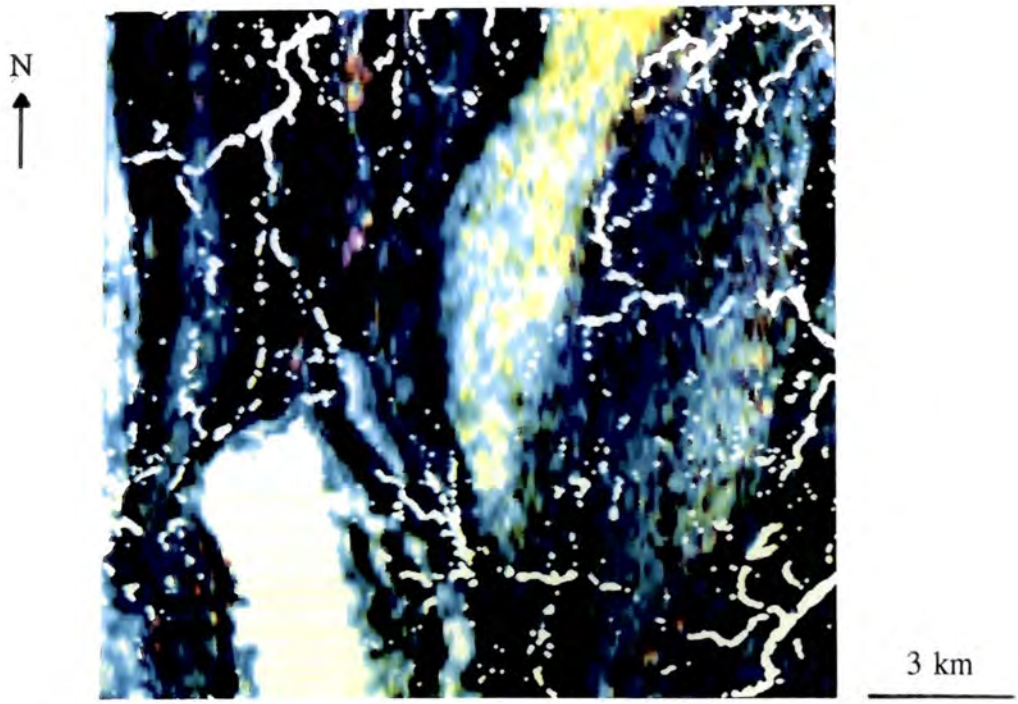

Plate 6.14 AGR colour composite NE of Burstall Granite (K = red, Th = green, U = blue) with creek network from TM vegetation ratio overlaid in white.

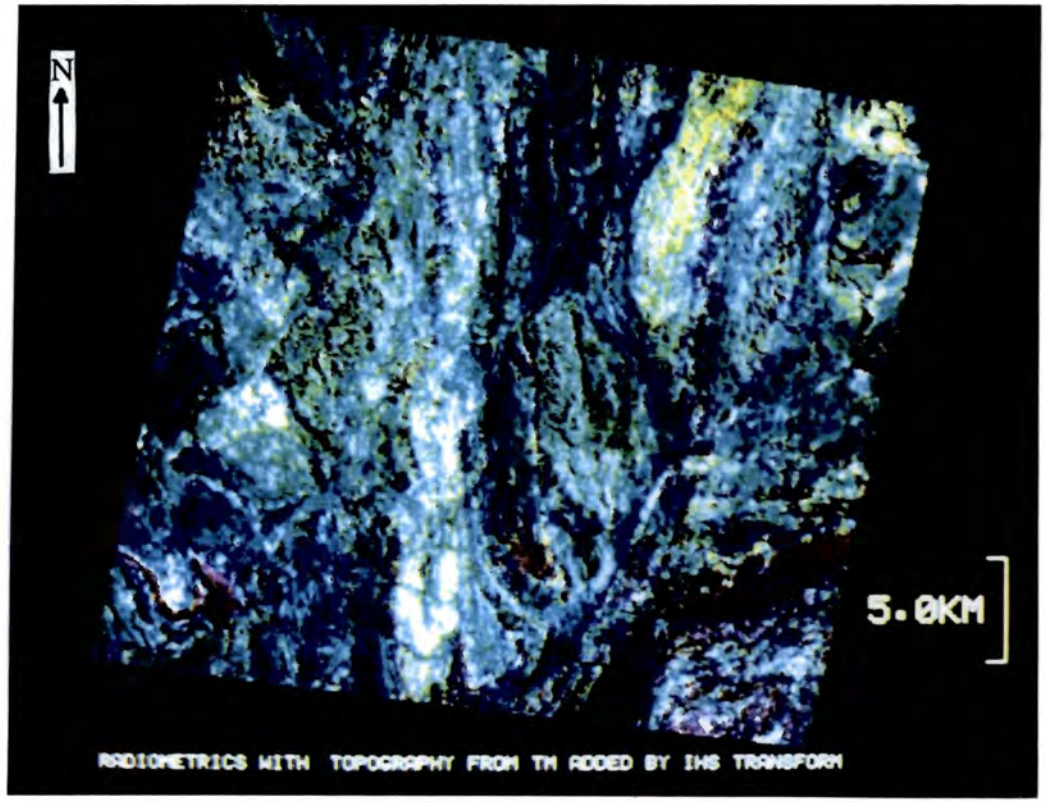

Plate 6.15 The HSI combination of the AGR and TM data over the whole field area. Red = potassium, green = thorium, blue = uranium, intensity variations are due to TM albedo from spectral mean values.

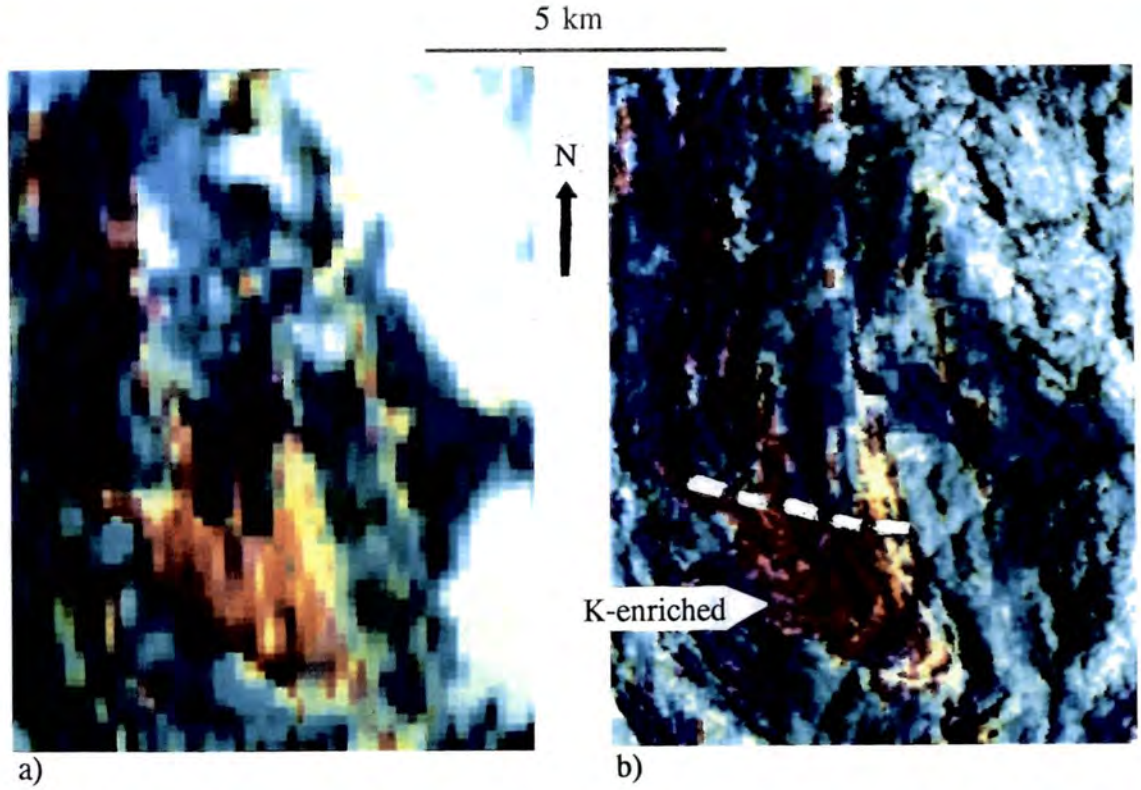

Plate 6.16 The Mary Kathleen Syncline. a) AGR data only, hues as Plate 6.5. b) Integrated AGR and TM data, interpretation criteria as for Plate 6.15.

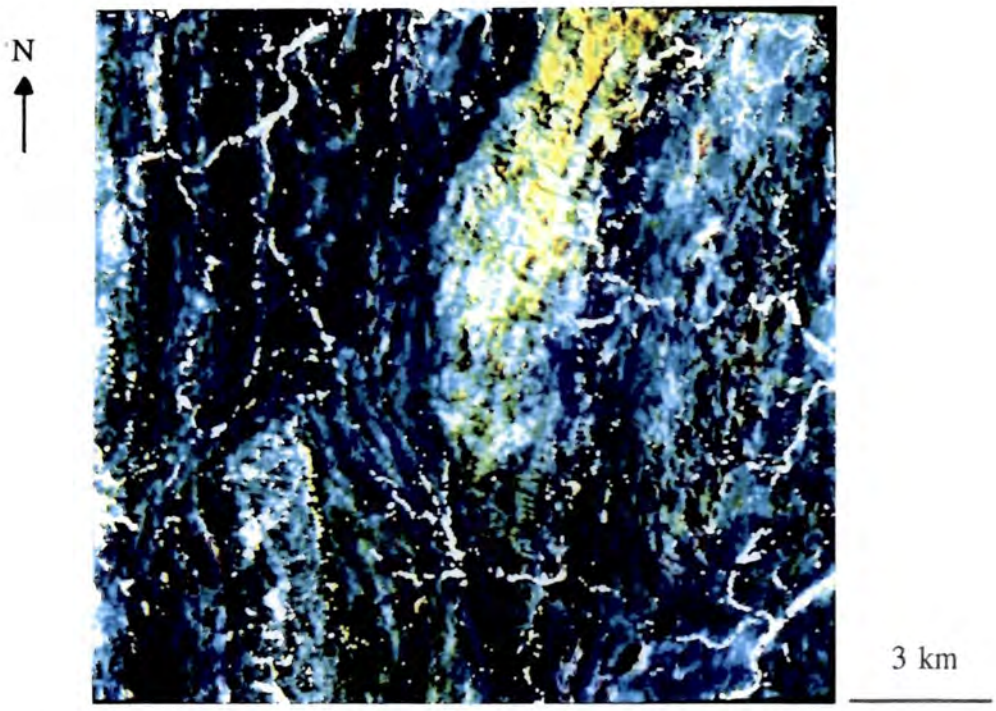

Plate 6.17 The combination of both types of TM terrain information with the AGR data NE of the Burstall Granite. Hues have the same meaning as in Plate 6.15, the intensity variation is due to the TM albedo and the creek network is overlaid in white.

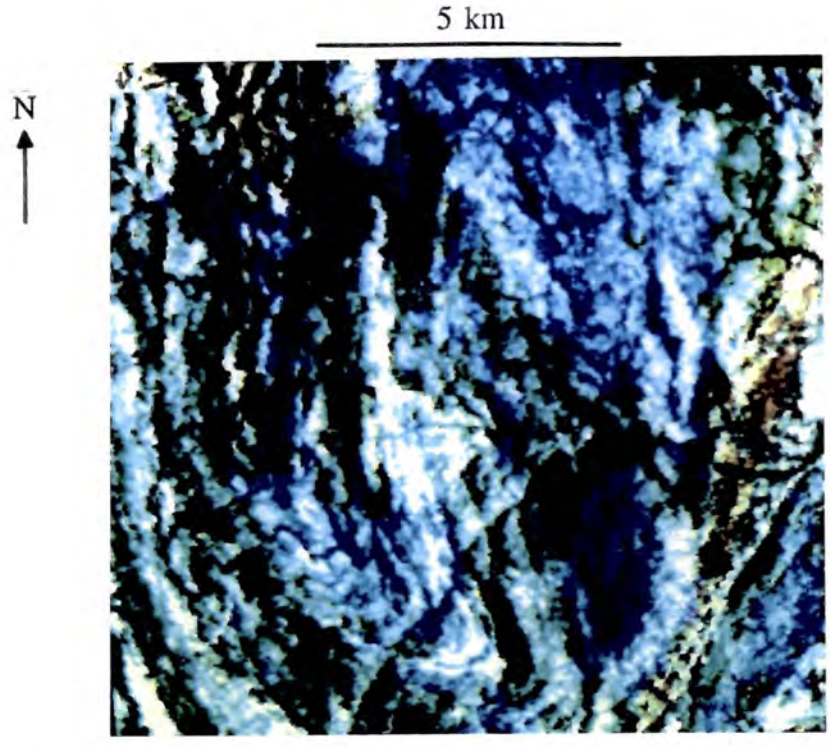

Plate 6.18 Threshold colour composite for the Mary Kathleen Syncline and southern mass of Burstall Granite. Intensity variations are due to the TM albedo, red = 0.83 μm absorption, green = 0.49 μm absorption, blue = high potassium count.

Line	To line	Apparent distance (m)	True distance (m)	Aspect ratio
275	941	6660	3600	1.85
1228	1974	7460	4300	1.73
2110	3040	9300	4300	2.16
3318	3812	4940	2800	1.76
1	3893	38920	19600	1.99

Table 6.1 Aspect ratios calculated for different portions of NS001 Flight Line 3.

Element	Minimum count	Maximum count	Mean count	σ
K	-32.2	+753	+217	+97.1
Th	+4.60	+713	+102	+53.5
U	+4.89	+652	+50.6	+20.9

Table 6.2 Statistics for the AGR data, showing the large differences in dynamic range for the three elements measured.

CHAPTER 7. RELATING THE REMOTELY SENSED DATA TO THE SOLID GEOLOGY

7.1 Introduction

Remote reflectance measurements are influenced by the top 50-100 μm of the exposed surface material (Buckingham and Sommer, 1983). In rare cases the erosional regime may lead to the exposure of fresh rock surfaces over a large enough area to dominate a pixel. Far more often, a pixel will be dominated at the surface by either weathered rock, soil derived from the lithology below, soil derived from other lithologies, vegetation or a mixture of these materials. As this study aims to map the solid geology, these complications must be accounted for so that the surface measured can be related to the lithologies of interest. This has been done through the use of the TM, NS001 and AGR data in the field. Samples collected have had their reflectance measured in the laboratory and have been analysed using X-Ray Diffraction (XRD).

In order to study the relationship of the geology and the field samples to the remotely sensed data, observations made in the field in this study have included structure, lithology, weathering characteristics, the nature of the surficial material, its relationship to the underlying lithology, vegetation, topographic setting and the relative proportions of each component at a given locality. Samples have been taken for each lithology of interest from fresh surfaces, weathered surfaces, in situ soils and transported materials. Dry vegetation has also been sampled as it may mask or modify the spectral response of the rock surface. Although it cannot be sampled, the influence of the shade component on the measurement made at the sensor has also been considered.

7.2 Laboratory techniques

Before discussing the results of the XRD analyses and laboratory reflectance studies, it is necessary to describe the techniques used.

7.2.1 Reflectance studies of field samples

Laboratory reflectance spectra have been measured using the GER Mk. IV Infrared Intelligent Spectroradiometer (IRIS). The use of this instrument has been described in Milton and Rollin (1987) and its operational configuration is shown in Plate 7.1. The IRIS was operated in high resolution mode, measuring the energy reflected from a sample's surface at 965 wavelengths between 0.4 and 2.5 μm. The measurements of the sample were made relative to a barium sulphate or spectrallon plate, which is nominally 100 % reflective, allowing subsequent conversion of the sample measurements to absolute reflectance. The resulting digital data were stored and analysed in this form on a personal computer.

Spectra have been measured for every sample taken. For a given locality the spectra measured depend on the nature and mix of the materials present. Where possible, the fresh rock surface, the weathered surface and the typical surface cover or soil have been measured so that the fresh rock may be related to its weathering products. In naming the spectra, the following convention has been used:

s	=	spectrum	
number	=	locality number	
no letter	=	fresh surface:	red in Figures
w	=	weathered surface:	blue in Figures
a,b,etc	=	soil:	purple in Figures

For example, three spectra have been measured for member Pkc_1 of the Corella Formation at locality 243. S243 is the fresh rock spectrum, S243w is the weathered surface spectrum and S243a the in situ soil spectrum. A similar convention, dropping the s, has been used for the XRD analyses. Appendix A lists all localities, the samples taken; the spectra measured and the minerals identified using this technique, and includes maps showing the position of each locality.

These laboratory spectra are used in the remaining chapters as ground truth and to investigate the weathering process for each lithology. They are particularly valuable for

comparison to the logarithmic residual pseudo-spectra. Examples of typical spectra are shown at relevant points in the text. The interpretations of these spectra are made by reference to Hunt (1977, 1980), Grove et al (1992), a CSIRO spectral library and a library of pure mineral spectra started by Hook (1989) and added to during this project. An additional experiment has been performed on one sample, soil 98a from the Lake Corella Dolerite, to investigate the effects of the change in particle size during the weathering process on the reflectance measured.

7.2.2 XRD analysis of field samples

XRD analysis has been performed using a Phillips PW 1130 2kW X-Ray Generator/Diffractometer Assembly with Co Ka radiation. Material from the surface to be measured was removed using a steel blade and collected in a mortar, where it was crushed to a fine powder with a pestle. The powder was suspended in an acetone solution, deposited on a glass slide and allowed to settle through the evaporation of the acetone. The slide was then mounted in the instrument in the path of the X-rays. Diffraction of the incident X-rays by the sample was measured for atomic spacings over the range 20.0 to 2.0 angstroms. The material's crystal structure was determined by analysis of the positions of diffraction peaks on the resultant chart. The crystalline mineralogy of the sample was then determined by reference to pure mineral standards compiled by the Joint Committee on Powder Diffraction Standards. In addition, the ratio of background response to major peak height was used to indicate the relative amount of amorphous iron oxide in a sample, such that a high background response correlates with high iron oxide content (R. Hardy, personal communication).

Unlike the laboratory reflectance measurements, geological considerations were not the only factors that dictated which samples were measured by XRD. The ease with which material could be removed from the surface of interest placed a further constraint on the choice of surfaces to be measured. Further, XRD is a time consuming process and the time available on the instrument must be used efficiently. Sample preparation time is longer than for IRIS measurements and in addition a sample takes 40 minutes to measure by XRD against 1 minute using the IRIS. Analogue data are produced by this particular XRD apparatus which require manual processing, compared with the digital

data produced by the IRIS which can be manipulated on a computer. Consequently it was not practical to measure all samples by XRD, as has been done using the IRIS. Samples have been chosen for XRD analysis from the Corella Formation, Hardway, Wonga and Burstall Granites, Lake Corella, Lime Creek and Dog Bone Dolerites and Magna Lynn and Lime Creek Metabasalts in order to address specific problems. Measurements have included fresh rock where possible, weathered surfaces and soils. XRD results are summarised at the appropriate points in this chapter (Tables 7.1 - 7.3: numbers in the Tables indicate strength of features detected for each mineral).

7.3 Weathering

Almost all outcrops are dominated by weathered surfaces and where rock does not outcrop the major surface cover is a mixture of soil (a particulate unconsolidated material with some organic content often akin to sand), weathered rock fragments and minor dry vegetation. Schwertmann (1985) has stated that iron oxides are among the most common products of rock weathering and the ubiquitous development of iron oxides through lateritic weathering is the dominant weathering process observed in the field, although some lithologies also develop clay minerals. The area is within eastern Australia's ferricrete zone (Figure 7.1) as depicted in Ollier (1984). Plate 7.2 shows the typical surface expression of the Lime Creek Metabasalt at locality 120 in the north of the field area. The weathered rock and the soil both show extensive development of iron oxides and hydroxides and the features of these minerals dominate the reflectance of this lithology. Plate 7.3 illustrates the development of clay minerals during the weathering of feldspar phenocrysts in the Wonga Granite at locality 106, in the centre of the field area. This difference in the weathering products of the basic and felsic lithologies suggests that they should be discriminated with ease in the remotely sensed data. Plate 7.4, however, shows a more general view of the Wonga Granite at locality 106 in which it is clear that iron oxide development is also an important factor in the weathering of felsic rocks. The balance between the development of iron oxides, iron hydroxides and clay minerals must thus be examined for each lithology to determine the likely reflectance characteristics of their exposed surfaces.

7.3.1 Basic rocks

Ollier (ibid.) states that clay minerals and iron oxides result from the weathering of basic rocks. The most important iron oxides are hematite and goethite (Schwertmann, 1985). Field study reveals that all the dolerites and metabasalts are characterised by the development of iron oxides and hydroxides in both weathered rock surfaces and soils. Plate 7.5 shows a profile through the Dog Bone Dolerite in a road cutting at locality 1. Fresh dolerite is found in the lower 2 m of the section. Above this there is increasing development of iron oxides, culminating in an iron oxide-rich horizon with a distinct red colouration in the top 50 cm. This outcrops at the surface alongside an iron oxide-rich soil. Enclosure 5.1 shows the logarithmic residual TM data over this lithology, with red meaning absorption at 2.22 μm, green absorption at 0.83 μm and blue absorption at 0.49 μm. The Dog Bone Dolerite is characterised by a strong absorption at 0.49 μm and a lesser absorption at 0.83 μm, typical of iron oxides. It can be clearly discriminated from the surrounding lithologies.

Figure 7.2 shows the IRIS spectra for the Dog Bone Dolerite at the same locality. The spectrum of the fresh rock from the base of the weathering profile, S1, is spectrally flat and of low reflectance, and has shallow broad absorptions at 0.64 μm, due to Fe charge transfer or crystal field effects, and at 0.96 μm, due to Fe crystal field effects. These features are typical of basic rocks (Figure 7.3). Poorly defined absorptions include a pair at 2.24 μm and 2.34 μm attributed to chlorite and a pair at 2.32 μm and 2.38 μm attributed to amphibole. The weathered surface spectrum, S1w, is dominated by the development of absorptions at 0.49 μm, due to Fe charge transfer effects, and 0.91 μm, due to Fe crystal field effects. The latter suggests goethite may be the dominant iron oxide present. A small absorption due to water is seen at 1.4 μm. The overall reflectance is increased and the features attributed to chlorite and amphibole are less clear. The soil spectrum, S1a, displays deepened features due to iron at short wavelengths and no features due to amphibole or chlorite. Deep asymmetric absorptions are seen at 1.42 μm and 1.93 μm, probably due to montmorillonite, a common clay where rocks containing bases are weathering (Ollier, 1984). The short wave infrared spectrum of montmorillonite is shown in Figure 7.4 for comparison.

The weathering sequence indicated is a basic rock developing iron oxides in its weathered surface and increasingly in its soil, with clay minerals becoming more significant in the soil, though no deep 2.2 μm absorption develops. The absorptions at 0.49 μm and 0.91 μm which develop during the weathering process lead to generally low reflectance in the visible and near infrared wavelength region and this is also seen in the remotely sensed data. Figure 7.5 shows a logarithmic residual pseudo-spectrum from a single pixel over the Dog Bone Dolerite.

Table 7.1 contains the XRD data for the weathered surface and soil at the same locality. The main minerals identified are amphibole, feldspar, mica and quartz, with chlorite, hematite and montmorillonite developing during weathering. This suite of minerals is broadly consistent with that identified by IRIS analysis. Both the weathered surface and the soil have very high background to peak ratios, suggesting they are rich in iron oxides, with the soil perhaps the richer of the two. This supports the assertion, made in the field and after analysis of the IRIS spectra, that iron oxides develop increasingly throughout the weathering process. Figure 7.6 shows background to peak ratio averaged for the weathered surfaces and soils of all basic rocks measured. The dominant pattern revealed is an increase in iron oxide content from the weathered surface to the soil.

The above weathering sequence is typical of all basic rocks analysed in this study. Different basic lithologies may develop different iron minerals, or proportions of them, in their weathering product, so that one group may be characterised by hematite and another by goethite. Schwertmann (1985) has suggested that the balance between hematite and goethite is related to a combination of climate, topographic setting and depth in the weathering profile. If such distinctions are found, and can be mapped using the remotely sensed data, some of the controversies involving these rocks may be resolved. This question will be fully addressed in chapter 8.

7.3.2 Granite

Quartz is resistant to weathering, feldspar often alters to kaolinite and sericite, and micas break down to form clay minerals and chlorite. Amphiboles alter to chlorite and clay minerals but also release bases into solution (Ollier, 1984). Field study suggests

that two weathering processes take place over the granites. These are the breakdown of the felsic components to form clay minerals and the production of iron oxides from the mafic components. At locality 102 within the Burstall Granite, seen in Plate 7.6, both iron oxides and clay minerals are visible. Clay minerals appear concentrated in the soil between outcrops, while the outcrops themselves develop iron oxide crusts on their weathered surfaces.

The Wonga Granite at locality 275, shown in Plate 7.7, has strong iron oxide development in its weathered surface. Plate 7.8 shows NS001 logarithmic residual data over part of this granite. The lithology's spectral response is varied, with large areas of the granite having absorption at 0.49 μm and smaller areas at 0.83 μm or 2.22 μm. The reasons for this varied spectral signature are clear in the field and when comparing the remotely sensed data with air photographs. Plate 2.5 shows a view over the Wonga Granite. The majority of the lithology has little significant outcrop and is covered by a deeply developed iron oxide soil forming a flat plain responsible for the large areas of 0.49 μm absorption seen in the imagery. Outcrop within this plain occurs as tors and areas dominated by iron oxide-rich weathered surfaces and these correspond in position to areas of 0.83 μm absorption in the imagery. The areas of 2.22 μm absorption occur over clay-rich soil and debris found on the flanks of the tors and between outcrops.

The different surfaces described above have been analysed using the IRIS. Figure 7.7 shows the IRIS spectra for the Wonga Granite at the tor seen in the NS001 data and covered by localities 112, 113 and 114. Spectrum S112 of the fresh rock is generally flat with a small absorption at 0.46 μm due to Fe charge transfer, a small water band at 1.4 μm, a small couplet at 2.17 μm and 2.19 μm attributed to Al-OH vibrational overtones in kaolinite and a poorly defined feature around 2.34 μm attributed to Mg-OH vibrational overtones, possibly in amphibole. In the spectrum for the weathered rock, S112w, the Fe charge transfer related absorption at 0.46 μm is better developed and is accompanied by a broad moderate absorption centred on 0.88 μm due to Fe crystal field effects, demonstrating the increase in iron oxide in the granite's weathered surface. The kaolinite feature around 2.2 μm is reduced due to the dominance of iron oxide. There is also a small absorption at 2.44 μm which is attributed to Mg-OH vibrational overtones in mica. The spectrum for the apparently clay-rich soil, S113a, has a

shallower absorption at both 0.49 μm and 0.88 μm, reflecting a reduction in iron oxides in this soil. Water absorption bands at 1.41 μm and 1.91 μm are deep, right asymmetric and attributed to quartz, of which these asymmetric water bands are typical (Figure 7.8). The most important feature of spectrum s113a is, however, the deep well developed absorption at 2.19 μm, with a couplet at 2.16 μm. These are both due to vibrational overtones in Al-OH and are characteristic of kaolinite, reflecting the clay rich nature of the granite soil. The spectrum of the soil from the debris plain, s114a, is in contrast dominated by a deep absorption at 0.47 μm and a broad absorption at 0.9 μm, indicating a high level of iron oxide. The 2.2 μm kaolinite feature is present but reduced in magnitude. Figure 7.9 shows a similar weathering sequence for the Burstall Granite at locality 104. Figure 7.10 shows TM LR pseudo-spectra for the clay soil and iron oxide soil typically exposed over the granites.

The weathering sequence illustrated by the IRIS data is in broad agreement with that postulated using the NS001 data in the field. Felsic components in the granites weather to clay minerals which accumulate in the soil, leaving behind iron oxide from mafic components in the weathered surface. Soils close to granite outcrops have the highest proportion of clay minerals to iron oxides, probably due to regular replenishment during weathering. Soils distant from outcrops have a higher proportion of iron oxides as they are further from the clay source and develop in situ.

Table 7.2 contains the XRD data for the Wonga Granite at these localities. Quartz, feldspar and mica are identified in the fresh surface, weathered surface, granite soil and debris plain soil. Kaolinite is identified in all but the debris plain soil. Amphibole is the main mafic mineral present. This pattern persists for all samples of the Wonga. The Burstall and Hardway Granite display a similar pattern, though kaolinite is not identified by XRD analysis in any of these lithology's soils.

For all three of the granites sampled, weathered surfaces have higher background to peak ratios than granite soils. This is the reverse of the situation found over the basic lithologies. The highest background to peak ratios for granitic lithologies occur in the Wonga debris plain soils. The average background to peak ratios shown in Figure 7.6 confirm the weathering pattern postulated in the field and with the IRIS data. Iron

oxides from the mafic minerals develop in the weathered surfaces, and clay minerals from the felsic minerals accumulate in the granite soils. The more developed soils on the granite debris plain are enriched in iron oxide by further in situ lateritic weathering, or the addition of iron oxide from another source, as will be discussed in section 7.4.2.1.

Study of the AGR data over the granites (Enclosure 6.1) shows that weathering affects the gamma radiometric data to a lesser degree. The Burstall Granite is markedly more homogeneous in the AGR imagery than in the TM imagery. The spectral differences between fresh rock, weathered rock and soils seen in the radiance data do not appear to have radiometric equivalents for this lithology. All three materials have a similarly high radiometric response. Only over the Wonga Granite are inhomogeneities seen. Areas of lower radiometric response occur over the iron-rich debris plain soil and areas of high response over the outcrop tors.

7.3.3 Metamorphic rocks

The Argylla Formation has a similar weathering pattern to the granites, being a predominantly felsic lithology of acid volcanic rocks and quartzites. In the field the development of clay minerals from feldspars (Plate 2.2) and iron oxide-enriched weathered surfaces is clear. Plate 7.9 shows the logarithmic residual NS001 data over this lithology, which is characterised by a mixture of 0.83 μm and 2.22 μm absorptions. This is consistent with the iron oxide-rich surfaces and clay minerals observed in the field.

Figure 7.11 shows the IRIS spectra for the fresh surface, weathered surface and soil of the Argylla Formation at locality 226. All three spectra have a moderate absorption at 2.21 μm with a couplet at 2.16 μm, characteristic of kaolinite. These features are not affected by the weathering process in this case. All three surfaces also have well defined Fe features with absorption at 0.47 μm and 0.87 μm, but these apparently reduce during weathering as the overall reflectance decreases. The other main feature of these spectra, moderate asymmetric water bands at 1.41 μm and 1.9 μm, are typical of quartz and are best developed in the weathered surface. The small absorptions in the

fresh and weathered surface spectra at 1.76 μm are attributed to lichen (Green et al, 1985).

The Ballara Quartzite is frequently in contact with the Argylla Formation (as in Plate 7.9) and they can be hard to tell apart, both in the remotely sensed data and in the field. They have the same development of clay minerals and both have some iron oxide enriched surfaces. Figure 7.12 shows the IRIS spectra for the Ballara Quartzite at locality 225, adjacent to the Argylla Formation sample described above. Fe charge transfer and Fe crystal field effects in iron oxides are responsible for absorptions at 0.47 μm and 0.9 μm respectively. For this sample they develop increasingly during weathering. A deep right-asymmetric water absorption at 1.9 μm, typical of quartz, also develops during weathering. The smaller left-asymmetric water band at 1.4 μm is more typical of kaolinite and is consistent with an absorption, deep in the soil, at 2.21 μm with a couplet at 2.16 μm also due to that clay mineral. The sharpness of the 1.4 and 2.21 μm absorptions suggests that muscovite (Figure 3.6) is also present. The spectral similarity of these two lithologies, particularly after weathering, is clear. Figure 7.13 shows the logarithmic residual TM pseudo-spectrum from the portion of the data over localities 255 and 256. The clay minerals developed during the weathering of these two lithologies produce an absorption at 2.22 μm in the remotely sensed data. As clay minerals are found in fresh and weathered surfaces as well as soils, this 2.22 μm absorption occurs consistently over the lithology, in marked contrast to the granites.

The metamorphic rock which outcrops over the largest area is the Corella Formation. The large variety of lithologies represented in this formation means that the weathering process cannot be easily characterised for the formation as a whole. In places the rocks are felsic and have similar weathering patterns to those described for the granitic rocks (Plate 7.10). Elsewhere, as seen in Plate 7.11, more basic lithologies occur and the weathering product is dominated by iron oxides. Many units are impure metamorphosed limestone and thus have solution of carbonate as the dominant weathering agent (see Plate 2.4 for example of characteristic vuggy weathering) (Ollier, 1984). The absence of a typical weathering sequence leads to the lithology having a variable spectral response, which is only constant for a particular facies. Many of these facies are not recognised by the existing division of the formation into three members.

Figure 7.14 shows the IRIS spectra for a schist from member Pkc_1 of the Corella Formation at locality 27. The fresh surface displays a small absorption due to iron oxide at 0.47 μm, accompanied by a very small broad absorption around 0.9 μm. The main feature of this spectrum is a very sharp water band at 1.41 μm, a shoulder at 2.12 μm and a very sharp absorption at 2.2 μm. These features, the latter due to Al-OH vibrational overtones, are typical of muscovite (Figure 3.6), which is consistent with the field observation that Pkc_1 is a schist at this locality. Features around 2.3 μm and 2.4 μm are poorly developed in the fresh surface. The weathered surface has a deeper iron oxide absorption at 0.45 μm, while the muscovite features are even more pronounced. The small absorption at 2.34 μm is also typical of micas and the small absorption around 2.41 μm may be due to amphibole. In the soil, the iron oxide absorption at 0.48 μm is slightly reduced, the formerly strong muscovite features are almost lost and there is a deep, broad water band at 1.92 μm whose asymmetry is typical of quartz. The weathered surface appears to be enriched in iron oxide compared to the soil, which is consistent with the felsic nature of this schist. **For this lithology then, the mineralogical signal of the primary muscovite may be obscured by the development of a soil rich in residual quartz and iron oxide.**

Figure 7.15 shows the IRIS spectra of member Pkc_2 at locality 130, which is described in the field as quartzite with cm scale calc-silicate bands. The fresh surface has small but well developed features attributed to Fe at 0.44 μm and 1.01 μm. The other main features are a water absorption at 1.9 μm, a small sharp 2.22 μm Al-OH absorption and a deeper 2.35 μm absorption due to C-O vibrational overtones probably in calcite. The weathered surface has much deeper iron oxide features at 0.46 μm and 0.9 μm, increased absorption due to water at 1.41 μm and 1.92 μm, and a less well defined calcite feature around 2.35 μm. The soils spectrum is similar in the shorter wavelengths where iron oxide still produces deep absorptions at 0.48 μm and 0.87 μm, but at longer wavelengths the spectrum displays a 2.21 μm absorption with a couplet at 2.19 μm, characteristic of Al-OH vibrational overtones in kaolinite. The calcite feature is almost lost in the soil, perhaps due to solution of the calcite as tufa deposits are found on rock surfaces in a nearby creek. In this case weathering again increases iron oxide but also produces clay minerals in the soil from the rock's silicate minerals.

At locality 27 the 2.2 μm feature due to muscovite in the fresh rock is lost during soil formation because another primary rock forming mineral, quartz, and iron oxides dominate the soil's spectrum. At locality 130, the 2.2 μm feature develops during weathering as clay minerals are formed from the felsic components in the rock and the spectral signature of primary minerals like calcite is masked. This illustrates the spectral differences which can be expected in the Corella Formation as the facies and weathering product vary. In fact, the entire range of spectral responses observed in the TM data are seen within this formation.

Table 7.3 contains the XRD data from an E-W traverse across the strike of the Corella Formation in the area to the northeast of the Burstall Granite. A detailed analysis of these data is given when the problems of mapping the Corella Formation are discussed in chapter 8. Initial inspection of the XRD data makes clear the variability of the formation even across this relatively small sample. The quartzite (e.g. 65), calcareous rocks (e.g. 58), micaceous sandstone (e.g. 92) and amphibole-rich rocks (e.g. 68) across this 10 km traverse all contain quartz, feldspar and mica but the other primary minerals and weathering products vary considerably, as do iron oxide contents.

The Corella Formation metasediments are generally more iron oxide rich than the granites. The metasediments' weathered surfaces have the same iron oxide content as the basic rocks (Figure 7.6), but after weathering to a soil the sediments are less iron-rich than the dolerite and metabasalt soils. Although they show the same pattern of iron oxide enrichment in weathered surfaces as the granites, there are more individual exceptions (e.g. 54 and 44 display the reverse), reflecting the metasediments' inhomogeneity. Each facies of the Corella Formation weathers in a way that requires individual consideration due to the large mineralogical variations that exist. While iron oxide development is a feature of weathering for the whole formation, the mineralogy of the exposed surface for a particular facies is determined by:

1. The development of clay minerals and their relative abundance in the weathering product compared to iron oxide.

2. The persistence or otherwise of features due to the primary mineralogy in the weathering product.

3. The presence or absence of an iron oxide enriched weathered crust and the relative proportions of this crust, fresher outcrop and soil.

7.3.4 Ubiquitous iron oxide

The presence of iron oxide as a weathering product of all lithologies, as seen in the field and determined by the IRIS analyses (appendix A), suggests that an iron oxide response should be seen in the remotely sensed data over the whole scene. If this were the case, it should not be possible to map one particular lithology using the presence of iron oxide in its weathering product. However, it is clear from study of all the data sets that the basic lithologies can be discriminated using an iron oxide response in both the ratio and LR data. This is because the ubiquitous iron oxide forms a background signal against which only higher iron oxide concentrations, such as those over a dolerite, register as absorptions.

Logarithmic residual analysis can be taken as an example. The logarithmic residuals technique involves the calculation of a spatial average at each wavelength, as explained in section 5.8. Taken together these can be thought of as the average spectrum for the scene. This scene-average spectrum contains features common to all pixels such as the instrument gain at each wavelength and, it is assumed, the atmospheric transmittance at each wavelength. For an individual pixel, these features are removed when the pixel is divided by the scene-average spectrum. The ubiquitous presence of iron oxide means that every pixel also has a moderate iron oxide related absorption, principally at 0.49 μm. The scene-average spectrum will also therefore contain a moderate 0.49 μm absorption, and thus division of an individual pixel's spectrum by the scene-average spectrum will remove any moderate iron oxide absorption. Only deeper 0.49 μm absorptions will remain after this normalisation to the scene average and thus rocks such as dolerite with a high concentration of iron oxide can be mapped in the data using this absorption.

A further consequence of this normalisation to a scene average containing some iron oxide features is that the few lithologies which do not have an iron oxide component may have a "not iron oxide" false reflectance peak at 0.49 μm in the LR data. Similarly, Green and Craig (1985) describe a "not Ca-clay" feature in the few portions of their LR data where this absorption was not found. This emphasises the need to look at absorptions only with LR data, by inverting the display device's lookup table when they are displayed.

7.3.5 The effects of mixing particle sizes on soil reflectance

Weathering processes mean that, within a pixel dominated by a single lithology, the sensor may not measure a uniform surface representing the mineralogy, as in the ideal case, but a mixture of surface types, particle sizes and textures such as that seen in Plate 7.12. In order to investigate the effects this may have on the measured reflectance, the soil sample 98a was sieved such that it was split into the following sizes: hand specimen, $>3/4$ inch, $>1/2$ inch, $>1/4$ inch and $<1/4$ inch. Reflectance spectra were recorded for all of these sizes, plus a mixture of them all (Plate 7.13), and are shown in Figure 7.16. It was found that the hand specimen (1), presenting the most uniform surface, had the brightest spectrum. Next brightest was the $>1/4$ inch sample (2), the small clasts presenting a relatively uniform surface. The $<1/4$ inch sample (3), effectively a sand, and the mixed sample (4) are of similar brightness, suggesting that either the fine material, or more likely a single large clast, dominated the mixed sample. The darkest samples were those involving larger clasts of $>1/2$ inch (5) and $>3/4$ inch (6). These samples present the least uniform surfaces, including a large proportion of shadow. All spectra have strong, water-related absorptions near 1.4 and 1.9 μm except the hand specimen, which is attributed to this sample being the least weathered.

It is hard to apply these results directly to the remotely sensed data as the sample measured by the IRIS, with a 2 cm x 2 cm "pixel", may be a poor analogue of, for example, a 28.5 m x 28.5 m TM pixel. It is possible to infer that, on the scale of the sensors used in this study, fairly flat and uniform surfaces such as soils are likely to be

bright. Fairly inhomogeneous surfaces with mixtures of soils and outcrop are likely to have reduced reflectance due to shadowing.

7.3.6 The relationship of IRIS and XRD results

Study of the XRD results presented in Tables 7.1 - 7.3 alongside the IRIS results shown in appendix A shows that, on the whole, the two analytical methods used in this study correlate, although some differences are apparent. IRIS measurements commonly reveal iron oxide and clay minerals in the samples where the XRD measurements more frequently record the presence of quartz, feldspars, pyroxenes, amphiboles and micas. For example, kaolinite is not found in XRD analyses of the Burstall Granite's soil. IRIS measurements, however, do lead to kaolinite being identified in this soil.

This inconsistency is explained by the fact that sample preparation of soils for XRD analysis by crushing leads to the interior bulk of grains forming a higher proportion of the sample than their surface coatings, where the clay minerals concentrate. Whereas the IRIS measurements reflect the mineralogy of the top 50-100 μm of the sample, the XRD powder inevitably contains a contribution from the interior of crushed grains below this surface coating. This is an important contrast between the two analytical techniques. The IRIS results are biased towards the weathered mineralogy while the XRD results reflect the primary mineralogy of the lithology. The former, being a surface-biased measurement, are a closer analogy to the remotely sensed data. A detailed study of the relationship between XRD and IRIS measurements, reaching similar conclusions, is described in Fraser (1990b).

7.3.7 Summary

The relationship between the solid geology and the surface measured by the sensor varies in complexity with lithology. For basic rocks, a simple direct relationship can be established between the fresh rock and both the weathered surface and the soil. For the granites and some other felsic lithologies a more complex relationship is found and the weathered surface and soil are spectrally distinct. The situation is further complicated within the metasediments due to mineralogical changes which accompany

facies variations. Within the same formation, one facies may develop a 2.2 μm absorption during weathering whilst another may have an existing 2.2 μm absorption due to primary mineralogy masked by the weathering process.

Within this framework, some broad observations can be made which hold true for the majority of the lithologies exposed in the area:

1. Iron oxide minerals develop during the weathering of almost all lithologies. The main iron oxide related absorption around 0.5 μm either develops for the first time during weathering or becomes more pronounced. Additional iron-related absorptions at around 0.9 μm also develop and deepen.

2. The absorptions due to molecular or free water at 1.4 μm and 1.9 μm develop, not being present in the fresh sample, appearing in the weathered surface reflectance and becoming a major feature in the soil's reflectance spectrum. This reflects an increase in water content and the development of clay minerals during weathering, and the presence of a quartz residuum with associated molecular water.

3. As the mineralogy changes during weathering, so does the lithology's spectral character. Absorption features present in the fresh surface spectrum are not seen in that of the soil, and vice versa. It may be difficult to relate the spectral response of the fresh rock surface to that of the exposed soil, or even the rock's weathered surface.

4. Basic rocks have a continual increase in iron oxide throughout the weathering process. Felsic rocks develop an iron oxide rich weathering crust and have reduced iron oxide in their soils.

5. The overall reflectance can be expected to increase during weathering, with the production of a uniform weathered surface and then a uniform soil. Extensive areas of soil will have high albedo.

6. IRIS and XRD results do not correlate directly but are broadly consistent. Differences are partly due to sample preparation methods. The IRIS data are easier to collect and analyse and form a closer analogue for the remotely sensed data as they are a measure of the surface layer only.

7. The AGR data are less affected by weathering than the TM data in this field area, as shown by the more homogeneous AGR response of most lithologies.

7.4 Erosion, transport and deposition of weathered material

So far the relationship between the solid geology and the material exposed in situ which has been derived from it directly through weathering has been considered. It is also necessary to consider the further stages of the denudation process and the effects these may have on the relationship between the material exposed at the surface and the bedrock.

7.4.1 Erosion

In some favourable settings, erosion of the weathered material may be sufficient to remove the materials masking the solid geology. An example of this phenomenon, from member Pkc_2 of the Corella Formation at locality 58, is seen in Plate 7.14. The iron oxide rich weathered surface covering this facies of the formation over most of its outcrop is absent in those outcrops which occur within the creek bed, where flash-flooding has eroded the weathered crust. In this example, however, the area covered by the fresher outcrop is on the order of a single TM pixel. It is difficult to perceive the effect in the remotely sensed data, where pixels in the creek are dominated by vegetation.

The Cameron River, seen from locality 115 in Plate 7.15, cuts across the strike of the Corella Formation in the north of the field area in a deep gorge. Within the gorge the normally dense green vegetation of the river course is reduced and there are larger expanses of fresher rock surfaces exposed. The spectral response of pixels within the

gorge is different to that of those along-strike away from the creek which are covered by a weathered surface.

In the TM data (Enclosure 5.1) the lithology is characterised by 0.83 μm absorption away from the creek, but the pixels in the creek have an additional absorption at 2.22 μm. This could be due to vegetation, but there is no corresponding 0.49 μm absorption and the 0.83 μm absorption remains. The lithology is a carbonate, and it seems likely that calcite, with an absorption centred on 2.34 μm which falls within TM band 7 (2.08-2.35μm), is responsible for the apparent 2.22 μm absorption. The same area is covered by the GMS data shown in Plate 7.16, which are of higher spectral resolution. In the short wave infrared, the lithology is characterised by absorption at 2.352 μm typical of calcite away from the creek. Within the creek, it appears that the same absorption persists and the river course is discontinuous in the image. The weathered crust is sufficient to mask the weak absorption caused by calcite in TM band 7, which is not well positioned to measure the 2.352 μm absorption. The GMS data measure the calcite absorption where it is strongest and can detect this signal even through the weathered crust. Thus the true spectral character of the lithology is seen in the GMS data over all its outcrop. In the TM data this is only the case when erosion removes the weathered crust.

7.4.2 The spread of weathering product from resistant lithologies

When using remotely sensed data to produce geological maps, it is common to draw boundaries between areas of different spectral response. These will only correspond to geological boundaries if the material exposed at the surface is directly related to the rock below for the boundary pixels. Often this is not the case.

7.4.2.1 Masked Lithologies

The Burstall Granite illustrates this problem well. This pluton is resistant to erosion in comparison to the Corella Formation metasediments which it intrudes. In particular the southern mass, seen from the south in Plate 2.8, forms a prominent hill with extensive outcrop and rugged topography. When the TM data are used to map this lithology, the

apparent boundaries of the pluton are inconsistent with the 1:100 000 geological map, and the results are worse still with the AGR data (Figure 7.17). All of the pluton and its surrounding debris have the same high radiometric response.

The reason for this inconsistency between the remotely sensed data and the geological map is clear in the field. The true position of the contact between the sediments and the granite is high up the hill. As seen in Plate 7.17 large amounts of granite debris eroding from the crags near the top of the hill are transported down slope, so that for between 100 and 300 m the outcrop of the Corella Formation is hidden below a cover of granite debris ranging from large boulders to soils. Plate 7.18 from locality 100, halfway up the slope, illustrates this problem. The bag is on Corella Formation outcrop which is almost entirely covered by granite debris. As the slope is uniformly steep and there is a continual supply of granite debris from above, the granite debris dominates the surface until the lower slope break is reached. The main part of the granite and the apron of debris can be discriminated in the NS001 LR data shown in Plate 7.19. The fresher granite boulders and clay rich soil on the debris slope cause 2.22 μm absorption. Another area of 2.22 μm absorption occurs in the centre of the pluton. The 0.83 μm absorption is related to outcrop slabs with an iron oxide crust and the 0.49 μm absorption to shade in this instance (due to a problem with the atmospheric correction for this data set which will be discussed in section 7.6.2.).

This locality, being near the mine site and other uranium prospects, is mapped at 1:10 000. This scale of mapping reveals the buried Corella Formation below the granite and allows the geological boundary to be placed with accuracy. Rapid mapping by traverses based on the TM data may not lead to a comparable accuracy being achieved. Even on a 1:100 000 scale map, the discrepancy in the position of the Burstall Granite's boundary as measured in the TM data could be up to 3 mm. Indeed, an easily eroded lithology may not be detected in the remotely sensed data at all.

The deep iron oxide-rich soil forming the debris plain over much of the Wonga Granite may provide another example of a masked lithology. This soil, the most iron oxide-rich surface measured for the Wonga Granite, may be developing in situ through lateritic weathering, as postulated in section 7.3. There is, however, a second possibility to

consider. The majority of the Wonga Granite forms a flat lowland area, seen in Plate 2.5, into which creeks feed from the adjacent high ground to east and west. These high relief areas contain both metadolerites and metasediments with iron oxide-rich weathered surfaces. These weathering products may be transported to the Wonga Granite plain where they will accumulate due to the change in gradient. It may be these materials which are responsible for the iron oxide-enriched debris plain soil, so that the large areas of 0.49 μm absorption found over the Wonga Granite are due to a soil derived from adjacent lithologies. The spectral signature of the granite, absorption at either 0.83 μm or 2.22 μm, is thus masked over much of the pluton.

Little of the Burstall Granite has a deep 0.49 μm absorption (that is, not in the TM or GMS data, but disregarding the NS001 data which have atmospheric correction problems), only showing 0.83 μm absorption, 2.22 μm absorption and a response typical of vegetation (Enclosure 5.1). If the iron oxide-enriched soil formed by in situ mature weathering of the Wonga Granite, it would also be expected to be found over at least part of the Burstall Granite, particularly in the central valley of the main mass which has extensive areas of stable soil accumulations. These are in fact characterised by 2.22 μm absorption attributed to clay minerals in the soil. This supports the hypothesis that much of the Wonga Granite is covered by a soil whose major spectral characteristic, absorption at 0.49 μm, is derived from adjacent unrelated lithologies. The difference could however be due to lithological contrasts between the two granites.

7.4.2.2 Mixing of lithologies at their boundaries

In the southwest of the field area at locality 258 (the southwest end of traverse 21), seen in Plate 7.20, the Corella Formation is in contact with the Ballara Quartzite, which forms a resistant ridge to the south. The slope of this ridge is reduced and it is possible to map, over a distance of approximately 500 m, a progression from 100 % quartzite debris, through a gradually changing mix of Ballara Quartzite debris and Corella Formation, as seen in Plate 7.21. This corresponds to a change seen in the TM LR data shown in Enclosure 5.1. The Ballara Quartzite has a strong 2.22 μm absorption and is red in this colour composite. The Corella Formation at this locality has a 0.49 μm absorption which would appear blue if the formation ever dominated a pixel. The mixed

area nearer the quartzite is seen in pink, indicating a mix of both these absorption features dominated by 2.22 μm in red. Further from the quartzite the mixed area appears purple, indicating that the proportion of 0.49 μm absorption, and therefore Corella Formation, in the mix has increased.

This effect again complicates the placing of geological boundaries in the remotely sensed data. Whilst a technique such as unmixing analysis (Settle, 1990) could be used to find the proportion of each lithology in each pixel, this would not necessarily help locate the geological boundary. The boundary could be placed at the "no Corella Formation" pixel, but this would only reduce the problem to that discussed in section 7.4.2.1., as the quartzite debris may mask Corella Formation outcrop completely at the top of the slope.

7.4.3 Summary

1) In exceptional circumstances, erosion may remove the weathered surface from a lithology and expose near-fresh rock surfaces to the sensor.

2) The mapping of geological units and their contacts is complicated by the spread of weathered material from upstanding resistant lithologies onto other lithologies. This problem is worse with the AGR data than with the TM data.

3) A lithology may be entirely masked by the resistant lithology's weathering product. Alternatively, a mixing may occur which effectively blurs geological boundaries.

7.5 Vegetation

A further difficulty in relating the surface measured by the sensor to the solid geology is presented by the vegetation cover.

7.5.1 Areas of 100 % vegetation cover

Total vegetation cover is found in very few parts of this semi-arid field area. Pixels which cover the major creeks may consist of 100 % green vegetation, where a dense canopy of Eucalypts fills the creek bed. Such an area within the Cameron River, at locality 115, is shown in Plate 1.2. Figure 7.18 shows a laboratory reflectance spectrum for green vegetation. The logarithmic residual pseudo-spectrum for a single pixel from the visible/near infrared GMS data over one of the main creeks is shown in Figure 7.19 for comparison. Figure 7.20 shows a TM pseudo-spectrum from within the Corella Formation, away from any creeks, which also has typical vegetation features. A few such pixels are found over this formation and over the granites, but they are uncommon. The correspondence of the two pseudo-spectra and the laboratory reflectance spectrum is evidence that the logarithmic residual technique produces a close approximation to reflectance.

In contrast, the creeks are not seen at all in the AGR data. Even areas of 100 % vegetation cover do not appear to mask the gamma radiometric response.

Areas of 100 % vegetation may still be geologically informative where the vegetation species can be related to a particular lithology or soil. In this field area, however, the vegetation is not related to the lithology but primarily to the presence of the creeks. Such pixels effectively contain no lithological information but may contain structural information where the creeks exploit features such as faults.

7.5.2 Other areas

Away from the main creeks, visual estimation in the field suggested that vegetation cover is usually limited to approximately 10 %, uniformly scattered within a pixel. The typical vegetation cover for the field area is shown in Plate 1.1 and consists of a mixture of low scrubby trees, spinifex grasses and dry wood. This level of vegetation cover does not obscure the geological signal but rather modifies it.

7.5.3 The effect of logarithmic residuals

The vegetation problem is reduced by the application of the logarithmic residuals process because the vegetation density is uniform across the majority of the scene. Every pixel therefore has a "10 % vegetation" component in its spectrum. The scene-average spectrum will also contain a "10 % vegetation" component, and thus division of an individual pixel's spectrum by the scene-average spectrum will remove the effects of this vegetation component. For this semi-arid area, the calculation of logarithmic residuals thus has an additional defoliant effect.

7.5.4 Least squares fit residuals

Where there is a local increase in vegetation density and thus in the vegetation component of the reflectance of each pixel, the greatest effect in terms of absorption occurs at 2.22 μm, particularly for dry vegetation (Figure 7.18). This is a problem where the geological material of interest also has a 2.22 μm absorption, for example a clay mineral. An area of 2.22 μm absorption in the imagery may thus be due to a geological material, a local increase in the vegetation density, or both. Whilst absorption features at other wavelengths are different for these materials, it is difficult to unequivocally attribute the 2.22 μm absorption to the presence of clay minerals rather than vegetation where the two materials mix in the pixel. Figure 7.21 shows a TM LR pseudo-spectrum from the Wonga Granite which has a 2.22 μm absorption but the features of vegetation at shorter wavelengths and probably represents such a mixed pixel. Fraser and Green (1987) describe a defoliant process termed least squares fit residuals designed to separate these two similar spectral responses. The technique is described in detail in section 5.7 and is assessed here for this field area.

The LSFit technique produces a band of predicted 2.22 μm data where the response of vegetation has been predicted from information at other wavelengths. Any remaining absorption at 2.22 μm is due to a mineral whose presence cannot be predicted using information at other wavelengths. These absorptions lead to a large value in the second residual band of the LSFit data. The LSFit residual band can be used to replace the 2.22 μm band of the LR data in colour composites, giving images such as that shown

in Plate 7.22. In this image, red represents 2.22 μm absorption which cannot be accounted for by the presence of vegetation in the pixel, green absorption at 0.83 μm and blue absorption at 0.49 μm.

The image in Plate 7.22 is very similar to the LR colour composite without the LSFit band shown in Enclosure 5.1, but there are some interesting differences. The most obvious difference is that the creeks are black in the LSFit image as their 2.22 μm absorption has been predicted. The tailings dam for the Mary Kathleen uranium mine, characterised by absorption at 2.22 μm in the original LR composite, no longer has a strong 2.22 μm absorption in the LSFit data. Plate 7.23 gives a view of the tailings dam and shows the increased vegetation density which covers it due to the water trapped within the dam. The LSFit technique has successfully predicted that this area of 2.22 μm absorption is also due to increased vegetation density rather than a material of geological interest. Interestingly, the tailings dam has a very high uranium response despite the vegetation cover, again suggesting that vegetation has little masking effect on the AGR data in this field area.

The apparent success of the technique in removing that part of the 2.22 μm absorption due to vegetation means that areas of 2.22 μm absorption indicated by the LSFit data can more confidently be attributed to absorptions near 2.22μm due to clay, sulphate or carbonate minerals. Areas of 2.22 μm absorption found in the LR data which persist in the LSFit data occur over the Argylla Formation, the Ballara and Deighton Quartzites, certain facies of the Corella formation and all the granites in the area, as well as some pegmatites in the extreme northeast. Thus, the majority of the 2.22 μm absorptions found in the TM data for this area have geological explanations. One notable exception is provided by parts of the Argylla Formation northwest of the Rosebud Syncline, which no longer display 2.22 μm absorption in the LSFit data. On the whole, however, vegetation represents a minor problem which is in part overcome through the application of the logarithmic residuals process.

7.5.5 Summary

1) 100 % vegetation mainly occurs in the creeks. Pixels containing 100 % vegetation in this setting contain no lithological information.

2) The close correspondence of laboratory vegetation spectra and logarithmic residual pseudo-spectra from two different data sets suggests that the LR process, when carefully applied, produces a close approximation to reflectance.

3) Where the vegetation component forms a small and relatively constant proportion of the reflectance of a pixel, it is removed or reduced by the application of logarithmic residuals.

4) Where vegetation remains a problem due to increased density, for local reasons, the LSFit technique is successful in separating 2.22 μm absorptions due to the vegetation component from those with a geological cause.

5) The majority of the 2.22 μm absorptions in the data over the Mary Kathleen area, away from the main creeks, are due to geological materials rather than a vegetation component.

6. The AGR data are largely unaffected by the levels of vegetation cover found in this field area, though they are affected in other areas (B. Dickson, personal communication).

7.6 The shade component

Although difficult to measure in the field, the shade component may also make it difficult to apply the remotely sensed data to geological mapping problems.

7.6.1 Band ratios

As discussed in section 5.6, provided that corrections have been made for the additive atmospheric path radiance and instrument offsets the band ratio technique should remove the shade component as it forms a constant. Constant ratio values result over homogeneous materials. In an area of total shade the radiance reaching the sensor not attributable to the atmosphere is zero and there is no geological information at all. Where the shade component forms anything less than 100 %, the ratio technique will remove it, but with rapidly decreasing success as the proportion of shade becomes high. Consider a material whose 1.65/2.22 μm ratio value is 2:

Bright area:	1.65 μm = 200 DN	2.22 μm = 100 DN
Dark area:	1.65 μm = 50 DN	2.22 μm = 25 DN
Darkest area:	1.65 μm = 2 DN	2.22 μm = 1 DN

All these DN values give a common ratio value of 2 as the ratio is proportional to the reflectance at each wavelength for that material and this does not change. Introduction of noise of just 1 DN to the 1.65 μm band for these pixels results in increasingly inaccurate ratio values as the proportion of shade increases:

Bright area:	1.65 μm = 201 DN	2.22 μm = 100 DN	Ratio = 2.01
Dark area:	1.65 μm = 51 DN	2.22 μm = 25 DN	Ratio = 2.04
Darkest area:	1.65 μm = 3 DN	2.22 μm = 1 DN	Ratio = 3.00

Ratios commonly have a very small range from a maximum of about 10 down to 0. When these values are scaled to byte for display the variation introduced by the noise becomes very significant. The ratio no longer has a single value over a single material. In effect, the shade component does not have to reach 100 % for there to be no geological information in a pixel.

7.6.2 Logarithmic residual data

Plate 7.19 shows the southern mass of the Burstall Granite in the NS001 data after atmospheric correction and logarithmic residual processing. Plate 7.24 shows the same part of the granite after atmospheric correction but without further processing. There is a correlation between areas of deep shade in the radiance data and areas of 0.49 μm absorption in the LR data. Clearly deep shade in the blue visible wavelength region is being misinterpreted during the logarithmic residual process as absorption at that wavelength. Thus, for a pixel in deep shade it would seem that the 0.49 μm datum is anomalously low in comparison to the spectral average for that pixel. A possible cause of this is under-correction of the additive atmospheric path radiance at this wavelength. As discussed in section 4.3.4.3, the majority of the data minima for NS001 Flight Line 3 lie within the lake. However, deep shade over the southern mass of the Burstall Granite has a lower DN value than the lake at 0.49 μm and at 0.56 μm.

This flight line was processed very rapidly prior to field work. Previous experience with the TM data indicated that atmospheric corrections based on water were better than those based on deep shade, and so the flight line was corrected using the Lake Corella minima values. The lower values in the shade at 0.49 μm and 0.56 μm were assumed to represent only a few pixels and attributed to noise. The correction performed set the minima values to 1 DN to avoid mathematical problems in later processing. As it was based on the Lake Corella values, any values lower than this would have been set to zero. The haste with which the correction was performed led to this problem being neglected, on the assumption that only a few noisy pixels would result. In fact, it is clear that there are many such pixels and they do not appear to be related to noise.

All the deep shade pixels set to zero at 0.49 μm and 0.56 μm by the correction applied have slightly higher DN values at the other wavelengths. Their 0.49 μm and 0.56 μm values are thus low in comparison to their spectral average. The result is a false absorption at these two wavelengths when logarithmic residuals are calculated.

Thus the explanation for this phenomenon is under-correction of the NS001 0.49 μm and 0.56 μm data. This problem must be considered when the data are interpreted. This

under-correction may only be one or two DN but it will still affect the logarithmic residual data in deep shade where the numbers involved in the divisional process are small. It would be avoided were more time taken over processing as not only the data minima indicated by the statistics but also the surrounding pixels would be checked interactively on screen.

7.6.3 Summary

Where shade is a significant component of a pixel, the signal is reduced to such an extent that even a small amount of noise or an under-correction of the data by one or two DN becomes significant. Techniques which rely on division, such as band ratioing and logarithmic residuals, may be unreliable in areas of deep shade. Such areas thus effectively contain no geological information. With the AGR data, the earth is the source of radiation and shade therefore has no effect.

7.7 General summary

The task of relating the remotely sensed data to the solid geology is complicated by weathering, erosion, transport and deposition of weathered material, the growth of vegetation and the presence of shade. The weathering process typically involves the production of iron oxide with or without clay minerals but must be understood for each individual lithology. In some cases there is no clear relationship between the spectral responses of the parent lithology and the weathered material, but the gamma radiometric response is usually unchanged between the two. The topographic setting of a lithology and its resistance to erosion often determine what type of surface covers that lithology. Some lithologies are wholly or partially masked by material weathered from adjacent unrelated rock types, particularly in the AGR data. Vegetation is rarely a major problem other than in the main creeks and does not appear to affect the AGR data at all. The effects of the shade component cannot be adequately removed where it forms a large proportion of a pixel, because the reduction in signal makes noise more significant. Such pixels contain no geological information. This problem does not affect the AGR data.

Figure 7.1 The distribution of Ferricrete in Eastern Australia, after Ollier (1984).

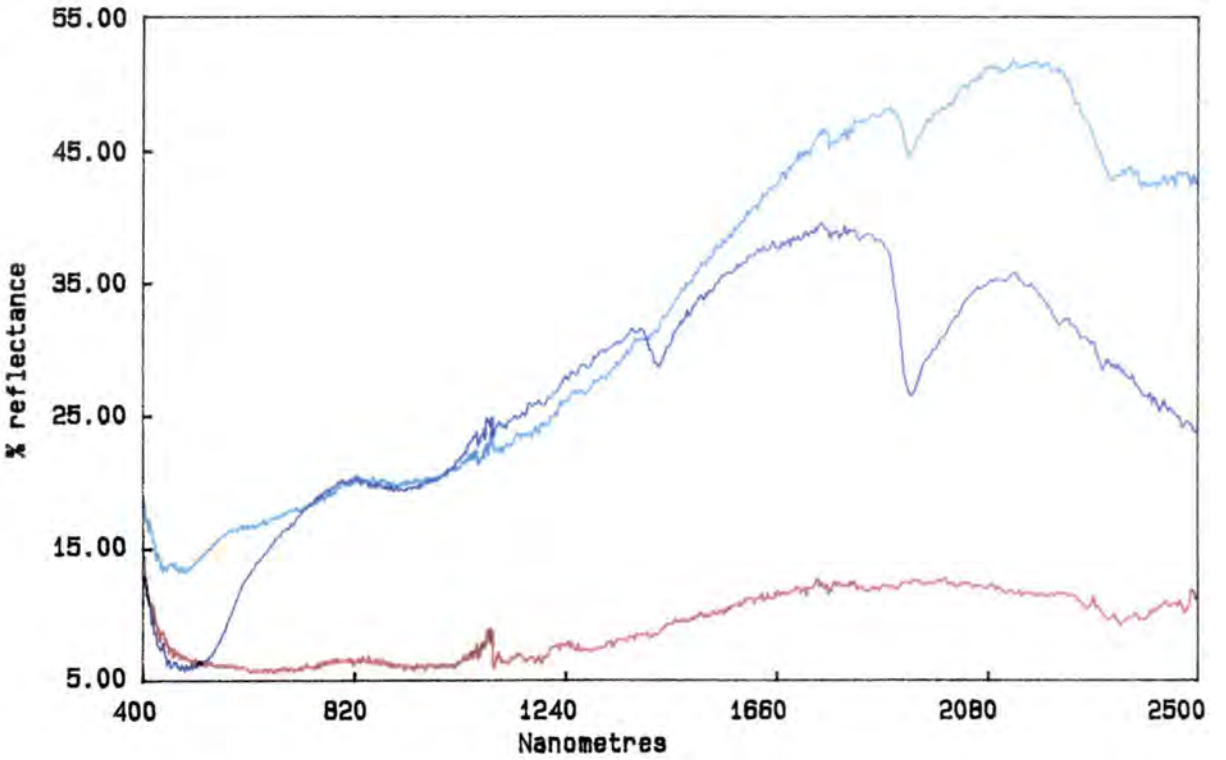

Figure 7.2 IRIS reflectance spectra for the fresh, weathered and soil surfaces of the Dog Bone Dolerite at locality 1. Colour coding of spectra is explained in the text.

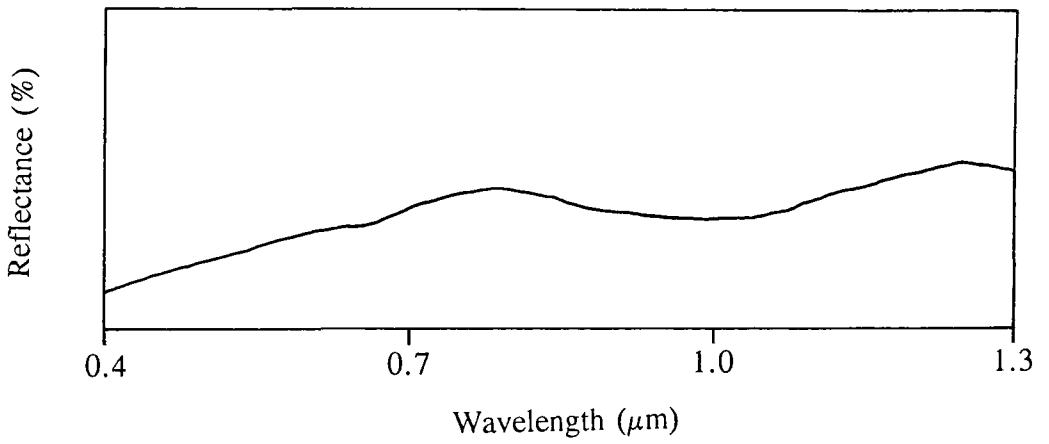

Figure 7.3 Typical laboratory reflectance spectrum of basic rocks (source: CSIRO).

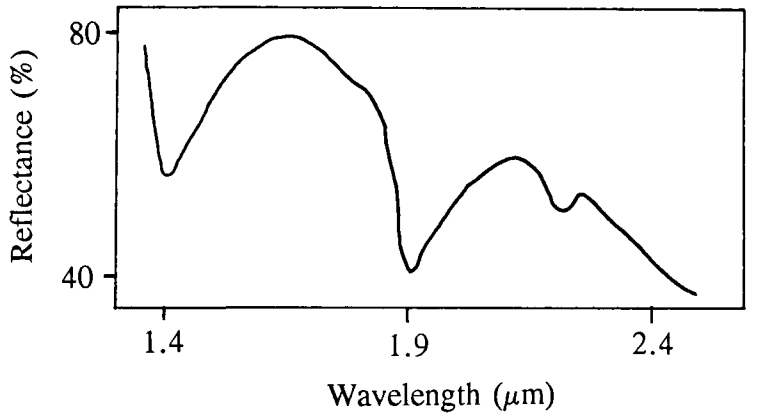

Figure 7.4 Laboratory reflectance spectrum of montmorillonite (source: Geoscan).

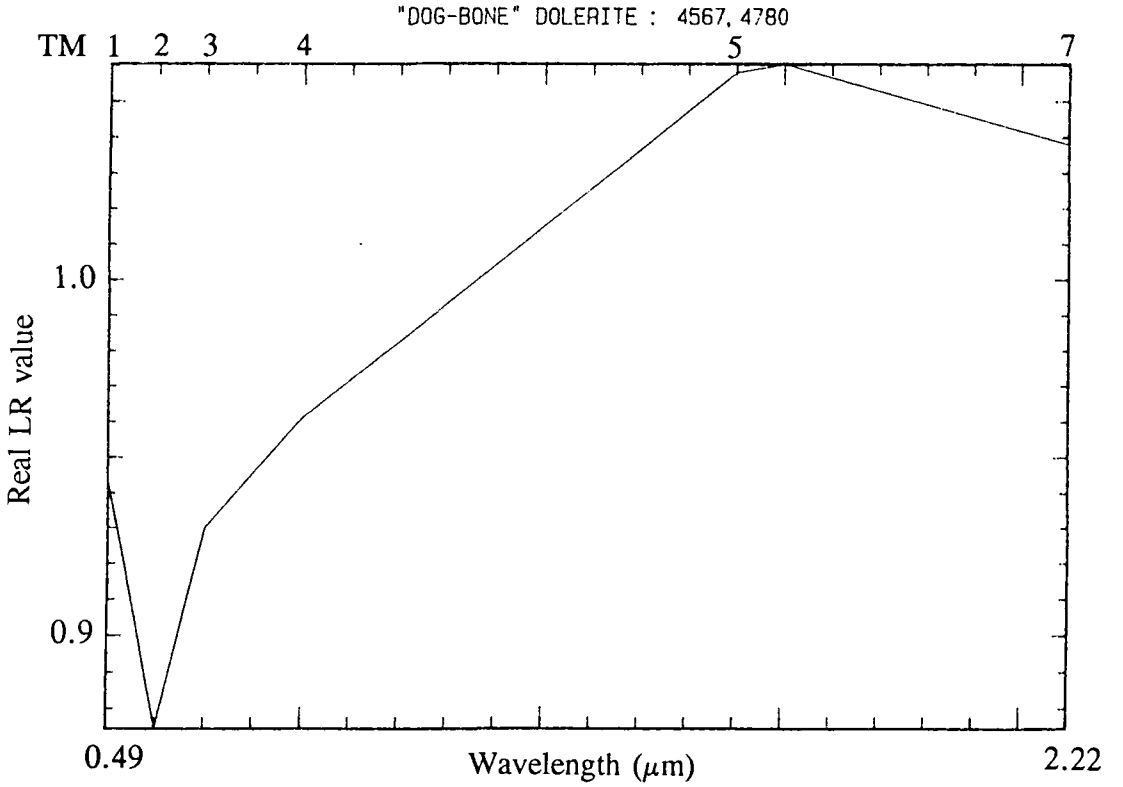

Figure 7.5 TM LR pseudo-spectrum for the Dog Bone Dolerite.

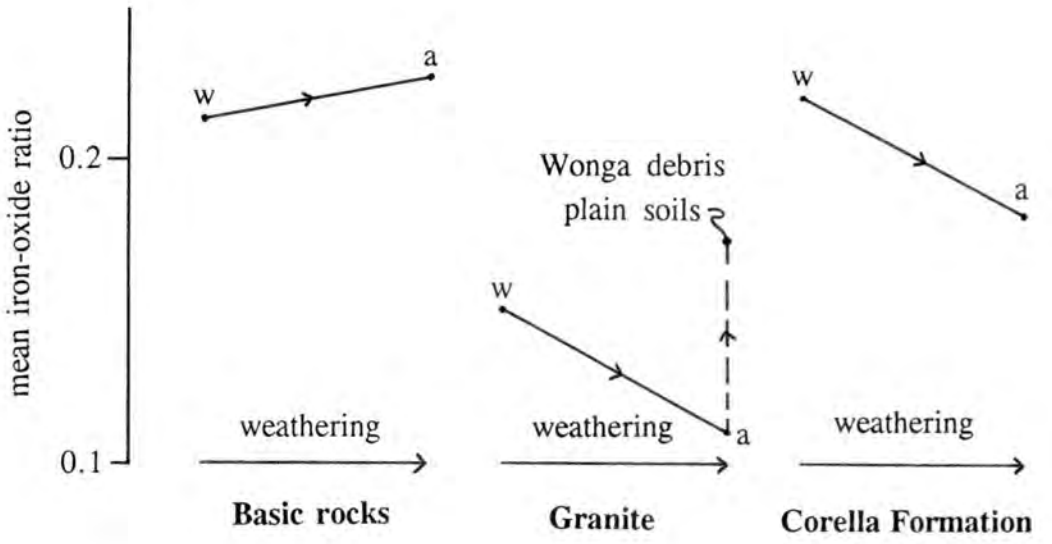

Figure 7.6 The change in the mean iron-oxide ratio of various rock types during the transition from weathered rock to soil.

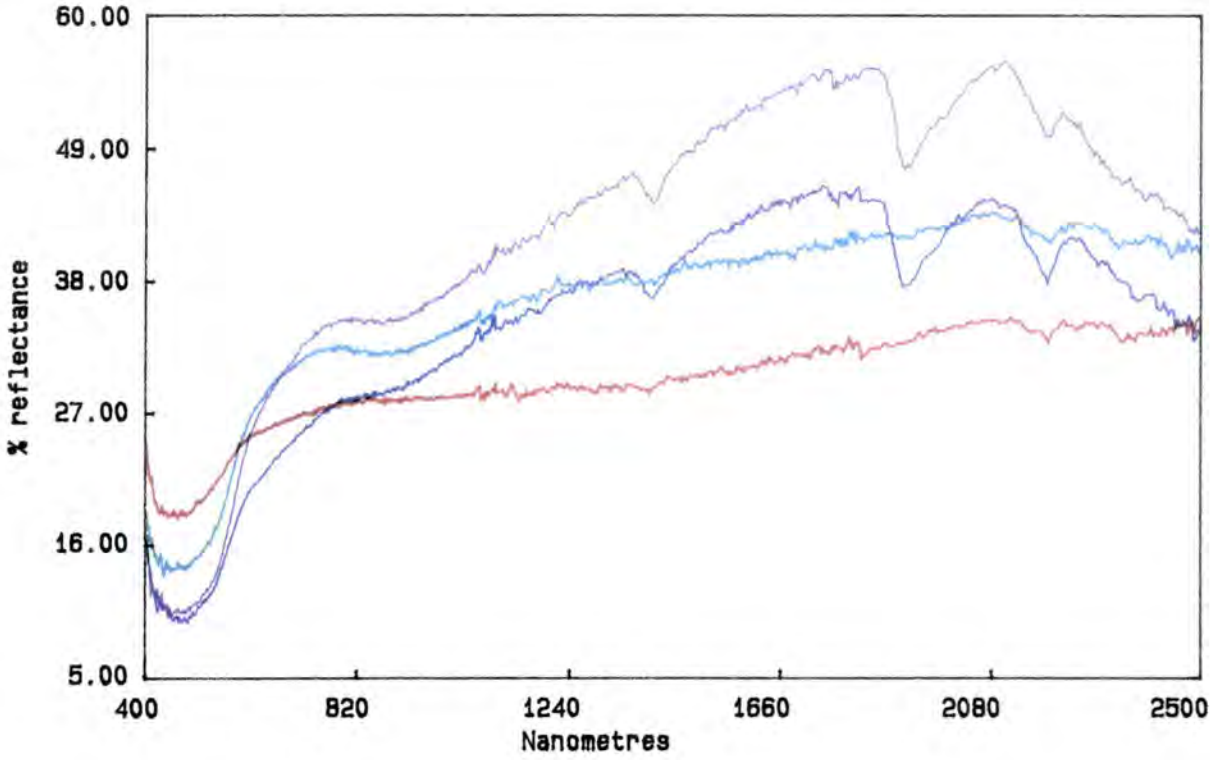

Figure 7.7 IRIS reflectance spectra for the Wonga Granite at localities 112 (fresh and weathered surfaces), 113 (soil) and 114 (debris plain soil, in purple).

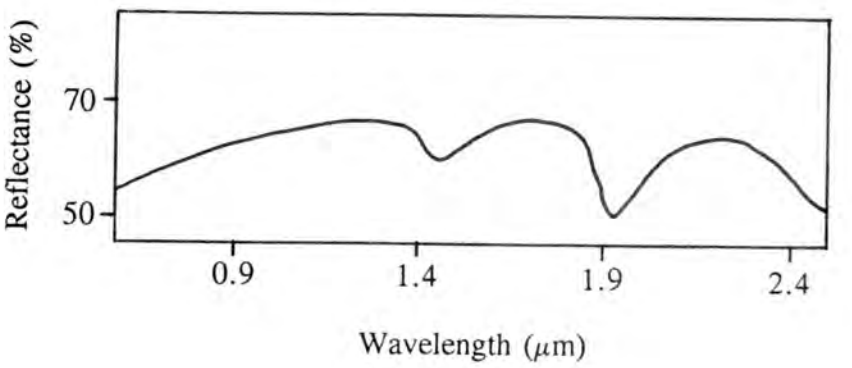

Figure 7.8 Laboratory reflectance spectrum of quartz, after Hunt (1980).

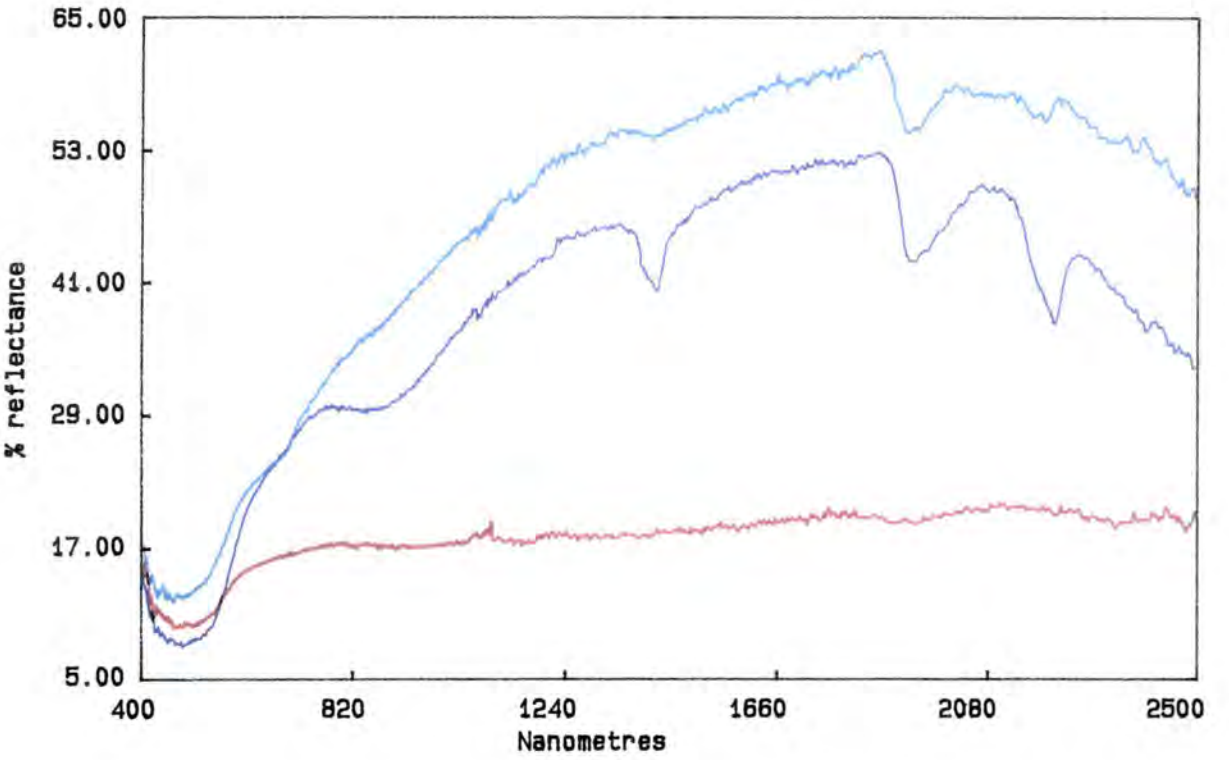

Figure 7.9 IRIS reflectance spectra for the Burstall Granite at locality 104.

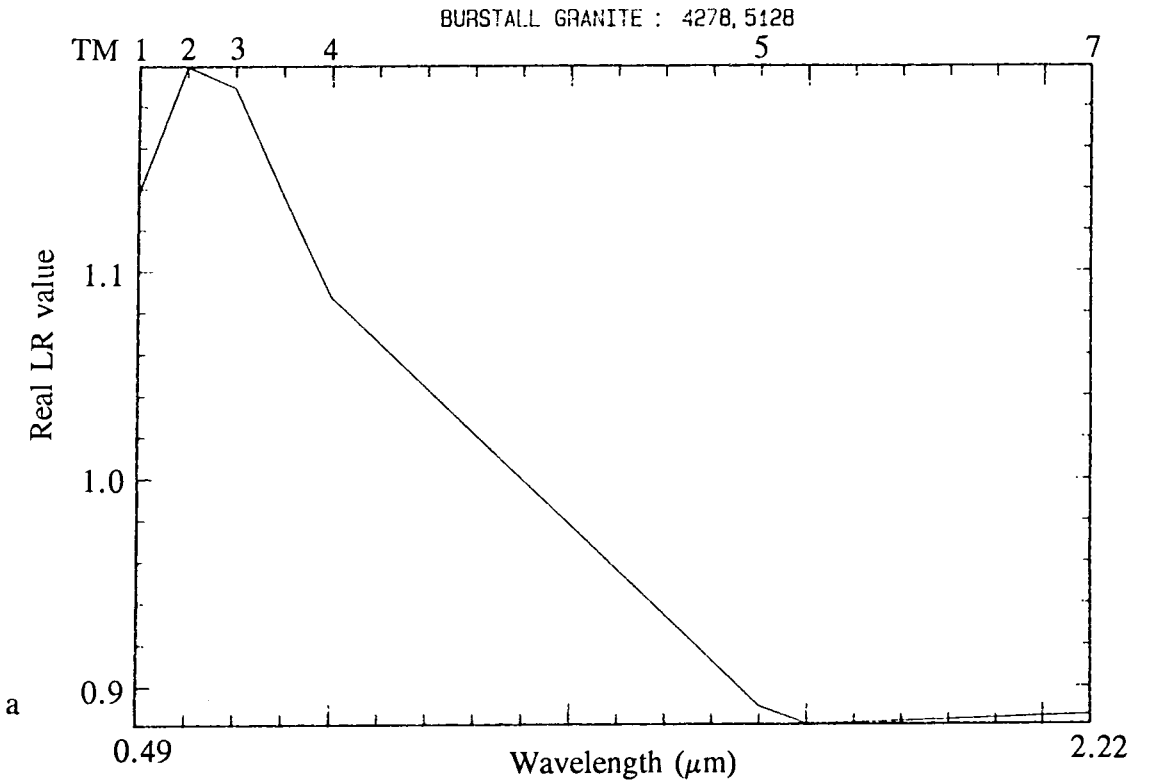

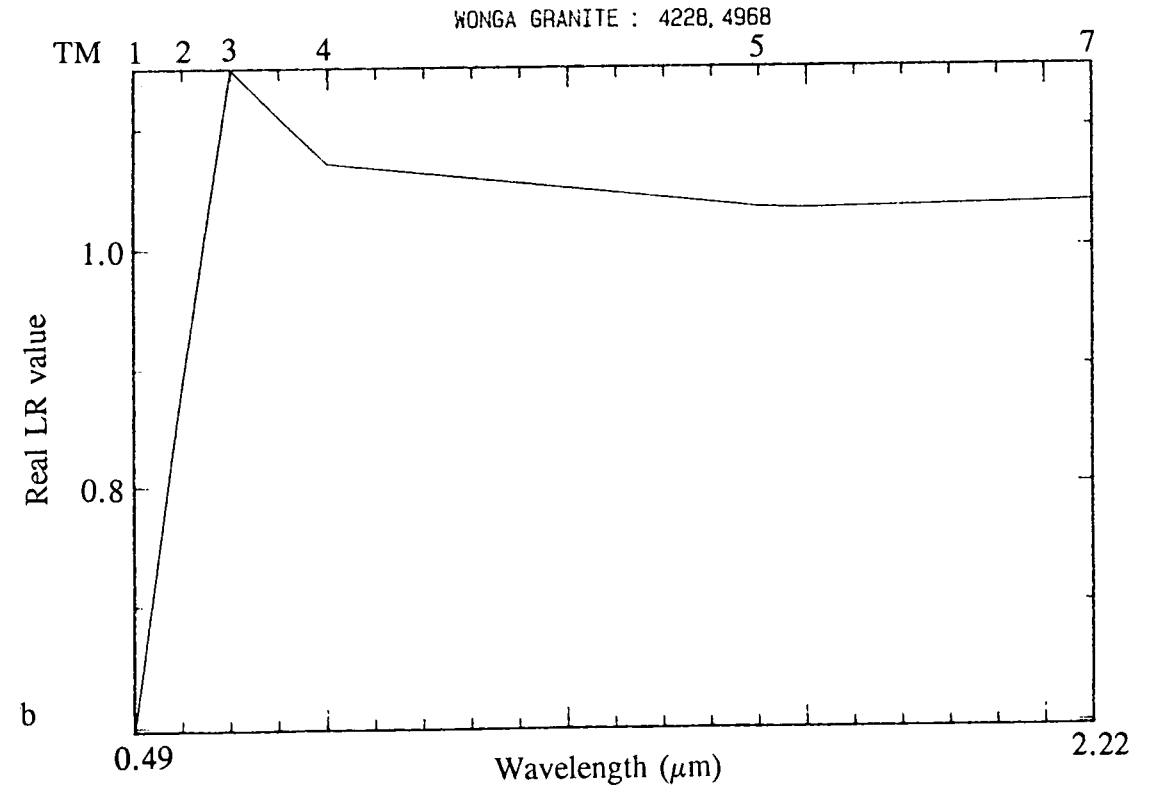

Figure 7.10 TM LR pseudo-spectra for the clay-rich soil (a - Burstall Granite) and more mature iron-oxide soil (b - Wonga Granite) commonly developed on the granites.

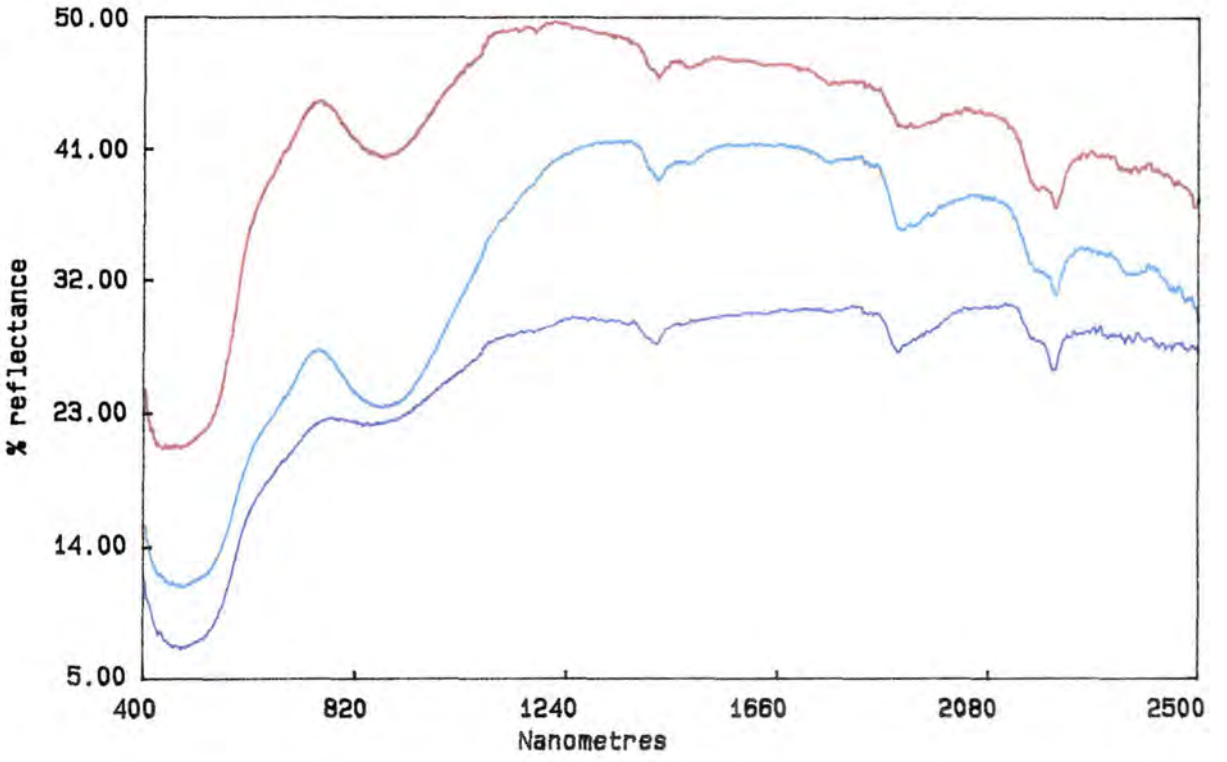

Figure 7.11 IRIS reflectance spectra for the Argylla Formation at locality 226.

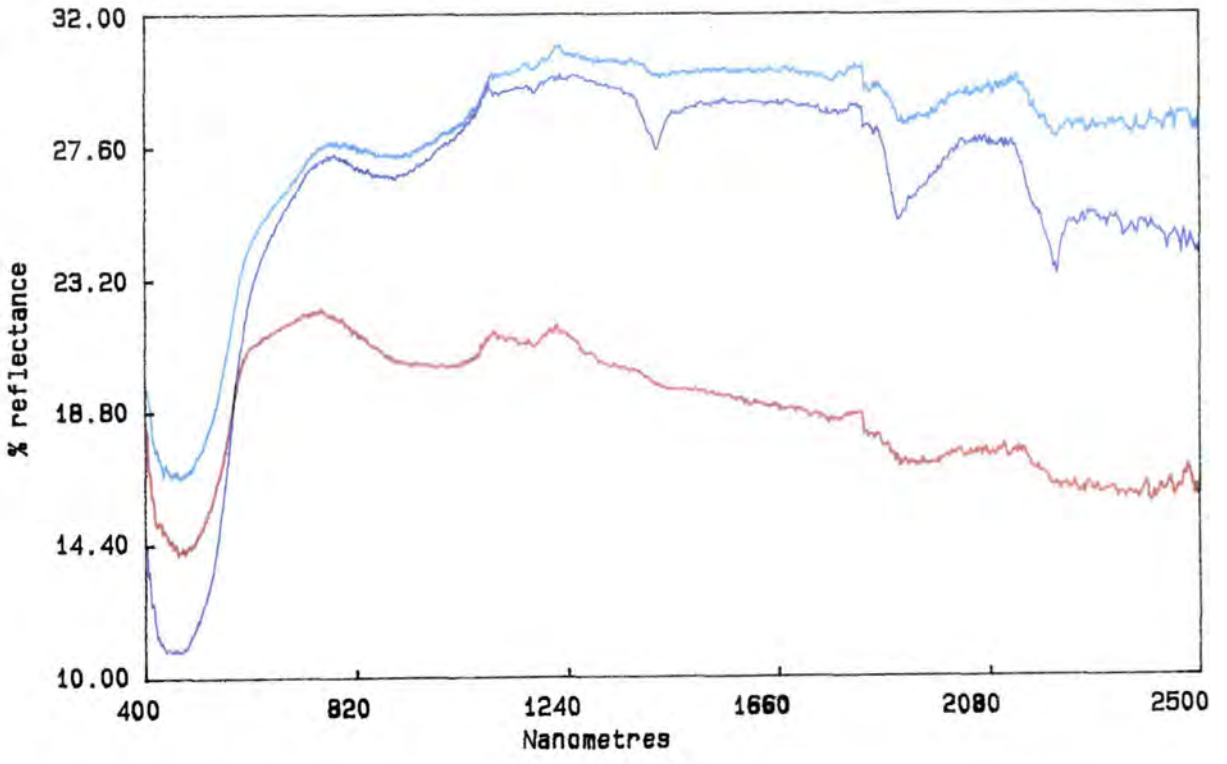

Figure 7.12 IRIS reflectance spectra for the Ballara Quartzite at locality 225.

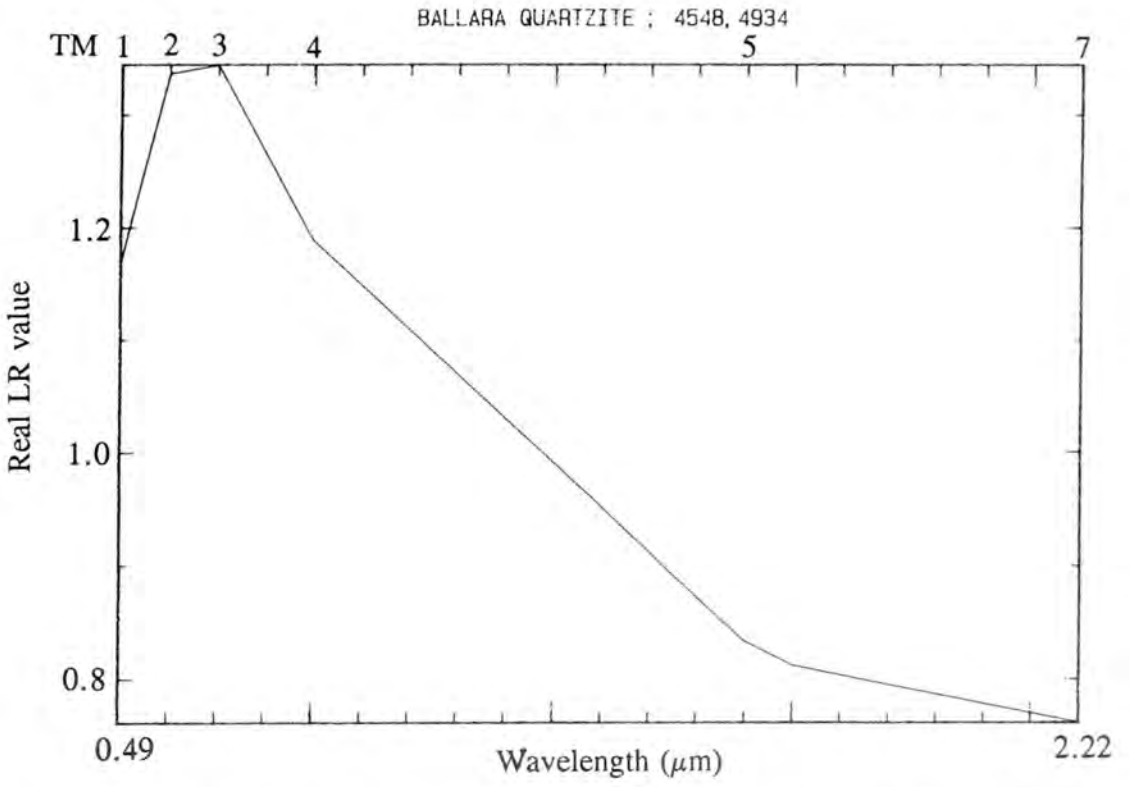

Figure 7.13 TM LR pseudo-spectrum for a prominent outcrop at the contact of the Argylla Formation and the Ballara Quartzite, localities 225 and 226.

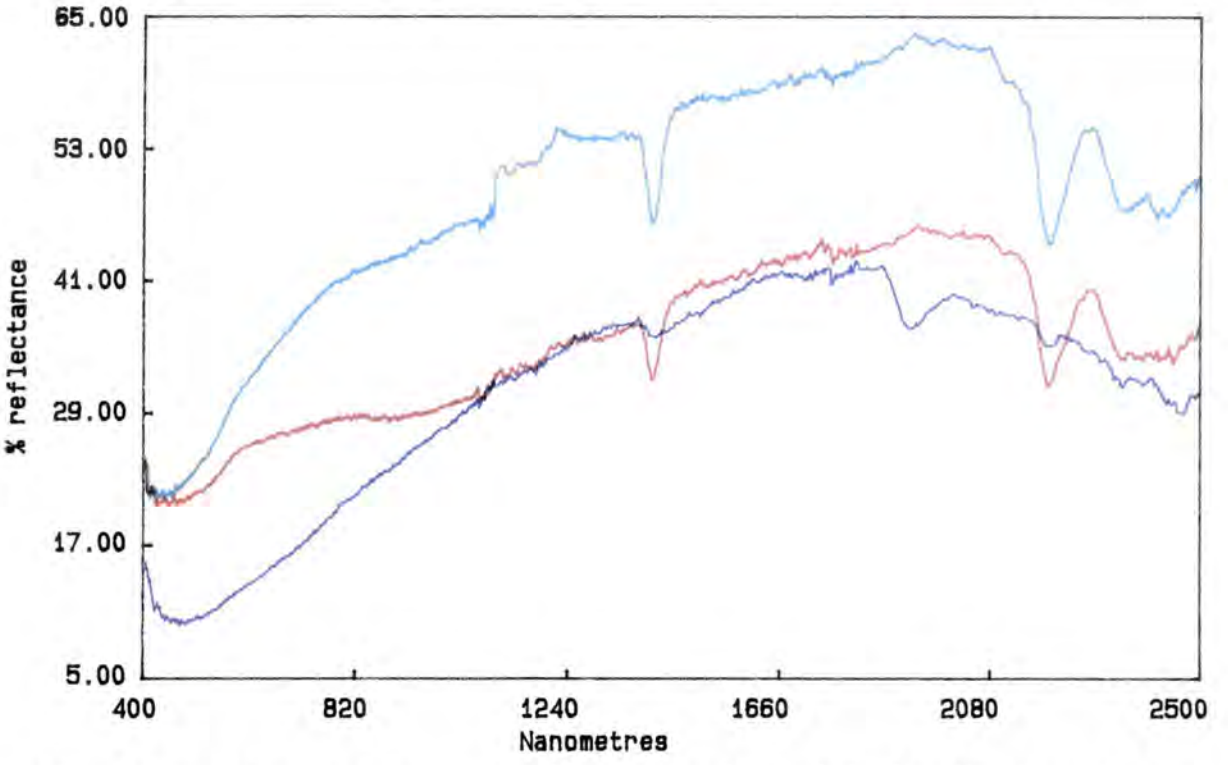

Figure 7.14 IRIS reflectance spectra for member Pkc_1 of the Corella Formation at locality 27 in the Rosebud Syncline.

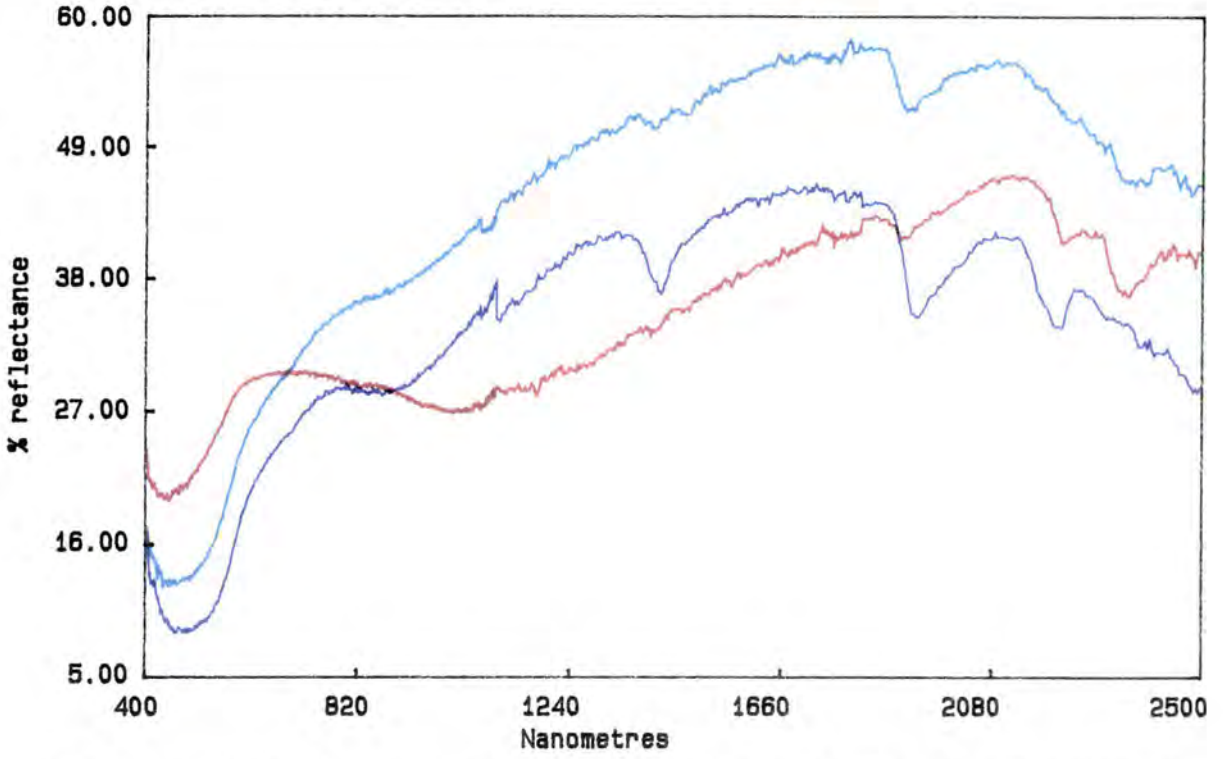

Figure 7.15 IRIS reflectance spectra for member Pkc_2 of the Corella Formation at locality 130 in the Mary Kathleen Syncline.

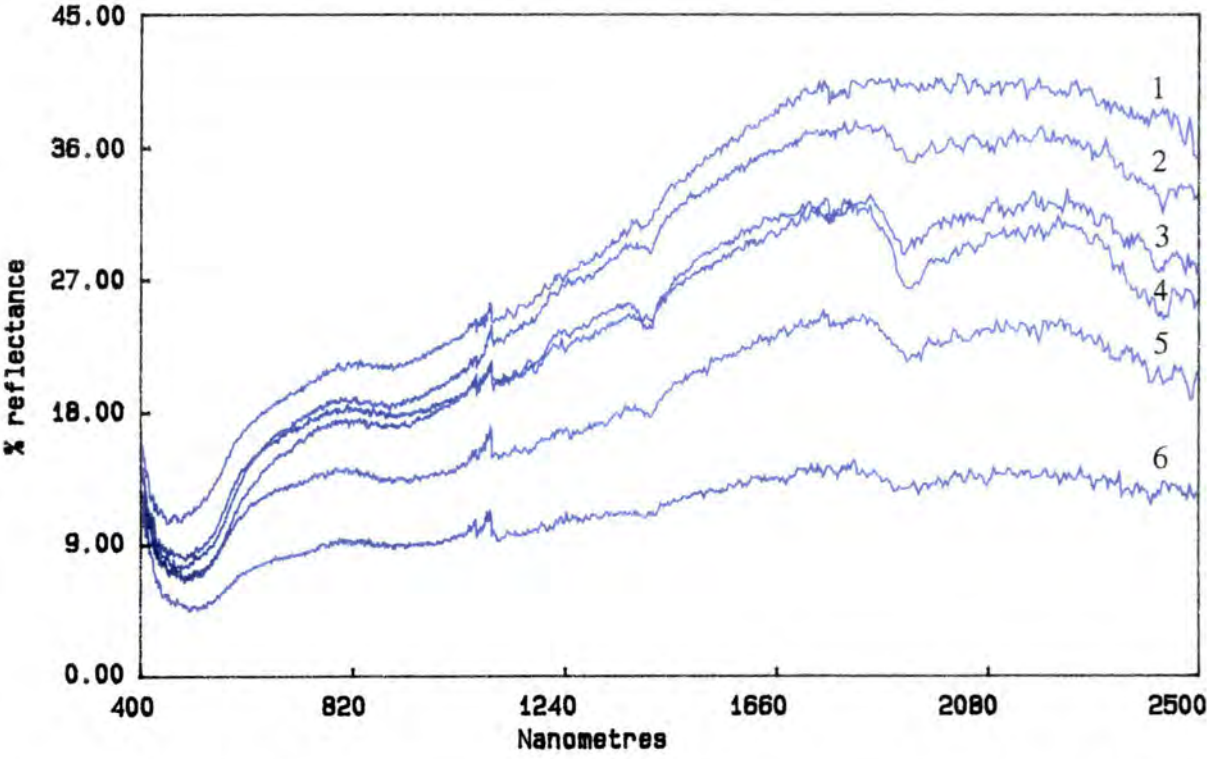

Figure 7.16 IRIS reflectance spectra for different particle sizes of sample 98a. Labels are explained in the text.

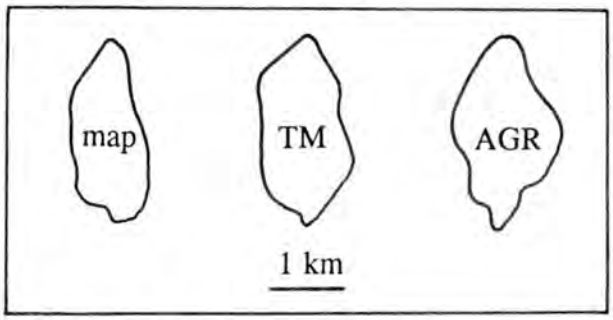

Figure 7.17 The apparent size of the Burstall Granite's southern mass in the TM and AGR data, with the size on the 1:100 000 map for comparison.

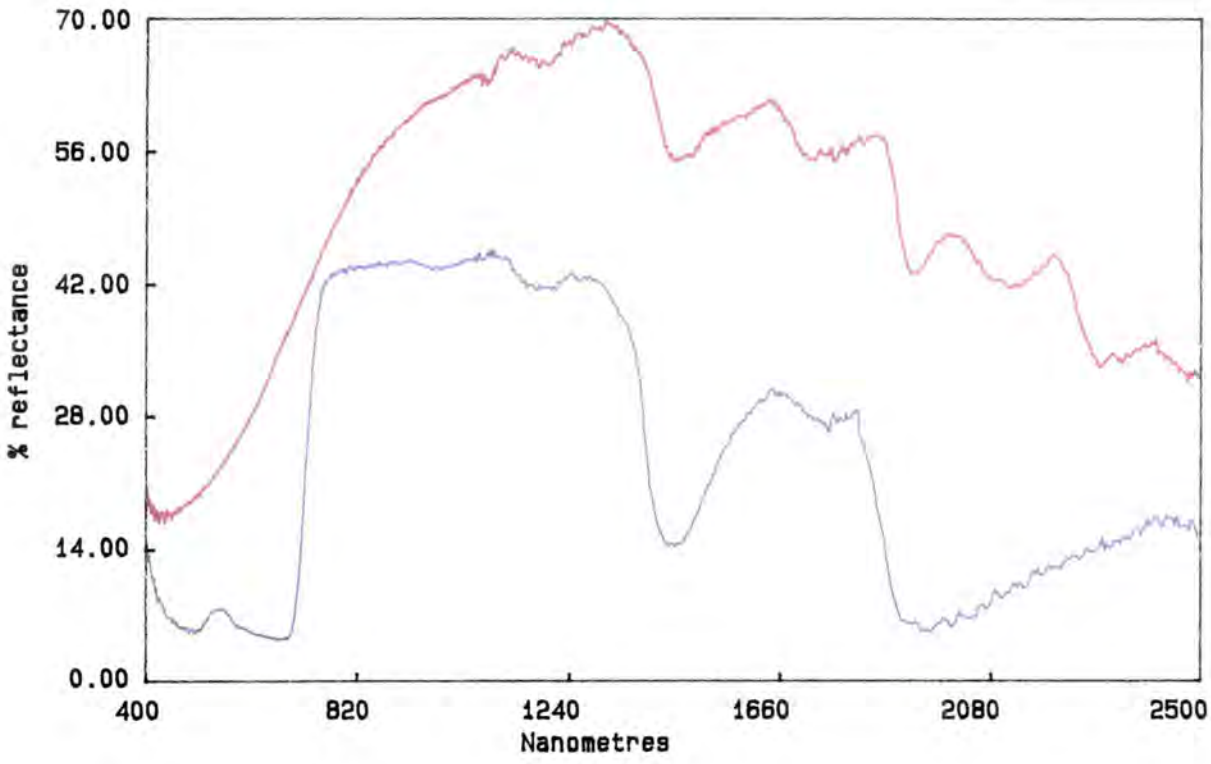

Figure 7.18 IRIS reflectance spectra for green (purple spectrum) and dry (red spectrum) vegetation. The dry vegetation sample was collected in the field area.

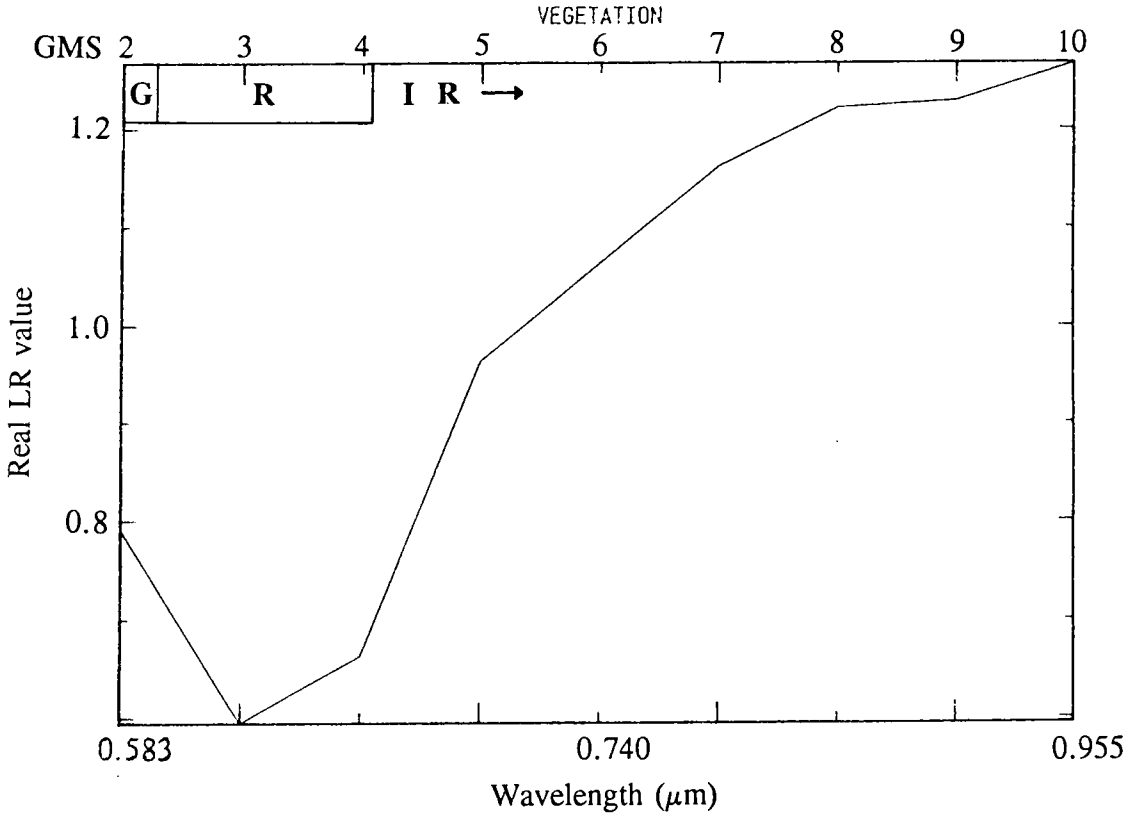

Figure 7.19 GMS LR pseudo-spectrum of green vegetation in the Cameron River.

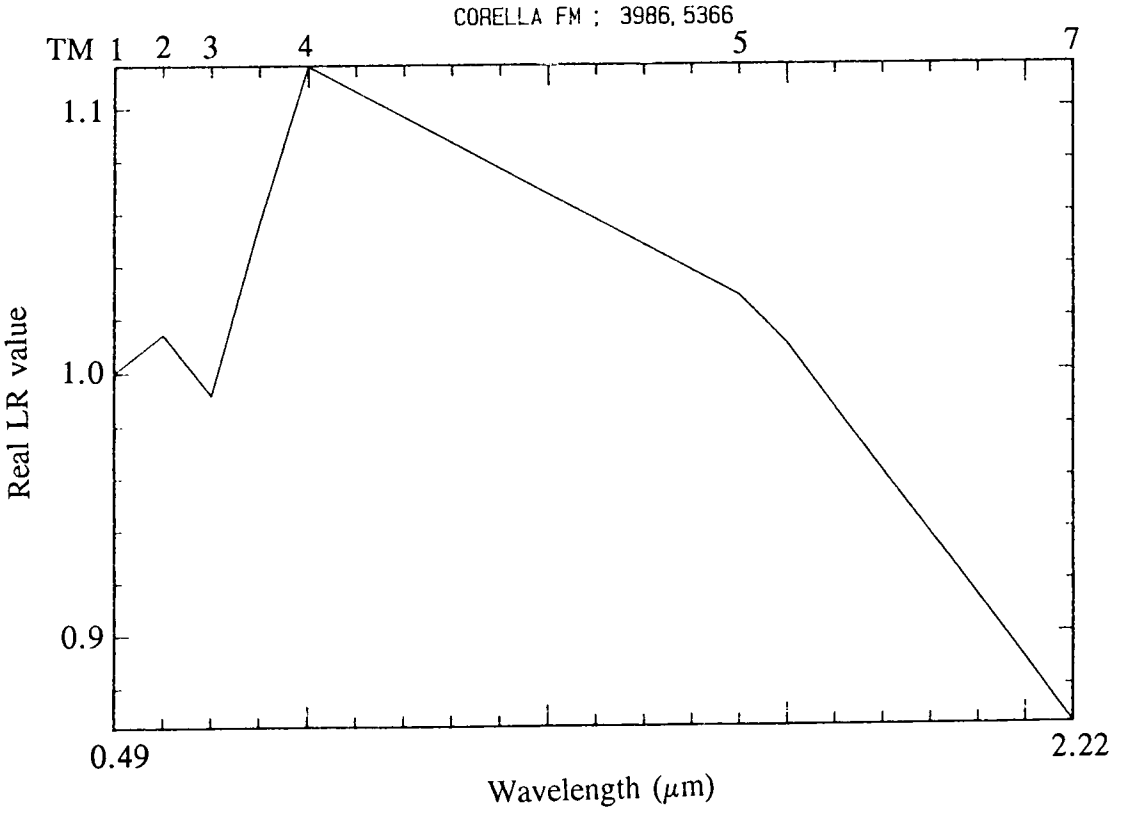

Figure 7.20 TM LR pseudo-spectrum from the Corella Formation in a part of the Mary Kathleen Syncline with increased vegetation density.

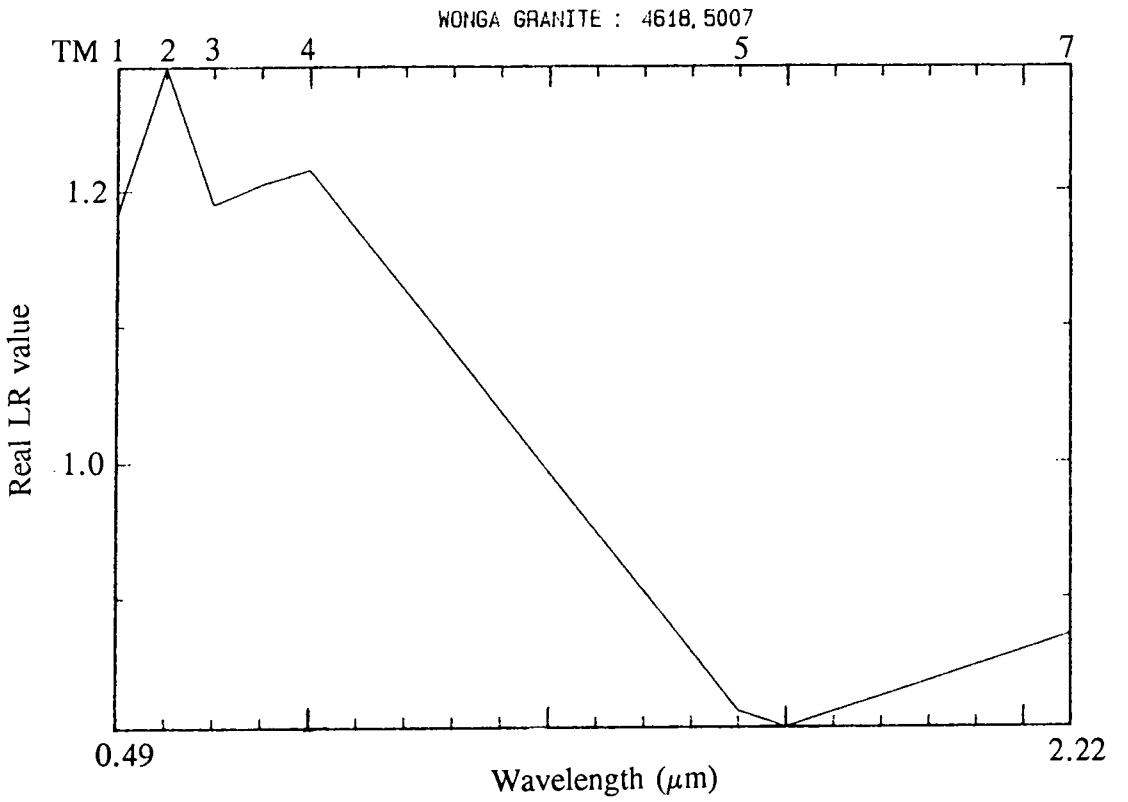

Figure 7.21 TM LR pseudo-spectrum from an area of the Wonga Granite where vegetation appears to modify, rather than obscure, the geological signal.

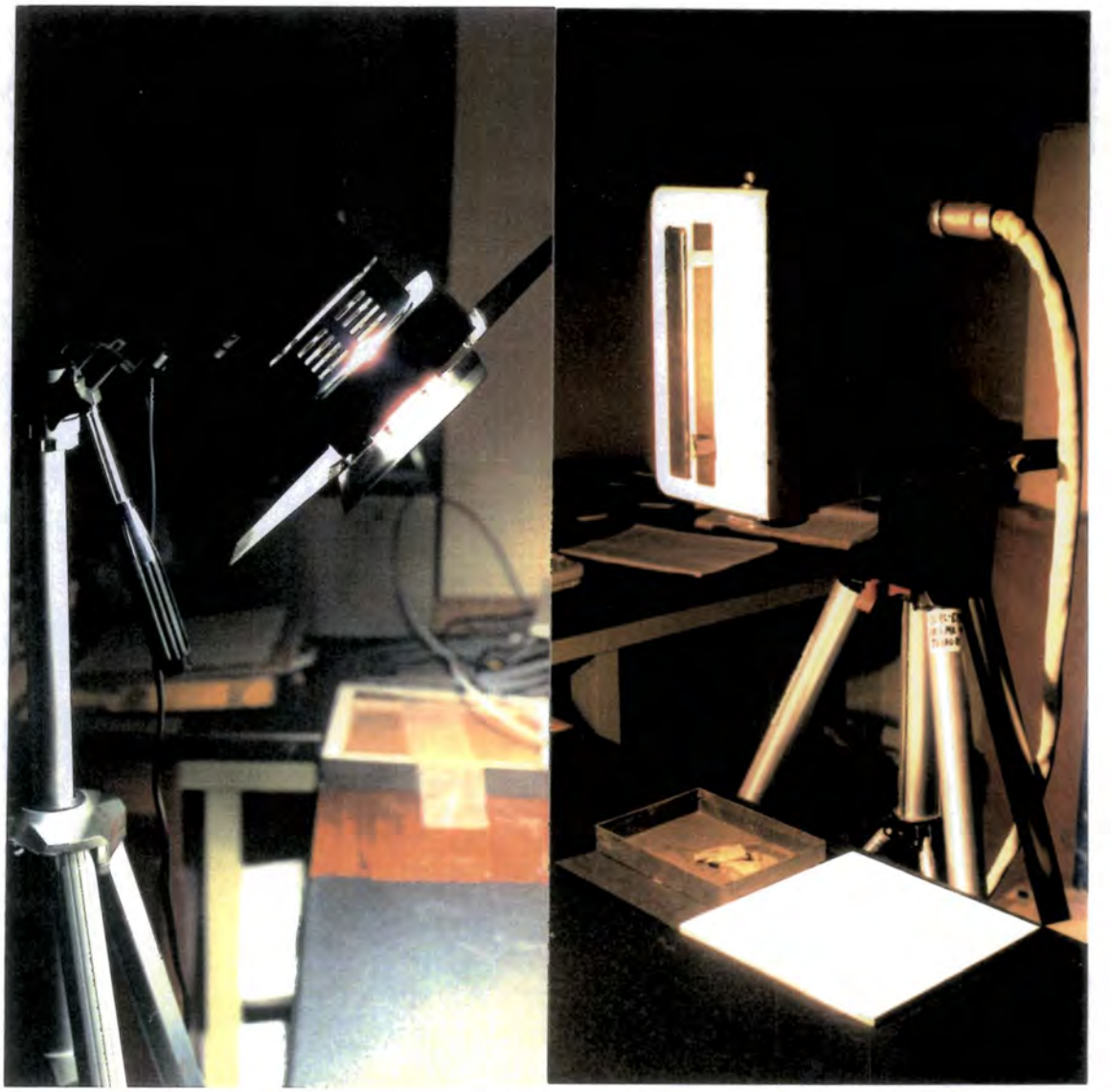

Plate 7.1 The operational configuration of the GER IRIS Mk.IV.

Plate 7.2 The Lime Creek Metabasalt at locality 120.

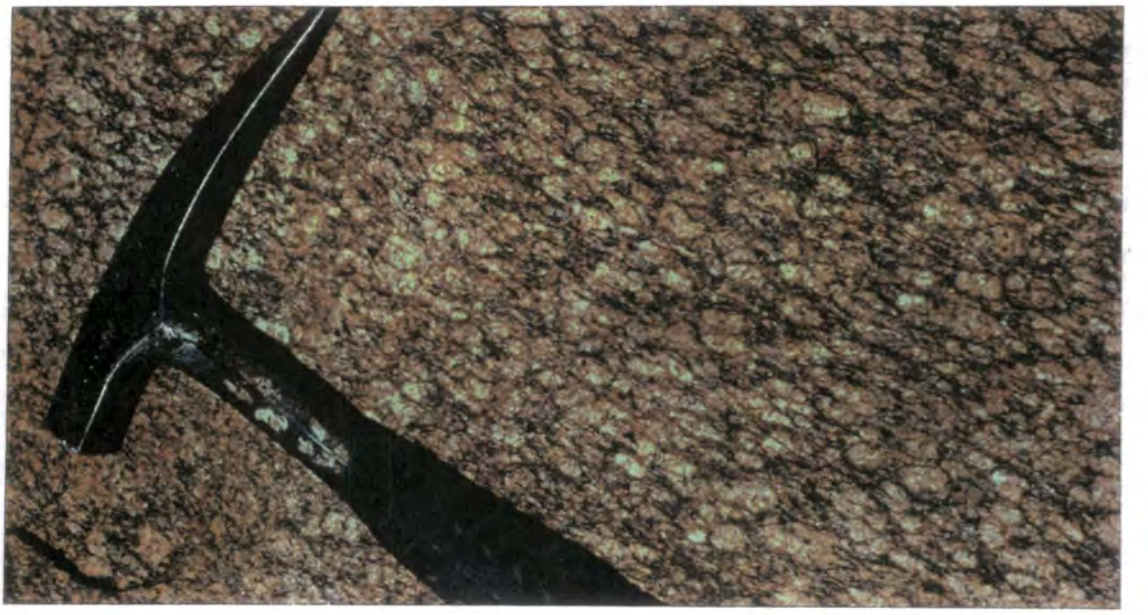

Plate 7.3 Clay minerals developing through weathering of feldspar phenocrysts in the Wonga Granite at locality 106.

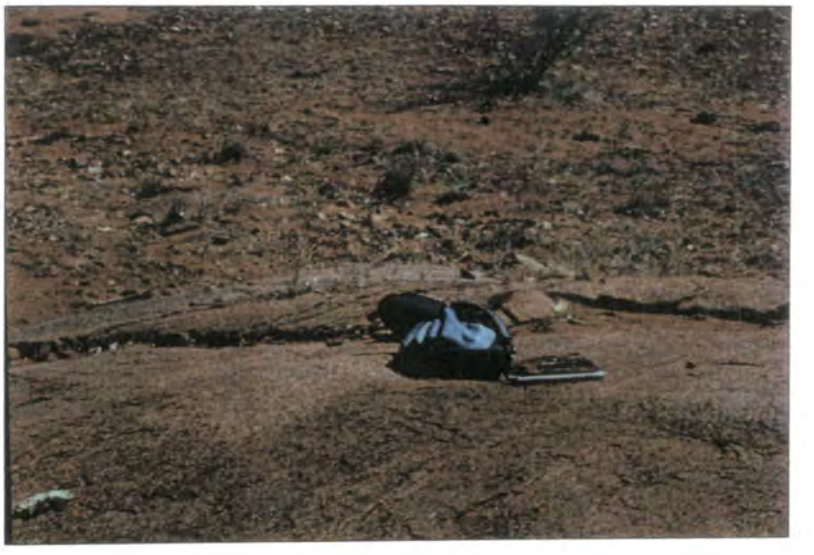

Plate 7.4 Iron-oxide development in the Wonga Granite at locality 106.

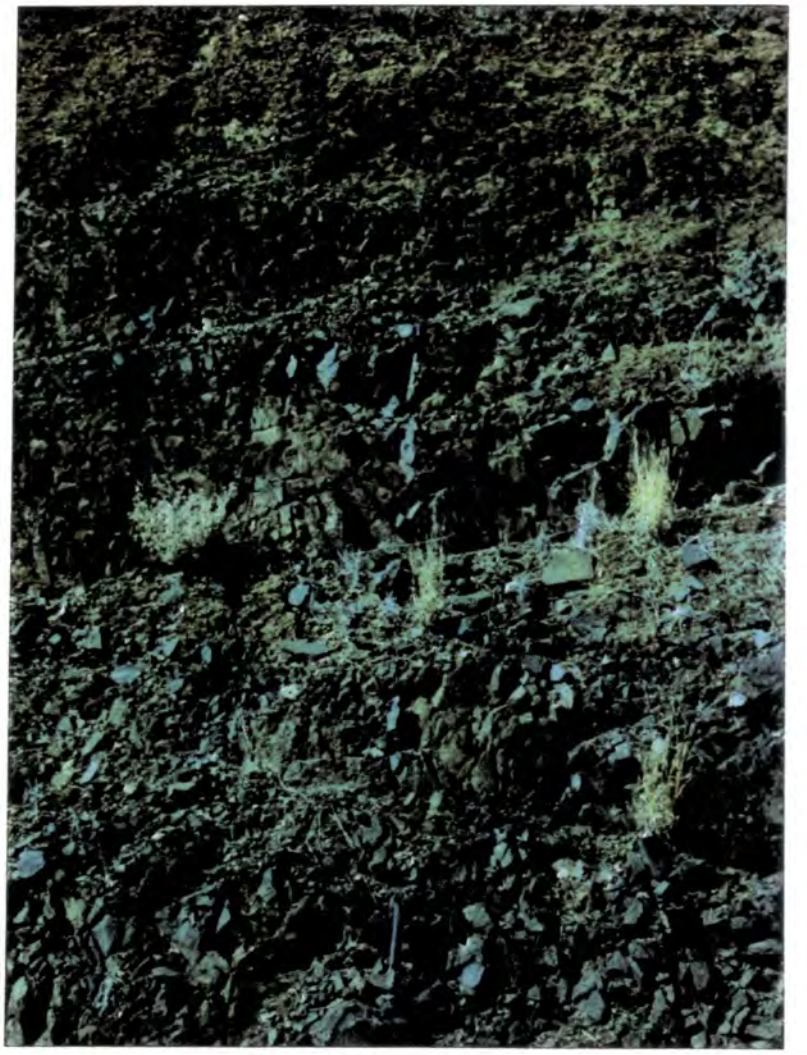

Plate 7.5 Profile through the Dog Bone Dolerite at locality 1 from fresh rock by the hammer to an iron-oxide rich weathering product at the top.

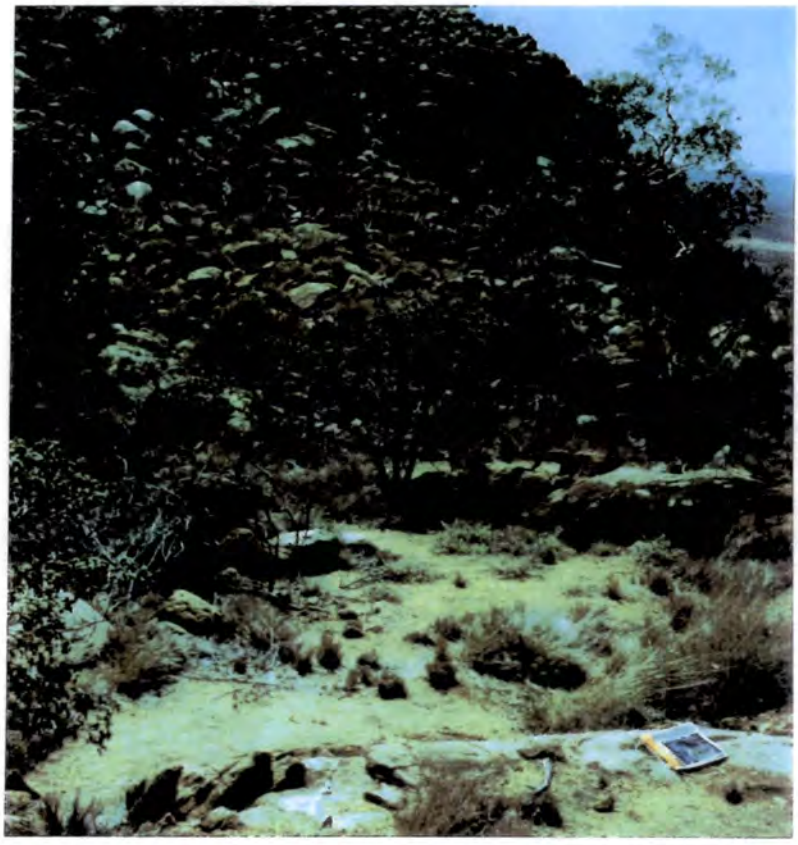

Plate 7.6 Locality 102 of the Burstall Granite, displaying iron-oxide enriched weathered surfaces on outcrops and a clay-rich soil in the hollow.

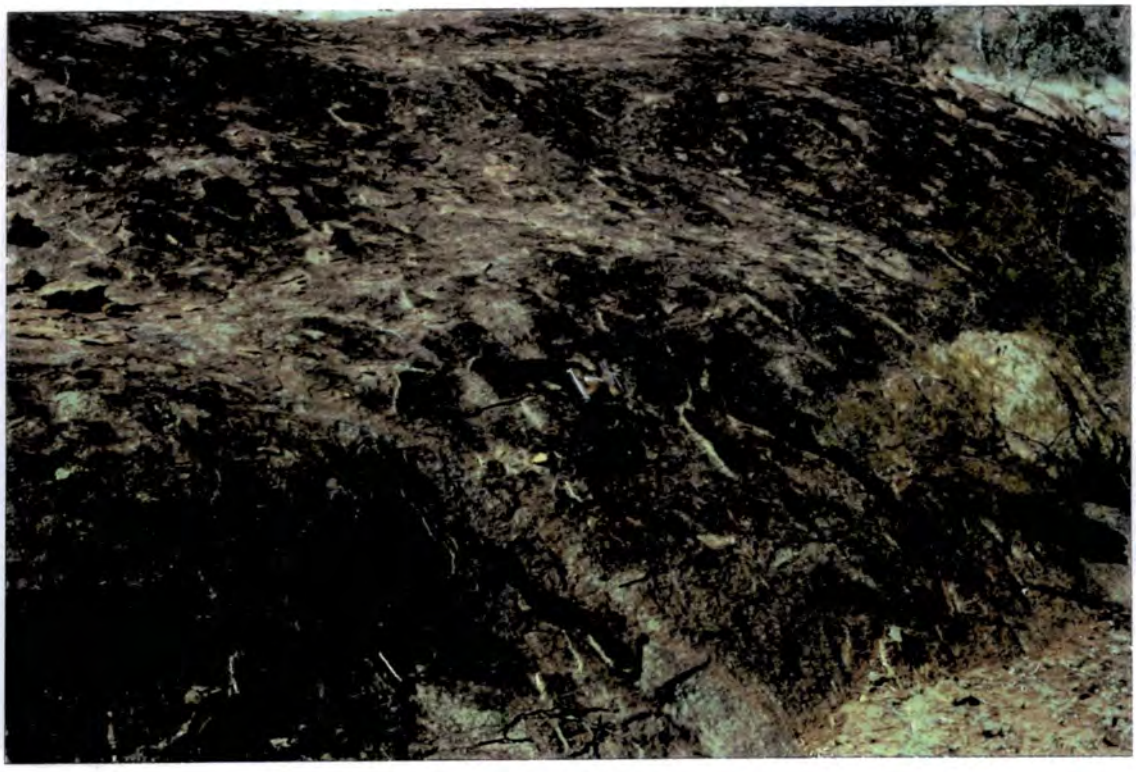

Plate 7.7 Iron-oxide weathered crust on the Wonga Granite at locality 275.

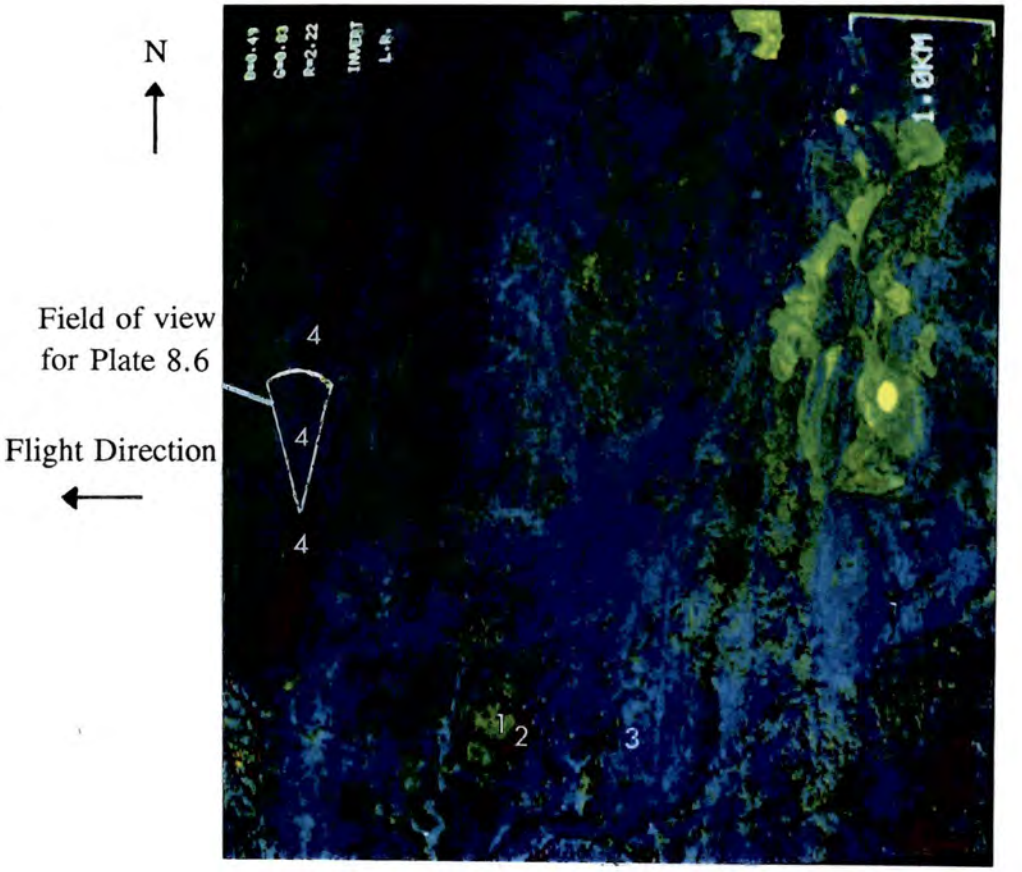

Plate 7.8 NS001 LR data over the Wonga Granite to the west of the open-pit. Red = 2.22 μm absorption, green = 0.83 μm absorption, blue = 0.49 μm absorption. Within Wonga Granite: 1 = weathered surfaces, 2 = clay-soil, 3 = iron-oxide soil. The along-strike discontinuity of the Ballara Quartzite is also labelled (4).

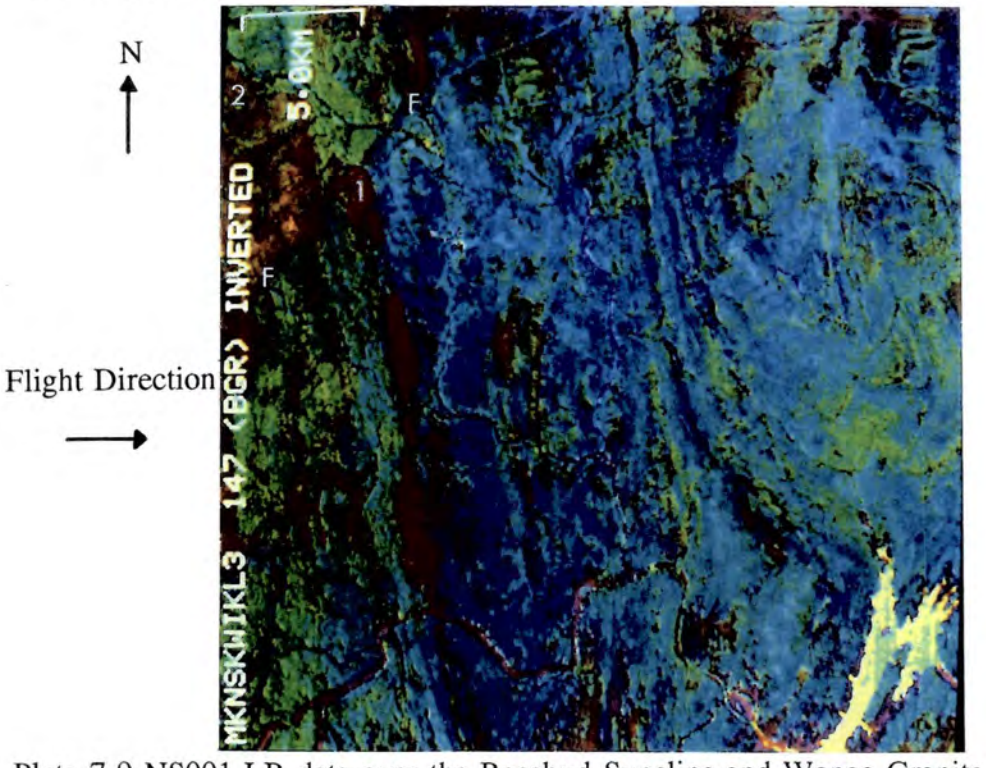

Plate 7.9 NS001 LR data over the Rosebud Syncline and Wonga Granite south of the Cameron Fault. Colours are as Plate 7.8. F = Cameron Fault, 1 = Argylla Formation and Ballara Quartzite in contact, 2 = Argylla Formation.

Plate 7.10 An area of the Corella Formation adjacent to the Dog Bone Dolerite which is seen in the distance as the red soil.

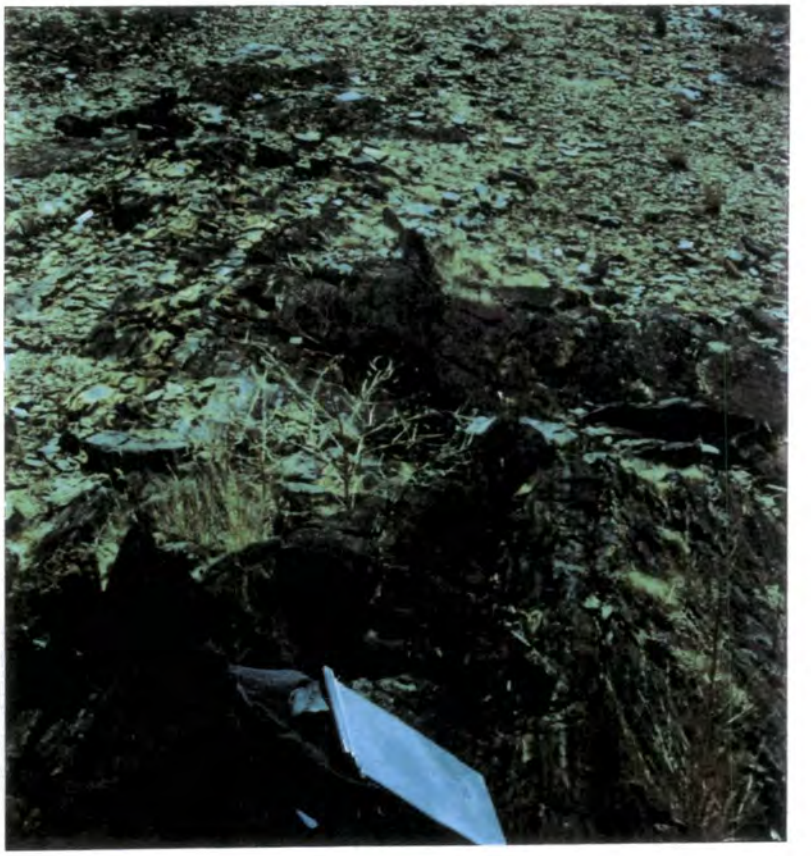

Plate 7.11 At locality 96 of the NE Corella Formation a more basic lithology occurs.

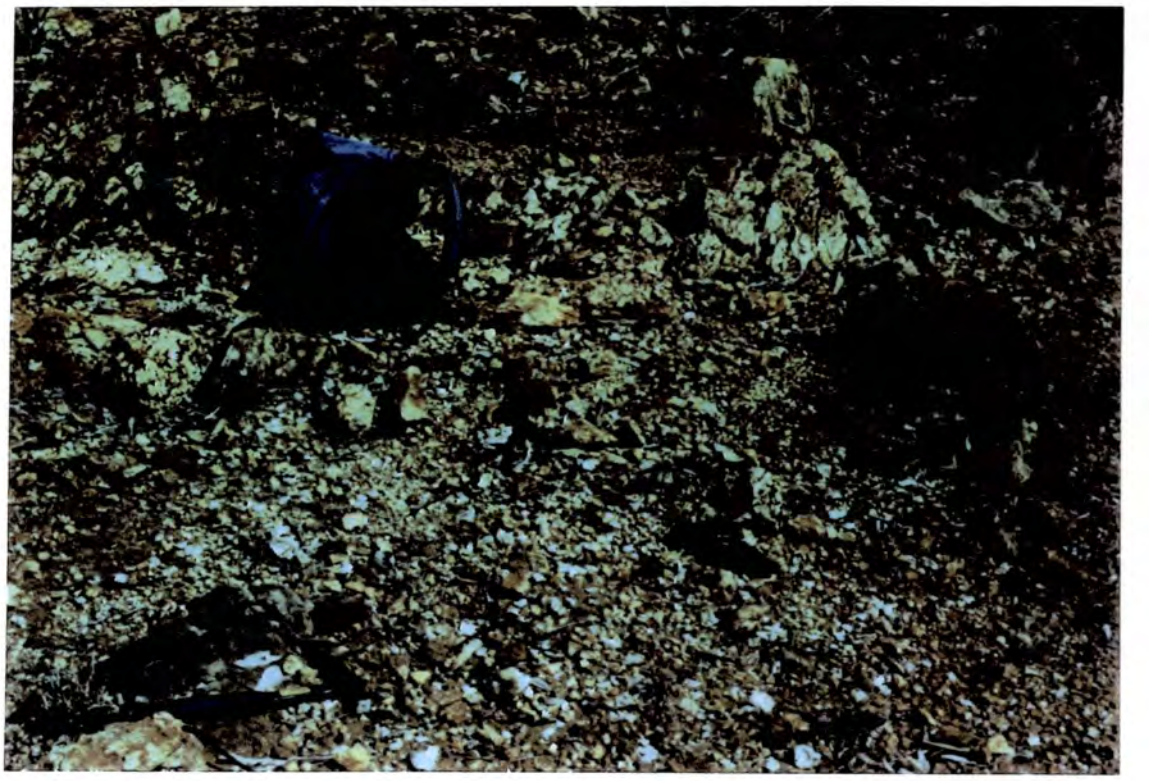

Plate 7.12 A mixed surface with a variety of clast sizes and shade.

Plate 7.13 The mixed sample in the IRIS particle size experiment.

Plate 7.14 View at locality 58 from weathered Corella Formation on the bank into a creek which contains fresh Corella Formation due to erosion during flash flooding.

Plate 7.15 View into gorge in the Cameron River from locality 115. Fresh outcrop is exposed over a wide area in the gorge.

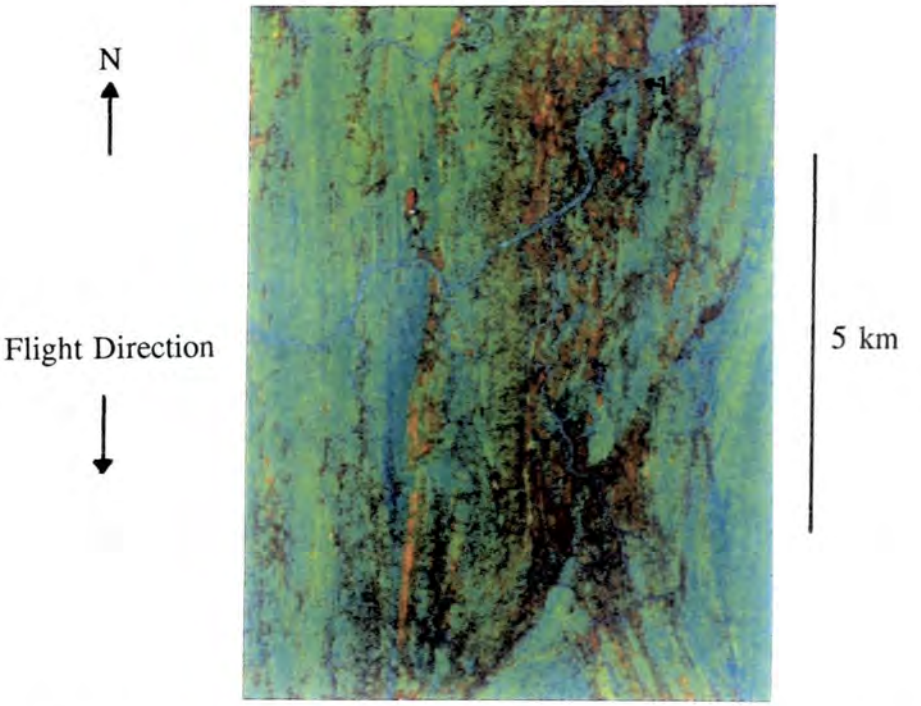

Plate 7.16 GMS LR data over the Cameron River (top right to middle left). Red = 2.352 μm absorption, green = 2.176 μm absorption, blue = 2.044 μm absorption. A unit characterised by 2.352 μm absorption meets the river in the top right of the image (1) and the spectral signature persists for most of the river's width.

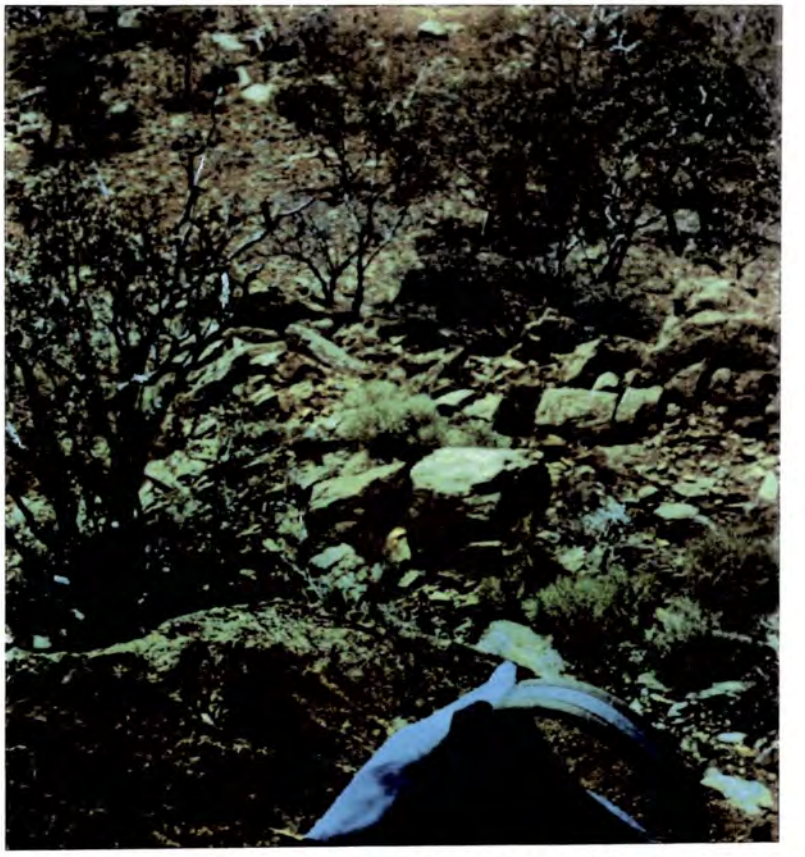

Plate 7.17 Granite debris eroding off the southern mass of the Burstall Granite to cover the adjacent Corella Formation outcrops.

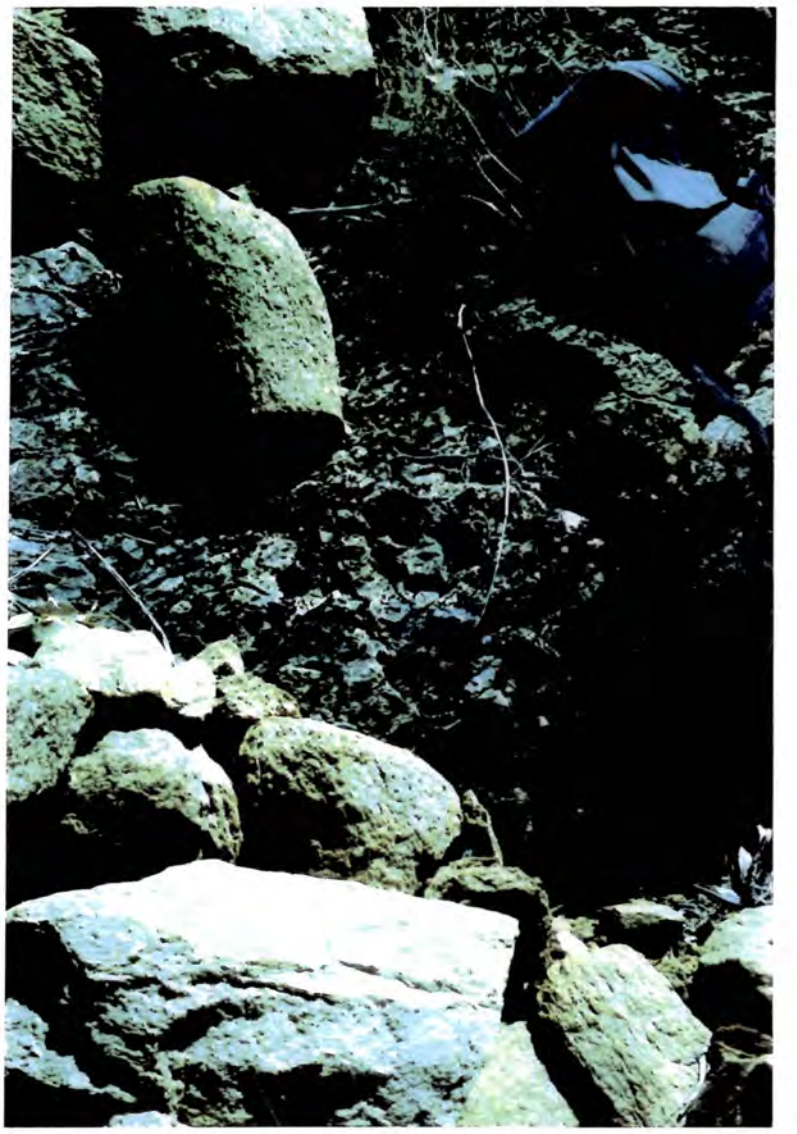

Plate 7.18 Boulders of Burstall Granite overlying the Corella Formation at locality 100.

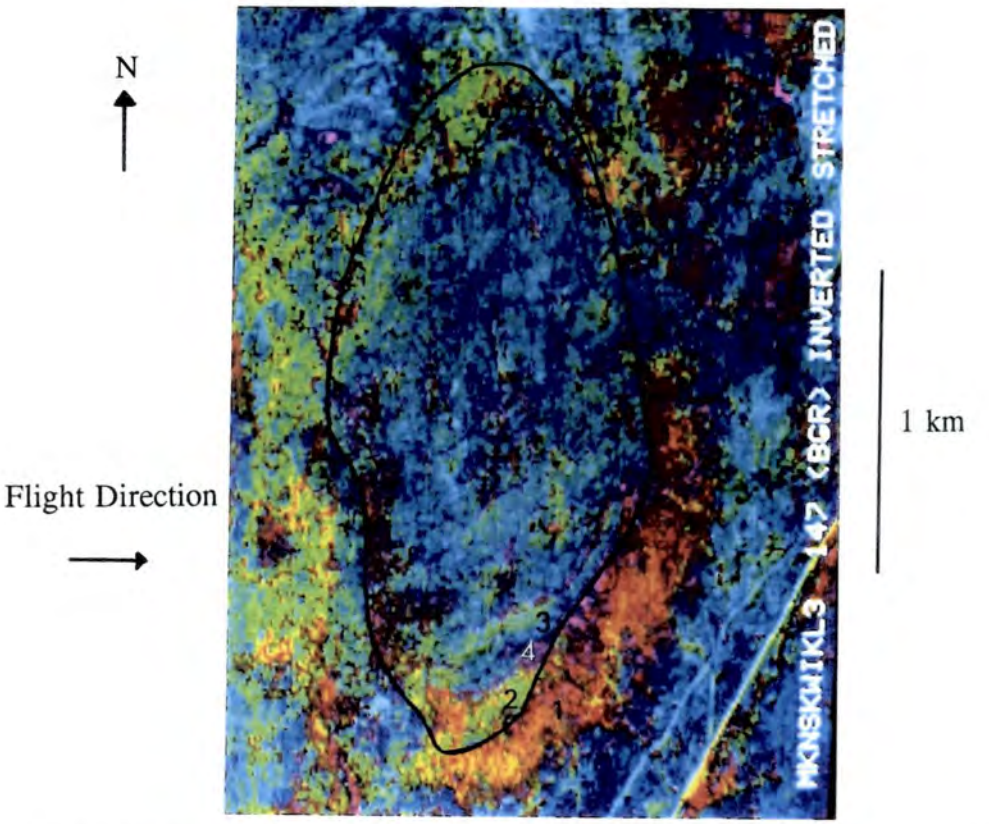

Plate 7.19 NS001 LR data over the southern mass of the Burstall Granite (line). Red = 2.22 μm absorption, green = 0.83 μm absorption, blue = 0.49 μm absorption. 1 = granite debris slope, 2 = weathered surfaces, 3 = shade, 4 = denser vegetation.

Plate 7.20 View southward toward the Ballara Quartzite which forms the prominent ridge near locality 258.

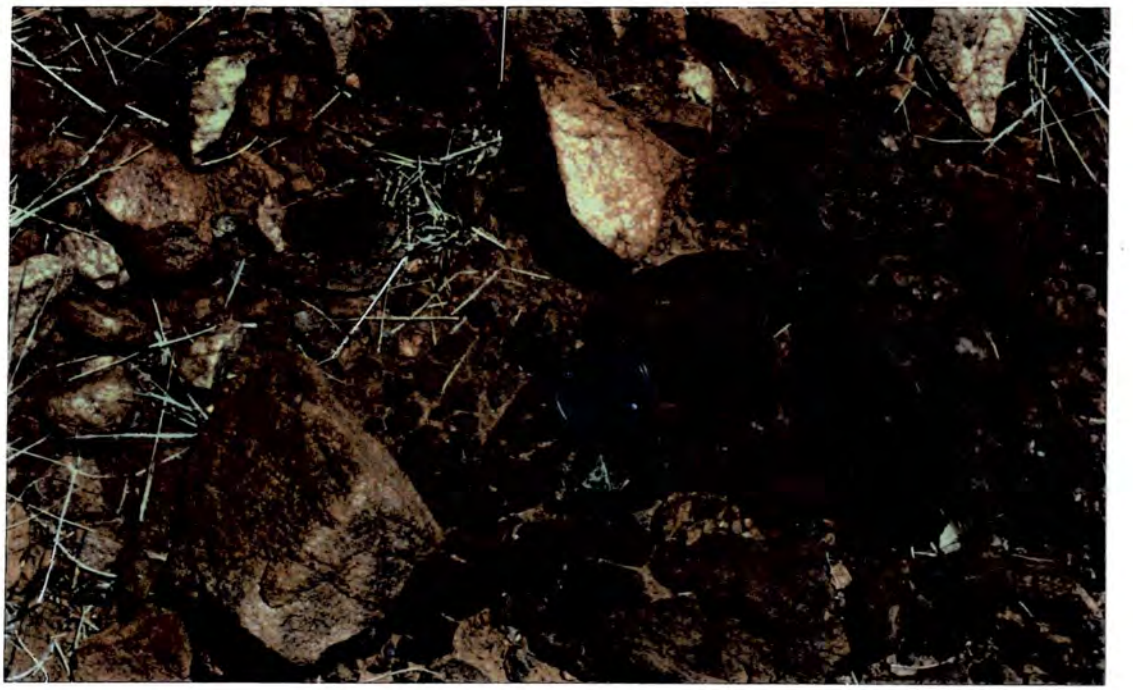

Plate 7.21 Moving north from the ridge the exposed surface is a mix of Corella Formation outcrop (dark grey) and quartzite debris (white, weathering orange).

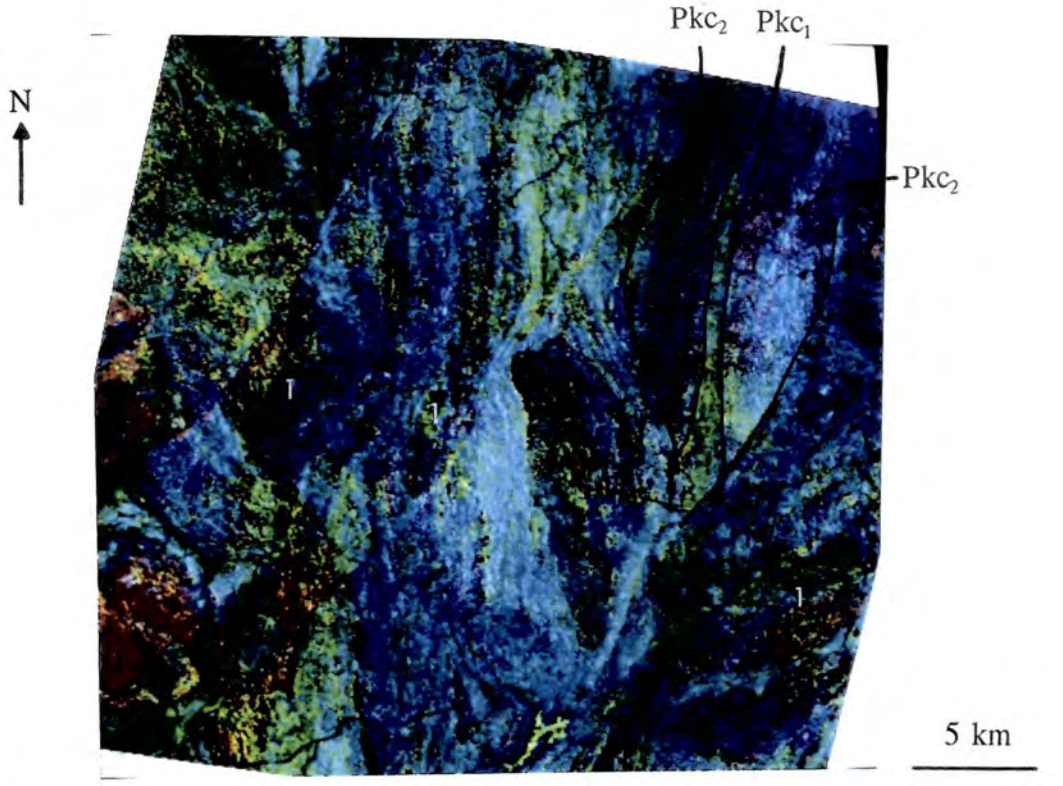

Plate 7.22 Colour composite of the whole field area with the LSFit residual of the TM 2.22 μm data in red, 0.83 μm absorption in green and 0.49 μm absorption in blue. 1 = areas where 2.22 μm absorption was due to vegetation rather than a mineral.

Plate 7.23 View westward across the Wonga plain to the tailing dams at the Mary Kathleen mine, on which a unique pale green vegetation appears to flourish.

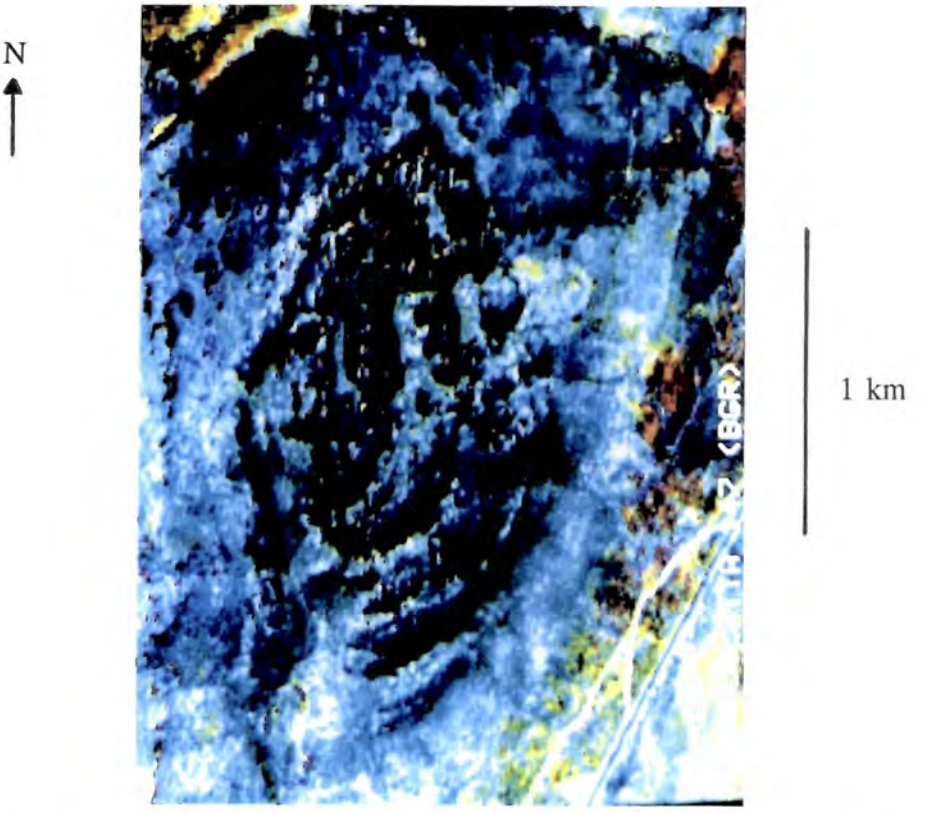

Plate 7.24 NS001 colour composite with atmospherically-corrected radiance data. Red = high radiance at 2.22 μm, green = high radiance at 0.83 μm, blue = high radiance at 0.49 μm. Deep shadow correlates with 0.49 μm absorption in Plate 7.19.

Lithology	Dog Bone Dolerite			Lake View Dolerite	
Sample	1w	1ww	1c	245w	245a
Amphibole	1	1	1	1	2
Feldspar	2	2	1	2	3
Quartz	4	4	?	2	1
Pyroxene			4		
Mica	3		6	3	4
Chlorite		3	3		5
Calcite					6
Hematite			5		
Montmorillonite		?	6		
Fe-oxide ratio	0.33	0.33	0.34	0.58	0.30

Lithology	Lake Corella Dolerite				
Sample	66w	66a	98w	98a	99w
Amphibole	1	1	1	1	1
Feldspar	2	2	2	3	2
Quartz	2	4	2	2	3
Mica			4		4
Chlorite	3	3			
Calcite				4	
Hematite		5			
Fe-oxide ratio	0.30	0.27	0.15	0.19	0.14

Table 7.1 Minerals identified in XRD analyses of the basic rocks, with background to peak ratios to give an indication of amorphous iron-oxide contents.

Lithology	Lime Creek Dolerite						
Sample	115w	116w	117a	118w	118a	125w	125a
Amphibole	3		1	1	1	1	1
Feldspar	1	2	3	2	2	2	2
Quartz	1	1	2		4	2	
Mica	4	3	4	4	5	4	3
Chlorite	4		4	2	3		4
Kaolinite	4						
Calcite		3		5	6		
Goethite			?				
Montmorillonite					6		
Fe-oxide ratio	0.13	0.10	0.15	0.16	0.15	0.15	0.16

Lithology	Lime Creek Metabasalt					
Sample	120w	120a	122w	122a	123w	123a
Amphibole	1	1	1	1	1	1
Feldspar	2	2	3	3	1	2
Quartz		2	2	2	3	3
Mica		5	5	4		5
Chlorite		4		5		
Kaolinite			4		4	4
Calcite				6		
Fe-oxide ratio	0.24	0.21	0.23	0.28	0.20	0.20

Table 7.1 Minerals identified in XRD analyses of the basic rocks, with background to peak ratios to give an indication of amorphous iron-oxide contents.

Lithology	Magna Lynn Metabasalt					
Sample	10w	11w	12w	13a	15w	206a
Amphibole	1	1	2	2	1	1
Feldspar	2	2	1	4	3	2
Quartz	2	3	5	3	2	2
Mica	6	4	2	1	4	3
Chlorite	4	5	4	5	4	4
Kaolinite			6	5		
Calcite			6	5		
Goethite	4			5		
Siderite				?		?
Fe-oxide ratio	0.32	0.23	0.13	0.23	0.27	0.26

Table 7.1 Minerals identified in XRD analyses of the basic rocks, with background to peak ratios to give an indication of amorphous iron-oxide contents.

Lithology	Wonga Granite						
Sample	106w	107a	109w	110w	111w	112	112w
Quartz	1	1	1	1	1	3	1
Feldspar	2	2	3	2	3	1	1
Mica	2	4	1	5	1	1	1
Amphibole	4	3	4	3	4		4
Chlorite				5			
Kaolinite	5		6			4	5
Calcite		4	5	4	5	4	
Fe-oxide ratio	0.15	0.13	0.14	0.15	0.10	0.18	0.20

Table 7.2 Minerals identified in XRD analyses of the granites, with background to peak ratios to give an indication of amorphous iron-oxide contents.

Lithology	Wonga Granite			Wonga debris plain soils			
Sample	113a	210w	214a	107b	108a	114a	215a
Quartz	1	1	1	1	1	1	1
Feldspar	1	3	2	1	2	1	2
Mica	3	1	3	3	3	4	
Amphibole		4		5	4		3
Chlorite						3	4
Kaolinite	4		4		5		
Calcite	5		4			5	5
Lepidocrocite							5
Grossular				4			
Periclase				?			
Gibbsite					?		
Dolomite						4	
Fe-oxide ratio	0.15	0.10	0.09	0.16	0.23	0.17	0.13

Lithology	Burstall Granite				
Sample	101	101w	102w	102a	103w
Quartz	4	2	1	1	2
Feldspar	1	1	2	2	1
Mica	1	3	3	3	
Amphibole	3	3	4	5	
Kaolinite	5	5	4		4
Calcite	5	4	6	4	3
Goethite			7		
Fe-oxide ratio	0.17	0.15	0.30	0.13	0.12

Table 7.2 Minerals identified in XRD analyses of the granites, with background to peak ratios to give an indication of amorphous iron-oxide contents.

Lithology	Burstall Granite			Hardway Granite		
Sample	104w	104a	105w	5a	6w	7a
Quartz	1	1	1	1	1	1
Feldspar	1	2	2	2	1	2
Mica				3	1	3
Amphibole	3			4		
Chlorite	5			5		
Kaolinite			3		4	
Calcite	4	4	4			
Lepidocrocite		3				
Fe-oxide ratio	0.14	0.11	0.15	0.10	0.10	0.07

Table 7.2 Minerals identified in XRD analyses of the granites, with background to peak ratios to give an indication of amorphous iron-oxide contents.

Lithology	Pkc_{2q}		Pkc_2 in west of structure					
Sample	65w	65a	68w	92w	92a	71w	74w	74a
Quartz	1	1	3	1	1	1	1	1
Feldspar	3	2	2	2	3	1	3	3
Mica		3	4	3	1	5	4	1
Amphibole			1					
Chlorite				4		3	1	
Calcite	4			5		4	5	
Dolomite				6				
Magnetite						6		
Goethite	5			6				
Kaolinite	2	4	5		5			3
Pyroxene					4			
Fe-oxide ratio	0.20	0.14	0.24	0.20	0.20	0.27	0.33	0.18

Table 7.3 Minerals identified in XRD analyses of the Corella Formation, with background to peak ratios to give an indication of amorphous iron-oxide contents.

Lithology	Pkc_1 in centre of structure							
Sample	76w	76a	77w	77a	78w	78a	64w	62w
Quartz	2	1	1	1	2	1	1	1
Feldspar	3	2	3	2	1	2	4	3
Mica		3	4	2		3	2	5
Amphibole	1			4	3			
Chlorite	4		2				3	2
Calcite								4
Dolomite		4						
Magnetite		5						
Goethite	4							
Kaolinite				5				
Hematite					4			6
Brucite	4							
Pyroxene			4					
Fe-oxide ratio	0.33	0.20	0.20	0.20	0.23	0.17	0.18	0.20

Table 7.3 Minerals identified in XRD analyses of the Corella Formation, with background to peak ratios to give an indication of amorphous iron-oxide contents.

Lithology	Pkc_1 in centre of structure				
Sample	60w	58	58w	54w	54a
Quartz	1	1	1	1	1
Feldspar	3	2	4	5	2
Mica	2	1	5	2	4
Amphibole				3	
Chlorite	4	4	2	4	4
Calcite		2			3
Dolomite		5	6		6
Kaolinite			3		
Hematite					7
Fe-oxide ratio	0.20	0.18	0.20	0.16	0.18

Lithology	Pkc_2 in east of structure							
Sample	53w	50w	48	48w	48a	46	44w	44a
Quartz	2	1	1	1	1	4	2	1
Feldspar	3	4	2	2	2	1	1	2
Mica	4	1	5	3	3	2	4	3
Amphibole			3				3	
Chlorite	1	1				3	4	
Calcite	6							
Dolomite	5		4					
Kaolinite		5		3	4			4
Siderite								5
Fe-oxide ratio	0.20	0.23	0.16	0.23	0.18	0.22	0.18	0.20

Table 7.3 Minerals identified in XRD analyses of the Corella Formation, with background to peak ratios to give an indication of amorphous iron-oxide contents.

CHAPTER 8. THE APPLICATION OF THE DATA TO GEOLOGICAL MAPPING PROBLEMS

8.1 Introduction

In the previous chapter the relationship between the surface measurements made by the sensors and the solid geology of interest was considered. Once this relationship has been established, the data from all four sensors can be used to address the geological problems of the field area. This chapter documents the application of the data both to the general problems of geological mapping in the area and the more specific areas of controversy highlighted in section 2.8. It is divided into sections on each metamorphic lithology, each intrusive lithology, structure, metamorphism and mineralisation.

Within each section, the sequence followed is based on the stratigraphy as described in chapter 2. Each lithology is addressed with all the available data but the emphasis is placed on those which contribute the most information. This may be because the lithology is not covered by the other sensors, or because the spatial or spectral attributes of one data set make it more suited to the study of a particular problem. Where appropriate the use of integrated data sets is also discussed and laboratory data are used to support the observations made with the remotely sensed data. Consequently, the reader is frequently referred back to previous Plates. Enclosures 2.1, 5.1 and 6.1 will prove useful in relating the imagery to the geology throughout this chapter.

8.2. Tewinga Group

The oldest rocks exposed in the area are the Leichhardt Metamorphics, which are overlain by the Magna Lynn Metabasalt and the Argylla Formation. Specific problems to be addressed in this section are the internal stratigraphy of the Argylla Formation and the discrimination of that formation from the older Leichhardt Metamorphics.

8.2.1. Leichhardt Metamorphics

As seen in Figure 2.3, the metamorphosed rhyolite flows of the Leichhardt Metamorphics outcrop along the western margin of the field area in the north and are covered by the TM and AGR data. These outcrops are difficult to access so the lithology was not visited in the field and is only considered briefly.

The TM LR data covering this lithology are shown in Enclosure 5.1. The Leichhardt Metamorphics are characterised by a mottled green and red tone in the image, due to a mixed pattern of 0.83 μm and 2.22 μm absorption. This pattern is similar to that described in chapter 7 over the outcrop tors of other felsic lithologies such as the Wonga Granite and the younger rhyolites of the Argylla Formation. It is thus likely that the areas of 0.83 μm absorption correlate with iron oxide rich weathered surfaces. The areas of 2.22 μm absorption may be related to the primary mineralogy, being due to mica, or the weathering product, being due to clay minerals produced from the breakdown of feldspar phenocrysts. Indeed, Derrick et al (1977) describe abundant potassium feldspar phenocrysts in this lithology. Accordingly, the AGR data records a moderate radiometric response dominated by potassium and thorium, rather than uranium (Enclosure 6.1).

The 1:100 000 map (Enclosure 2.1) records undivided Leichhardt Metamorphics, Pel, and a dacitic unit occurring toward the top of the formation immediately below the Magna Lynn Metabasalt, Pel_d. As both are metamorphosed, the dacite is difficult to differentiate from the rhyolite in the field and the majority of its boundaries with the rhyolites are mapped as uncertain. The differentiation of this lithology into rhyolite and dacite units would improve the mapping and stratigraphy in the area. The transition from rhyolite to dacite is marked by an increase in feldspathic components relative to quartz (Best, 1982). This increase in feldspar should be reflected in the AGR data by an increase in potassium. The study of weathering in chapter 7 showed that quartz-rich rocks commonly have iron oxide enriched weathered surfaces while feldspar weathers to clay minerals. The TM data should also therefore record the change to dacite as an increase in 2.22 μm, and decrease in 0.83 μm, absorption.

Looking again at the TM data in Enclosure 5.1, it is clear that in the north of the lithology 2.22 μm absorption dominates, whilst 0.83 μm absorption increases to the south. That part of the signal due to the Al-OH component is thus more common in the north. Study of the ratio-normalised AGR data (Plate 6.11) reveals that the potassium count also increases northward. This northward increase in the potassium and clay mineral signal corresponds to the mapped dacite occurrences, but also shows that the extent of the dacite is greater than indicated on the 1:100 000 map. The TM and AGR data pick up the mineralogical change to increased feldspar wherever it occurs, not only where it is detectable during fieldwork. There is a second area of probable dacite indicated by the TM data immediately northwest of the Wonga Fault which is mapped as undifferentiated Leichhardt Metamorphics. This area displays increased 2.22 μm absorption and is stratigraphically below another occurrence of the Magna Lynn Metabasalt. In the absence of field checking, however, the extrapolation of the stratigraphy to this part of the sequence must remain speculative. Figure 8.1 shows the wider area over which study of the TM and AGR data indicates dacite occurs.

8.2.2 Magna Lynn Metabasalt

This black, fine-grained, foliated and crystalline lithology outcrops above, and thus northeast of, the Leichhardt Metamorphics in the west of the field area. Plate 8.1 shows the red-brown soil produced when the lithology weathers. XRD analyses have been performed on samples 10w, 11w, 12w, 13a, 15w and 206a and are summarised in Table 7.1. They consistently indicate that the primary mineralogy is amphibole/feldspar/mica/quartz/chlorite. Weathering leads to iron oxide, usually goethite and/or siderite, as well as small amounts of clay minerals and calcite. The iron oxide content of the lithology is moderate to high as shown in Table 7.1 and appears to increase throughout weathering. Exposed surfaces can be expected to have an iron oxide response in the TM and NS001 data which, along with the AGR data, cover this lithology. The exposure of the Magna Lynn Metabasalt in the northwest of the field area is covered by the TM data in Enclosure 5.1, where the lithology is characterised by 0.83 μm and 0.49 μm absorption. A TM LR pseudo-spectrum typical of this basalt is shown in Figure 8.2 and displays this absorption plus one at 0.65 μm both of which are probably related to crystal field effects in iron oxide.

Amphibole, mica and goethite are commonly identified in IRIS spectra as well as quartz, clay minerals, calcite and epidote. This is in general agreement with the XRD analyses. Figure 8.3 shows the IRIS spectra for the fresh and weathered surface at locality 15 and the soil at locality 13. The fresh surface is spectrally flat and of low reflectance, a characteristic feature of basic rocks (Figure 7.3). Small absorptions at 2.32 μm and 2.39 μm are attributed to amphibole. The weathered surface develops better defined absorptions at 0.47 μm and 0.92 μm which are more typical of goethitic iron oxide. Amphibole features are still present but poorly defined, as are small Al-OH related absorptions around 2.2 μm, attributed to mica, chlorite or a clay mineral. The soil spectrum displays similar features but is darker and like most soils has a moderate water band at 1.91 μm. The absorptions seen in the TM data around 0.65 μm and 0.83 μm are therefore explained by the goethite developed during weathering.

The NS001 data in Plate 6.2 cover the southern outcrops of this lithology near the Hardway Granite. In spectral terms these data are similar to the TM data, though 0.49 μm absorption is more common. The increased spatial resolution of the NS001 data set has led to the discovery of faults unseen in the TM data and not appearing on the 1:100 000 map which better explain the basalt's relations with the Argylla Formation. These are discussed in section 8.8.

The AGR data over the Magna Lynn Metabasalt (Enclosure 6.1) show that it has a low radiometric count for all three elements. This is typical of basic rocks and consequently radiometric data usually reveal little information over these lithologies. The ratio normalised AGR data in Plate 6.11 reveal that the low count over the Magna Lynn Metabasalt and many other basic lithologies is dominated by uranium. There are two possible explanations for this, one geological and the other noise-related. As radiometric concentrations decrease from "hot" rocks to "cold" rocks, the uranium count typically decreases at about half the rate of the thorium and potassium count (B. Dickson, personal communication). Thus "cold" rocks such as basalt may have a uranium dominated response. Alternatively, the general low count could lead to the response being dominated by any remaining atmospheric radon signal, which only affects the uranium channel. As the noise has been treated, the geological explanation is perhaps the more likely.

All workers agree on the stratigraphic position of the Magna Lynn Metabasalt, which the data confirm as being unconformable on the Leichhardt Metamorphics. The lithology cannot be further divided. It will be considered further when the status of some of the dolerites in the area is reviewed in section 8.7.4.

8.2.3 Argylla Formation

The acidic metavolcanics of the Argylla Formation are exposed to the northeast of the Magna Lynn Metabasalt and flanking the Wonga Granite over much of the western half of the field area. They also outcrop in the southeast corner in the core of an anticlinal structure. They are covered by the TM, NS001 and AGR data sets. In addition to rhyolite, lithologies seen in the field include garnet-mica schist, foliated mica schist, pelites, glassy quartz-rich crystalline metamorphics and quartzites. Their acidic composition leads to a pale colour (Plate 8.2) and weathering leads to an orange soil.

All exposures sampled are in the western half of the field area, where the Argylla Formation is mapped as undifferentiated Pea rhyolite with some quartzite beds. The variety of lithologies which are represented lead to a varied spectral response, so that the TM data shown in Plate 8.3 again have a mottled look, with mixed 0.83 μm and 2.22 μm absorption. In places, such as flanking the Little Beauty and Rosebud synclines, 2.22 μm absorption dominates (Plates 8.3 and 7.9). Figure 8.4 shows the IRIS spectra for the fresh and weathered surface at locality 8, where the lithology is mica schist and the radiance data are dominated by 2.22 μm absorption. The main features of both spectra are absorption at 0.44 μm, 0.68 μm (weathered surface) and 0.90 μm, which deepen as goethitic iron oxide develops during weathering, and sharp absorptions at 1.42 μm and 2.20 μm particularly in the fresh surface, which are typical of muscovite (Figure 3.6). Small absorptions at 2.36 μm and 2.45 μm also relate to muscovite. The absorption at 1.92 μm is attributed to montmorillonite (Figure 7.4), a clay mineral associated with acidic tuffs. In this case the goethite features lead to 0.83 μm absorption in TM, while the 2.22 μm absorption in TM is due to muscovite in the primary mineralogy. For other samples the 2.22 μm absorption is due instead to kaolin, developed from feldspar phenocrysts such as those shown in Plate 8.4. The

weathering sequence, described for this lithology in section 7.3, explains the TM response. The gamma radiometric count is moderate.

One of the problems to be addressed in this area is that of establishing the correct stratigraphy for this formation. Within undifferentiated Pea in the west of the field area, variation has been noted between areas where 2.22 μm absorption dominates and areas of mixed 0.83 μm and 2.22 μm absorption. This suggests that a division of the formation in the west may be possible. In the southeast of the field area, the Argylla Formation is subdivided on the 1:100 000 map (Enclosure 2.1). The divisions from oldest to youngest are: Pea (mainly rhyolite), Pea_2 (a feldspathic quartzite), Pea_3 (a dacitic unit), and Pea_5 (another feldspathic quartzite). The TM and AGR data have been investigated to determine whether these divisions can be seen in the data. If they are, it may be possible to apply them to the western exposures, where variation has already been detected.

Enclosures 5.1 and 6.1 cover the southeast of the field area. The feldspathic quartzites and the dacitic unit are characterised by 2.22 μm absorption. In contrast, mixed 0.83 and 2.22 μm absorption is seen over the undifferentiated rhyolite. Thus, using the TM data a two-fold division can again be established. Unfortunately, both dacites and quartzites have a dominant 2.22 μm absorption. Further differences are required to separate them, and these are seen in the AGR data (Enclosure 6.1). The feldspathic quartzites are characterised by low radiometric counts for all three elements, a response typical of quartzite. The dacite, however, has a higher radiometric count dominated by potassium as was the case with the dacite unit in the Leichhardt Metamorphics. Thus by using both data sets a threefold division can be made:

Pea:	mixed 0.83 μm and 2.22 μm absorption, moderate count
Pea_2 and Pea_5 :	2.22 μm absorption, low count
Pea_3:	2.22 μm absorption, higher count.

These divisions may be responsible for the variation noted in the west (Figure 8.5). Exposures southeast of the Wonga Fault have moderate radiometric counts but can be split into a unit with mixed 0.83 μm/2.22 μm absorption correctly mapped as Pea and

a unit dominated by 2.22 μm absorption. This latter unit thus has the character of a dacite and may be equivalent to Pea_3. At the top of the sequence, on the flanks of the Rosebud Syncline, the NS001 data in particular are dominated by 2.22 μm absorption, as seen on the east of the syncline in the Plate 8.5. A low radiometric count is found dominated by potassium. These beds are described in the field as quartzite, difficult to distinguish from the overlying Ballara Quartzite. Given their spectral and radiometric character and their stratigraphic position, they are likely to be feldspathic quartzite, probably equivalent to Pea_5.

In the Little Beauty Syncline in the northwest of the field area, Argylla Formation occurs between Magna Lynn Metabasalt and Ballara Quartzite in the west limb of the fold. The whole of the exposed Argylla Formation, mapped as Pea, is dominated by 2.22 μm absorption. Study of the AGR data shows that this exposure also has a high radiometric count dominated by potassium. An apparently full sequence of the Argylla Formation bounded below by the Magna Lynn Metabasalt and above by the Ballara Quartzite thus shows the typical features of the dacitic unit, Pea_3, and none of the others are represented. This demonstrates the difficulty of generally applying an established stratigraphy to this formation. The Little Beauty area was not visited in the field and so these observations cannot be confirmed. It is clear, however, that the rocks mapped as Pea in this area are different to those by the Wonga Fault to the south, also mapped as Pea. It is possible to subdivide the Argylla Formation in the west, allowing the problems highlighted in chapter 2 to be partly addressed. Further fieldwork utilising the remotely sensed data would allow them to be solved more satisfactorily.

8.2.4 Summary

The major divisions of the Tewinga Group into an acidic lower formation, a basic middle formation and an acidic upper formation are clearly seen in all data sets studied. The Leichhardt Metamorphics are rhyolitic at their base and dacitic towards the top. This is seen in the data due to a raised potassium count, reflecting an increase in potassium feldspar, and more consistent 2.22 μm absorption because of the increased clay from weathering feldspar. The Magna Lynn Metabasalt is characterised by 0.83 μm absorption due to iron oxide, probably goethite, developing from amphibole

and other mafic minerals. Above this the rhyolites of the lower Argylla Formation pass upwards into more feldspathic units of either quartzite or dacite, but this sequence cannot be established for all exposures. In places rhyolitic Argylla Formation lies on the Magna Lynn Basalt, while elsewhere feldspathic dacites are directly above the basalt. By using a combination of TM and AGR data the divisions of Pea on the eastern MARABBA 1:100 000 sheet can be recognised and tentatively extended to areas of undivided Pea in the eastern MARY KATHLEEN sheet.

Study of Enclosure 6.1 shows that the Leichhardt Metamorphics can be discriminated from the similar Argylla Formation due to their having a stronger potassium signal. The numerous similarities between the two rhyolitic sequences are clear, however, and it remains difficult to confidently separate them. The problems of the internal stratigraphy of the Argylla Formation described in chapter 2 have been partly addressed with the TM and AGR data, but it has not been possible to solve them to satisfaction. This is due to the great similarity of the rocks rather than a failing of the data; the formation is as variable as the mapping suggests. The relationship of the Argylla Formation with the Ballara Quartzite will be discussed after the Ballara Quartzite has been described in section 8.4.1.

8.3 Malbon Group

In the southeast of the area the Cone Creek metabasalt outcrops above the Argylla Formation, and is overlain by the Mitakoodi Quartzite which contains the Wakeful Metabasalt (Enclosure 2.1). This basalt-quartzite-basalt-quartzite sequence is covered by the TM and AGR data.

In the TM data the spectral signatures are typical of such rocks (Enclosure 5.1). Figure 8.6 shows a TM LR pseudo-spectrum for the Cone Creek Metabasalt, with absorptions in the visible and near infrared typical of a weathered basic rock. The smaller outcrop of the Wakeful Metabasalt is difficult to see in the TM data, but can be discriminated when the data are analysed on-screen and is of similar spectral character. Figure 8.7 shows the TM LR pseudo-spectrum for the Mitakoodi Quartzite, which displays absorption at 0.83 μm and 2.22 μm, a common quartzite signature. In the AGR data

(Enclosure 6.1) the metabasalts have low counts for all three elements. The quartzites have moderately low counts dominated by potassium in the same way as other quartzites described previously.

The two data sets can be used to reproduce the divisions of the three units seen on the 1:100 000 map, but no further detail can be added in this case. Derrick et al (1977) postulated that the Mitakoodi Quartzite may be the eastern equivalent of the Ballara Quartzite in the west. The two quartzites occur at the same point in the stratigraphy and have the same spectral and radiometric character. The latter is however true of other quartzites in the area. The data allow the discrimination of a particular lithology, rather than a particular stratigraphic unit in this case.

8.4 Mary Kathleen Group

The oldest lithology in this group is the Ballara Quartzite. The relationship of this lithology to the underlying Argylla Formation is a matter of dispute (section 2.8.1) and will be discussed in this section. Above this the bulk of the group is made up of the Corella Formation, which includes the Overhang Jaspilite and the Lime Creek Metabasalt. There has been much debate about the Corella Formation's stratigraphy (section 2.8.2) and these problems are the focus of this section.

8.4.1 Ballara Quartzite

The Ballara Quartzite occurs in the west of the field area, thinning eastward (Enclosure 2.1). Where sampled, it consists of quartzite, usually fine grained or medium grained, crystalline and weathering orange, as seen in Plate 8.6, at locality 223 on the east side of the Rosebud Syncline. The Ballara Quartzite has been studied using the TM, NS001 and AGR data.

In the TM data and NS001 data the lithology is uniformly characterised by 2.22 μm absorption. Plate 8.3 shows the TM LR data over the massive, rugged exposures of quartzite in the southwest of the field area. Plate 8.5 shows the thinner quartzite exposures which form the limbs of the Rosebud Syncline as seen in the NS001 LR data.

A TM LR pseudo-spectrum for the quartzite is shown in Figure 8.8 and is dominated by 2.22 μm absorption. Derrick et al (1977) described clay minerals in the quartzite and IRIS spectra confirm their presence. Figure 8.9 shows the IRIS spectra for the weathered surface and soil of the Ballara Quartzite at localities 220, 223 and 231 on the east limb of the Rosebud Syncline. All six spectra display 2.2 μm absorption and some have the characteristic 2.17 μm absorption doublet of kaolin. The deep asymmetric water band at 1.9 μm and fall in reflectance towards 2.5 μm are characteristic of quartz (Figure 7.8). Iron oxide related features are strongest in the weathered surface, rather than the soil, as is typical of quartz rich lithologies.

In the AGR data (Enclosure 6.1) the quartzite has very low radiometric counts for all three elements. The whole count normalisation technique suggests that, like basic rocks, the quartzite's low count is dominated by uranium and the same explanations apply. A quartzite containing feldspar would be expected to have a radiometric response dominated by potassium so that in this case the clay minerals do not seem to be weathering products but are probably sedimentary in origin.

In the southwest, analysis of the data confirms the mapped boundaries. More problems exist in the thinner exposures east of the Rosebud Syncline, where boundaries with the Argylla Formation are marked as uncertain on the 1:100 000 map and problems have been reported by numerous previous workers (section 2.8). It is clear in the TM data and NS001 data that two problems exist in these exposures. The first is that the Argylla Formation and Ballara Quartzite are similar compositionally and therefore spectrally. The second is that moving north along-strike, the strong 2.22 μm absorption is discontinuous (Plate 7.8). The photograph in Plate 8.6 was taken from the first major area of the 2.22 μm absorption north of the Cameron Fault looking northwards across an area of weak absorption towards a second area of absorption further north. The area of no 2.22 μm absorption coincides with an area of reduced outcrop, subdued topography and increased soil. The point where the 2.22 μm absorption strengthens again is marked by outcrop increasing when the high ridge recommences, top left in the photograph. The spectral response between the two prominent ridges is more typical of iron oxide. Thus, along-strike facies variation and the spectral similarity of the two lithologies make the boundary difficult to map in the images, as it is in the field.

It is possible to separate the Argylla Formation from the Ballara Quartzite using the AGR data, because the former has a higher radiometric response dominated by potassium where it is adjacent to the Ballara Quartzite. This is shown very clearly in the integrated data set shown in Plate 6.12. In this image, the Argylla Formation in the west limb of the Little Beauty Syncline is yellow, due to its having both a 2.22 μm absorption (red) and a moderately high potassium count (green). The Ballara Quartzite only has the 2.22 μm absorption and is therefore red in this image. The same discrimination is possible in the integrated data shown in Plate 6.13 and can be extended to the Rosebud Syncline, though with less certainty. The division is apparent in the Rosebud Syncline south of the Cameron Fault, but becomes more difficult to see to the north as the fold closes. The thick limb of 2.22 μm absorption covering both lithologies in the LR colour composites can be split into two thinner units in the integrated data due to the differing potassium content of the two lithologies.

The discovery of this distinction led to a re-examination of the TM data. Whilst the lithologies cannot be separated by their 2.22 μm absorption, there are subtle differences at other bands. These are visually picked out by the ratio image shown in Plate 8.7. The Argylla Formation and the Ballara Quartzite both have moderately high 4/5 (blue) and 5/7 (red) ratios, leading to their being displayed in magenta tones in this image. The Argylla Formation, however, is more blue, suggesting 4/5 is higher for this lithology, whilst the Ballara Quartzite is redder, showing 5/7 is higher for this lithology. This suggests there is an increase in vegetation on the Argylla Formation, a possibility noted in chapter 7 after analysis of the LSFit data shown in Plate 7.22.

The analysis of the integrated data sets has made possible the discrimination of two lithologies which are difficult to distinguish in the field. Controversy remains over the nature of their boundary. If the Ballara Quartzite is derived from the Argylla Formation, erosion of the latter and hence a time gap is required and the contact is an unconformity. It could be suggested that the radiometric difference between the two and the predominance of clay in the quartzite compared to mica in the Argylla Formation may preclude the derivation of one from the other. Alternatively the sedimentary clay minerals in the Ballara Quartzite may be derived from weathering of the feldspars in the dacitic parts of the Argylla Formation. The difference in potassium content gives

strength to the former suggestion. Outcrop patterns around the fold structures do not suggest an unconformity as the two lithologies have the same strike at their boundary. On balance the data support the view that the contact is conformable, but a more detailed study than is possible with remotely sensed data would be necessary to prove this.

8.4.2 Corella Formation

In the west of the field area the Corella Formation outcrops in the southwest corner, in the Rosebud Syncline and in the Little Beauty Syncline. In the centre of the area its outcrop is dominated by the Mary Kathleen Syncline to the west of the Burstall Granite. In the east of the field area, the Corella Formation occurs in a large anticlinal sedimentary sequence. All four sensors cover the formation, which is spectrally the most variable found in the area. It is thus difficult to describe a typical spectral response or weathering sequence, as has been done for other lithologies.

The scale at which the Corella Formation has been mapped in different parts of the field area varies considerably. This affects the amount of new information which the remotely sensed data can provide at any given location. The western exposures are limited and have been mapped in some detail, but there are places where new information is apparent. The central Corella Formation in the Mary Kathleen Syncline has been mapped at scales of up to 1:10 000 due to the economic uranium mineralisation. It is more difficult to add information in an area such as this. The eastern exposures have largely been mapped by air photograph interpretation and traverses. This study has made a big contribution to the mapping of the Corella Formation in this northeastern area.

Blake (1982) has recognised differences between the western Corella, which he refers to as Zone A, and the eastern and central Corella, referred to as Zone B. It is clear from the TM imagery studied that these differences are reflected in spectral variations and these differences have been more strongly highlighted by successive processing stages (Plates 5.1 - 5.3 and 5.6). Further differences may exist within Zone B between

the central and eastern Corella Formation. The western, central and eastern exposures will thus be discussed separately in that order.

8.4.2.1 Western exposures

The western exposures are covered by TM, NS001 and AGR data. The 1:100 000 maps (Enclosure 2.1) depict a full Corella Formation sequence of Pkc_1, Pkc_2, Pkc_3 in the Rosebud Syncline, while the southwest corner exposures are dominantly Pkc_1. An E-W traverse across the Rosebud Syncline revealed the mapped boundaries to be correct. Pkc_1 is commonly carbonate or impure marble, weathering in a pitted style typical of carbonate rocks (Plate 8.8). Pkc_2 is less calcareous and more schistose, especially where Pkc_{2c}, a cordierite-biotite schist, occurs (Plate 8.9). Pkc_3 does not occur on this traverse. It is clear that despite the differences in lithology, the two units weather in a very similar fashion.

This is further demonstrated by IRIS spectra along the traverse, the analysis of which is summarised in Figure 8.10. The carbonates of Pkc_1 are characterised primarily by calcite and goethite absorptions, as seen in Figure 8.11, which shows the IRIS spectra for the fresh, weathered and soil surfaces at locality 35. The weathered surface loses the calcite absorption in the short wave infrared and is dominated by iron oxide. The soil has very much reduced reflectance, though the calcite absorption can again be seen. Analysis of the TM ratio image in Plate 8.7 shows that a 2.22 μm absorption occurs over this lithology in places, although this is not seen in the TM LR data, in which this lithology is dominated by iron oxide absorption. Figure 8.12 shows the IRIS spectra for the fresh, weathered and soil surfaces at locality 27 within Pkc_2. The deep, sharp features at 1.4 and 2.2 μm in the fresh and weathered surface are typical of muscovite, but are lost in the soil spectrum which again has much reduced reflectance. The weathering of this lithology produces a low reflectance soil dominated by iron oxide features, as seen in places in the TM ratio imagery.

The Corella Formation depicted in the Little Beauty Syncline has a similar spectral response. These exposures are a repetition of those to the south brought about by the change in the plunge of the fold from southward in the Rosebud Syncline to northward

in the Little Beauty Syncline. In the AGR data the Corella Formation in both synclines has a moderate radiometric response. The rest of the western exposures, almost all consisting of Pkc_1, frequently have the same spectral and radiometric response. The Corella Formation in the west appears to be reasonably consistent, but there are places where this is not the case. A good example occurs along the northern edge of the Dog Bone Dolerite where the TM data are dominated by consistent 2.22 μm absorption (Enclosure 5.1). These exposures are clearly different to the rest of the western Corella Formation, and will be reconsidered in relation to the rest of the formation in the central and eastern exposures.

8.4.2.2 Central exposures

The central part of the Corella Formation in the mapping area is dominated by the Mary Kathleen Syncline. Due to the uranium mineralisation, this area has been mapped in great detail over many years. Pkc_1 is represented by a thin unit down the west limb of this northward plunging syncline, but the majority of the exposures are Pkc_2. Several subdivisions of Pkc_2 are mapped, but not consistently through the whole structure. In the north of the Mary Kathleen Syncline, the detail depicted within Pkc_2 around the uranium mine on the 1:100 000 map (Enclosure 2.1) is not all seen in the TM or AGR data sets. There are, however, clear N-S bands of alternating 0.49 and 2.22 μm absorption apparent in Plate 8.7. In the south of the syncline these alternations persist, though each bed of Pkc_2 is considerably thinner. The fold structure can be clearly traced around the nose of the syncline. These alternations are not shown for the nose of the syncline on the 1:100 000 map.

The Mary Kathleen Syncline is better displayed in the higher resolution GMS data. Plate 8.10 shows colour composites over the northern and southern portions of the syncline using the GMS LR data from the shortwave infrared region. Absorption 2.352 μm is displayed in red, absorption at 2.176 μm in green and absorption at 2.044 μm in blue. Figure 8.13 depicts the relationship between the GMS band passes and the short wave infrared reflectance spectra for various minerals. The alternations seen in the TM ratio imagery are also seen in the GMS LR data. In the short wave infrared they are between 2.176 μm absorption, typical of kaolinite, and 2.352 μm

absorption typical of calcite and epidote. Plate 8.11 shows the site of one of these divisions in the field. The less massive rock on the right forming the debris slope is a more quartz rich unit, while the more massive rock on the left is a more calcareous lithology. The 2.176 μm absorption occurs over the siliceous unit and the 2.352 μm absorption over the calc-silicate.

These alternating carbonate/silicate units have been sampled in the area covered by localities 126-131 and IRIS results are summarised in Figure 8.14. The more quartz rich rocks do contain kaolin, explaining their 2.176 μm absorption in the GMS LR data. Amphibole, mica, chlorite and calcite are found in the calc-silicate rocks. Figure 8.15 shows a GMS LR spectrum over an area of 2.352 μm absorption. Comparison with Figure 8.13 suggests that the spectrum could be caused by calcite or epidote, both of which absorb near 2.352 μm. The low 2.044 μm value is, however, more typical of calcite, which correlates with the IRIS results. The southern section of the Mary Kathleen Syncline again displays a similar alternation of kaolinitic and calcite response in the GMS data, further confirming the synclinal structure in the south. This patterns breaks down in the northwest of the syncline around the ore body. Here the GMS data depict a series of discontinuous units which end suddenly just south of the open pit. These data will therefore be used to address mineralisation in section 8.9.

8.4.2.3 Eastern exposures

The most extensive exposures of Corella Formation occur northeast of the Burstall Granite. The 1:100 000 map (Enclosure 2.1) depicts a thin N-S striking limb of Pkc_1 between two limbs of Pkc_2, both members affected by complex folding. All the data sets used in this study have demonstrated that the divisions shown on the 1:100 000 map are incorrect. The TM LR data shown in Plate 8.12 depict the most obvious difficulty. Member Pkc_2 in the eastern limb is spectrally quite different from member Pkc_2 in the western limb. The central, Pkc_1, limb has a spectral character similar to that displayed by the Corella Formation in the Rosebud Syncline, with a dominant 0.83 μm absorption. The eastern limb of Pkc_2 has many similarities with Pkc_2 in the Mary Kathleen Syncline, being dominated by 0.45 μm absorption. The western limb, also depicted as Pkc_2 on the map, has a quite different spectral character with much internal

detail. Unusually for the Corella Formation, some units are dominated by 2.22 μm absorption, particularly in the south, and others by 0.83 μm absorption or a mixed pattern of both. Complex folding and along-strike facies changes are needed to explain the distribution of these western units. The 0.45 μm absorption typical of the eastern limb of Pkc_2, does not occur to any extent in the western limb Pkc_2. The spectral contrasts seen in the TM data are confirmed by the NS001 LR data, seen in Plate 8.13.

The AGR data in Plates 6.5 and 6.14 show that whilst the radiometric responses of the eastern limb of Pkc_2 and the central limb of Pkc_1 are comparable with other exposures of the Corella Formation, the western limb of Pkc_2 has a quite different character. The ratio-normalised AGR data in Plate 6.11 show that the latter's moderately high radiometric count is dominated by potassium and thorium. Contrastingly, the response of the eastern and central limbs is dominated by potassium and/or uranium. Pkc_2 west is the only part of the Corella Formation with a consistently high thorium count. The presence of these differences in the AGR data is evidence that the difference between the eastern and western limbs is lithological and not related to vegetation. No vegetational contrast was apparent in the field, and the LSFit data shown in Plate 7.22 depict the same variation.

This section of the Corella Formation was studied in detail to address the problems with the Corella Formation stratigraphy described in section 2.8 and made clear by initial studies with all four of the data sets. The sequence northeast of the Burstall Granite was traversed in several places, usually along east-west creeks, and sampled extensively. Hence, XRD (Table 7.3) and IRIS (Appendix A) analyses can also be brought to bear on the problem. Figure 8.16 synthesises the results of this study. Throughout the following, the reader is referred to Enclosure 8.1, an image-based revised geological map for the NE Corella Formation.

Eastern limb of Pkc_2: this unit can be divided into two, with a third area being discriminated to the north. The eastern-most Pkc_2 by the Fountain Range Fault is schistose and characterised by absorption at 0.49 μm in the TM data (Figure 8.17). Figure 8.18 shows the IRIS spectrum typical of this unit. Absorptions seen are typical of iron oxide (0.45 μm, 1.91 μm), mica (1.41 μm, 2.2 μm), epidote (2.34 μm,

1.54 μm, 2.24 μm) and quartz. The second unit of the eastern limb of Pkc_2 has increased 0.83 μm absorption in comparison (Figure 8.19) and was found to be pink-green calc-silicate with little outcrop and an orange-red soil (Plate 8.14). The features shown by this unit are clear in the IRIS spectra shown in Figure 8.20 from locality 241. This spectrum has all the features of epidote (Figure 8.13), plus iron oxide and a small amount of Al-OH. Thus, epidote is found in both units. The contrasts picked up in the TM data are in the shorter wavelengths. As the spectra have similar iron oxide features, these must be due to differences in the balance of soil and outcrop.

Both these units show 2.352 μm absorption typical of epidote in the short wave infrared GMS LR data displayed in Plate 8.15. Consequently they cannot be separated using these data. In the visible and near infrared the GMS LR data highlight the remaining noise (Plate 8.16) and it is again difficult to separate the two units. Thus the GMS data, whilst revealing more about the mineralogy of the two units by identifying epidote, do not allow their separation, whereas the lower resolution TM data do.

In the north of the eastern limb of Pkc_2, a third unit can be discriminated. The whole unit has reduced 2.22 μm reflectance and several narrow elongate zones of 2.22 μm absorption are seen. The TM LR pseudo-spectrum of one of these elongate zones is shown in Figure 8.21. The absorption occurs over pegmatites related to the Burstall Granite intrusion but not visited in the field. They are described by Derrick et al (1977), as having quartz, potassium feldspar, mica and tourmaline mineralogy. Both mica and weathering feldspar cause 2.22 μm absorption in other parts of the field area. Two improvements can be made to the mapping of these pegmatites. Within the known zone, several pegmatite bodies not shown on the map can be delineated. More importantly, a second zone of pegmatites can be seen which does not appear at all on the 1:100 000 map. This new zone lies to the east of the known occurrences and appears to be a repetition of the first zone brought about by folding. The eastern limb of Pkc_2 has a similar TM spectral signature to the Pkc_2 mapped in the Mary Kathleen Syncline. Uranium and rare earth element mineralisation in the Mary Kathleen syncline occurs where the Burstall Granite intrudes Pkc_2 host rocks. The eastern Pkc_2 may also form a suitable host rock and is intruded by Burstall-related pegmatite. Pegmatites are known to contain uranium and rare earth element mineralisation (Best, 1982). Thus,

Pkc_2 in this eastern limb forms a prospect for further mineralisation. Study of the AGR data in Plate 6.11 suggests that, while counts are only moderate over these exposures, they are dominated by uranium.

Central limb of Pkc_1: The central limb has a quite different spectral character, dominated by absorption at 0.65 μm and 0.83 μm, as seen in the TM LR pseudo-spectrum in Figure 8.22. In the field, there is a correspondingly clear lithological change. In Plate 8.14, the far distance is formed by a ridge of more resistant rocks in the west which correspond to the start of Pkc_1. The commonest lithology of these more massively outcropping metamorphics is fine grained limestone (Plate 8.17). XRD analyses reveal that the major change across this boundary is an increase in the importance of calcite and reduction in Al-OH content. The dominant mineral recognised in analyses of IRIS spectra is calcite, in contrast to the epidote mineralogy of Pkc_2 in the east limb. Figure 8.23 shows calcite in IRIS spectra locality 242 within Pkc_1. Though some of the features also suggest epidote is present, calcite is the dominant mineral, in agreement with the XRD results. The spectra also show that short wave infrared features are subdued in the soil. The dominance of iron oxide explains the TM response and the calcite signal is not detected in the TM data. The spectral signature of the calcite is however seen in the short wave infrared GMS LR data, where it can also be distinguished from epidote, with absorption at 2.352 μm (Pkc_2 in the east limb) due to calcite's lower 2.044 μm reflectance noted in section 8.4.2.2 (Plate 8.15).

There is one locality where the calcite signal can be detected in the TM data. At locality 89 shown in Plate 8.18 there is a large calcite quarry, with near-perfect calcite crystals in the form of chippings covering the ground over an area several hundred square metres. Plate 8.12 shows that this area has a strong 2.22 μm absorption in the TM data and is seen in the image as a bright orange-red patch. The TM LR pseudo-spectrum for locality 89 is shown in Figure 8.24. Though similar to that seen for clay and mica-related absorptions within other lithologies (e.g. Figure 8.8), there are subtle differences at wavelengths other than 2.22 μm which allow the two to be separated, particularly the lack of an iron oxide-related absorption at 0.49 μm in the calcite pseudo-spectrum. The IRIS spectrum from the same locality is shown in Figure 8.25 and the calcite mineralogy is quite clear.

Thus, under ideal circumstances the calcite/epidote absorption minimum around 2.35 μm is not at too long a wavelength to be detected by using TM's wide band centred on 2.22 μm. Where the weathered surface interferes, however, the features of iron oxide make the features of calcite too weak to be detected by the use of TM. Marsh et al (1992) have found the same phenomenon in Cretaceous limestones in the Sinai Desert. The GMS data have a well positioned band to detect the 2.35 μm absorption and can thus detect even the weakened calcite signal, so the calcite quarry is not clearly seen as a separate feature in the short wave infrared GMS LR data.

There are also internal divisions within the central limb of Pkc_1. These consist of an intermediate unit on each side between Pkc_1 and Pkc_2, only 100 m across. The soil has the character of Pkc_1, but the outcrop is reduced and less obviously calcareous. Like in the east limb of Pkc_2, epidote is more frequently identified in IRIS analyses. The spectral contrasts accompanying these changes are subtle, but do produce a mappable, separate unit in both cases. Finally, moving north along the strike of Pkc_1, there is a change north of the calcite pit from 0.83 to 0.49 μm absorption in the TM data. This corresponds to an along-strike facies change to a finer grained pure carbonate with an orange soil (Plate 8.19), which does not appear to be structurally controlled.

Western limb of Pkc_2: Pkc_2 in the western limb is distinguishable from Pkc_2 in the eastern limb both lithologically and structurally. Two lithologies are found, whose outcrop pattern is defined by a series of tight folds which can be mapped using the TM data. The boundary with the central Pkc_1 exposures is probably fault controlled, being very linear and cutting obliquely across the strike of the central limb. Immediately across this fault, a distinctive unit displaying 2.22 μm absorption is seen. This unit, mapped in the field as micaceous sandstone, is unlike any other portions of the Corella Formation described so far. An increase in kaolinite is detected across this boundary by XRD, and also in IRIS spectra and the GMS data. The spectra in Figure 8.26 from locality 244 displays iron oxide-related absorptions at short wavelengths, but the striking feature is the development of muscovite-related absorptions at 1.41 μm and 2.21 μm, particularly in the weathered surface and the soil, which was observed as being mica-rich in the field. Quartz is also indicated by the right-asymmetric water band at 1.9 μm. Well developed features at 2.26 μm and 2.37 μm are attributed to chlorite.

Figure 8.27 shows a TM LR pseudo-spectrum from the same locality, which displays absorption at 2.22 μm due to the mica. In contrast to the calcite pseudo-spectrum shown in Figure 8.24, 0.49 μm absorption related to iron oxide is also present.

The photograph in Plate 8.20 is taken standing on the second main unit of the western limb of PKC_2, looking eastward toward the micaceous sandstone unit. This second unit has more massive outcrop with vuggy carbonate weathering to a dull brown soil and is more like Pkc_1 than Pkc_2, displaying 0.83 μm absorption in the TM data (Figure 8.28). The IRIS spectra of this lithology at locality 88 are shown in Figure 8.29. The fresh surface displays absorption due to amphibole at 2.34 μm and 2.38 μm, as well as an Al-OH feature at 2.22 μm. The weathered surface and soil also display these absorptions, but all except the Al-OH feature become less clear as iron oxide develops. The soil has a broad absorption around 0.9 μm, which explains the 0.83 μm absorption seen in the TM LR data. At locality 88, there is also still some 2.22 μm absorption, causing a reduced 2.22 μm value in the TM data (Figure 8.28). Elsewhere, the carbonate/amphibole assemblage dominates. Several interbeds of micaceous sandstone/carbonate metamorphics are seen, affected by folding and faulting. The structure in this area is difficult to map on the ground due to lack of clear bedding, steep dips and tight folding (D. Blake, personal communication). The remotely sensed data allow this problem to be addressed.

8.4.2.4 Summary

The base of the Corella Formation is defined as the first calcareous unit above the Ballara Quartzite. In the western part of the field area this contact is clearly seen in the Rosebud Syncline and appears to be conformable. Pkc_1 is calcareous and Pkc_2 more arenaceous, with schist being common. It may also be possible to map Pkc_3, though it was not covered by that part of the Rosebud Syncline studied here. As Blake (1982) suggests, the three member division of the Corella Formation can be seen in this western sequence. The Mary Kathleen Syncline, in the centre of the field area, contains a thin limb of Pkc_1 along its western edge before a thick sequence of calc-silicates is encountered occupying the bulk of the syncline. It may be that Pkc_1 thins and Pkc_2 thickens eastward. Again the contact with the underlying Ballara Quartzite is seen and

appears broadly conformable. The top of the sequence is not recorded at all in the Mary Kathleen sequence, though Pkc_3 may occur stratigraphically above Pkc_2 to the north of the Burstall Granite in a continuation of the same synclinal structure. Where sampled, Pkc_3 contains granofels, limestone and calc-silicate metamorphics and it has the spectral character of Pkc_1. IRIS spectra for the two samples taken (localities 121 and 124) reveal amphibole, mica, chlorite and calcite plus iron oxide, which is similar again to Pkc_1. From the limited exposure in this area, however, it is difficult to put Pkc_3 into context with the rest of the Corella Formation.

It is far more difficult to establish the full sequence in the east of the field area. The central limb of Pkc_1 is typical of Pkc_1 elsewhere but contacts with the underlying Ballara Quartzite are not seen. The eastern limb of Pkc_2 is comparable to Pkc_2 elsewhere both lithologically and spectrally. The western limb of Pkc_2, however, is unlike the Corella Formation anywhere else in the field area. It clearly does not belong to the normal Corella Formation stratigraphy and is a less calcareous lithology either deposited at a different time or in a different part of the basin. The divisions shown in Figure 2.5 may thus be approaching the correct interpretation. The area northeast of the Burstall Granite, Zone A of Blake (1982) is thus unsuitable for a type section of the Corella Formation and Blake's proposal that these beds be downgraded to the Corella Beds is supported by all the data analysed in this study.

Where the Corella sequence is clear, the top of the formation is not seen. Only in the extreme west of the field area is the overlying Mount Albert Group exposed. The contact is, at the least, unconformable and may be fault controlled and will be further considered after the Mount Albert Group has been described.

8.5 Mount Albert Group

This group, covered by the TM and AGR data, only outcrops at the western margin of the field area (Enclosure 2.1), forms inaccessible high ground and was not visited in the field. The Deighton Quartzite displays the characteristic quartzite signature of 2.22 μm absorption (Enclosure 5.1) and low radiometric count (Enclosure 6.1) previously described for the Ballara Quartzite. The 2.22 μm absorption is probably

explained by the presence of feldspar and white kaolinitic sandstones as described by Derrick et al (1977). These two quartzites cannot be separated using the TM data, the AGR data or a combination of the two (Plate 6.12). The schist, phyllite and limestone of the White Blow Formation barely outcrop within the field area. 0.49 μm absorption is seen over a slate unit and 2.22 μm absorption occurs over a quartzite unit.

As noted in section 2.8.2, the status of the Mount Albert Group is contentious. Loosveld and Schreurs (1987) equate it with the Corella Formation and place a thrust at the contact between the two, rather than the mapped unconformity. In the remotely sensed data it is clear that the contact cuts across several lithologies, but this could equally well be due to an unconformity as a thrust. It is difficult to identify a thrusted contact using remotely sensed data except where older rocks are brought above younger, which is not the case here. The remotely sensed data may, however, allow the equivalence or otherwise of the two groups to be tested. The Mary Kathleen Group is characterised by a thinner, lower quartzite formation and a much thicker carbonate/metamorphic formation, leading to small areas of 2.22 μm absorption and vast areas of iron oxide dominated response. In contrast, the Mount Albert Group has a thick lower quartzite formation and, in this area at least, a very restricted carbonate/metamorphic sequence above this. Even allowing for this and the similarity of the two quartzites, the White Blow Formation is quite different to the lowest member of the Corella Formation, Pkc_1, in the TM data and there is no obvious similarity in the AGR data, either. Given these differences and the opposite balance of quartzite and carbonate formations it is unlikely that the two equate and the separate Mount Albert Group should be retained. As there are no other rocks lower in the stratigraphic column of which the Mount Albert Group could be an equivalent, it is likely that this group tops the sedimentary sequence.

8.6 Granites

The main acidic extrusives have been considered as part of the metamorphic sequence so far described. The acidic rocks remaining to be covered are intrusive, namely the Wonga, Hardway and Burstall Granites.

8.6.1 Wonga Granite

This lithology outcrops in an elongate N-S belt through the centre of the field area (Enclosure 2.1) and is covered by the TM, AGR and NS001 data. In the field, the granite forms widely separated upstanding tors within a low-lying flat plain covered in a red, iron-enriched soil. The lack of topography and uniform soil leads to the granite having a high albedo, and it is thus conspicuous in the albedo image created during the logarithmic residual process (Plate 5.5). XRD analyses (Table 7.2) give the bulk mineralogy as quartz-two feldspar-mica-amphibole and this is also clear in the field.

The most common spectral signature of the Wonga Granite in the TM data, shown in Plate 8.3, is a deep 0.49 μm absorption. Fieldwork reveals that this occurs over the red iron enriched soil covering much of the lithology. Increased vegetation density in places modifies this signal by lowering the 2.22 μm value. Over outcrop tors the TM response changes to mixed areas of 2.22 μm and 0.83 μm absorption. It is clear that some areas have stronger 2.22 μm absorption while others are dominated by 0.83 μm absorption. At the spatial resolution of the TM data, however, the two components which may be responsible for this pattern cannot be separated with certainty. Field work suggested that the 2.22 μm absorption is related to a clay-rich soil (as in Figure 7.10 from the Burstall Granite's clay soil) and the 0.83 μm absorption to iron-rich weathered surfaces. Figure 8.30 shows TM LR pseudo-spectra over an outcrop tor (a) and the debris plain soil (b).

The increased spatial resolution of the NS001 data helps to solve this problem, allowing clear separation of the granite weathered faces, granite soil and debris plain soil. Plate 8.5 shows the NS001 LR data over a prominent linear tor of Wonga Granite shown outcropping in Plate 8.21. In this area the 2.22 μm absorption clearly corresponds with the slopes to the east of the tor, which have little outcrop and are covered by an orange soil and granite boulders with clean surfaces due to their recent erosion. The 0.83 μm absorption occurs along the crest of the tor and on the far side, where large weathered surfaces are preserved in granite slabs with iron-enriched crusts, as discussed in chapter 7. To the SE by the E-W creek visible in both the image and the field photograph, smaller tors meet the debris plain with little or no slope of soil and boulders. Only

0.83 μm absorption is seen over these tors. Plate 8.22 shows one such low-lying granite tor from this area.

In the above example, it is clear that the increase in spatial resolution of the NS001 data also affects the effective spectral resolution of those data. Increasing the spatial sampling frequency means that components mixing at scales below TM's spatial resolution can be separated. Thus, while a mixed signal occurs in the TM data the NS001 data record two separate signals and the effective spectral resolution of the data is increased. This is the reverse of the effect noted by Barnsley and Kay (1990) where image variance decreases toward the edge of the flight line as the true pixel size increases with increasing look angle.

The XRD data for the Wonga Granite (Table 7.2) support the explanation of the remotely sensed data given above. The weathered surface of the granite is enriched in iron oxide, whereas the soil near outcrops has anomalously low iron oxide. Weathering products detected by XRD include kaolinite. The debris plain soil is iron-enriched compared to the granite soil, and contains other minerals such as periclase and grossular not associated with the granite. An analysis of this soil in the field revealed clasts of quartzite, schist, metasediment, carbonate, vein quartz, dolerite as well as granite, suggesting a transported element in the soil which covers the majority of the Wonga Granite. Figure 8.31 shows the IRIS spectrum of the fresh and weathered surface at locality 210 of the Wonga Granite. The fresh surface displays kaolinite features at 2.17 μm and 2.22 μm, which are almost lost in the weathered surface. The latter has a deeper iron oxide absorption, again demonstrating the iron-enrichment of granite weathered surfaces and explaining their 0.83 μm absorption.

Figure 8.32 shows the IRIS spectra for the two contrasting soils. The Wonga Granite soil found around outcrop tors displays a deep, sharp absorption at 2.21 μm due to muscovite, with water bands typical of quartz at 1.91 μm and mica and/or quartz at 1.41 μm. Either mica, as in this case, or kaolin, found in many of the soil samples from the tor areas, explains the 2.22 μm absorption. The soil at locality 215 on the debris plain shows the same features, but the muscovite feature is reduced while those due to quartz are increased and the iron oxide absorption is deeper and better defined.

This case suggests that the debris plain soil with 0.49 μm absorption found over much of the Wonga Granite is iron-enriched due to lateritic weathering in-situ. A transported component may add to this but is of less importance.

The majority of the Wonga Granite has a high radiometric count, with a lower response over parts of the debris plain soil and major dolerite dykes. The ratio-normalised AGR data reveal that thorium dominates this granite's radiometric response. The boundaries of the granite are seen very clearly in these data despite the soil cover (Plate 6.11). The latter's strong effect on the spectral response makes this difficult with the radiance data.

8.6.2 Hardway Granite

The Hardway Granite outcrops in three masses to the west of the Wonga Granite (Enclosure 2.1) and is covered by the TM and AGR data. XRD analysis shows the bulk mineralogy to be quartz, two feldspars, mica and amphibole.

The majority of the granite is again characterised by 0.49 μm absorption, as seen in the TM LR pseudo-spectrum in Figure 8.33 The similarity of this pseudo-spectrum to that from the Wonga Plain soil (Figure 8.30b) suggests that a similar iron-rich soil also occurs over the Hardway Granite. Iron-enrichment of this granite during weathering is clear in the field at locality 7 (Plate 8.23), where a track cutting exposes a weathering profile. The XRD data in Table 7.2 again show an increase in iron oxide for the weathered surface in comparison to adjacent granite soil. The spectral effects of this weathering sequence at locality 5 are illustrated by the IRIS spectra in Figure 8.34. The fresh surface has a flat IRIS spectrum, with small features due to Al-OH and quartz and a moderate iron oxide absorption. Weathering leads to a deeper iron oxide absorption and right asymmetric water bands at 1.42 μm and 1.92 μm develop which are attributed to quartz. The 2.2 μm feature develops a couplet around 2.17 μm and is thus related to kaolinite.

The TM albedo image (Plate 5.5) shows that the style of outcrop and topography are similar for both the Hardway and Wonga granites. The mineral assemblage found is the same as that found for the Wonga Granite and the two show the same spectral features.

The Hardway Granite has even fewer areas of 2.22 μm absorption, however, suggesting that outcrop tors and their associated soils are less common. The lack of large outcrop tors, means that the Hardway Granite is even more dominated by 0.49 μm absorption.

The only data which show a difference between the Wonga and Hardway granites are the AGR data. Compared to the Wonga Granite, the Hardway Granite has a lower radiometric count less obviously dominated by thorium, with increased inhomogeneity. This could be related to the lack of outcrop tors, but may indicate a more fundamental difference between the two granites.

8.6.3 Burstall Granite

The Burstall Granite outcrops in two masses in the centre of the field area, the larger to the north, and also in the form of smaller dykes and/or pegmatites (Enclosure 2.1). It has been studied using all four data sets. The bulk composition given by XRD is quartz-two feldspar-mica-amphibole (Table 7.2).

Whilst mineralogically similar to other granites in the area, the Burstall Granite shows clear differences to them in the TM data. Study of the TM albedo image in Plate 5.5 shows that the Burstall Granite forms high ground, as is clear in Plate 8.24, with the rugged topography causing a lot of shadowing. There is therefore a basic difference in topography and amount of outcrop between the Burstall Granite and those previously considered. There is also a clear spectral difference. The Burstall Granite does not display the 0.49 μm absorption associated with the accumulation of a deep iron-enriched soil in a flat plain. It is characterised by extensive 2.22 μm absorption in the TM LR data (Enclosure 5.1, Figure 8.35), with areas of increased 0.49 μm absorption probably due to local increases in vegetation density (Figure 8.36). There are also some areas of 0.83 μm absorption, probably related to outcrop slabs (Figure 8.37).

With the NS001 LR data over the southern mass of Burstall granite (Plate 7.19), despite problems due to shadowing, correlations can be made between; increased vegetation and combined 0.49/2.22 μm absorption; accumulating clay minerals and mica in the soil between outcrops and 2.22 μm absorption; large weathered slabs of granite with an

iron-enriched surface layer and 0.83 μm absorption; deep shade and anomalous 0.49 μm absorption, as discussed in chapter 7. The spectral responses seen in the TM and NS001 data are caused by the same components as were found over the other granites in the area, but these components occur in differing proportions on the Burstall Granite. 2.22 μm absorption is far more common, as large areas of fresh granite soil and granite boulders cleaned of their weathered surfaces by recent erosion are found.

The IRIS spectra for locality 105 on the main mass of granite and 101 on the southern mass are shown in Figure 8.38. Both fresh surface spectra are largely flat, with the main features attributable to iron oxide. During weathering, quartz features become stronger in both cases, with a right asymmetric absorption either appearing at 1.91 μm or becoming deeper. The iron oxide features also become deeper. Finally, a 2.2 μm absorption develops. At locality 101 this is probably related to mica as the feature is sharp and there is no doublet, whereas kaolin probably causes the 2.2 μm and 2.17 μm absorption seen at locality 105. These IRIS data support the explanation of the data TM and NS001 data postulated in the field.

The higher spectral resolution GMS data were also used to study the Burstall Granite. Plate 8.10 shows the short wave infrared LR data over the Burstall Granite's southern mass. The granite can be clearly distinguished from the surrounding metasediments of the Corella Formation. The sediments display 2.352 μm absorption related to their carbonate/epidote mineralogy for which a GMS LR spectrum was shown in Figure 8.15 In contrast, the granite displays absorptions related to the Al-OH component of its mineralogy. Figure 8.39 shows a GMS LR spectrum typical of the Burstall granite, with absorption at 2.22 μm and a lesser absorption at 2.176 μm allowing kaolinite to be identified (Figure 8.13).

The radiometric response over the Burstall Granite is distinct from that over the Wonga and Hardway Granites because high intensity occurs for all three elements over the whole area of the granite. The impression gained is that the Burstall Granite is in some way different, especially as it is associated with uranium mineralisation. It is likely, however, that it is once again the difference in amount of outcrop and soil cover which causes this effect, as prominent tors of the Wonga Granite also have high radiometric

counts for all three elements. Ratio normalisation of the AGR data shows that, as for the Wonga Granite, the radiometric response is dominated by thorium.

8.6.4 Discussion

The major controversy involving the granitic rocks of the area centres on their relationships to each other and their ages. Whilst various correlations have been proposed (section 2.8.3) the situation was summarised by Scott and Scott (1985) who said that the age and relations of the granites remain unclear. Precise ages cannot be obtained from the data in this study. The differences noted in the remotely sensed data between these three granites, however, can be used to help deduce their inter-relationships and thus relative ages.

The differences between the three granites noted in the previous sections are summarised in Table 8.1. The Burstall Granite is unlike the others in the area, both in terms of albedo and spectrally. The Wonga and Hardway granites appear more closely related. The spectral differences between the granites are not due to contrasting mineralogy, which is broadly similar for all three. Rather, they are related to contrasting styles of topography and outcrop, particularly between the Burstall and the Wonga Granites. This must be related to the ease with which they are eroded, with the Wonga the more easily eroded of the two. The Wonga Granite's greater deformation and inhomogeneity compared to the Burstall Granite are the probable reason for this. The large areas of deep iron-rich soil detected in the TM and NS001 data over the Wonga Granite, and absent from the Burstall Granite, suggest the former is in a more mature stage of weathering and is the oldest granite of the three, as proposed by Derrick et al (1977). The Burstall, being comparatively undeformed, must be the youngest.

In the memoir (Derrick et al, ibid.), the Hardway Granite is correlated with the Burstall Granite as they both intrude the Mary Kathleen Group. Study of the TM LR data in Enclosure 5.1 suggests, however, that the contact between the Hardway Granite and the Mary Kathleen Group, which lies along the north edge of the Dog Bone Dolerite, may be inaccurately mapped. The rocks mapped as Corella Formation here display a

2.22 μm absorption. The only other such absorption in the Corella Formation occurs northeast of the Burstall granite in rocks that should be down-graded to the Corella beds, of unknown age. The rocks causing the 2.22 μm absorption in the Corella Formation by the Hardway Granite are seen in the field to be acidic metamorphics more reminiscent of the Argylla Formation, which frequently displays 2.22 μm absorption. Thus, the Hardway Granite may not intrude the Corella Formation of the Mary Kathleen Group at all but only the Argylla Formation, like the Wonga Granite. This is consistent with the similarity between the Hardway and Wonga Granites previously noted and so they may well be equivalent.

8.7 Basic Lithologies

The majority of the basic rocks in the area are either intrusive dolerites or extrusive basalt flows. There is one pluton, the Lunch Creek Gabbro.

8.7.1 Lunch Creek Gabbro

The Lunch Creek Gabbro occurs in the centre of the field area, intimately associated with the main body of Burstall Granite (Enclosure 2.1). It has been studied using the TM and AGR data. As it was not visited in the field it will only be considered in brief.

In the TM LR data, the east side of the Burstall Granite has an irregular pattern of 0.49 μm absorption both within and to the east of the granite. In places, this can be resolved into separate occurrences of gabbro, but commonly the two lithologies are closely associated and difficult to discriminate with TM's spatial resolution. Figure 8.40 shows a typical TM LR pseudo-spectrum for the Lunch Creek Gabbro. The main features is a sharp absorption to 0.49 μm. Only one of the Lunch Creek Gabbro pseudo-spectra studied has any 0.83 μm absorption. The gabbro is thus spectrally distinct from the basic rocks so far described and either weathers in a different fashion or has a different mineralogy which is still detectable in exposed surfaces. Green et al (1985) have described an iron oxide response from a red soil in aircraft scanner data over the Lunch Creek Gabbro. As the pseudo-spectra most like those of the Lunch Creek Gabbro are those over the Wonga Granite's debris plain, it seems likely that deep

weathering leading to iron enriched soils is responsible for the spectral character of the Lunch Creek Gabbro.

The major outcrops of gabbro are clearer still in the AGR data (Enclosure 6.1) as the gabbro, with a low radiometric count for all elements, is in extreme contrast to the Burstall Granite.

8.7.2 Dolerites

The majority of the dolerites exposed in the area are the older do_3, including the sills in the cores of the Little Beauty and Rosebud Synclines, the Lake Corella Dolerite dyke, the Lime Creek Dolerite and the Dog Bone Dolerite (Enclosure 2.1). The younger do_6 dolerites are only represented by the Lake View Dolerite. Where it is has a strong contrast with the host rock this dolerite can be seen in the TM LR data (Plate 8.12) despite being only 50 m across (Plate 8.25). This is the narrowest unit detected with the TM data in this study.

The spectral characteristics of the dolerite rocks have been described in chapter 7. Their iron content leads to a weathering process dominated by the production of an iron oxide-rich soil. This in turn leads absorptions at 0.49 μm and 0.83 μm in the TM LR data. All the dolerites show both absorptions, but one is commonly stronger or occurs over more of the outcrop. Study of Enclosure 5.1 shows that all except the Lime Creek Dolerite are dominated by the 0.49 μm absorption. The Lime Creek Dolerite, dominated by 0.83 μm absorption, is quite distinct from the others and this will be of significance when the status of some of the dolerites is reconsidered in section 8.7.4. Examples of both 0.49 μm and 0.83 μm absorption in the Lime Creek Dolerite are shown in Figure 8.41.

The XRD data shown in Table 7.1 show that the dolerites all have very similar mineralogy. The only major difference between the Lime Creek Dolerite, with dominant 0.83 μm absorption, and the other dolerites, dominated by 0.49 μm absorption, is in the weathering product. Compared to the other dolerites, the Lime Creek Dolerite appears to have a reduced iron oxide ratio. In addition to this, the iron

mineral identified may be goethite, while hematite has been identified in some of the other dolerites. This difference in weathering product between the two groups of dolerites may be causing the variation between 0.49 μm and 0.83 μm absorption in the TM data.

It should be possible to separate goethite and hematite in IRIS spectra, as the absorption minima for hematite (0.58 and 0.85 μm) are distinct from those for goethite (0.45 and 0.91 μm and minor 0.68 μm absorption) (Figure 3.5). Using these criteria almost all the samples taken are goethitic (appendix A). Only the Lake Corella Dolerite has any features resembling those of hematite. The reason for this disagreement with the XRD data is unclear. Fraser (personal communication) has stated that separation of goethite from hematite is more difficult in field samples than in pure mineral samples and this may explain the problem.

8.7.3 Metabasalts

The Magna Lynn, Lime Creek, Cone Creek and Wakeful Metabasalts, occur in the field area (Enclosure 2.1). These lithologies are easily discriminated from other rocks by their iron oxide response. All except the Cone Creek Metabasalt are dominated by 0.83 μm absorption in the TM LR data (Enclosure 5.1). Pseudo-spectra for the Lime Creek Metabasalt showing 0.83 μm and less common 0.49 μm absorption are shown in Figure 8.42

The dominance of near infrared absorption over short wave infrared absorption is also seen in the GMS data. Figure 8.43 shows a GMS pseudo-spectrum for the Lime Creek Metabasalt in which the dominant absorption occurs at 0.915 μm. The 0.83 μm LR value is also reduced, explaining the 0.83 μm absorption in the TM LR data. The improved spectral resolution of the GMS data, with a band ideally placed to measure goethite's 0.91 μm absorption, allows the mineral to be identified in this case.

In the XRD data (Table 7.1) both the sampled metabasalts have the same basic mineralogy. Goethite is identified in the weathering product of the Magna Lynn Metabasalt. Iron contents indicated by peak to background ratios are generally lower

than those of the dolerites, with some exceptions. The IRIS data also suggest goethite is the iron mineral present in the metabasalts' weathering product. One sample of Lime Creek Metabasalt has a the diagnostic third goethite absorption at 0.67 μm. Thus the dominance of 0.83 μm absorption in the TM LR data over the metabasalts is explained by the presence of goethite in their weathering product.

8.7.4 Discussion

Table 8.2 summarises the differences between the dolerites and metabasalts. Discrimination is seen in the TM LR data between the majority of the dolerites, dominated by 0.49 μm absorption, and the majority of the metabasalts, dominated by 0.83 μm absorption. The XRD data in particular suggest that the dolerites are hematitic, whilst the metabasalts are more goethitic.

Hematite can be separated from goethite using high spectral resolution AVIRIS data (Kruse, 1990a). Such discrimination of two similar iron oxide minerals using lower spectral resolution TM data has only previously been described where economic concentrations of each mineral are exposed in open-pits where the other does not occur (Fraser, 1990a). In this field area the two minerals are probably occurring together and only form a lower concentration weathering product and it is significant that any discrimination is achieved at all. Fraser (op. cit.) achieved discrimination between hematite and goethite in TM data by using directed PCs on 0.66/0.49 μm and 0.83 μm/0.49 μm ratios. This method exploits differences between the two minerals' spectra in TM's 0.49 and 0.83 μm bands, the same bands that have been used to discriminate hematite and goethite in this field area.

The discrimination of hematitic dolerites from goethitic dolerites may allow another of the geological problems detailed in chapter 2 to be addressed. Blake (1982) has proposed that many of the dolerite dykes within the Corella Formation are in fact extrusive units. The Lime Creek Dolerite is clearly unlike the other dolerites in the area, displaying 0.83 μm absorption in the TM data and having a goethitic weathering product in the XRD data. It appears far more like the metabasalts (Table 8.2). Figure 8.44 shows the IRIS spectra of both the Lime Creek Dolerite and Lime Creek

Metabasalt and emphasises the overall spectral similarity of these rocks. The Lime Creek Dolerite is shown in Plate 8.26 and the Lime Creek Metabasalt in Plate 8.27. The similarity of the two lithologies, especially their weathering products, is clear. The conclusion is that all the Lime Creek rocks are mineralogically and spectrally the same, and seem more typical of the metabasalts in the area than the dolerites.

The redefinition of the Lime Creek Dolerite as metabasalt would fit Blake's (ibid.) hypothesis. This redefinition cannot be made using the remotely sensed data, however, despite the apparent spectral similarities between the Lime Creek Dolerite and the metabasalts. This is because the distinction between extrusive and intrusive rocks is not mineralogical. Textural evidence such as the presence of pillows and field relations such as cross-cutting contacts are required. As both rocks are metamorphosed, recognition of such features has been difficult. Thus the remotely sensed data provide extra information by demonstrating the anomalous nature of the Lime Creek Dolerite and its affinity with the Lime Creek Metabasalt, but cannot be used to solve the problem to satisfaction.

8.8 Structure

The existing geological map is the product of extensive air photograph interpretation and most of the major structures are mapped correctly. It is clear to any geologist who has used aerial photography as part of a mapping exercise that the synoptic view available from an airborne platform provides a powerful tool in the mapping of geological structures (Drury, 1987). Such structures are a dominant control on topography in many areas, even where exposure is poor or non-existent. The TM albedo image (Plate 5.5) is therefore an effective tool for mapping structure and all the structures on the 1:100 000 map can be identified (Enclosure 2.1). The Mary Kathleen Syncline, the existence of which has been disputed by Hawkins (1975), is seen clearly plunging to the south in the centre of the field area.

8.8.1 Confirmation of uncertain faults

Some faults which are mapped as uncertain are clearly seen as features in the satellite imagery. An example of this occurs parallel to and SE of the Wonga Fault, and is shown in Figure 8.5. Examination of Enclosure 5.1 reveals a clear lineation along the proposed fault. Detection of such a feature makes it likely that the proposed fault is present, and field checking can be rapid and effective.

The detection of faults and folds in imagery does not only rely on their having a physical expression in the topography. In the above example, there is also a spectral contrast across the southern end of the fault. This closely corresponds to an offset in the proposed outcrop of Pea_3 in this area, as depicted in Figure 8.5.

8.8.2 Spectral signature of faults

Examination of the NS001 LR data in Plate 7.9 suggests that increased 2.22 μm absorption occurs along the Cameron Fault in places. Plate 8.28 is a view of this fault in the field, which forms a clear negative feature in the landscape. Such a feature will form a deeper soil and have increased moisture, especially in the wet season. Hence, as is seen in the distance, a greater vegetation density results along parts of the fault. Greenbaum and Amos (1991) report a similar coincidence of increased vegetation and lineaments in TM data over Zimbabwe.

8.8.3 Masked faults

As faults tend to form negative topographic features they are also often covered by the weathering product of one or other of the adjacent lithologies. Whichever forms the higher feature will appear to cover more area than in reality, and the position of the fault will appear displaced in the imagery. Plate 8.29 is taken from the south of the Cameron Fault, on the Argylla Formation, looking across the fault to the Corella Formation on the northern side. The fault plane lies along the field assistant's arms, but is covered by weathering product from the Argylla Formation for up to 100 m northward across the fault. In the enlargement of the NS001 imagery shown in Plate 6.2

the fault is clearly obscured by Argylla Formation debris with 2.22 μm absorption at this point.

8.8.4 New Faults

Plate 8.30 is a 1:25 000 scale enlargement of the NS001 LR data over a portion of the Magna Lynn Metabasalt covered by traverse 17. The area of 0.49 μm and 0.83 μm absorption (blue-green hues) is the metabasalt and the area of 0.83 μm and 2.22 μm absorption (green-red hues) is the Argylla Formation. On the 1:100 000 map the latter is shown enclosing the metabasalt and also occurring within it as an enclosed, folded limb (Figure 8.45). In the NS001 data several unmapped faults are detected which alter the interpretation significantly. The apparent folds within the enclosed Argylla Formation are in fact offsets of a single unit due to faulting.

In the TM data the enclosed limb of the Argylla Formation cannot be discriminated from the metabasalt at all. The increased spatial resolution of the NS001 data not only allows more accurate mapping of the outcrop pattern, but also the separation of two spectrally distinct units which the TM cannot discriminate when mixed at this scale. This again shows that increased spatial resolution also increases the effective spectral resolution by increasing the sampling frequency.

8.9 Mineralisation

The remotely sensed data can contribute to the debate about the origin of the mineralisation described in section 2.8.6, which centres on the source of the uranium, the importance of structural controls and the relationships of the rocks involved.

The AGR data suggest only one reasonable source for the uranium, that being the Burstall Granite. This body has consistently high counts for all three radioelements, and is close to the site of the mineralisation within the adjacent Corella Formation sediments to the west. The TM data also show that the Burstall Granite is unlike the others in the area. The importance of the link between the Burstall Granite and the adjacent sediments in the Mary Kathleen Syncline is also seen in Plate 8.31, which shows TM's

thermal infrared band over the granite and syncline. Both have a similar dark tone, as do other quartz-rich rocks in the area such as the quartzites in the SW. Magnetic data over the area suggest that granite lies below the syncline (D. Richards, personal communication). This association of a granite rich in radioelements and the calcareous rock of the Corella Formation is intimately associated with the uranium mineralisation at Mary Kathleen. Both the Burstall Granite and the Corella Formation have distinctive spectral responses which would be detectable in TM data over other areas. A prospective area has been defined using the TM data over some pegmatites related to the Burstall Granite which intrude member Pkc_2 of the Corella Formation with the correct spectral signature in the NE of the field area (section 8.4.2.3).

The integrated TM and AGR data shown in Plate 6.16 and Plate 6.18 depict a division between the northern and southern parts of the Mary Kathleen Syncline. As this division cuts directly across-strike it is more likely to be related to the mineralisation than the original sediments, but the significance of this division could not be identified during a rapid traverse in the field. The potassium enrichment of the sediments in the nose of the syncline could however be further evidence that circulating fluids from the Burstall granite were involved in the mineralisation. In the GMS data shown in Plate 8.10 the shear described by some workers is seen running N-S to the east of the deposit and there is a spectral contrast across it. The pit area has 2.352 μm absorption typical of calc-silicates but east of the shear the absorption seen is more typical of clay minerals. This may be related to a calcium rich smectite reported east of the shear by Green et al (1985). This outcrop pattern is local to the mine area and the shear is seen to swing westward and terminate against the Argylla Formation, isolating the mineralisation. The GMS visible and near infrared data are very noisy (Plate 8.32) but a change eastward across the shear from absorption at longer wavelengths more typical of goethite to absorption at shorter wavelengths more typical of hematite is seen. The importance of the shear is underlined.

Thus the important factors in the mineralisation appear to be a shear associated with a change in both clay and iron oxide mineralogy, and the intrusion of member Pkc_2 of the Corella Formation by the Burstall Granite.

8.10 Metamorphism

Metamorphism received little attention in this project, as no specific problem requiring attention came to light during research at the start of the work. The mineral assemblages described in section 2.4 have not been identified in the remotely sensed data. The metamorphic minerals rarely dominate an exposed surface sufficiently to be detectable, due to the ubiquitous development of iron oxides during weathering.

8.11 Summary

The major geological divisions can be mapped in all of the data sets studied. In many places much new geological information can be gained from the remotely sensed data, allowing the known geological problems in the area to be addressed more rapidly than would be possible by conventional mapping. Improvements have been made to the mapping of the Tewinga and Mary Kathleen Groups and the Wonga and Burstall Granites in particular. The remotely sensed data strongly support the downgrading of the Corella Formation in the east of the area to the Corella Beds. Uncertain structures have been confirmed and new ones discovered. Finally, recommendations have been made for future mineral exploration in the area, based on the remotely sensed data.

All the data sets have contributed to this process. The integration of the TM and AGR data proved particularly useful in some instances, making clear geological divisions which could not easily be mapped in other data sets or in the field. Of the processing techniques used on the radiance data, logarithmic residuals was the most informative. The LR technique aided structural mapping and data integration, through the production of an albedo image. Discrimination was greatly enhanced in the LR data. Finally, the LR data allowed the goal of identification to be addressed. The near-reflectance produced by the technique was consistent between all three radiance data sets. Even with the lower resolution TM data the treatment of the data as having a physical meaning was worthwhile. Two different iron oxide minerals were discriminated, and several materials causing 2.22 μm absorption where separated due to differing near-reflectance values at other wavelengths. Figure 8.46 illustrates the success achieved in distinguishing spectrally similar materials using the logarithmic residual technique.

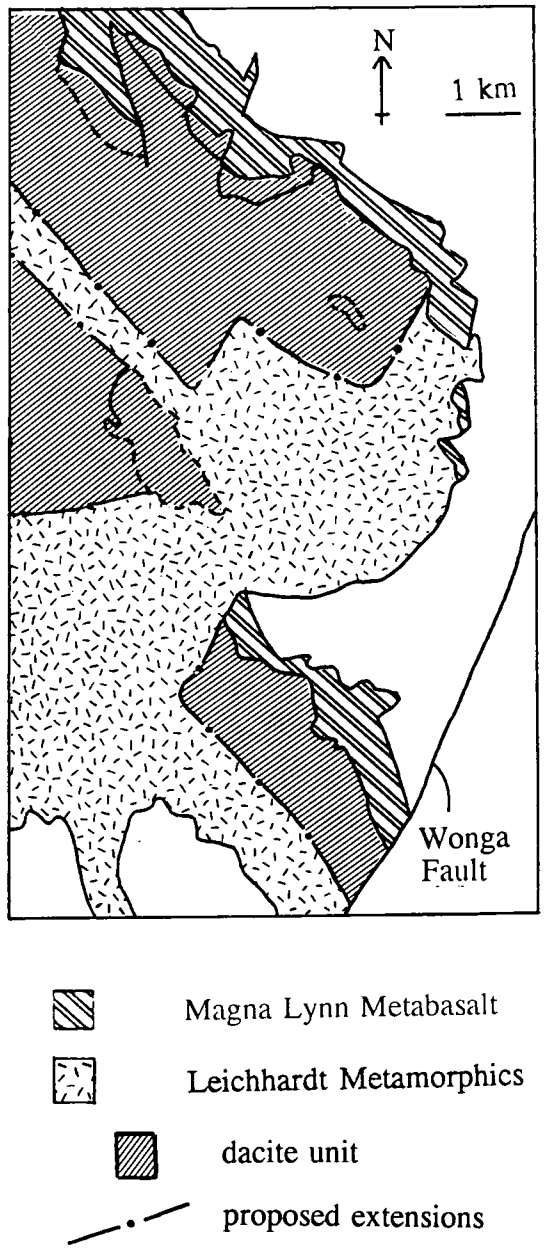

Figure 8.1 Geological map of the Leichhardt Metamorphics NW of the Wonga Fault, depicting proposed extensions to the dacite unit.

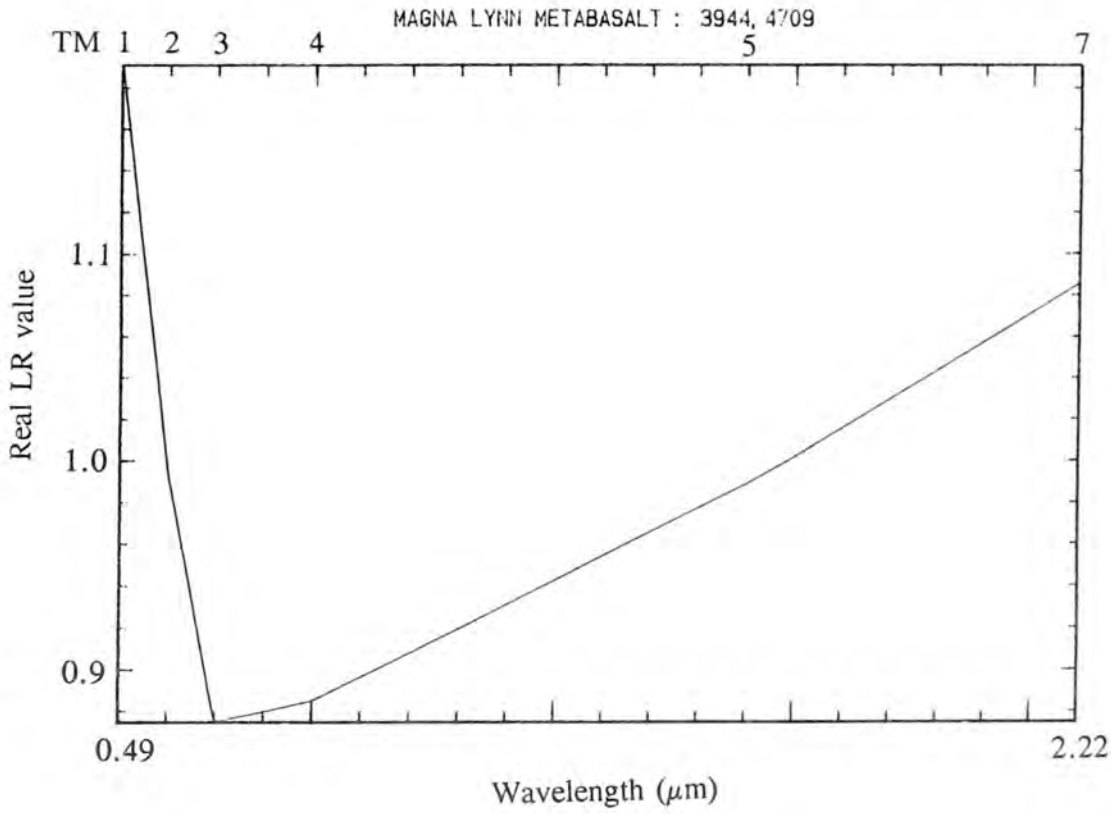

Figure 8.2 TM LR pseudo-spectrum of the Magna Lynn Metabasalt in NE of field area.

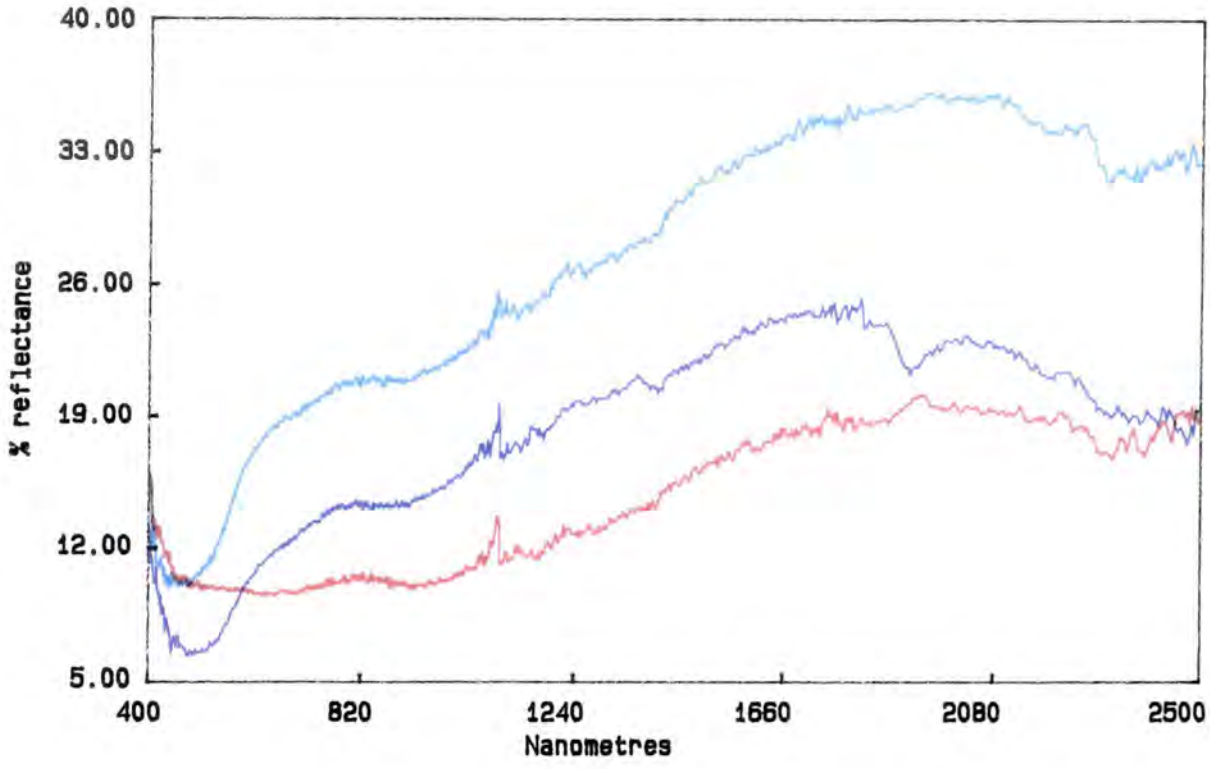

Figure 8.3 IRIS spectra for the Magna Lynn Metabasalt at locality 13.

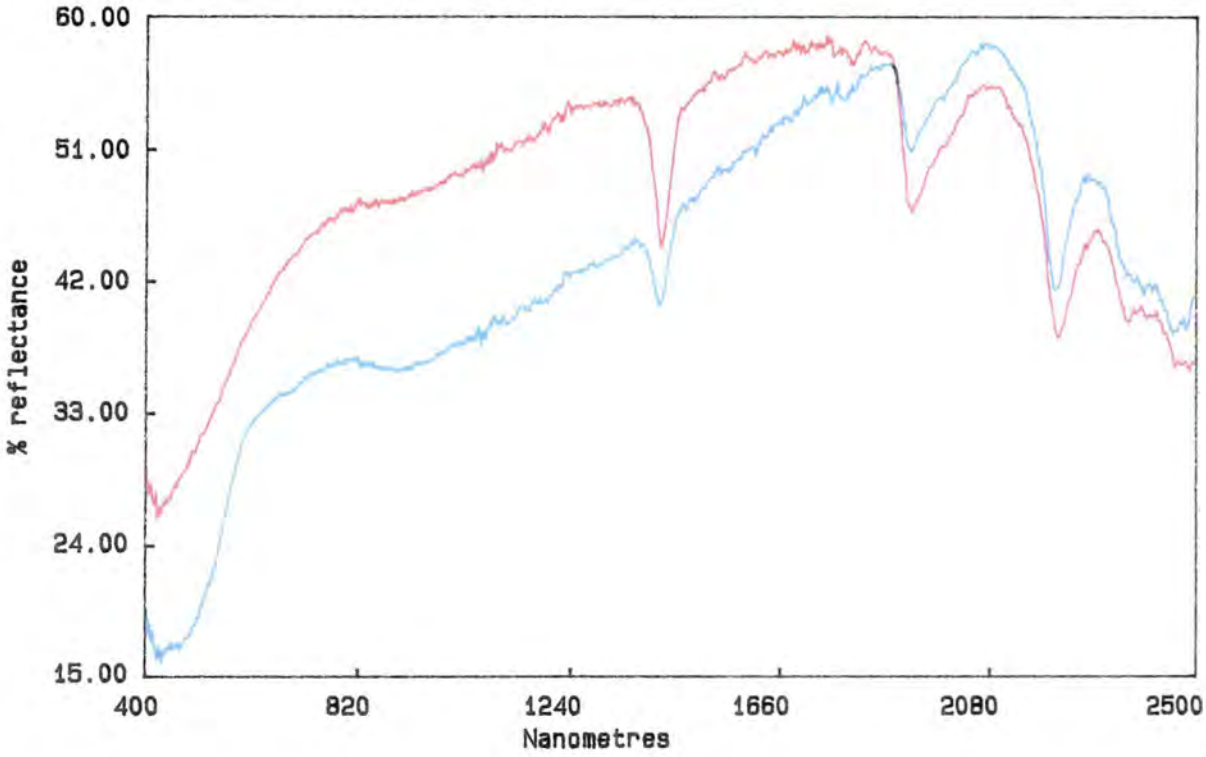

Figure 8.4 IRIS spectra for a mica-schist of the Argylla Formation at locality 8.

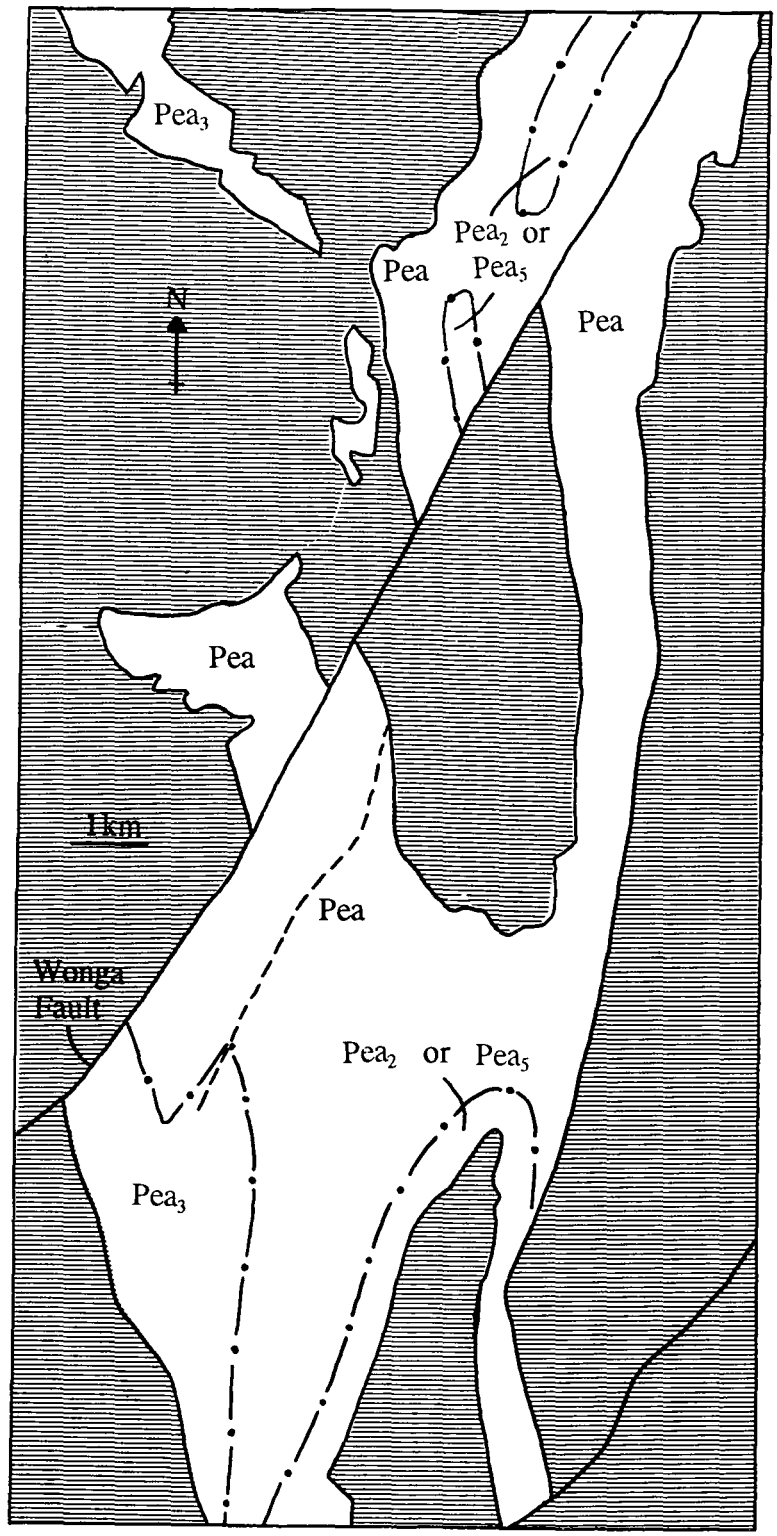

Figure 8.5 Proposed revisions to the Argylla Formation's stratigraphy in the west of the field area made using a combination of TM and AGR data.

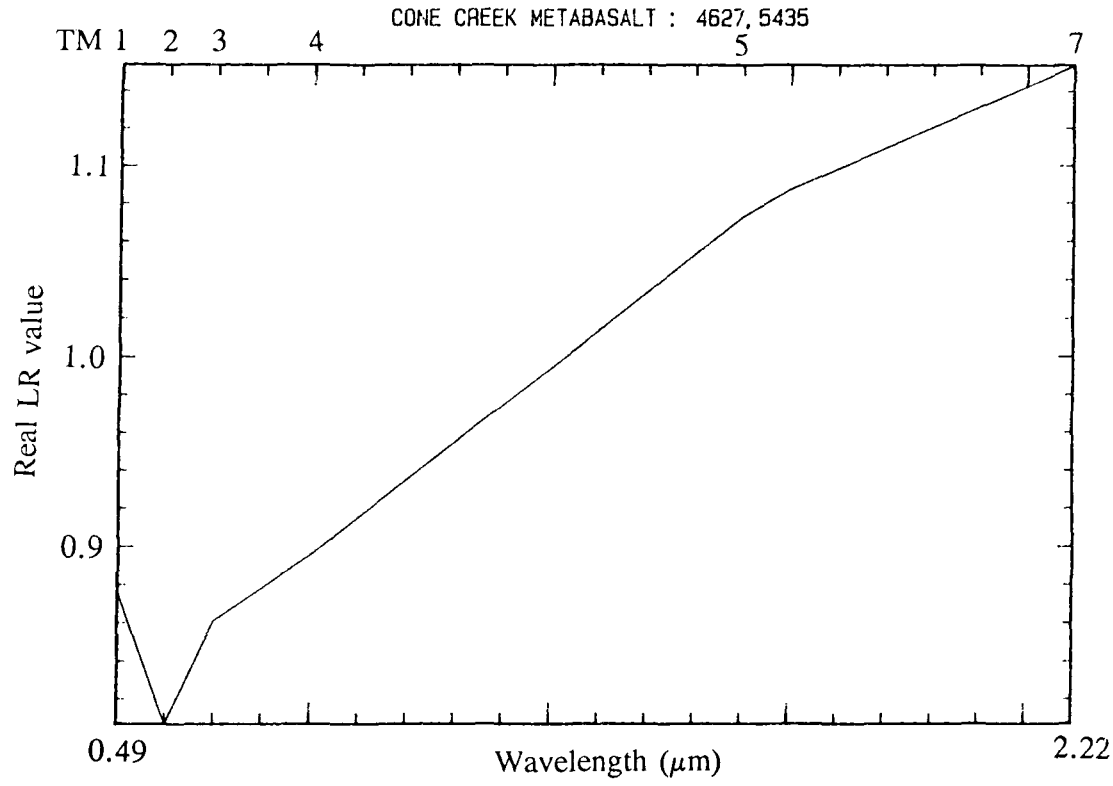

Figure 8.6 TM LR pseudo-spectrum for the Cone Creek Metabasalt.

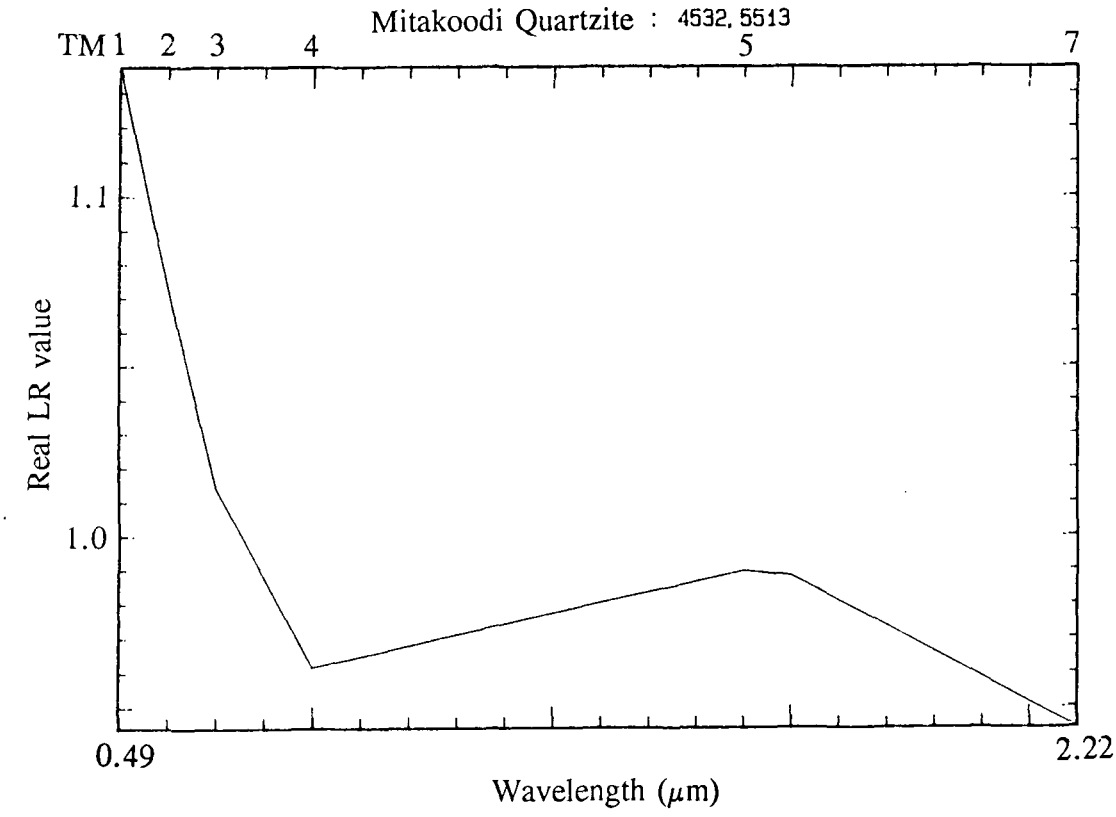

Figure 8.7 TM LR pseudo-spectrum for the Mitakoodi Quartzite.

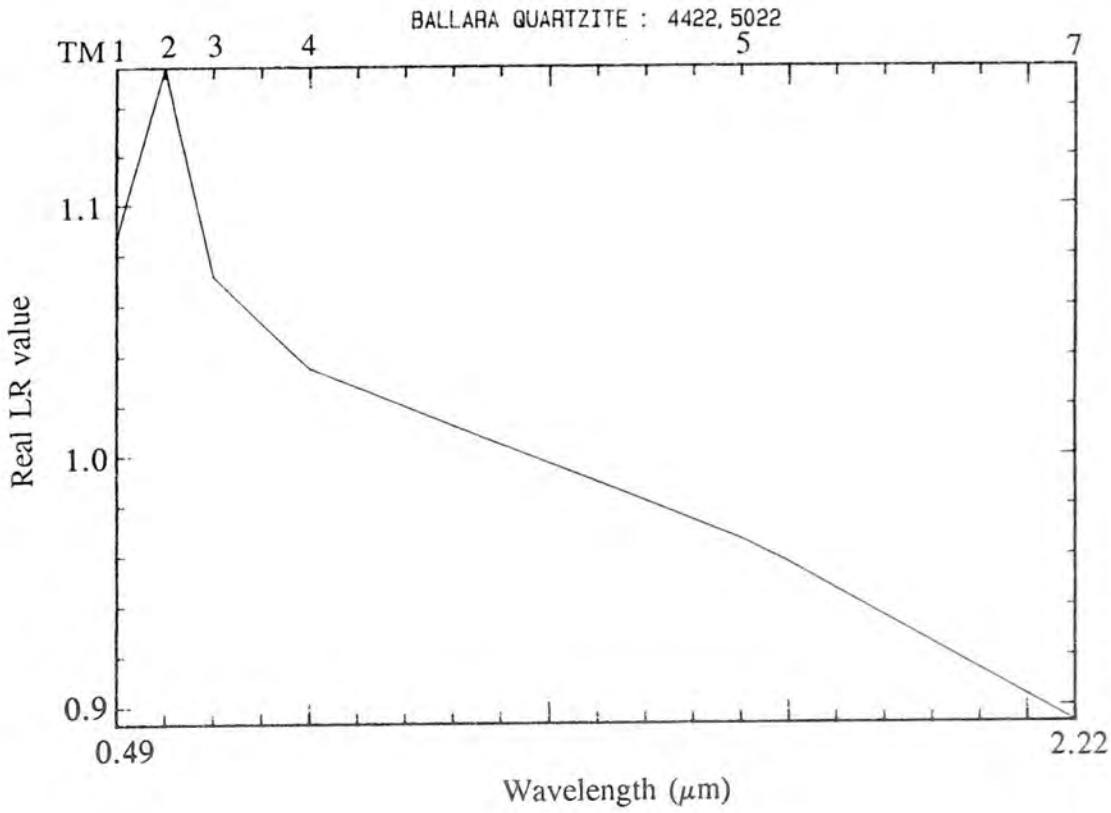

Figure 8.8 TM LR pseudo-spectrum for the Ballara Quartzite.

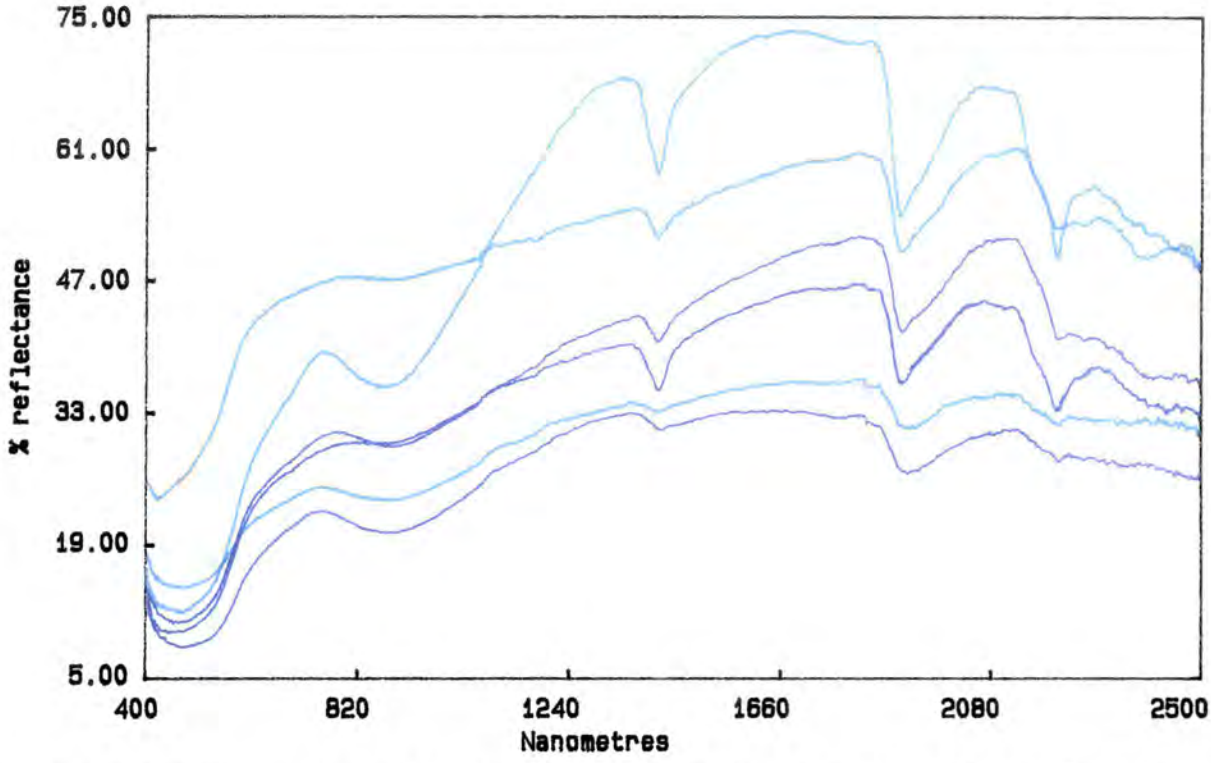

Figure 8.9 IRIS spectra for the Ballara Quartzite at localities 220, 223 and 231 along the east limb of the Rosebud Syncline.

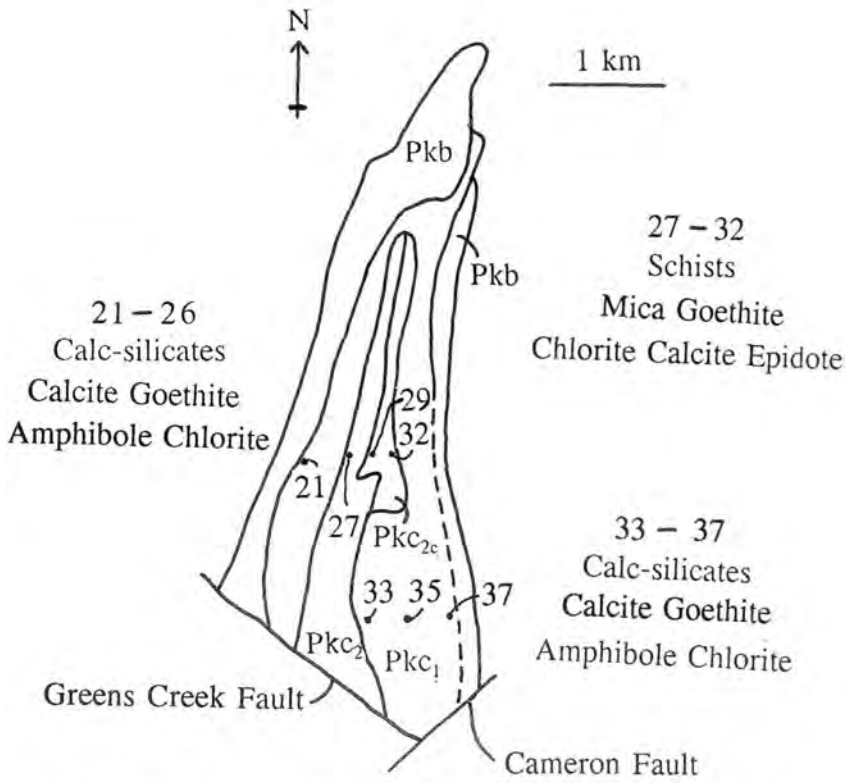

Figure 8.10 Summary of the IRIS results from traverses 2 and 3 across Corella Formation in the Rosebud Syncline.

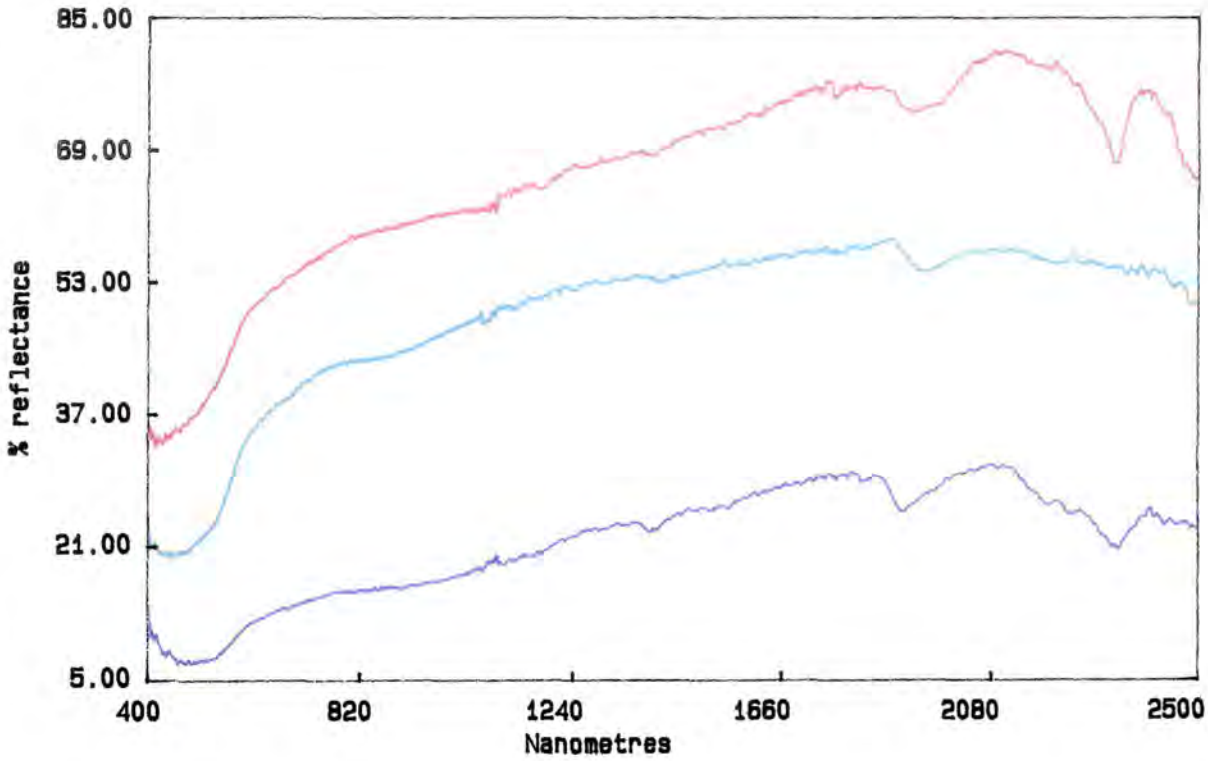

Figure 8.11 IRIS spectra of Pkc_1 carbonate in the Rosebud Syncline at locality 35.

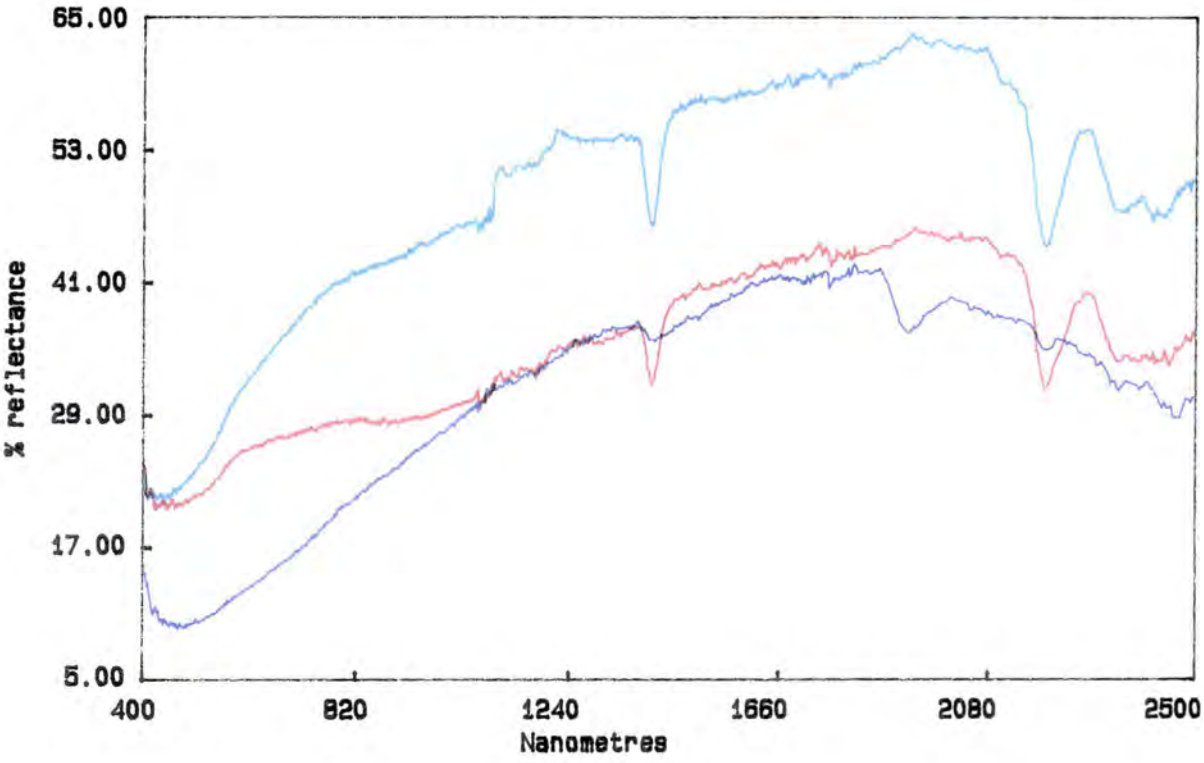

Figure 8.12 IRIS spectra of Pkc_2 schist in the Rosebud Syncline at locality 27.

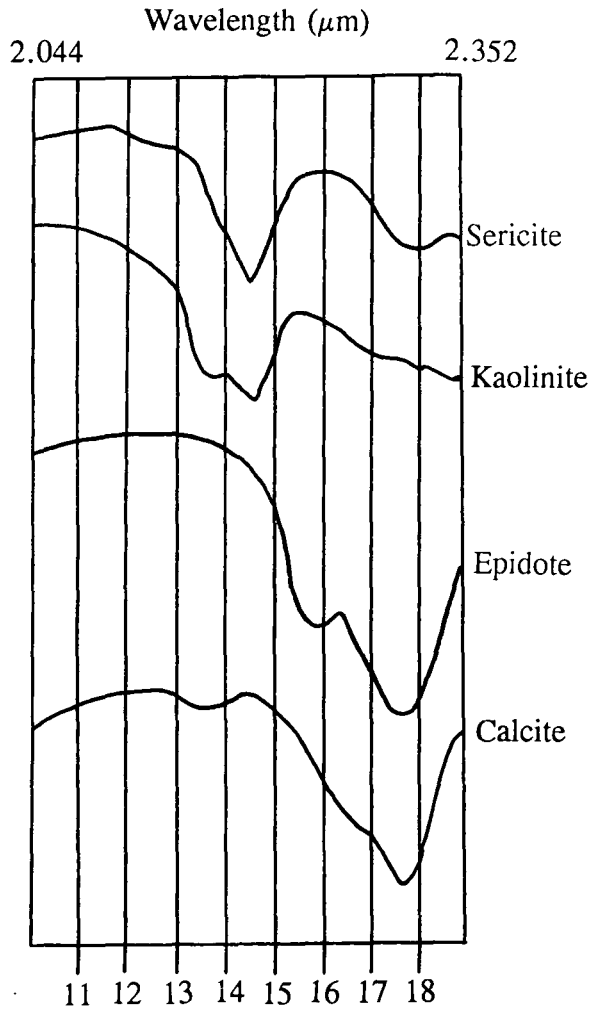

Figure 8.13 The reflectance of various minerals across the GMS band passes.

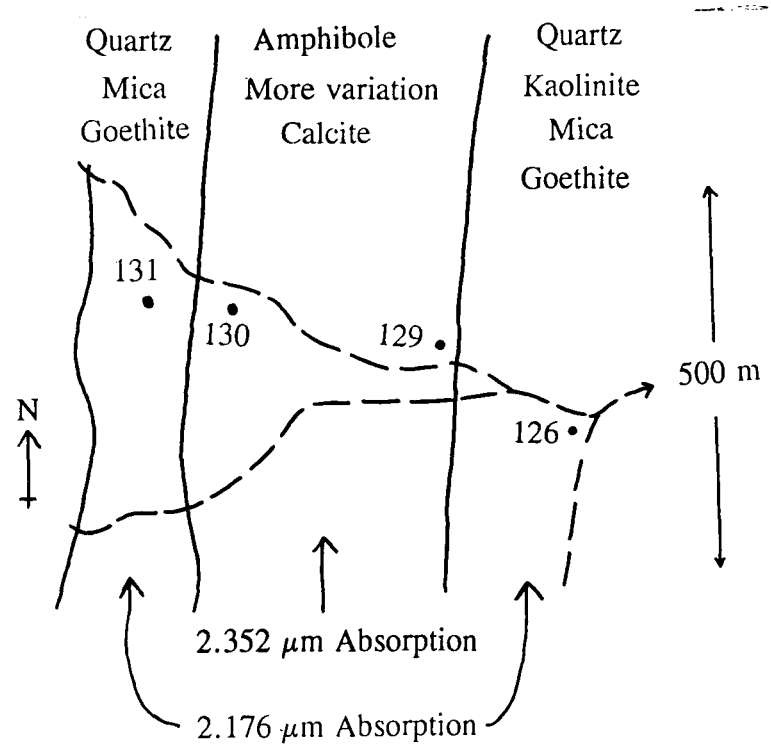

Figure 8.14 Summary of the IRIS results for the Corella Formation along the Final Creek traverse in the Mary Kathleen Syncline.

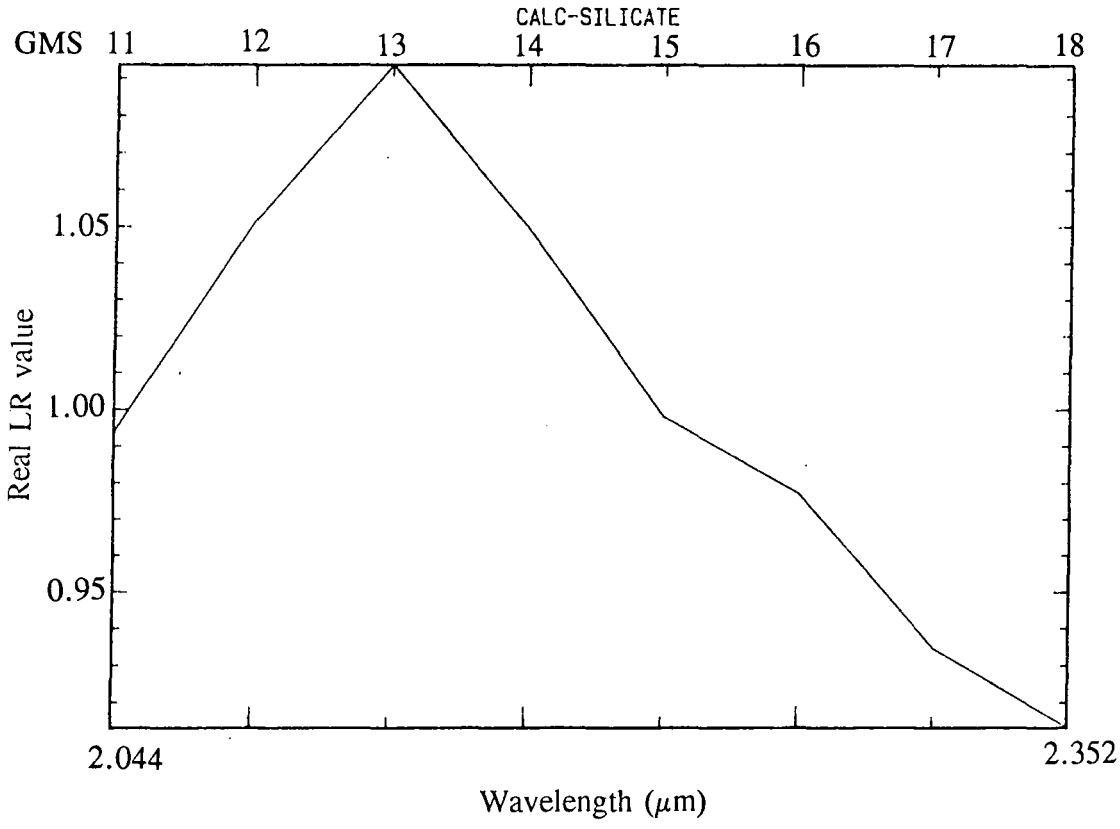

Figure 8.15 GMS LR spectrum the over calc-silicates of the Corella Formation in the Mary Kathleen Syncline.

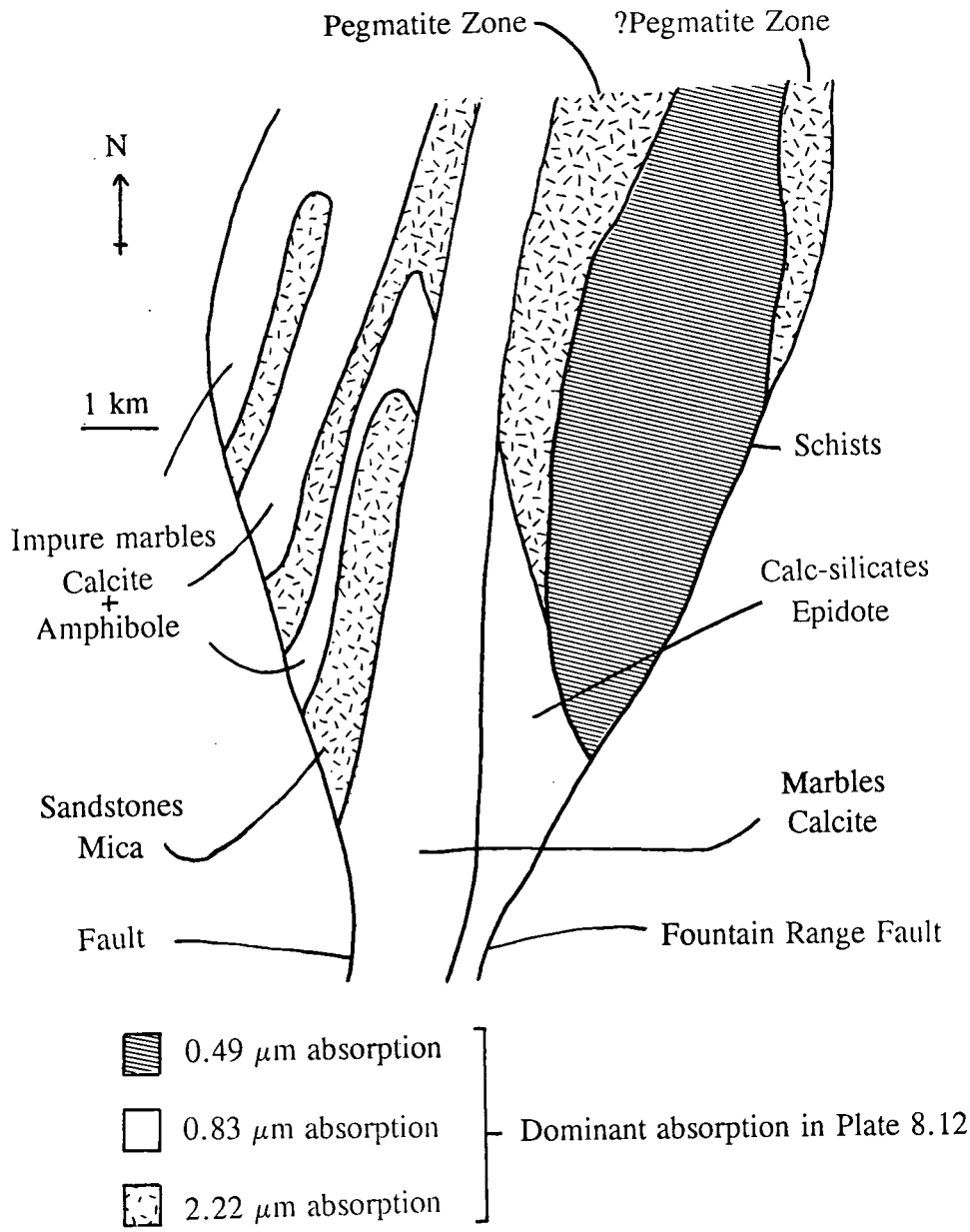

Figure 8.16 A synthesis of the studies findings in the Corella Formation NE of the Burstall Granite. The divisions shown are spectral, and are not intended to form a map. A revised map for the area is included in the back pocket as Enclosure 8.1.

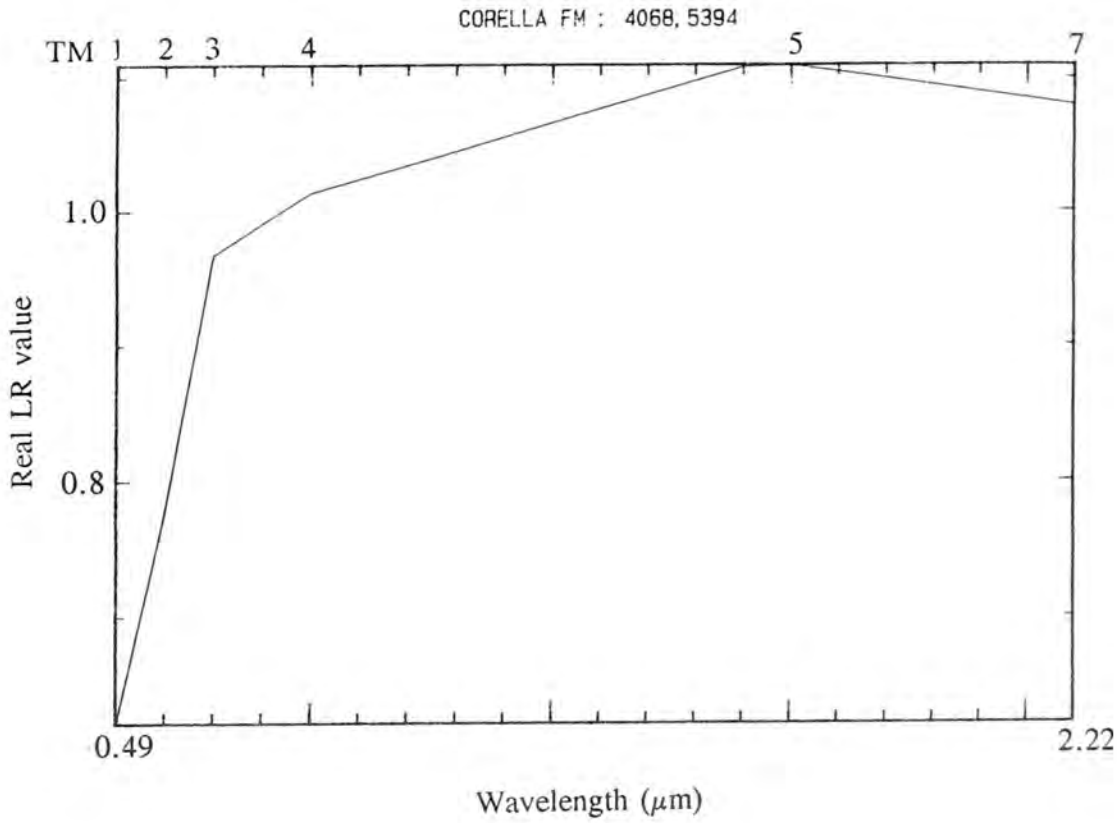

Figure 8.17 TM LR pseudo-spectrum for Pkc_2 schists in the eastern limb of the Corella Formation's eastern exposures.

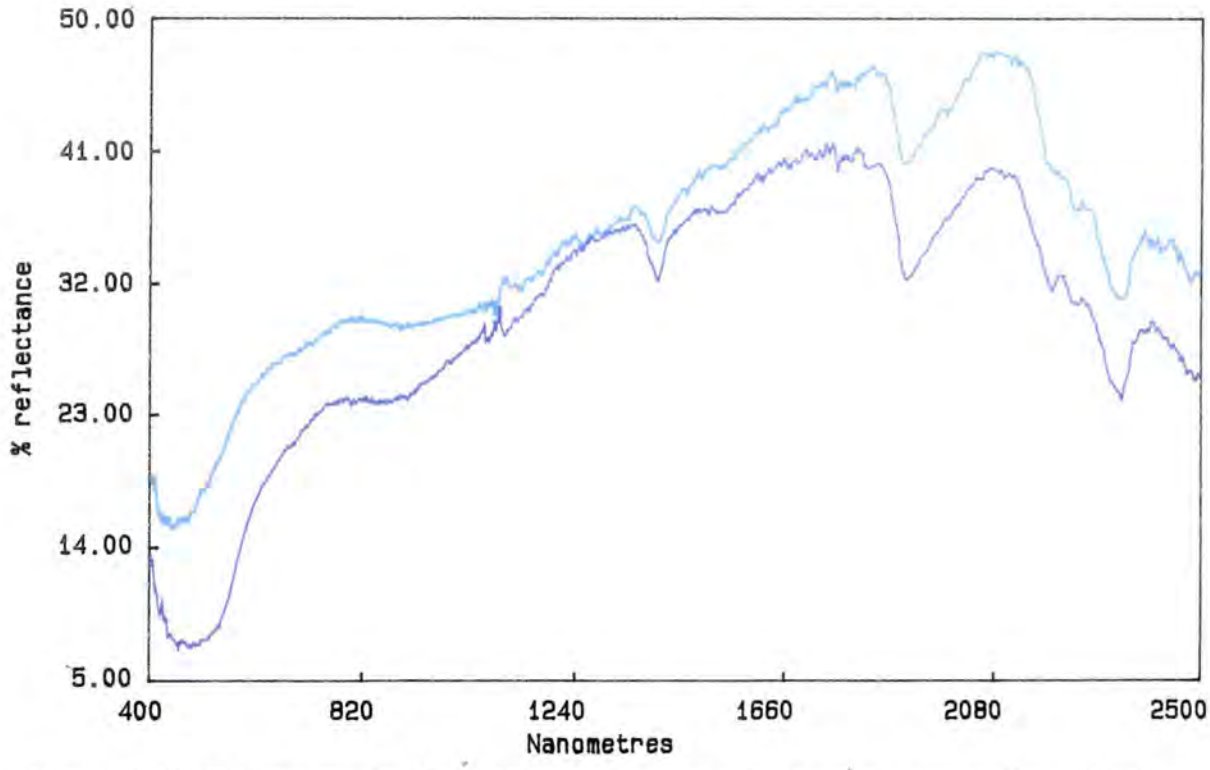

Figure 8.18 IRIS spectra for Pkc_2 schists in the eastern limb of the Corella Formation's eastern exposures.

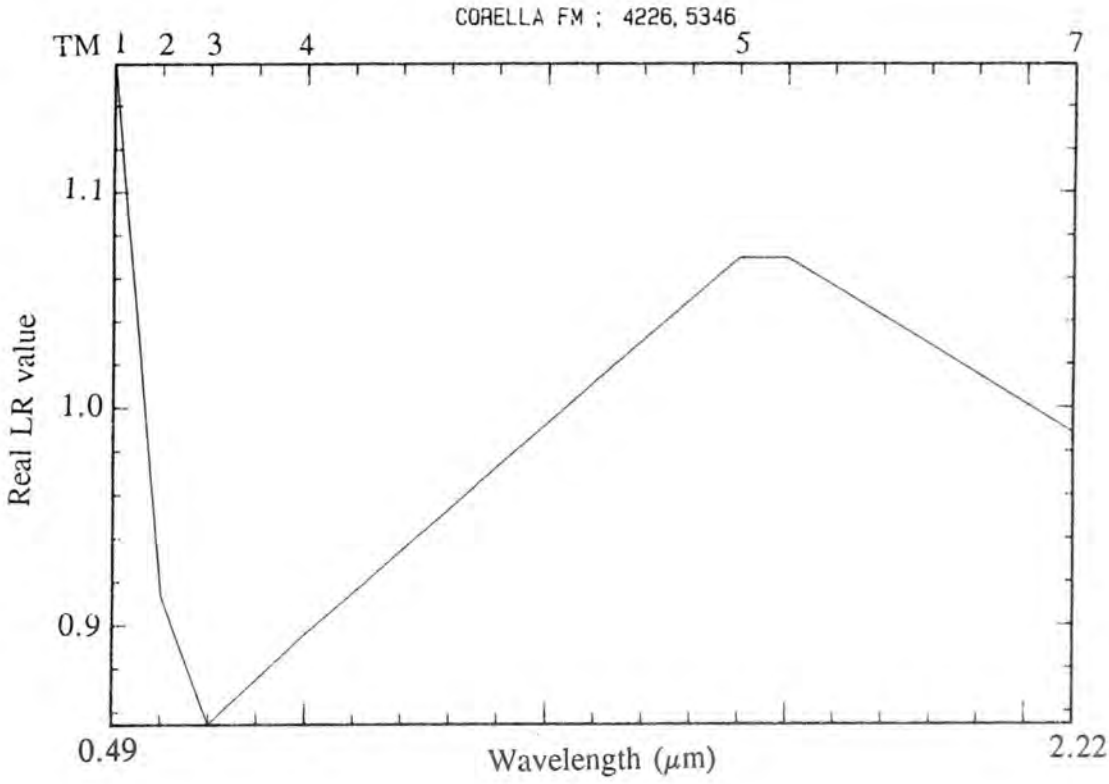

Figure 8.19 TM LR pseudo-spectrum for Pkc_2 calc-silicates in the eastern limb of the Corella Formation's eastern exposures.

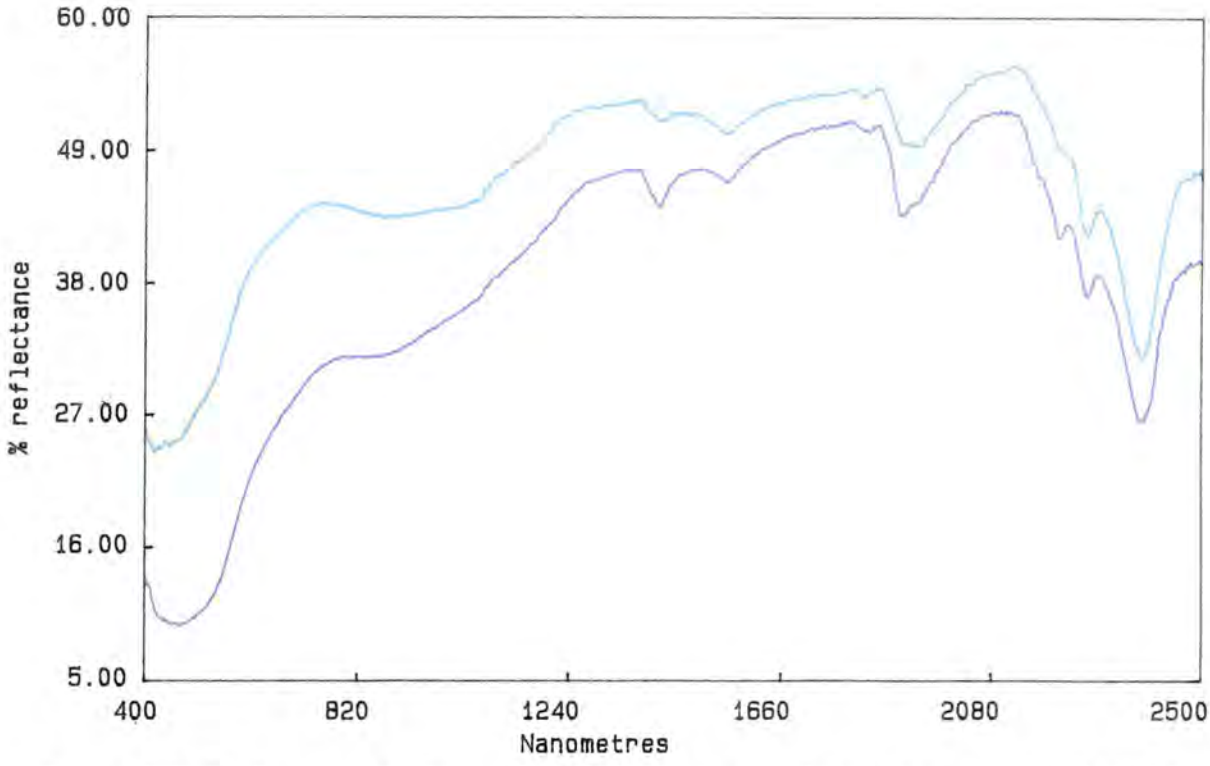

Figure 8.20 IRIS spectra for Pkc_2 calc-silicates at locality 241 in the eastern limb of the Corella Formation's eastern exposures.

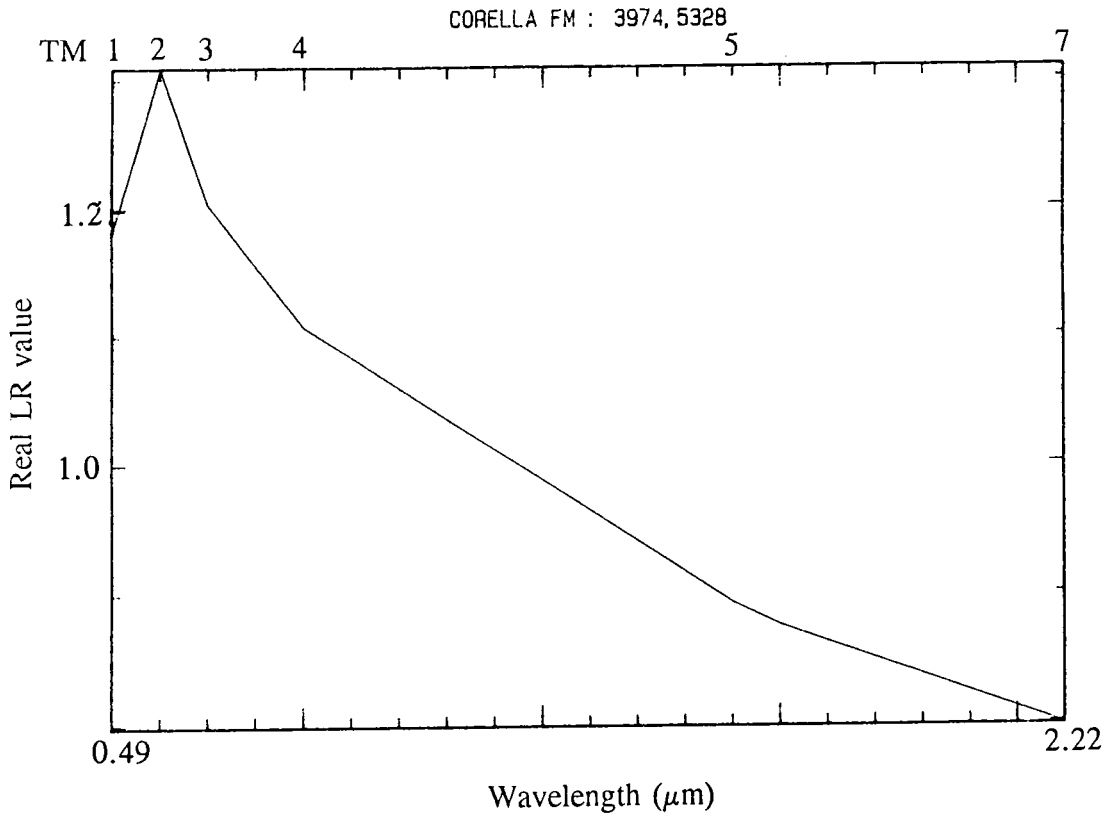

Figure 8.21 TM LR pseudo-spectrum for the pegmatite zone in the eastern limb of the Corella Formation's eastern exposures.

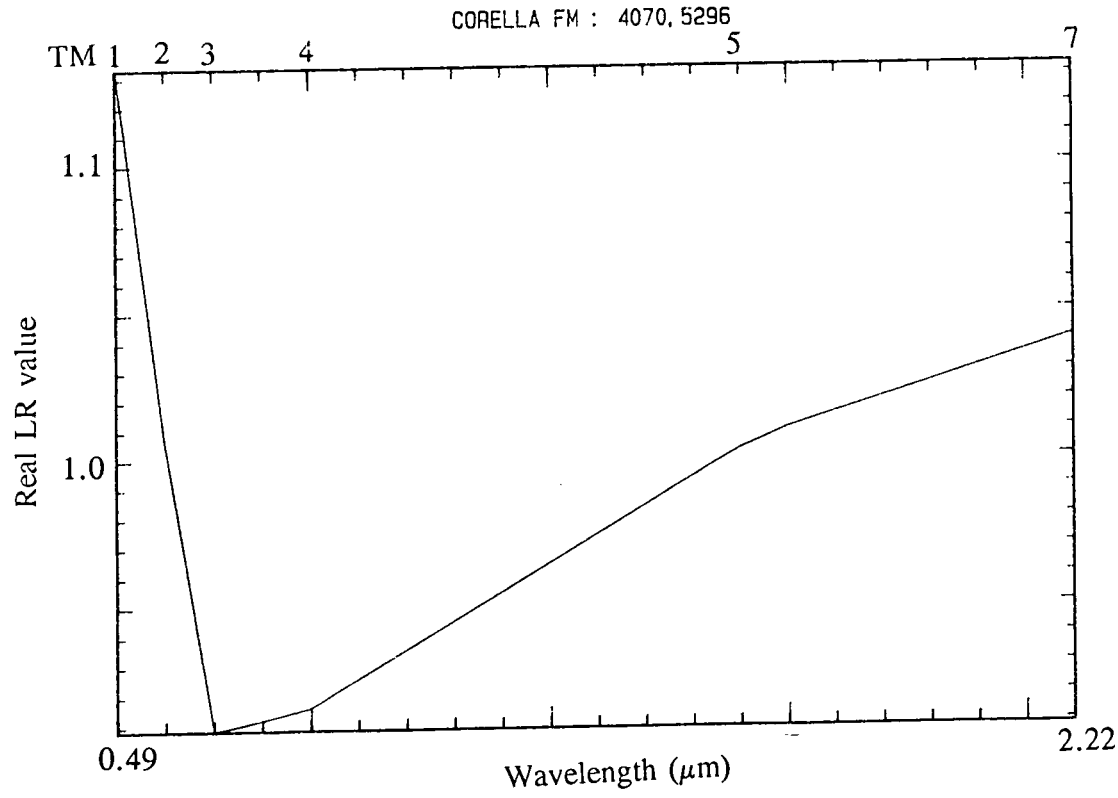

Figure 8.22 TM LR pseudo-spectrum for Pkc_1 in the central limb of the Corella Formation's eastern exposures.

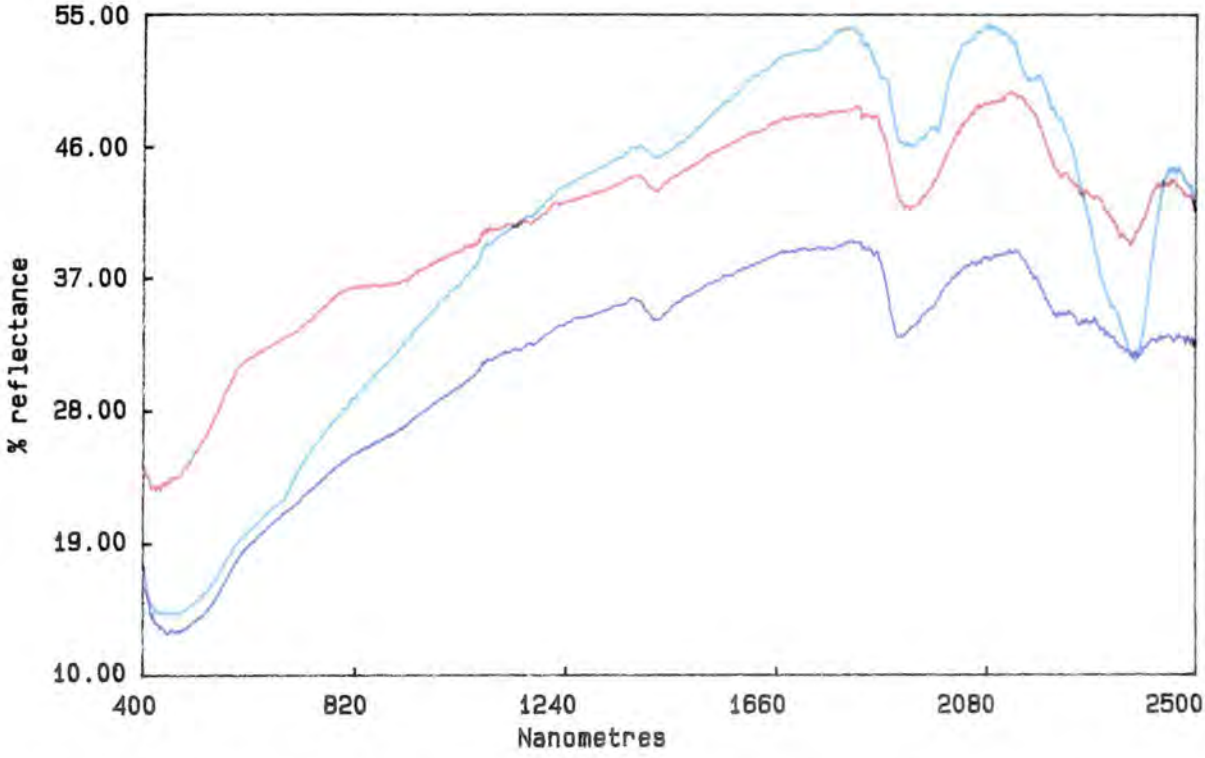

Figure 8.23 IRIS spectra for Pkc_1 at locality 242 in the central limb of the Corella Formation's eastern exposures.

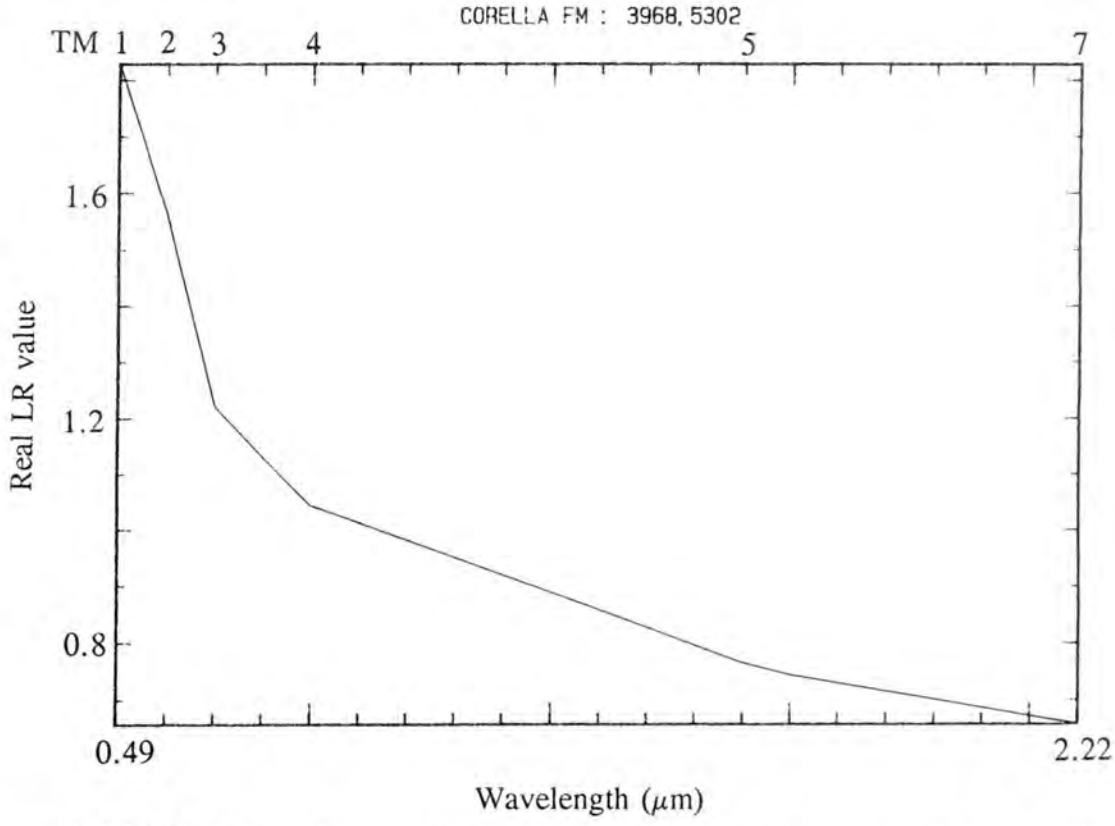

Figure 8.24 TM LR pseudo-spectrum for the calcite pit at locality 89 within Pkc_1 in the central limb of the Corella Formation's eastern exposures.

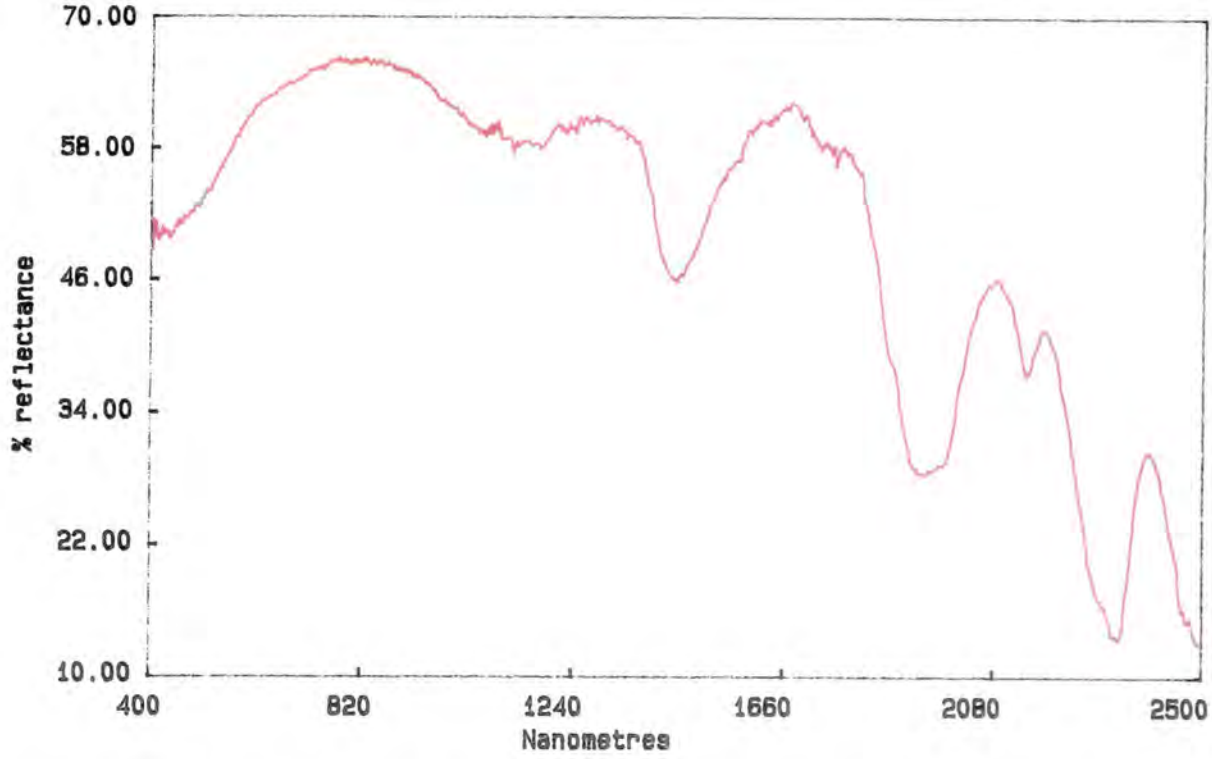

Figure 8.25 IRIS spectrum for the calcite pit at locality 89 within Pkc_1 in the central limb of the Corella Formation's eastern exposures.

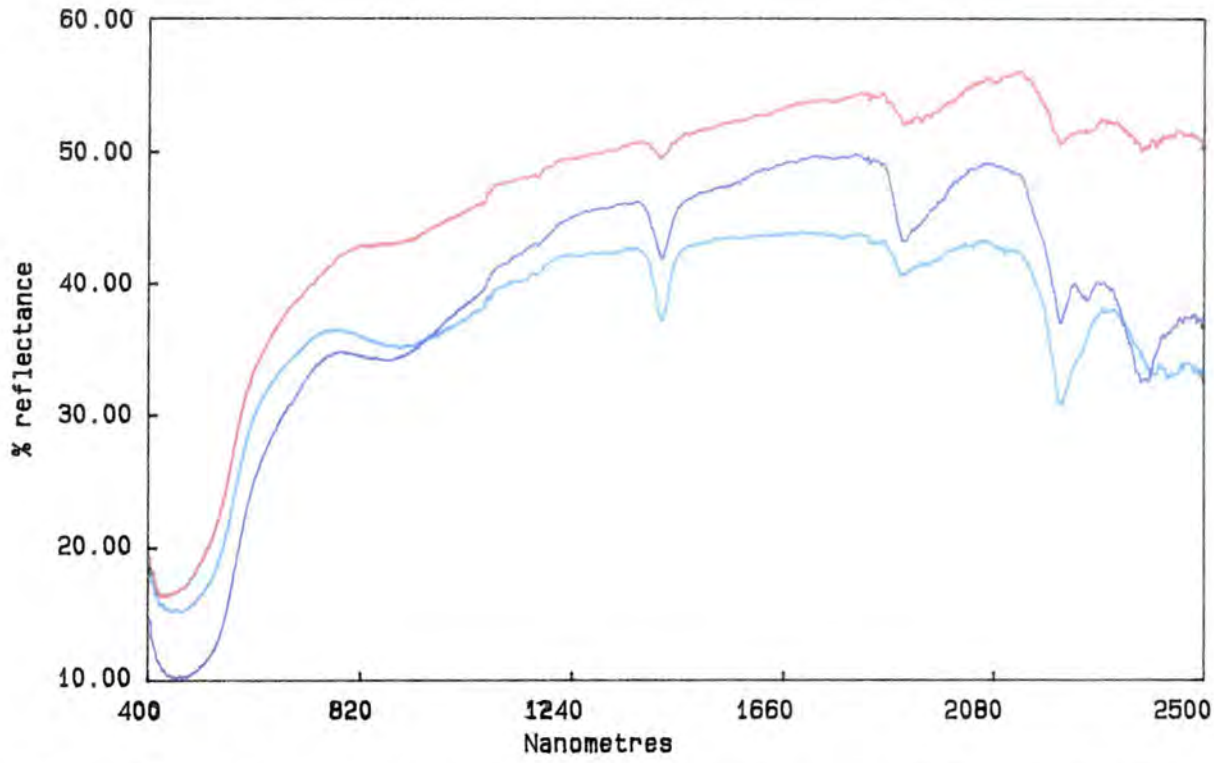

Figure 8.26 IRIS spectra for Pkc_2 at locality 244 in the western limb of the Corella Formation's eastern exposures: micaceous sandstone unit.

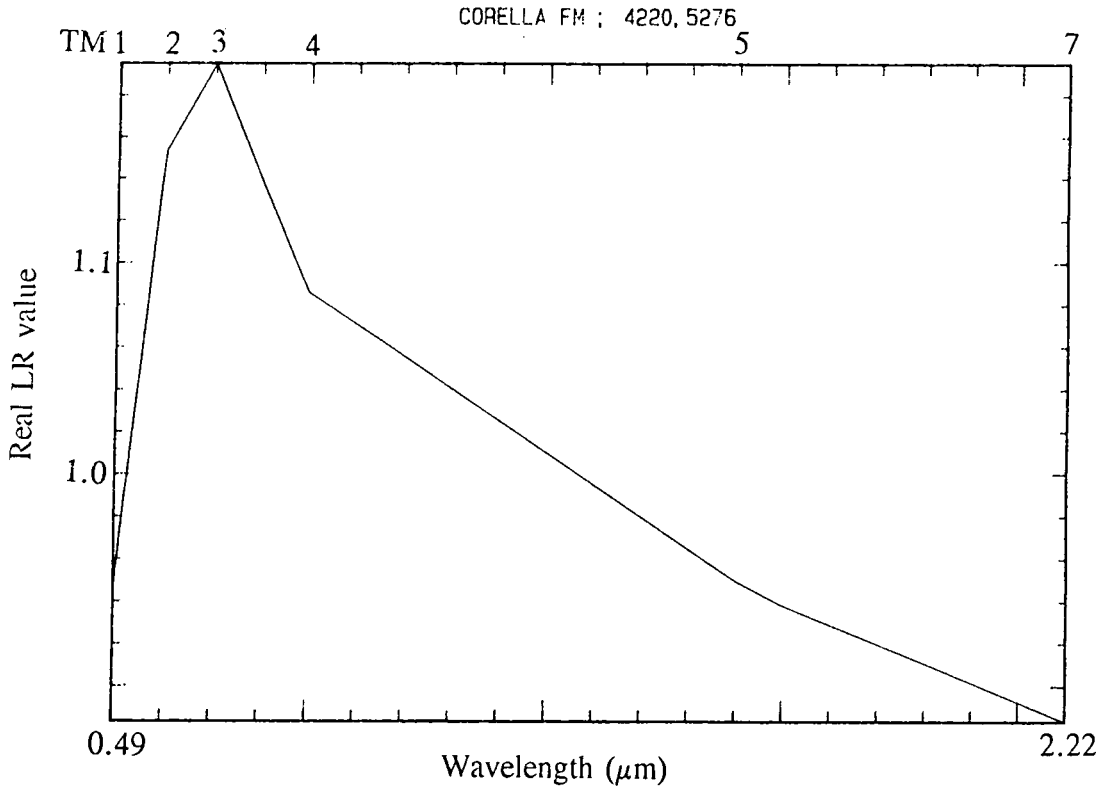

Figure 8.27 TM LR pseudo-spectrum for Pkc_2 in the western limb of the Corella Formation's eastern exposures: micaceous sandstone unit.

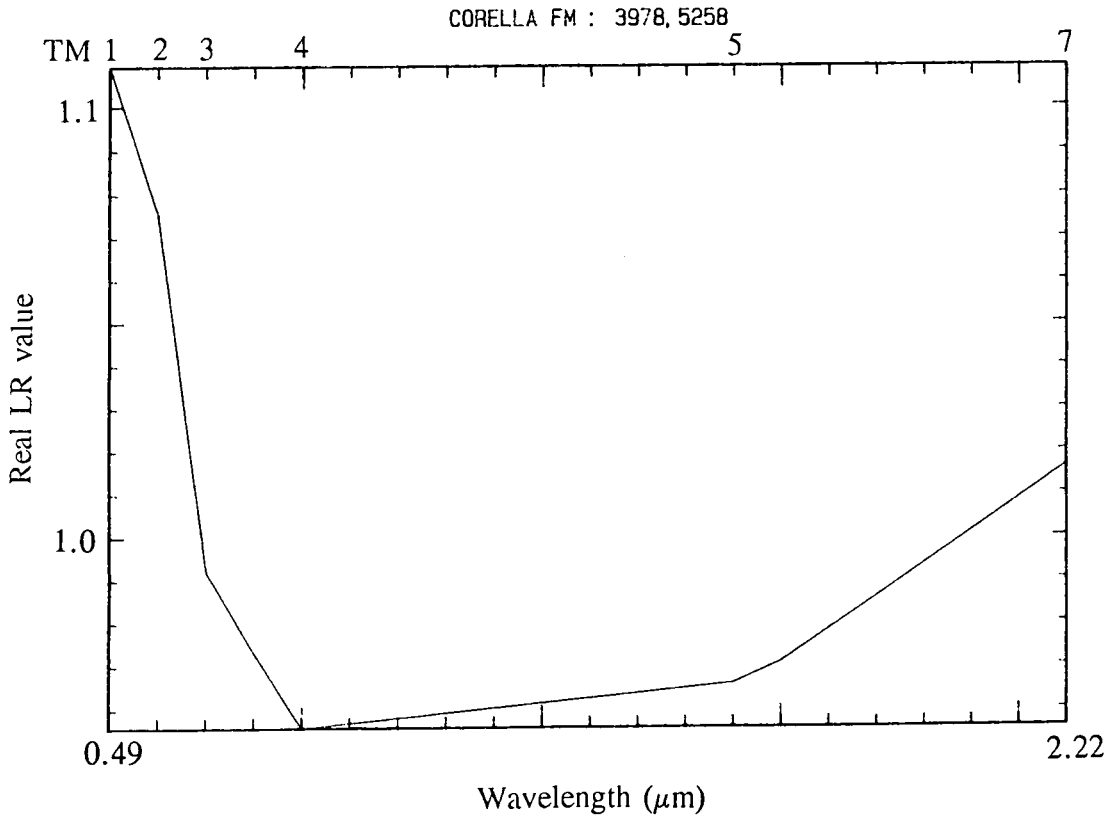

Figure 8.28 TM LR pseudo-spectrum for Pkc_2 in the western limb of the Corella Formation's eastern exposures: carbonate unit.

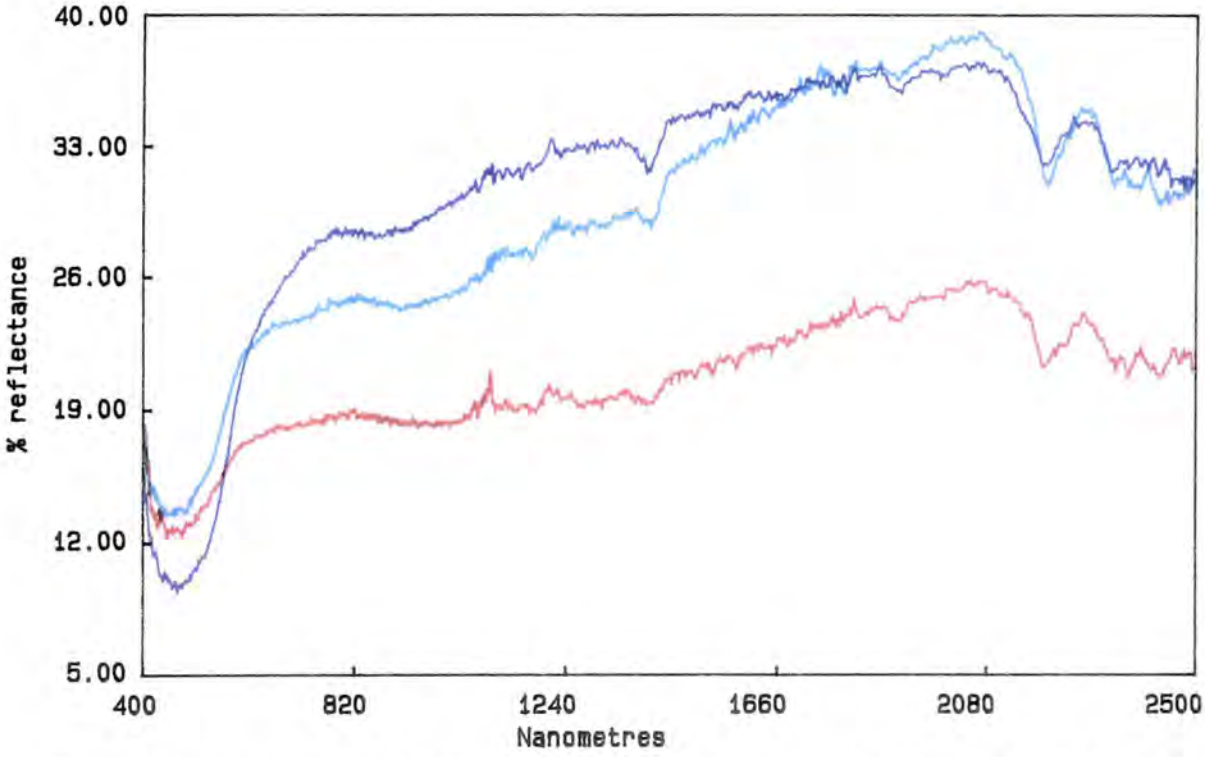

Figure 8.29 IRIS spectra for Pkc_2 at locality 88 in the western limb of the Corella Formation's eastern exposures: carbonate unit.

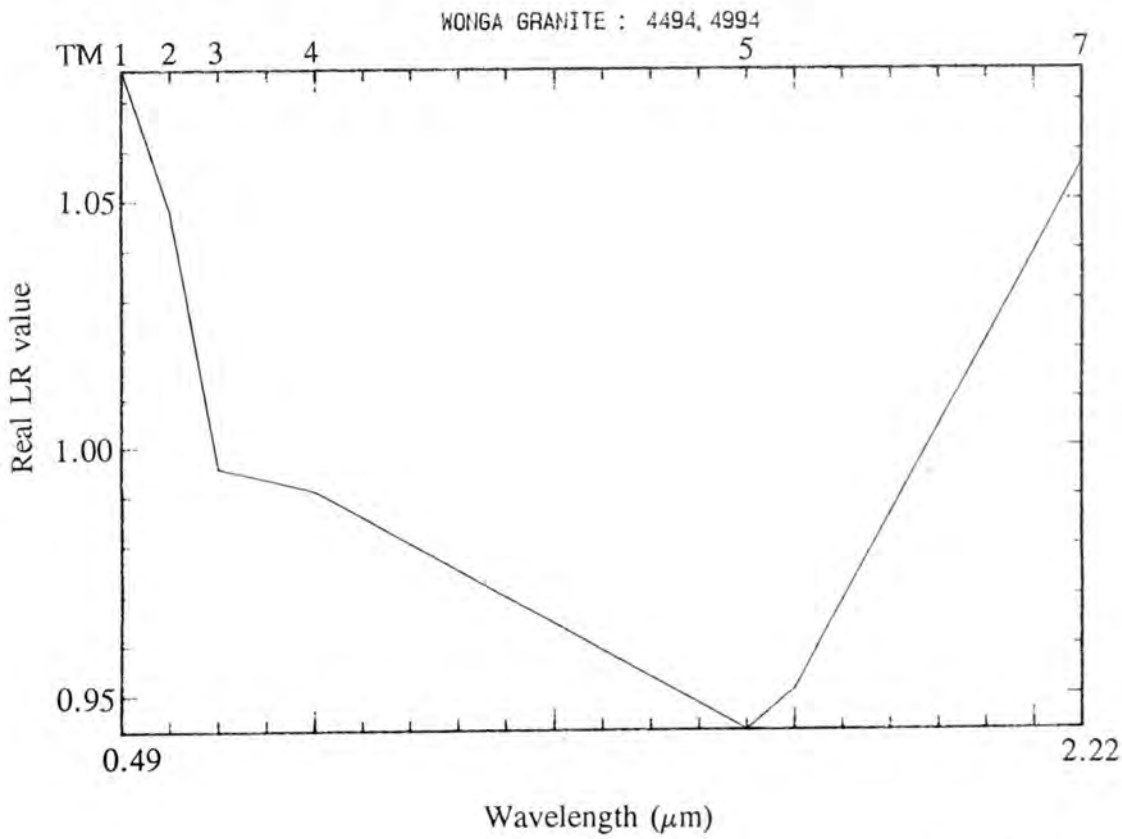

Figure 8.30 a) TM LR pseudo-spectrum over the Wonga Granite's weathered surface.

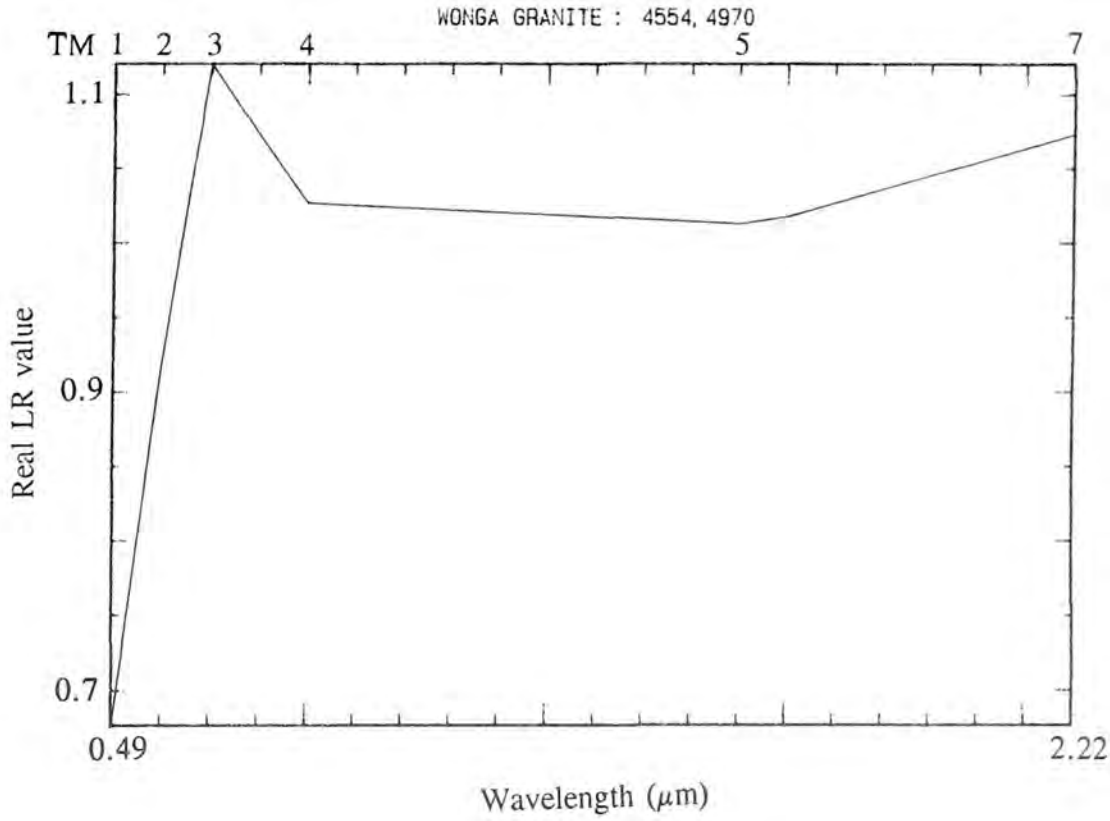

Figure 8.30 b) TM LR pseudo-spectrum over the deep iron enriched Wonga soil.

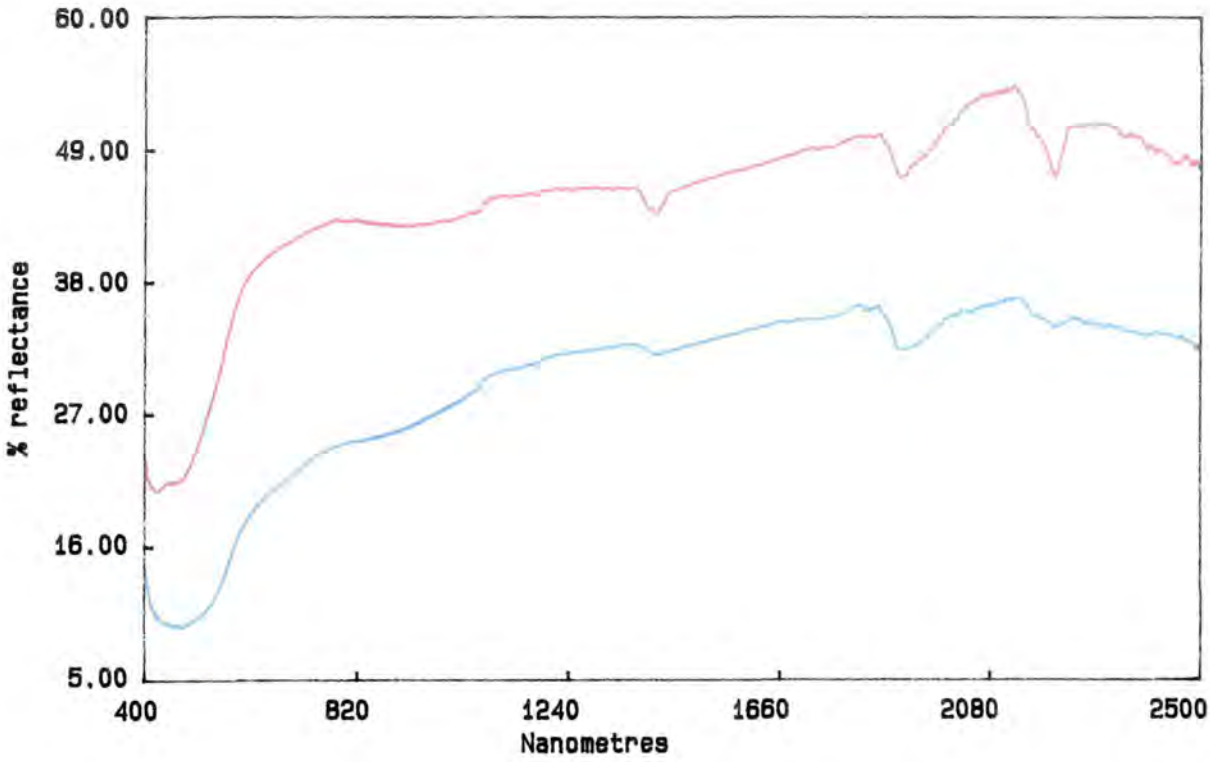

Figure 8.31 IRIS spectra for the Wonga Granite at locality 210.

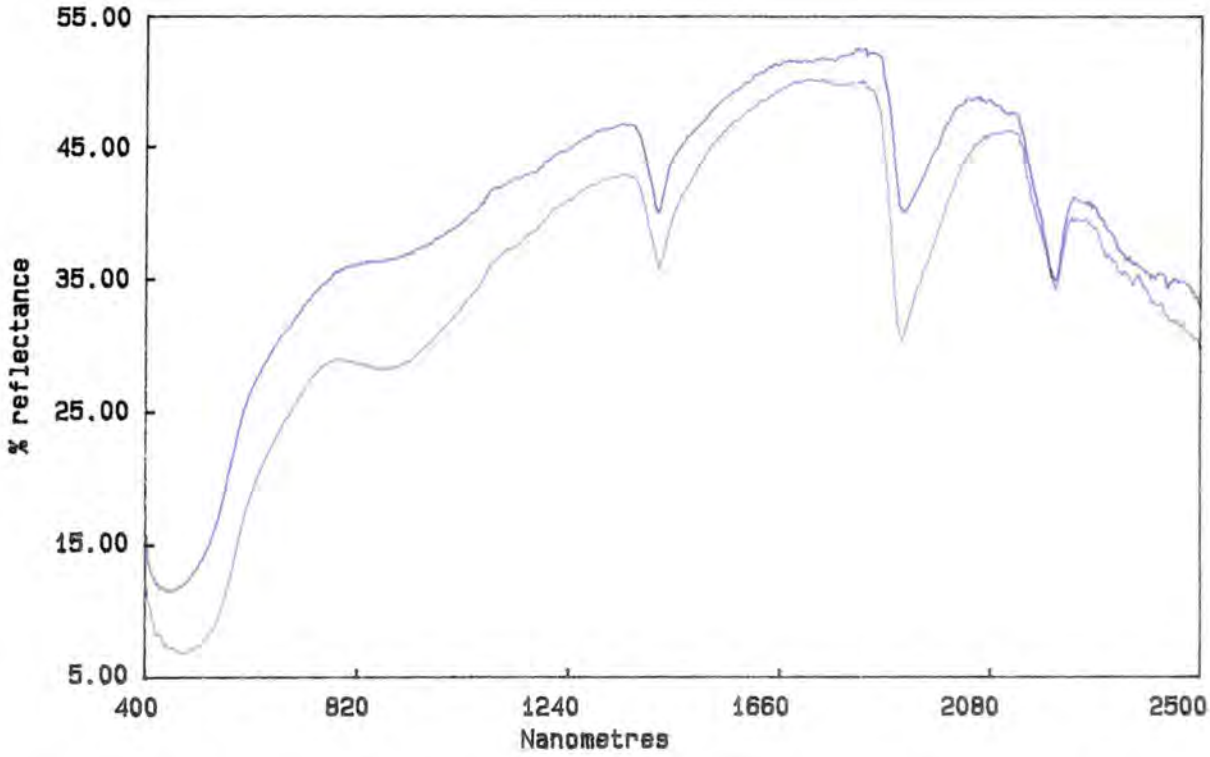

Figure 8.32 IRIS spectra for the two types of soil occurring over the Wonga Granite. The soil from the outcrop tors is in blue and the debris plain soil in purple.

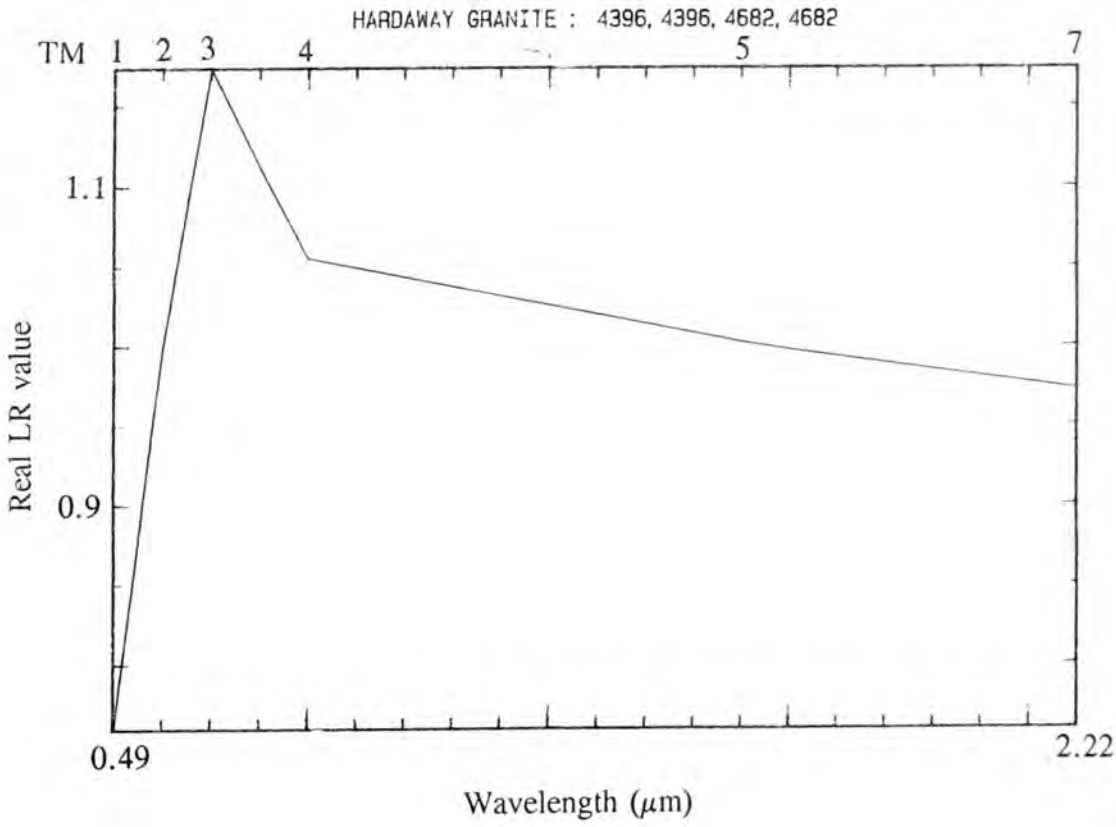

Figure 8.33 TM LR pseudo-spectrum for the Hardway Granite.

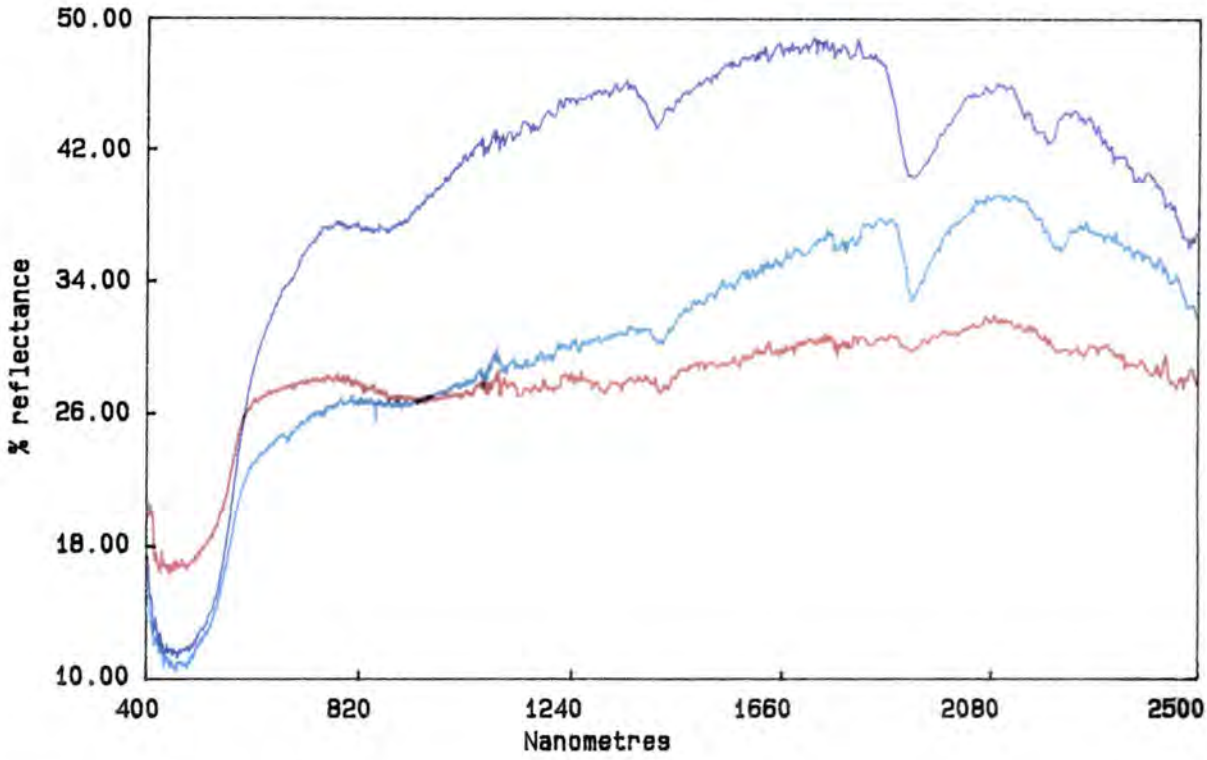

Figure 8.34 IRIS spectra for the Hardway Granite at locality 5.

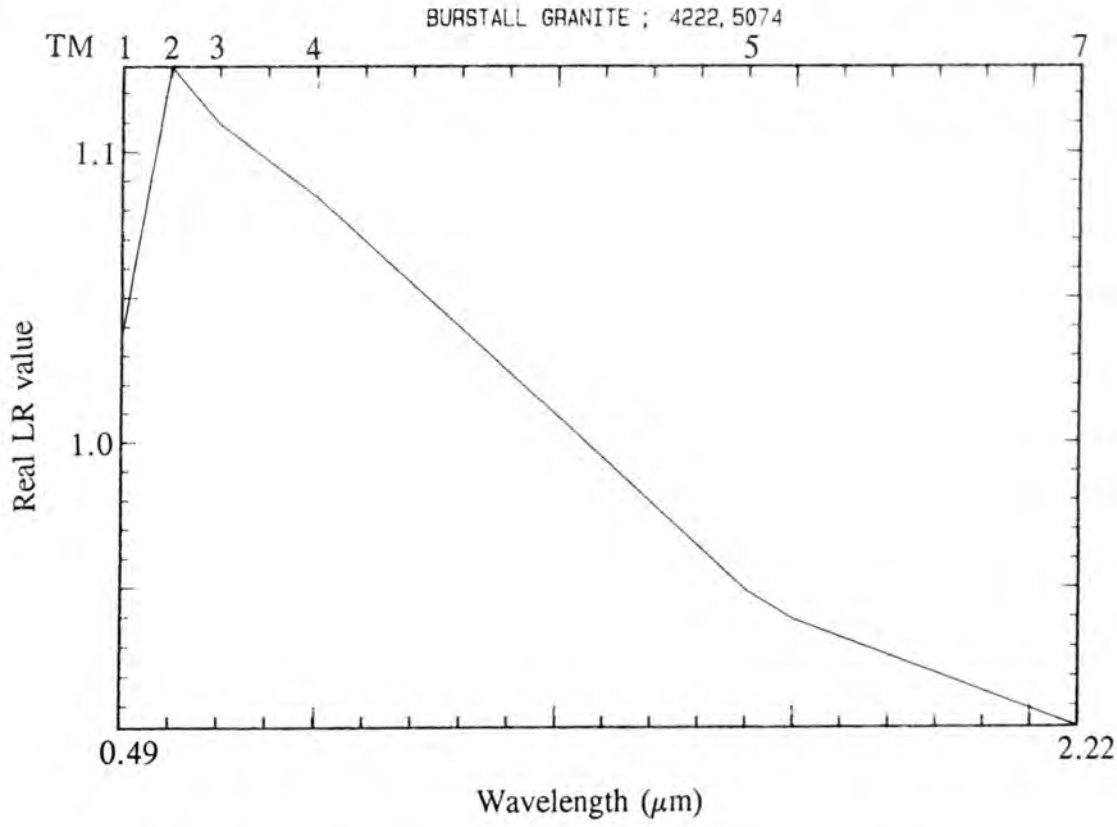

Figure 8.35 TM LR pseudo-spectrum for the Burstall Granite - clay soil.

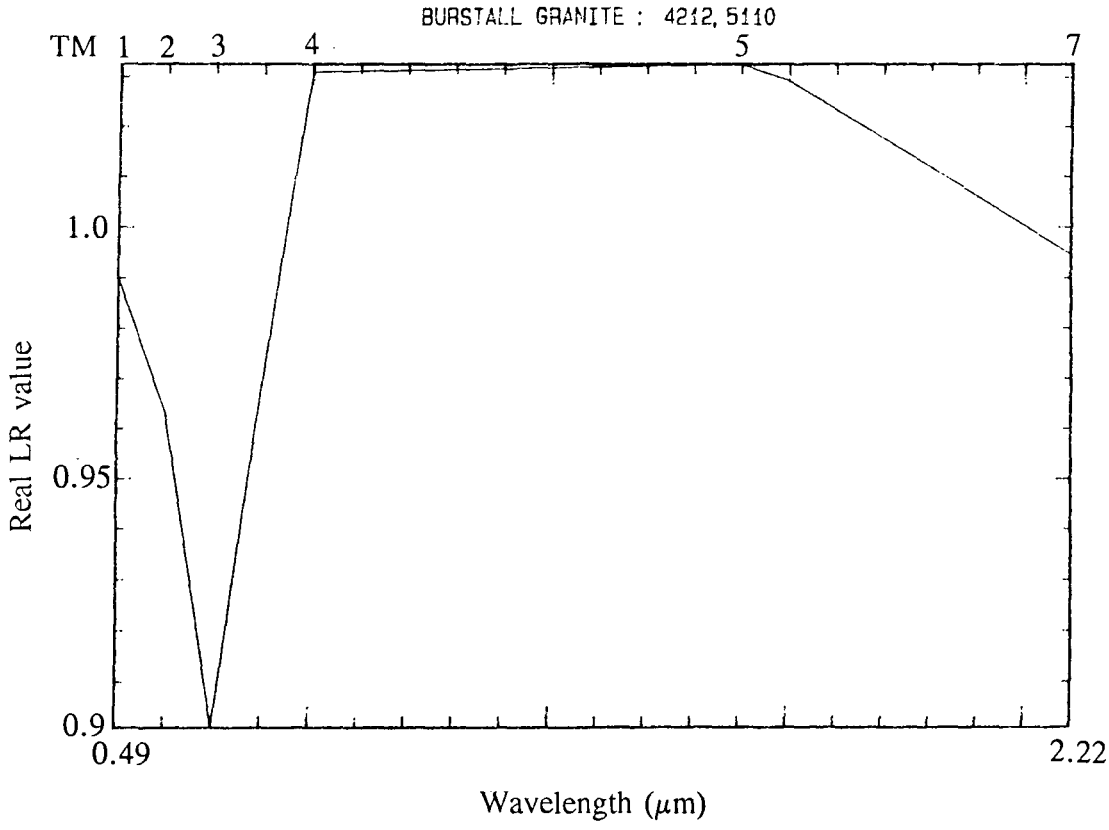

Figure 8.36 TM LR pseudo-spectrum for the Burstall Granite - vegetation.

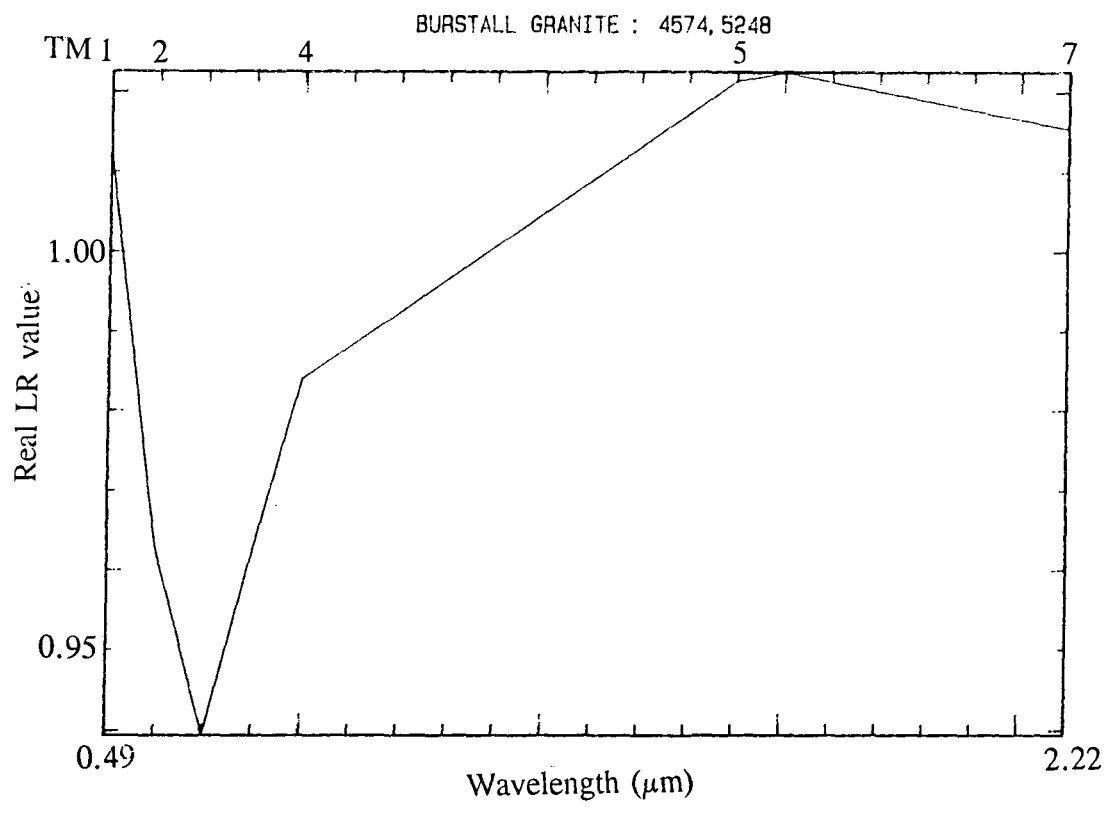

Figure 8.37 TM LR pseudo-spectrum over the Burstall Granite - weathered surface.

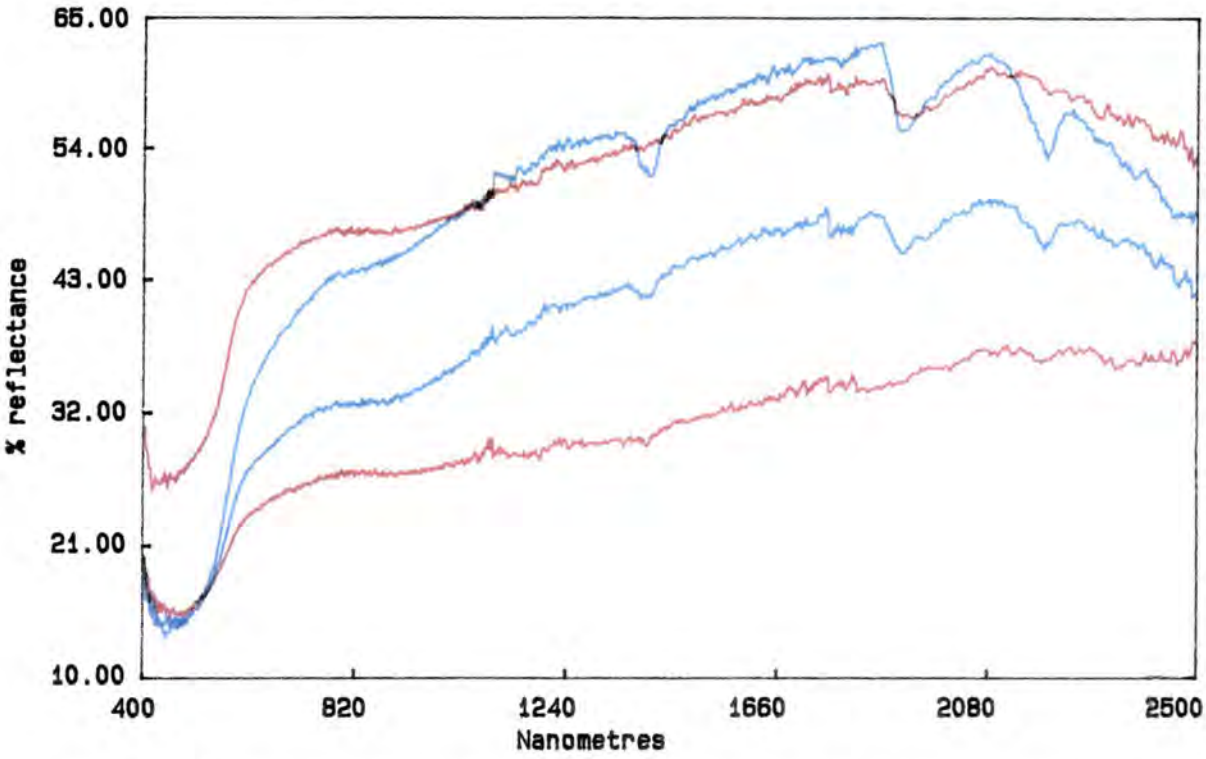

Figure 8.38 IRIS spectra for the Burstall Granite at locality 105 (bottom) and 101 (top).

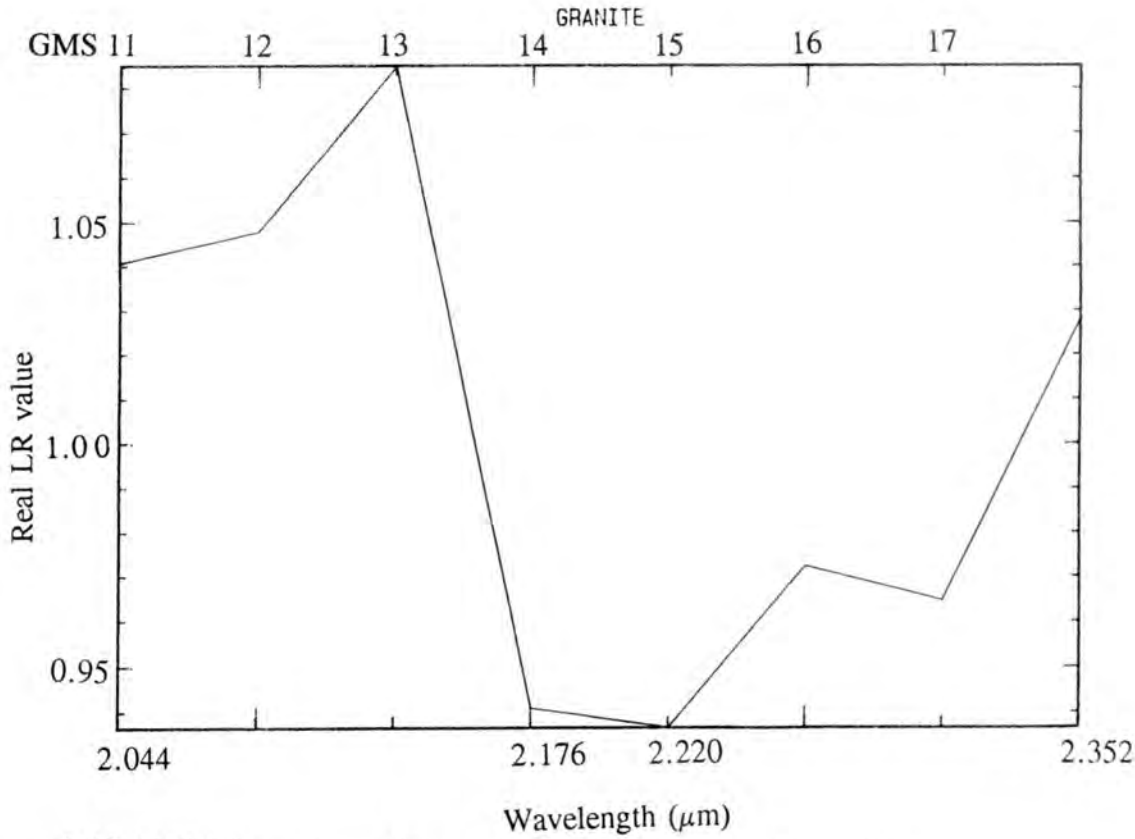

Figure 8.39 GMS LR spectrum for the southern mass of the Burstall Granite.

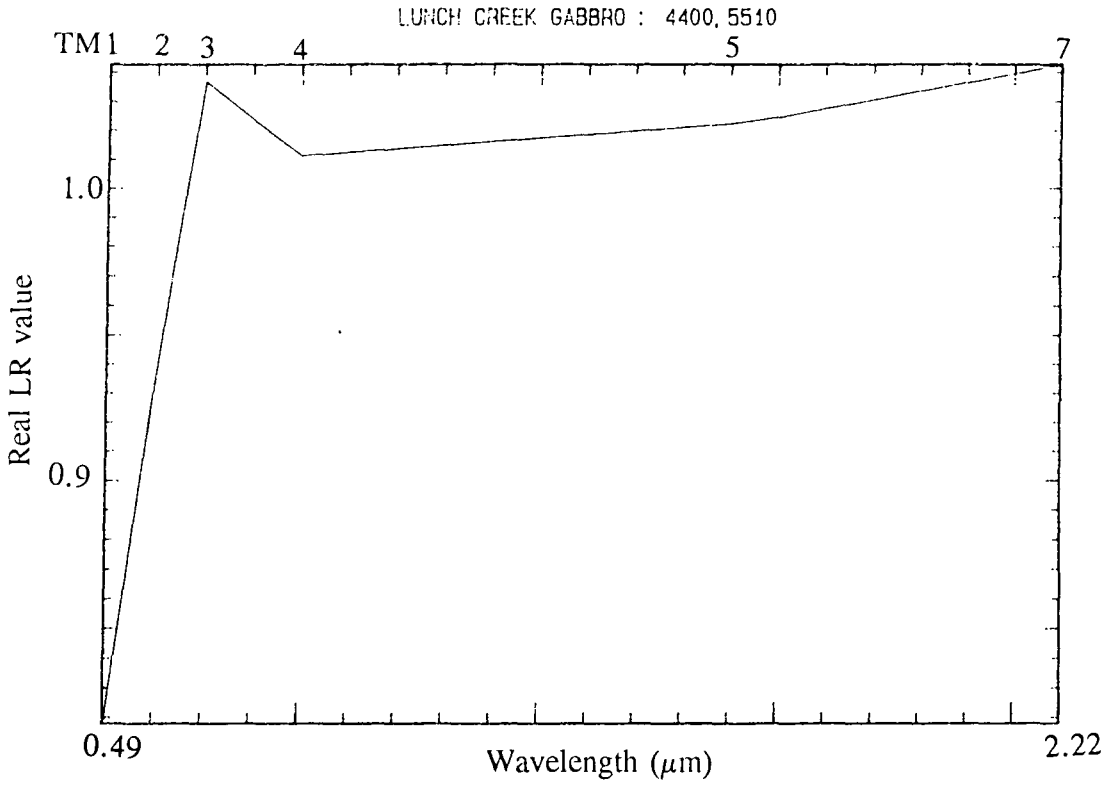

Figure 8.40 TM LR pseudo-spectrum over the Lunch Creek Gabbro.

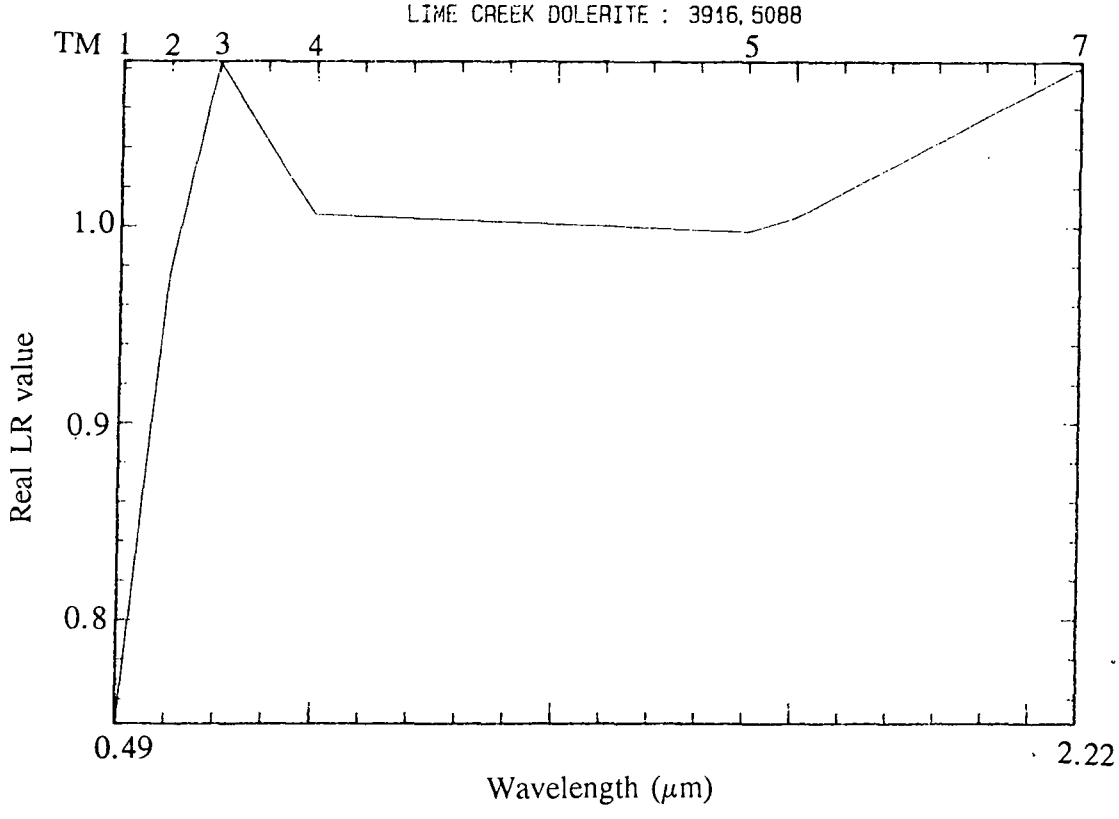

Figure 8.41 a) TM LR pseudo-spectrum for the Lime Creek Dolerite - 0.49 μm absorption.

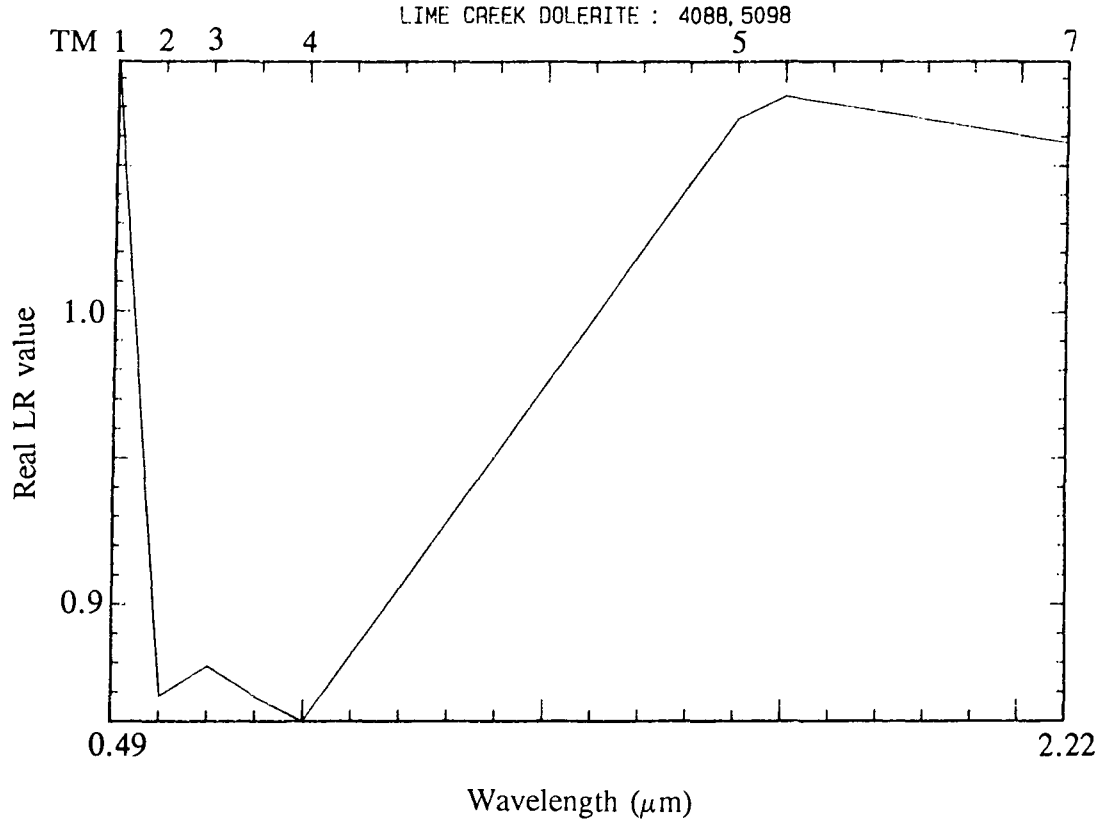

Figure 8.41 b) TM LR pseudo-spectrum for the Lime Creek Dolerite - 0.83 μm absorption.

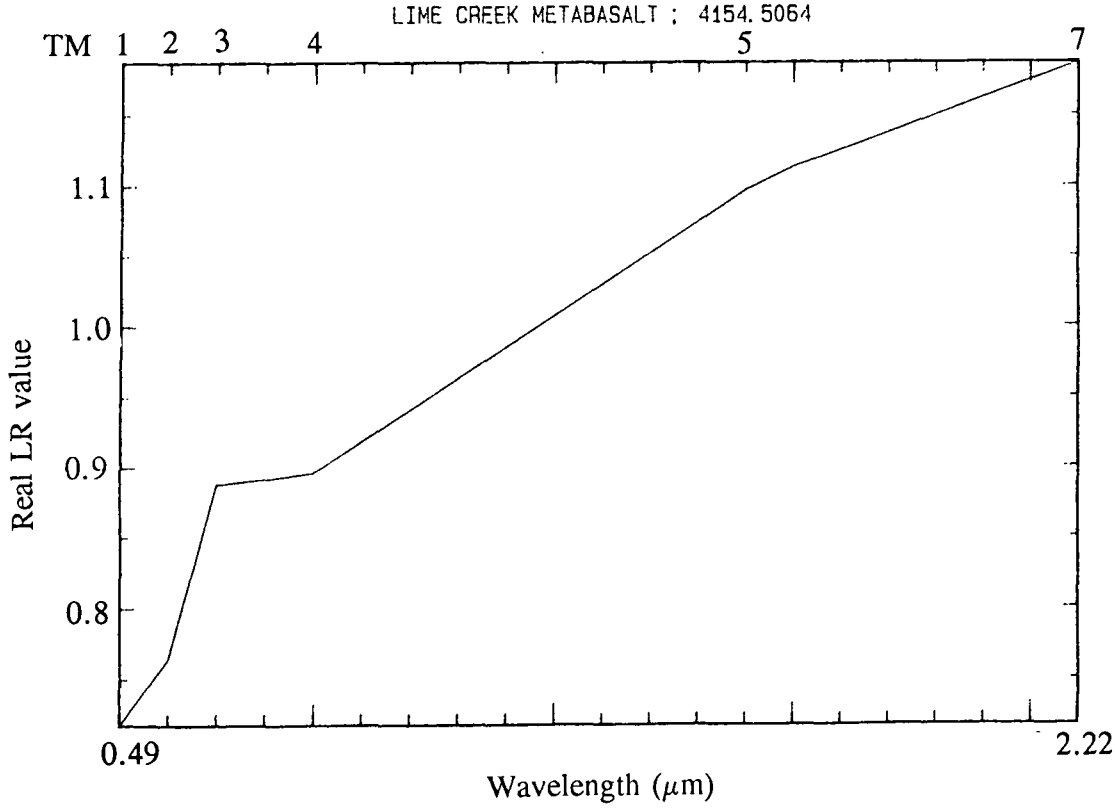

Figure 8.42 a) TM LR pseudo-spectrum for the Lime Creek Metabasalt - 0.49 μm absorption.

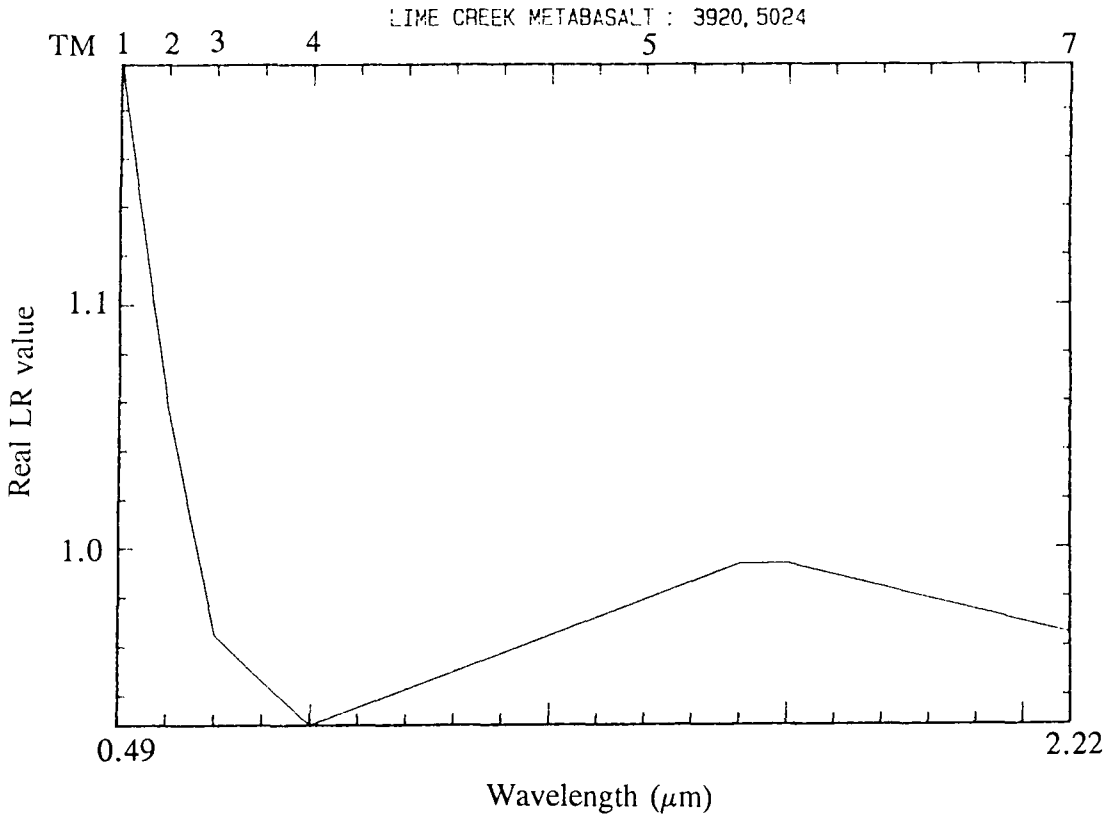

Figure 8.42 b) TM LR pseudo-spectrum for the Lime Creek Metabasalt - 0.83 μm absorption.

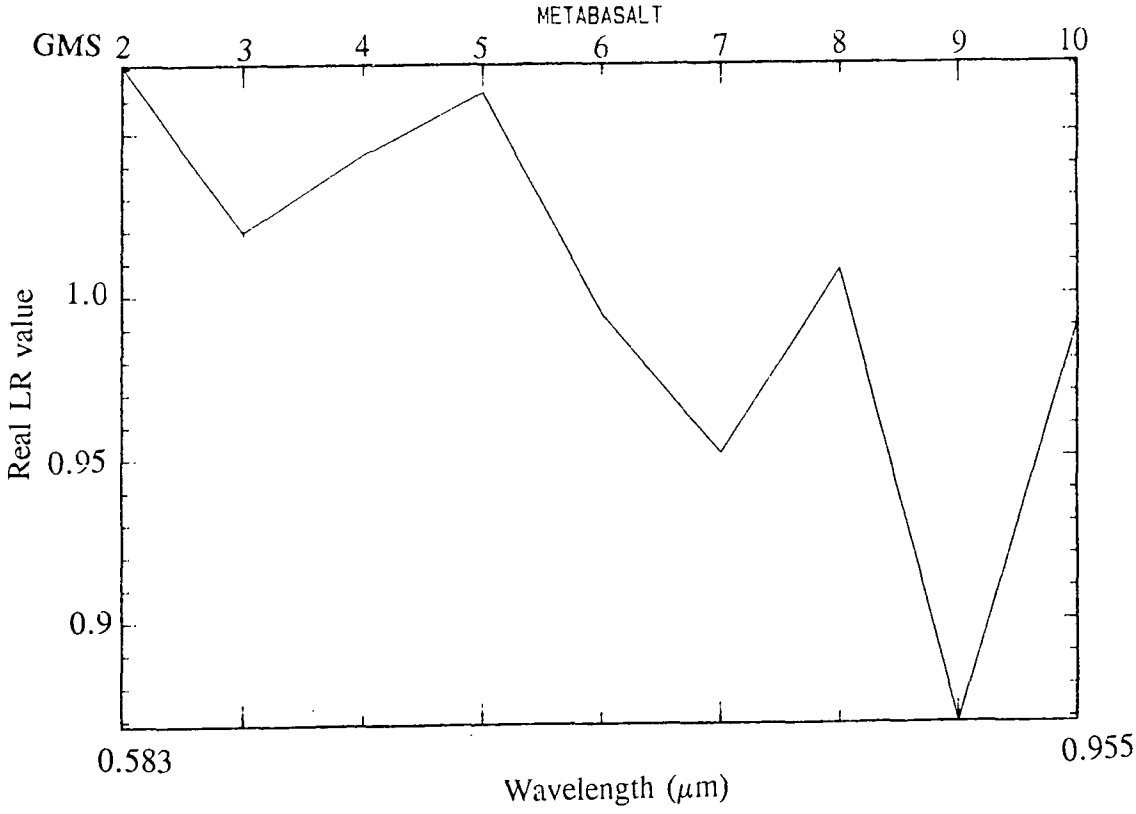

Figure 8.43 GMS LR pseudo-spectrum for the Lime Creek Metabasalt.

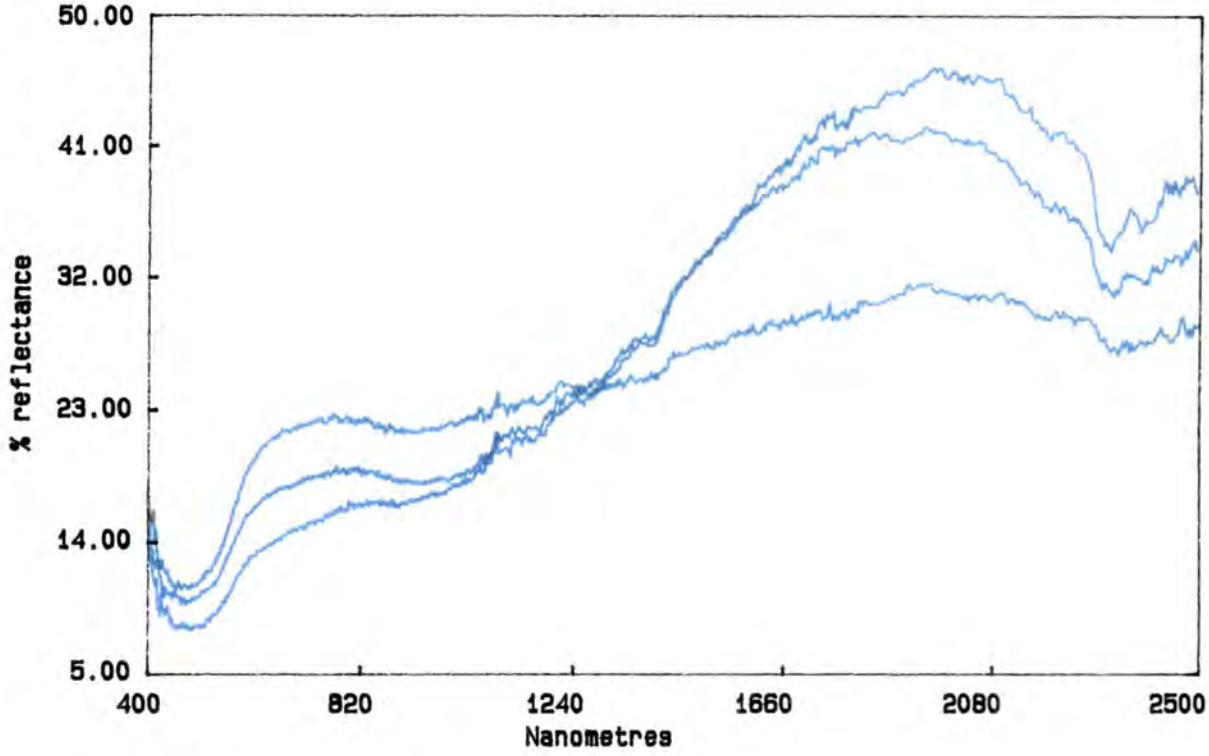

Figure 8.44 a) IRIS spectra for the Lime Creek Metabasalt.

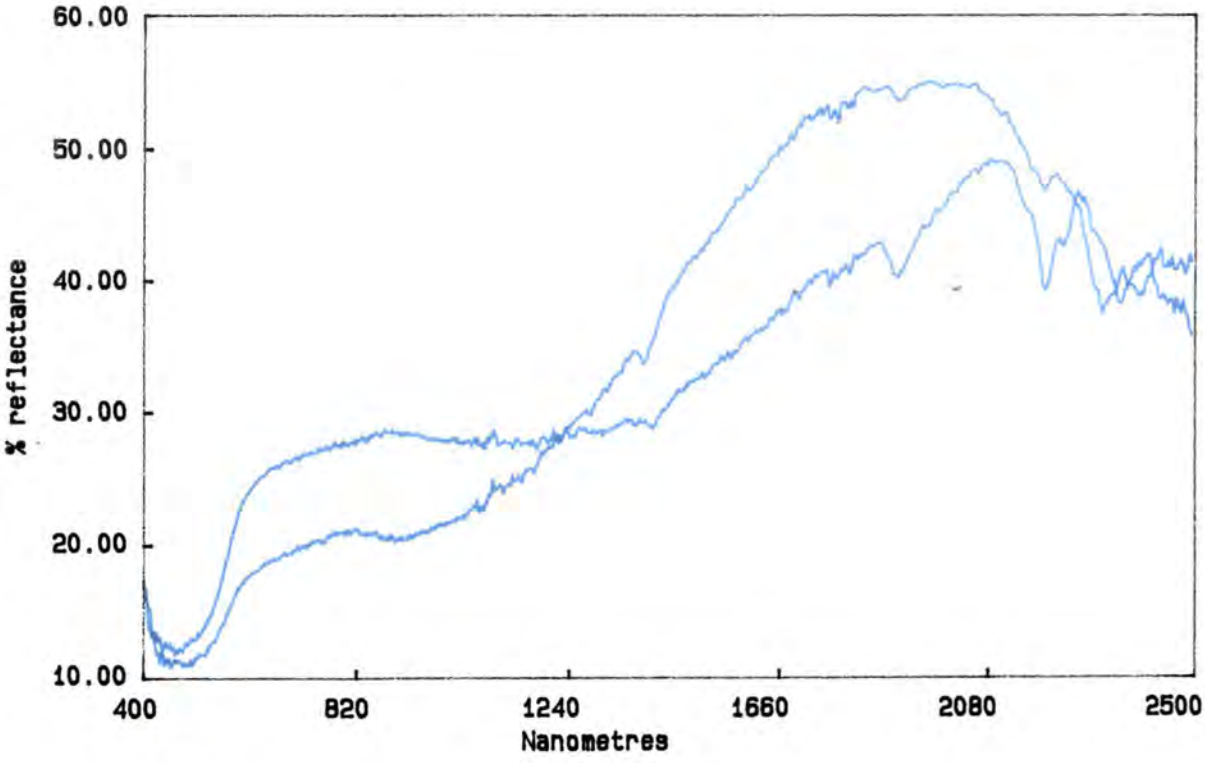

Figure 8.44 b) IRIS spectra for the Lime Creek Dolerite.

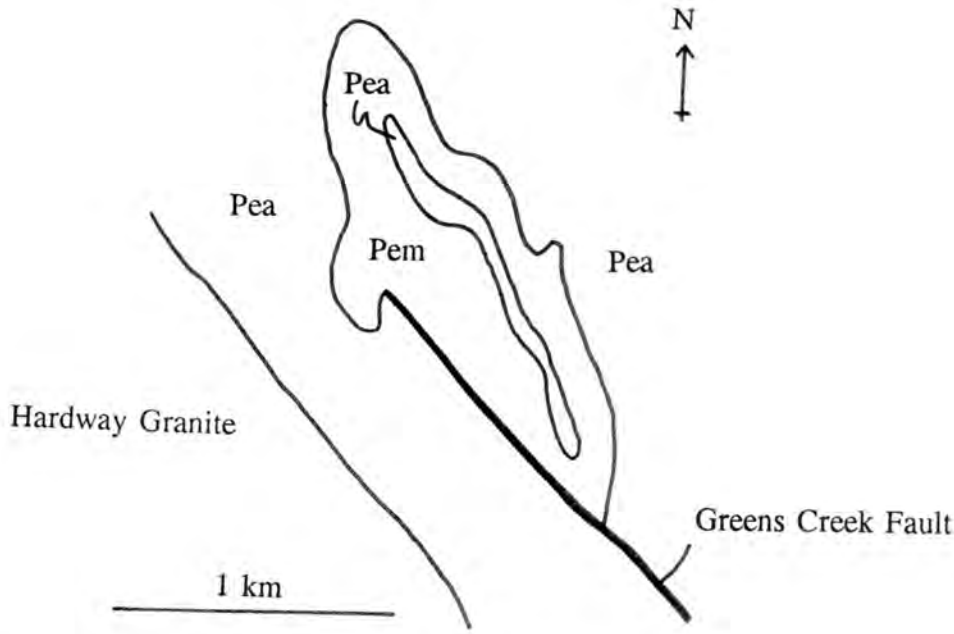

Figure 8.45 The disposition of the Argylla Formation and Magna Lynn Metabasalt by the Greens Greek Fault as on the 1:100 000 MARABBA sheet.

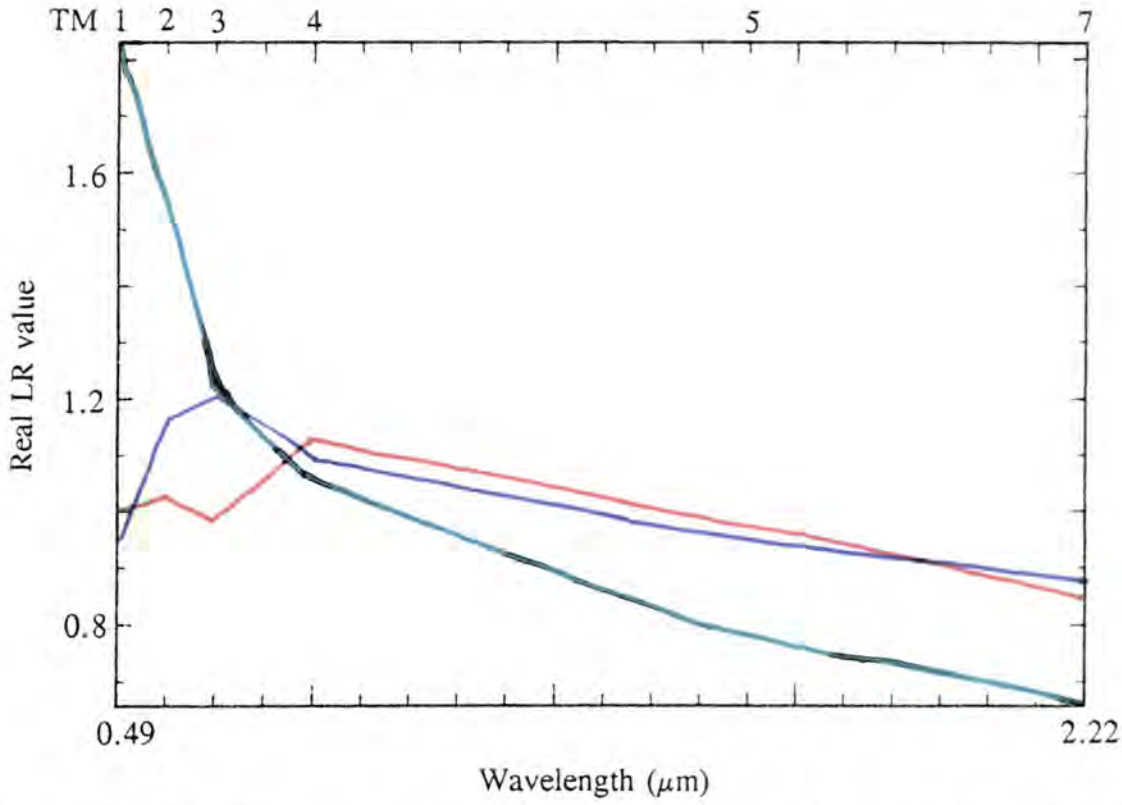

Figure 8.46 TM LR pseudo-spectra for three materials which all display 2.22 μm absorption. Green = calcite, purple = mica, red = vegetation.

Plate 8.1 The Magna Lynn Metabasalt between two units of the Argylla Formation near the Greens Creek Fault.

Plate 8.2 The foreground is the Argylla Formation and the background the Corella Formation, over the Cameron Fault.

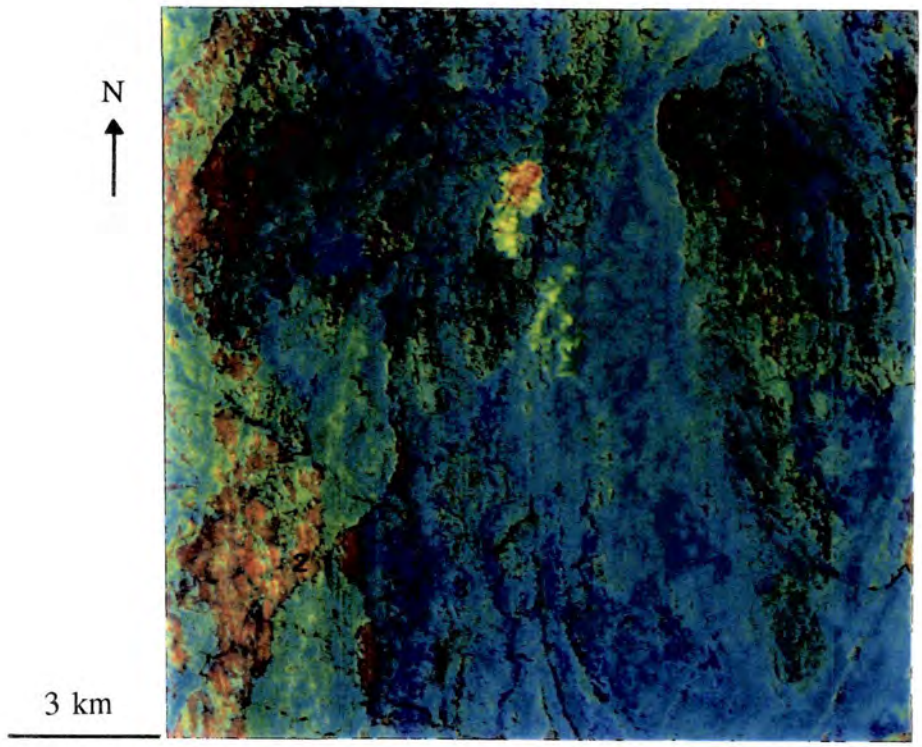

Plate 8.3 TM LR data over the Burstall Granite (top right) and the Rosebud Syncline (bottom left) in the southwest of the field area. Red = 2.22μm absorption, green = 0.83 μm absorption, blue = 0.49 μm absorption. 1 = Argylla Formation, 2 = Ballara Quartzite, 3 = 0.49 μm absorption over the Wonga Granite debris plain.

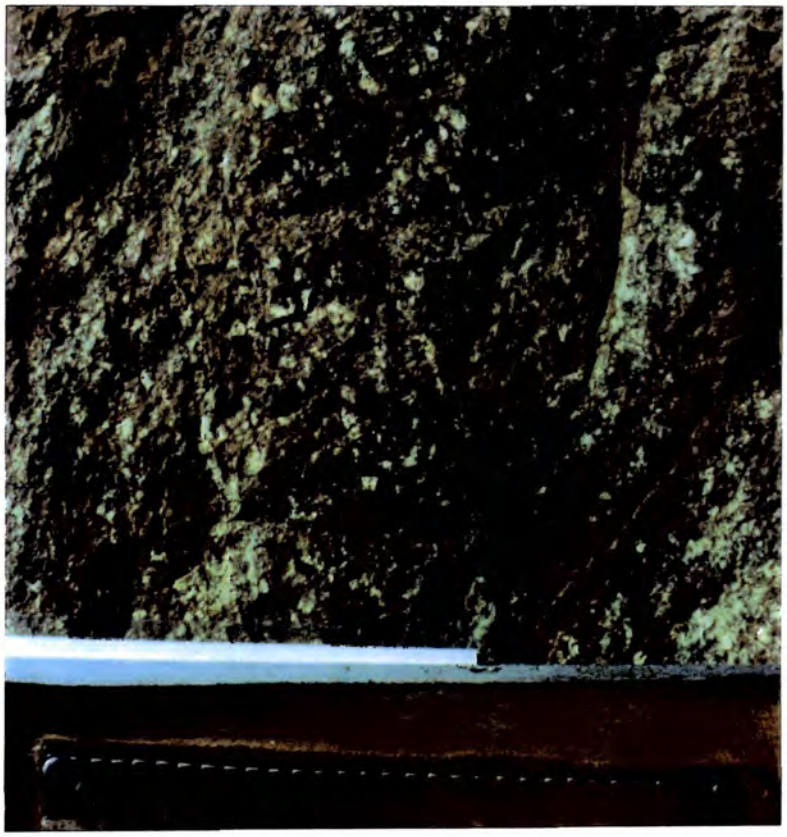

Plate 8.4 Clay weathering from feldspar phenocrysts in the Argylla Formation at locality 14 near the Greens Creek Fault.

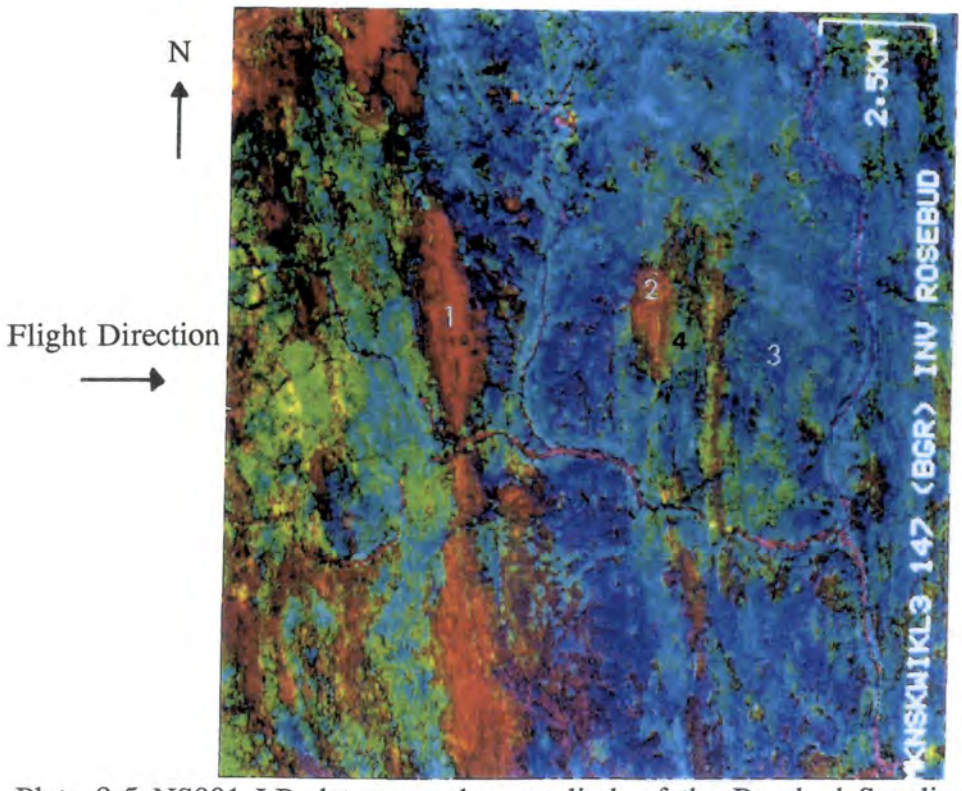

Plate 8.5 NS001 LR data over the east limb of the Rosebud Syncline and adjacent exposures of the Wonga Granite. Colours as Plate 8.3. 1 = the Argylla Formation and Ballara Quartzite in the limb of the syncline. Within the Wonga Granite 2 = clay soil, 3 = iron soil, 4 = weathered outcrop slabs.

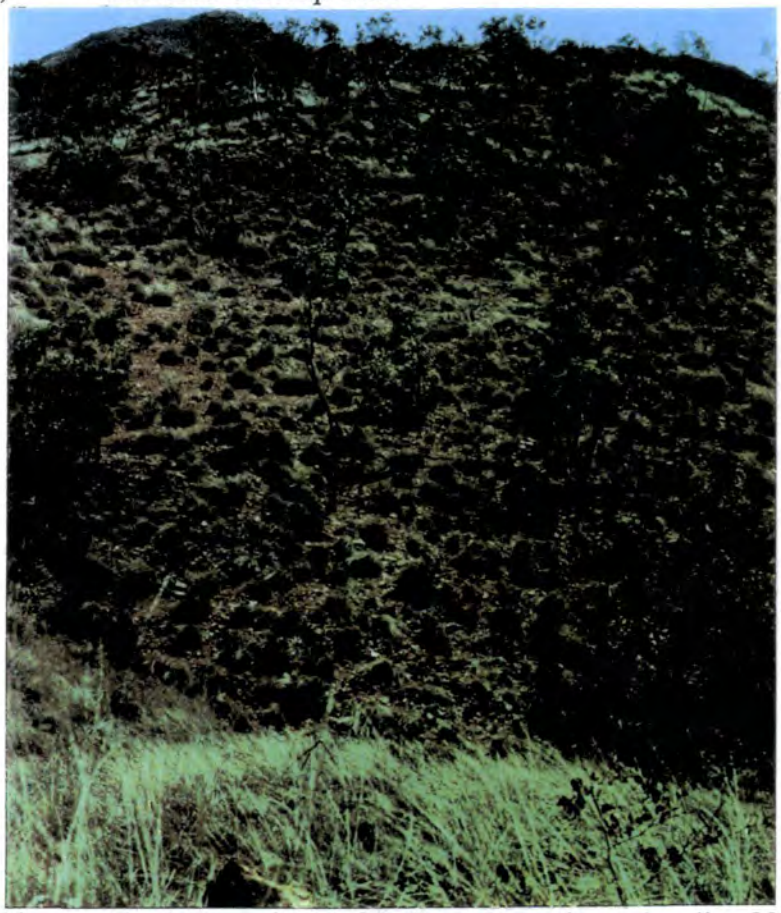

Plate 8.6 Looking north along a ridge of Ballara Quartzite at locality 223 on the east limb of the Rosebud Syncline. This photograph's field of view is shown on Plate 7.8.

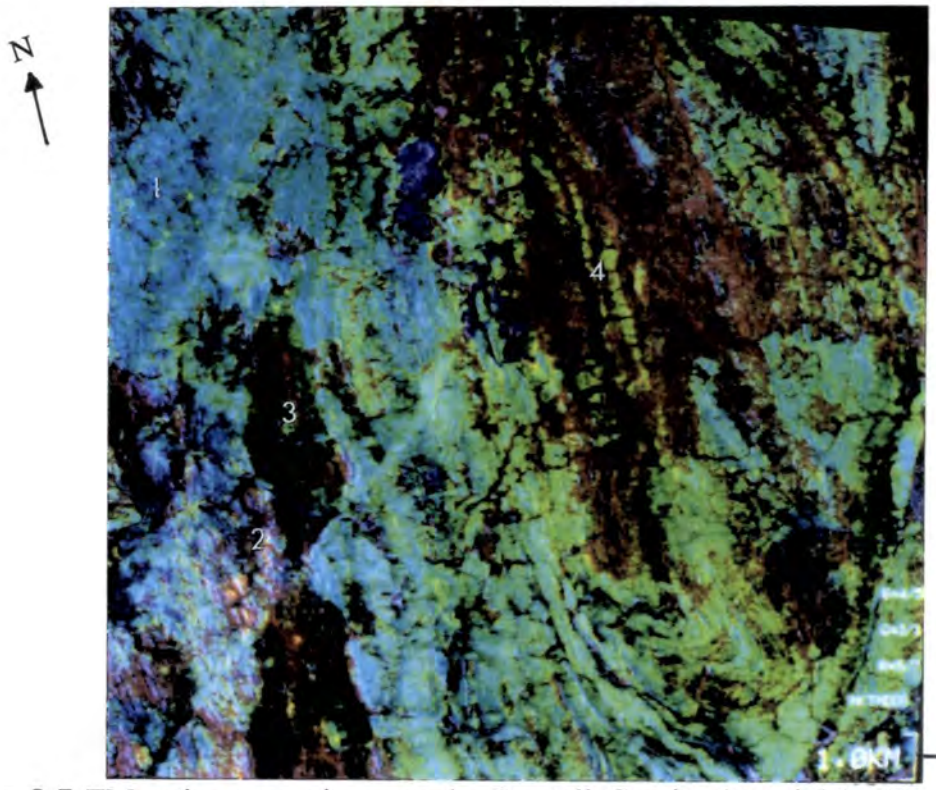

Plate 8.7 TM ratio composite over the Burstall Granite (top right), Wonga Granite (centre) and Rosebud Syncline (bottom left). Red = 1.65/2.22 μm, green = 0.83/1.65 μm, blue = 0.66/0.49 μm. 1 = Argylla Formation, 2 = Ballara Quartzite, 3 = Pkc in the Rosebud Syncline, 4 = Pkc in the Mary Kathleen Syncline.

Plate 8.8

Plate 8.9

Plate 8.8 Corella Formation carbonate, Pkc_1 in the Rosebud Syncline.

Plate 8.9 Corella Formation cordierite-biotite schist, Pkc_2 in the Rosebud Syncline.

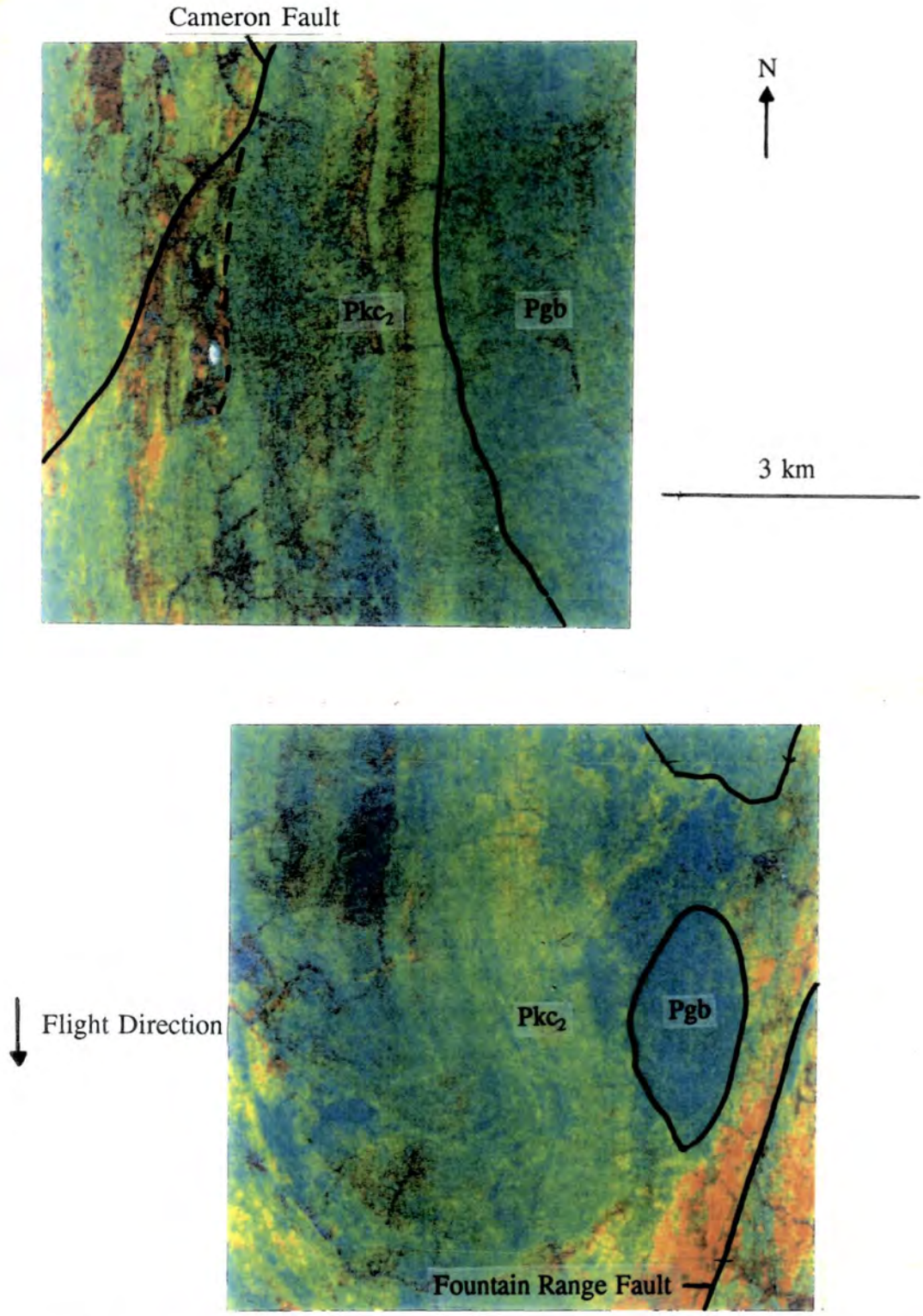

Plate 8.10 GMS LR data over the Mary Kathleen Syncline between the Cameron and Fountain Range Faults. Red = 2.352 μm absorption, green = 2.174 μm absorption, blue = 2.044 μm absorption. The Corella Formation (Pkc_2) and Burstall Granite (Pgb) are labelled and the shear proposed by some workers marked with a dashed line.

Plate 8.11 The contact of the quartzite (right - locality 128) with the calc-silicate (left - locality 129) in the Mary Kathleen Syncline.

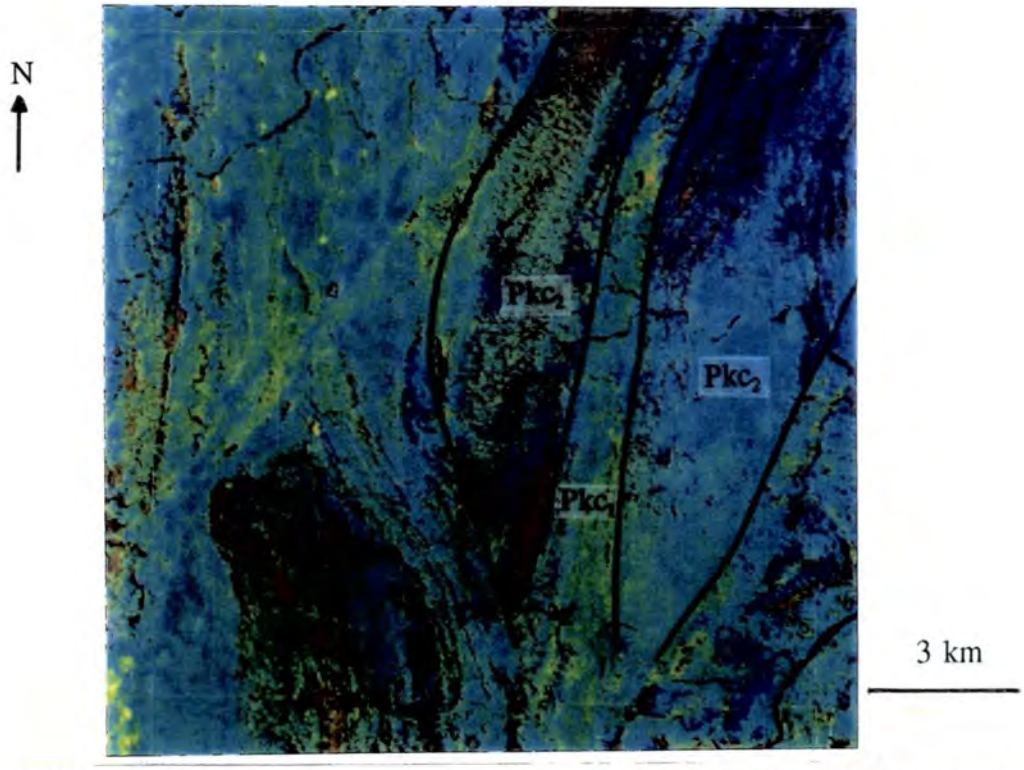

Plate 8.12 TM LR data over the eastern exposures of the Corella Formation in the NE of the field area. Colours as Plate 8.3. The divisions of the Corella Formation on the 1:100 000 map are shown. 1 = calcite pit, 2 = Lake View Dolerite. Enclosure 8.1 contains a detailed interpretation of this plate where it covers the Corella Formation.

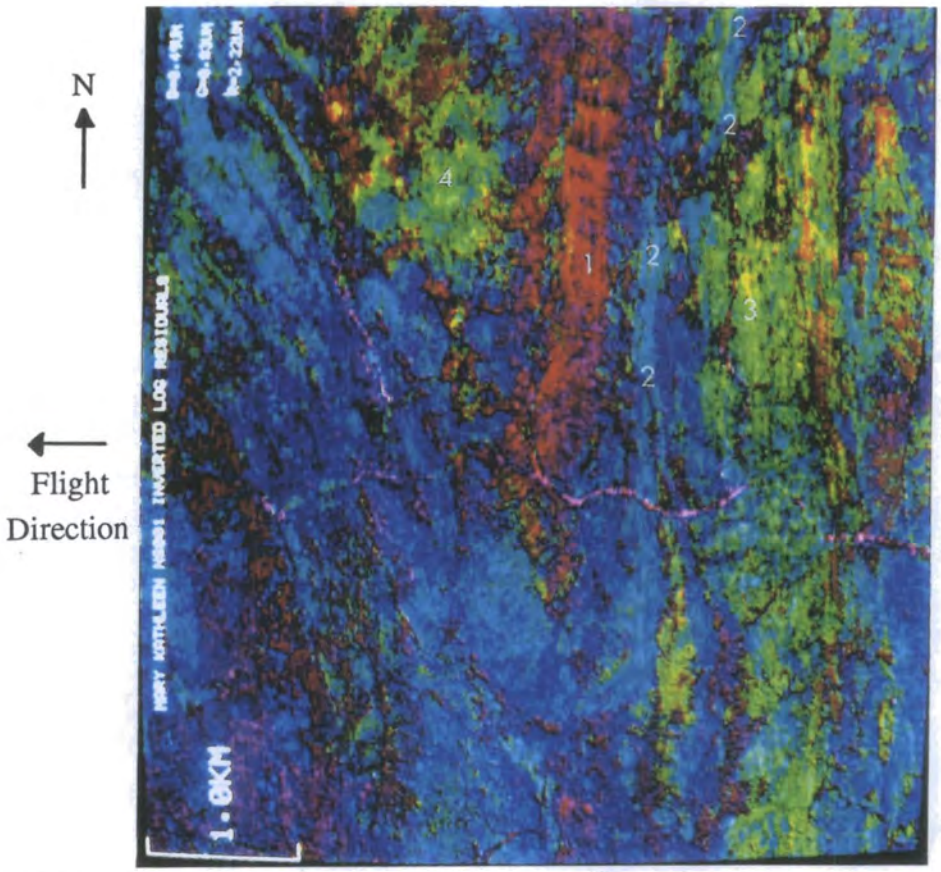

Plate 8.13 NS001 LR data of the south part of the sequence depicted in Plate 8.12. Colours as Plate 8.3. 1 = micaceous sandstone of Pkc_2 , 2 = Lake View Dolerite, 3 = central Pkc_1, 4 = impure marble unit of Pkc_2.

Plate 8.14 Pkc_2 in the eastern limb. Pkc_1 forms the ridge in the distance.

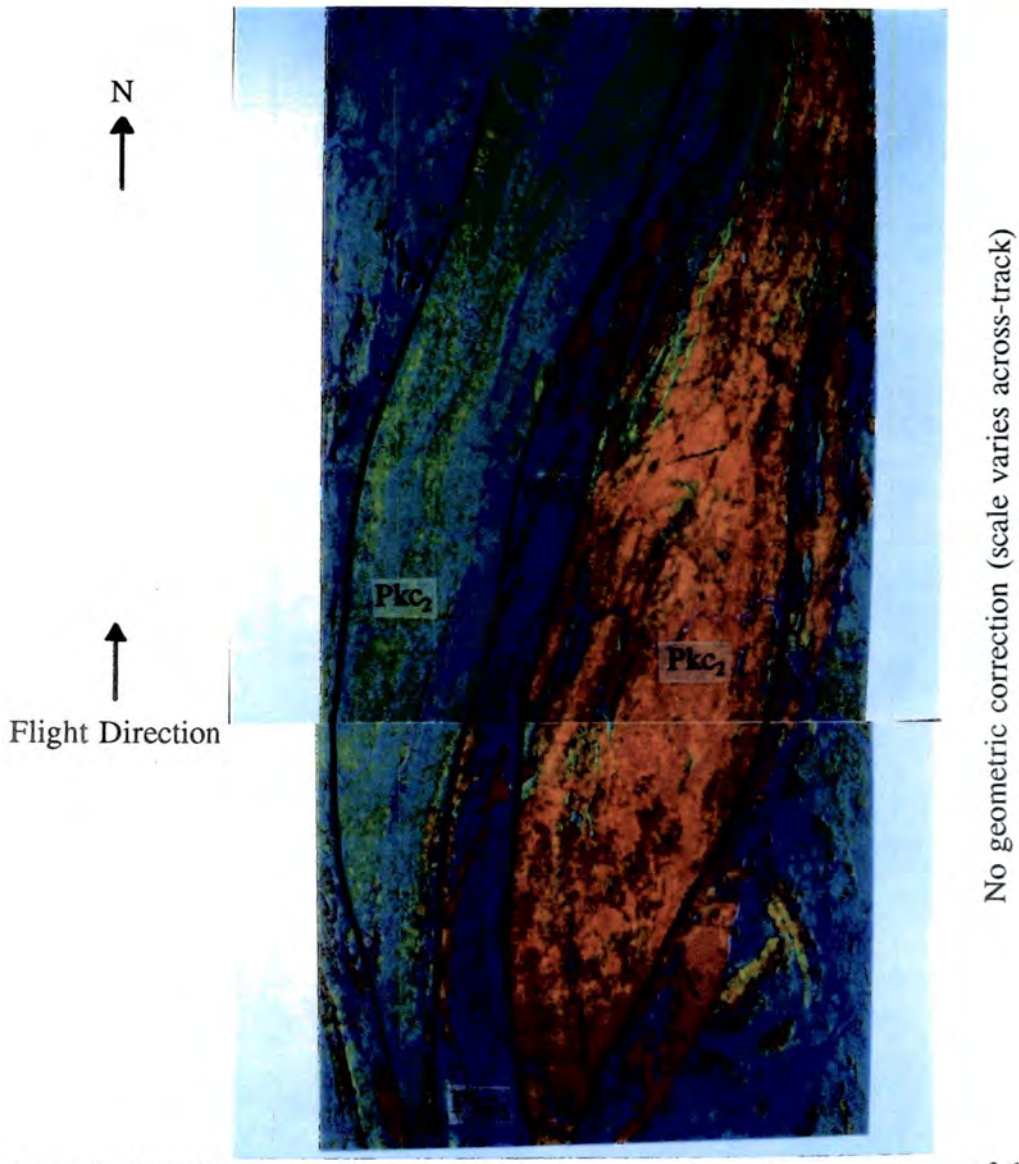

Plate 8.15 GMS short wave infrared LR data over the eastern exposures of the Corella Formation. Colours as Plate 8.10. Pkc_1 and Pkc_2 shown as depicted on 1:100 000 map.

Plate 8.16 GMS visible and near infrared LR data for the central part of Plate 8.15. Red = 0.955 μm absorption, green = 0.830 μm absorption, blue = 0.740 μm absorption. Pkc_1 and Pkc_2 shown as depicted on 1:100 000 map.

Plate 8.17 Pkc_1 in the central limb of the Corella Formation's eastern exposures.

Plate 8.18 Exposed calcite crystals in the calcite quarry at locality 89.

Plate 8.19 Pure marble occurring in extreme north of Pkc_1 in the central limb.

Plate 8.20 View from an impure marble unit of Pkc_2 in the western limb looking east toward the micaceous sandstone unit.

Plate 8.21 View of the Wonga Tor covered by the NS001 LR data in Plate 8.5.

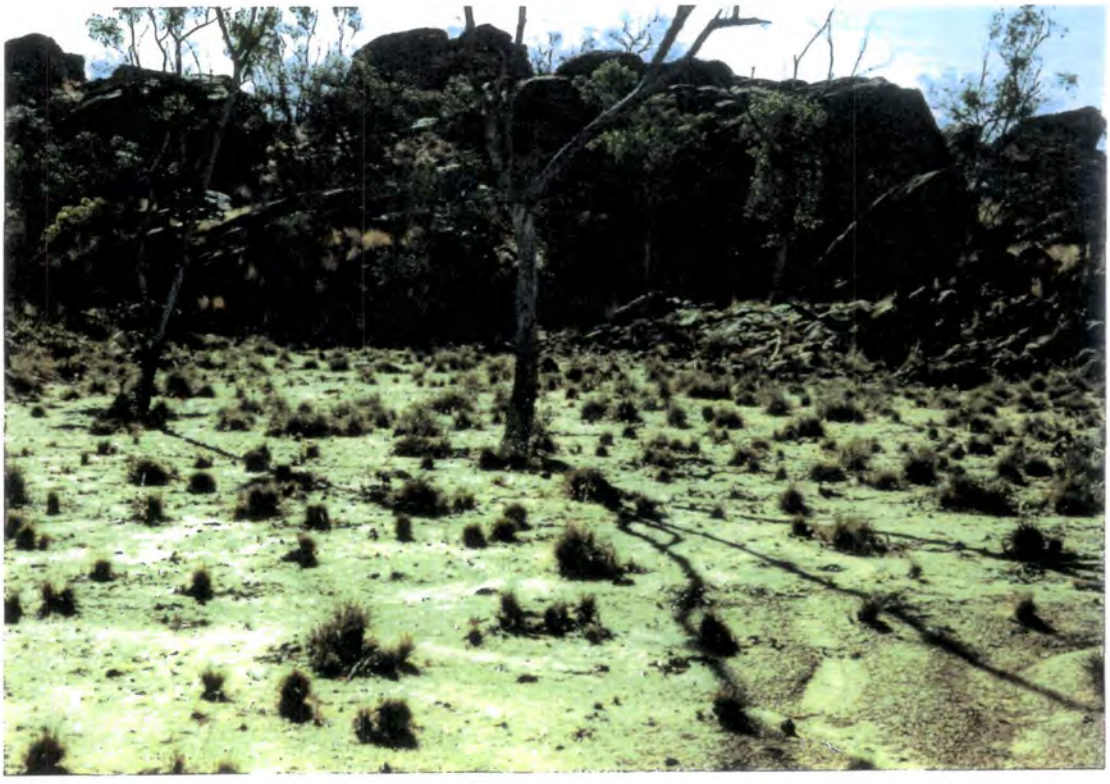

Plate 8.22 A low tor of Wonga Granite with no associated clay soil accumulations.

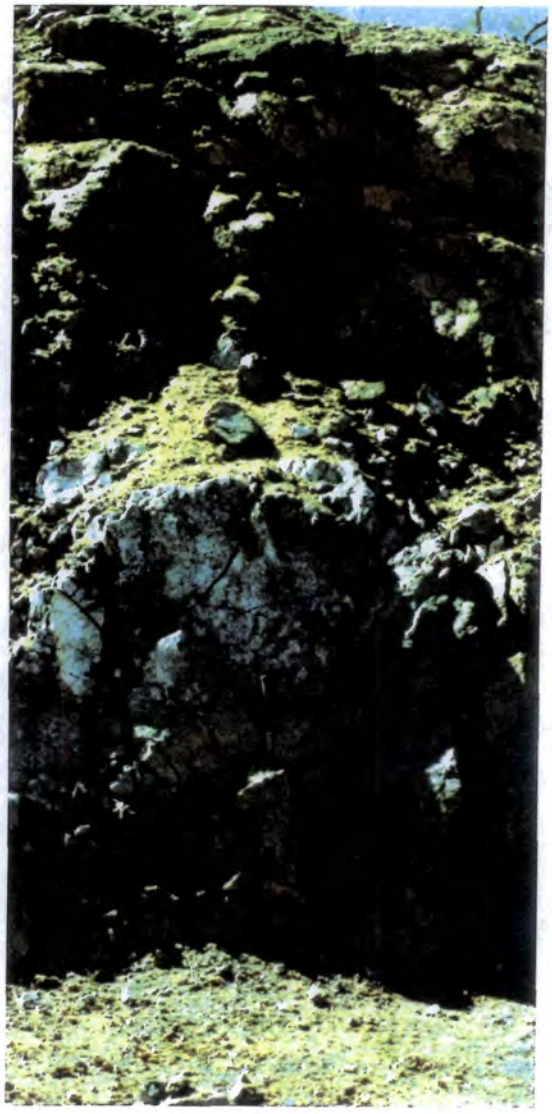

Plate 8.23

Plate 8.24

Plate 8.23 A profile through the Hardway Granite at locality 7 showing the development of iron oxides in the weathered surface. Hammer for scale.

Plate 8.24 Taken from the high crags which characterise the southern mass of the Burstall Granite, showing the contrast in relief compared to the Wonga Granite.

Plate 8.25 The 50 m wide Lake View Dolerite forming a negative feature between two ridges of Corella Formation, Tramline Dyke traverse.

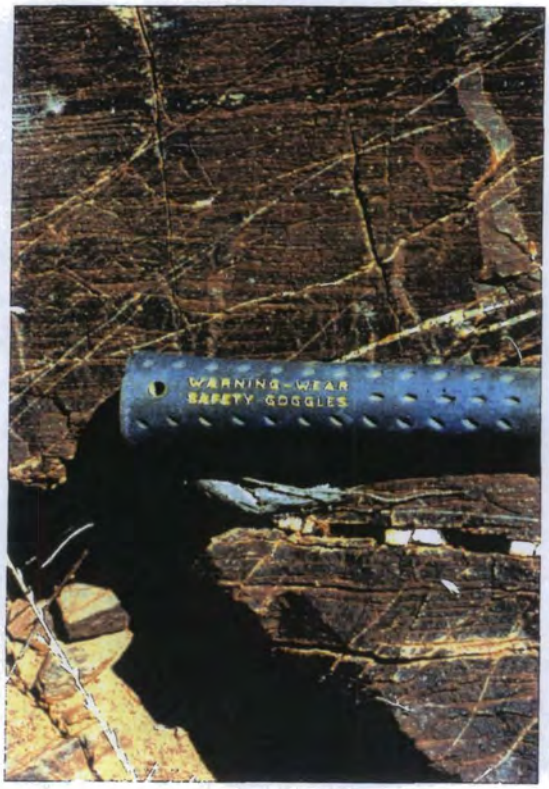

Plate 8.26

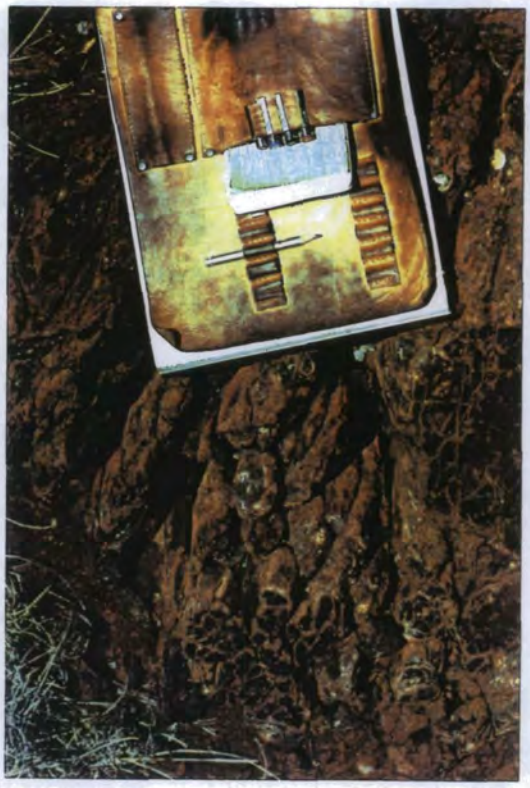

Plate 8.27

Plate 8.26 The Lime Creek Dolerite at locality 116, showing possible flow banding.

Plate 8.27 The Lime Creek Metabasalt at locality 120, with possible pillow structures.

Plate 8.28 The Cameron Fault (central depression) cutting the Argylla Formation (left) and the Corella Formation (right), on the east limb of the Rosebud Syncline.

Plate 8.29 The field assistant is on the Argylla Formation, debris from which covers the Cameron Fault (field assistant's arms) where it cuts the Rosebud Syncline.

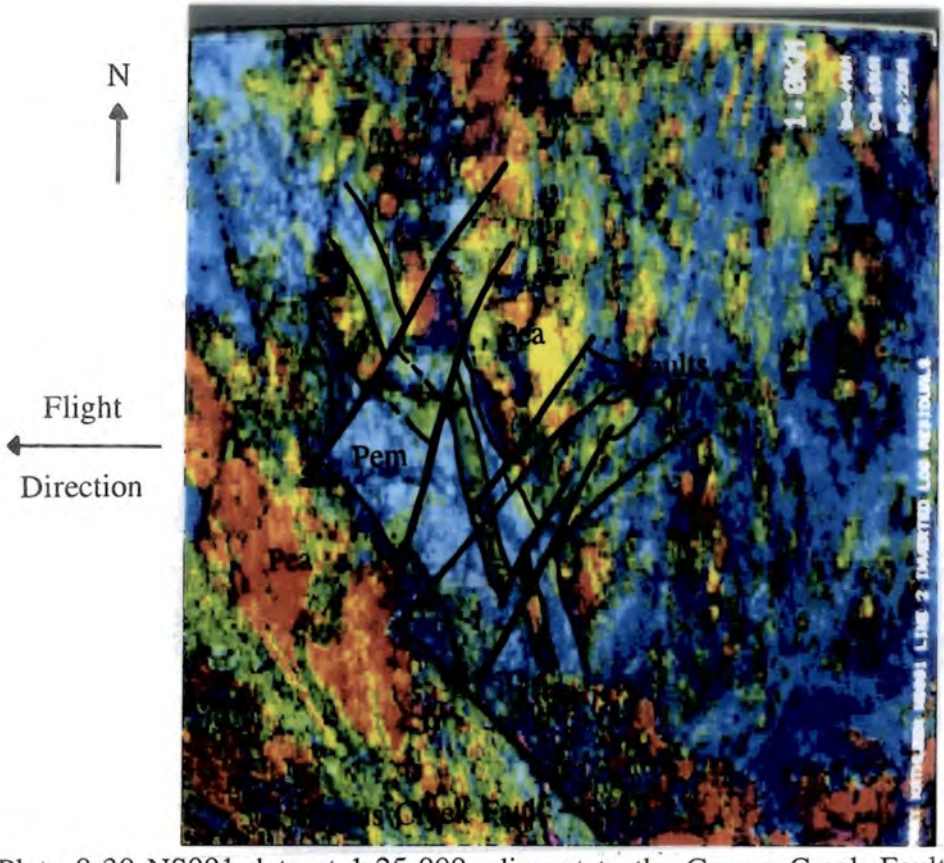

Plate 8.30 NS001 data at 1:25 000 adjacent to the Greens Creek Fault. The detailed interpretation shows a limb of Argylla Formation (Pea) enclosed within the Magna Lynn Metabasalt (Pem) and repeatedly broken up by faulting. Colours as Plate 8.3.

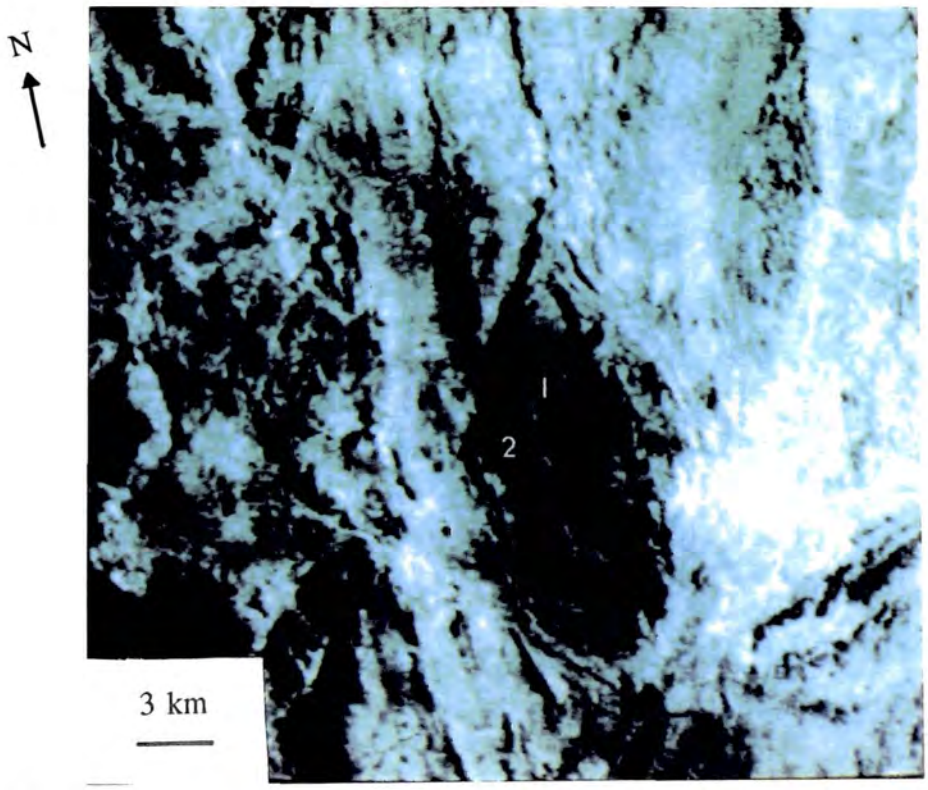

Plate 8.31 TM's thermal infrared band over the Burstall Granite (1) and the Corella Formation in the Mary Kathleen Syncline (2).

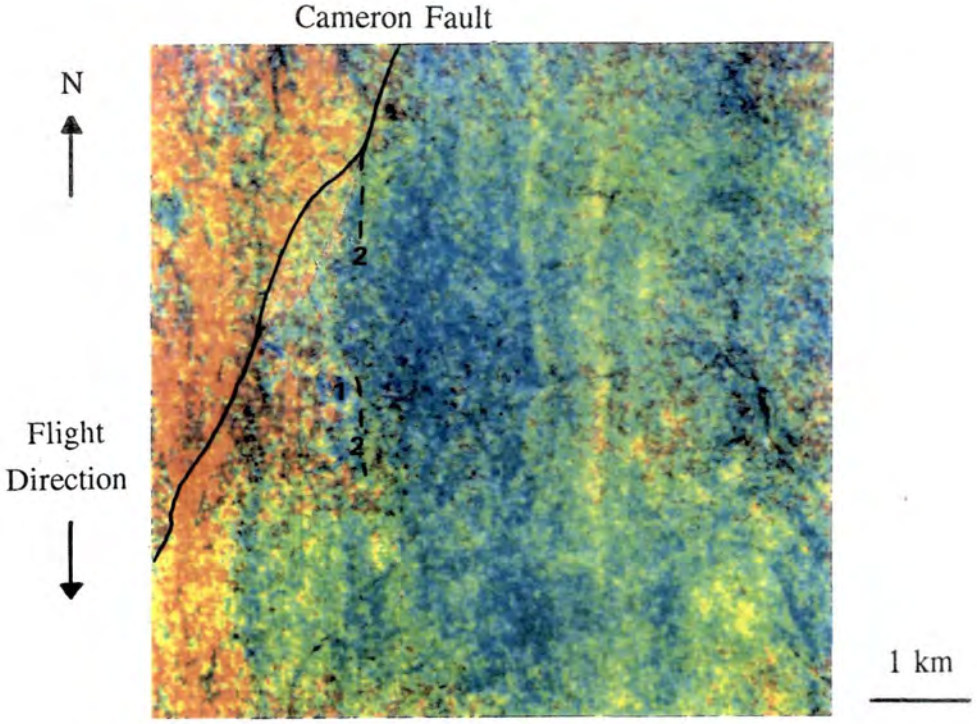

Plate 8.32 GMS visible and near-infrared data over the Mary Kathleen Syncline, showing the open-pit (1) and assocciated shear (2). Colours as for Plate 8.16

	WONGA	HARDWAY	BURSTALL
Albedo	High	High	Low
2.22 μm absorption	Some	Little	Much
0.83 μm absorption	Some	Some	Some
0.49 μm absorption	Much	Much	Little
Radiometric intensity	Patchy high and moderate	Moderate	High
Dominant elements	Th	Th/U	Th
Outcrop type	Low lying plain with tors	Low-moderate hills	High hills with much outcrop
Mafic segregations	Common	-	Rare
Dolerite dykes	Many	Many	Few
Deformation	Frequent	-	Infrequent
Relationship to other soils and lithologies	Often covered by other soils and lithologies	-	Often covering other lithologies

Table 8.1 The differences between the three main granites in the field area.

Lithology	Dominant absorption in TM LR (μm)	Fe-oxide identified in XRD	Mean Fe-oxide ratio	Fe-oxide identified in IRIS spectra
Dog Bone Dolerite	0.49	hematite	0.33	goethite
Lake View Dolerite	0.49		0.30	goethite
Lake Corella Dolerite	0.49	hematite	0.21	hematite/ goethite
Little Beauty Dolerite	0.49			
Rosebud Dolerite	0.49			
Lime Creek Dolerite	0.83	goethite	0.14	goethite
Lime Creek Metabasalt	0.83		0.23	goethite
Magna Lynn Metabasalt	0.83	goethite	0.24	goethite
Cone Creek Metabasalt	0.49			

Table 8.2 A Summary of the TM, XRD and IRIS data over the basic rocks.

CHAPTER 9. CONCLUSIONS AND RECOMMENDATIONS

9.1 Introduction

The aim of this study was to assess the utility of TM, NS001, GMS and AGR data for improving and refining the process of geological mapping. The real question to be addressed for each data set is:

What is the balance between effort expended and information gained?

To answer this question, it is necessary to first consider all those processes which must be performed on the data to emphasise the geological information content. The amount of new geological information gained from the data should then be assessed. This should make clear which data set, or combination of data sets, is most suited to addressing geological problems in this semi-arid environment.

9.2 What effort must be expended?

Before the data can be geologically analysed they must be acquired, loaded into an image analysis system and processed in some way. Both the ease of each of these operations and the number of processes required varies between the data sets.

9.2.1 Data acquisition

The TM data are acquired repeatedly over most of the globe and are relatively inexpensive, as the purchaser does not have to explicitly pay for all data acquisition costs. The NS001, GMS and AGR data are all acquired from an aircraft, and data acquisition must be specifically requested and paid for in most cases. For many study areas TM data are likely to already be available, unless the area is frequently cloud-covered. In the latter case it may be particularly difficult to get data from the desired season, with reduced vegetation or a low sun-angle to emphasise topography. Despite this, in many cases the ready availability of TM and other satellite data gives them a major advantage over aircraft data, whose acquisition must be planned well in advance.

9.2.2 Image analysis systems

Until recently image analysis systems have not been geared toward high resolution data, or the handling of real number data. Almost every image analysis system can handle TM data, but spectral analysis packages suitable for analysing GMS data are less common. TM data are easier for the user to handle. This advantage will diminish now that spectral analysis packages are becoming available for PCs and Workstations. The AGR data are also becoming easier to handle as more analysis packages are modified to handle real numbers.

9.2.3 Data processing

If the goal of a study is only geological discrimination, the data set which can achieve maximum discrimination for minimum processing is the AGR. Comparison of the unprocessed AGR data in Plate 6.5 with the least processed TM data in Plates 5.1 and 5.2 makes this clear. Despite the higher spatial resolution of the radiance data sets they are less geologically discriminating than the AGR data when unprocessed. This is because far more non-geological factors affect the radiance data than affect the AGR data, so more processing is necessary to remove them.

The first processing step necessary is noise removal. The uranium data require cleaning and the operation has largely been successful. Of the radiance data, the TM data are almost noise-free, the NS001 data have minimal noise and the visible and near infrared GMS data are almost too noisy to be used. The ease with which this noise can be removed follows a similar pattern. Noise removal techniques are more successful if the noise is first separated from the signal. The LSFit and MAF techniques have proved equally successful at performing this separation.

Satellite data have two further advantages over the aircraft-borne data that relate to the geometry of their acquisition. The high altitude of the TM sensor means that a small field of view is required to image a large area on the ground. Geometric distortions are minimal and across-track shading non-existent. In contrast the NS001 and GMS data are acquired at lower altitudes with large fields of view. There is a corresponding

increase in geometric distortion and across-track shading in the aircraft data, which must be removed before the data can sensibly be applied to geological problems. The TM data require no such processing before they can be used in the field. The stability of the platform is also important and the satellite data have a clear advantage being acquired outside the turbulence of the atmosphere. Of the aircraft radiance data, the GMS data are far superior to the NS001 data in this respect, being acquired from a gyroscopically stabilised platform. These problems do not affect the AGR data.

A detailed geological study requires any data used to be compatible with map-based information. The registering of TM data to a grid system is relatively straightforward and has become routine in many applications. AGR data are always gridded. The geometric problems described for the aircraft-borne radiance data increase the difficulty of this operation, particularly for the NS001 data.

9.2.4 Data enhancement

Once these processing steps have been performed, all radiance data sets can be processed to highlight geological information with equal ease. The GMS data are, however, time consuming to process for the same ground area as the TM data due to the increased volume of data which is a consequence of the improved spatial and spectral resolution.

If discrimination is the only goal then a PC analysis of the data after minimal processing is the obvious data processing choice. If however identification is the goal then it is necessary to consider what physical meaning the data have. All radiance data sets contain the parameter reflectance and thus measure a physical attribute of the earth's surface. In the past the visual impression made by satellite images and the coarse spectral resolution has tended to obscure this fact for TM data. The limited spectral resolution of TM is, however, no reason to ignore the physical meaning of the data. In this study, processing TM data to near-reflectance has enabled spectrally similar lithologies such as micaceous sandstone and pure calcite to be discriminated. TM data contain more information than is routinely extracted from them.

If the data are to be treated as having a physical meaning, an atmospheric correction must be performed. This is equally time consuming for all radiance data sets. Automatic correction methods developed in arid regions which rely on homogeneous surfaces being exposed are not successful in this semi-arid region because increased vegetation density makes all surfaces inhomogeneous. This is the biggest problem caused by vegetation in this area. Corrections based on shadow minima are also poor because true shadow does not exist in practice. Atmospheric corrections based on water are the best option at the present time if reliable atmospheric data are not available.

The logarithmic residual technique has been a very effective tool for geological mapping in this area, producing both a highly discriminatory image and data which appear to have consistent physical meaning for all three radiance data sets. Comparison of logarithmic residual values to laboratory reflectance values has shown that the technique produces a close approximation to the true reflectance. As the technique produces discrimination and an albedo image of a similar quality to a PC analysis but also allows identification of surface minerals it is highly suited to the tasks set out for this study. PC analysis is equally time-consuming and produces data which are more difficult to interpret geologically, particularly without field work.

9.3 What information has been gained?

A large amount of new geological information has been gained from all of the data sets studied. The main contributions have been:

1. The proposed extension of the Argylla Formation's stratigraphy to those areas where it is currently undivided.

2. The separation of the Argylla Formation from the overlying Ballara Quartzite.

3. Improvements to the stratigraphy of the Corella Formation, including the confirmation that parts should be downgraded to the Corella Beds.

4. The demonstration of the differences between the Wonga and Burstall Granites which indicate their relative ages.

5. The provision of further evidence that some of the units within the Corella Formation mapped as intrusive may in fact be extrusive.

In this section, the relative contribution of each data set in achieving these results will be discussed. This relates to the data's spectral and spatial resolution and the degree to which they are affected by weathering, erosion, transport of weathered material and vegetation. The latter processes must be understood for each lithology before geological analysis of the data is possible.

9.3.1 Spectral Resolution

In terms of discrimination, higher spectral resolution does not always appear to be advantageous. In the Corella Formation NE of the Burstall Granite the high spectral resolution GMS data are in places less discriminating than the low spectral resolution TM data. This is because, although a wide variety of minerals are present in the rocks of this area and could be remotely sensed if exposed, weathering in this semi-arid area produces a few simple mineral groupings. The most dominant of these, clay minerals and iron oxides, have spectral signatures which TM is ideally designed to detect. The discrimination of a lithology often relies on these weathering products rather than the primary mineralogy of the rock, which is frequently masked.

Where the goal is identification, the higher spectral resolution data are clearly advantageous. Calcite, epidote, mica, kaolinite and vegetation all cause absorptions which fall within TM's 2.22 μm band. LSFit analysis has shown that the majority of 2.22 μm absorption in this field area is due to minerals rather than vegetation. The minerals causing this absorption can be separated using the GMS data, and to a lesser degree with the logarithmic residual TM data. The identification which can be achieved with the GMS data, and the near-identification possible with TM, calls into question the need for many contiguous spectral bands in future sensors.

9.3.2 Spatial resolution

The work reported here suggests that spatial resolution can be more important than spectral resolution. The 30 m spatial resolution of TM is insufficient in some instances to resolve geological components mixing on a similar scale, despite strong spectral contrasts between these components. The 10 m spatial resolution of the NS001 data overcomes this problem in many cases. The spatial resolution most appropriate for geological needs appears to be 10 m.

TM data can be used for detailed mapping at scales up to 1:50 000. The narrowest geological unit resolved with the TM data is a dolerite dyke 50 m across, which is seen where spectral contrasts with its host rock are strong. The NS001 data can be used at scales of up to 1:10 000, a significant improvement bringing the data into the realm of non-regional mapping. A major advantage of GMS data is that they can be flown with any spatial resolution desired. Reproduction of the AGR data at even 1:100 000 begins to present analytical problems.

9.3.3 Data integration

The AGR data are difficult to use in the field. Integration of the AGR data with the higher spatial resolution TM data overcomes this problem and should be routinely implemented. The HSI technique is the most appropriate method for integrating the TM and AGR data sets.

9.4 Final conclusions and recommendations

On balance, the TM data provide the most cost effective operational mapping tool for geologists. The full potential of these data is yet to be realised. TM data are superior to aircraft data of the equivalent spectral resolution in most respects, except in the important area of spatial resolution. Ten metre spatial resolution is required as a minimum for detailed analysis of geological problems. Data with the spectral resolution of the GMS data can be used to identify minerals. This suggests that, in many operational geological situations, high spectral resolution data such as those from the

AVIRIS sensor with 224 bands may represent over-kill. The implication is that the identification of minerals may not require 224 bands but a lesser number of well placed bands. This requires detailed investigation.

An ideal radiance remote sensing system for geological mapping would be satellite-borne, have on the order of 20 bands split evenly between the visible, near and short wave infrared and more importantly have 10 m spatial resolution. The acquisition of stereo imagery would also be advantageous. More work is needed aiming specifically to define the minimum number of bands needed, their band widths and where they should be positioned. Japan's Earth Resource Satellite 1 is a step in the right direction.

Such a system should include updated calibration values in the data it relays to earth. If reliable atmospheric data were still unavailable, the strategy to apply to data from such a system would involve an atmospheric correction, based on the automated technique for arid areas and water bodies for semi-arid areas. The author is involved in further work to improve these atmospheric correction techniques. Logarithmic residual processing should follow to produce near-reflectance data. This technique requires further testing in a variety of areas to confirm the consistency of the data it produces. The author is currently involved in studies using the technique in arid Egypt and semi-arid Namibia, with encouraging results. With noise-free, distortion-less satellite data this should become a routine procedure and form a part of all geological mapping.

BIBLIOGRAPHY

Abrams, J.M., Brown, D., Lepley, L. and Sadowski, R. 1983. Remote Sensing for Porphyry Copper Deposits in Southern Arizona. *Economic Geology*, **78**, 591-604.

Abrams, J.M. and Brown, D. 1985. Silver Bell, Arizona, Porphyry Copper Test Site Report, in Paley, H.N., ed., *Joint NASA/Geosat Test Case Project, Final report, Part 2*, **1**, American Association of Petroleum Geologists, Tulsa, OK, 4-1 - 4-83.

Barnsley, M.J. and Kay, S.A.W. 1990. The relationship between sensor geometry, vegetation-canopy geometry and image variance. *International Journal of Remote Sensing*, **11**, 1075-1083.

Best, M.G. 1982. *Igneous and Metamorphic Petrology*. W.H.Freeman and Company, New York, 630pp.

Blake, D.H. 1980. The early geological history of the Proterozoic Mt. Isa Inlier, NW Queensland: an alternative interpretation. *Bureau of Mineral Resources Journal of Australian Geology and Geophysics*, **5**, 243-256.

Blake, D.H. 1982. A review of the Corella Formation, Mt. Isa Inlier, Queensland. *Bureau of Mineral Resources Journal of Australian Geology and Geophysics*, **7**, 113-118.

Blake, D.H and Page, R.W. 1988. Early Proterozoic migmatitic basement in the Kalkadoon-Leichhardt belt of the Mt. Isa Inlier, NW Queensland. *Bureau of Mineral Resources Journal of Australian Geology and Geophysics*, **10**, 323-328.

Blom, R.G. and Daily, M. 1982. Radar image processing for rock-type discrimination. *IEEE Transactions on Geoscience Electronics*, **GE-20**, 876-887.

Buckingham, W.F. and Sommer, S.E. 1983. Mineralogical characterisation of rock surfaces formed by hydrothermal alteration and weathering - application to remote sensing. *Economic Geology*, **78**, 664-674.

Canas, A.A.D. and Barnett, M.E. 1985. The generation and interpretation of false-colour composite principal component images. *International Journal of Remote Sensing*, **6**, 867-881.

Carrere, V. 1990. Mineral Identification and Hydrothermal Alteration Mapping using Airborne Visible/Infrared Imaging Spectrometer (AVIRIS) data. Examples from the Goldfield Mining District, Nevada. *Proceedings of the Fifth Australasian Remote Sensing Conference*, **1**, Perth, WA, 135-145.

Chavez, P.S., Jr., Berlin, G.L. and Mitchell, W.B. 1977. Computer enhancement techniques of Landsat MSS digital images for land use/land cover assessments. *Remote Sensing of Earth Resources*, **6**, University of Tennessee, Tullahoma, TN, 259-275.

Chavez, P.S., Jr., Sides, S.C. and Anderson, J.A. 1991. Comparison of three different methods to merge multiresolution and multispectral data: Landsat TM and Spot Panchromatic. *Photogrammetric Engineering and Remote Sensing*, **57**, 295-306.

Clark, R.N., Gallagher, A.J. and Swayze, G.A. 1990a. Material Absorption Band Depth Mapping of Imaging Spectrometer Data using a Complete Band Shape Least Squares Fit with Library Reference Spectra. *Proceedings of the Second Airborne Visible/Infrared Imaging Spectrometer (AVIRIS) Workshop, JPL Publication*, **90-54**, Jet Propulsion Laboratory, Pasedena, CA, 176-186.

Clark, R.N., Swayze, G.A., King, T.V.V., Middlebrook, B., Calvin, W.M. and Gorelick, N. 1990b. The U.S. Geological Survey Digital Spectral Library and Analysis Software. *Proceedings of the Second Airborne Visible/Infrared Imaging Spectrometer (AVIRIS) Workshop, JPL Publication*, **90-54**, Jet Propulsion Laboratory, Pasedena, CA, 208-215.

Conel, J.E. and Alley, R.E. 1985. Lisbon Valley, Utah, Uranium Test Site Report, Appendix C: Principal Components for Lisbon Valley images, in Paley, H.N., ed., *Joint NASA/Geosat Test Case Project, Final report, Part 2*, **1**, American Association of Petroleum Geologists, Tulsa, OK, 8-121 - 8-136.

Conel, J.E., Green, R.O., Vane, G., Bruegge, C.J. and Alley, R.E. 1987. AIS-2 Radiometry and a comparison of methods for the recovery of Ground Reflectance. *Proceedings of the Third Airborne Imaging Spectrometer Data Analysis Workshop, JPL Publication*, **87-30**, Jet Propulsion Laboratory, Pasedena, CA, 18-47.

Creasy, J. 1990. Integrating GER64 aircraft data with a DEM generated from Spot Panchromatic satellite data. *Unpublished poster presentation, Fifth Australasian Remote Sensing Conference*, Perth, WA.

Crippen, R.E. 1987. The Regression Intersection Method of adjusting image data for Band Ratioing. *International Journal of Remote Sensing*, **8**, 137-155.

Crippen, R.E. 1988. The dangers of underestimating the importance of data adjustments in band ratioing. *International Journal of Remote Sensing*, **9**, 767-776.

Crosta, A.P. and Moore, J.McM. 1989. Geological mapping using Landsat Thematic Mapper imagery in Almeria Province, southeast Spain. *International Journal of Remote Sensing*, **10**, 505-514.

Cruickshank, B.I., Ferguson, J. and Derrick, G.M. 1980. The association of uranium and skarn development in the Mary Kathleen area, Queensland, in Ferguson, J. and Goleby, A.B., eds., *Uranium in the Pine Creek Geosyncline*, International Atomic Energy Agency, Vienna, 693-706.

Day, R.W., Whitaker, C.G., Murray, I.H. and Grimes, K.G. 1983. *Queensland Geology - A companion volume to the 1:2 500 000 scale geological map.* Geological Survey of Queensland Publication, **383**, Brisbane, Qld, 194pp.

Derrick, G.M. 1977. Metasomatic history and origin of uranium mineralisation at Mary Kathleen, northwest Queensland. *Bureau of Mineral Resources Journal of Australian Geology and Geophysics*, **2**, 123-130.

Derrick, G.M., Wilson, I.H., Hill, R.M., Glickson, A.Y. and Mitchell, J.E. 1977. Geology of the Mary Kathleen 1:100 000 Sheet area, northwest Queensland. *Bureau of Mineral Resources, Australia, Bulletin*, **193**, 114pp.

Derrick, G.M. and Wilson, I.H. 1981. The early geological history of the Proterozoic Mt. Isa Inlier, NW Queensland: an alternative interpretation - Discussion. *Bureau of Mineral Resources Journal of Australian Geology and Geophysics*, **6**, 267-271.

Derriman, M.D.J. and Agar, R.A. 1990. Gold and base metal exploration in the Pilbara Craton, Western Australia, using the Geoscan Airborne Multispectral Scanner. *Proceedings of the Fifth Australasian Remote Sensing Conference*, **2**, Perth, WA, 924-927.

Donoghue, D.N.M., Robinson, D.W.C. and Hook, S.J. 1990. Analysis of high spectral resolution data on a personal computer. *Proceedings of the Second Airborne Visible/Infrared Imaging Spectrometer (AVIRIS) Workshop, JPL Publication*, **90-54**, Jet Propulsion Laboratory, Pasedena, CA, 216-223.

Drury, S.A. 1987. *Image Interpretation in Geology.* Allen and Unwin, London, 243pp.

Drury, S.A. and Hunt, G.A. 1988. Remote Sensing of Laterized Archaean Greenstone Terrain: Marshall Pool area, Northeastern Yilgarn Block, Western Australia. *Photogrammetric Engineering and Remote Sensing*, **54**, 1717-1726.

Dudgeon, G.S., Nilsson, C.S. and Fry, W.B. 1990. Rangeland vegetation monitoring using the NOAA AVHRR data 1. Improving the spatial and radiometric accuracy of NDVI data. *Proceedings of the Fifth Australasian Remote Sensing Conference*, **1**, Perth, WA, 208-217.

Dwivedi, R.S. 1991. Technical note. The effects of band to band mis-registration on multispectral classification. *International Journal of Remote Sensing*, **12**, 1593-1597.

Fernandez-Alonso, M. and Tahon, A. 1991. Lithological discrimination and structural trends in W-Rewanda (Africa) on images of Airborne Radiometric and Aeromagnetic surveys, co-registered to a Landsat TM scene. *Photogrammetric Engineering and Remote Sensing*, **57**, 1155-1162.

Fraser, S.J., Gabell, A.R., Green, A.A. and Huntington, J.F. 1986. Targeting epithermal alteration and gossans in weathered and vegetated terrains using aircraft scanners: successful Australian case histories. *Proceedings of the Fifth Thematic Conference: 'Remote sensing for Exploration Geology'*, Reno, NV, 63-84.

Fraser, S.J. and Green, A.A. 1987. A software defoliant for geological analysis of band ratios. *International Journal of Remote Sensing*, **8**, 525-532.

Fraser, S.J. 1990a. Discrimination of ferric iron oxides on satellite Thematic Mapper data: a Mt. Newman case study. *Proceedings of the Fifth Australasian Remote Sensing Conference*, **1**, Perth, WA, 645-653.

Fraser, S.J. 1990b. A study of the surficial clay distribution at Mt. Leyshon: a comparison between XRD and spectral reflectance techniques. *Proceedings of the Fifth Australasian Remote Sensing Conference*, **2**, Perth, WA, 906-914.

Gabell, A.R., Huntington, J.F. and Green, A.A. 1985. US/Australia Joint Scanner Project: *CSIRO Institute of Energy and Earth Resources, Restricted Internal Report*, **1616R**, 209pp.

Gillespie, A.R. 1980. *Digital techniques of Image Enhancement,* in B.S.Siegal and A.R.Gillespie, eds., *Remote Sensing in Geology*, John Wiley and Sons, New York, 139-226.

Gillespie, A.R., Kahle, A.B. and Walker, R.E. 1986. Colour enhancement of highly correlated images. I Decorrelation and HSI Contrast Stretches. *Remote Sensing of Environment*, **20**, 209-235.

Goetz, A.F.H., Rock, B.N. and Rowan, L.C. 1983. Remote Sensing for Exploration: An Overview. *Economic Geology*, **78**, 573-590.

Green, A.A. and Craig, M.D. 1984. Integrated analysis of image data for mineral exploration. *Proceedings of the International Symposium on Remote Sensing of Environment, Third Thematic Conference, Remote Sensing for Exploration Geology*, **1**, Colorado Springs, CO, 131-137.

Green, A.A. and Craig, M.D. 1985. Analysis of aircraft spectrometer data with Logarithmic Residuals. *Proceedings of the First Airborne Imaging Spectrometer Data Analysis Workshop, JPL Publication*, **85-41**, Jet Propulsion Laboratory, Pasedena, CA, 111-119.

Green, A.A., Huntington, J.F., Gabell, A.R., Fraser S.J., Horsfall, C.L., Cocks, T. and Craig, M.D. 1985. An assessment of the exploration value of Aircraft TM data for Gold Exploration in Queensland. *CSIRO Institute of Energy and Earth Resources, Restricted Internal Report*, **1609R**.

Green, A.A., Berman, M., Switzer, P.S. and Craig, M.D. 1988. A transformation for ordering multispectral data in terms of image quality with implications for noise removal. *IEEE Transactions on Geoscience and Remote Sensing, GE-26*, **1**, 65-74.

Green, R. 1990. Reflectance recovery from Imaging Spectrometer radiance using a radiative transfer code for Lithological Mapping in the Clark Mountains, California. *Proceedings of the Fifth Australasian Remote Sensing Conference*, **1**, Perth, WA, 123-134.

Greenbaum, D. and Amos, B.J. 1991. Progress report on the use of remote sensing for hydrogeological mapping, in Greenbaum, D and others, Development of techniques for hydrogeological mapping and borehole siting: Progress Report for 1991. *British Geological Survey Technical Report,* WC/91/6, Keyworth, UK.

Gribble, C.D. and Hall, A.J. 1985. *A Practical Introduction to Optical Mineralogy.* George Allen and Unwin Ltd., London, 249pp.

Grove, C.I., Hook, S.J. and Paylor, E.D. 1992. Laboratory reflectance spectra of 160 minerals, 0.4 to 2.5 μm. *JPL Publication,* 92-2, Jet Propulsion Laboratory, Pasadena, CA, 406pp.

Harding, A.E. and Forrest, M.D. 1988. Image processing methods for the presentation of multiple geological data sets from the English Lake District. *Proceedings of the IGARSS-88 Symposium*, 3, Edinburgh, Scotland, 1659-1662.

Harris, R. 1987. *Satellite Remote Sensing. An Introduction.* Routledge and Kegan Paul Ltd., London, 220pp.

Hawkins, B.J. 1975. Mary Kathleen uranium deposit, in Knight, C.L., ed., *Economic Geology of Australia and Papua New Guinea: 1. Metals*, Australasian Institute of Mining and Metallurgy, Melbourne, 398-402.

Hill, J. and Sturm, B. 1991. Radiometric correction of multitemporal Thematic Mapper data for use in agricultural land-cover classification and vegetation monitoring. *International Journal of Remote Sensing,* 12(7), 1471-1491.

Holcombe, R.J. and Fraser, S.J. 1979. Structural and stratigraphic problems of the Argylla Formation near Mary Kathleen, Queensland. *Journal of the Geological Society of Australia*, 26, 419-434.

Hook, S.J. 1989. *An Evaluation of NS001 and TIMS Data for Lithological Mapping and Mineral Exploration in Weathered Vegetated Terrain.* Unpublished Ph.D. thesis, University of Durham, U.K., 306pp.

Hook, S.J. 1990. The combined use of multispectral remotely sensed data from the short wave infrared (SWIR) and thermal infrared (TIR) for lithological mapping and mineral exploration. *Proceedings of the Fifth Australasian Remote Sensing Conference*, **1**, Perth, WA, 371-380.

Hunt, G.R. 1977. Spectral signatures of particulate minerals in the visible and near infrared. *Geophysics*, **42**, 501-513.

Hunt, G.R. 1980. Electromagnetic radiation: The communication link in Remote Sensing, in B.S.Siegal and A.R.Gillespie, eds., *Remote Sensing in Geology*, John Wiley and Sons, New York, 5-45.

Huntington, J.F. 1984. Interpretation of visible, near and short wavelength infrared, field and airborne spectra from Mary Kathleen, Queensland, Australia. *Abstract in Proceedings of the International Symposium on Remote Sensing of Environment, Third Thematic Conference, Remote Sensing for Exploration Geology*, **1**, Colorado Springs, CO, 227.

Huntington, J.F., Green, A.A. and Craig, M.D. 1989. Identification - the goal beyond discrimination. *Proceedings of IGARSS-89/12th Canadian Symposium on Remote Sensing*, Vancouver, BC, 6-11.

Huntington, J.F., Craig, M.D., Munday, T.J. and Churchill, J. 1990. Eight bands can map minerals. *Unpublished oral presentation, Fifth Australasian Remote Sensing Conference*, Perth, WA.

Irons, J.R. and Labovitz, M.L. 1982. A Data Analytic approach to look-angle Radiance Adjustment. *Journal of Applied Photographic Engineering*, **8**, 128-137.

Jacques, A.L., Blake, D.H. and Donchak, P.J.T. 1982. Regional metamorphism in the Selwyn Range area, NW Queensland. *Bureau of Mineral Resources Journal of Australian Geology and Geophysics*, **7**, 181-196.

Kimes, D.S. 1983. Dynamics of Directional Reflectance Factor distributions for Vegetation Canopies. *Applied Optics*, **22**, 1364-1372.

Kealy, P.S. 1990. *Lithological Mapping by Remote Sensing using Emittance Information in the Thermal Infrared Region.* Unpublished Ph.D. thesis, University of Durham, U.K., 135pp.

Kruse, F.A. 1990a. Analysis of Airborne Visible/Infrared Imaging Spectrometer (AVIRIS) data for the Northern Death Valley Region, California/Nevada. *Proceedings of the Second Airborne Visible/Infrared Imaging Spectrometer (AVIRIS) Workshop, JPL Publication*, **90-54**, Jet Propulsion Laboratory, Pasedena, CA, 100-106.

Kruse, F.A. 1990b. Identification and Mapping of Alteration Minerals with the Airborne Visible/Infrared Imaging Spectrometer. *Proceedings of the Fifth Australasian Remote Sensing Conference*, **1**, Perth, WA, 146-154.

Laughlin, W.P. 1991. Principal component analysis for alteration mapping. *Photogrammetric Engineering and Remote Sensing*, **57**, 1163-1170.

Lillesand, T.M. and Keifer, R.W. 1987. *Remote Sensing and Image Interpretation (2nd edition).* John Wiley and Sons, New York, 721pp.

Loosveld, R. and Schreurs, G. 1987. Discovery of thrust klippen, northwest of Mary Kathleen, Mt. Isa Inlier, Australia. *Australian Journal of Earth Sciences*, **34**, 387-402.

Lyon, R.J.P. and Honey, F.R. 1989. Spectral Signature extraction from airborne imagery using the Geoscan MK.II Advanced Airborne Scanner in the Leonora, Western Australia Gold District. *Proceedings of IGARSS-89/12th Canadian Symposium on Remote Sensing*, Vancouver, BC, 2925-2930.

Maas, R., McCulloch, M.T. and Campbell, I.H. 1987. Sm-Nd isotope systematics in uranium-rare earth mineralisation at the Mary Kathleen Uranium mine, Queensland. *Economic geology*, 82, 1805-1826.

Mackin, S. 1989. *Mineral Mapping using airborne Imaging Spectrometry data.* Unpublished Ph.D. thesis, University of Durham, U.K., 101pp.

Markham, B.L. and Barker, J.L. 1986. Landsat MSS and TM post-calibration dynamic ranges, exoatmospheric reflectances and at-satellite temperatures. *EOSAT LANDSAT Technical Notes,* 1, 3-8.

Marsh, S.H. 1990. Geological Mapping with Landsat Thematic Mapper data in the Proterozoic Mt. Isa Inlier, NW Queensland. *Proceedings of the Fifth Australasian Remote Sensing Conference*, 1, Perth, WA, 635-644.

Marsh, S.H. 1991. The effect of increased Spatial Resolution on Spectral Resolution: Geological Mapping with NS001 Aircraft Thematic Mapper data in NW Queensland, Australia. *Proceedings of the Eighth ERIM Thematic Conference*, Denver, CO, 481-489.

Marsh, S.H., O'Connor, E.A. and Greenbaum, D. 1992. Industrial minerals exploration in Egypt using Landsat TM. *Proceedings of the Sixth Australasian Remote Sensing Conference*, 3, Wellington, NZ, 314-323.

Mather, P.M. 1987. *Computer processing of remotely-sensed images: an introduction.* John Wiley & Sons, New York, 352pp.

Matheson, R.S. and Searl, R.A. 1956. Mary Kathleen uranium deposit, Mt. Isa - Cloncurry district, Queensland, Australia. *Economic Geology*, 51, 528-540.

Milton, E.J. and Rollin, E.M. 1987. *The GER IRIS Mk.IV Spectroradiometer: A Guide for UK users*, Department of Geography, University of Southampton, 138pp.

Ollier, C. 1984. *Weathering (2nd edition)*, Geomorphology texts; 2, Longman Inc., New York, 270pp.

Oliver, N.H.S., Pearson, P.J. and Holcombe, R.J. 1985. Chronology of magmatism, skarn formation and uranium mineralisation, Mary Kathleen, Queensland, Australia - a discussion. *Economic Geology*, **80**, 513-520.

Page, R.W. 1983. Chronology of magmatism, skarn formation and uranium mineralisation, Mary Kathleen, Queensland, Australia. *Economic Geology*, **78**, 838-853.

Plumb, K.A., Derrick, G.M. and Wilson, I.H. 1980. Precambrian geology of the McArthur River - Mt. Isa region, Northern Australia, in Henderson, R.A. and Stephenson, P.J., eds., *The Geology and Geophysics of Northeastern Australia*, Geological Society of Australia, Queensland Division, Brisbane, 71-88.

Podwysocki, M.H., Segal, D.B. and Abrams, M.J. 1983. Use of Multispectral Scanner Images for assessment of Hydrothermal Alteration in the Marysvale, Utah, Mining Area. *Economic Geology*, **78**, 711-722.

Porter, W.M., Chrien, T.G., Hansen, E.G. and Sarture, C.M. 1990. Evolution of the Airborne Visible/Infrared Imaging Spectrometer (AVIRIS) flight and ground data processing system. *Imaging Spectroscopy of the Terrestrial Environment, SPIE Proceedings*, **1298**, 11-17.

Qari, M.Y.H.T. 1989. Lithological mapping and structural analysis of the Proterozoic rocks in part of the Arabian Shield using Landsat images. *International Journal of Remote Sensing*, **10**, 499-503.

Ramsay, C.R. and Davidson, L.R. 1970. The origin of scapolite in the regionally metamorphosed rocks of Mary Kathleen, Queensland, Australia. *Contributions to Mineralogy and Petrology*, **25**, 41-51.

Rothery, D.A. 1987. Improved discrimination of rock units using Landsat Thematic Mapper imagery of the Oman Ophiolite. *Journal of the Geological Society, London*, **144**, 587-597.

Scott, A.K. and Scott, A.G. 1985. Geology and genesis of uranium-rare earth deposits at Mary Kathleen, Northwest Queensland. *Bulletin of the Australasian Institute of Mining and Metallurgy Proceedings*, **290**, 79-89.

Schwertmann, U. 1985. Formation of secondary iron-oxides in various environments, in Drever, J.I., ed., *The Chemistry of Weathering*, D. Reidel Publishing Company, Dordrecht, 119-120.

Settle, J. J. 1990. Contextual models and the use of Dirichlet Priors for unmixing problems. *Proceedings of the Fifth Australasian Remote Sensing Conference*, **1**, Perth, WA, 314-323.

Slater, P.N. 1980. *Remote Sensing: Optics and Optical Systems.* Addison and Wesley, Reading, MA, 575pp.

Smith, R.J. 1985. Geophysics in Australian mineral exploration. *Geophysics*, **50**, 2637-2665.

Sultan, M., Arvidson R.E. and Sturchio, N.C. 1986. Mapping of Serpentine in the Eastern Desert of Egypt by using Landsat Thematic Mapper Data. *Geology*, **14**, 995-999.

Switzer, P., Kowalik, W.S. and Lyon, R.J.P. 1981. Estimation of Atmospheric Path-Radiance by the Covariance Matrix Method. *Photogrammetric Engineering and Remote Sensing*, **47**, 1469-1476.

USGS, 1984. *Landsat 4 data users handbook.* US Geological Survey, Alexandria, VA, 86pp.

Wilson, I.H. 1978. Volcanism on a Proterozoic Continental Margin in NW Queensland. *Precambrian Research*, **7**, 205-235.

Wilson, I.H. 1983. Discussion: A review of the Corella Formation, Mt. Isa Inlier, Queensland. *Bureau of Mineral Resources Journal of Australian Geology and Geophysics*, **8**, 161-163.

Windeler, D.S.Jr. and Lyon, R.J.P. 1991. Discriminating dolomitization of marble in the Ludwig Skarn near Yerington, Nevada, using high resolution airborne infrared imagery. *Photogrammetric Engineering and Remote Sensing*, **57**, 1171-1177.

APPENDIX A. SAMPLE LOCALITIES

Samples were taken at 208 localities. During the first field season, samples 1 - 131 were collected. Sample numbering began at 200 in the second field season, when samples 200 - 276 were collected. The samples were collected along the 22 traverses depicted in Figure A.1. There follows a list of every sample locality for each traverse, together with the name of the lithology and the main minerals identified by analysis of IRIS spectra.

1. Barkly Highway: from west to east crossing the Dog Bone Dolerite, Argylla Formation, Magna Lynn Metabasalt, Corella Formation and Hardway Granite.

1	Dog Bone Dolerite	Basic rocks, chlorite, amphibole
1w		Goethite, amphibole
1a		Goethite, quartz, amphibole, Al-OH
2	Pkc_1	Amphibole, calcite, Fe-oxide
3	Pkc_1	Amphibole, calcite, quartz, Al-OH
3w		Goethite, amphibole, calcite, quartz, Al-OH
4	Pkc_1	Fe-oxide, amphibole
5	Hardway Granite	Fe-oxide, Al-OH, quartz
5w		Goethite, quartz, kaolinite
5a		Goethite, quartz, kaolinite, mica, amphibole
6	Hardway Granite	Goethite, Al-OH, chlorite, mica
6w		Goethite, Al-OH, chlorite, mica
7w	Hardway Granite	Goethite, Al-OH, chlorite
7ww		Goethite, quartz, Al-OH
8	Argylla Formation	Quartz, muscovite
8w		Goethite, muscovite, montmorillonite
9w	Argylla Formation	Goethite, quartz, mica
10w	Magna Lynn Metabasalt	Goethite, Al-OH, amphibole, mica
11w	Magna Lynn Metabasalt	Goethite, amphibole, mica, montmorillonite
11	Argylla Formation	Muscovite, amphibole, calcite
12	Magna Lynn Metabasalt	Noisy spectrum

13a	Magna Lynn Metabasalt	Goethite, amphibole, calcite
14	Argylla Formation	Fe-oxide
14w		Fe-oxide, goethite
15	Magna Lynn Metabasalt	Basic rocks, amphibole
15w		Goethite, amphibole, chlorite
16w	Argylla Formation	Goethite, amphibole, calcite, mica

2. **Solitary Prospector East:** from west to east across the Corella Formation, Ballara Quartzite and Argylla Formation on the Rosebud Syncline's east limb.

17	Pkc_1	Goethite, calcite
17w		Goethite, calcite, amphibole
17a		Goethite, calcite, chlorite
18	Pkc_1 (Cu-mineralised)	Chrysocolla, gibbsite
33w	Pkc_1	Goethite, calcite
34w	Pkc_1	Goethite, calcite
34a		Goethite, calcite, chlorite, kaolinite
35	Pkc_1	Goethite, calcite
35w		Goethite
35a		Goethite, calcite, chlorite, Al-OH
36w	Pkc_1	Goethite, calcite, epidote
36a		Goethite, calcite, amphibole
37w	Pkc_1	Goethite, kaolinite, amphibole
38w	Pkc_1	Goethite, amphibole
39w	Pkb/Pea?	Goethite, kaolinite, chlorite
39a		Goethite, kaolinite, quartz
40w	Pkb/Pea?	Goethite, muscovite, quartz
40a		Goethite, kaolinite, quartz
41w	Pea/Pkb?	Goethite, kaolinite, mica
42w	Pea/Pkb?	Goethite, kaolinite

3. Solitary Prospector West: from west to east across the Ballara Quartzite and Corella Formation in the Rosebud Syncline's west limb.

20w	Pkb_2	Goethite, quartz
21w	Pkc_1	Goethite, calcite, mica
21a		Goethite, quartz, Al-OH
22	Pkc_1	Goethite, chlorite, Al-OH
22w		Goethite, chlorite, Al-OH
23w	Pkc_1	Goethite, calcite, chlorite, Al-OH
24	Pkc_1	Goethite, amphibole
24w		Goethite, amphibole, Al-OH
25w	Pkc_1	Noisy spectrum
25a		Goethite, calcite
26w	Pkc_1	Goethite, chlorite, amphibole, kaolinite
27	Pkc_2	Goethite, muscovite
27w		Goethite, muscovite
27a		Fe-oxide, quartz, mica
28w		Goethite, muscovite, calcite
29w	Pkc_2	Goethite, chlorite, amphibole, calcite, Al-OH
29a		Goethite, calcite, kaolinite
30w	Pkc_2	Goethite, epidote, phlogopite, calcite
30a		Goethite, epidote, mica
31w	Pkc_2	Goethite, calcite, chlorite
31w	(Second rock type)	Goethite, epidote, mica
32	Pkc_2	Goethite, mica, chlorite
19w	Pkc_2	Goethite, mica, chlorite

4. Billabong Creek: from west to east across the Corella Formation northeast of the Burstall Granite.

65w	Pkc_{2q}	Goethite, quartz, kaolinite
65a		Goethite, quartz, kaolinite
66	Lake Corella Dolerite	Basic rock, amphibole, calcite

66w		Goethite, amphibole, calcite, epidote
66a		Goethite, calcite, epidote
67w	Pkc_2	Goethite, kaolinite
67a		Goethite, kaolinite, calcite, amphibole
68	Pkc_2	Goethite, kaolinite, calcite
69	Pkc_2	Goethite, kaolinite, amphibole
69w		Goethite, kaolinite
70w	Pkc_2	Goethite
71	Pkc_2	Goethite, chlorite, calcite, amphibole
71w		Goethite, calcite, amphibole
72a	Pkc_2	Fe-oxide, calcite, amphibole, kaolinite
73	Pkc_2	Goethite, amphibole, kaolinite
73w		Goethite, amphibole, kaolinite
74	Pkc_2	Basic rock, amphibole, epidote
74a		Goethite, calcite, amphibole, kaolinite
75w	Pkc_1	Goethite, calcite, kaolinite
76w	Pkc_1	Goethite, amphibole, calcite, epidote
76a		Goethite, epidote, amphibole, kaolinite
77w	Pkc_1	Goethite, chlorite, amphibole
77a		Goethite, amphibole, chlorite, kaolinite
64w	Pkc_1	Goethite, amphibole, calcite, kaolinite
64a		Goethite, calcite, kaolinite
63	Pkc_1	Goethite, basic rock, amphibole, chlorite
243	Pkc_1	Goethite, epidote, calcite, Al-OH
243w		Goethite, epidote, calcite, kaolinite
243a		Goethite, kaolinite, epidote, calcite
62	Pkc_1	Fe-oxide, calcite, chlorite
62w		Goethite, calcite, chlorite
61	Pkc_1	Fe-oxide, amphibole, calcite
61w		?Hematite/goethite, amphibole, kaolinite
60w	Pkc_1	Goethite, calcite, amphibole, kaolinite
59w	Pkc_1	Goethite, calcite, chlorite
58	Pkc_1	Goethite, calcite, kaolinite

58w		Goethite, calcite, kaolinite
57w	Pkc_1	Goethite, calcite, chlorite, Al-OH
56	Pkc_1	Goethite, amphibole, calcite, mica
56w		?Hematite/Goethite, Chlorite, amphibole, Al-OH
55w	Pkc_1	Goethite, chlorite, calcite, amphibole
242	Pkc_1	Goethite, epidote, Al-OH
242w		Goethite, epidote, calcite
242a		Goethite, epidote
54	Pkc_1	Goethite, calcite, mica
54w		?Hematite/Goethite, epidote, calcite, chlorite
54a		Fe-oxide, epidote, calcite
241w	Pkc_2	Goethite, epidote
241a		Goethite, epidote, kaolinite
53w	Pkc_2	Goethite, chlorite, calcite
52w	Pkc_2	Fe-oxide, calcite, amphibole
52a		Calcite, kaolinite
51w	Pkc_2	Goethite, calcite, epidote
50w	Pkc_2	Goethite, epidote, chlorite, calcite, amphibole
49	Pkc_2	Goethite, epidote, chlorite, calcite
49w	Pkc_2	Goethite, calcite, kaolinite
48w	Pkc_2	Goethite, calcite, epidote
48a		Hematite, calcite, epidote
47w	Pkc_2	Goethite, epidote, calcite
46	Pkc_2	Calcite
45w	Pkc_2	Goethite, epidote, calcite
44w	Pkc_2	Goethite, calcite, amphibole, chlorite
44a		Goethite, calcite, chlorite, kaolinite
43w	Pkc_1	Goethite, amphibole
43a		Goethite, epidote, calcite, Al-OH

5. Tramline Dyke: from west to east within the Corella Formation and north along the Lake View Dolerite.

244	Pkc_2	Goethite, muscovite, quartz, chlorite
244w		Goethite, muscovite, quartz, chlorite
244a		Goethite, muscovite, chlorite
245w	Lake View Dolerite	Goethite, epidote, quartz, mica
245a		Goethite, mica, quartz
239	Pkc_1	Goethite, calcite, quartz, Al-OH
239w		Goethite, amphibole, kaolinite, quartz
239a		Goethite, amphibole, kaolinite, quartz
238	Lake View Dolerite	**Lost by DHL**
240w	Pkc_1	Fe-oxide, amphibole, chlorite, Al-OH
78w	Pkc_1	Goethite, calcite
78a		Goethite, calcite, kaolinite
79w	Lake View Dolerite	Goethite, basic rock, amphibole
80	Pkc_1	Goethite, amphibole
80w		Goethite, chlorite, calcite, amphibole
237	Pkc_1	Goethite, calcite, mica, chlorite
237w		Goethite, calcite, mica, chlorite, amphibole, quartz
237a		Goethite, calcite, mica, amphibole, quartz
236w	Pkc_1	Goethite, calcite, epidote, Al-OH
235w	Pkc_1	Goethite, chlorite, Al-OH
235a		Goethite, quartz, kaolinite
234	Pkc_1	Goethite, basic rock, chlorite, amphibole
234w		Goethite, chlorite, amphibole, Al-OH

6. Birdsong Creek: eastward across the Corella Formation north of the Billabong Creek Traverse.

88	Pkc_2	Goethite, basic rock, amphibole, Al-OH
88w		Goethite, amphibole, Al-OH
88a		Goethite, amphibole, Al-OH

87w	Pkc_2	Goethite, muscovite, quartz
87a		Goethite, muscovite, quartz
86w	Pkc_1	Goethite, amphibole
86a		Goethite, amphibole, kaolinite
85w	Pkc_1	?Hematite/goethite, muscovite, epidote
85a		?Hematite/goethite, epidote, muscovite
84w	Pkc_1	Fe-oxide, epidote, calcite
84a		Goethite, epidote, kaolinite
83w	Pkc_2	Fe-oxide, chlorite, kaolinite
83a		Goethite, kaolinite, chlorite, calcite
82	Pkc_2	Basic rock, epidote, Al-OH
82w		Goethite, epidote, Al-OH
82a		Goethite, epidote, kaolinite
81w	Pkc_2	Goethite, epidote, calcite, Al-OH
81a		Goethite, epidote, calcite, kaolinite

7. Calcite Pit Traverse: eastward across the Corella Formation and north of the Birdsong Creek Traverse and along-strike within Pkc_1.

92	Pkc_2	Fe-oxide, amphibole, kaolinite
92w		Goethite, amphibole, calcite, chlorite, kaolinite
92a		Goethite, calcite, amphibole, kaolinite
93	Pkc_2	Goethite
93a		Goethite, muscovite
94w	Pkc_2	Goethite, muscovite
94a		Goethite, muscovite, quartz
90	Pkc_1	Goethite, mica, kaolinite
95w	Pkc_1	Goethite, chlorite, Al-OH
95a		Fe-oxide, Al-OH, quartz
89	Pkc_1	Calcite
89a		Calcite
250	Pkc_1	**Lost by DHL**
91	Pkc_2	Goethite, calcite

91w		Goethite, calcite, chlorite, mica
91a		Goethite, calcite, kaolinite

8. Parrot Creek: eastward across the Corella Formation north of the Billabong Creek Traverse.

246	Pkc_2	**Lost by DHL**
247	Pkc_2	**Lost by DHL**
248	Pkc_2	**Lost by DHL**
249	Pkc_2	**Lost by DHL**
97	Pkc_2	Fe-oxide, calcite, kaolinite
97w		Goethite, calcite, kaolinite
96w	Pkc_2	Goethite, mica, quartz, calcite, amphibole
96a		Goethite, mica, quartz

9. Mt. Burstall North: from the Burstall Granite across the Corella Formation to the Lake Corella Dolerite.

102a	Burstall Granite	Quartz, kaolinite
101	Burstall Granite	Goethite, mica, Al-OH
101w		Goethite, mica, quartz, kaolinite
100	Pkc_2	Goethite, chlorite, kaolinite
100w		Goethite, chlorite, amphibole, kaolinite
103		Noisy spectrum
99	Lake Corella Dolerite	?Hematite/goethite, amphibole, mica, chlorite
98w	Lake Corella Dolerite	Noisy spectrum
98a		Amphibole, Al-OH

10. Enormous Termite Mounds: two localities only, on the southwest margin of the Burstall Granite's main mass.

104	Burstall Granite	Fe-oxide, flat spectrum
104w		Goethite, mica, amphibole, kaolinite

104a		Goethite, quartz, muscovite, kaolinite
105	Burstall Granite	Fe-oxide, flat spectrum
105w		Goethite, kaolinite, quartz

11. East Wonga Creek: north-south within the Wonga granite.

108a	Soil on Wonga Granite	Goethite, kaolinite, quartz (deep iron absorption)
107a	Wonga soil	Goethite, kaolinite, quartz, chlorite
107b	Soil on Wonga Granite	Goethite, quartz, kaolinite, chlorite (deep iron absorption)
106	Wonga Granite	Goethite, amphibole, Al-OH
106w		Goethite, amphibole, kaolinite

12. Rosebud: from the northwest to the southeast across the Wonga Granite, east of the Rosebud Syncline.

109	Wonga Granite	Flat spectrum
109w		Goethite, kaolinite
110	Wonga Granite	Goethite, kaolinite
271	Wonga Granite	**Lost by DHL**
272	Wonga Granite	**Lost by DHL**
273	Wonga Granite	**Lost by DHL**
274	Wonga Granite	**Lost by DHL**
275	Wonga Granite	**Lost by DHL**
276	Soil on Wonga Granite	**Lost by DHL**

13. Central Wonga: a series of outcrop tors to the east of Mary Kathleen township.

111w	Wonga Granite	Goethite, kaolinite, mica
112	Wonga Granite	Fe-oxide, kaolinite
112w		Goethite, kaolinite, mica
113a	Wonga Granite	Goethite, quartz, kaolinite, mica

114a	Soil on Wonga Granite	Goethite, quartz, kaolinite, calcite (deep iron absorption)
210	Wonga Granite	Goethite, quartz, muscovite, kaolinite
210w		Goethite, quartz, muscovite, kaolinite
211	Wonga Granite	**Lost by DHL**
212	Wonga Granite	**Lost by DHL**
213	Wonga Granite	**Lost by DHL**
214a	Wonga Granite	Goethite, kaolinite, quartz, muscovite
215a	Soil on Wonga Granite	Goethite, quartz, muscovite, kaolinite
216	Wonga Granite	**Lost by DHL**
217	Wonga Granite	**Lost by DHL**

14. Cameron River: an eastward traverse following the river course across the strike of the Corella Formation, Lime Creek Metabasalt and Lime Creek Dolerite.

120w	Lime Creek Basalt	Goethite, amphibole
120a		Goethite, amphibole, Al-OH
121	Pkc_3	Goethite, amphibole
121w		Goethite, amphibole
121a		Goethite, amphibole, mica
119a	Debris on Lime Creek Metabasalt	Noisy spectrum
118w	Lime Creek Dolerite	Goethite, amphibole, kaolinite
118a		Goethite, amphibole, montmorillonite
117a	Lime Creek Dolerite	Fe-oxide, amphibole, Al-OH
116	Lime Creek Dolerite	Goethite, basic rock, calcite, montmorillonite
116w		Goethite, kaolinite, chlorite, calcite
115	Lime Creek Dolerite	Goethite, amphibole
115w		Goethite, amphibole, kaolinite

15. Loopback Creek: the same sequence as Traverse 14, but further south.

123w	Lime Creek Basalt	Goethite, amphibole

123a		Fe-oxide, amphibole, Al-OH
122w	Lime Creek Basalt	Goethite, amphibole
122a		Goethite, amphibole, Al-OH
124w	Pkc_3	Noisy spectrum
124a		Fe-oxide, chlorite, amphibole, mica
125	Lime Creek Dolerite	Noisy spectrum

16. Final Creek: a traverse across the Corella Formation in the Mary Kathleen Syncline.

131w	Pkc_2	Goethite, quartz
131a		Goethite, quartz, phlogopite
130	Pkc_2	?Goethite/hematite, quartz, Al-OH, calcite
130w		Goethite, quartz, calcite
130a		Goethite, quartz, kaolinite
129	Pkc_2	Goethite, chlorite, kaolinite
129w		Goethite, amphibole, Al-OH
128w	Pkc_2	Goethite, amphibole, mica
127a	Pkc_2	Goethite, kaolinite, quartz
126	Pkc_2	Goethite, kaolinite, mica
126w		Goethite, kaolinite, mica

17. Magna Lynn: a series of sample localities across interleaved Argylla Formation and Magna Lynn Metabasalt.

209	Argylla Formation	**Lost by DHL**
208	Argylla Formation	**Lost by DHL**
207	Argylla Formation	**Lost by DHL**
206a	Magna Lynn Basalt	Goethite, amphibole, epidote, kaolinite
205a	Quartz float	Goethite, kaolinite, quartz, montmorillonite
204	Magna Lynn Basalt	**Lost by DHL**
203	Magna Lynn Basalt	**Lost by DHL**
202	Magna Lynn Basalt	**Lost by DHL**

201	Magna Lynn Basalt	**Lost by DHL**
200	Argylla Formation	Goethite, amphibole, muscovite, montmorillonite, quartz
200w		Goethite, amphibole, muscovite, quartz

18. Rosebud Ridge North: a north-south traverse along the Argylla Formation/Ballara Quartzite contact on the east limb of the Rosebud syncline.

223w	Ballara Quartzite	Goethite, muscovite, kaolinite, quartz
223a		Goethite, muscovite, kaolinite, quartz
222w	Ballara Quartzite	Goethite, muscovite, quartz, kaolinite
222a		Goethite, quartz, Al-OH
220w	Ballara Quartzite	Goethite, quartz, kaolinite
220a		Goethite, quartz, Al-OH
221w	Argylla Formation	Fe-oxide, quartz, kaolinite, chlorite, amphibole
221a		Goethite, quartz, montmorillonite/quartz, kaolinite
219a	Ballara Quartzite	Goethite, kaolinite, quartz
218	Ballara Quartzite	**Lost by DHL**
224w	Argylla Formation	Goethite, quartz, muscovite, kaolinite

19. Rosebud Ridge South: two parallel eastward traverses across the east limb of the Rosebud Syncline, south of the Cameron Fault.

225	Ballara Quartzite	Fe-oxide, basic rock, mica
225w		Goethite, kaolinite, quartz
225a		Goethite, kaolinite, quartz
226	Argylla Formation	Goethite, kaolinite, amphibole, quartz
226w		Goethite, kaolinite, amphibole, quartz
226a		Goethite, kaolinite, amphibole, quartz
227	Argylla Formation	Goethite, quartz, kaolinite, mica
227w		Goethite, quartz, muscovite
228	Argylla Formation	Goethite, quartz, kaolinite
228w		Goethite, quartz, kaolinite

229a		Goethite, kaolinite
230	Pkc_1	Fe-oxide, amphibole
230w		Goethite, calcite, kaolinite, quartz
230a		Goethite, quartz, kaolinite
231w	Ballara Quartzite	Goethite, quartz, kaolinite, muscovite, chlorite
231a		Goethite, quartz, kaolinite
232w	Argylla Formation	Goethite, quartz, muscovite, kaolinite
233	Argylla Formation	**Lost by DHL**

20. Distant Traverse: west-east across the west side of the northeast Corella Formation.

251	Pkc_2	**Lost by DHL**
252	Pkc_2	**Lost by DHL**
253	Pkc_2	**Lost by DHL**
254	Pkc_2	**Lost by DHL**
255	Pkc_2	**Lost by DHL**
256	Pkc_2	**Lost by DHL**

21. Dog Bone Traverse: sampling the Corella Formation at its contact with the Ballara Quartzite, and also the Dog Bone Dolerite.

264	Pkc_1	**Lost by DHL**
263	Pkc_1	**Lost by DHL**
262	Pkc_1	**Lost by DHL**
261	Pkc_1	**Lost by DHL**
260	Dog Bone Dolerite	**Lost by DHL**
259	Pkc_1	**Lost by DHL**
258	Mixed Ballara Quartzite and Corella Fm.	**Lost by DHL**
257	Ballara Quartzite	**Lost by DHL**

22. Mt. Burstall South: a series of sample localities on the south of Mt. Burstall, including the granite and Corella Formation it obscures.

265	Burstall Granite	**Lost by DHL**
266	Burstall Granite	**Lost by DHL**
267	Pkc_2	**Lost by DHL**
268	Pkc_2	**Lost by DHL**
269	Pkc_2	**Lost by DHL**
270	Burstall Granite	**Lost by DHL**

*Of three boxes of samples from the second field season sent to the UK via DHL, only two arrived at Durham University.

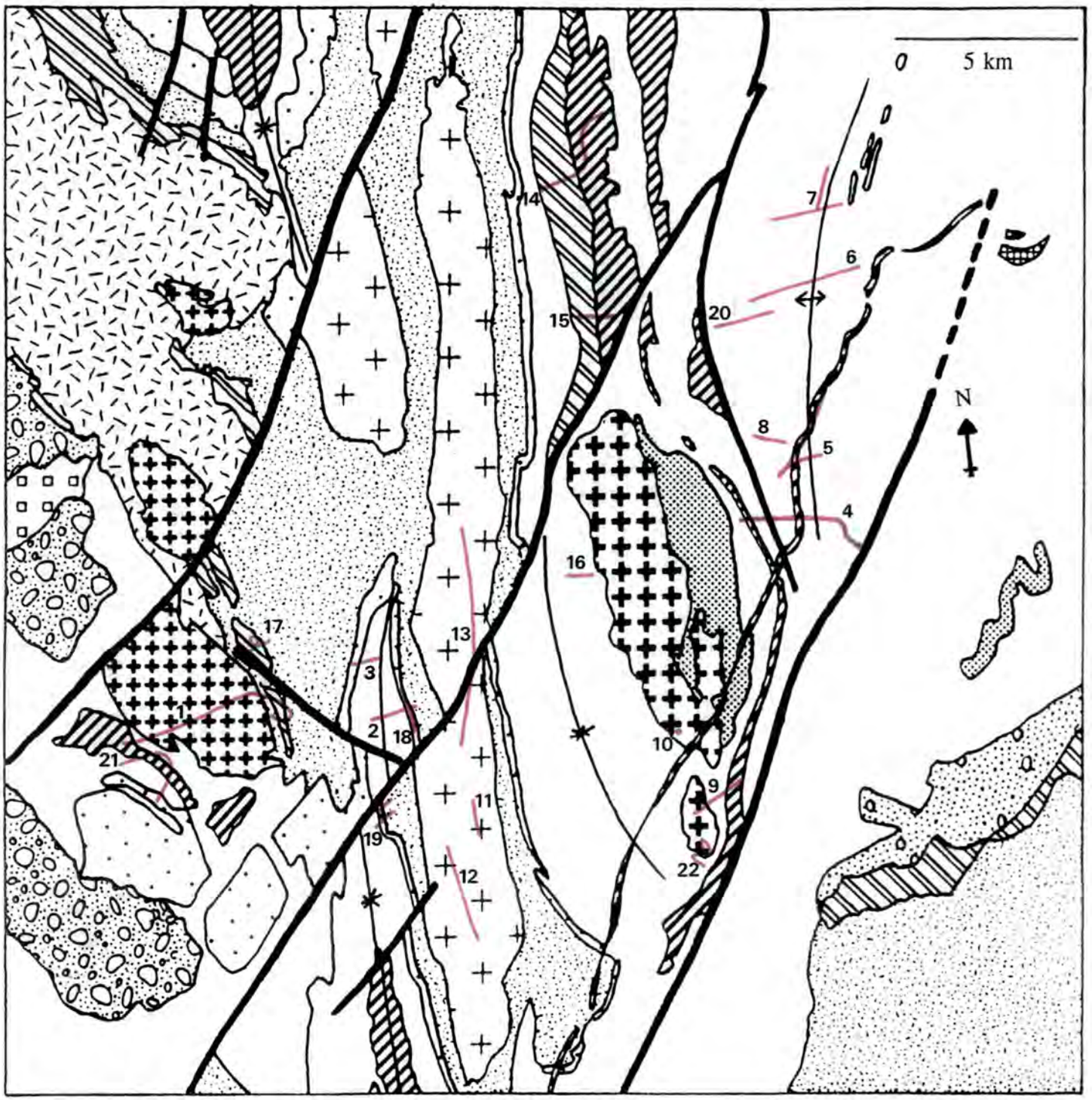

Figure A.1 The locations of the 22 field traverses.

Enclosure 2.1 The geology of the study area at 1:100 000 scale as depicted on the MARABBA and MARY KATHLEEN sheets.

Enclosure 6.1 AGR colour composite with the geology of the study area for comparison. **In the image**, potassium is in red, thorium in green and uranium in blue. **On the map**, circle = Mary Kathleen. Dolerites and metabasalts: 1 = Magna Lynn, 2 = Cone Creek, 3 = Lime Creek, 4 = Little Beauty, 5 = Dog Bone, 6 = Rosebud, 7 = Lake Corella, 8 = Lake View. Burstall Pegmatite dykes = 9. Faults: A = Wonga, B = Cameron, C = Fountain Range, D = Greens Creek. To allow comparison of the image and units on the map, an overlay is provided which *schematically* relates the geological boundaries and faults to the image.

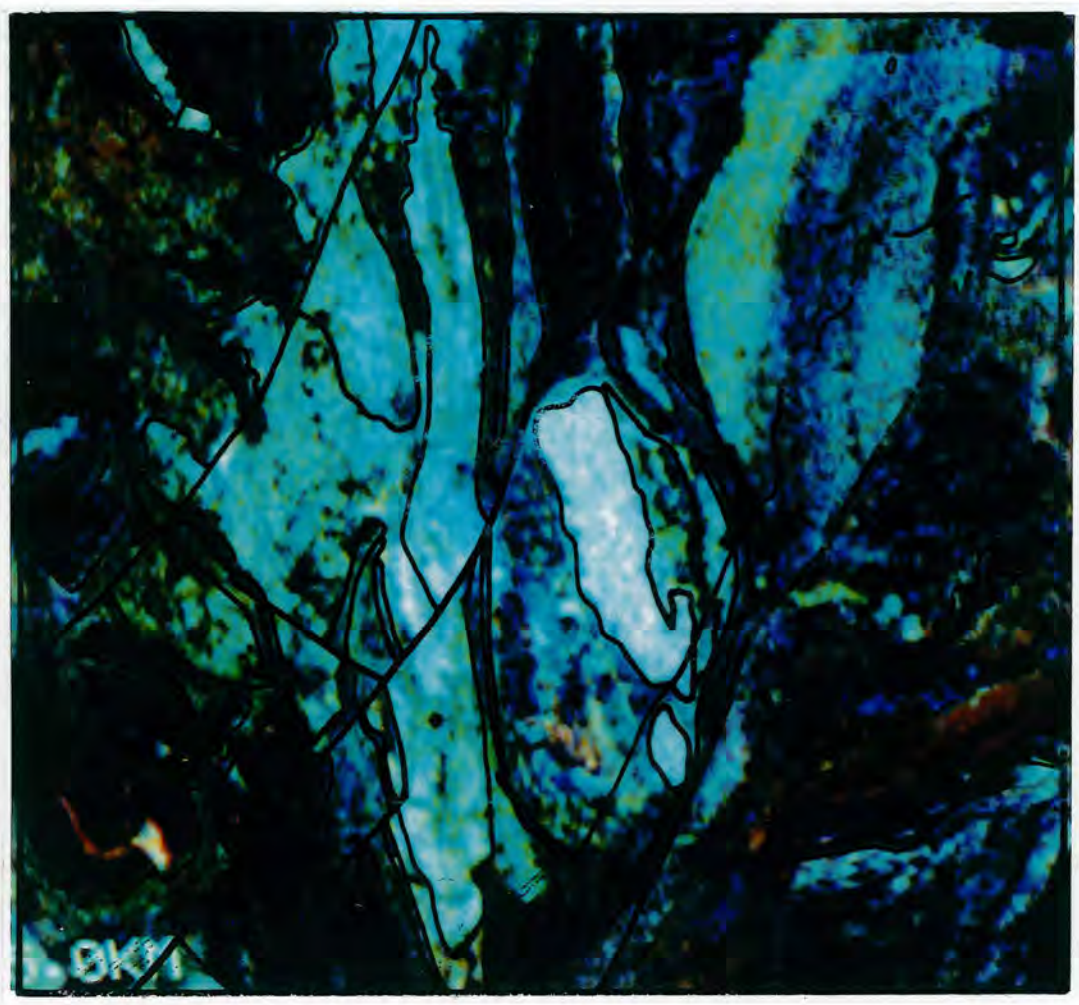

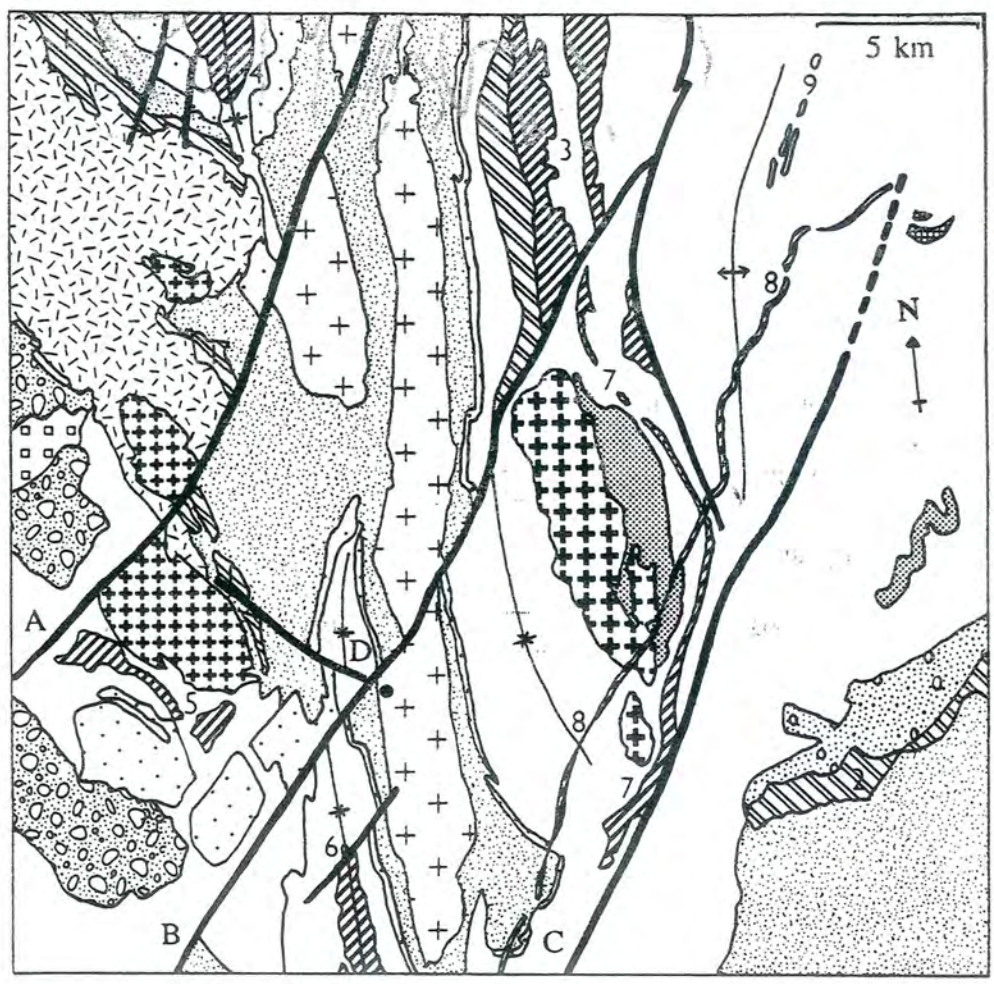

Syncline; Anticline

Dolerite

Metabasalt

Lunch Creek Gabbro

Tommy Creek Microgranite

Hardway Granite

Burstall Granite

Wonga Granite

Major Faults

White Blow Formation

Deighton Quartzite

Corella Formation

Ballara Quartzite

Mitakoodi Quartzite

Argylla Formation

Leichhardt Metamorphics

(major features only)

- Geological boundary
- Unconformity
- Anticline, showing plunge
- Syncline, showing plunge
- Overturned anticline, showing plunge
- Overturned syncline, showing plunge
- Fault, showing relative horizontal movement
- Fault, (D, U indicate relative movement down, up)

Cainozoic: soil, sand, alluvium

Dolerite dykes

TOMMY CREEK MICROGRANITE

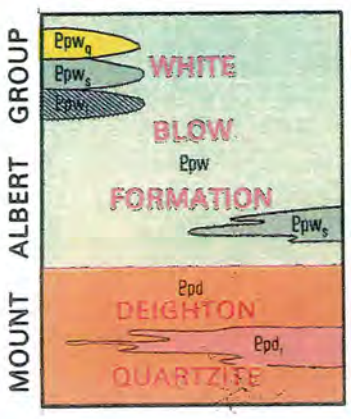

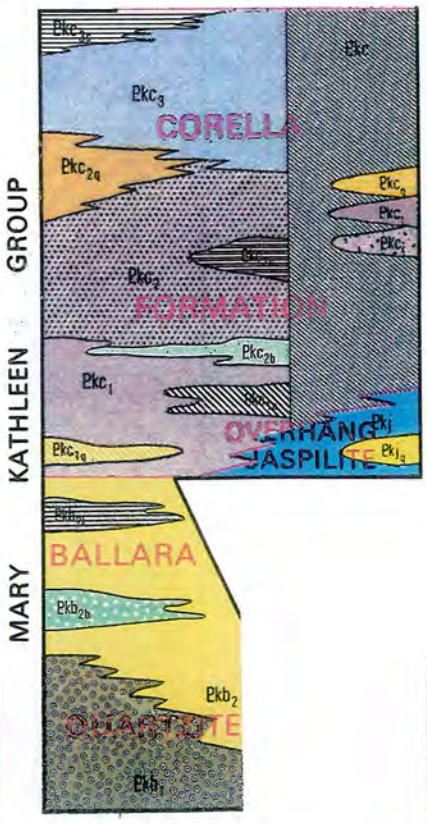

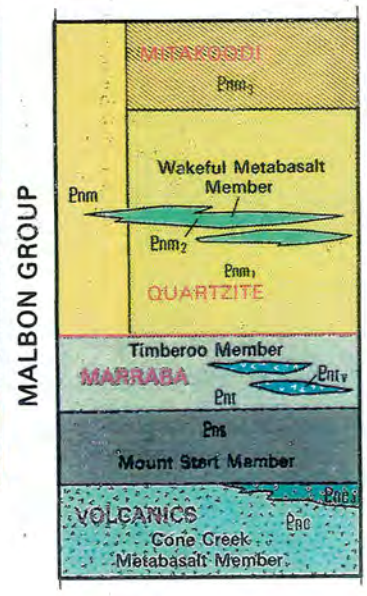

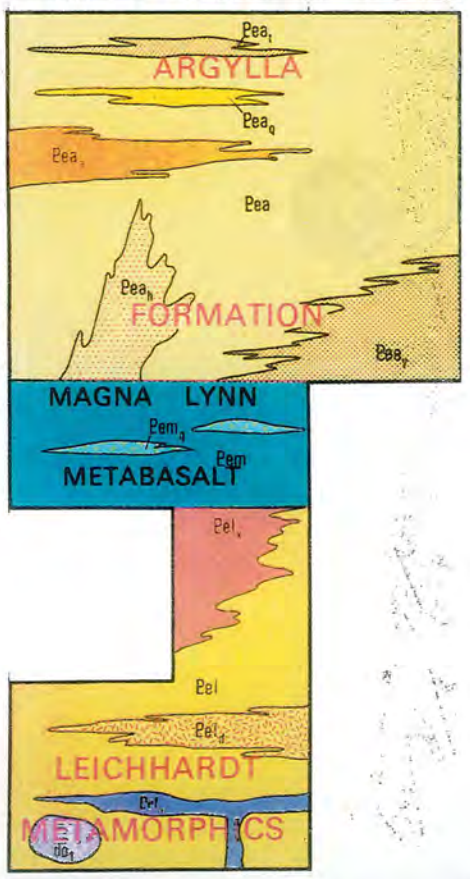

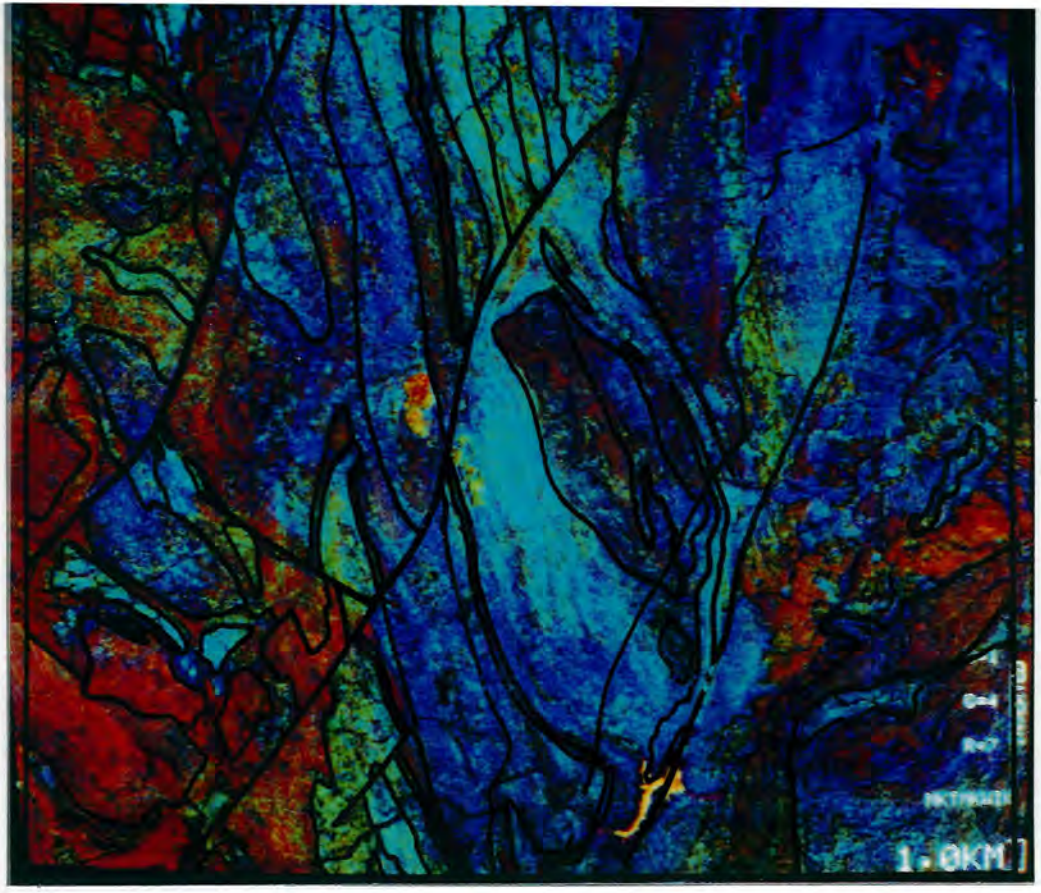

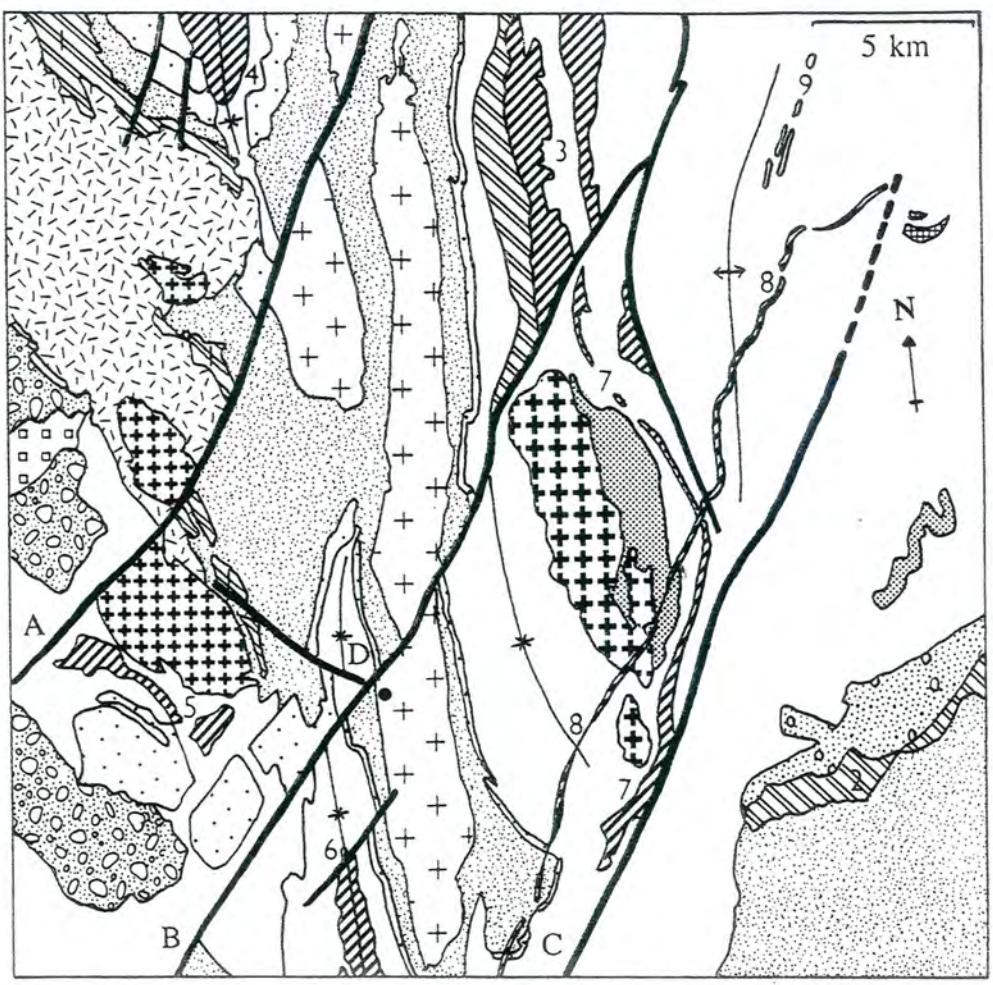

Syncline; Anticline

Dolerite

Metabasalt

Lunch Creek Gabbro

Tommy Creek Microgranite

Hardway Granite

Burstall Granite

Wonga Granite

Major Faults

White Blow Formation

Deighton Quartzite

Corella Formation

Ballara Quartzite

Mitakoodi Quartzite

Argylla Formation

Leichhardt Metamorphics